Part 2

SESSION IV - OPERATING PROBLEMS AND POTENTIAL SOLUTIONS
Chairman: H. W. Schmidt

22. WAKE VORTEX ATTENUATION FLIGHT TESTS: A STATUS REPORT 387 1/A14
Marvin R. Barber and Joseph J. Tymczyszyn

23. BASIC RESEARCH IN WAKE VORTEX ALLEVIATION USING A VARIABLE TWIST WING 409 1/C8
Dana J. Morris and G. Thomas Holbrook

24. PNEUMATIC BOOT FOR HELICOPTER ROTOR DEICING 425 1/D11
Bernard J. Blaha and Peggy L. Evanich

25. AIRCRAFT OPERATING EFFICIENCY ON THE NORTH ATLANTIC - A CHALLENGE FOR THE 1980'S 445 1/F3
Robert Steinberg

26. FIREWORTHINESS OF TRANSPORT AIRCRAFT INTERIOR SYSTEMS 453 1/F12
John A. Parker and D. A. Kourtides

27. COMBUSTION TOXICOLOGY OF EPOXY/CARBON FIBER COMPOSITES 481 2/A14
D. E. Cagliostro

28. THE USE OF ANTIMISTING KEROSENE (AMK) IN TURBOJET ENGINES 499 2/C10
Harold W. Schmidt

29. NASA/FAA GENERAL AVIATION CRASH DYNAMICS PROGRAM 511 2/D8
Robert G. Thomson, Robert J. Hayduk, and Huey D. Carden

SESSION V - FLIGHT EXPERIENCES AND GROUND OPERATIONS
Chairman: J. L. McCarty

30. CURRENT RESEARCH IN AIRCRAFT TIRE DESIGN AND PERFORMANCE 543 2/F12
John A. Tanner and John L. McCarty

31. REVIEW OF ANTISKID AND BRAKE DYNAMICS RESEARCH 555 2/G10
Sandy M. Stubbs and John A. Tanner

32. STUDIES OF SOME UNCONVENTIONAL SYSTEMS FOR SOLVING VARIOUS LANDING PROBLEMS 569 3/A12
T. J. W. Leland, J. R. McGehee, and R. C. Dreher

33. RECENT PROGRESS TOWARDS PREDICTING AIRCRAFT GROUND HANDLING PERFORMANCE 583 3/B12
Thomas J. Yager and Ellis J. White

34. THE NASA DIGITAL VGH PROGRAM - EARLY RESULTS 613 3/D14
Norman L. Crabill and Garland J. Morris

35. EVALUATION OF EMERGENCY-LOCATOR-TRANSMITTER PERFORMANCE IN REAL AND SIMULATED CRASH TESTS 625 3/E12
Huey D. Carden

36. EXTINGUISHING IN-FLIGHT ENGINE FUEL-LEAK FIRES WITH DRY CHEMICALS 655 3/G14
Robert L. Altman

SESSION VI - ACOUSTICS AND NOISE REDUCTION
Chairman: H. G. Morgan

37. RECENT DEVELOPMENTS IN AIRCRAFT ENGINE NOISE REDUCTION TECHNOLOGY 671 4/B4
James R. Stone and Charles E. Feiler

38. SOURCES, CONTROL, AND EFFECTS OF NOISE FROM AIRCRAFT PROPELLERS AND ROTORS 699 3/D4
John S. Mixson, George C. Greene, and Thomas K. Dempsey

39. NASA PROGRESS IN AIRCRAFT NOISE PREDICTION 721 4/E12
J. P. Raney, S. L. Padula, and W. E. Zorumski

40. AIRPORT NOISE IMPACT REDUCTION THROUGH OPERATIONS 759 5/A13
Richard DeLoach

ATTENDEES 779 5/C5

APR 2 1981
Item 830-H-10
NAS 1.55:2170/pt.2

NASA Conference Publication 2170
Part 2

COMPLETED
ORIGINAL

1980 Aircraft Safety and Operating Problems

Proceedings of a conference
held at NASA Langley Research Center
Hampton, Virginia
November 5-7, 1980

NASA

418

NASA Conference Publication 2170
Part 2

1980 Aircraft Safety and Operating Problems

Joseph W. Stickle, ***Compiler***
Langley Research Center
Hampton, Virginia

Proceedings of a NASA conference
held at Langley Research Center
Hampton, Virginia
November 5-7, 1980

NASA
National Aeronautics
and Space Administration

Scientific and Technical
Information Office

1981

BLANK PAGE

BLANK PAGE

PREFACE

This Conference Publication contains the proceedings of the 1980 NASA Aircraft Safety and Operating Problems Conference held at the Langley Research Center, Hampton, VA, on November 5-7, 1980. The purpose of the conference was to report results of research activities within NASA in the field of aircraft safety and operating problems. The last conference reporting on this subject was held at Langley on October 18-20, 1976.

The 1980 conference contained sessions on: Terminal-Area Operations; Avionics and Human Factors; Atmospheric Environment; Operating Problems and Potential Solutions; Flight Experiences and Ground Operations; and Acoustics and Noise Reduction. In many instances the verbal presentations summarized the work of several researchers in a particular area. The published proceedings provided for individual reporting of the research efforts. In addition, a few research activities which were not selected for presentation due to other recent exposure have been included in order to more accurately portray the scope of the Aircraft Safety and Operating Problems Program within NASA.

The size of the compilation necessitated publication in two parts (Parts 1 and 2). A list of attendees, by organizational affiliation, is included at the back of Part 2.

Use of trade names or names of manufacturers in this report does not constitute an official endorsement of such products or manufacturers, either expressed or implied, by the National Aeronautics and Space Administration.

Joseph W. Stickle
Allen R. Tobiason
Conference Cochairmen

BLANK PAGE

BLANK PAGE

CONTENTS

Part 1*

PREFACE iii

1. INTRODUCTORY REMARKS 1
Roger L. Winblade

SESSION I - TERMINAL-AREA OPERATIONS
Cochairmen: T. A. Walsh and R. L. Kurkowski

2. TEST RESULTS OF FLIGHT GUIDANCE FOR FUEL CONSERVATIVE DESCENTS IN A TIME-BASED METERED AIR TRAFFIC ENVIRONMENT 7
Charles E. Knox and Lee H. Person, Jr.

3. A PILOT'S SUBJECTIVE ANALYSIS OF A COCKPIT DISPLAY OF TRAFFIC INFORMATION (CDTI) 29
Gerald L. Keyser, Jr.

4. GUIDANCE AND CONTROL SYSTEM RESEARCH FOR IMPROVED TERMINAL AREA OPERATIONS 51
R. M. Hueschen, J. F. Creedon, W. T. Bundick, and J. C. Young

5. OPERATIONAL CONSIDERATIONS IN UTILIZATION OF MICROWAVE LANDING SYSTEM APPROACH AND LANDING GUIDANCE 83
William F. White and Leonard V. Clark

6. AUTOMATED PILOT ADVISORY SYSTEM TEST AND EVALUATION AT MANASSAS MUNICIPAL AIRPORT 113
John L. Parks, Jr.

7. A METHOD FOR DETERMINING LANDING RUNWAY LENGTH FOR A STOL AIRCRAFT 127
D. M. Watson, G. H. Hardy, J. F. Moran, and D. N. Warner, Jr.

8. FLIGHT TESTS OF IFR LANDING APPROACH SYSTEMS FOR HELICOPTERS 145
J. S. Bull, D. M. Hegarty, L. L. Peach, J. D. Phillips, D. J. Anderson, D. C. Dugan, and V. L. Ross

9. A HEAD-UP DISPLAY FORMAT FOR TRANSPORT AIRCRAFT APPROACH AND LANDING. 165
Richard S. Bray and Barry C. Scott

---

*Papers 1 to 21 are published under separate cover.

SESSION II - AVIONICS AND HUMAN FACTORS
Cochairmen: M. D. Montemerlo and A. B. Chambers

10. AN EVALUATION OF HEAD-UP DISPLAYS IN CIVIL TRANSPORT OPERATIONS 197
John K. Lauber, Richard S. Bray, and Barry C. Scott

11. GENERAL AVIATION SINGLE PILOT IFR AUTOPILOT STUDY 201
Hugh P. Bergeron

12. APPLICATION OF THE EPIDEMIOLOGICAL MODEL IN STUDYING HUMAN ERROR IN AVIATION 219
Ed S. Cheaney and Charles E. Billings

13. HOW A PILOT LOOKS AT ALTITUDE 237
Amos A. Spady, Jr., and Randall L. Harris, Sr.

SESSION III - ATMOSPHERIC ENVIRONMENT
Cochairmen: D. W. Camp and L. J. Eherenberger

14. SUMMARY OF FLIGHT TESTS OF AN AIRBORNE LIGHTNING LOCATOR SYSTEM AND COMPARISON WITH GROUND-BASED MEASUREMENTS OF PRECIPITATION AND TURBULENCE 251
Bruce D. Fisher and Norman L. Crabill

15. WALLOPS SEVERE STORMS MEASUREMENT CAPABILITY 279
Robert E. Carr and John C. Gerlach

16. THE 1979 CLEAR AIR TURBULENCE FLIGHT TEST PROGRAM 293
E. A. Weaver, L. J. Ehernberger, B. L. Gary,
R. L. Kurkowski, P. M. Kuhn, and L. P. Stearns

17. PULSED DOPPLER LIDAR FOR THE DETECTION OF TURBULENCE IN CLEAR AIR 313
E. A. Weaver, J. W. Bilbro, J. A. Dunkin, S. C. Johnson
W. D. Jones, C. E. Harris, and C. A. DiMarzio

18. FLIGHT TESTS OF A CLEAR-AIR TURBULENCE ALERTING SYSTEM 329
Richard L. Kurkowski, Peter M. Kuhn, and Lois P. Stearns

19. CLEAR AIR TURBULENCE STUDIES WITH MICROWAVE RADIOMETERS 351
Bruce L. Gary

20. IN-FLIGHT DIRECT-STRIKE LIGHTNING RESEARCH 359
Felix L. Pitts and Mitchel E. Thomas

21. MAGNITUDE AND FREQUENCY OF WIND SPEED SHEARS AND ASSOCIATED DOWNDRAFTS 373
Margaret B. Alexander and C. Warren Campbell

Part 2

SESSION IV - OPERATING PROBLEMS AND POTENTIAL SOLUTIONS
Chairman: H. W. Schmidt

22. WAKE VORTEX ATTENUATION FLIGHT TESTS: A STATUS REPORT 387
Marvin R. Barber and Joseph J. Tymczyszyn

23. BASIC RESEARCH IN WAKE VORTEX ALLEVIATION USING A VARIABLE TWIST WING 409
Dana J. Morris and G. Thomas Holbrook

24. PNEUMATIC BOOT FOR HELICOPTER ROTOR DEICING 425
Bernard J. Blaha and Peggy L. Evanich

25. AIRCRAFT OPERATING EFFICIENCY ON THE NORTH ATLANTIC - A CHALLENGE FOR THE 1980'S 445
Robert Steinberg

26. FIREWORTHINESS OF TRANSPORT AIRCRAFT INTERIOR SYSTEMS 453
John A. Parker and D. A. Kourtides

27. COMBUSTION TOXICOLOGY OF EPOXY/CARBON FIBER COMPOSITES 481
D. E. Cagliostro

28. THE USE OF ANTIMISTING KEROSENE (AMK) IN TURBOJET ENGINES 499
Harold W. Schmidt

29. NASA/FAA GENERAL AVIATION CRASH DYNAMICS PROGRAM 511
Robert G. Thomson, Robert J. Hayduk, and Huey D. Carden

SESSION V - FLIGHT EXPERIENCES AND GROUND OPERATIONS
Chairman: J. L. McCarty

30. CURRENT RESEARCH IN AIRCRAFT TIRE DESIGN AND PERFORMANCE 543
John A. Tanner and John L. McCarty

31. REVIEW OF ANTISKID AND BRAKE DYNAMICS RESEARCH 555
Sandy M. Stubbs and John A. Tanner

32. STUDIES OF SOME UNCONVENTIONAL SYSTEMS FOR SOLVING VARIOUS LANDING PROBLEMS 569
T. J. W. Leland, J. R. McGehee, and R. C. Dreher

33. RECENT PROGRESS TOWARDS PREDICTING AIRCRAFT GROUND HANDLING PERFORMANCE 583
Thomas J. Yager and Ellis J. White

34. THE NASA DIGITAL VGH PROGRAM - EARLY RESULTS 613
Norman L. Crabill and Garland J. Morris

35. EVALUATION OF EMERGENCY-LOCATOR-TRANSMITTER PERFORMANCE IN REAL AND SIMULATED CRASH TESTS 625
Huey D. Carden

36. EXTINGUISHING IN-FLIGHT ENGINE FUEL-LEAK FIRES WITH DRY CHEMICALS 655
Robert L. Altman

SESSION VI - ACOUSTICS AND NOISE REDUCTION
Chairman: H. G. Morgan

37. RECENT DEVELOPMENTS IN AIRCRAFT ENGINE NOISE REDUCTION TECHNOLOGY 671
James R. Stone and Charles E. Feiler

38. SOURCES, CONTROL, AND EFFECTS OF NOISE FROM AIRCRAFT PROPELLERS AND ROTORS 699
John S. Mixson, George C. Greene, and Thomas K. Dempsey

39. NASA PROGRESS IN AIRCRAFT NOISE PREDICTION 721
J. P. Raney, S. L. Padula, and W. E. Zorumski

40. AIRPORT NOISE IMPACT REDUCTION THROUGH OPERATIONS 759
Richard DeLoach

ATTENDEES 779

SESSION IV - OPERATING PROBLEMS AND POTENTIAL SOLUTIONS

BLANK PAGE

BLANK PAGE

WAKE VORTEX ATTENUATION FLIGHT TESTS: A STATUS REPORT

Marvin R. Barber
NASA Dryden Flight Research Center

Joseph J. Tymczyszyn
FAA Western Region

SUMMARY

Flight tests have been conducted to evaluate the magnitude of aerodynamic attenuation of the wake vortices of large transport aircraft that can be achieved through the use of static spoiler deflection and lateral control oscillation. These methods of attenuation were tested on Boeing B-747 and Lockheed L-1011 commercial transport aircraft. Evaluations were made using probe aircraft, photographic and visual observations, and ground-based measurements of the vortex velocity profiles.

The magnitude of attenuation resulting from static spoiler deflection was evaluated both in and out of ground effect. A remotely piloted QF-86 drone aircraft was used to probe the attenuated vortices in flight in and out of ground effect, and to make landings behind an attenuated B-747 airplane at reduced separation distances.

INTRODUCTION

The National Aeronautics and Space Administration has conducted extensive research and testing to determine the feasibility of aerodynamically attenuating the wake vortices of large transport aircraft. This program has been underway since 1974, and it has resulted in numerous flight and ground facility tests. Much of the early work conducted under this program was reported in the Wake Vortex Minimization Symposium held in 1976 (ref. 1). This paper reviews all of the flight work that has been conducted during the program, with an emphasis on the results of the work done after the symposium.

Table I summarizes the flight experiments that were reported at the 1976 symposium. All of the methods shown in the table were successful in attenuating the vortices to some degree. However, each method had some attendant characteristic that resulted in its not being practical for actual airline usage. The means of attenuation for all of these tests were defined in various ground facilities that were developed to support the minimization research. The capabilities of the ground facilities are reported extensively in reference 1, and are not mentioned here except in passing.

Two series of flight tests have been conducted since the Wake Vortex Minimization Symposium (table II). The objectives of these tests can be categorized as follows:

(1) An evaluation of the effectiveness of altered spoiler deflections on the L-1011 aircraft to attenuate wake vortices.

(2) An evaluation of the effectiveness of altered spoiler deflections on the B-747 aircraft to attenuate wake vortices. These tests included an evaluation of ground effects, which involved flying a remotely controlled drone into the spoiler-attenuated vortices at low altitudes. The tests also included landings behind an attenuated B-747 aircraft at reduced separation distances.

(3) An evaluation of the attenuation that resulted from the excitation of dynamic vortex instabilities. This series of tests used the L-1011 airplane as the vortex-generating aircraft. However, the tests were inspired by the results of the tests conducted with the B-747 airplane in the first series of tests, which showed that significant attenuation resulted from oscillating the spoilers and ailerons.

As shown by the number of test flights made with altered spoiler deflections, an emphasis was placed on that concept for vortex attenuation. This concept was emphasized because spoiler deflection alterations would probably be easier to incorporate in an existing fleet of aircraft than any of the other concepts. In addition, the number of possible combinations of altered spoiler deflections results in a rather large test matrix.

SYMBOLS

AGL	above ground level
b	wingspan, m
C_L	lift coefficient
C_l	rolling-moment coefficient
DME	separation distance, n. mi.
I_x	rolling moment of inertia, kg-m^2
p	roll rate, deg/sec
$\dot{p}$	roll acceleration, deg/sec^2
p_{s_b}	boom-mounted static pressure, N/m^2
q	dynamic pressure, N/m^2
S	wing area, m^2

V_t	true airspeed, m/sec
δ_a	aileron position, deg
φ	bank angle, deg

Subscripts:

max	maximum
tw	trailing wing
v	vortex

FLIGHT TEST METHODS

Figure 1 shows the L-1011 vortex-generating test aircraft equipped with the smoke generators that are used to mark the vortices so that a probe aircraft can fly into them. Four smoke generators are installed on each wing of the test aircraft. Each smoke generator marks one of the points of aerodynamic discontinuity on the wing (the wingtip, the outboard edge of the outboard flap, the outboard edge of the inboard flap, and the wing root). Smoke-marked vortices are shown in figure 2. A depiction of a light aircraft probing the vortices is presented in figure 3; as indicated by the figure, this study is concerned primarily with the probe aircraft's roll response.

During the tests, vortices were probed at distances as great as 12 nautical miles and as small as 2 nautical miles. The objective of the vortex attenuation effort, however, was to make it possible for light aircraft to fly as close as 3 nautical miles behind aircraft classed as heavy on landing approach, in contrast to the present requirement for a separation distance of 6, 5, 4, or 3 nautical miles, depending on the class of the following aircraft. Therefore, the major effort of this program has been concentrated on the 3-nautical-mile separation distance, as depicted in figure 3. The distance between the two airplanes was measured with an onboard distance-measuring radio and recorded in the probe airplane.

The probe airplanes were equipped with response-measuring instrumentation that enabled real time calculations to be made of the rolling moment induced on the probe airplane by the vortex. Figure 4 shows time histories of the variables that are used to compute the vortex-induced rolling-moment coefficient, which is calculated as follows:

$$C_{l_v} = \frac{\dot{p}I_x}{qSb} = \left(C_{l_{\delta_a}}\delta_a + C_{l_p}\frac{pb}{2V_t}\right)$$

Roll acceleration, $\dot{p}$, is obtained by differentiating the roll rate measurement. A calculation of the vortex-induced rolling-moment coefficient is desirable because it is difficult to evaluate the severity of a vortex encounter in terms of bank angle, roll rate, or roll acceleration. The difficulty arises from the fact that the pilot of the probe aircraft must constantly maneuver the airplane to attempt to stay in the vortex wake. The calculation of the rolling-moment coefficient enables the masking effects of the ailerons and of roll damping to be subtracted from the airplane's total response, leaving a direct measurement of the airplane's response to the vortex. Reference 2 describes the derivation of the vortex-induced rolling-moment coefficient and discusses its use as a measure of aircraft response to a vortex encounter.

In addition to using a probe airplane to determine the upset potential of attenuated and unattenuated vortices, measurements of the vortex velocities were made by using a laser-Doppler velocimeter (LDV) and a monostatic acoustic sensing system (MAVSS). These devices, which are described in detail in reference 3, belonged to the Department of Transportation's Transportation Systems Center (TSC). Their use in the wake vortex minimization program reflected the desire on the part of both agencies to minimize the difficulties that result from the wake vortices of large aircraft. Figure 5 shows the LDV in use during one of the flight tests.

The general approach for the most recent flight tests, which were made with the L-1011 airplane, was to evaluate the effectiveness of the vortex attenuation of each static or dynamic configuration visually and photographically and to explore only the most promising configurations with in-flight probes and measurement with the LDV and MAVSS.

RESULTS AND DISCUSSION

Selected Static Spoiler Deflection

Figure 6 presents the vortex-induced rolling-moment coefficients on a T-37B probe aircraft that resulted from a conventionally configured B-747 aircraft, and from the same aircraft using the best spoiler attenuation configuration that was defined at the time of the Wake Vortex Minimization Symposium. The figure shows that the spoilers did attenuate the vortices, but that the vortices were still significantly more powerful than T-37B roll control capability. To see whether vortex attenuation resulted when selected spoilers were deflected on other heavy transports, wind tunnel and tow tank facility tests were made on L-1011 and DC-10 models (refs. 4 and 5, respectively). The results of these tests were encouraging and led to subsequent flight tests with an L-1011 airplane, which yielded the results shown in figure 7. The spoilers again provided attenuation, but not to a level that the T-37B controls could overpower. An interesting finding of this test series was that the deflection of three spoiler panels provided more attenuation than the two spoilers that were deflected on the B-747 airplane. This prompted additional wind tunnel tests with a B-747 model to determine the magnitude of attenuation that the deflection of three spoiler panels would produce on that airplane (ref. 6). The results of those wind tunnel tests are presented in figure 8. The figure shows that more attenuation would be achieved. Another surprising result was that a spoiler deflection on the three panels of 15° yielded more attenuation than a larger deflection. Since deflecting the spoilers induces buffet and performance penalties on the airplane, the greater attenuation with less deflection was particularly attractive.

Because the wind tunnel tests were so promising, flight tests were initiated to evaluate the effectiveness of deflecting the three spoiler panels on the B-747 airplane. The results of those tests are presented in figure 9. The three spoiler panels did yield more attenuation than the two panels previously tested. However, unlike the wind tunnel prediction, 15° of spoiler deflection yielded less attenuation than the 30° deflection.

The attenuation achieved by deflecting the three B-747 spoiler panels was greater than any that had been achieved by using spoilers on either the B-747 or L-1011 aircraft. Figures 10(a) and 10(b) present time histories of T-37B roll response to typical vortex encounters resulting from the conventional B-747 landing configuration and the B-747 configuration with three spoilers deflected. The conventionally configured B-747 (fig. 10(a)) caused several bank angle excursions that exceeded 90° and one upset that completely inverted the T-37B airplane. The static pressure measurement in the time history comes from a nose-boom-mounted static pressure orifice. The static pressure transducer is sensitive and has a washout to compensate for altitude changes and a pilot reset to null it. Its function is to identify the sharp drops in pressure that occur when the airplane encounters a vortex core. The time history for the spoiler-attenuated vortex encounter (fig. 10(b)) shows much smaller roll and bank angle responses, and the variations in the nose boom static pressure are much smaller. The figure shows that the pilot is able to keep the airplane's bank angle variation within approximately 30°, with one excursion as great as 60°. The time history also shows that the roll and bank angle excursions have a slower onset rate, which is very important to an unsuspecting pilot. The slowing of the excursions would be expected from the data presented in figure 9, since that figure shows that the upset potential of the vortex is only slightly greater than the roll control power of the airplane.

Low Altitude Tests

The upsets resulting from the vortices of the attenuated configuration were small enough and slow enough so the pilots felt they could cope with vortex encounters at separation distances of 3 nautical miles at altitudes as low as 70 meters. This permitted the evaluation of a previously untested hypothesis: that if the ground effects provided some additional vortex attenuation, landings might be possible at the desired 3-nautical-mile separation distance. Therefore, an effort was made to evaluate the vortices in and out of ground effect, with a remotely controlled QF-86 drone used as a probe.

Before low altitude probes were made in flight, a piloted simulation was developed to help determine the problems associated with vortex encounters at low altitude. The simulation utilized the vortex velocities measured by the LDV during the previous flight tests. Unfortunately, the LDV has not yet been refined to the point where it can measure attenuated vortices in ground effect. Therefore, the simulation did not contribute to an understanding of the effects of ground effect on attenuated vortices, although it indicated that ground effect did reduce the severity of unattenuated vortices.

The results of flying the remotely controlled aircraft probe at low altitudes 3 nautical miles behind the attenuated B-747 configuration are presented in figure 11. The data show that bank angle excursions as large as 60° were produced at altitudes as low as 20 meters, well within the ground effect of the B-747 airplane. The remotely controlled probe aircraft was also landed seven times 4 nautical miles behind the attenuated B-747 configuration. The pilot was able to maintain maximum exposure to the visible wake vortex during the entire approach until it became necessary to concentrate on lining up with the runway for the landing itself. Slight wind variations made it difficult to place the vortex trail precisely over the center of the runway, so it could not be positively determined that the drone was in the vortex wake during the most critical portion of the landing approach and flare.

Oscillating Spoiler and Aileron Tests

During the remotely controlled aircraft probe tests, a test was run to evaluate the effects on the vortices of oscillating the lateral controls of the B-747 in the attenuated configuration. It was theorized that the interplay of the ailerons and the spoilers during such oscillation and the resulting changes in lift distribution might produce hard spots in the wake. Therefore, a test was made wherein the B-747 pilot was asked to oscillate the lateral control wheel at a frequency of about 6 seconds per cycle. The resulting wake was probed by the T-37B airplane to see if hard spots did in fact result. Unexpectedly, however, the T-37B pilot reported that the wake was completely devoid of coherent rotary motion at the 3-nautical-mile separation distance. Because of this result, additional tests were conducted, first to verify the finding, and then to try to determine whether the attenuation was due to spoiler and aileron control motion or if B-747 wing rocking was causing the effect. Table III lists the tests conducted and gives a qualitative assessment of the results.

For the first tests shown in table III, the spoilers and ailerons were oscillated simultaneously through the pilot's roll control wheel. For these oscillations, spoilers 2, 3, and 4 were preset in the 30° position used in the attenuated configuration and then allowed to oscillate with the roll control inputs. This caused the three spoilers on the rising wing to retract and the affected spoilers on the falling wing to become further extended. A test was then made with aileron deflection only, that is, the ailerons oscillated with the pilot's roll control wheel and the spoilers were locked in the retracted position. For all of the above tests, the pilot oscillated the roll control wheel nearly its full deflection at the 6 second per cycle frequency, and the resulting bank angle oscillations were approximately ±7°. The spoiler-alone oscillation shown in table III was performed by having the pilot modulate the speed brake lever between 15° and 30°. The speed brakes were modulated symmetrically, so no aircraft roll motion resulted from their deflection.

Figure 12 presents a time history of T-37B response to a wake produced with both the spoilers and ailerons oscillating. The figure shows bank angle variations so small that it is difficult to tell whether they are the result of wake encounters or the result of pilot attempts to encounter the wake. There are none of the large variations in static pressure that indicate that high velocity, low pressure vortex cores are present. The maximum rolling-moment coefficient for this run is approximately 0.045, and only one deviation of this magnitude occurs during the run. The deviation may be the result of B-747 pilot inputs that were somewhat out of phase with the oscillation inputs, so that there was a single hard spot in the wake. A comparison of figure 12 with figures 10(a) and 10(b) shows that in general the wake attenuated by oscillating the ailerons and spoilers causes much less roll and bank angle response than the wake produced by either of the other two configurations. In fact, the probe airplane pilots commented that oscillating the ailerons and spoilers produced a wake that was somewhat comparable to light or light-to-moderate atmospheric turbulence.

A summary of the maximum rolling-moment coefficients for the five oscillating aileron and spoiler runs is presented in figure 13. The induced rolling-moment coefficients fall mostly within the roll control power of the T-37B. Since the pilot's ability to control the airplane becomes marginal when the rolling-moment coefficients approximate the roll control power of the probe airplane, few uncontrollable bank angle excursions occurred at these values, allowing the probe pilot to report the nearly total conversion of rotary motion to random turbulence. The time histories that generated the data in figure 13 show only one or two large values of C_{l_v} during a run. Again, the larger deviations may be indicative of pilot inputs that were out of phase with the B-747 oscillations.

The attenuation achieved by oscillating the ailerons and spoilers of the B-747 is technically exciting, in that it demonstrates once again that essentially total wake vortex attenuation can be achieved as close as 2.5 nautical miles behind a large transport aircraft in the landing configuration. (Total wake vortex attenuation was first achieved at a separation distance of 2.5 nautical miles by altering the deflection of the inboard and outboard flaps (ref. 1), as shown in table I. However, the attenuation occurred only when the landing gear was not extended, thus making it impractical for operational use.) Obviously, oscillating the ailerons and spoilers and the resulting airplane roll is not practical for airline transports on final approach. However, the desire to understand the mechanism of the attenuation prompted further testing.

The first of these tests is being conducted in the Langley vortex flow facility with a B-747 model that has control surfaces capable of being oscillated. (The wing is kept level, however.) If the model tests reproduce the attenuation experienced in flight successfully, they will make it possible to refine the technique and minimize the objectionable airplane response.

Oscillating control tests were also conducted with the L-1011 aircraft to see whether the vortex attenuation could be duplicated with another aircraft configuration. The L-1011 was particularly attractive for this test because it incorporates a direct lift control (DLC) system and an active aileron control system (AACS), which assured flexibility for oscillating the control surfaces. The capabilities of the two systems are described in tables IV and V, respectively. The AACS provides gust load alleviation.

The L-1011 tests were completed in the summer of 1980. Table VI summarizes the results of those tests. The table identifies the concepts that were tested, the configurations used to test the concepts, and the results. Perhaps the most significant result was that the L-1011 could not reproduce the B-747 vortex attenuation that resulted from oscillating the ailerons and spoilers. The inability to reproduce the attenuation may be due to the L-1011 control system, which did not permit the exact duplication of the B-747 maneuver. The L-1011 spoilers 2, 3, and 4 can be extended but not retracted from a preset position as a result of a pilot roll control input, whereas the B-747 spoilers did both. Therefore, to simulate the B-747 maneuver, the copilot had to retract the spoilers from the preset position by using the speed brake control handle while the pilot was making roll control inputs. Further, the speed brake handle activates spoiler panel 5 in addition to three other spoiler panels. These differences, though subtle, may underlie the inability of the L-1011 to reproduce the extremely favorable attenuation achieved by the B-747.

Perhaps the most interesting result of the recent L-1011 flight tests was that oscillating the spoilers alone permitted the Crow instability (ref. 7) to be manipulated. It could also be manipulated by oscillating the ailerons and spoilers in combination, whether asymmetrically or symmetrically. Even though the Crow instability could be manipulated, however, the total time necessary for the vortices to decay did not seem to decrease until the control oscillation rate was high. The 2.3 second per cycle symmetrical oscillation of the ailerons and spoilers did cause the vortices to decay significantly more rapidly than the vortices generated during the 9.2 or 4.6 second per cycle oscillations. However, both visual observation and probing flights (fig. 14) indicated that the configuration still had an unacceptable upset potential. Nevertheless, high frequency control oscillation may have potential for purposes of wake vortex attenuation.

CONCLUDING REMARKS

Flight tests have shown that the wake vortices of large transport aircraft can be attenuated by several methods, including altered span loading, turbulence ingestion, altered span loadings and turbulence ingestion in combination, and by the excitation of dynamic vortex instabilities. Only two of the methods have resulted in the nearly total attenuation of vortices at the 3-nautical-mile separation distance desired for air traffic operation in terminal areas. They are altered span loading and the excitation of dynamic instabilities. Both of these methods are impractical for operational use, however. The reason for the attenuation that results from altered span loading is already understood, but further testing will be necessary to understand the reason for the attenuation that results from oscillating the lateral controls. An understanding of the mechanism might allow refinements of the method that would make it more attractive in airline applications.

REFERENCES

1. Wake Vortex Minimization. NASA SP-409, 1977.

2. Smith, Harriet J.: A Flight Test Investigation of the Rolling Moments Induced on a T-37B Airplane in the Wake of a B-747 Airplane. NASA TM X-56031, 1975.

3. Burnham, D. C.; Hallock, J. N.; Tombach, I. H.; Brashears, M. R.; and Barber, M. R.: Ground-Based Measurements of the Wake Vortex Characteristics of a B-747 Aircraft in Various Configurations. FAA-RD-78-146, Fed. Aviation Admin., Dec. 1978.

4. Croom, Delwin R.; Vogler, Raymond D.; and Williams, Geoffrey M.: Low-Speed Wind-Tunnel Investigation of Flight Spoilers as Trailing-Vortex-Alleviation Devices on a Medium-Range Wide-Body Tri-Jet Airplane Model. NASA TN D-8360, 1976.

5. Croom, Delwin R.; Vogler, Raymond D.; and Thelander, John A.: Low-Speed Wind-Tunnel Investigation of Flight Spoilers as Trailing-Vortex-Alleviation Devices on an Extended-Range Wide-Body Tri-Jet Airplane Model. NASA TN D-8373, 1976.

6. Croom, Delwin R.: Low-Speed Wind-Tunnel Parametric Investigation of Flight Spoilers as Trailing-Vortex-Alleviation Devices on a Transport Aircraft Model. NASA TP-1419, 1979.

7. Crow, S. C.; and Bate, E. R, Jr.: Lifespan of Trailing Vortices in a Turbulent Atmosphere. AIAA J. Aircraft, vol. 13, no. 7, July 1976, pp. 476-482.

TABLE I.—VORTEX ATTENUATION FLIGHT EXPERIMENTS CONDUCTED TO 1976

Method of attenuation	Means of attenuation	Vortex-generating aircraft	Vortex-probing aircraft	Number of test flights	Time period for test flights
Altered span loading	Altered inboard/ outboard flap deflections	B-747	Learjet-23 (LR-23) Cessna T-37B	≈17	1974
Turbulence ingestion	Splines	C-54G	Piper Cherokee (PA-28)	≈20	1973
Mass and turbulence ingestion	Altered inboard/ outboard engine thrust levels	B-747	LR-23 T-37B	≈2	1974/1975
Altered span loading and turbulence ingestion	Wingtip-mounted spoiler	CV-990	LR-23	≈2	1969
	Altered spoiler deflections	B-747	LR-23 T-37B **McDonnell Douglas DC-9**	≈15	1975/1976

TABLE II.—VORTEX ATTENUATION FLIGHT EXPERIMENTS CONDUCTED FROM 1976 to 1980

Method of attenuation	Means of attenuation	Vortex-generating aircraft	Vortex-probing aircraft	Number of test flights	Time period for test flights
Altered span loading and turbulence ingestion	Altered spoiler deflection	B-747, L-1011	T-37B, QF-86	45	1976 to 1980
Excitation of dynamic instabilities	Oscillating spoilers and ailerons	B-747, L-1011	T-37B	9	1979 to 1980

TABLE III.—VORTEX ATTENUATION WITH FIXED AND OSCILLATING B-747 CONTROLS

Control oscillated	Number of tests	Results
Spoilers 2, 3, and 4 (0° to 45°) and ailerons	5	Wake devoid of coherent rotary flow at 3 nautical miles
Aileron oscillation only (spoilers locked in retracted position)	1	Wake similar to unattenuated wake
Spoiler oscillation only (spoilers 2, 3, and 4 modulated symmetrically 15° to 30° at 6 sec/cycle)	1	Wake similar to statically attenuated spoiler wakes

TABLE IV.—L-1011 SPEED BRAKE AND DIRECT LIFT CONTROL SYSTEM
[Six spoiler panels per wing]

Normal operation:

In cruise configuration (flaps up), spoilers 1 to 6 can be used manually as speed brakes. Maximum deployment is 60°.

In approach configuration (flaps down)—

Spoilers 2 to 6 can be deployed for roll assistance. Deflection is proportional to inboard aileron position. Maximum overall spoiler deflection is 40°.
With direct lift control system operating, spoilers 1 to 4 modulate ±8° about 8° null. Modulation is proportional to pitch control column motion about its trim position.

Test aircraft capabilities:

If flaps are down, spoilers 1 to 6 can be operated manually or through DLC system, but this defeats roll assist.
Spoilers can be activated in symmetrical left/right pair combinations.

TABLE V.—L-1011 ACTIVE AILERON CONTROL SYSTEM

Normal operation:

Outboard ailerons modulate symmetrically about a null bias that is proportional to a combination of wingtip and body vertical accelerations

Null bias position is variable—

In cruise configuration (flaps up), null is at 2° down aileron
In approach configuration (flaps down), null is at 8° up aileron

Authority (command limits)—

Production aircraft: 21.1° trailing edge up, 17.4° trailing edge down
Test aircraft: 12° trailing edge up, 12° trailing edge down

Test aircraft capabilities:

Null bias is variable according to outboard aileron position
Outboard ailerons can be oscillated symmetrically by using a separate function generator
Computation command path can be open or closed loop

TABLE VI.—L-1011 1980 TEST CONFIGURATIONS AND RESULTS

Concept being evaluated	Configuration	Test results
Baseline	Normal landing configuration: gear down, flaps deflected 33°, no DLC, no AACS	------------------------------
Baseline with AACS and DLC	AACS and DLC	No significant improvement over baseline configuration
Effect of selected spoiler deflection on vortex wake	Spoilers 2, 3, and 4 deflected 45°	Same as previous test (table II)
Effect of aileron and selected spoiler oscillation on vortex wake	Ailerons and spoilers 2, 3, 4, and 5 oscillated Ailerons and spoilers 2 and 5 oscillated Ailerons oscillated alone	Could not reproduce B-747 result
Effect of static outboard aileron and spoiler deflection on wingtip vortices	Ailerons up 5°, 7½°, 10° and 15° Ailerons down 5°, 7½°, 10°, and 15° Spoilers 2, 3, and 4 deflected 30° for all tests	Up ailerons diffused tip wake Down ailerons augmented tip wake Small down aileron deflection shows a slight attenuating effect
Effect of spoiler modulation on vortices	Spoilers modulated through selected ranges: 0° to 10°, 0° to 15°, 20° to 35°, 15° to 45°, and 0° to 45° Frequencies tested were 9.2 and 4.6 sec/cycle	Excites and changes period of Crow instability
Vortex attenuation through inciting instability by pulsing spanwise center of lift	Oscillate ailerons and spoilers 2, 3, and 4 at 9.2, 4.6, and 2.3 sec/cycle asymmetrically and symmetrically	2.3 sec/cycle produced greatest L-1011 vortex attenuation to date. Pulsing excites and changes period of Crow instability
Incite instability through spanwise center of lift pulsing	Oscillate spoilers 1 and 6 asymmetrically and symmetrically, with or without ailerons	Potential for altering vortex characteristics on one side of airplane for comparative and vortex merging studies

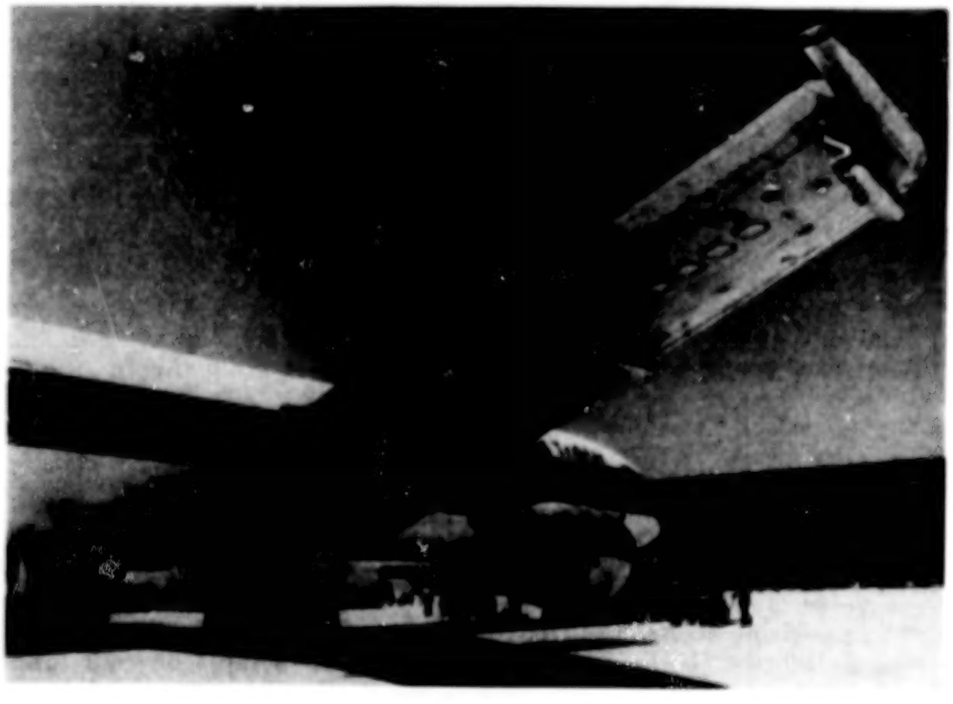

Figure 1. L-1011 vortex-generating test aircraft with vortex-marking smoke generators installed.

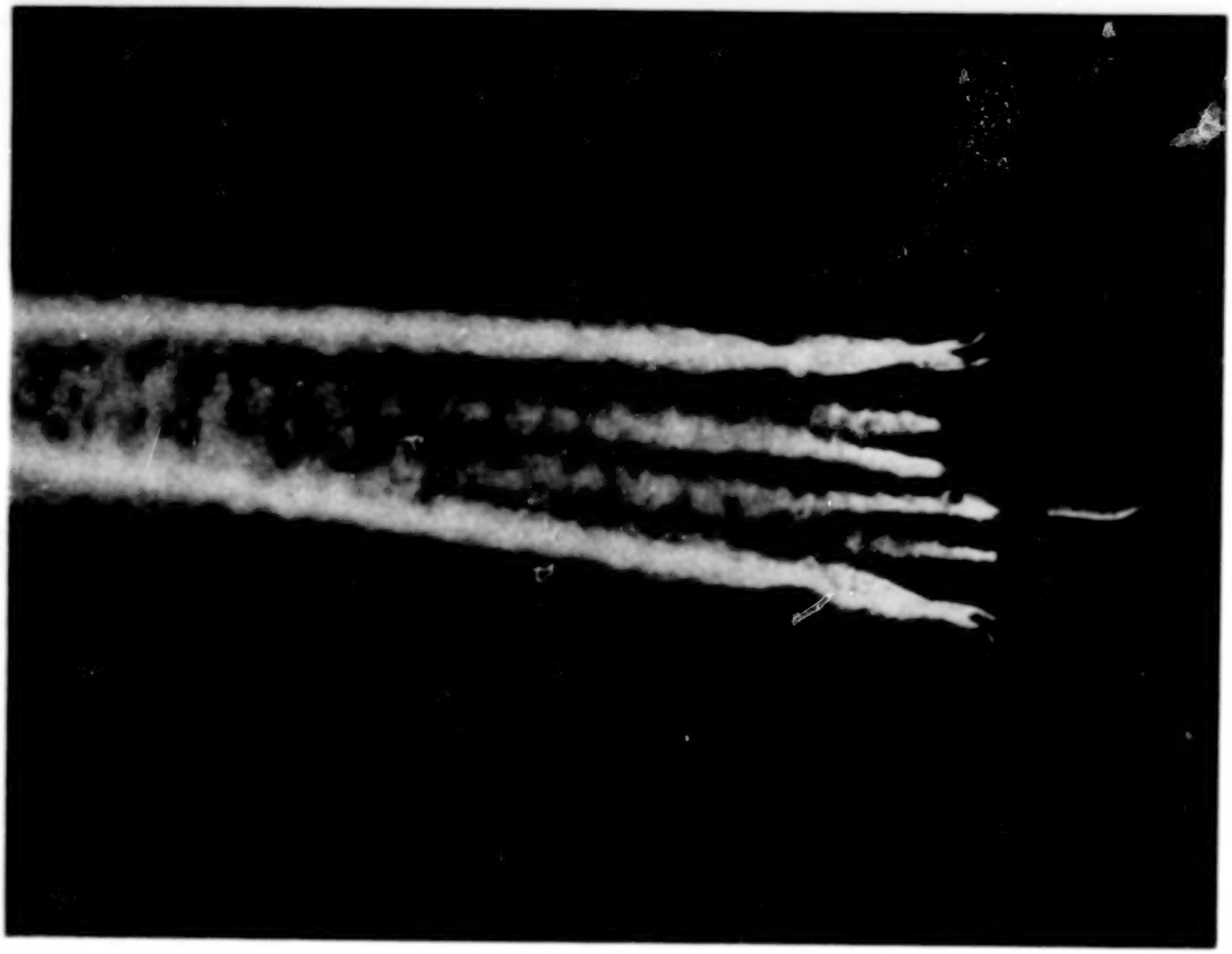

Figure 2. Smoke-marked vortices.

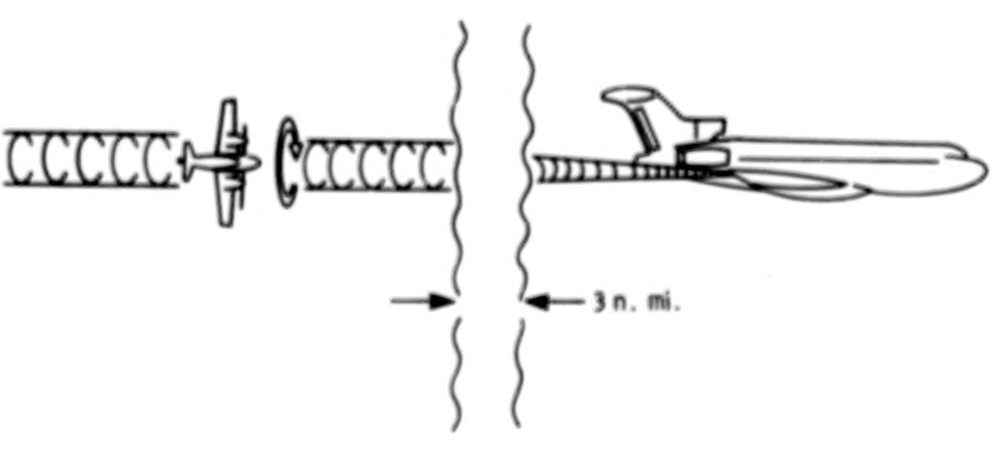

Figure 3. Light aircraft probes.

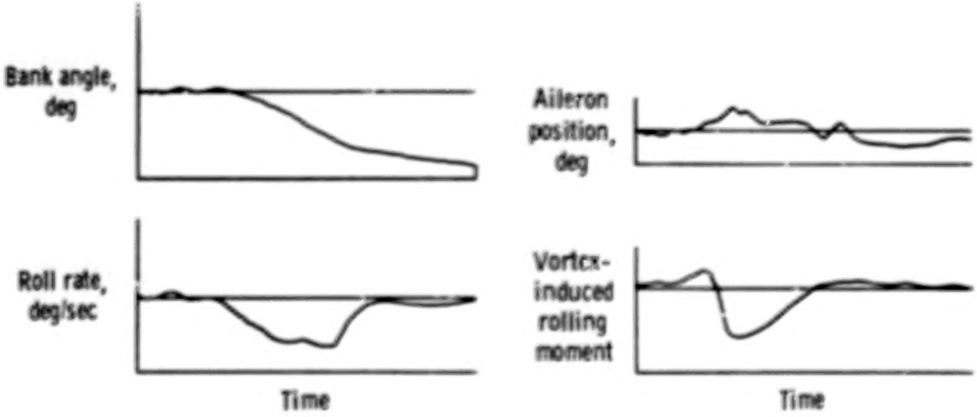

Figure 4. Real time wake vortex data reduction.

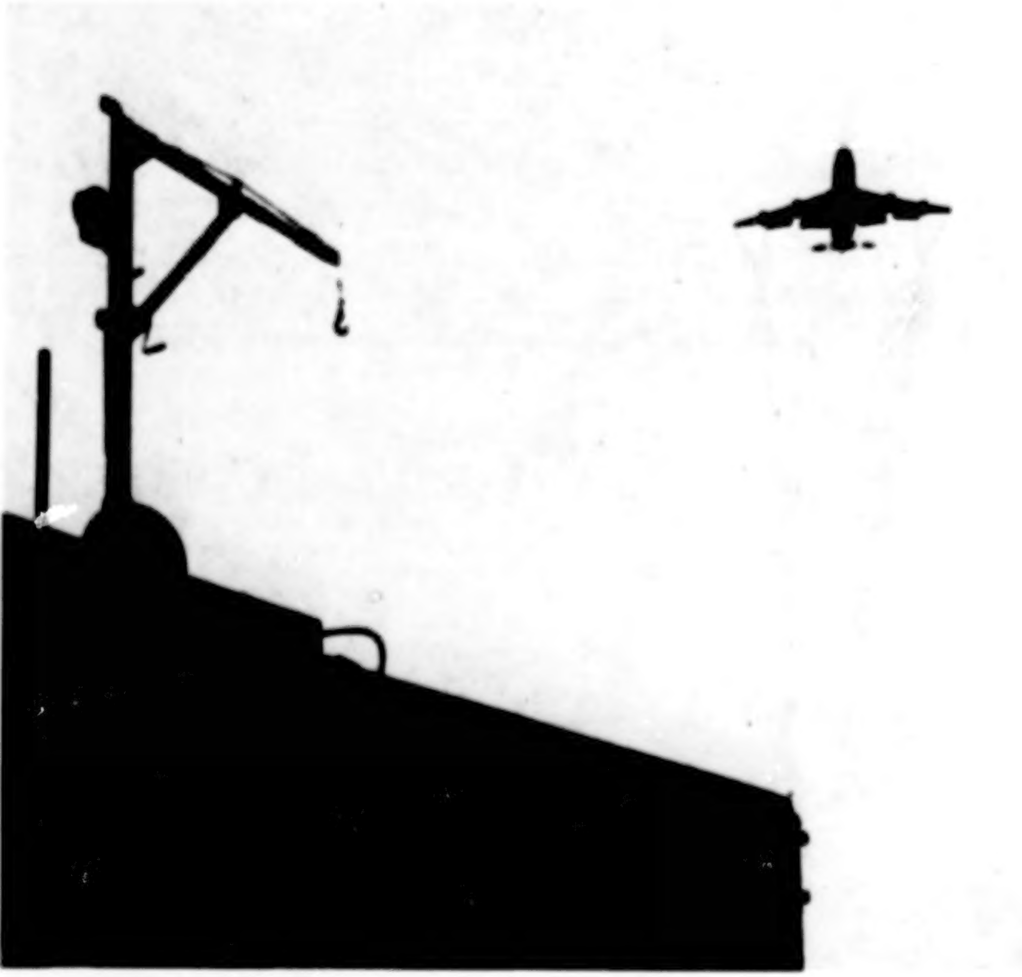

Figure 5. LDV system monitoring wake vortices generated by a B-747 aircraft at Rosamond Dry Lake.

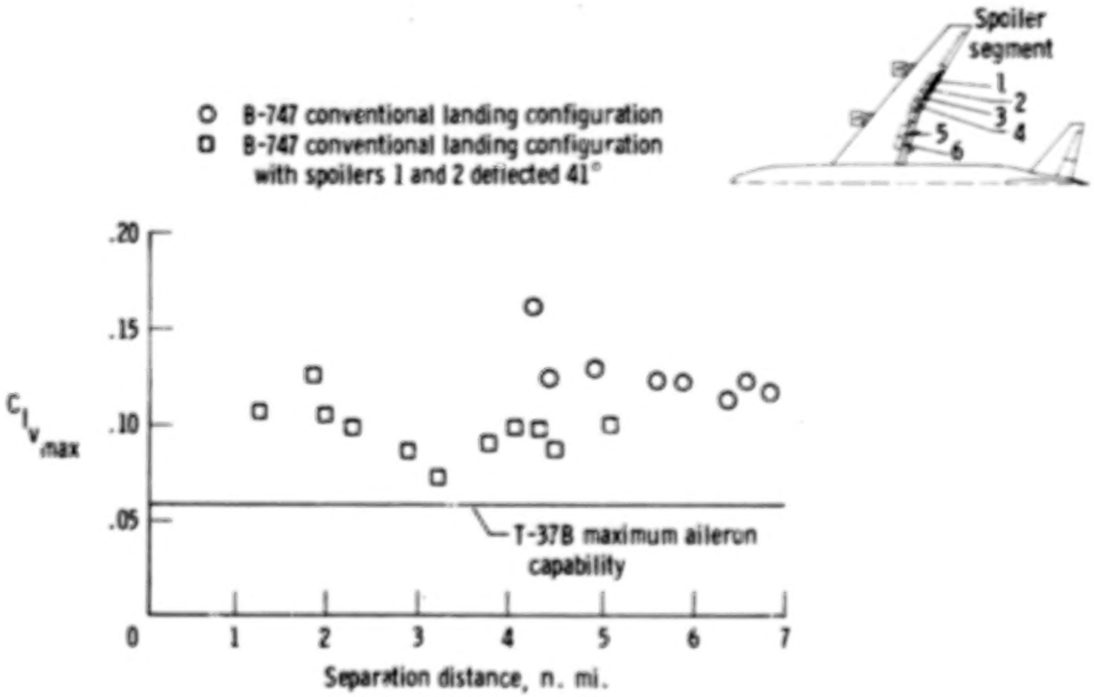

Figure 6. B-747 wake vortex upset potential for a T-37B probe airplane.

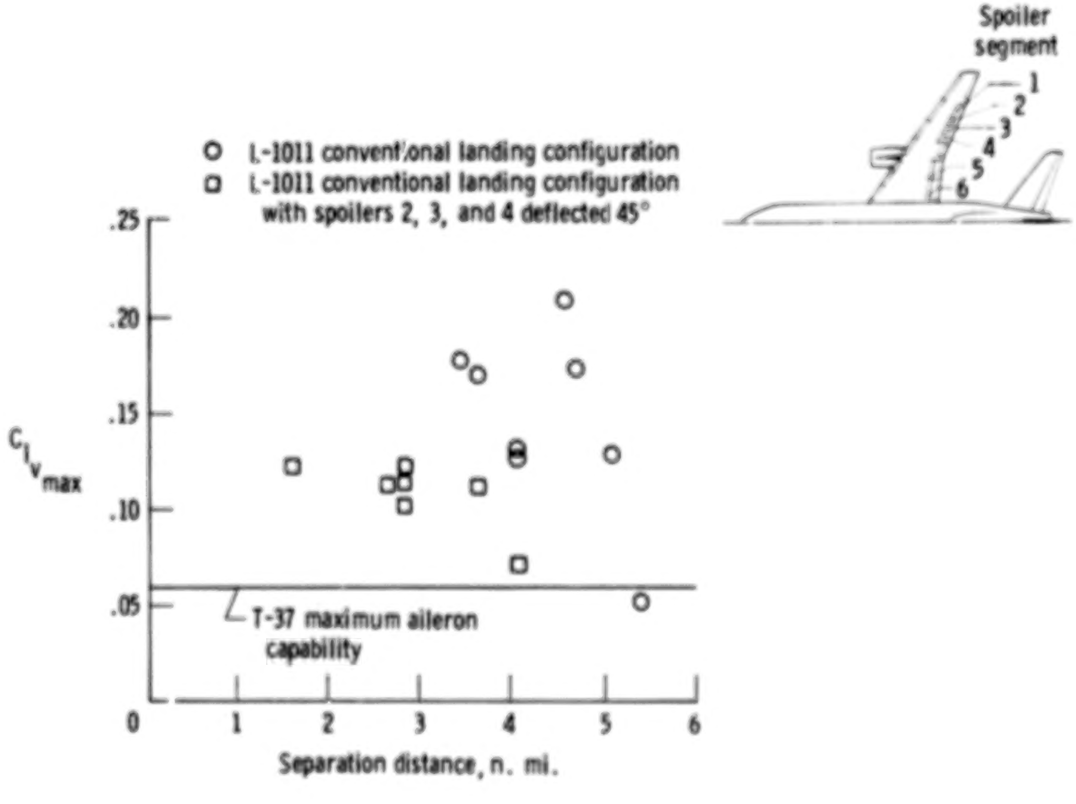

Figure 7. L-1011 wake vortex upset potential for a T-37B probe airplane.

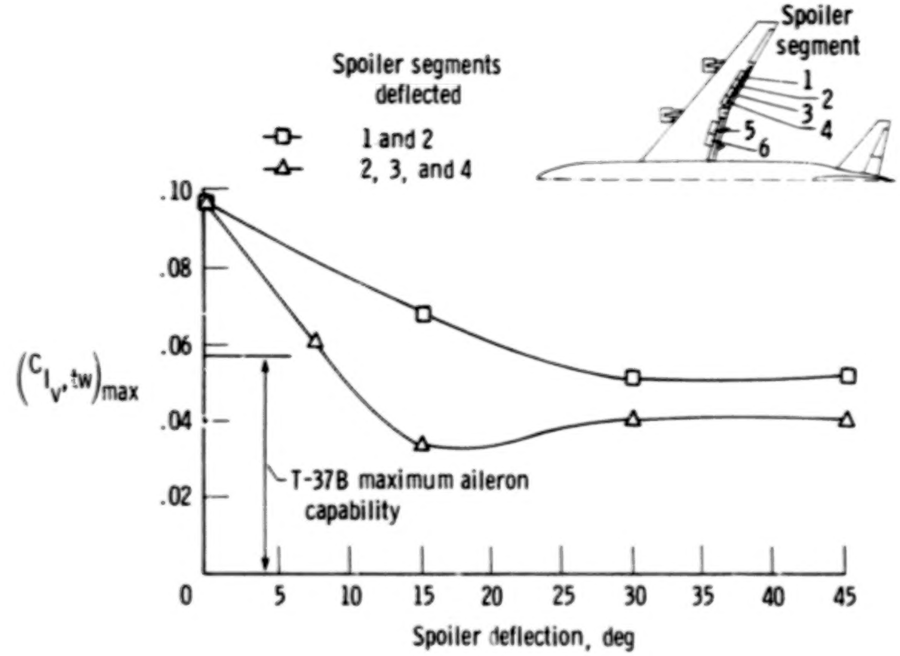

Figure 8. Trailing wing rolling-moment coefficient. B-747 model; gear down; $C_L = 1.2$. LearJet trailing model, 7.8 spans downstream.

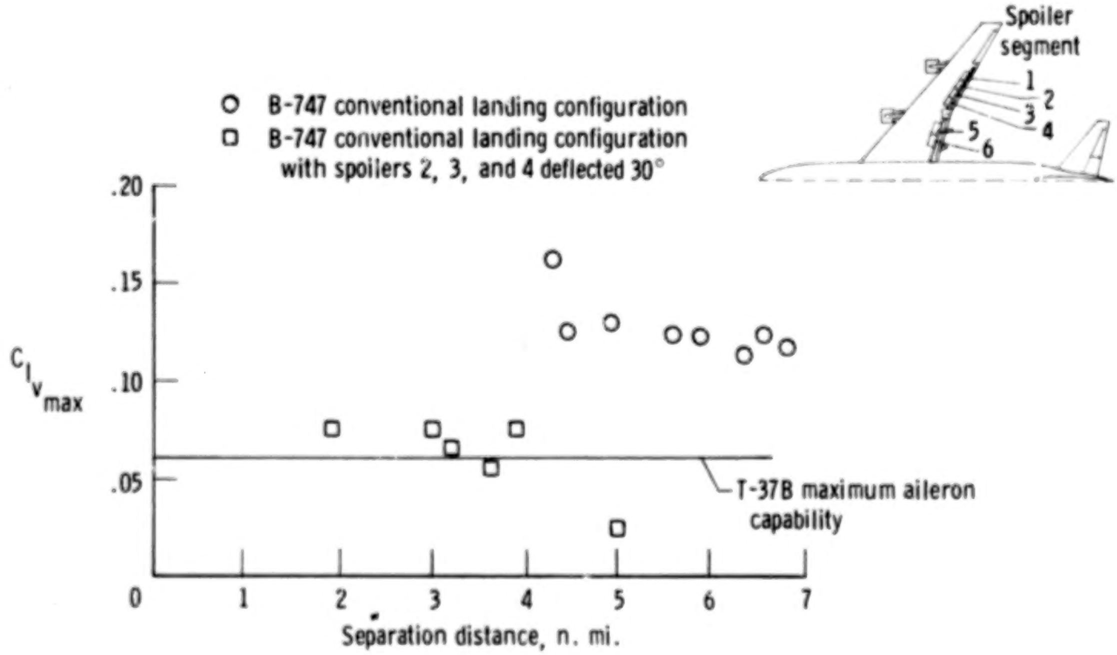

Figure 9. B-747 wake vortex upset potential for a T-37B probe airplane.

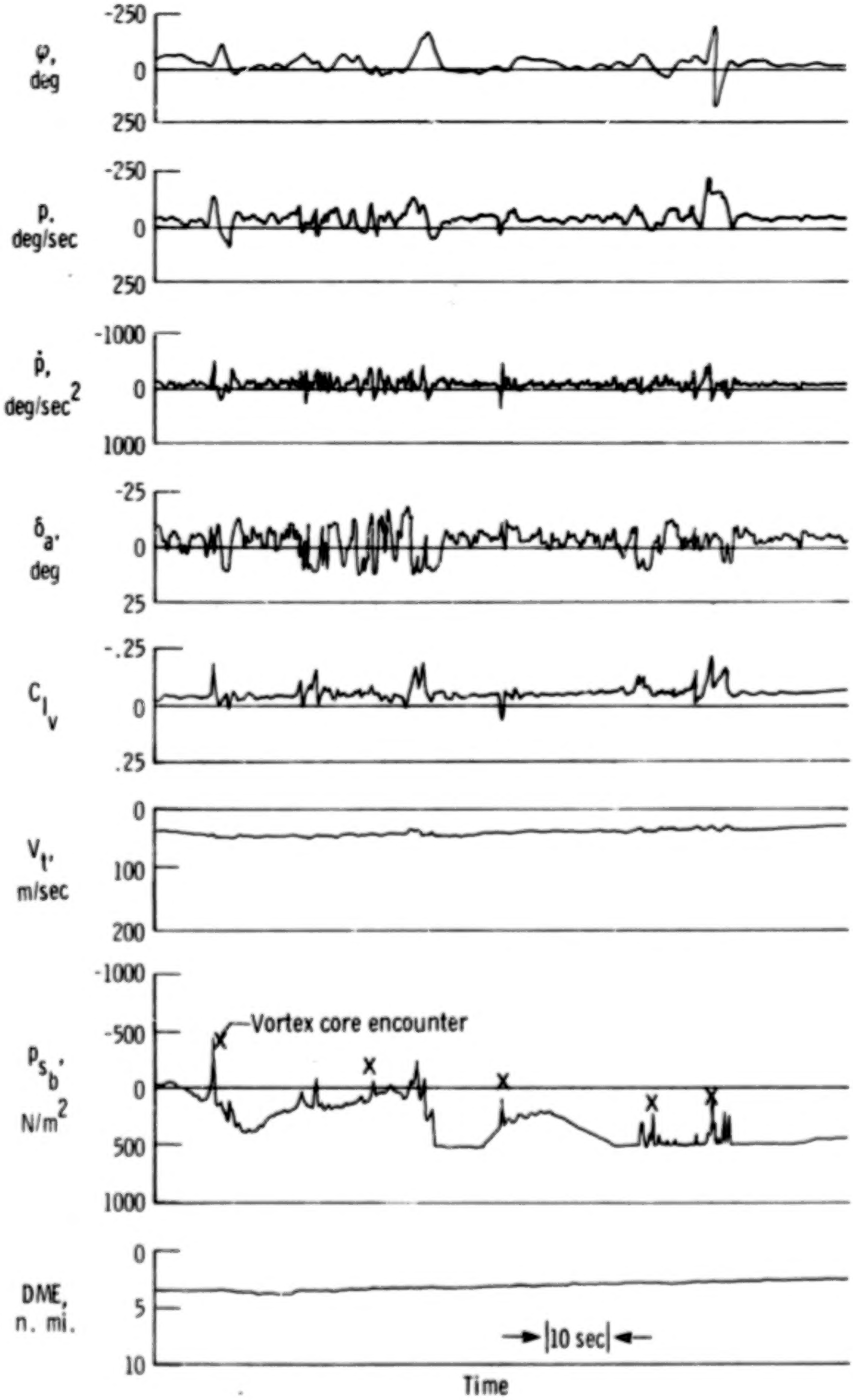

(a) B-747 in conventional landing configuration.

Figure 10. T-37B vortex encounter behind B-747 airplane.

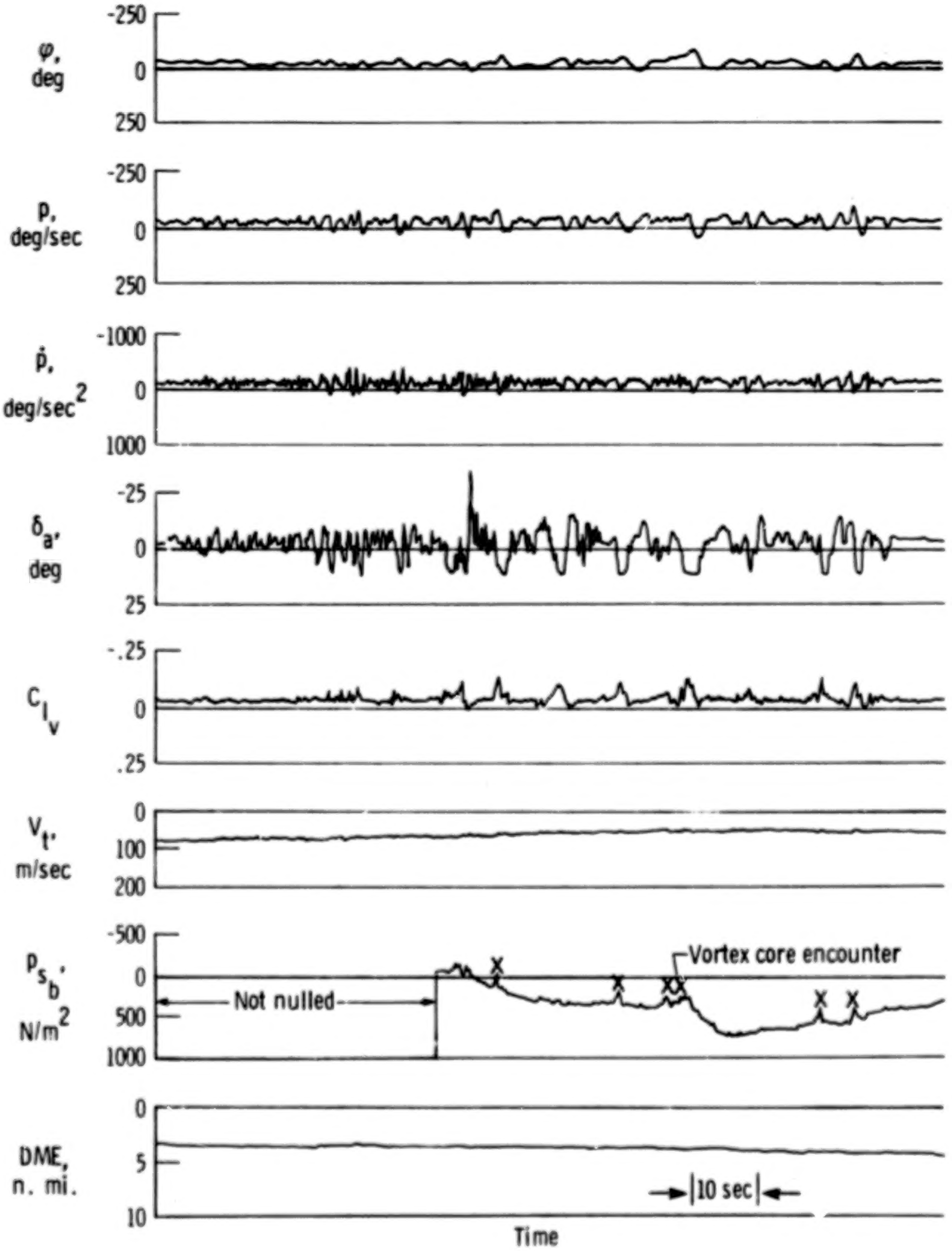

(b) B-747 in conventional landing configuration with spoilers 2, 3, and 4 extended 30°.

Figure 10. Concluded.

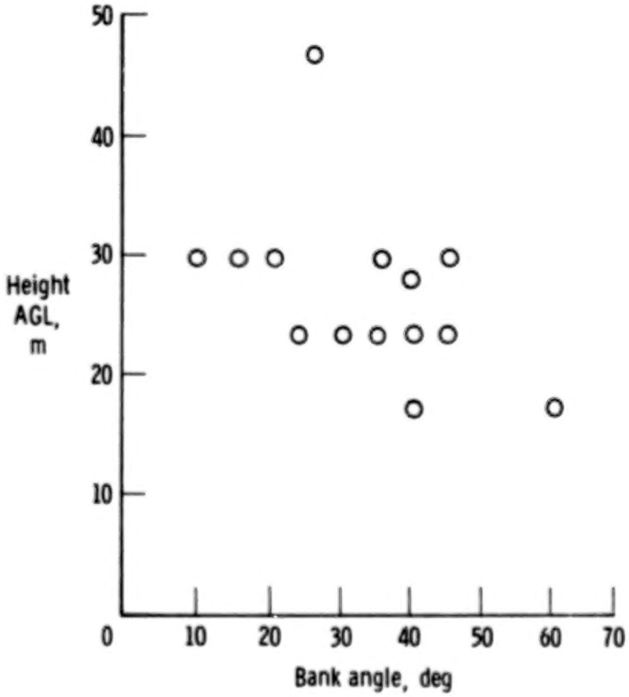

Figure 11. QF-86 bank angle excursions 3 nautical miles behind a spoiler-attenuated B-747 aircraft.

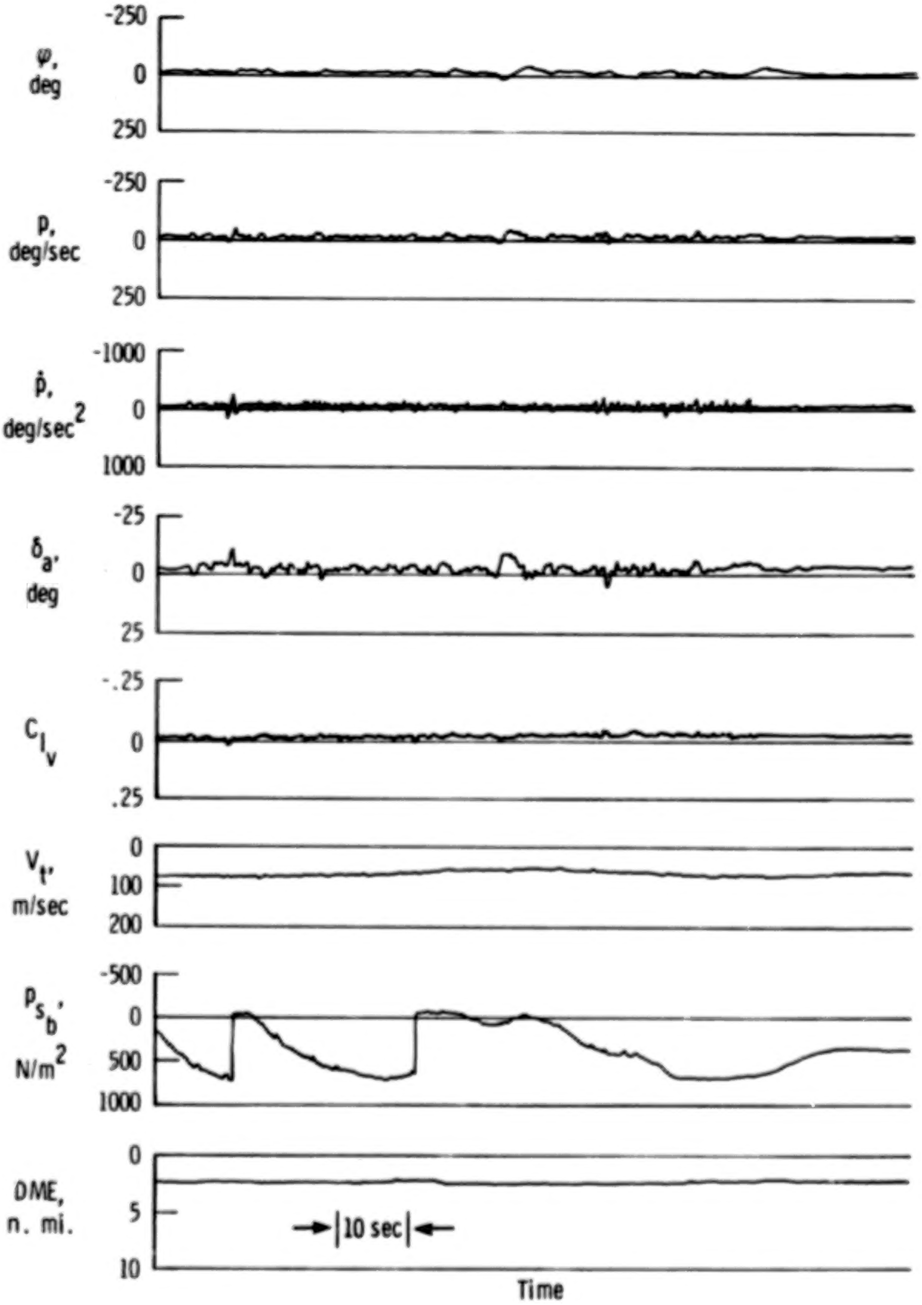

Figure 12. T-37B vortex encounter behind B-747 landing configuration with spoilers 2, 3, and 4 extended 30° and with oscillating ailerons and spoilers.

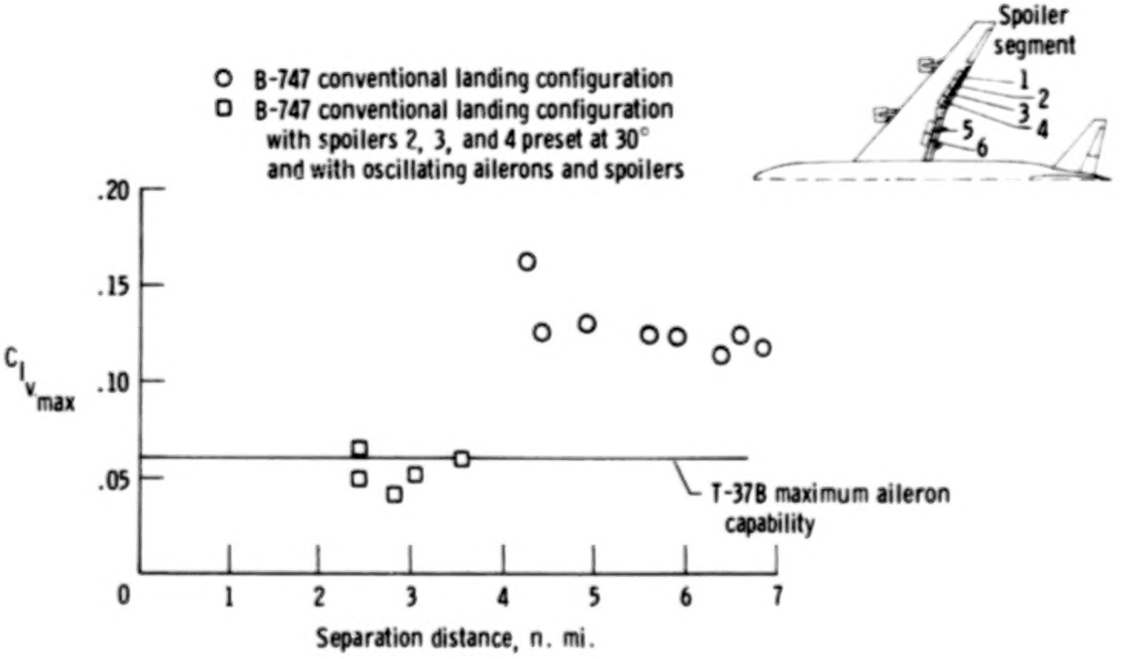

Figure 13. B-747 wake vortex upset potential for a T-37B probe airplane.

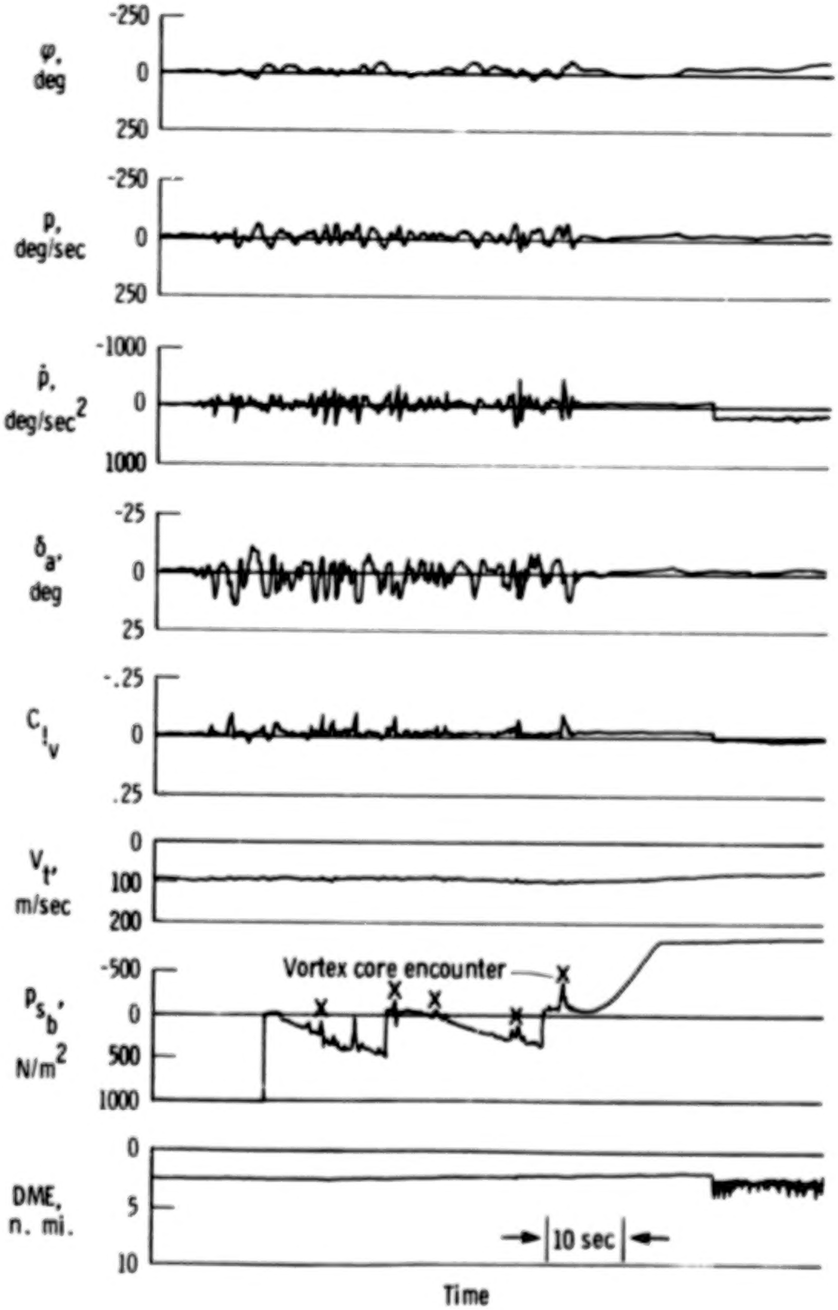

Figure 14. T-37B vortex encounter behind L-1011 landing configuration with spoilers 2, 3, and 4 extended 30° and ailerons and spoilers 2, 3, 4, and 5 pulsing asymmetrically at 2.3 seconds per cycle.

BASIC RESEARCH IN WAKE VORTEX ALLEVIATION

USING A VARIABLE TWIST WING

By Dana J. Morris and G. Thomas Holbrook
NASA Langley Research Center

INTRODUCTION

Aircraft trailing vortices are one of the principal factors affecting aircraft acceptance and departure rates at airports. Minimization of the hazard posed by the vortex would allow reduction of the present spacing requirements. Such reductions would allow full utilization of advances in automatically aided landing systems while maintaining or improving safety within the terminal area. For several years, NASA has been conducting an in-house and contractual research effort involving theoretical and experimental studies of various wake vortex minimization techniques (refs. 1 and 2). This work was done in conjunction with the Federal Aviation Administration's investigation of various sensing devices for detecting the presence of vortices within the terminal area.

This work has identified several methods of reducing the vortex strength behind an aircraft. These involve the redistribution of lift (vorticity) spanwise on the wing and drag (turbulence) distribution along the wing. NASA's continued effort involves experiments and theoretical analysis aimed at improving the understanding of the physics of vortex dissipation. This report summarizes one area of NASA's basic research in wake vortex alleviation and contains the highlights of model tests using a variable twist wing to investigate various wing span-load and drag distributions.

SYMBOLS

All force and moment data are referenced to the wind axes.

b	reference wing span, m
$\bar{c}$	wing mean aerodynamic chord, m
c_l	sectional lift coefficient
C_D	drag coefficient, $\frac{\text{Drag force}}{q_\infty S}$
C_L	lift coefficient, $\frac{\text{Lift force}}{q_\infty S}$
C_l	trailing-wing rolling-moment coefficient, $\frac{\text{Rolling moment}}{q_\infty S b}$
C_p	pressure coefficient, $\frac{p - p_\infty}{q_\infty}$

P	static pressure, Pa
q	dynamic pressure, Pa
S	reference wing area, m^2
u	component of velocity parallel to the x-axis, m/sec
V	resultant velocity magnitude, m/sec
VTW	refers to Variable Twist Wing
v	component of velocity parallel to the y-axis, m/sec
w	component of velocity parallel to the z-axis, m/sec
x	longitudinal axis referenced to Variable Twist Wing centerline, positive aft, m
y	lateral axis referenced to Variable Twist Wing centerline, positive out right wing, m
z	vertical axis referenced to Variable Twist Wing quarter-chord line, positive above wing, m
$\Delta\alpha$	wing-segment twist angle relative to wing center panel, wing leading edge up is positive, deg
η	vorticity, counterclockwise flow is positive, per sec

Subscripts:

TW	refers to trailing wing
VTW	refers to Variable Twist Wing
∞	refers to free-stream conditions

TEST FACILITIES

The tests were conducted in the Langley V/STOL Tunnel and, under contract, in the Hydronautics Ship Model Basin.

V/STOL Wind Tunnel

The test section of the V/STOL tunnel has a height of 4.42 m, a width of 6.63 m, and a length of 14.24 m. The Variable Twist Wing was blade mounted and maintained at 2.2 m above the test section floor (floor-to-wing center panel trailing edge) during test runs. Angle of attack was determined from an accelerometer mounted in the fuselage (ref. 3). A six-component strain-gage balance measured lift, drag, and pitching-moment data.

A survey rig (see fig. 1) was utilized in these tests for crossplane sampling of the three wake velocity components or rolling moment on a trailing wing in the wake of the Variable Twist Wing. The survey rig could be positioned anywhere from 1.2 m to 13.7 m downstream of the wing. The appropriate sensor was mounted to a motor-driven traverse mechanism on the survey rig to allow moving the sensor both laterally and vertically. Digital encoders on the mechanism output the lateral and vertical position of the sensor during test runs.

Hydronautics Ship Model Basin

The Hydronautics Ship Model Basin is a water tank 125 m long and 7.3 m wide, with a water depth of 3.8 m. Two independently powered carriage systems propel the Variable Twist Wing and trailing wing down the tank (see fig. 2). The Variable Twist Wing was located 0.56 span below the water line and attached to the lead carriage by a strut mounted to a tilt table. The tilt table provided for angle-of-attack adjustment (ref. 3). Balances internal to the model center body measured lift, drag, and pitching-moment data.

The trailing-wing carriage has a motor-driven vertical-scan system allowing a 0.46-m vertical survey of the wake during runs at a scanning rate of 0.04 m/sec. The lateral position of the trailing wing is changed manually between runs. The separation distance between the two models was determined using the time differential for the two carriages to pass a point half-way down the tow tank and the measured speed of the carriages.

MODELS

Variable Twist Wing

The Variable Twist Wing (VTW), shown in figure 3, is a unique research model capable of generating a desired span loading by twisting spanwise wing segments to the proper local angle of attack. In this manner, the effect of highly varied span loadings on the rolled-up wake can be investigated. The effect of turbulence on the rolled-up wake can be determined from tests made with various turbulence injection devices attached to the VTW model.

The aspect-ratio 7 metal wing has a span of 2.489 m. As shown in figure 4, the fixed 0.35-m center span is bounded on each end by 36 independently movable sections, each about 0.03 m wide. The 20 instrumented spanwise locations, each with 29 pressure ports, were electronically scanned and recorded in about one-tenth of a second to obtain pressure coefficient data, C_p, during tests in the V/STOL tunnel.

Trailing Wing

Rolling moment on a smaller trailing wing has been used as a means of estimating the hazard posed by a vortex wake system. The aspect-ratio 5.35 trailing wing used for these tests has a span 13 percent of the VTW span. A photograph and dimensions of the unswept trailing-wing model installed on the V/STOL survey rig are presented in figure 5. In each test facility, the model was mounted on a roll balance and attached to a traverse mechanism capable of positioning the model both laterally and vertically in the VTW wake. The model and its roll-balance system were used to measure the rolling moment caused by the vortex flow downstream of the VTW model.

METHOD OF TESTING AND ANALYSIS

The tests were all made at a Variable Twist Wing C_L of 0.6 and a Reynolds number of about one million, based on wing chord. A matrix of the configurations tested is shown in table I. Figure 6 shows schematically the types of data taken at the different downstream locations.

Lift distributions for each configuration tested in the V/STOL tunnel were calculated from the measured C_p data. During the tests, an on-line computer program utilized about half the pressure port data to produce rough plots of spanwise loading. This enabled "fine tuning" of the VTW twist distribution to match the desired loading.

Force and moment data (lift, drag, and pitching-moment) on the Variable Twist Wing were taken throughout an angle-of-attack range in the V/STOL tunnel. Generally, only the force and moment data necessary to assure testing at $C_{L_{VTW}} = 0.6$ were taken in the water towing tank.

Measured trailing-wing rolling-moment coefficients given in this report represent an averaged $C_{l_{TW}}$ for V/STOL data and a peak $C_{l_{TW}}$ for the water-tank data. The V/STOL technique for measuring rolling moment is to position the probe and take 10 data points per second over a 5-second period. These data points are averaged and used as the $C_{l_{TW}}$ for that y,z location. Data are taken at a sufficient number of y,z positions to insure location of the position of the maximum $C_{l_{TW}}$ value obtained by this method. The Hydronautics technique for measuring rolling moment uses the probe to traverse the wake vertically for a single lateral position. Sufficient runs are made at different probe lateral positions to insure locating the y,z position for the peak $C_{l_{TW}}$. The Hydronautics measured $C_{l_{TW}}$ thus represents the maximum instantaneous value of rolling moment obtained in the y,z crossplane of the wake. On several VTW configurations, multiple vortices were shed from each wing semispan. Only the maximum strength vortex is noted in this report.

Three-component wake velocity measurements were made using a three-component hot-film probe, mounted in the V/STOL survey rig. Hot-film voltages and y,z potentiometer outputs from the traverse mechanisms were signal conditioned and recorded on magnetic tape. This tape was digitized to a matrix of y, z, u, v, and w data values over a 1.524 m × 1.524 m, 0.0254-m mesh, crossplane grid. Vorticity contours were computed from the crossplane velocities at each of the downstream data stations. Comparison of velocity and vorticity plots at the downstream sampling planes shows the development of the wake. Additionally, the data from the half-span downstream station were used as initial conditions for the two-dimensional, time marching, viscous wake simulation computer code (WAKE). (See ref. 4.)

RESULTS

Data were taken at the discrete locations shown in table I and all the data curves shown are faired through these data points. Among the tests (table I) were three relatively simple VTW loadings, each of which resulted in a rolled-up wake with one significant strength semispan vortex. These three configurations (1, 2, and 4) and their measured $C_{l_{TW}}$ values are compared in figure 7. The comparative values of $C_{l_{TW}}$ are as expected, with the simulated rectangular (2) loading generating the maximum rolling moment and the simulated triangular (4) loading creating the minimum. The relative relationship of $C_{l_{TW}}$ data for configurations 1 and 4 also agrees between test facilities. Thus, up to a 30-percent reduction in trailing-wing rolling moment can be achieved in a single semispan vortex wake by span-load alteration on the generating wing. Turbulence differences are considered to be insignificant since the C_D is nearly identical for the three configurations at a C_L of 0.6.

The lift distribution for configuration 7 is similar to that of an 80-percent flapped wing and results in a downstream semispan wake composed of an inboard, or flap, vortex and an outboard, or wingtip, vortex. For this configuration, the flap vortex is highly dominant - in the V/STOL tunnel, the wake velocity data indicate vorticity levels for the flap vortex are at least 30 percent greater than those for the wingtip vortex at 3 spans downstream and, in the water tank, $C_{l_{TW}}$ for the flap vortex was measured as 60 percent greater than the wingtip vortex. Addition of a spoiler centered at $0.61(b_{VTW}/2)$ (configuration 7S) results in a far downstream semispan wake with only one vortex and, as shown in figure 8, a significantly lower $C_{l_{TW}}$. It is important to note that the lift distribution for configuration 7S varies greatly from that of configuration 7, as does the turbulence distribution (evidenced by a 230-percent increase in C_D for configuration 7S at a C_L of 0.6). Therefore, the reduction in measured $C_{l_{TW}}$ may result from the modified lift and turbulence distributions, the increased turbulence level, or a combination of these factors.

In an effort to separate the effect of turbulence from that of span load, the VTW was adjusted (configuration 9) to match the span load of configuration 7 with the spoiler (configuration 7S). Figure 10 compares configurations 7, 7S, and 9. It is apparent that configuration 9 does not achieve the complete

$C_{l_{TW}}$ reduction between configurations 7 and 7S. In fact, the V/STOL tunnel data, for $x/b_{VTW} < 5.5$, show a large increase in $C_{l_{TW}}$ for configuration 9 as opposed to configuration 7. However, at an x/b_{VTW} of 35, the water-tank data indicate an 11-percent reduction in $C_{l_{TW}}$ from configuration-7 values as opposed to an overall 32-percent reduction between configurations 7 and 7S. Thus, it seems that one-third of the measured $C_{l_{TW}}$ reduction between configurations 7 and 7S may be accounted for by span-load alteration - the remainder occurring due to turbulence distribution and level changes.

The nondimensional vorticity contours for configuration 7S are shown in figure 11. The four vortices present one-half span behind the wing have merged into two vortices by five-and-one-half spans downstream. The measured values at the half-span station were used to initialize the WAKE code to predict the development downstream. The vorticity contours predicted by WAKE at five-and-one-half spans downstream are shown in figure 12 for comparison with the measured values shown in figure 11(c). While the predicted vorticity levels are higher than those measured, the locations and shapes of the contours are approximately the same.

CONCLUDING REMARKS

The Variable Twist Wing concept has been used to investigate the relative effects of lift and turbulence distributions on the rolled-up vortex wake. The extensive data gathered will assist in understanding the development and decay of the wake. Also, initial attempts to use the Variable Twist Wing velocity data to validate the WAKE computer code have shown a strong correlation, although the vorticity levels were not exactly matched. Further data analysis and verification of the computer code is proceeding.

REFERENCES

1. Wake Vortex Minimization. NASA SP-409, 1976.

2. Proceedings of the Aircraft Wake Vortices Conference. March 15-17, 1977. Report No. FAA-RD-77-68.

3. Stickle, Joseph W.; and Kelly, Mark W.: Ground-Based Facilities for Evaluating Vortex Minimization Concepts. Wake Vortex Minimization. NASA SP-409, 1977, pp. 129-155.

4. Bilanin, Alan E.; Hirsh, Joel E.; Teske, Milton E.; and Hecht, Arthur M.: Atmospheric-Wake Vortex Interactions. ARAP Report No. 331, 1978.

TABLE I.- DATA TAKEN WITH THE VARIABLE TWIST WING

Designation	Description of wing loading or configuration being simulated	Test facility		Type of data								
		V/STOL	Hydronautics	Force and moment	C_p	$C_{l_{TW}}$, x/b_{VTW} =				u,v,w; x/b_{VTW} =		
						3.0	5.5	20.	35.	0.5	3.0	5.5
1	Straight wing	✓		✓	✓	✓	✓					
1	Straight wing		✓	✓			✓	✓	✓			
2	Rectangular loading	✓		✓	✓	✓	✓					
3	Parabolic loading	✓		✓	✓	✓	✓					
4	Triangular loading	✓		✓	✓	✓	✓			✓	✓	✓
4	Triangular loading		✓	✓			✓	✓	✓			
5	Flapped wing to 40% semispan	✓		✓	✓	✓	✓					
6	Flapped wing to 60% semispan	✓		✓	✓	✓	✓					
7	Flapped wing to 80% semispan	✓		✓	✓	✓	✓			✓	✓	✓
7	Flapped wing to 80% semispan		✓	✓			✓	✓	✓			
7S	Configuration 7 with spoiler centered at $0.61(b_{VTW}/2)$	✓		✓	✓	✓	✓			✓	✓	✓
7S	Configuration 7 with spoiler centered at $0.61(b_{VTW}/2)$		✓	✓			✓	✓	✓			
7X	Configuration 7 with spline centered at $0.61(b_{VTW}/2)$		✓	✓			✓	✓	✓			
8	Twisted wing simulation of 7S lift distribution	✓		✓	✓	✓	✓					
8.5	Twisted wing simulation of 7S lift distribution	✓		✓	✓	✓	✓			✓	✓	✓
8.5X	Configuration 8.5 with flat plate aft of wing centered at $0.61(b_{VTW}/2)$	✓		✓	✓		✓					
9	Twisted wing simulation of 7S lift distribution	✓		✓	✓	✓	✓					
9	Twisted wing simulation of 7S lift distribution		✓	✓			✓	✓	✓			
9X	Configuration 9 with spline centered at $0.61(b_{VTW}/2)$		✓	✓			✓	✓	✓			

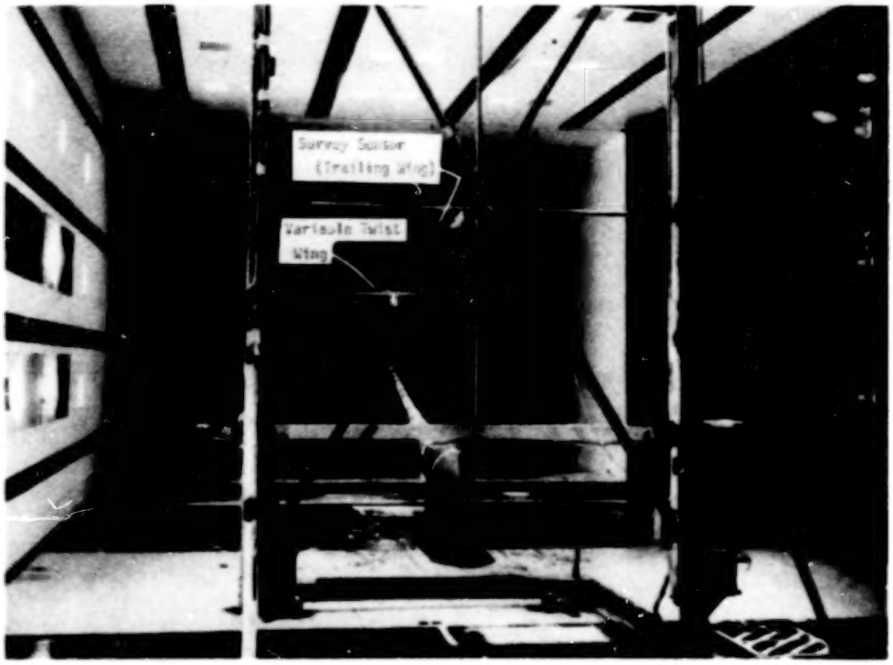
Survey Sensor
(Trailing Wing)
Variable Twist
Wing

Figure 1.- Survey rig in Langley V/STOL Tunnel (with trailing-wing model attached to traverse mechanism.

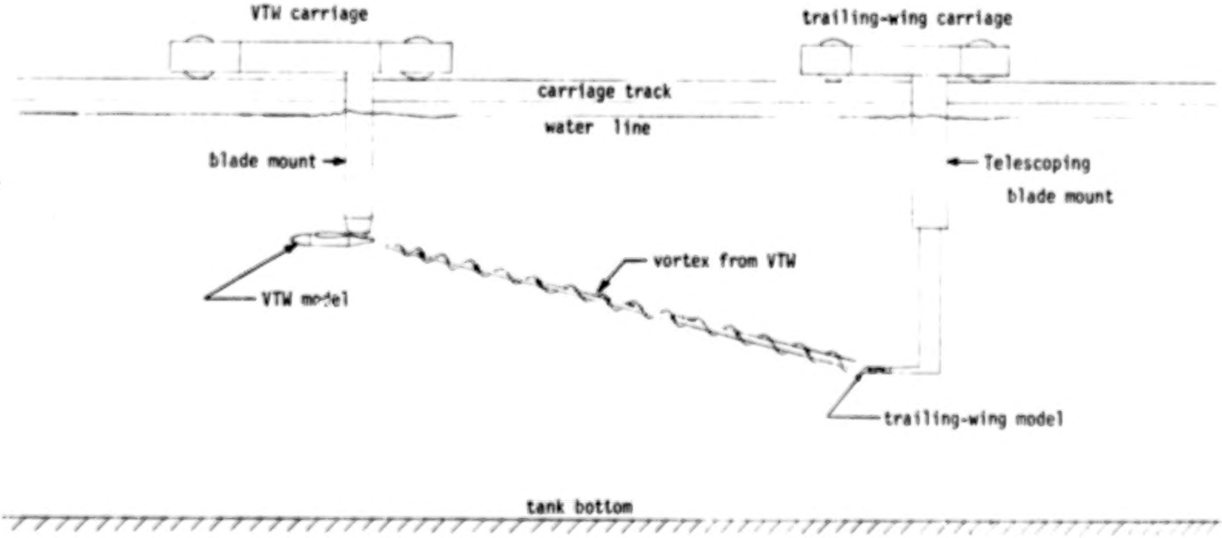
VTW carriage
trailing-wing carriage
carriage track
water line
blade mount
Telescoping
blade mount
vortex from VTW
VTW model
trailing-wing model
tank bottom

Figure 2.- Diagram of Hydronautics Ship Model Basin.

Figure 3.- Variable Twist Wing model, blade mounted in Langley V/STOl Tunnel test section.

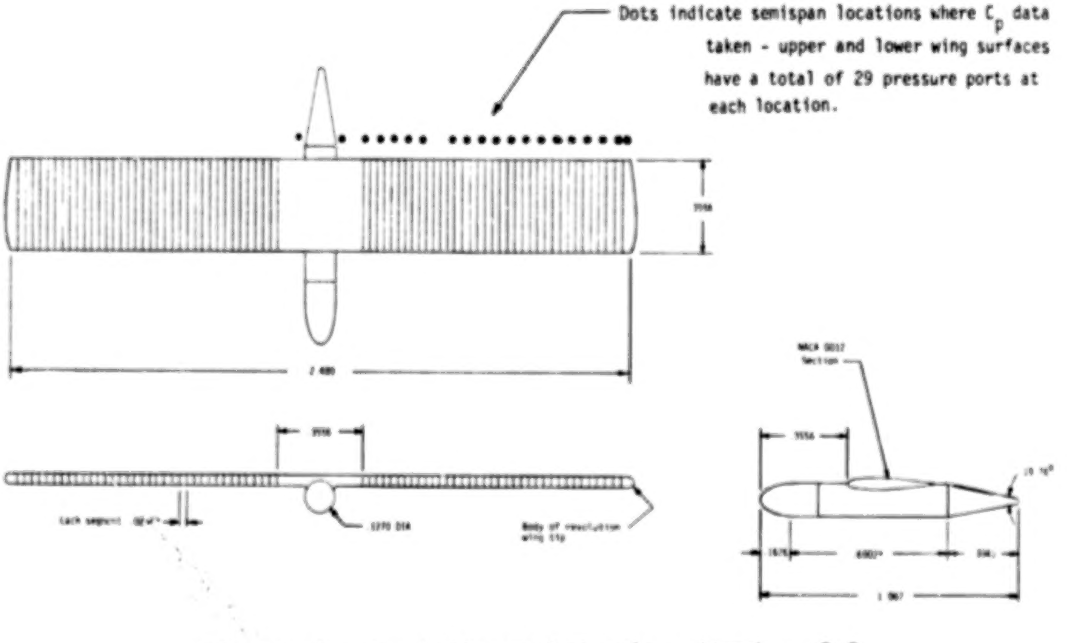

Dots indicate semispan locations where C_p data taken - upper and lower wing surfaces have a total of 29 pressure ports at each location.

.3556
2.400
.3556
Each segment .024"
.1270 DIA
Body of revolution wing tip
NACA 0012 Section
.3556
.1575
.6002
1.067

Figure 4.- Variable Twist Wing (VTW) model.

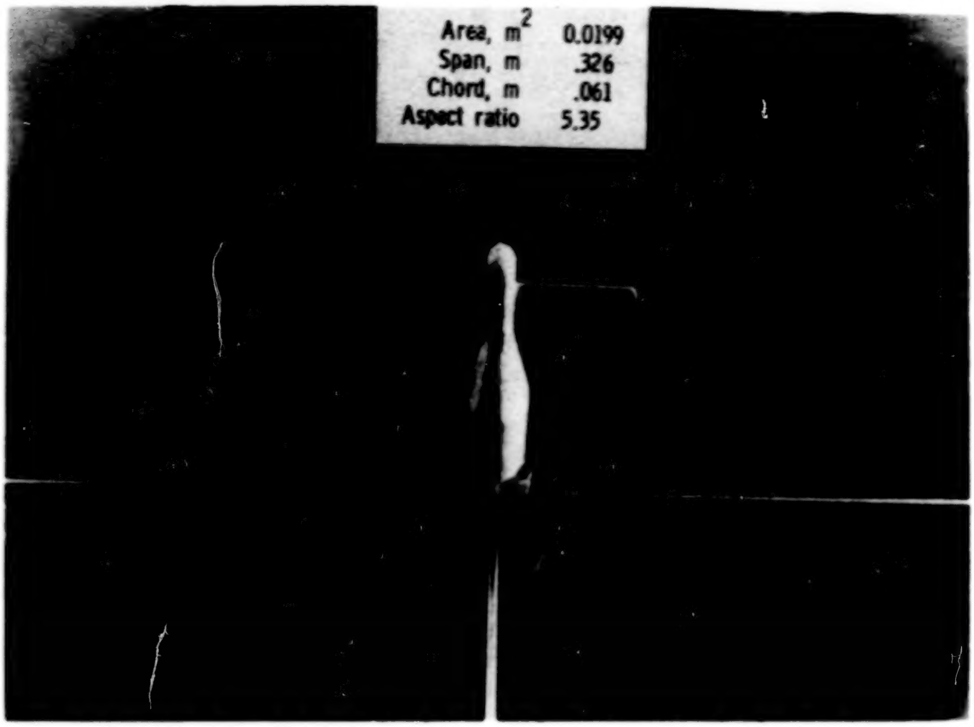
Area, m^2 0.0199
Span, m .326
Chord, m .061
Aspect ratio 5.35

Figure 5.- Photograph and dimensions of unswept trailing-wing model on traverse mechanism. Model has NACA 0012 airfoil section.

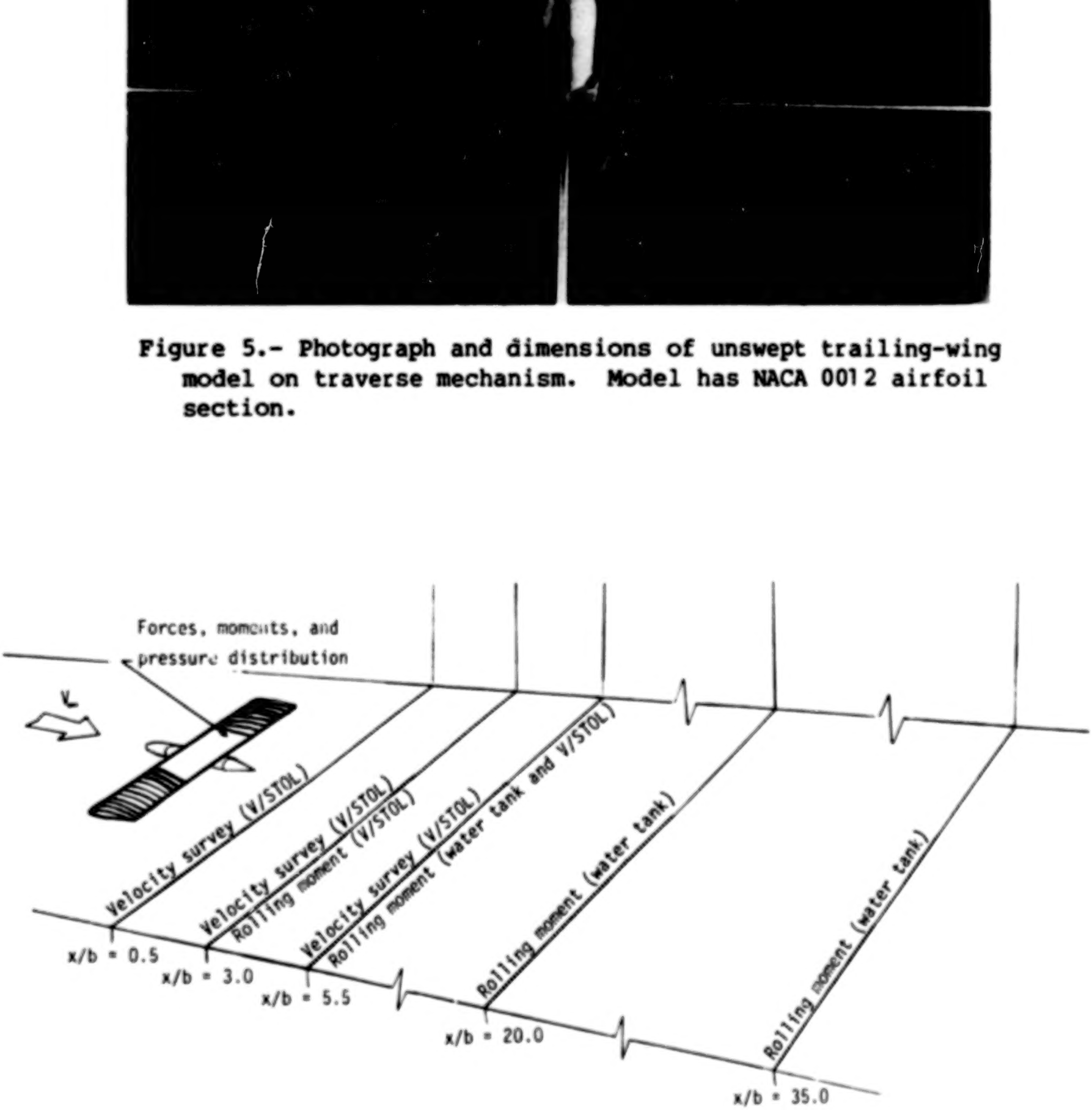
Forces, moments, and pressure distribution
V
Velocity survey (V/STOL)
Velocity survey (V/STOL)
Rolling moment (V/STOL)
Velocity survey (V/STOL)
Rolling moment (water tank and V/STOL)
Rolling moment (water tank)
Rolling moment (water tank)
x/b = 0.5
x/b = 3.0
x/b = 5.5
x/b = 20.0
x/b = 35.0

Figure 6.- Types of data taken with Variable Twist Wing model.

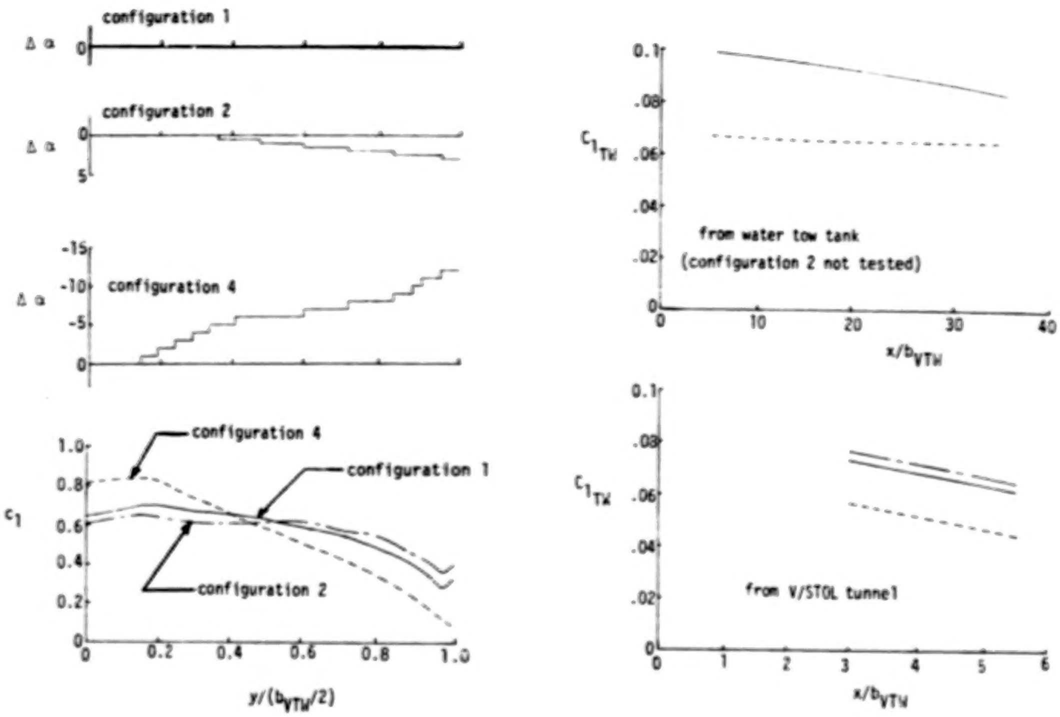

Figure 7.- Wing twist, wing loading, and trailing-wing rolling-moment comparisons for VTW configurations 1, 2, and 4.

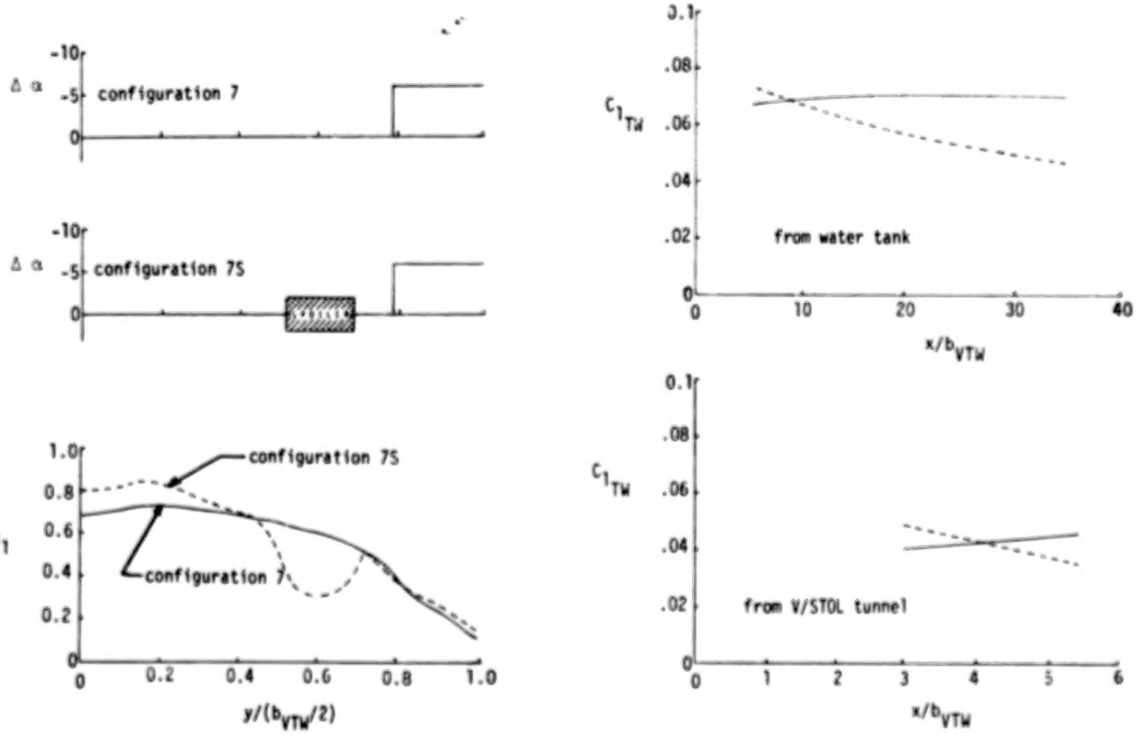

Figure 8.- Wing twist, wing loading, and trailing-wing rolling-moment comparisons for VTW configurations 7 and 7S.

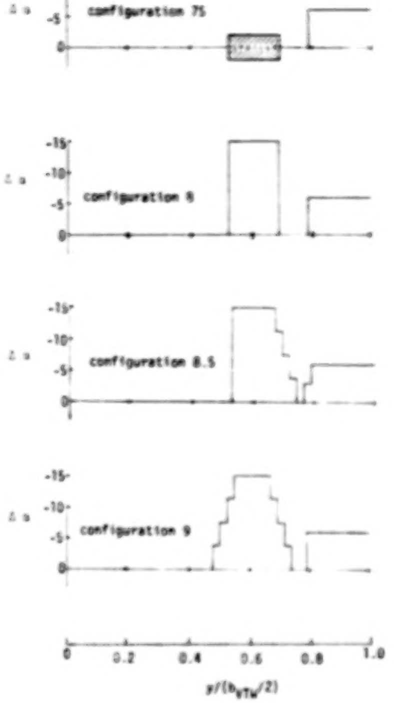

Figure 9.- Comparison of different wing twist distributions used to simulate lift distribustion attained with configuration 7S.

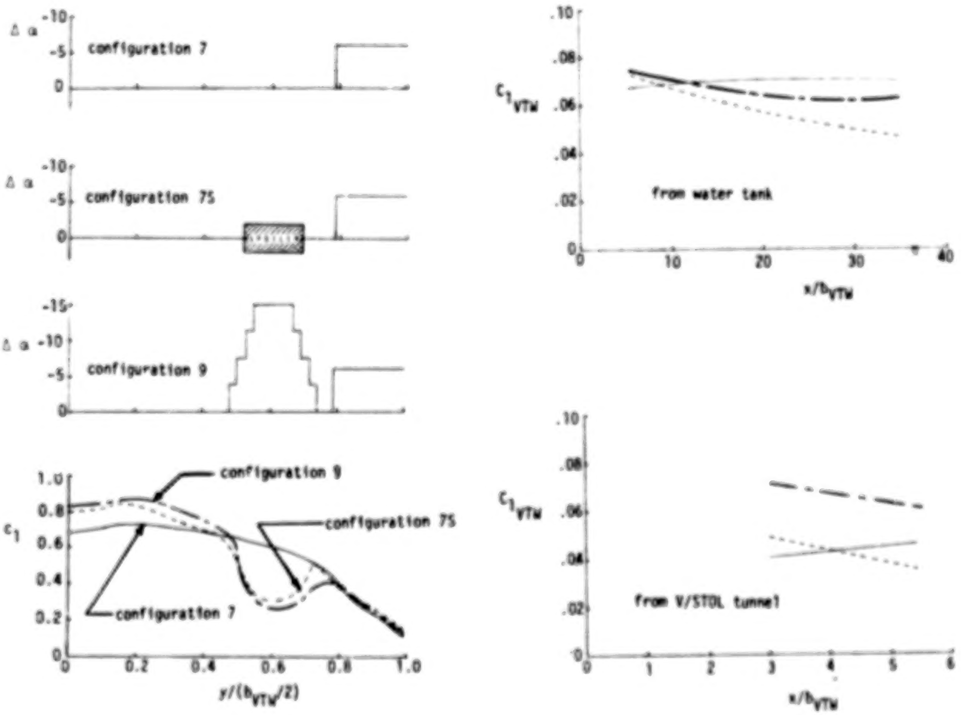

Figure 10.- Wing twist, wing loading, and trailing-wing rolling-moment comparisons for VTW configurations 7, 7S, and 9.

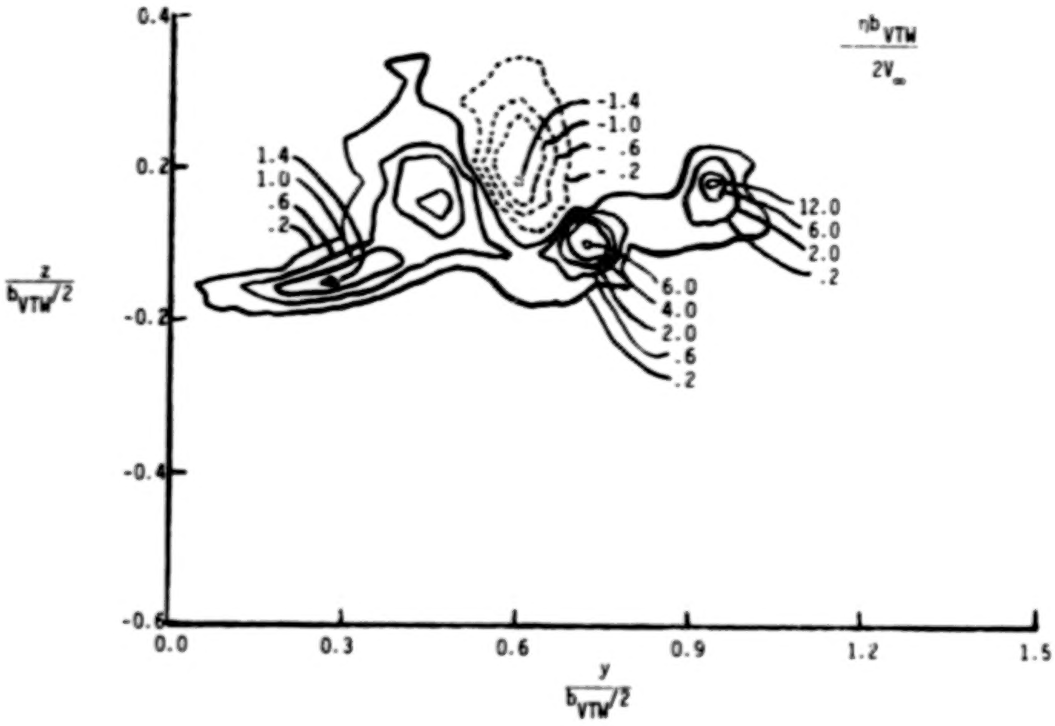

(a) $x/b_{VTW} = 0.5$.

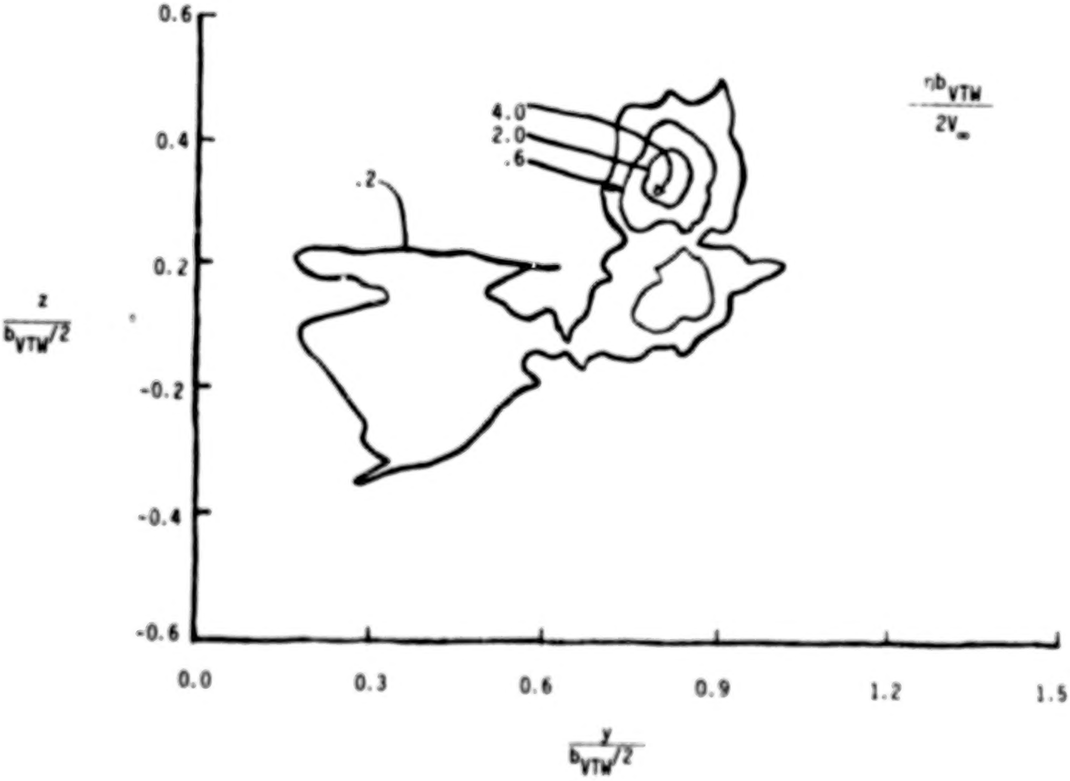

(b) $x/b_{VTW} = 3.0$.

Figure 11.- Vorticity contours measured behind configuration 7S.

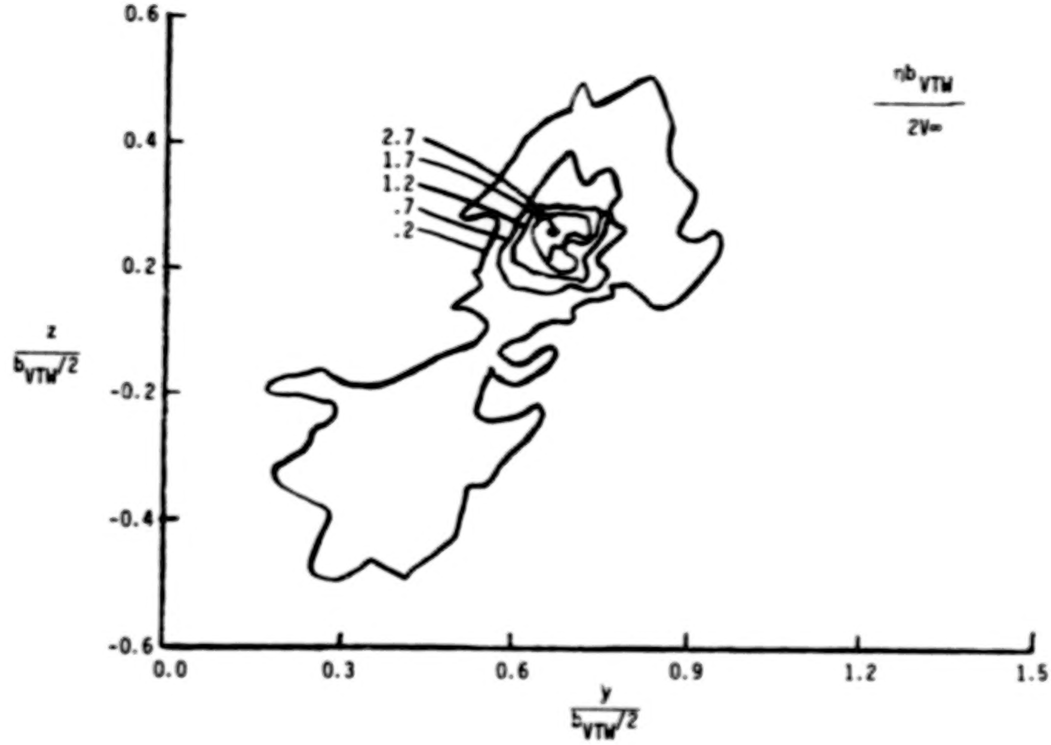

(c) $x/b_{VTW} = 5.5$.

Figure 11.- Concluded.

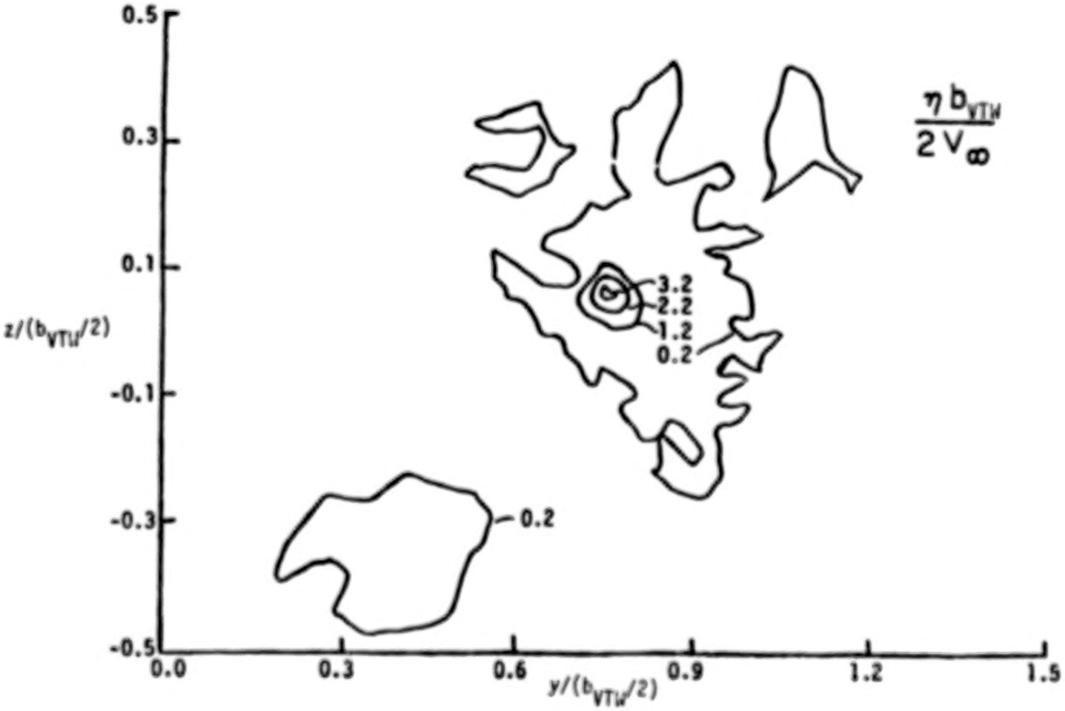

Figure 12.- Predicted vorticity contours at 5.5 spans downstream of configuration 7S.

BLANK PAGE

BLANK PAGE

PNEUMATIC BOOT FOR HELICOPTER ROTOR DEICING

Bernard J. Blaha and Peggy L. Evanich
Lewis Research Center

SUMMARY

Although they have many desirable characteristics, pneumatic deicer boots have received little consideration for application to helicopters. Modern polyurethane pneumatic deicer boots are light in weight, low in power consumption, easy to control, and capable of field repair. The Lewis Research Center, in cooperation with the B. F. Goodrich Company, has tested pneumatic deicer boots for helicopter rotor blades. The tests were conducted in the Lewis 6- by 9-ft Icing Research Tunnel on a stationary section of a UH-1H helicopter main-rotor blade. The boots were effective in removing ice and in reducing aerodynamic drag due to ice. Results of these tests are presented in this paper. Because of these promising results a program was begun at the NASA Ames Research Center to test boots on full-scale, rotating UH-1H rotor blades.

INTRODUCTION

To date, there are no U.S.-manufactured helicopters certified to fly into forecasted icing conditions. None are expected to be certified for at least 2 years. However, much work is in progress to develop both certification criteria (which currently are not defined exclusively for rotorcraft) and deicing systems for rotors (ref. 1). The rotor deicing systems being developed employ the electrothermal concept (ref. 1). The pneumatic boot concept for rotor blade ice protection was analyzed in 1973 by the Lockheed-California Company and rejected (ref. 2). Although the strong advantages of low weight, low power, blade leading-edge protection, and simple controls were pointed out in this study, Lockheed listed several reasons for questioning the pneumatic boot concept. These reasons included materials problems, possible adverse aerodynamic effects, and basic icing questions. Of the reasons listed, the most damaging centered on the materials technology of the day. A primary question was whether the pneumatic boot could withstand the severe dynamic environment of the helicopter rotor blade. A specific concern was that the boots might be damaged or completely torn off by the high centrifugal forces. Furthermore the rain abrasion resistance of neoprene was unacceptable. Also there were possible adverse aerodynamic effects of the inflated tubes on the small-chord, thin airfoils of a rotor. These problems were sufficient to eliminate the boot from further consideration.

As a result of these early studies the B. F. Goodrich Company has further investigated materials and techniques of pneumatic boot manufacture and has conducted limited testing. They claim that a polyurethane elastomeric material, rather than the currently used neoprene, can be compounded to exhibit many superior properties, such as abrasion (rain and sand) resistance (3 to 5 times greater than that of neoprene), field repairability, greater compatibility to ester oils, higher strength and fatigue resistance, and minimal distortion under high centrifugal forces.

A schematic diagram of the pneumatic system applied to a UH-1H helicopter is shown in figure 1 (ref. 1). According to reference 1 this system would approximately 13.6 kg (30 lb) (43 percent of the electrothermal system weight), would apply to existing rotor blades, and would cost much less than the proposed electrothermal system.

In an initial attempt to evaluate the deicing capability and aerodynamic performance of boots for rotor blades, tests were conducted in 1979 in the NASA Lewis 6- by 9-ft Icing Research Tunnel (IRT) on a 1.83-m (6-ft) span, full-scale segment of a stationary UH-1H rotor blade. In these tests three boot geometries were evaluated. These boots comprised both spanwise and chordwise tubes. Since the model blade was stationary during a run, neither the rotating nor vibrating loads of a real rotor were simulated. Also the high rotor tip speeds could not be simulated since the maximum tunnel air speed was 134 m/sec (i.e., $M_0 \sim 0.4$). Angle of attack was varied from 0° to 16° (stall) without ice and from 0° to 10° with ice. The lower air speeds and the absence of rotor dynamic loads in these tests probably made this a conservative test of the boot's effectiveness as a deicer because both dynamic loads and higher air speeds should aid in removing the ice. Some tests were made to roughly simulate the cyclic motion of a rotor blade by icing the model at one angle of attack and deicing the model at another. With the best boot configuration a series of model drag measurements were made with a translating wake-survey probe. The test results are included herein along with a description of a NASA Ames-Lewis program plan to test the pneumatic boot concept with full-scale, rotating UH-1H blades.

SYMBOLS

C_d	section drag coefficient, $2\int \frac{V}{V_0}\left(1 - \frac{V}{V_0}\right) dz$
c	wing chord, 0.533 m (1.75 ft)
D_{med}	droplet median volume size, μm
H	local stagnation pressure
H_0	free-stream stagnation pressure
LWC	liquid water content, g/m^3
M_0	free-stream Mach number
P_0	free-stream static pressure

T_0	free-stream stagnation temperature, °C
X,Z	position coordinates, m
V	velocity, m/sec
V_0	free-stream velocity, m/sec
α	section angle of attack at tunnel centerline, deg

TEST APPARATUS AND PROCEDURE

The test model was made from a 1.83-m (6-ft) span segment of a full-scale UH-1H rotor blade and was mounted vertically in the test section of the Lewis 6- by 9-ft Icing Research Tunnel (fig. 2). Since the model was cut from an actual rotor blade, it included a uniform twist of approximately 0.5° per foot or about 3° from floor to ceiling. The rotor blade on a UH-1H helicopter is 14.63 m (48 ft) in diameter and incorporates a constant-chord (0.533 m (1.76 ft)) NACA 0012 airfoil section. The model was mounted on the tunnel floor-plate, and the angle of attack could be varied from near zero to stall.

The pneumatic boots were applied over the external surface of the leading edge, and the supply air line was routed inside the model and through the tunnel floorplate. The control system for the boot test was the same as that shown in figure 1. For the wind tunnel tests the turbine bleed air was replaced by regulated tunnel service air. This system is also the same as the one currently used on fixed-wing aircraft. The system was designed around a two-position valve (ejector flow control valve) that used a venturi orifice to provide vacuum to the boot when it was not activated. Upon activation this valve closed and higher pressure air ($10.5\mathrm{x}10^3$ to $21\mathrm{x}10^3$ kg/m^2 (15 to 30 psig)) was provided to rapidly inflate the boot. This system can be operated either manually or automatically with a programed pulse sequence and timing.

A translating wake-survey probe was used to help evaluate the deicing performance of the boot configurations. The probe, as shown in figure 3, consisted of a single stagnation pressure tube that could be retracted down behind a wind screen. When the airfoil was exposed to the tunnel icing cloud, the probe was retracted behind the windscreen. Then after the cloud was turned off, the probe was inserted into the air stream and the wake survey was made. This probe, which was located about one chord downstream of the airfoil at midspan, was installed as shown in figure 4 to yield the velocity decrement ratio V/V_0 in the airfoil wake. By translating laterally through the wake a plot of V/V_0 as a function of position X was obtained. Integration of the wake defect gave a measurement of airfoil section drag coefficient.

Sketches of the pneumatic boot designs tested are shown in figures 5 and 6. In the initial part of the test program three candidate designs were screened in terms of their deicing capability. These boots were designed to use a combination of both chordwise and spanwise tubes. Results from tests performed in the 1950's (ref. 3) on pneumatic boots for fixed wings suggested that the aerodynamic effect of inflating the tubes was less with chordwise tubes than with spanwise configurations. Because the rotor airfoil section was both shorter and thinner than fixed wings, it was felt that the boot for a helicopter rotor should incorporate primarily chordwise tubes. However, with the small leading-edge radius of a rotor blade, it was evident that chordwise tubes would crimp over in the leading-edge region and not provide the deflection necessary to fracture and remove the ice. As a result it was necessary to also incorporate into the boot design a spanwise tube (or tubes) at the leading edge. Two boot geometries were tested initially: a small-diameter-tube configuration (similar to fig. 5, but with a single spanwise tube) and a larger-diameter-tube configuration (fig. 6). These boot configurations incorporated tube sizes that were in the same range (1.27 to 3.18 cm diam) as those currently used on larger chord, fixed-wing aircraft. For the smaller-chord rotor airfoils it would be desirable to use smaller diameter tubes to minimize the aerodynamic effect, especially upon accidental or multiple inflation. However, getting the deflections required to break the ice with smaller tubes would require higher inflation pressures than available on existing rotorcraft. Consequently the tube sizes used in this program were from 5 to 7 times larger, relative to the chord length, than those currently used for fixed wings. The boots were designed to provide coverage of about 20 percent of the chord on the upper surface and 30 percent on the lower. When choosing the amount of chordwise boot coverage, both the limits of impingement of water-droplet trajectories and runback should be taken into account.

During the initial deicing tests the two configurations with a single spanwise tube on the leading edge were ineffective in removing the ice. Therefore, as discussed in the section RESULTS AND DISCUSSION, the boot design was modified by splitting the single spanwise tube into two tubes (fig. 5). Once it was determined that the boot with two spanwise tubes on the leading edge was effective in deicing the blade, the translating probe was installed. Measurements of airfoil section drag near the model centerline were made over a range in angle of attack from 0° to stall (~16° without ice, and ~9.4° with ice). Data were obtained, both with and without the boot installed, at tunnel speeds of 67 and 112 m/sec (150 and 250 mph). These speeds are lower than those near the outboard sections of a rotor blade; therefore compressibility effects and aerodynamic heating effects were not simulated. Data were initially taken at the lower speed, without ice, to check out the probe and to check the stall characteristics of the rotor blade. Stall was determined by applying tufts to the suction surface of the blade and observing where the flow began to reverse direction or become unstable. When it was determined that the probe could withstand the turbulence generated by the model, data were taken at the higher speed with ice.

Data were obtained at various icing conditions and at various angles of attack. By selecting tunnel temperature both glaze (-6.1° C) and rime (-14.4° C) ice conditions were investigated. In all cases the icing cloud conditions were kept constant at a volume median droplet size D_{med} of 20 μm and a liquid water content (LWC) of 1 g/m^3. Most icing and deicing sequences were done at constant angles of attack, but for some conditions the model would be iced at one angle of attack and deiced at another. The angles of attack were kept within the range of those typically expected on a rotor blade, namely, between 0° and 8°. For example the model would be iced at 1.4° and deiced at 5.4°, or vice versa; the model was also iced at 5.4° and deiced at 9.4°. These variations were an attempt to simulate, in a very slow way, the cyclic pitch variations of a real rotor blade.

In each icing test sequence about 1 cm of ice was accreted on the blade before deicing was attempted. One centimeter of ice was chosen as a good test condition for two reasons. First, for the pneumatic boot to work, a certain amount of ice has to be present. If too little ice is present, the ice will be fractured into small pieces, but the interfacial bonds will not be broken and consequently the ice will not be removed. Second, from unpublished flight data from recent rotorcraft icing tests behind the HISS (U.S. Army helicopter icing spray system) tanker and at the Ottawa spray rig, it was evident that, when ice accretions exceeded approximately 1 cm on the rotor, torque rose greatly.

RESULTS AND DISCUSSION

As was noted in the previous section the pneumatic boot configurations that had a single spanwise tube at the leading edge proved to be inadequate for these deicing tests of a stationary rotor blade. Inflation of the boots at various conditions of tunnel speed, temperature, and model angle of attack resulted in the ice being severely fractured, but the ice cap would not leave either the upper or lower surfaces. After each of these tests the ice adhesion was found to be so significantly reduced that the ice could be easily removed by wiping the surface of the model. However, the aerodynamic forces would not remove the ice. Similar results were observed with both tube sizes. It was decided therefore to change the basic boot design by splitting the single spanwise tube on the leading edge into two tubes (fig. 5). With this new design the aerodynamic forces were effective in removing the ice on the suction surface. Therefore this new boot configuration was used throughout the remainder of the testing with the wake-survey probe. It must be noted, however, that these initial tests, since there was no blade rotation with the corresponding centrifugal acceleration and blade vibration, can be considered as preliminary and probably conservative. It is possible that even the single-spanwise-tube configuration would work in a real rotor environment.

Airfoil Drag

The model section drag coefficient data without ice are presented in figure 7 as a function of section angle of attack. In this figure data are presented for the clean model without the boot and for the model with the boot, both deflated and inflated. Also shown in figure 7 are published data (ref. 4) for a NACA 0012 airfoil section, both smooth and with standard roughness. These data provide a means to evaluate and validate the measurements made with the wake-survey probe. Figure 7 also includes the results of the flow separation studies, made by observing tufts, which show the effect of the pneumatic boot on the airfoil stall characteristics.

The data in figure 7 are for a tunnel speed of 67 m/sec (150 mph). As noted in the previous section, data were obtained at two tunnel speeds, 67 and 112 m/sec (150 and 250 mph). Since both speeds were well below the region where compressible flow effects become important (i.e., $M_0 \geq 0.4$), the drag coefficients were essentially the same for the two test speeds. Figure 7 shows that the clean-model data agreed very well with the smooth-airfoil reference data, thereby validating the probe results. The data with the boot installed, but uninflated, indicate a drag penalty that decreased with angle of attack. This penalty was about 20 percent at low angles and decreased to zero at higher angles. However, this penalty could probably be reduced to zero if the boot were recessed flush with the surface of the wing. In any case the penalties were less than the difference between the smooth and standard-roughness reference airfoil drag data.

The drag associated with the inflation of the boot was quite large, with drag increases ranging from about 50 percent at the low angles of attack to nearly 300 percent at higher angles of attack. Similar results were observed in the stall angle data. With the boot deflated, the stall angle of attack was about 16°, nearly the same as that of the smooth reference airfoil. When the boot was inflated, however, the stall angle was reduced to about 9.4°. This result, although severe, may still be acceptable since the rotor blade cyclic pitch excursions result in angles of attack that are typically less than 8°. Consequently accidental boot inflation should not cause blade stall.

Figure 8 presents plots of drag coefficient as a function of angle of attack for two cases: (1) data repeated from figure 7 for the inflated boot without any ice present; and (2) the envelope of the drag data taken when the test section had about 1 cm of ice on its leading edge. (Data from both rime and glaze ice conditions are included within this envelope.) As noted earlier, helicopter pilots and test engineers have told us in informal conversations that helicopters like the UH-1H can tolerate about 1 cm of ice on the main rotors without severe consequences, such as inordinate torque rise caused by ice drag or excessive shaking and vibration due to unsymmetrical ice shedding on the main rotors.

Figure 8 shows that with 1 cm of ice on the leading edge the flow separates when the angle of attack exceeds about 6°. Therefore we should expect that with 1 cm of ice the airfoil performance will deteriorate drastically for angles of attack greater than 6°. On the other hand, figure 8 shows that with the boot inflated and no ice, the airflow separated at about 9.5° and the drag coefficient was about the same or lower than it was with 1 cm of ice. We therefore conclude that, since the helicopter can fly with 1 cm of ice, the inflation of the boot with no ice should not produce severe or catastrophic results.

Deicing Performance

The pneumatic boot deicing performance and characteristics are evaluated in figures 9 to 19. In figures 9 to 13, comparing the drag measured before and after actuating the boot yields a direct indication of the boot deicing performance. Figures 14 to 19 are a series of photographs of the boot for several deicing sequences. Figures 9 to 13 show data for the two types of icing-deicing sequences. In figures 9 and 10 the model was iced and deiced at the same angle of attack. In figures 11 to 13 the model was iced at one angle and deiced at another. In each case the first angle listed is the angle at which the model was iced, and the second is the deicing angle. Data are presented for two tunnel temperatures, namely -6.1° C (21° F) and -14.4° C (6° F). These temperatures gave representative glaze and rime ice conditions, respectively. For each temperature shown, ice accretion resulted in a significant increase in drag coefficient. However, the increases in drag coefficient were generally less at the colder temperature than at the warmer temperature. This result is consistent with the fact that rime ice shapes are smoother than glaze ice shapes. As shown in figures 9 to 13 activating the pneumatic boot at either temperature resulted in a significant decrease in these penalties. The residual drag was due to the residual ice left on the model (both on the boot and behind the boot). In each case shown, the data represent one cycle of boot inflation; however, additional cycling of the boot seemed to have little additional effect on removing the residual ice. The residual drags shown are therefore a direct measurement of the boot performance, and as shown in figure 9 the boot was quite effective especially at the warmer temperatures. The boot tended to be less effective at the colder temperatures, but in each case the boot resulted in a reduction in drag that could be the difference between a rotorcraft completing its mission or getting into serious difficulty. For example, in figure 13 (for $T_0 = -14.4°$ C) even though the residual drag at the cold temperatures was 55 percent, activating the boot at 9.4° angle of attack resulted in the flow over the blade reverting from a separated to an attached condition. Comparing the two types of icing-deicing sequences tested did not show any definite trend. It is inconclusive whether the slow variation in cyclic pitch used here could in any way be representative of the real rotor motion.

Typical icing-deicing sequences are depicted in figures 14 to 19 for both the upper (suction side) and lower (pressure side) surfaces. Figures 14 to 17 show the glaze icing condition (i.e., at warmer temperatures) at two different angles of attack. As shown in these photographs the icing limits along the chord, since both of these test points were at positive angles of attack, were greater on the lower surface than on the upper surface. Also the icing limit on the lower surface increased with increasing angle of attack. Figures 18 and 19 show a rime ice condition. Compared with the previous two photographic sequences, the ice at this lower temperature was much whiter and grainier and was not as peaked or double-horn shaped at the leading edge. In each of the deicing cases shown, the boot was fairly effective in removing ice on the upper surface but not as effective in removing ice on the lower surface. Also the effectiveness of removing ice from the lower surface was less at the lower temperatures. Comparing these results with the drag results given previously indicated that most of the observed drag rise resulted from the ice on the upper surface. This was especially evident for the rime ice case (figs. 18 and 19), where very little of the lower ice was removed but, as shown in figure 13 (for $T_0 = -14.4°$ C), the drag was reduced from a large value with separated flow to a lower value with attached flow. Again, as shown in figures 14 to 19, the residual ice was greater for the rime ice case and resulted in higher residual drags. In all the sequences shown the residual ice was well fractured, and therefore the boot performance should be better if the centrifugal and vibratory forces on a real rotor were present.

NASA Ames-Lewis Rotor Program

The next step in this program is to see how pneumatic deicer boots perform on full-scale rotating blades. NASA Ames has begun a program to test boots on a UH-1H helicopter. A series of nonicing tests will first be performed - including tie-down, hover, and full-flight evaluation. If these nonicing tests are successful, icing tests should follow.

CONCLUDING REMARKS

These initial tests of a pneumatic deicer boot on a helicopter rotor blade yielded some answers to several of the basic aerodynamic questions posed by the Lockheed-California Company in 1973. Since the blade was fixed in the tunnel (nonrotating) and since the tunnel speeds were limited to Mach numbers less than 0.4, these tests could not simulate the mechanical, rotational, cyclic pitch, vibrational, and high-tip-speed environment of an operational rotor. However, some important results were observed. First, the drag penalties of uninflated boots were small as compared with drag penalties caused by 1 cm of ice. These penalties were no worse than experienced with today's blade foreign-object-damage shields and would probably be eliminated if the boots were recessed flush on new blade designs. Second, although the aerodynamic effect of inflating the boot without ice was sizable, for most angles of attack the penalties were no worse than those already accepted on fixed-wing aircraft. Even the relatively larger tube diameters on the small-chord airfoil did not lower the stall angle into the normal region of rotor operation. At the same time these penalties proved to be significantly less than those observed with 1-cm accretions of ice. Third, the pneumatic boot proved to be an effective deicer even at low temperatures (-14.4° C) and in a probably very conservative test environment. It must be noted, however, that some of these results could be different on a real rotor, especially the aerodynamic effects at the higher tip speeds, but in that case the deicing performance would probably be more effective.

Because the pneumatic boot effectively reduced the icing drag penalty without causing any other serious aerodynamic penalties, NASA Ames has begun a program that includes full-scale flight testing of the pneumatic boot on helicopter rotors. If the boot material withstands the severe rotor environment in flight and if no further significant aerodynamic penalties arise, perhaps the pneumatic boot can be developed into a lightweight, low-cost, low-power, and easily maintained deicer system for rotor applications.

REFERENCES

1. Aircraft Icing. NASA CP-2086, 1979. (Also FAA-RD-78-109.)

2. Werner, J. B.: Ice Protection Investigation for Advanced Rotary-Wing Aircraft. LR-25327-10, Lockheed-California Co., 1973. (USAAMRDL-TR-73-38, AD-771182.)

3. Bowden, Dean T.: Effect of Pneumatic Deicers and Ice Formations on Aerodynamic Characteristics of an Airfoil. NACA TN-3564, 1956.

4. Abbott, Ira H.; and von Doenhoff, Albert E.: Theory of Wing Sections. Dover Publications, Inc., 1959.

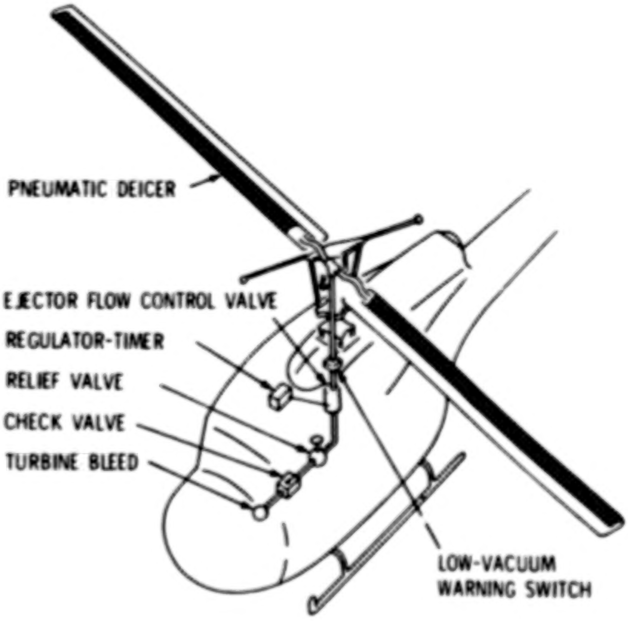
PNEUMATIC DEICER
EJECTOR FLOW CONTROL VALVE
REGULATOR-TIMER
RELIEF VALVE
CHECK VALVE
TURBINE BLEED
LOW-VACUUM
WARNING SWITCH

Figure 1.- Main rotor application pneumatic deicer.

Figure 2.- Pneumatic boot on rotor model installed in 6 × 9 ft. NASA Lewis Icing Research Tunnel.

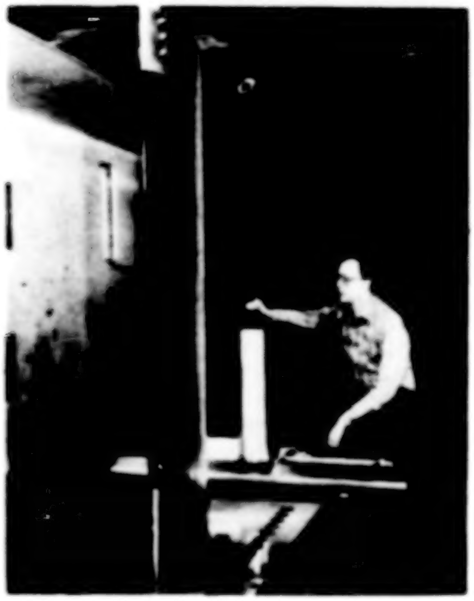

Figure 3.- Pneumatic boot on rotor model and wake survey probe in NASA Lewis Icing Research Tunnel.

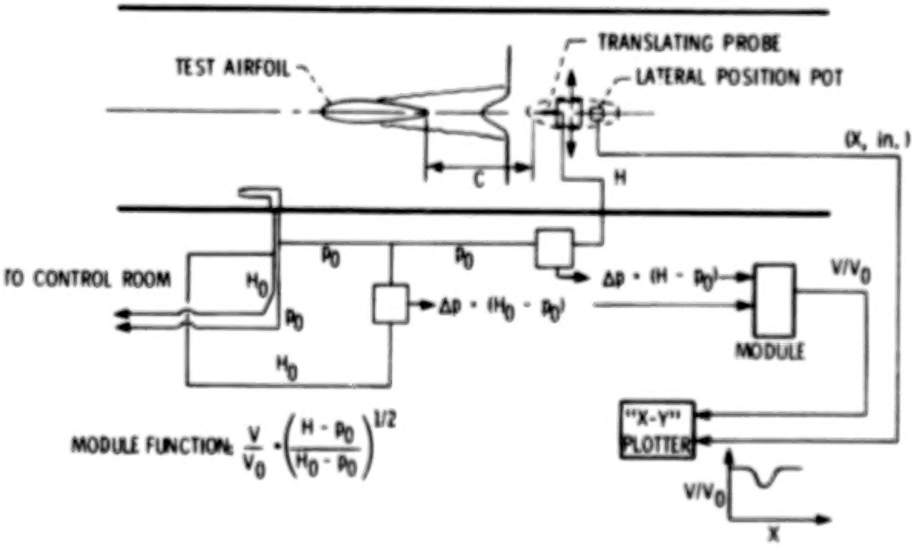
TRANSLATING PROBE
TEST AIRFOIL
LATERAL POSITION POT
(X, in.)
C
H
P_0
P_0
TO CONTROL ROOM
H_0
P_0
H_0
$\Delta p = (H - P_0)$
$\Delta p = (H_0 - P_0)$
V/V_0
MODULE
"X-Y" PLOTTER
V/V_0
X
MODULE FUNCTION: $\frac{V}{V_0} = \left(\frac{H - P_0}{H_0 - P_0}\right)^{1/2}$

Figure 4.- Translating probe instrumentation.

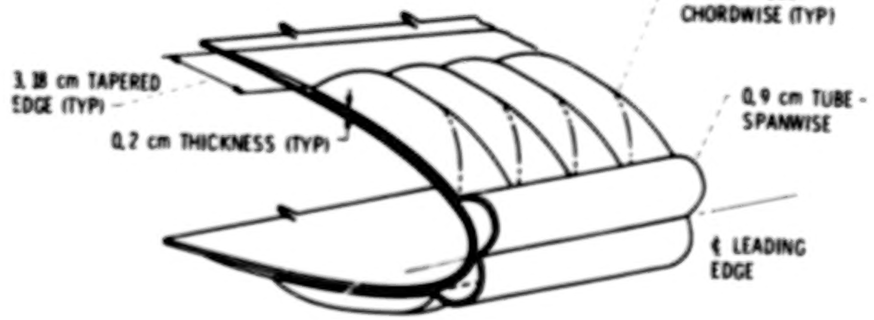
1.27-cm TUBE - CHORDWISE (TYP)
3.18 cm TAPERED EDGE (TYP)
0.2 cm THICKNESS (TYP)
0.9 cm TUBE - SPANWISE
℄ LEADING EDGE

Figure 5.- Typical cross section of installed deicer (inflated), small tube.

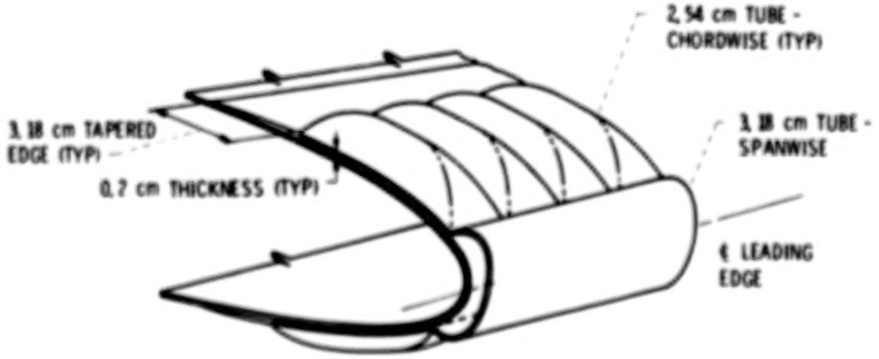
2.54 cm TUBE - CHORDWISE (TYP)
3.18 cm TAPERED EDGE (TYP)
0.2 cm THICKNESS (TYP)
3.18 cm TUBE - SPANWISE
℄ LEADING EDGE

Figure 6.- Typical cross section of installed deicer (inflated), large tube.

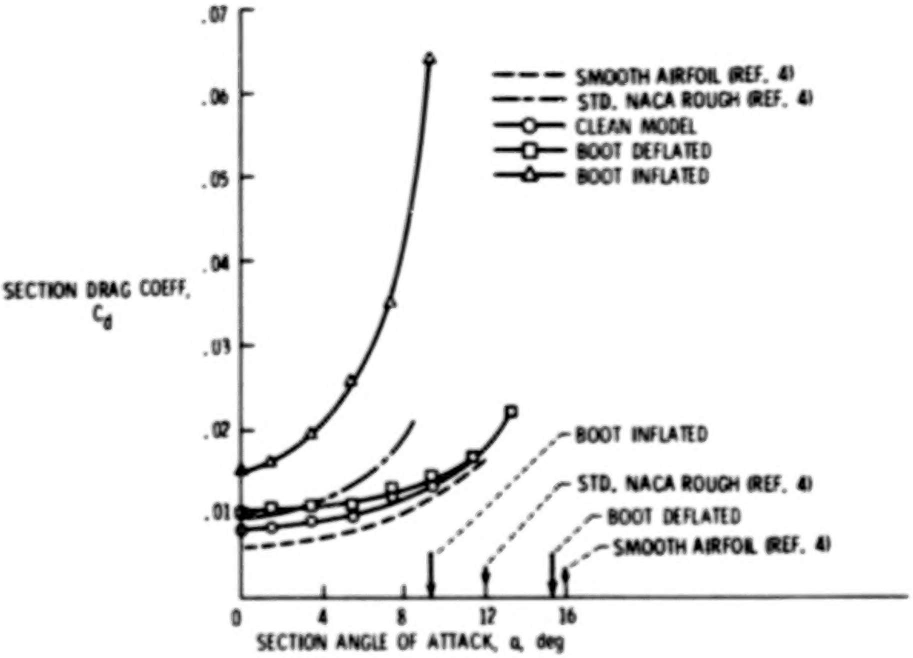

Figure 7.- Helicopter rotor model section drag. NACA 0012 airfoil (no ice); V = 67 m/sec.

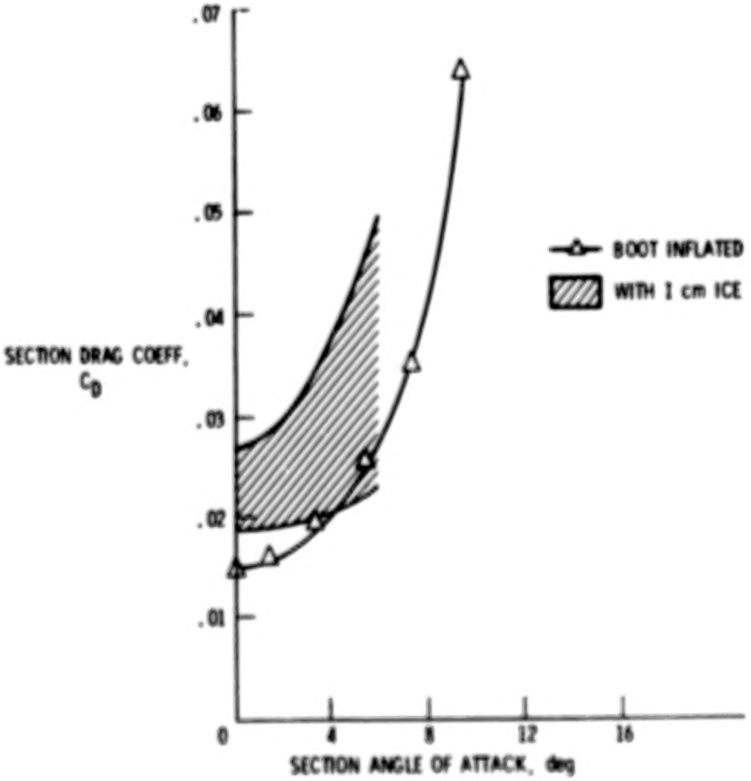

Figure 8.- Helicopter rotor model section drag. NACA 0012 airfoil; V_0 = 112 m/sec.

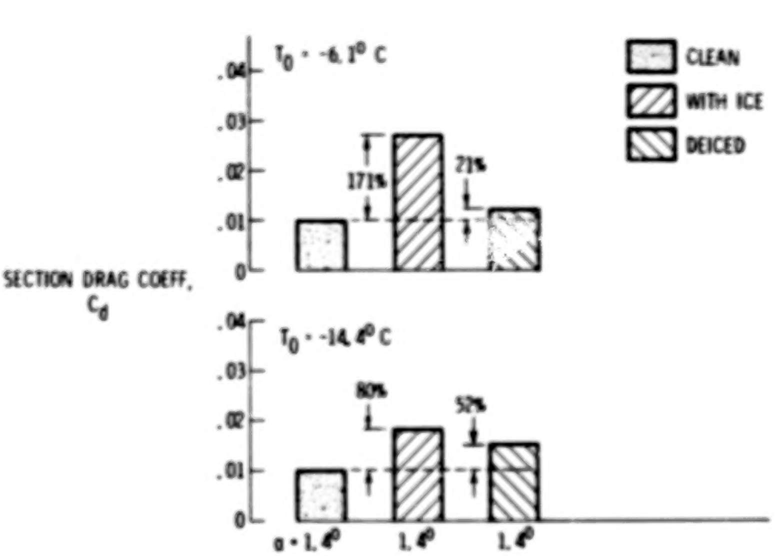

Figure 9.- Section drag of helicopter rotor model with pneumatic boot. Ice-deice sequence; $\alpha = 1.4^\circ/1.4^\circ$; $V_0 = 112$ m/sec.

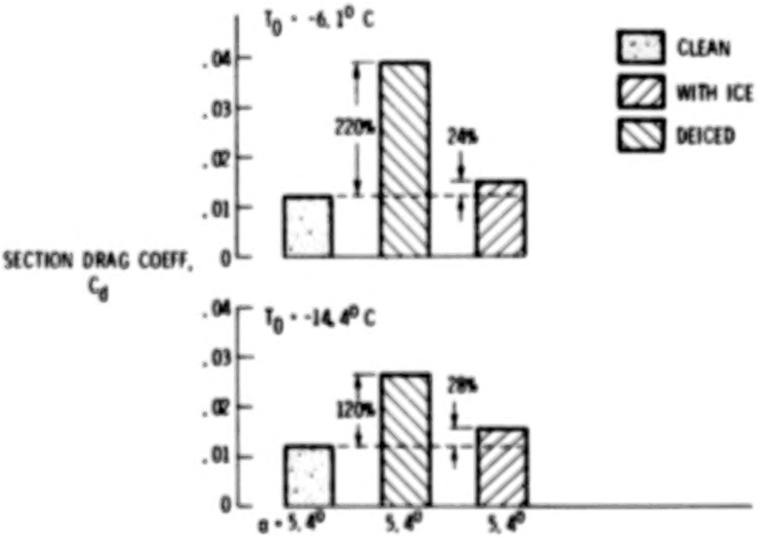

Figure 10.- Section drag of helicopter rotor model with pneumatic boot. Ice-deice sequence; $\alpha = 5.4^\circ/5.4^\circ$; $V_0 = 112$ m/sec.

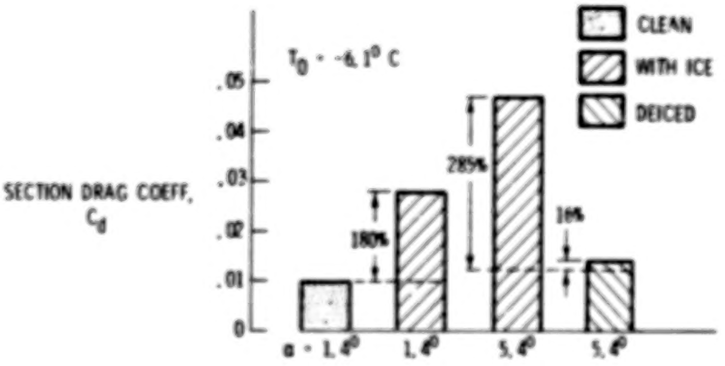

Figure 11.- Section drag of helicopter rotor model with pneumatic boot. Ice-deice sequence; $\alpha = 1.4^{\circ}/5.4^{\circ}$; $V_0 = 112$ m/sec.

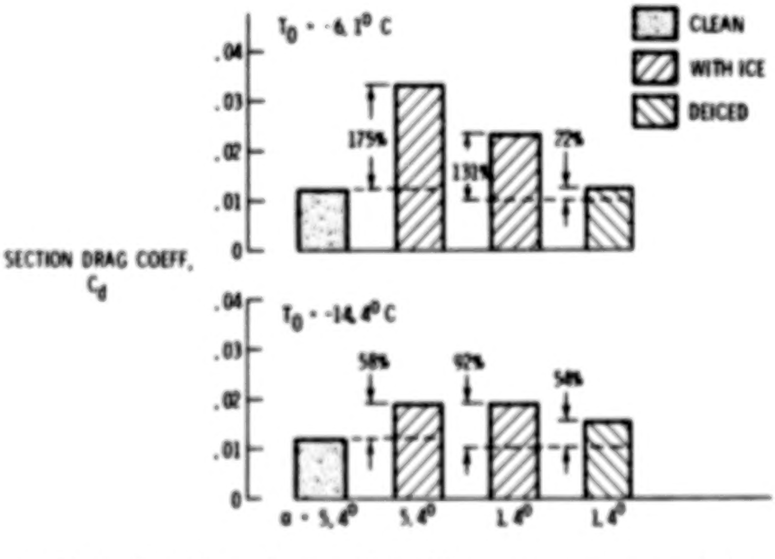

Figure 12.- Section drag of helicopter rotor model with pneumatic boot. Ice-deice sequence; $\alpha = 5.4^{\circ}/1.4^{\circ}$; $V_0 = 112$ m/sec.

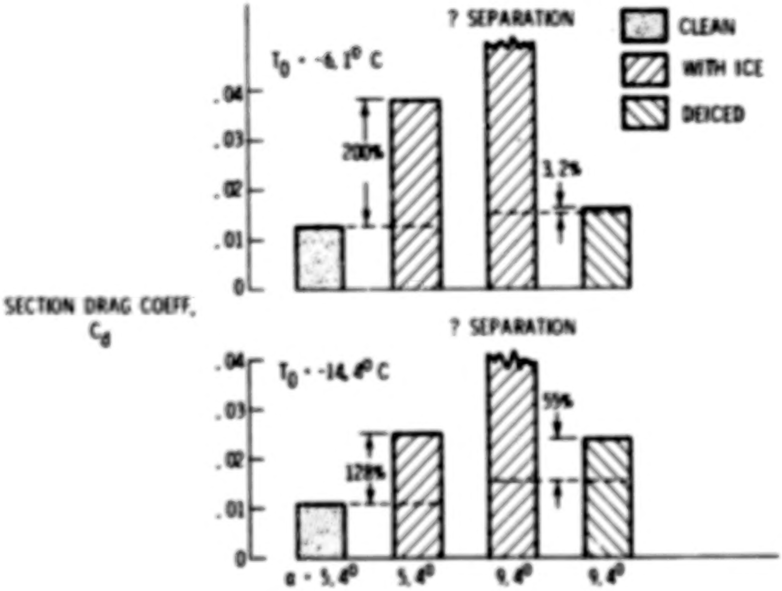

Figure 13.- Section drag of helicopter rotor model with pneumatic boot. Ice-deice sequence; $\alpha = 5.4^\circ/9.4^\circ$; V_0 = 112 m/sec.

WITH ICE
DEICED

Figure 14.- Typical ice-deice sequence. Upper surface; $\alpha = 1.4^\circ/5.4^\circ$; $T_0 = -6.1^\circ C$; V_0 = 112 m/sec.

WITH ICE DEICED

Figure 15.- Typical ice-deice sequence. Lower surface; $\alpha = 1.4^{\circ}/5.4^{\circ}$; $T_0 = -6.1^{\circ}C$; $V_0 = 112$ m/sec.

WITH ICE DEICED

Figure 16.- Typical ice-deice sequence. Upper surface; $\alpha = 5.4^{\circ}/5.4^{\circ}$; $T_0 = -6.1^{\circ}C$; $V_0 = 112$ m/sec.

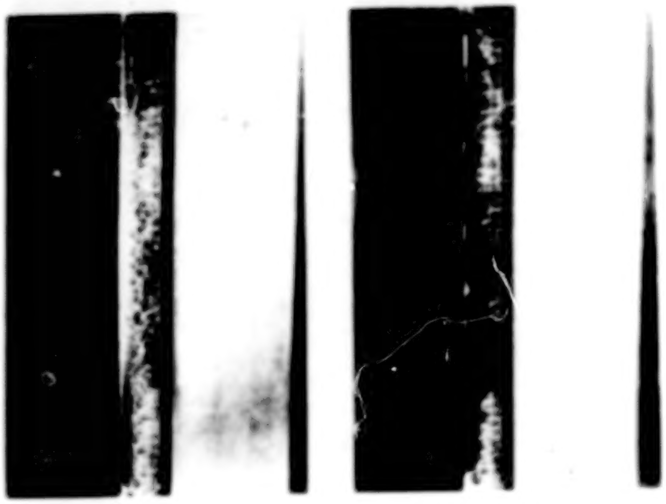

WITH ICE

DEICED

Figure 17.- Typical ice-deice sequence. Lower surface; $\alpha = 5.4^\circ/5.4^\circ$; $T_0 = -6.1^\circ C$; $V_0 = 112$ m/sec.

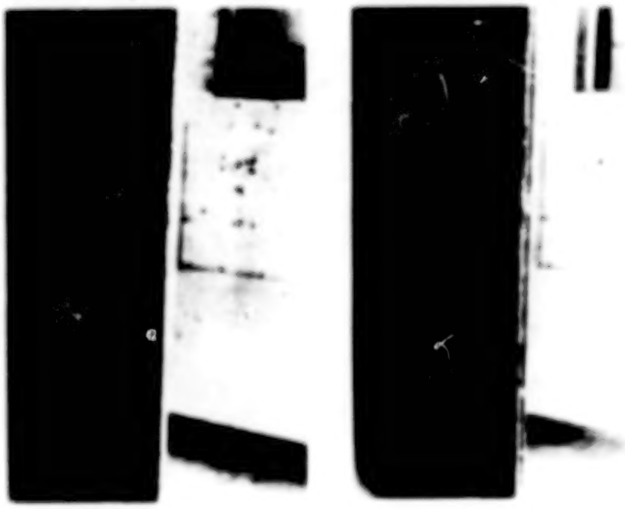

WITH ICE

DEICED

Figure 18.- Typical ice-deice sequence. Upper surface; $\alpha = 5.4^\circ/9.4^\circ$; $T_0 = -14.4^\circ C$; $V_0 = 112$ m/sec.

WITH ICE

DEICED

Figure 19.- Typical ice-deice sequence. Lower surface; $\alpha = 5.4^\circ/9.4^\circ$; $T_0 = -14.4^\circ C$; $V_0 = 112$ m/sec.

BLANK PAGE

BLANK PAGE

AIRCRAFT OPERATING EFFICIENCY ON THE NORTH ATLANTIC

A Challenge for the 1980's

Robert Steinberg
NASA Lewis Research Center
Cleveland, Ohio

Introduction

It is anticipated that more United States air carriers than ever will be providing service across the North Atlantic during the 1980's. As additional cities in both the south and the mid-west achieve gateway status, the twice daily setting of the North Atlantic Organized Track System will become more demanding. This will be compounded further by the need to fly minimum fuel tracks in order to maintain a competitive edge in today's deregulated environment.

There are a number of changes which will take place within the next 24 months which could have important consequences for Atlantic flight operations for the next decade. The purpose of this paper is: (1) to identify these changes and discuss their impact on aircraft operating efficiency, (2) to review possible alternatives for North Atlantic air carriers and (3) to suggest strategies and actions which may have a considerable impact on fuel savings for years to come.

Background

The North Atlantic Track System (NATS) consists of an array of movable tracks which are designed to provide safe transit for high volume air traffic crossing the North Atlantic and normally consists of seven to ten tracks each separated by 222 km*(120 miles) and each providing a choice of altitudes between 9.5 km (31,000 feet) and 11.9 km (39,000 feet) with a 600 m (2000 foot) vertical separation. The air traffic control centers at Gander, Newfoundland and Prestwick, Scotland are respectively responsible for the east- and west-bound traffic flow. The location of the NATS changes twice in any given 24-hour period and is dependent mainly on the current weather, air traffic control (ATC) considerations, desired routing, and traffic density. A detailed knowledge of the wind and temperature fields is essential if the traffic flow is to take full advantage of prevailing meteorological conditions.

Changes on the North Atlantic

A number of important changes relating to the track spacing, numerical forecast models used for weather prediction and ATC operations will be occurring over the next 24 months, which if considered singularly could have an important impact on flight operations; however, when taken collectively they have the potential for determining the operating efficiency on the North Atlantic for the next decade. I refer specifically to the following:

---

*Changed to 110 km (60 miles) in October 1980.

1. The change in the latitudinal track separation from 222 km (120 nautical miles) to 110 km (60 nautical miles). This reduction, in the latitudinal separation, will provide an opportunity for a greater number of aircraft to fly closer to the minimum fuel track (MFT).

   However, in order to take full advantage of this change and improve operating efficiency, it will be necessary to more accurately define the location and intensity of the jet streams as a function of time. In short, a more representative prediction model is needed to maximize the advantage of this change to the air carriers.

   There is one view that if one is able to better define the optimal route then every carrier would request the same track (and altitude), and the delays thus created would have, on balance, a negative impact. While there is a modicum of truth in this especially if one could always predict the location of the most fuel efficient route, the fact of the matter is that our current information concerning the exact whereabouts of the jet streams is far from perfect. Figure 1 shows the route requests from five carriers between London and New York. This case is not atypical and indicates that there is a difference of opinion. In a closely spaced track system this difference could be critical. A small error in the placement of the jet stream can place an aircraft in substantially differing wind regimes and could lead to a dramatic reduction in a tail wind (ending up on the cyclonic shear side of the jet) or worse still, an increase in air temperature accompanying the drop-off in wind speed.

2. The availability of an advanced operational forecast model from Bracknell (British Weather Service) outputted in the Suitland format. Bracknell plans to provide an advanced analysis and forecast model which is expected to be operational in early 1982. While many of the details have not been released, it is anticipated that Optimal Interpolation will be used in the analysis and a 15 level grid point model will be used to advance the analysis in time, with the data outputted in the Suitland (Marsden Square) format of 2-1/2^{0} x 5^{0}. Bracknell will be using a Cyber 203 computer which should greatly increase the computing power available for the 1980's. In fact, four complete daily analyses and forecasts are probably within the capability of this system. The current forecast from Bracknell is available about 4-1/2 hours after synoptic time (0000Z, 1200Z) and is transmitted within 1-1/2 hours. Bracknell is also planning to develop a fine-mesh model limited to the North Atlantic Ocean basin.

3. The availability of an advanced operational forecast model from Suitland (United States National Weather Service). Suitland expects to incorporate an analysis model using Optimal Interpolation in

about 1-1/2 years. Their advanced 12 level spectral forecast model is already operational (August 12, 1980). It is anticipated that Suitland will have a new computer installed by the middle of 1982. Currently, Suitland provides a forecast between 5-1/2 to 6-1/2 hours after synoptic time (000Z, 1200Z) and transmits this data to the air carriers within two to four hours.

4. Gander will shortly be installing a new computer system (GATTS II) which should provide for improved operating efficiency. Although flight following is still done with paper strips, CRT displays are used to advantage throughout. The system has the potential for a considerably faster response time than GAATS I and has built-in provision for expansion. While the algorithm for calculating a minimum time track (MTT) remains essentially unchanged, the Suitland forecast used to develop the MTT no longer requires conversion to punched paper tape, but goes directly into the GAATS II computer. Gander uses the Suitland forecast in the development of an MTT for the east-bound flow.

   Substantial improvements in operating efficiency will be possible as ATC allows more aircraft to obtain requested enroute step climbs. However, any major improvement must await the availability of more accurate and/or timely weather data on which to develop MTT's.

5. Prestwick ATC will go to a fully computerized system. Track analysis, planning functions, allocation of flight paths as well as conflict and avoidance prediction and resolution will be within the automated capabilities of the new computer system. Prestwick presently, although it calculates an MTT, relies on the MFT's sent in by air carriers 20 hours before departure to develop the daily tracks. The MFT's sent in by air carriers are based on at least four forecast models (United States, England, France, Federal Republic of Germany). In theory, the Prestwick approach to the development of an MTT is sound; however, in practice it is somewhat limited because of differences between various weather prediction models as well as differences between the various algorithms used by air carriers to calculate their MFT's.

   Prestwick will also have the ability to talk computer-to-computer with all oceanic ATC centers. It is important that the forecast information base be the same because of the development of estimated times of arrival at check points and is especially important in transferring control of aircraft at 30° west from Prestwick to Gander.

Possible Alternatives

It is clear that given all the changes which are in progress, the overall impact on carrier operating efficiency will be greatest if the result is a more accurate track determination by Gander and Prestwick. The North Atlantic air carriers also stand to benefit from the introduction of improved weather prediction models, but the extent of that benefit remains to be determined. It may be that even these forecast models may not provide the required spatial resolution. Each time the model resolution is doubled, the computer running time is increased by a factor of eight.

It is possible that a more cost effective approach might be through the use of multiple daily analyses (rather than forecasts) which could provide more timely data. For example, if four analyses were available each 24-hour period (instead of the current 2) it could be possible to fly the Atlantic on a 6 to 8-hour old analysis rather than a 24-hour forecast. Use of the analysis not only has the advantage of providing more current data on which to base an MFT, it also can be made available much earlier (less computer running time) since it does not require a translation in time (a forecast). In reality a simple non-dynamic forecast could be included with no substantial increase in computer running time.

In essence, it is suggested that an alternative to high resolution prediction models might be the use of multiple analyses which retain the meteorologically significant structure (through advanced assimilation techniques) of the atmosphere and provide this information in a timely fashion.

An alternate approach could be to use a fine-mesh model limited to the North Atlantic Ocean basin to provide a more detailed space-time description of the jet streams. This could produce a high resolution forecast yet because the model is not global, would require a much shorter running time on the computer.

Helping the Carriers

The air carriers, including Gander and Prestwick, need to know which advanced forecast model more accurately represents their region of interest (i.e., 20 kN/m^2 (200 mb) - 30 kN/m^2 (300 mb) level). Since both the Suitland and Bracknell products will be available in the same output format, it should be relatively simple to run comparisons on the North Atlantic with actual data to make this determination. A parallel effort also needs to be made to evaluate the potential of using more timely analyses as the basis for an MTT rather than a forecast. In essence, comparisons similar to those suggested above are presently being made in the NASA Commercial Aircraft Fuel Savings Program; however, it will involve comparing the older forecast models in use in 1979, rather than the more advanced assimilation and prediction models which will be in operation within 24 months.

The limited area fine-mesh model for the North Atlantic basin, which may become available through Bracknell, will also need to be evaluated from a carrier/ATC point of view.

Given the new methods of data assimilation and the higher spatial resolution of the new forecast models, Gander and Prestwick will need to review the way they calculate MTT's. For example, when using the Bracknell 15 level grid point model, a linear interpolation in the vertical near the tropopause may no longer be valid. Also in light of the 110 km (60 nautical miles) longitudinal separation, should a more accurate algorithm be used to develop the MTT?

There is also a question of the methods of interpolation as well as the algorithms presently used by the air carriers in developing their MFT's, since it is these MFT's which Prestwick currently uses as the basis for its daily track determination. There are indications that at the very least these calculational techniques need to be reviewed and perhaps standardized, especially in view of the higher resolution forecast models which will soon become operational.

Since the trend is toward more data rather than less coming from National Meteorological Centers, the current data transmission rates (1050 baud from Suitland) need to be reviewed. As more timely data becomes available, it becomes more important to be able to provide this data to the carriers in a mode such that the time for transmission is only a small fraction of that required to develop the forecast (or analysis). Currently Suitland develops a forecast in 5-1/2 to 6-1/2 hours after synoptic time. The transmission time (including requests for repeats due to errors) runs between 2 to 4 additional hours. Technically there would be no difficulty in going to 2400, 4800 or even 9600 baud to improve the transmission time. More than likely the additional cost for transmission would more than be made up by the advantage gained from more timely flight planning.

Gander and Prestwick have somewhat differing philosophies concerning the daily development of the track system. Although both centers develop the tracks based on a 24 to 30 hour forecast, Gander depends heavily on its computer developed MTT (as well as other ATC considerations) whereas Prestwick depends more on the daily carrier initiated (MFT) route requests. As a result of differences in forecast models and/or carrier MFT algorithms (as well as the location of departure cities) the Prestwick track system tends to be broad while the Gander system more closely straddles the MTT. Because of the somewhat larger track selection offered by Prestwick, it becomes more important that the west-bound carriers develop their flight plans on 12-hour old data rather than 24. In many cases this has not been possible because a forecast based on the 000Z observation is not available in time. This situation can be improved for the carriers if Bracknell's current plans to produce four analyses per day are put into operation. The analysis would have to be outputted in the Suitland format but probably could be available to the carriers within several hours after synoptic time, which should be sufficient for flight planning.

Conclusion

The present economic situation places severe limitations on what individual air carriers can do to improve aircraft operations on the North Atlantic. Yet it is because of the economics superimposed on a deregulated environment that efforts need to be made to assist the United States air carriers in improving their operating efficiency. The author has pointed out areas of interest to the carriers where a continuing and updated knowledge of present and future ATC and National Weather Service operations (here and abroad) as well as carefully considered and developed strategies may be required to maximize opportunities for improved operating efficiency.

It might be beneficial to the carriers if they more fully understood the details of how the new forecast models will impact their future operations. The soon to be available improved prediction models using more sophisticated data assimilation techniques in the analysis scheme as well as increased levels in the vertical hold the promise of more accurately reflecting the observed data and thus representing the space-time distribution Atlantic weather in a more realistic way. However, the carriers need to be able to evaluate these different models as well as multiple analyses schemes on a continuing basis so they can provide both input and direction to the National Weather Service and ATC on meteorological matters before they impact flight operations.

Because the changes which are about to take place over the next 24 months will have such a long term impact on North Atlantic flight operations, it is important that the carriers begin to explore these opportunities now.

Acknowledgments

The work described in this paper as well as the NASA Commercial Aircraft Fuel Savings Program which provided the basis for this investigation would not be possible without the continuing support and encouragement of Mr. Warner Stewart, Director of Aeronautics, Lewis Research Center and Mr. Donald L. Nored, Chief of the Transport Propulsion Office, Lewis Research Center.

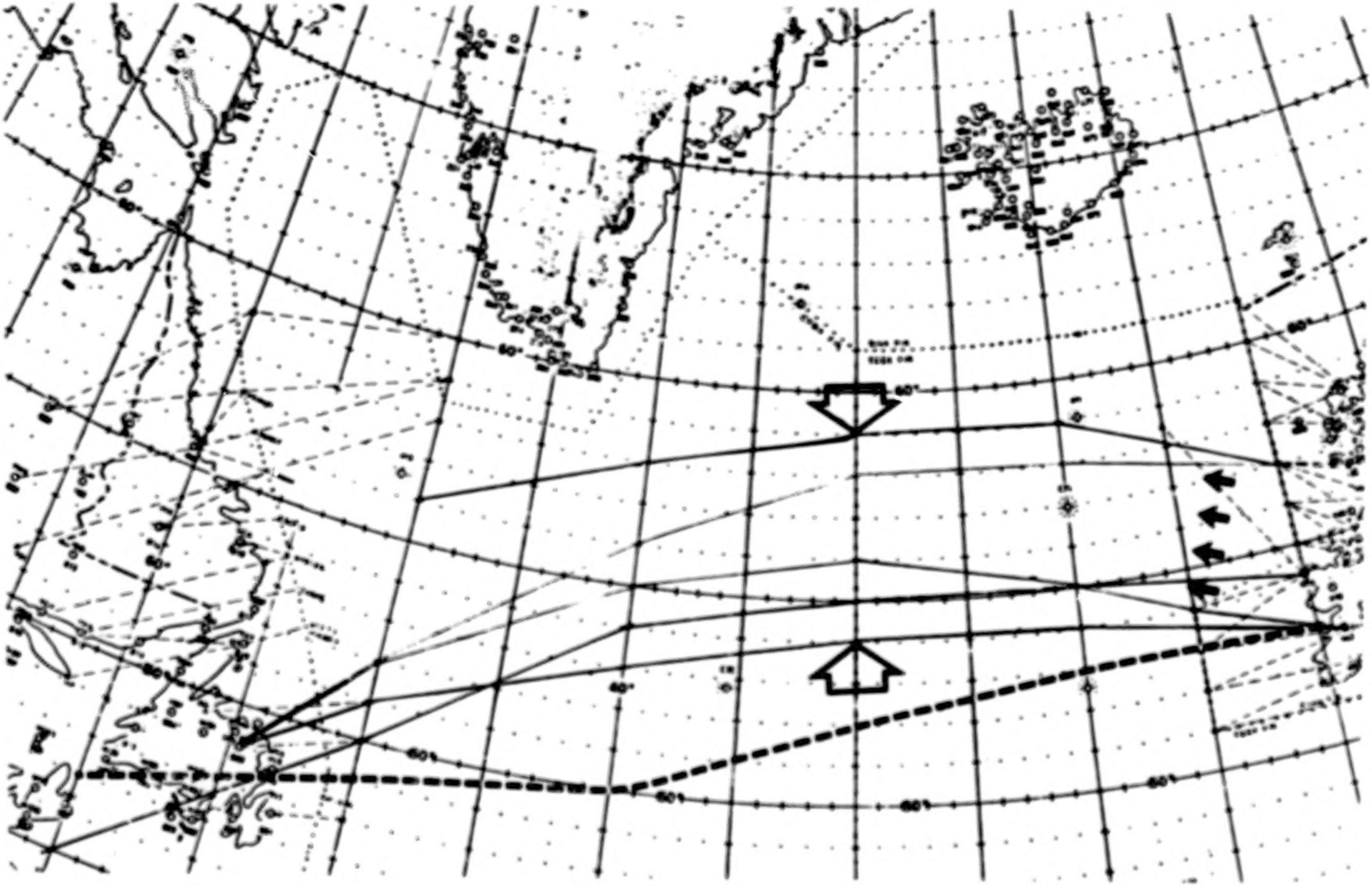

Figure 1.- Route requests from five carriers between London and New York. The dashed line indicates the previous 12-hour east-bound MTT.

BLANK PAGE

BLANK PAGE

FIREWORTHINESS OF TRANSPORT AIRCRAFT INTERIOR SYSTEMS

John A. Parker and D. A. Kourtides

Ames Research Center

INTRODUCTION

This paper presents an overview of certain aspects of the evaluation of the fireworthiness of air transport interiors. First, it addresses the key materials question concerning the effect of interior systems on the survival of passengers and crew in the case of an uncontrolled transport aircraft fire. Second, it examines some technical opportunities that are available today through the modification of aircraft interior subsystem components, modifications that may reasonably be expected to provide improvements in aircraft fire safety. Cost and risk benefits still remain to be determined.

Space permits only the discussion of three specific subsystem components: interior panels, seats, and windows. By virtue of their role in real fire situations and as indicated by the results of large-scale simulation tests, these components appear to offer the most immediate and highest payoff possible by modifying interior materials of existing aircraft. These modifications have the potential of reducing the rate of fire growth, with a consequent reduction of heat, toxic gas, and smoke emission throughout the habitable interior of an aircraft, whatever the initial source of the fire. It will be shown that these new materials modifications reduce the fire hazard not only because of their unique ablative properties, which help to contain or isolate the fire source, but also because there is a significant reduction in their characteristic flame spread, heat release, and smoke and toxic gas emissions.

SURVIVABILITY CRITERIA FOR AIRCRAFT FIRES

Significantly destructive fires, which have been encountered by transport aircraft, can be classified generally into three kinds (fig. 1): the in-flight fire, the ramp fire, and the survivable postcrash fire. Historical surveys taken over periods of 10 to 15 years for a variety of aircraft under a wide range of operating conditions have shown that the postcrash fire accounts by far, perhaps by a factor of 10, for most of the aircraft fire deaths. As indicated in figure 1 for a 270 passenger aircraft, the probable interaction of the 37,000 to 75,000 liters of jet fuel and ignition sources generated by damaged engines produces a fire source that interacts with the airframe and then with the interior systems to introduce the survivability fire parameters listed in the figure. The in-flight fire, whatever its source, can interact directly with the interior subsystems to ignite and cause them to burn.

It is a basic premise of all subsequent arguments that any vehicle interior will become a totally lethal environment if the fire source is large enough. It is also tacitly assumed that any and all material subsystems of an aircraft interior comprising organic polymeric materials (as shown as fuel load in fig. 1) can also contribute by means of (or may be limited by the fire parameters shown) to the formation of a lethal environment if the fire source and fire growth rate are sufficiently large. It is really unimportant when considering the flammability of the aircraft interior whether the fire source derives from, for example, the ignition of spilled fuel, a cargo bay fire, or arson. What is important, however, is how flammable the interior subsystems are and how large a fire source is encountered. Effects of crash impact on human survivability and of vehicle crashworthiness on the growth of the fuel fire have not been considered in this paper. Only the time rate of change in cabin temperature and the concurrent release of smoke and toxic gas from the combination of the fire source and the fire involvement of the interior have been considered as significant factors in establishing allowable egress times for passengers and crew members. It has been a goal of NASA's "FIREMEN" program to improve the allowable egress time by a factor of 2, that is, from 2.5 to 5 min, by modifying the materials used in aircraft interior subsystems to better understand the conditions imposed by postcrash fuel fire sources.

The ground rules of the SAFER Committee (ref. 1) excluded the in-flight fire case from considerations. This limited somewhat their specific recommendations concerned with the fireworthiness of aircraft interiors systems, such as toxic fume hoods, and fire-fighting methods. The Federal Aviation Regulation (FAR) burner flammability test remains as a recommendation which all must agree has not been related to materials aircraft fire safety. It is reasonable to infer from the foregoing that once an interior system has been ignited with a sufficient fire source that the survival time for the in-flight case can be closely related to the allowable egress time in the postcrash case.

The SAFER Committee has postulated that the evidence from aircraft fire death statistics makes in-flight fires relatively insignificant and that only postcrash fires deserve immediate attention. Postcrash fires cause about 30 deaths per year; recent congressional testimony (ref. 2) suggests that there have been over 300 fire deaths in in-flight fires since 1969. About 419 fatalities are attributed to survivable postcrash fires during the 1969-1978 period according to the same testimony. This recent record of in-flight events should moderate an exclusive interest in postcrash fires. SAFER made two other assumptions: (1) that the principal fire source in aircraft fire deaths is that arising from ignition of a misted-fuel cloud resulting from tank rupture during impact; and (2) that the heat, smoke, and toxic gases produced by the burning fuel are principal factors in the formation of a lethal cabin environment. One might conclude, after considering these two assumptions, that the fireworthiness of aircraft interiors may be a matter of little concern in most cases, and, indeed current activities with antimisting kerosene (AMK) correctly reflect this hypothesis and dominate the SAFER recommendation. SAFER, however, did endorse full-scale simulation of survivable postcrash fires, using a C-133, as a means of assessing the role of the fuel fire on human survivability. Recent results from C-133 tests (to be discussed below), reported in reference 3, seem to indicate that the flammability of interior systems may be the principal factor in the allowable egress time, even in the postcrash fire. Detailed analysis of the fireworthiness of transport aircraft incidents (ref. 4) indicates that under many conditions the flammability of interior systems may be significant in postcrash as well as in-flight aircraft fires. Recent fires in both rapid ground transportation and transport aircraft suggest that under the appropriate conditions, vehicle interiors are destructively flammable, independent of the nature of the large fire source.

INTERIOR SYSTEMS FROM A FIRE POINT OF VIEW

There are two identifiable, distinct, and separate thermochemical mechanisms by which interior materials systems can interact with a given fire source. These mechanisms have been defined in this paper as fire isolation (containment) and fire involvement. The first interaction depends only on the ablation efficiency of the material subsystem component; the second depends on combustion mechanisms that have been shown to depend on the pyrolysis vapor production rate and on the composition of the pyrolysis gases.

Neel et al. (ref. 5) have demonstrated, in a full-scale test with an intact C-47 fuselage, that the lethal effects of a complete burn with an 18,925-liter fuel fire source can be completely excluded from the aircraft interior by means of a lightweight organic ablative foam applied to the aircraft interior skin. No protection from fire penetration is provided by current plastic-bagged fuselage insulation. At present this ablative insulation systems approach has not been found practical by aircraft manufacturers. Kourtides et al. (ref. 6) have demonstrated in full-scale fire containment tests against simulated fuel fire sources, that ablative foams or honeycomb fillers and edge closeouts can effect as much as a fivefold improvement in the fire containment capacity of various kinds of aircraft panels, such as ceilings, walls, lavatories, and cargo bays, while at the same time maintaining the required structural strengths without an appreciable weight penalty.

Here then is a simple, available, and producible new kind of aircraft panel concept ready for application. It is believed that inert ablation efficiency of these new panel systems may be particularly effective in controlling fires in unattended areas of the aircraft. One need only optimize (modify the foam density) the ablation efficiency of these panel structures to provide the required containment times to a designed back-face temperature, probably about 200° C for the expected heat load from probable fire sources. Specific examples of applying the ablative fire-containment method to the fire-blocking-layer concept in aircraft seating and window systems will be described further in this paper.

Fire involvement, largely dependent on material pyrolysis and flammability, is a somewhat separate matter from ablative fire containment. Fire involvement comprises the interaction of a number of factors that contribute to the generation of lethal cabin conditions — ease of ignition, flame spread rate, heat release, and smoke and toxic gas emission. All of these factors interact cooperatively to reduce the probability either of passengers escaping or surviving when trapped. These properties depend on the thermochemical properties of the basic polymer out of which the component has been constructed as well as on the size and intensity of the applied fire source. Unfortunately, most usual laboratory flammability tests (ref. 7) have been carried out at cold-wall radiant heating rates of 2.5 W/cm^2 or less. As will be discussed below, it has been found that the combustible vapor production rate at the wall of the material is the controlling rate process for all of the fire involvement factor. This controlling rate is an intrinsic property of the material and of the applied heating rate. A heating rate of 2.5 W/cm^2 is much too low to characterize materials in the usual fire environment, in which case heating rates are found to vary from as little as 0.5 W/cm^2 to as much as 14 W/cm^2.

A typical example of an aircraft panel construction is shown in figure 2. Current films, inks, substrate films, and face sheets are made up of as much as 25% of contemporary materials of low char yield polymers (to be explained below). They are characterized in terms of ease of ignition by the standard limiting oxygen index test with values from 16 to 23 (percent oxygen in the ignition mixture required for sustained burning with an ignition source of about 1-2 W/cm^2). One should expect them to burn in air under the sustained fire impact of less than 2 W/cm^2 and to burn with increasing rates as the fire source is increased.

Standard panels of this kind were evaluated by Parker et al. (ref. 8) in a full-scale lavatory mock-up using a 2.5-kg hydrocarbon fuel source, with unrestricted ventilation. The fire source burned for about 10 min, with an average peak heating rate of about 8 W/cm^2, typical of a moderate aircraft trash fire. The lavatory panels, when exposed to this critical fire size, lead to flashover which produces a totally lethal environment in different size structures with different materials.

It was concluded from these tests that the high vapor production rate for low-char-yield materials comprising the decorative surfaces and face sheets coupled with this critical fire size combined to achieve this fatal condition. Characterization of the survivability at fire sizes with this lavatory system at less than the critical flashover fire size seems to depend on all the factors listed above that describe the total fire involvement.

Currently, attempts are being made to arrive at a "combined hazards index" or CHI (ref. 9) comprising the lethality of a material exposed to a fire source less than the flashover critical size; the index would combine the rate of heat released, the smoke obscuration, and time to incapacitation due to toxic gas emissions. So far this has required very complex testing, involving animal exposures, variable heating rates, and complex computer data reduction for fire models which depend on vehicle geometry and a presupposed fire scenario.

What is needed is a simple test for materials suppliers and users alike which would permit the selection of polymeric components for design and construction of system components on the basis of the components' enhancement of survivability in an aircraft fire. Parker and Winkler (ref. 10) showed earlier in 1967 that the anaerobic char yield could be estimated from the polymer structure and the cross-linking reactions of the polymer at elevated temperatures. It may be safely inferred from the foregoing that the tools exist with which to design and synthesize polymers with any set or limiting set of fire-involvement properties that the application demands.

Later, Kourtides (ref. 11) and van Krevelen (ref. 12) showed that these char-yield rules could also be applied to calculating the limiting oxygen index (LOI) of thermoplastics in addition to the thermoset system described by Parker and Winkler (ref. 10). Kourtides et al. (ref. 13) took advantage of this rule by developing criteria for selecting thermoplastic molding components for aircraft applications by correlating a linear combination of fire involvement properties with the measured anaerobic char yield. It was also found that when atoms such as chlorine, bromine, sulfur, fluorine, or nitrogen are contained in the polymer, a simple correction in the proportionality constant relating char yield to LOI could account for the variation in flammability properties of the neat polymer. As far as polymer selections are concerned, Fish and Parker (ref. 14) first showed that as long as the polymer did not melt and flow (as do, for example, epoxides, urethanes, and phenolics) all of the significant fire involvement properties of the bulk polymers, such as flame spread rate, ease of ignition, smoke obscuration, and toxic gas production, vary in a regular way (usually linearly) with the vapor production rate of the polymer being heated. Moreover, Fish and Parker showed that this relative vapor production rate can be accurately determined by the simple thermogravimetric analysis of the anaerobic char yield.

In figure 3 it can be seen that the simple and single value of the char yield can readily be used to rank the fire involvement characteristics of individual polymers for selection of candidates for the fabrication of interior system components. It turns out that the materials flammability properties, such as net heat released and the amount of smoke and gas generated at a fixed heating rate (radiative cold wall), are all unique and regular functions of this easily measured or calculated anaerobic char yield value. It should be pointed out, however, that what one is concerned with in estimating the probability of survivability is the rate of the production of these lethal products.

Even though the char yield as defined is more or less independent of the applied heating rate, the rate of char formation and the related flammability properties are determined by the ablation rate, which in turn increases with increasing heating rate. Because the material will encounter a variable heating rate, depending on scenario, SAFER (ref. 1) has recommended that these relative rates should be determined in the Ohio State heat-release calorimeter, in which the heat release and other rates can be measured at variable heating rates. Presumably these rates then can be used to construct any desired heating rate curve to estimate the time-dependent rates of heat, smoke, and gas production. Since these rates may be expected to vary with the thermal history of the sample and with the nature of the flame chemistry, we have preferred to use a propane burner; the burner can accurately simulate the actual time-dependent heating rate functions with a reasonable simulation of the fire-source flame chemistry. Initial screening of samples may be done with radiant-panel sources at a fixed average heating rate at 5-10 W/cm^2. The measured rates in radiant-panel tests related to a real and variable heat source can be determined by a propane gas burner preprogrammed to simulate the time-dependent heating rate encountered with a real fire source. For most cases that involve the fuel fire sources encountered in aircraft fires, the flammability of materials systems can be compared by means of a radiant panel providing an average heating rate of 5-8 W/cm^2, with pilot flame ignition. These results can be correlated with the measured anaerobic char yield, which usually gives a reasonable measure of the combined hazard index. Correlations with char yields have been reported in many studies, and Hilado et al. (ref. 15) have stated that this method is adequate in 90% of the cases studied. On a char-yield scale from zero (polymethylmethacrylate) to 100 (graphite), most contemporary aircraft materials are rated at less than 23, whereas the advanced materials offered in this paper all have values greater than 35. The latter are virtually nonflammable in air and produce little or no smoke or toxic gas.

The ablation efficiency in the fuel-fire environment of bulk polymers and their component derivatives is a different matter, as shown in figure 3. In this case the ablation efficiency increases with increasing char yield from about 23% to about 50%, after which it decreases abruptly. Although most of the flammability properties continue to decrease at char yields greater than 50%, it has been found that materials with char yields between 45% and 60% give the best combination of fire containment and fire involvement properties. Since it is probably true that the ablation efficiency is the principal parameter that governs the change in heat release, smoke, and toxic gas production rates, as these rates vary with applied heating rate, it is not surprising that the polymers, such as phenolics, bismaleimides, and others with char yields in the range of 45 to 60, show very low rates that change very little over an applied heating rate range from 3 to 10 W/cm^2. If it were possible to restrict the choice of advanced aircraft materials to this char yield range, which gives the best combination of fire-resistant properties, correlation of existing laboratory tests with full-scale performance would be highly simplified.

A rather simple correlation of the fire ablation efficiency of experimental aircraft panels in which the face sheets have been modified by choosing high char yield resins is shown in figure 3. The test method has been described by Riccitiello et al. (ref. 16). Here, comparable panels are exposed to a combined radiant and convective source, which has been found to correlate well with a full-scale fuel test. In the figure, the time to back-face temperature rise has been plotted as a function of the exposure time in seconds. The time required to reach a back-face temperature of 200° C has been selected to complete the relative fire ablation efficiencies of the candidate panels. It can be seen, as anticipated by the general trend in fire ablation efficiency of the face-sheet matrix resin composites, that the low-char-yield epoxies and the highest-char-yield conventional polyimides, with char yields of 23% and 70%, respectively, gave the shortest times to back-face temperature rise to 200° C; the bismaleimides and phenolics with char yields of the order of 45% to 60% gave the best performance.

Candidate phenolic and bismaleimide panels selected from this screening study were evaluated by Williamson (ref. 17), in full-scale fire-containment tests in which a variable propane burner was used to simulate the effect of actual burning of aircraft trash bags. It was found that the best fire retarded epoxy panels as baseline with face-sheet resin char yields of 23% reached a back-face temperature of 200° C in about 5 min, whereas the bismaleimide and phenolic panels with a peak heating rate of 6.5 W/cm^2 contained the simulated fire for as much as 15 min at a back-face temperature of 200° C.

On the basis of these tests, a full-scale wide-body transport lavatory was fabricated of phenolic panels (fig. 4). The fire-containment capability of this lavatory with the door closed and with the normal ventilation rate was evaluated in the Douglas cabin fire simulator (CFS). A sustained fire, which reached a peak heating rate of 12 W/cm^2 in 10 min, was started in the lavatory, using simulated aircraft trash. The fire burned itself out in about 1 hr. The effect of the fire on the lavatory is shown in figure 4. The only evidence of any lack of containment is shown in the figure as a slightly scorched area along the door edge. It is believed this slight fire penetration was a result of the limited fire containment of a small amount of polyurethane foam used at the edge of the door, a problem that can be easily corrected by replacing the polyurethane with phenolic foams. The slight damage did not propagate the fire. Otherwise the panels did not burn through or reach back-face temperatures in excess of 200° C over most of their surfaces.

No significant toxic gas was observed in the adjacent cabin area, as evidenced by the survival there of an animal (rat) test subject. A completely survivable environment existed within the cabin for 1 hr; animal subjects survived that period without adverse effects.

It can be concluded that the panels fabricated from the phenolic resins did an adequate job in containing a substantial compartment fire. However, the fact that most of the lavatory outer surface did not reach the design temperature of 200° C suggests that the fire protection ablative system was not fully exploited in this test. It is clear from various studies that the burn times and peak heating rates are controlled by the ventilation rate and the amount of fuel and its distribution in the compartment. One might say that the size of the fire in the test (fig. 4) was conservative. The simulation results with the propane gas burner support a conclusion that these panels could be expected to contain a compartment fire of a much greater severity for 3 to 5 times as long as the standard epoxy panels. The phenolic panels should be able to provide a margin of safety at least 3 times greater than the epoxy panels. This is especially important since similar panel construction is used throughout the aircraft interior where more severe fire sources (postcrash fires) may be encountered, for example, in cargo bays and side wall and ceiling panels.

The effects of face-sheet matrix resin type on the time required for complete fire involvement in a simulated cabin compartment were evaluated in a large-scale flashover fire test facility (fig. 5). A flashover fire test facility was constructed as a modification of the corner test described by Williamson (ref. 17). A ceiling extension panel constructed of the same materials as the wall panels was included. The propane burner shown in the corner, which had been calibrated with aircraft trash bags by metering the propane gas flow, was used as a fire source. The heating rate changes with time, as measured by calorimeters installed in the walls and ceiling, duplicated those of the aircraft trash bags. An arbitrary flash-over criterion was adopted as the time for the center ceiling thermocouple No. 57 to reach 500° C. In a baseline test with Transite (noncombustible and thermally inert), 500° C was reached in about 2 min; this value is represented in figure 6 as T3. With ceilings and wall panels constructed of standard epoxy, the critical temperature of 500° C was reached in less than 30 sec (T0) as observed on thermocouple No. 57, the process being accompanied by large amounts of dense smoke, shown in a separate test, to be largely due to the epoxy resin component of the panel. Next, a fire retardant epoxide panel was evaluated which extended the flashover time to more than 50 sec (T1). As expected with fire-retardant additives, enormous amounts of dense black smoke were generated from these panels almost immediately, but the flashover time was extended by a factor of 2.

Similar constructions were tested using the same phenolic and bismaleimide panels as those used in the fire-containment tests described by Williamson (ref. 17) using the same fire scenario. Very little smoke was observed in either test. The phenolic panels gave a ceiling temperature of 500° C in 60 sec (T2), and the bismaleimide gave a flash-over time greater than 90 sec (T3), the bismaleimide panel being somewhat less resistant to total involvement than the inert Transite panels. In this test, an improvement by a factor of 3 for the time to full fire involvement was observed in comparing the state-of-the-art epoxy panel with the advanced bismaleimide panel; moreover, there was virtually no smoke obscuration. It remains to be seen if a similar relationship will hold for full-scale testing of these advanced panels in the C-133.

It is of interest to see if the flashover times in this test can be correlated with the anaerobic char yields of the constituent resins and the respective oxygen indices. A best correlation was obtained by plotting the product of the time to flashover, T, and the applied heating rate observed at that time due to the burner fire source, as a function of the observed anaerobic char yield or limiting oxygen index. The change in the shape of the fire response curve approaches the limit for the inert Transite. It is interesting to note that the intermediate char-yield materials, the bismaleimide and the phenolic (45-60%), show the same relative ranking in this test as that observed in the fire-containment case. This suggests that not only the char yield but also the fire ablation rate of char formation (slower in the case of the bismaleimides at these heating rates) are factors in the time required for full fire involvement. Even though both face-sheet matrix resin systems produce little observable smoke and presumably low levels of toxic gas, the best panel as determined in both fire-containment and fire-involvement studies seems to be the one derived from the bismaleimide.

At present, the phenolic resin system is the one of choice mainly due to resin costs and processibility. Anderson et al. (ref. 18) have shown that a positive cost benefit can be derived from using this phenolic panel system. This report details the result of a contractual program with the Boeing Commercial Airplane Company to examine the fire characteristics of sandwich panels, using laboratory-scale test procedures. The program had the multiple objectives of improving flammability, smoke emission, and toxic gas emission characteristics of sandwich panels without sacrificing manufacturability or mechanical or aesthetic qualities of the panels.

Figure 2 shows a typical configuration of a sandwich panel considered in the Boeing program. The various laminating resins and the test matrix used for these panels are also shown in this figure.

A full matrix of testing was acomplished and the test results were combined mathematically with material and fabrication costs to arrive at a relative ranking of the candidate materials. The mathematical procedure utilized a weight distribution of parameters (fig. 7); this ranking method identified phenolic as the preferred resin system.

Figure 8 shows the contrast between flame-retardant epoxy resin and phenolic resin sandwich panels with respect to flammability, smoke, and toxic gas emission characteristics. It illustrates the improvements that phenolic resins exhibit over the baseline epoxy system.

Figure 2 is an example of a sandwich panel constructed with a phenolic resin. This construction, similar to that of a 747 partition panel, uses Tedlar (polyvinyl fluoride) as the decorative surface.

Phenolic resins have subsequently been developed further and will be used in the new generation commercial aircraft (e.g., 757 and 767). They will be utilized in a sandwich panel composite configuration, but it will be a crushed-core design concept. This provides for use of the weight advantages of sandwich panels while allowing more intricate contours to be achieved.

Figure 9 shows an example of a crushed-core sandwich panel; the panel shown is similar to that which will be utilized on the 757 and 767 aircraft.

ADDITIONAL REMARKS ON PANEL SYSTEMS AS CEILINGS

The results of the postcrash fire simulation with contemporary materials in the C-133, which will be discussed below, focus attention on the role of the flammability of ceiling panels in propagating the fire, once the fire is started by burning seats. In figure 2, it can be seen that in addition to the composite face sheets, contemporary panels also comprise a decorative surface system that consists of an outer layer of clear polyvinyl fluoride, PVF, and interlayers of additional PVF, acrylate inks, and adhesives. All of these materials are highly flammable. They are present in such small amounts in comparison with the composite matrix resin that they contribute very little to the time to flash-over in the tests already described. However, as mounted horizontally above the seats, they ignite and drip as flaming debris and promote the rapid propagation of the fire throughout the aircraft interior. Even if the new fire-resistant seat is not ignited directly by the intrusion of the fuel fire, direct contact with the ceiling structure may spread the fire rapidly.

Durable, transparent thin films — easy to process by existing decorating methods and with the same excellent maintainability characteristics as contemporary materials — have been exceedingly difficult to find. Although research at Ames has discovered a large number of high-char-yield transparent films that are finding wide application in aircraft windows and military canopies, none of them has the combination of properties required. New polymer research at Ames has identified several candidate polymers generally related to polyesters and polycarbonates that may be long-term solutions. A new high-char-yield polyether-ether-ketone (PEEK) (ref. 19) now being developed is an outstanding candidate to replace the existing polyvinyl fluoride film component. The PVF film has been found to give as little as 18% char yield with a limiting oxygen index of 16%, whereas the new polyether-ether-ketone gives values of 45% for the char yield and a limiting oxygen index of 37%, properties that are theoretically very close to ideal from a flammability point of view. This new film, intended for at least ceiling applications, has been also found to exhibit excellent maintenance characteristics. It will have to be applied with fire-resistant adhesives and inks. Two new polymers have been discovered which may serve this purpose. New fire-resistant ink and adhesive systems based on phosphorylated epoxides and tetrabromoepoxy acrylates are being developed by Kourtides, Parker et al. (ref. 20) to meet these special requirements. In the short term, fire-resistant bismaleimide composites, decorated with an ablative coating or with no decorative system, may be required for the highly fire-sensitive ceiling gases.

Summarizing the panel research and technology program developed under the NASA "FIREMEN" program at Ames Research Center, we have shown that the theory, materials, laboratory tests, large-scale tests, and production-ready panels — with which it would be possible to screen, select, and provide advanced panel systems — are available. And it is known that the advanced panels have a reasonable probability of enhancing human survivability when the interior system of a transport aircraft is subjected to a substantial fire source, whatever its origin. What remains to be done to establish the fireworthiness of these advanced panels is to evaluate them in all full-scale tests of a cabin interior system in the FAA C-133 simulator, using the impact of a real fire threat drawn from likely scenarios. On the basis of heat, smoke, and toxic gas evolved, including the time to full fire involvement, it is anticipated that the increase in allowable egress time will be determined.

POSTCRASH FIRE SIMULATIONS IN THE C-133

Although planned for (ref. 21), there are no satisfactory models for the postcrash fire. Hill and Sarkos (ref. 22) have designed an empirical test that is based on three levels of severity with respect to fire penetration and ignition of the interior systems. Their purpose is to answer the question: "Does the severity of the external fuel fire so dominate the available egress time that the inherent flammability of contemporary systems contributes little or nothing to the available egress time?" Stated otherwise: What is the cost-benefit in modifying the fuel system versus modifying the interior aircraft system? It is certainly not possible to make this trade-off at this time. However, the C-133 test method provides a means of uncoupling the survivability effects of spilled ignited fuel from those of the interior materials system.

This full-scale mock-up, as described by Hill and Sarkos (ref. 22), is shown in figure 10. It comprises a carefully simulated and instrumented C-133 fuselage to permit the evaluation of the external pool fire at three different levels of fire intensity within the fuselage. A fire representing an infinite fire course is created by a 1.2- by 1.2-m (4- by 4-ft) fuel pan placed in front of the open forward door. This opening may simulate some average damage to the aircraft fuselage during a crash-survivable fire with an open door and permits radiation-only penetration of the fuselage under a zero-wind condition. The transfer of heat and mass from the fuel fire is said to be rate-determined by the direction and velocity of the wind at the door.

Only the zero-wind condition (the mildest condition) will be referenced in this paper. An evaluation of this condition, namely about 14 W/cm^2 at the doorway is found to decay to about 0.5 W/cm^2 at the aircraft centerline. The evaluation of the interior environment in the absence of interior aircraft systems suggest that between 5 and 10 min are available for the passengers to escape from the unfurbished aircraft. However, when a simulation was conducted with 16 seats in typical rows with paneling and mock-up thermoplastic occupying about 10% of the aircraft, it was found that the fire that ensued might reduce the egress time to less than 2 min.

One may draw two conclusions from the above: (1) that as far as the qualifying materials for the effect of postfire environment the bunsen burner flammability test does not represent the above; and (2) at least under these conditions, the fire involvement characteristics of the interior materials play a large role in determining the human survivability at least in this scenario.

PROPAGATION OF THE FIRE CHAIN IN THE C-133 POSTCRASH FIRE SIMULATION

A tentative mechanism for the propagation of the fire chain due to the impact of the external fuel fire has been made by Eklund (ref. 23). It has been suggested that the wool-and-nylon-covered polyurethane cushions nearest the door are ignited by a radiant heat pulse with a radiative input greater than 8 W/cm^2, even in the absence of free flame. This threshold has been verified by Hartzell (ref. 24) in separate radiant panel tests. Once ignited, the fire from the seat reaches the ceiling panels; quickly thereafter the so-called "two zone effect," that is, downward radiation of the heat from the hot gas layer, ignites the remaining seats and a complete fire involvement ensues. Based on this scenario significant attention has been given to a short-term fix by applying a fire-blocking layer to the outboard seats. It is believed that the use of a highly efficient elastomeric ablative material, used for thermal protection for the extremely flammable urethane cushioning, may be sufficient.

SEAT DESIGN AND DEVELOPMENT BASED ON COMPONENT RESPONSE TO THE POSTCRASH FIRE

It is clear from the foregoing C-133 test results with contemporary materials in a zero-wind postcrash fire simulation that ignition and burning of the outboard seats seems to be the principal fire source inside the cabin. It has been shown by Bricker and Duskin (ref. 25) that the extremely rapid burning of aircraft seats is due to the polyurethane cushions of the seats. Little benefit can be obtained by making the polyurethane fire retardant. Either the polyurethane elastic foam must be replaced with a completely fire-resistant cushioning foam or the polyurethane must be protected by a compatible fire-blocking ablative material. Both of these approaches are being investigated in efforts to find ways of breaking the fire chain and restricting the spread of the fire throughout the interior of the cabin.

The ablative efficiency of foamed polychloroprene (neoprene) as a fire-blocking layer to protect military aircraft fuel tanks against external pool fires was first demonstrated by Pope et al. in 1968 (ref. 26). Foamed neoprene is currently the ablative material of choice, specifically low-smoke L-200 neoprene, because of its high charring ablation efficiency, moderate cost, and availability. Neoprene cushioning cannot be fabricated at useful densities much less than 46 kg/m^3 (6 lb/ft^3) as compared with standard polyurethane at 24 kg/m^3 (1.5 lb/ft^3). It has been estimated that replacement of all the cabin seat polyurethane seat cushioning with neoprene foam would impose a weight penalty of about 907 kg (2000 lb) for a wide-body jet aircraft. Hence, the use of the foamed neoprene as a fire layer between the fabric and polyurethane foam may be the only way in the short term to control fire propagation through the aircraft interior of contemporary design.

It has been estimated from recent preliminary tests that optimization with regard to blocking-layer thickness and position of the heat-blocked seats in the aircraft could result in a weight penalty for the wide-body transport of between 68 and 136 kg (150-300 lb). When a neoprene foam is used as a fire-blocking interlayer in a thickness of 1.3 cm (0.5 in.) between the seat covering and the polyurethane foam, it has been found that this configuration results in no fire propagation at a 2 W/cm^2 radiant heat source with a free-flame-ignition source about as well as an all neoprene seat. Surprisingly, few if any of the irritating gases normally expected from the pyrolysis of chloroprene (e.g., hydrogen chloride) have been observed in cabin fire simulator tests. It has also been observed that the neoprene fire-blocking layer covering the polyurethane and covered with wool-nylon fabric seems to surpress the flame spread across the fabric. It may be conjectured that the low-smoke neoprene not only protects the underlying cushioning foam but also, through char-swelling and hydrogen chloride evolution, inhibits flame spread of the fabric covering. These fire-suppression mechanisms observed in the cabin-fire simulator may be of considerable importance in preventing fire propagation into the aircraft interior ceiling, as was observed in the C-133 baseline test.

A sketch of an advanced seat concept is shown in figure 11. This seat has been designed with the best material options available, both with respect to functionality and to fire resistance; it has been described by Fewell et al. (ref. 27). It takes advantage of an imide foam with a somewhat lower density than standard polyurethane but with a much reduced flammability. Since this low density polyimide foam may still require some fire-blocking protection, a neoprene foam fire-blocking layer has also been included. A wool-kermel blend rather than wool-nylon is used in this advanced seat to further reduce the flame spread from external ignition sources.

A three-seat array of this advanced seat is shown in figure 12. It is planned to evaluate seats of this kind at higher heating rates than 3 W/cm^2 in the Douglas Aircraft cabin-fire simulator as a back-up for the fire-blocking neoprene-polyurethane system, especially for the case of outboard seats.

It may be concluded that the most cost-effective option available in the short term to break the fire chain generated by the external postcrash fire as it attempts to penetrate the interior system through a damaged fuselage or open door may be the use of a neoprene fire-blocking layer in contemporary seats. Neoprene foams in the form of vonar and low-smoke L-200 are commercially available and only somewhat more expensive than currently used polyurethane cushioning. It is believed that the weight penalty incurred by using the neoprene layer can be minimized by designing the thickness to accomodate the fire sources encountered in a survivable postcrash fire. Special material options are available using the neoprene fire-blocking layer with no significant weight penalty. Application of the NASA charring materials ablation code, CMA, is available (ref. 28) and is being modified to optimize these systems. The radiant panel facilities available in the Douglas Aircraft cabin-fire simulator and the Ames postcrash fire simulator can be used to evaluate this optimization technique.

WINDOW SYSTEMS FOR POSTCRASH FIRE PROTECTION

It has been reported by SAFER (ref. 1) that the contemporary panels of a wide-body transport aircraft provide sufficient protection to prevent fire penetration of the fuselage when exposed to an external fuel fire of very short duration. However, the present acrylate window systems shrink, as should be expected, and drop out, allowing direct fire penetration long before the failure of the airframe structure. Earlier, Bricker and Duskin (ref. 25) demonstrated that contemporary polymethyl methacrylate windows were burned through in 50 to 60 sec under the heat flux typically encountered in a postcrash fire.

Parker et al. (ref. 29) have developed physically equivalent windows, composed of a high-char-yield epoxy trimethoxyboroxine transparent polymer system, that resist burn-through for up to 10 min. Eklund et al. (ref. 30) confirmed that state-of-the-art windows do indeed shrink and fall out in less than 1 min, whereas the high-yield windows do not fall out but survive for at least 6 min.

A generalized plot of window performance is shown in figure 13. Here the back-side temperature change with time is plotted for contemporary windows, which burn through (as shown) in 1.5-2 min. It can be seen that the advanced materials provide continuing protection at times greater than 8 min. In comparing the slopes of the temperature-time plots the superior ablation efficiency of the new high-char-forming windows is apparent. In order to apply this fire resistant transparent window to maximize the window systems functionality, that is, scratch, ultraviolet resistance, etc., and provide a fireworthy window system design, it has been necessary to apply the new window material as interlayer with fire hardened edge attachment as shown in figure 14. This type of assembly has been developed into full-scale canopies for military aircraft.

Various options have been examined to apply this fire-resistant transparent material to a conventional window system (fig. 15). It is now believed that the most effective and practical way to use the epoxy window as a fire barrier is as the secondary fail-safe inner window shown in figure 16. Of course, similar fire-resistant edge-attachment methods as shown for the military canopy will have to be applied to optimize the fire performance of these new candidate windows.

DATA BASE LIBRARY FOR AIRCRAFT INTERIOR MATERIALS

The purpose of the study is to provide NASA and the FAA with several design options for a library of data for materials that are currently or can potentially be used in aircraft interiors.

It was recognized that for many years the aircraft community has been studying the contribution of materials used in aircraft interiors to aircraft fire safety. Although the fire safety record in commercial aircraft has been continuously improved there is an ongoing attempt to alleviate the threat of severe aircraft cabin fires with state-of-the-art technology and new material developments. It is the responsibility of government organizations such as the FAA to regulate the introduction of new materials to aircraft interior use based on the material's contribution to the fire hazard. In order to effectively regulate the use of new materials, these organizations must recognize and evaluate the potential benefit and associated costs of utilizing them in the cabin interior. However, data on the material's fire performance, cost, processing, and maintenance, which must be utilized in this evaluation, are not available in a centralized repository.

The SAFER Committee recognized the need to select materials for aircraft applications that would provide the highest performance in a fire scenario while still meeting design and cost criteria. The Committee also recognized the lack of agreed-upon standard tests and fire threat scenarios, the proprietary nature of industry materials data, the continuing development of hundreds of new materials per year, and the lack of a large-scale, computer-based "clearing house" or data base for these materials and their properties.

Data about aircraft materials are generated by many members of the materials and aircraft community, including material suppliers, aircraft manufacturers, and government organizations involved in R&D, testing, and the development of standards. While some of the data are published and therefore distributed to other interested groups, much of it is available only to the group generating the data. To decrease the redundancy in testing and to distribute the information required for material evaluation, the SAFER Committee agreed that a centralized repository for these data should be established by the FAA.

In addition, there are conflicting viewpoints as to which testing methods should be used in materials evaluation and selection. It is recognized that a centralized data repository would provide an improved ability to compare test results from different test methods and therefore facilitate decisions about the most desirable testing methods.

The study is organized into three major tasks aimed at generating several design options for the data base. The design options will be defined by the data contents, data suppliers, required administrative support, applicable computer software and hardware, and various plans for user accessibility.

The first task is to survey potential users of the data base and suppliers of data, with emphasis on characterization of the data that is both desired and available. The kinds of data potentially to be contained with the data library include:

1. Material descriptions
2. Fire performance properties
3. Physical properties
4. Mechanical properties
5. Processing and maintenance characteristics
6. Cost information

The second task involves four subtasks aimed at estimating the requirements, in terms of manpower and cost, for configuring a data base to respond to the needs of the potential user community. Included in task 2 is a survey of applicable commercial software and hardware to select those systems which may be appropriate to the various options. This task results in a recommendation to NASA and the FAA of the most effective and efficient library configuration(s).

Task 3 reviews the anticipated applications of the materials data library and will be performed in conjunction with the first two tasks. Figure 16 shows an outline of the three major tasks and their subtasks.

The study has proceeded on schedule during the first 3 months. ECON has indicated that initial design-option descriptions and cost estimates will be completed by early November. These design options will incorporate the results of the surveys of potential data-bank users and data suppliers and the screening of commercially available computer hardware and software that are now in progress. At such time these initial options will be presented to Ames Research Center and to the FAA Test Center for preliminary review and discussion.

CONCLUDING REMARKS

It has been shown in this paper that there exists a substantial technology base for the selection, evaluation, and application of fire-resistant subsystem components that can reasonably be expected to improve human survivability in aircraft fires involving aircraft interiors. This technology can, in the short term, effect improvements in aircraft fire safety as well as provide a sound basis for further long-term improvements in new aircraft.

REFERENCES

1. Final Report of the Special Aviation Fire and Explosion Reduction Advisory Committee (SAFER), June 1980.

2. Aviation Safety — Interior Compartment Materials. Hearings before the Subcommittee on Oversight and Review of the Committee on Public Works and Transportation, House of Representatives, 96th Congress, U.S. GPO Report 96-12, April 1979, p. 61.

3. Sarkos, C. P.; and Hill, R. G.: Preliminary Wide Body (C-133) Cabin Hazard Measurements During a Postcrash Fuel Fire. Federal Aviation Administration, National Aviation Facilities Experimental Center, Report No. NA-78-28-LR, 1978.

4. Study of Aircraft Crashworthiness for Fire Protection. Douglas Aircraft Co., Interim Report, NASA Contract NAS2-10583, July 1980.

5. Neel, C. B.; Parker, J. A.; and Fish, R. H.: Heat Shields for Aircraft: A New Concept to Save Lives in Crash Fires. Astronaut. & Aeronaut., Nov. 1971.

6. Kourtides, D. A.; Parker, J. A.; et al.: Fire Containment Tests of Aircraft Interior Panels. Journal of Fire and Flammability, Apr. 1976.

7. Radiant Panel Tests. ASTM report E 162-67.

8. Parker, J. A.; Kourtides, D. A.; Fish, R. H.; and Gilwee, W. J.: Fire Dynamics of Modern Aircraft from a Materials Point of View. Proceedings of the AGARD Propulsion and Energetics Panel, Rome, Italy, Apr. 1975.

9. Combined Hazards Index. Interim Report, Douglas Aircraft Co., FAA Technical Center Contract, 1979.

10. Parker, J. A.; and Winkler, E. L.: The Effects of Molecular Structure on the Thermochemical Properties of Phenolics and Related Polymers. NASA TR R-276, 1967.

11. Kourtides, D. A.: Flammability and Thermochemical Properties of Some Thermoplastics and Thermoset Polymers — A Review. Journal of Polymer Plastics Technology and Engineering, vol. 11, no. 2, 1978, pp. 159-198.

12. Van Krevelen, D. W.: Some Basic Aspects of Flame Resistance of Polymeric Materials. Polymer, vol. 16, 1975, p. 615.

13. Kourtides, D. A.; Parker, J. A.; and Hilado, C. J.: Thermochemical Characterization of Some Thermoplastic Polymers. Journal of Fire and Flammability, vol. 8, no. 1, 1977, pp. 59-95.

Part 2

SESSION IV - OPERATING PROBLEMS AND POTENTIAL SOLUTIONS
Chairman: H. W. Schmidt

22. WAKE VORTEX ATTENUATION FLIGHT TESTS: A STATUS REPORT 387 1/A14
Marvin R. Barber and Joseph J. Tymczyszyn

23. BASIC RESEARCH IN WAKE VORTEX ALLEVIATION USING A VARIABLE TWIST WING 409 1/C8
Dana J. Morris and G. Thomas Holbrook

24. PNEUMATIC BOOT FOR HELICOPTER ROTOR DEICING 425 1/D11
Bernard J. Blaha and Peggy L. Evanich

25. AIRCRAFT OPERATING EFFICIENCY ON THE NORTH ATLANTIC - A CHALLENGE FOR THE 1980'S 445 1/F3
Robert Steinberg

26. FIREWORTHINESS OF TRANSPORT AIRCRAFT INTERIOR SYSTEMS 453 1/F12
John A. Parker and D. A. Kourtides

27. COMBUSTION TOXICOLOGY OF EPOXY/CARBON FIBER COMPOSITES 481 2/A14
D. E. Cagliostro

28. THE USE OF ANTIMISTING KEROSENE (AMK) IN TURBOJET ENGINES 499 2/C10
Harold W. Schmidt

29. NASA/FAA GENERAL AVIATION CRASH DYNAMICS PROGRAM 511 2/D8
Robert G. Thomson, Robert J. Hayduk, and Huey D. Carden

SESSION V - FLIGHT EXPERIENCES AND GROUND OPERATIONS
Chairman: J. L. McCarty

30. CURRENT RESEARCH IN AIRCRAFT TIRE DESIGN AND PERFORMANCE 543 2/F12
John A. Tanner and John L. McCarty

31. REVIEW OF ANTISKID AND BRAKE DYNAMICS RESEARCH 555 2/G10
Sandy M. Stubbs and John A. Tanner

32. STUDIES OF SOME UNCONVENTIONAL SYSTEMS FOR SOLVING VARIOUS LANDING PROBLEMS 569 3/A12
T. J. W. Leland, J. R. McGehee, and R. C. Dreher

33. RECENT PROGRESS TOWARDS PREDICTING AIRCRAFT GROUND HANDLING PERFORMANCE 583 3/B12
Thomas J. Yager and Ellis J. White

34. THE NASA DIGITAL VGH PROGRAM - EARLY RESULTS 613 3/D14
Norman L. Crabill and Garland J. Morris

35. EVALUATION OF EMERGENCY-LOCATOR-TRANSMITTER PERFORMANCE IN REAL AND SIMULATED CRASH TESTS 625 3/E12
Huey D. Carden

36. EXTINGUISHING IN-FLIGHT ENGINE FUEL-LEAK FIRES WITH DRY CHEMICALS 655 3/G14
Robert L. Altman

SESSION VI - ACOUSTICS AND NOISE REDUCTION
Chairman: H. G. Morgan

37. RECENT DEVELOPMENTS IN AIRCRAFT ENGINE NOISE REDUCTION TECHNOLOGY 671 4/B4
James R. Stone and Charles E. Feiler

38. SOURCES, CONTROL, AND EFFECTS OF NOISE FROM AIRCRAFT PROPELLERS AND ROTORS 699 3/D4
John S. Mixson, George C. Greene, and Thomas K. Dempsey

39. NASA PROGRESS IN AIRCRAFT NOISE PREDICTION 721 4/E12
J. P. Raney, S. L. Padula, and W. E. Zorumski

40. AIRPORT NOISE IMPACT REDUCTION THROUGH OPERATIONS 759 5/A13
Richard DeLoach

ATTENDEES 779 5/C5

14. Fish, R. H.; and Parker, J. A.: The Performance of Lightweight Plastic Foams Developed for Fire Safety. Proceedings of the NASA Conference on Materials for Improved Fire Safety, May 10, 1970, pp. 11-1/11-20.

15. Hilado, C. J.; Kourtides, D. A.; Barnes, G. J.; and Parker, J. A.: The Use of the High Flux Furnace in the Smoke Chamber to Measure Ignitability and Smoke Evaluation of Composite Panels. Journal of Fire and Flammability, vol. 8, no. 3, 1977.

16. Riccitiello, S. R.; Fish, R. H.; Parker, J. A.; and Gustafson, E. J.: Development and Evaluation of Modified Polyisocyanurate Foams for Low Heating Rate Thermal Protection. Proceedings of the 28th ANTEC-SPE Conference, May 1970.

17. Williamson, R. B.: Large Scale Fire Testing of Aircraft Interiors: Construction and Development of Criteria to Represent the Level of Threat. University of California, Berkeley, NASA Grant Interim Report NSG-2026-A.

18. Anderson, R. A.; Arnold, D. B.; and Johnson, G. A.: Development of Aircraft Lavatory Compartments with Improved Fire Resistance Characteristics. NASA CR-152120, 1979.

19. Polyether Ether Ketone Provisional Data Sheet. ICI Plastics Division, PJK/AGS/CM, Nov. 1979 (Ref. No. PK PD7).

20. Kourtides, D. A.; Parker, J. A.; et al.: Thermophysical and Flammability Characterization of Phosphorylated Epoxy Adhesives. Proceedings of the Adhesives for Industry Conference, Society of Plastics Engineers, Los Angeles, Calif., June 1980.

21. Engineering and Development Program Plan — Aircraft Cabin Fire Safety. U.S. Dept. of Transportation, Federal Aviation Administration, Report No. FAA-E-18-7, June 1980.

22. Hill, R. G.; and Sarkos, C. P.: Postcrash Fuel Fire Hazard Measurements in a Wide Body Aircraft Cabin. Journal of Fire and Flammability, vol. II, apr. 1980, pp. 151-163.

23. Eklund, T. I.: Preliminary Evaluation of the Effects of Wind and Door Openings on Hazard Development Within a Model Fuselage from an External Pool Fire. Federal Aviation Administration, NAFEC, Letter Report NA-79-1-LR, Feb. 1979.

24. Hartzell, G.: Fire Test Methodology for Aerospace Materials. Southwest Research Institute, NASA Final Report NAS-10140.

25. Bricker, R. W.; and Duskin, F.: 737 Aircraft Flammability Testing. NASA TM-78523, 1978.

26. Pope, R. B.; Riccitiello, S. R.; and Parker, J. A.: Evaluation of a Polyurethane Foam for Ablative Protection at Low Heating Rates. J. Spacecraft & Rockets, vol. 6, 1968, p. 74.

27. Fewell, L. L.; Duskin, F.; et al.: Release-Rate Calorimetry of Multilayered Materials for Aircraft Seats. SAMPE Quarterly, Apr. 1980.

28. Analytical Modeling of Intumescent Coating Thermal Protection System in a JP-5 Fuel Fire Environment. Aerothern Final Report, NASA Contract NAS2-7709, June 1974.

29. Parker, J. A.; Fohlen, G. M.; and Sawko, P. M.: Development of Transparent Composites and Their Thermal Responses. Presented at Conference on Transparent Aircraft Enclosures, sponsored by Air Force Materials Laboratory and Air Force Flight Dynamics Laboratory, Las Vegas, Nev., Feb. 5-8, 1973.

30. Eklund, Thor I.; Wright, Joseph A.; Fann, Franklin D.; and Berenotto, Joseph F.: Preliminary Evaluation of the Performance of Advanced and Conventional Aircraft Windows in a Model Fire Environment. NAFEC Technical Letter Report NA-80-17-LR, Federal Aviation Administration, Atlantic City, N.J.

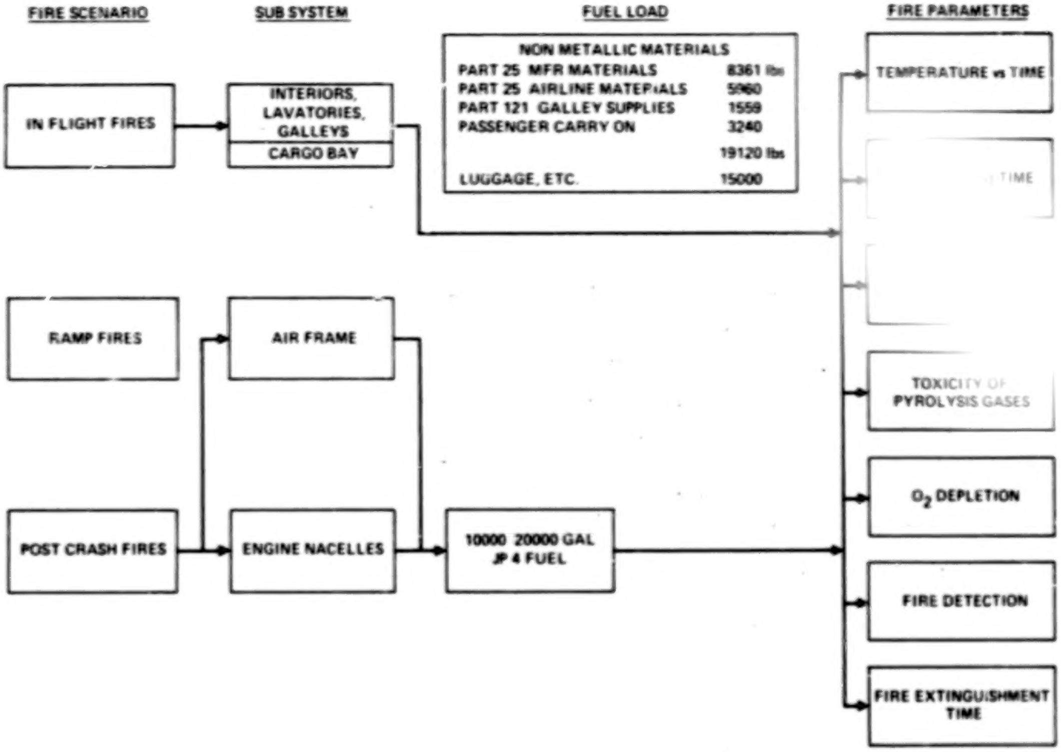
FIRE SCENARIO
SUB SYSTEM
FUEL LOAD
FIRE PARAMETERS
IN FLIGHT FIRES
INTERIORS, LAVATORIES, GALLEYS
CARGO BAY
NON METALLIC MATERIALS
PART 25 MFR MATERIALS 8361 lbs
PART 25 AIRLINE MATERIALS 5960
PART 121 GALLEY SUPPLIES 1559
PASSENGER CARRY ON 3240
19120 lbs
LUGGAGE, ETC. 15000
TEMPERATURE vs TIME
TIME
RAMP FIRES
AIR FRAME
TOXICITY OF PYROLYSIS GASES
O_2 DEPLETION
POST CRASH FIRES
ENGINE NACELLES
10000 20000 GAL JP 4 FUEL
FIRE DETECTION
FIRE EXTINGUISHMENT TIME

Figure 1.- Survivability criteria for aircraft fires (270 passenger aircraft). (Note: 1 lb = 0.454 kg and 1 gal = 0.378 liters.)

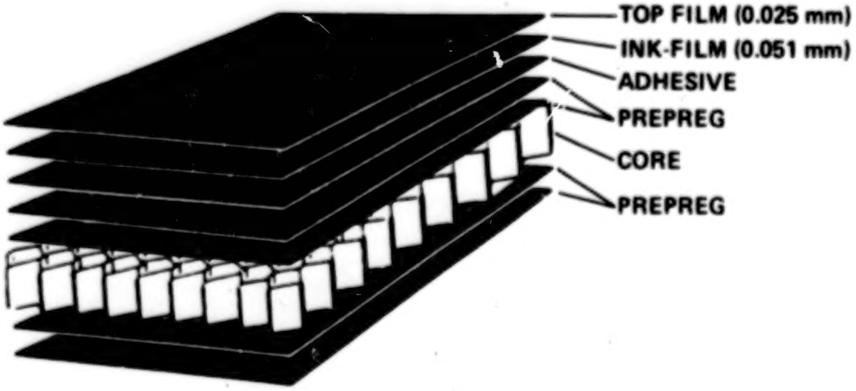
TOP FILM (0.025 mm)
INK-FILM (0.051 mm)
ADHESIVE
PREPREG
CORE
PREPREG

- CANDIDATE RESIN SYSTEMS FOR PREPREG
  - BASELINE EPOXY
  - BISMALEIMIDE
  - PHENOLIC
  - POLYIMIDE
- TESTING MATRIX
  - FLAMMABILITY, SMOKE, AND TOXICITY
  - MECHANICALS AND AESTHETICS

Figure 2.- Sandwich panel configuration.

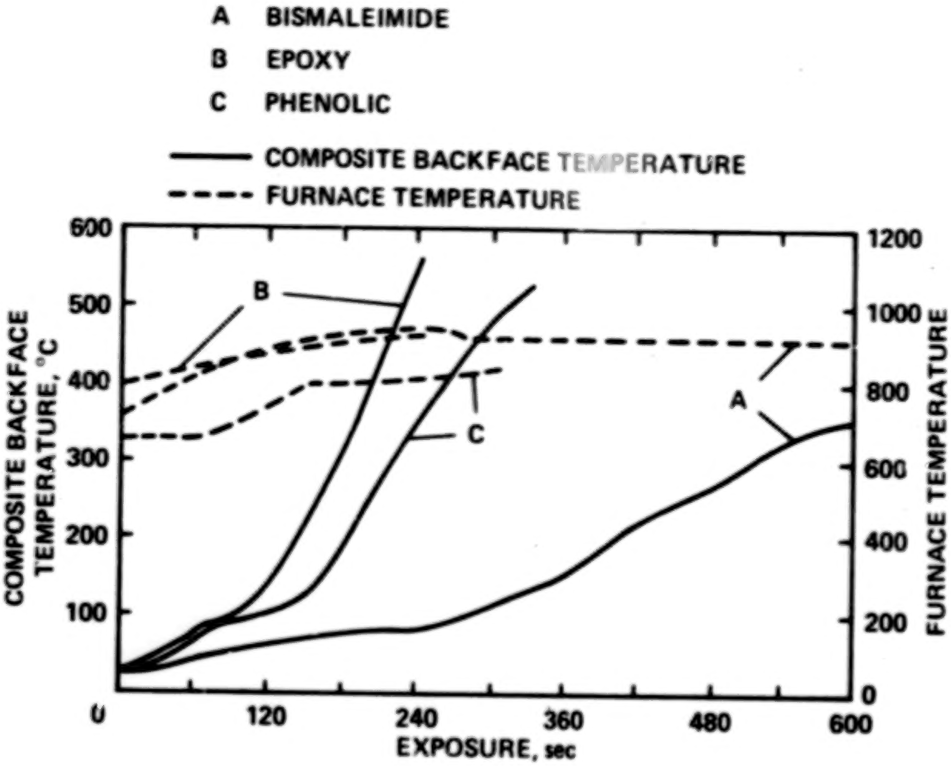

Figure 3.- Thermal efficiency of panels.

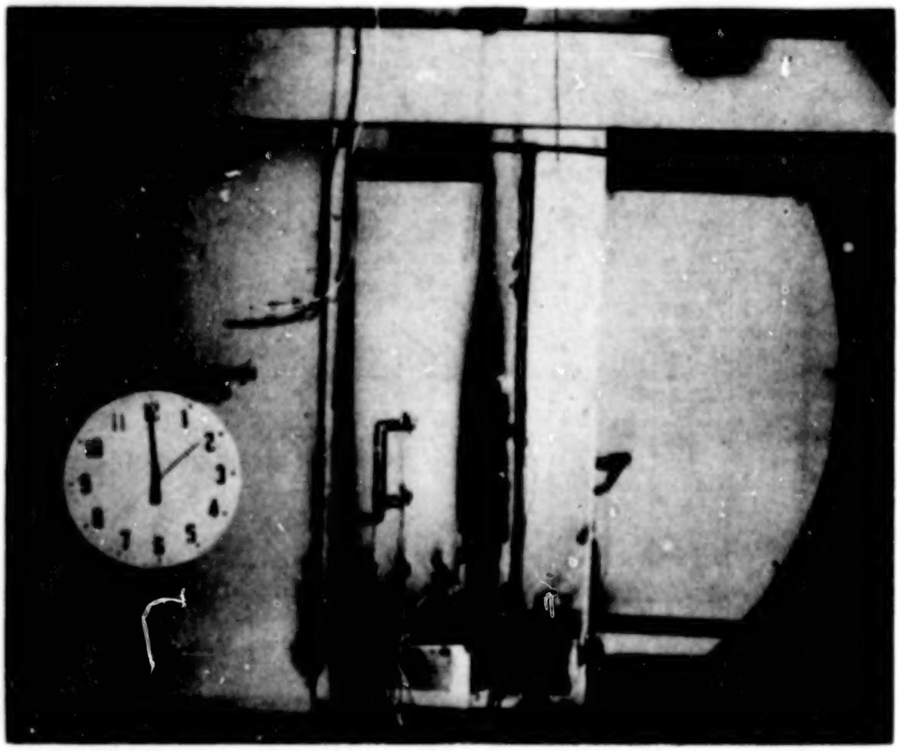

Figure 4.- Laboratory setup in cabin fire simulator.

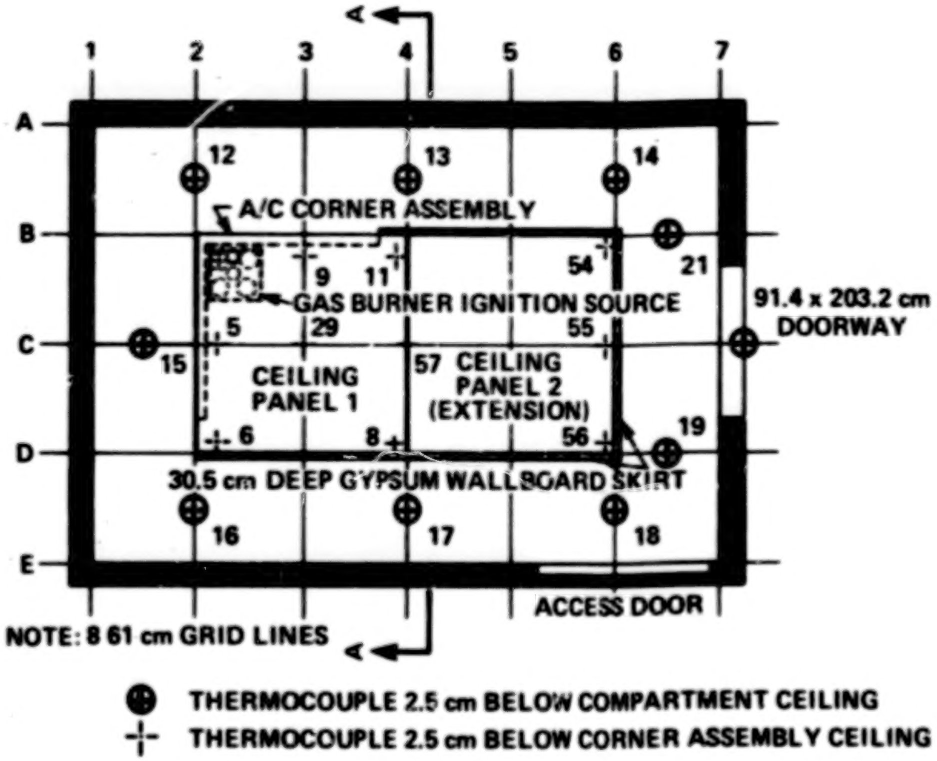
A
1
2
3
4
5
6
7
A
B
C
D
E
12
13
14
A/C CORNER ASSEMBLY
9
11
54
21
GAS BURNER IGNITION SOURCE
91.4 x 203.2 cm DOORWAY
5
29
55
15
CEILING PANEL 1
57
CEILING PANEL 2 (EXTENSION)
6
8
56
19
30.5 cm DEEP GYPSUM WALLBOARD SKIRT
16
17
18
ACCESS DOOR
NOTE: 8 61 cm GRID LINES
A
THERMOCOUPLE 2.5 cm BELOW COMPARTMENT CEILING
THERMOCOUPLE 2.5 cm BELOW CORNER ASSEMBLY CEILING

Figure 5.- Flashover test facility.

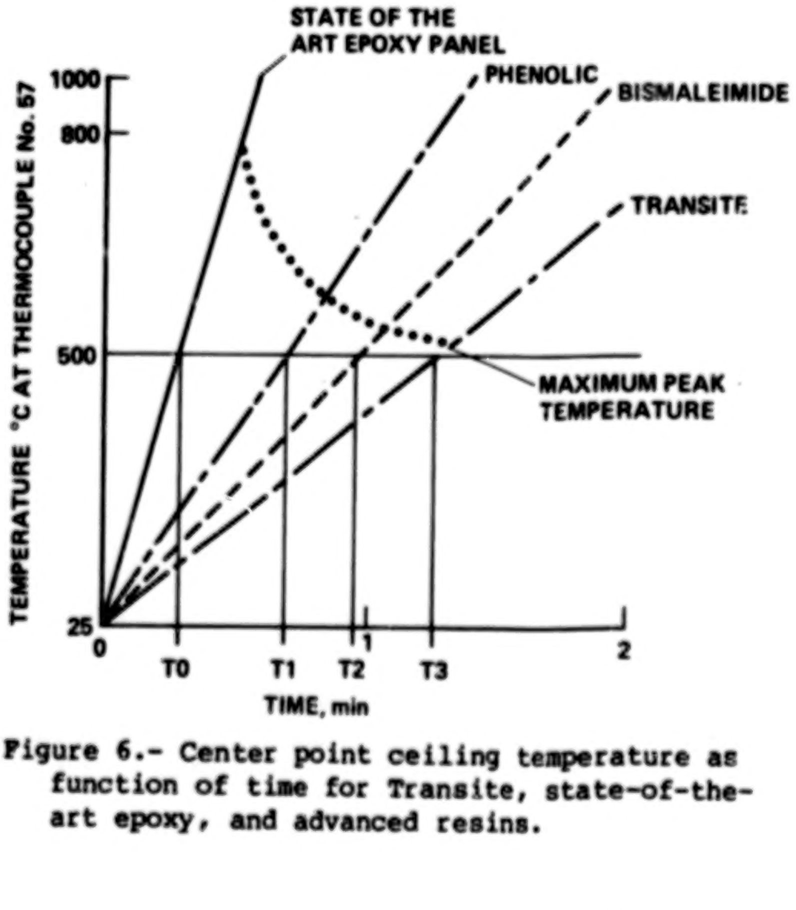

Figure 6.- Center point ceiling temperature as function of time for Transite, state-of-the-art epoxy, and advanced resins.

- LABORATORY TESTS—WEIGHT DISTRIBUTION
  - FLAMMABILITY—10%
  - SMOKE EMISSION—20%
  - TOXIC GAS EMISSION—10%
  - HEAT RELEASE—20%
  - HEAT RELEASE RATE—20%
  - THERMAL CONDUCTIVITY—4%
  - MECHANICAL STRENGTH—6%
  - DENSITY—10%

- MATERIAL AND FABRICATION
  - 15%
  - LABORATORY TESTS--85%

Figure 7.- Ranking procedure.

	BASELINE EPOXY	DEVELOPED PHENOLIC
• PROPENSITY TO BURN (LOI)		
• FACE SHEET	29.0	100^+
• BOND PLY	27.7	53.5
• SMOKE EMISSION (D_s @ 4 min) NBS		
• 2.5 W/cm^2	62.8	2.5
• 5.0 W/cm^2	96.5	8.4
• HEAT RELEASE (J/cm^2) OSU		
• 2.5 W/cm^2	177.2	126.0
• 5.0 W/cm^2	512.4	96.3
• CHAR YIELD, 800°C, N_2, %	38.0	61.0

Figure 8.- Flammability and smoke.

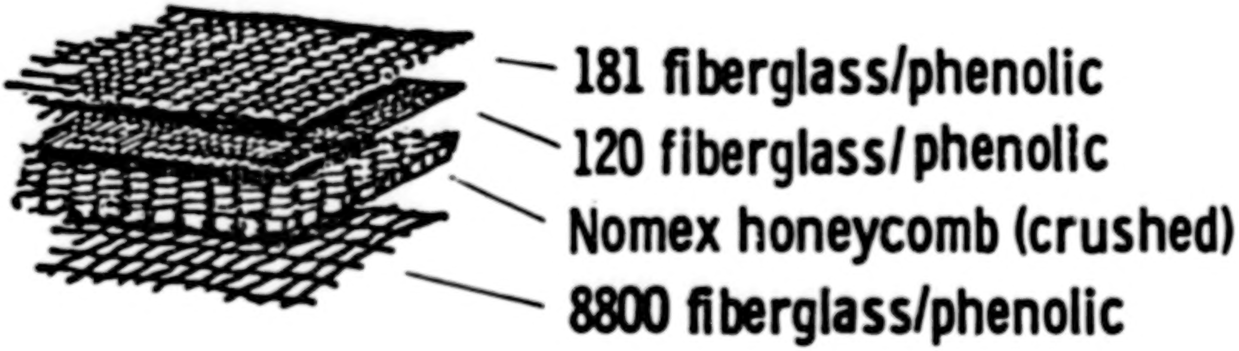
181 fiberglass/phenolic
120 fiberglass/phenolic
Nomex honeycomb (crushed)
8800 fiberglass/phenolic

Figure 9.- Crushed-core sandwich panel.

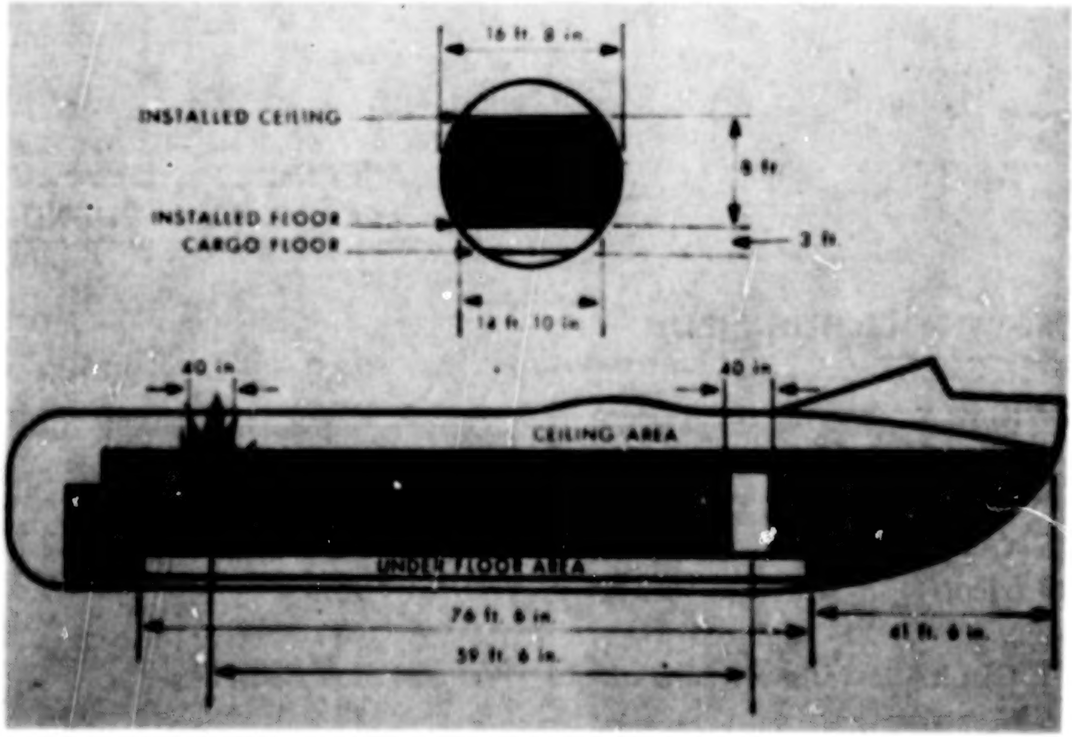
16 ft. 8 in.
INSTALLED CEILING
8 ft.
INSTALLED FLOOR
CARGO FLOOR
3 ft.
14 ft. 10 in.
40 in.
40 in.
CEILING AREA
UNDER FLOOR AREA
76 ft. 6 in.
41 ft. 6 in.
59 ft. 6 in.

Figure 10.- C-133 wide body cabin fire test article.
(Note: 1 ft = 0.3048 m.)

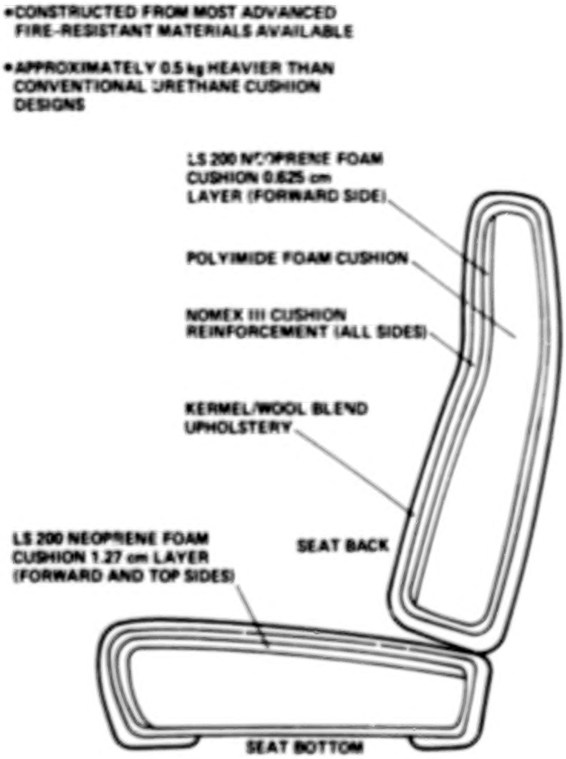
•CONSTRUCTED FROM MOST ADVANCED FIRE-RESISTANT MATERIALS AVAILABLE
•APPROXIMATELY 0.5 kg HEAVIER THAN CONVENTIONAL URETHANE CUSHION DESIGNS
LS 200 NEOPRENE FOAM CUSHION 0.625 cm LAYER (FORWARD SIDE)
POLYIMIDE FOAM CUSHION
NOMEX III CUSHION REINFORCEMENT (ALL SIDES)
KERMEL/WOOL BLEND UPHOLSTERY
LS 200 NEOPRENE FOAM CUSHION 1.27 cm LAYER (FORWARD AND TOP SIDES)
SEAT BACK
SEAT BOTTOM

Figure 11.- NASA fire-resistant passenger seat cushion construction.

Figure 12.- Three-seat array of advanced seats.

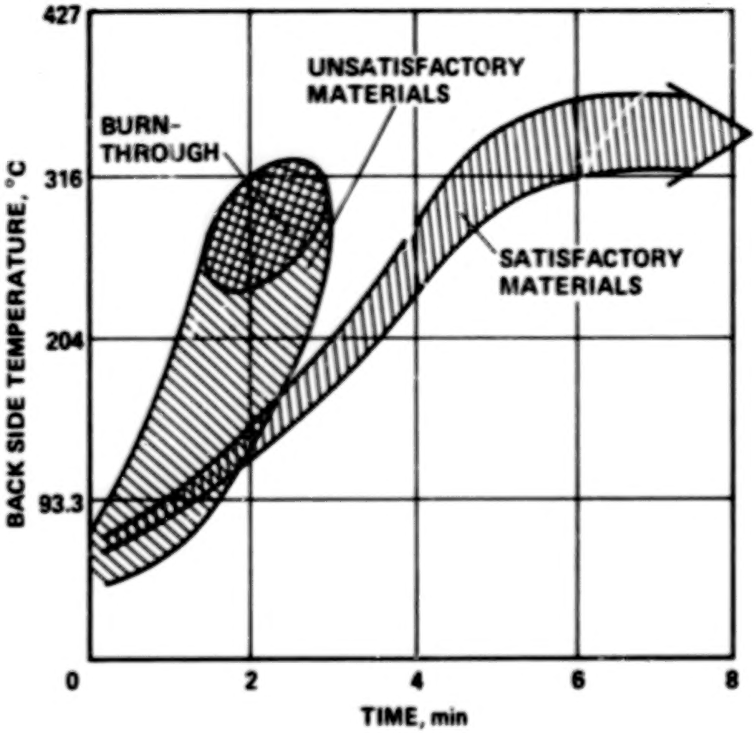

Figure 13.- General data plot of Ames Research Center's T-3 fire test results.

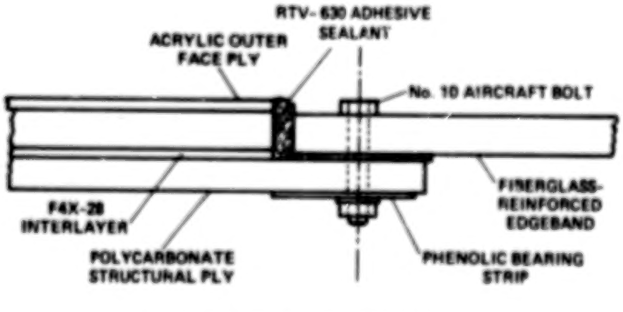
RTV-630 ADHESIVE SEALANT
ACRYLIC OUTER FACE PLY
No. 10 AIRCRAFT BOLT
FIBERGLASS-REINFORCED EDGEBAND
F4X-28 INTERLAYER
POLYCARBONATE STRUCTURAL PLY
PHENOLIC BEARING STRIP

DETAILS OF EDGE ATTACHMENT DESIGN

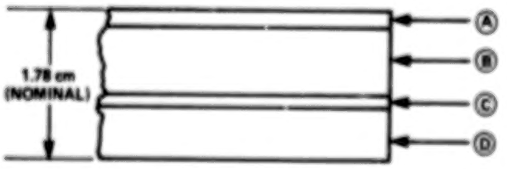
1.78 cm (NOMINAL)
Ⓐ
Ⓑ
Ⓒ
Ⓓ

Ⓐ 2.03 cm OUTER PLY OF ACRYLIC
Ⓑ 0.813 cm EX-112 PLY DIRECTLY BONDED TO THE ACRYLIC
Ⓒ 0.127 cm OF SILICONE INTERLAYER
Ⓓ 0.635 cm POLYCARBONATE STRUCTURAL PLY

Figure 14.- Fire-resistant transparent composite.

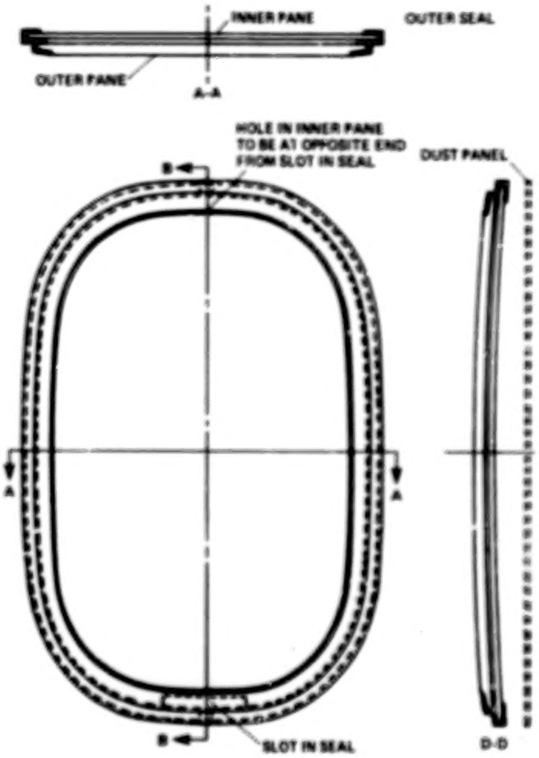
INNER PANE
OUTER SEAL
OUTER PANE
A-A
HOLE IN INNER PANE TO BE AT OPPOSITE END FROM SLOT IN SEAL
DUST PANEL
B
A
A
B
SLOT IN SEAL
D-D

Figure 15.- Air transport passenger window.

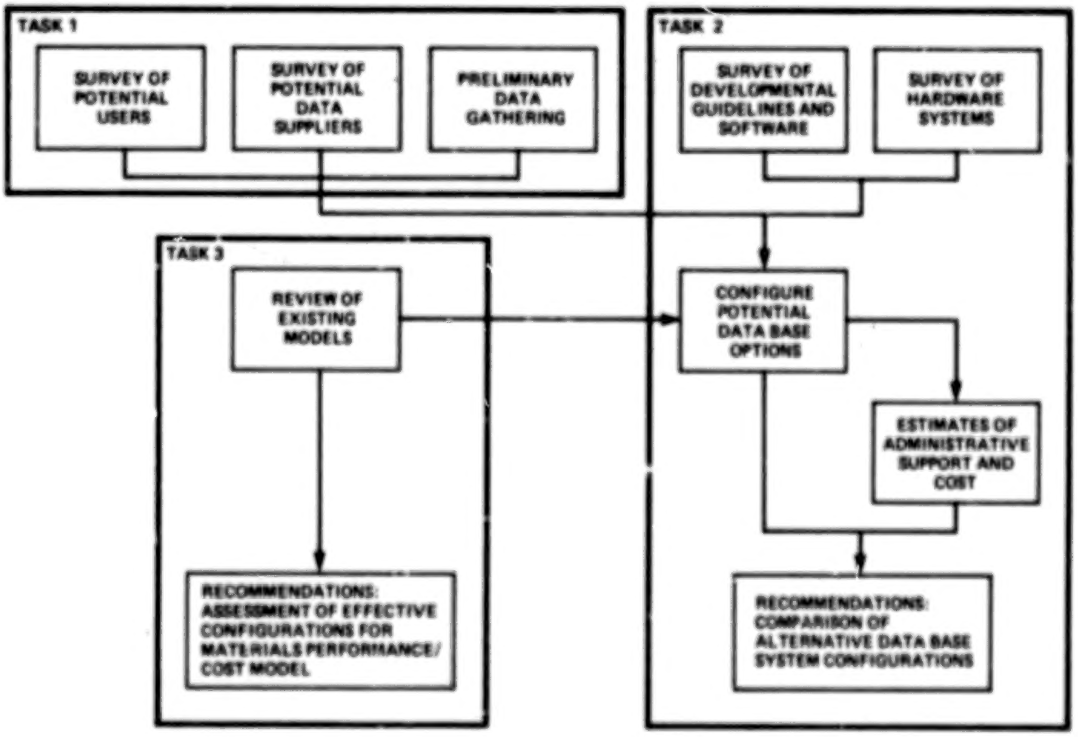
TASK 1
SURVEY OF POTENTIAL USERS
SURVEY OF POTENTIAL DATA SUPPLIERS
PRELIMINARY DATA GATHERING
TASK 2
SURVEY OF DEVELOPMENTAL GUIDELINES AND SOFTWARE
SURVEY OF HARDWARE SYSTEMS
TASK 3
REVIEW OF EXISTING MODELS
CONFIGURE POTENTIAL DATA BASE OPTIONS
ESTIMATES OF ADMINISTRATIVE SUPPORT AND COST
RECOMMENDATIONS: ASSESSMENT OF EFFECTIVE CONFIGURATIONS FOR MATERIALS PERFORMANCE/ COST MODEL
RECOMMENDATIONS: COMPARISON OF ALTERNATIVE DATA BASE SYSTEM CONFIGURATIONS

Figure 16.- Overview of study tasks.

BLANK PAGE

BLANK PAGE

COMBUSTION TOXICOLOGY OF EPOXY/CARBON FIBER COMPOSITES

D. E. Cagliostro

Ames Research Center

INTRODUCTION

The Chemical Research Projects Office has a continuing effort in researching and developing materials for aerospace applications. Many of these materials are polymeric systems for high temperature and/or long-term use. An outgrowth of this effort has been the development of polymers with improved fire safety. In the recent study of risks (or nonrisks) using epoxy/carbon fibers in commercial transport operations, fire effects on the release of fibers was important; therefore, the fire effects on the epoxy composite were studied. Experimental programs were established in the Navy because some advanced aircraft contain epoxy composites. The Navy was also interested in developing a safety protocol, especially with regard to exposure of experimentalists and ship's crew to the pyrolysis products of the epoxy composite. These results could also help establish a data base for subsequent industrial or military fires.

EXPERIMENTAL SYSTEM

In our laboratory a combustion toxicology test is being developed to screen new materials. This system is called the radiant panel test facility. Presented here are a description of the facility and some preliminary results from tests on a Navy 3501-6AS composite, a typical composite for fighter aircraft.

The test facility was designed

1. To expose a material to a simulated fire condition.
2. To determine the pyrolysis products generated.
3. To study the effects of the pyrolysis products on test animals.

Figure 1 shows an overall view of the test system. At the top of the chamber is the sample exposure area; at the bottom are the atmospheric and animal test areas. Figure 2 shows the sample exposure area. Suspended in a vertical configuration from a load cell, the sample can be exposed to a radiant flux and/or a small JP-5 pool fire or small hydrogen ignition flame. The radiant source is an electrically powered panel which can provide up to

5 W/cm^2 flux at the sample surface. The JP-5 pool fire is achieved by burning JP-5 in a small pan beneath the sample. Ventilation of the chamber can be varied.

In the atmospheric analysis area, there are 3 kinds of atmospheric probes, shown in figure 3. A hypodermic syringe was used to obtain samples of volatile components such as CO, O_2, and CO_2. These were analyzed by chromatography and infrared. Aerosol samples were trapped on a 1 µm filter. In some cases aerosol samples were also obtained from scrapings of deposits on the chamber walls. Samples were analyzed using chromatography and mass spectrometry. Where possible, photomicrographs of the aerosols were also taken to examine size. A scrubber was used to absorb acidic or basic gases, such as HCN, H_2S, and NH_3. Scrubbing solutions were analyzed using specific ion electrodes.

Two types of test animals were studied, rats and mice. Rats were restrained so they only inhaled the atmospheres. Their respiratory and cardiac responses were recorded during exposure. The rat module is shown in figure 4. Blood enzymes in the rats were also analyzed. The concentration of these was indicative of tissue necrosis in the lungs and the neural, cardiovascular, liver, and kidney systems. The rats were also autopsied a few days after exposure.

Mice in the tests were conditioned to jump on a pole to avoid an electric shock in a grid on the cage floor. The test module is shown in figure 5. The mice learned to jump given a light or sound signal warning that the grid was to be electrified. Delays in reaction time due to exposure are a measure of the animals' ability to escape. The time delay given the light or sound is a measure of the loss of avoidance response; the delay given the shock is a measure of the loss of escape response. This test is a modification of one developed at the Stanford Research Institute.

In all tests both types of animals were observed for overt symptoms during exposure. In some cases tests for mutagenicity were also run.

In the original panel chamber design, the ratio of the sample weight to chamber volume was scaled similar to the ratio of panel weight to passenger cabin volume in a wide-bodied jet. At the beginning of the Navy tests, this ratio was not available for military applications, so the wide-bodied jet weight-to-volume ratio was used. Future tests will include a lower ratio indicative of composite usage on advanced aircraft in aircraft carrier hangar decks. In one of the present tests, the smallest sample, this ratio also was similar to that proposed for a fuel saving application of epoxy/carbon fiber composites as face sheets for wall panels in advanced commercial aircraft. Tables 1 and 2 summarize these typical weight-to-volume ratios.

RESULTS AND DISCUSSION

The epoxy resin tested has a molecular structure similar to that shown in figure 6. Thermogravimetric analyses (TGAS) of the resin in nitrogen and in air are shown in figure 7.

The resin in both cases begins to pyrolyze at about 300° C. In nitrogen it gives a char yield of about 35% at 650° C. In air, at 650° C, it is about 2% or almost totally consumed.

A summary of the actual test conditions for the preliminary experiments is shown in table 3. Besides sample weight or a different sample mounting, the major difference between experiments was a flame or nonflame condition. The kinds of atmospheres generated varied markedly depending on whether the resin burned. The sample burned only when both radiation and an ignition source (the hydrogen flame) were present.

When flames occurred there was an increase in CO_2 and decrease in O_2 compared to a nonflame case. Flames also resulted in large quantities of HCN being generated, while little was generated in the nonflame case. In one case a flash-over condition resulted and HCN was even more evident. Flames also changed the nature of the aerosol; aerosol material found as major components in the nonflame case was not apparent in the flame case. Typical atmospheric analyses exemplifying these characteristics are shown in tables 4-7.

Toxic effects were more severe for the flaming condition in the animal tests. In the nonflame case, although animals survived the test, they exhibited symptoms which could represent a decrease in ability to escape (see table 8). These animals also were exposed to one potential carcinogen, aniline, and therefore might show long-term health effects. (The fertilized egg tests also showed the atmosphere generated had potential mutagenic and other effects.) In the flame case not only was there a decrease in ability to escape, measured by the avoidance and escape response, but also many mice died. Although the rats survived these tests, on autopsy there was extensive pulmonary edema and kidney damage. Some typical results are shown in table 9, and figures 8 and 9.

FUTURE WORK

Additional tests are planned with a 5208 resin at lower weight-to-volume ratios similar to aircraft stored in a hangar deck. These tests will include exposure to a small JP-5 fuel fire. The JP-5 test system is shown in figure 10. A typical test on a small JP-5 fire in the chamber without epoxy or test animals is shown in table 10 and figure 11. The toxic effect of the JP-5 fuel pyrolysis alone will be studied as a baseline for comparison.

In addition, separate studies with test animals are underway to try to determine whether the animal symptomology can be correlated with just the histories of CO, HCN, or HCN/CO mixtures generated in previous panel tests. Tests using just the aniline histories may determine if aniline or its reaction products cause the kidney damage. Because of the presence of potential carcinogens, a new host mediated assay is being developed to test for mutagenicity of aerosols reaching the lungs of test animals.

TABLE 1.- TYPICAL PANEL WEIGHT TO VOLUME RATIOS

	Cabin volume	Panel weight	Ratio
Commercial aircraft Wide-bodied jet			
Case A - Total panel - state-of-the-art (fiberglass facesheet and honeycomb)	840 m^3	136×10^6 g	1.62×10^{-3} g/cm^3
Case B - Advanced aircraft Face sheet alone Epoxy/carbon fiber construction	840 m^3	4.05×10^5 g	4.82×10^{-4} g/cm^3
Case C - Military application Advanced aircraft in hangar deck	3.16×10^4 m^3	3.16×10^6 g	1.36×10^{-4} g/cm^3

TABLE 2.- SAMPLE RATIOS IN RADIANT PANEL SYSTEM

Chamber volume	Sample size (g)	Ratio (g/cm^3)	% Involvement		
			Case A	Case B	Case C
113.3 liters	200.0	1.76×10^{-3}	108	365	1294
	184.0	1.62×10^{-3}	100	--	--
	100.0	8.8×10^{-4}	54	182.5	647
	54.8	4.82×10^{-4}	--	100	--
	50.0	4.4×10^{-4}	27	91.3	323.5
	15.5	1.36×10^{-4}	--	--	100
	10.0	8.8×10^{-5}	5.4	18.3	64.7
	5.0	4.4×10^{-5}	2.7	9.1	32.4

TABLE 3.- EXPERIMENTAL CONDITIONS

[Navy 3501-6AS epoxy/graphite panels; 0.51 cm thick, 40 plys; chamber volume 113.3 liters]

Experiment no.	Sample size	Sample weight, g	Flux, W/cm^2	Exposure time, min	Flame	Mount	Atmospheric probes	Animal tests
3501-6AS-1	15.24 cm × 15.24 cm	198.2	2.25	20	None	Water-cooled block	Aerosol, gas, scrubber	Fertilized eggs
3501-6AS-2	↓	198.3	2.48	↓	None	Load cell	Aerosol, gas	Mice
3501-6AS-3	↓	199.1	↓	↓	H_2 flame	↓	Gas, scrubber	Mice/ rats
3501-6AS-4	↓	198.0	↓	↓	↓	↓	Aerosol, gas, scrubber	None
3501-6AS-5	7.62 cm × 7.62 cm	48.0	↓	↓	↓	↓	Aerosol, gas, scrubber	Mice/ rats

TABLE 4.- NO FLAME — AEROSOL ANALYSIS[a]
[Radiant-panel test 3501-6AS-2]

Organic volatile material	Aerosol concentration			
	No. 2[b]	No. 3[c]	No. 2[b]	No. 3[c]
	ppm in gas form		mg liquid/m^3	
Aniline	83.8	68.3	320	260
n,n dimethylaniline	7.4	11.0	37	55
p-toluidine	7.9	10.9	35	48
n-etaniline	2.0	1.8	10	9
Methylquinoline	17.3	8.2	102	48
Quinoline	13.2	7.5	7	40
Indole	5.6	2.2	27	11
Methylindole	9.6	4.4	52	24

[a] Aerosol no. 1 was too diluted for analysis.

[b] Time was 5-10 min; total gas was 0.982 liters; total volume of methanol was 2.7 ml.

[c] Time was 10-20 min; total gas was 1.964 liters; total volume of methanol solution was 2.5 ml.

TABLE 5.- FLAME — SCRUBBER ANALYSIS — CN^- GAS CONCENTRATION IN ANIMAL TEST AREA[a]
[Radiant-panel test]

	Flame	Flame	Flashover
Time, min	3501-6AS-3	3501-6AS-4	3501-6AS-5
	CN^-, ppm[b]	CN^-, ppm[c]	CN^-, ppm[d]
0-7	6.2	Trace	400
7-13	533	460	1052
13-17	446	302	972
17-20	180	304	890

[a] Hydrogen cyanide analysis may have had H_2S interference. Analysis being refined. Hydrogen sulfide, however, is also very toxic.

[b,c] Sample flowrate 80 ml/min.

[d] Sample flowrate 160 ml/min.

TABLE 6.- NO FLAME — GAS ANALYSIS[a]
[Radiant-panel test 3501-6AS-2]

Time, min	CO, ppm	CO_2, %	O_2, %	CH_4, ppm	CH_2CH_2, ppm	CH_3CH_3, ppm	Propane, ppm	Propylene, ppm
5	0	0.68	20.13	---	---	---	---	---
7	200	.83	20.06	10	---	---	---	---
9	510	.83	20.08	26	70	200	40	250
12.5	1000	1.03	19.9	500	70	340	120	340
15	1480	1.04	19.7	618	130	440	310	400
18	2040	1.20	19.5	720	150	500	230	430
20	2200	1.26	19.5	694	140	520	270	380

[a] SO_2 and HCN were not found. Two unknown peaks may be COS and CH_3Cl. Maximum concentration for COS was 300 ppm, and maximum concentration for CH_3Cl was 650 ppm.
Flux level 2.48 watts/cm^2

TABLE 7.- FLAME (FLASHOVER) — GAS ANALYSIS IN ANIMAL CHAMBER
[Radiant-panel test 3501-6AS-3]

Time, min	Gas concentration			
	CO_2, %	CO, ppm	O_2, %	Hydrocarbons
0	1.54	0	17.92	Trace
4	1.65	0	17.44	
8	2.96	1060	16.3	
12	3.17	2200	15.47	
16.4	4.14	2620	15.01	
20.2	3.90	2500	15.12	

Flux level 2.48 watts/cm^2

TABLE 8.- OBSERVATIONS OF MICE DURING THE BURN AND POST EXPOSURE
[Radiant Panel Test 3501-6AS-2]

Time into burn	Observations
0 min	Animals moving, exploring, cleaning movements, active; no sweating apparent. All animals appeared normal.
2 min	Appearance of smoke at feed-through.
3.5 - 4.0 min	Appearance of smoke in chamber. Mice agitated.
5.0 - 7.0 min	Much movement, agitation, jumping behavior, attempts to climb chamber walls. Beginning to exhibit loss of coordination, some staggering.
10 min	Mice jumping, attempting to escape. Some cleaning motions. Chamber very smoky and poor visibility.
15 min	Only 1 mouse observed moving; most not visible. Animals moving on top of box appeared normal, exploring, and active. Appearance of sweat and/or aerosol deposition (yellow) on fur.
20 min	Mice were active. Fur moist with yellow sweat or aerosol.
25 min	Animal movements unsteady. Some mice obviously moribund. Movements slow and disorganized.
30 min	Animals appeared incapacitated and unable to move in a coordinated manner. Movements weak.

TABLE 8.- CONCLUDED

Time post-exposure	Observations
15 min	Brownish deposit on fur and skin of all mice. Rinsing in H_2O did not remove this. Movements slow and labored; ataxic. Breathing difficult and rapid in all mice. Appeared to be able to see, but some mice squinting and/or eyes partially closed. Perhaps some sensory irritation. Two mice appeared extremely ill.
95 min	All mice active, cleaning themselves (this would be an additional source of toxicants). Feeding, active, some scratching (irritation?). #10 possible eye damage; eye closed. Darting movement and shaking of extremities as if to get rid of irritant.
24 hr	Animals huddled together sleeping. Some eye squinting and scratching. After weighing, the animals were active and eyes appeared normal. Much cleaning and grooming.
48 hr	In general all animals appeared normal, healthy, and active, with slightly rapid breathing. Little deposition is left on their coats; somewhat more on tails and ears. Occasional squinting was observed. Animals appeared slightly jittery and exhibited very quick responses to sound (almost overly so). When removed for weighing they began exploring actively. When left undisturbed they tended to huddle in the corners, sleeping.
120 hr	All animals clean. Eyes and behavior appeared normal.

BLANK PAGE

BLANK PAGE

TABLE 9.- FLAME — SUMMARY OF BEHAVIORAL CHANGES IN MOUSE RESPONSE EXPERIMENTS

Test no.	Time of behavioral changes, sec		
	Loss of avoidance response	Loss of escape response	Estimated time of death
3501-6AS-3	352	704	985
3501-6AS-5	218	478	[a]

[a] Not possible to estimate.

TABLE 10.- JP-5 PYROLYSIS GAS ANALYSIS

Run No.	Time (min)	O_2 (%)	CO_2 (%)	CO (ppm)	Hydrocarbons (ppm)	Comments
3-2	0	21.2	0.05	0	0	Circular pan ~4 in.^{2} 5.5 g fuel, 1.41 g lost, analyses near animal test area, no HCN or H_2S detected
	2	19.1	1.5	200	--	
	5	17.4	2.76	400	--	
	10	17.37	2.76	500	50	
3-3	0	20.8	0.04	0	0	Circular pan ~4 in.^{2} 3.54 g fuel, 1.22 g lost, analyses near animal test area, no HCN or H_2S detected
	2	18.9	1.98	160	0	
	5	18.0	2.76	450	0	
	10	17.7	2.82	340	--	
	20	18.3	2.0	220	--	
3-7	0	21.2	0.04	0	0	Circular pan ~4 in.^{2} 3.53 g fuel, 1.37 g lost, analyses near flame, no HCN or H_2S detected
	1	11.9	8.24	1,300	280	
	2	14.4	6.23	820	110	
	3	16.4	4.28	500	40	
	5	17.54	2.84	330	0	
	11	17.46	2.78	350	0	

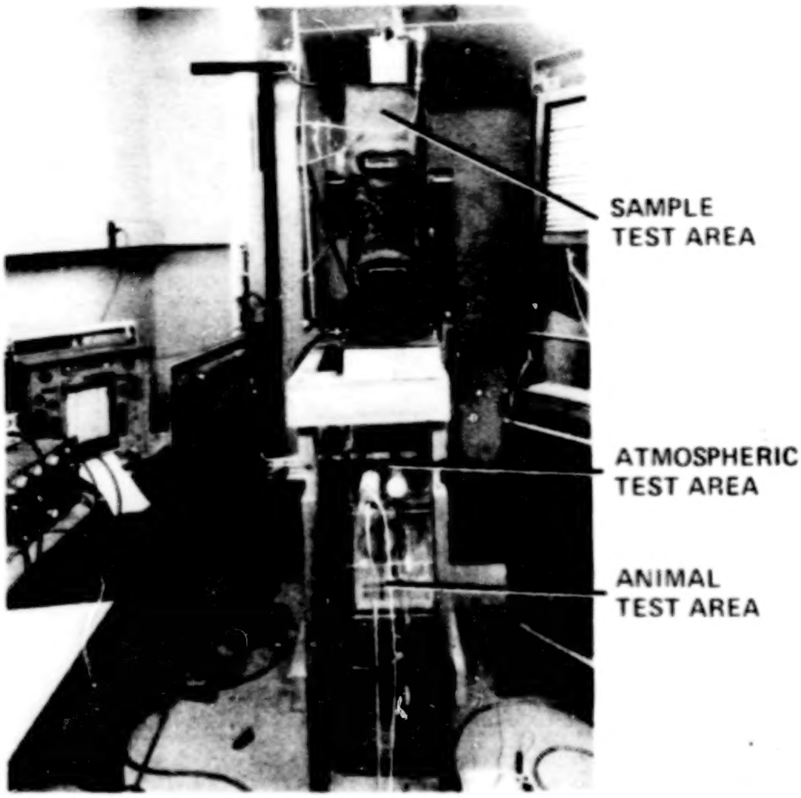
SAMPLE
TEST AREA
ATMOSPHERIC
TEST AREA
ANIMAL
TEST AREA

Figure 1.- Radiant panel facility.

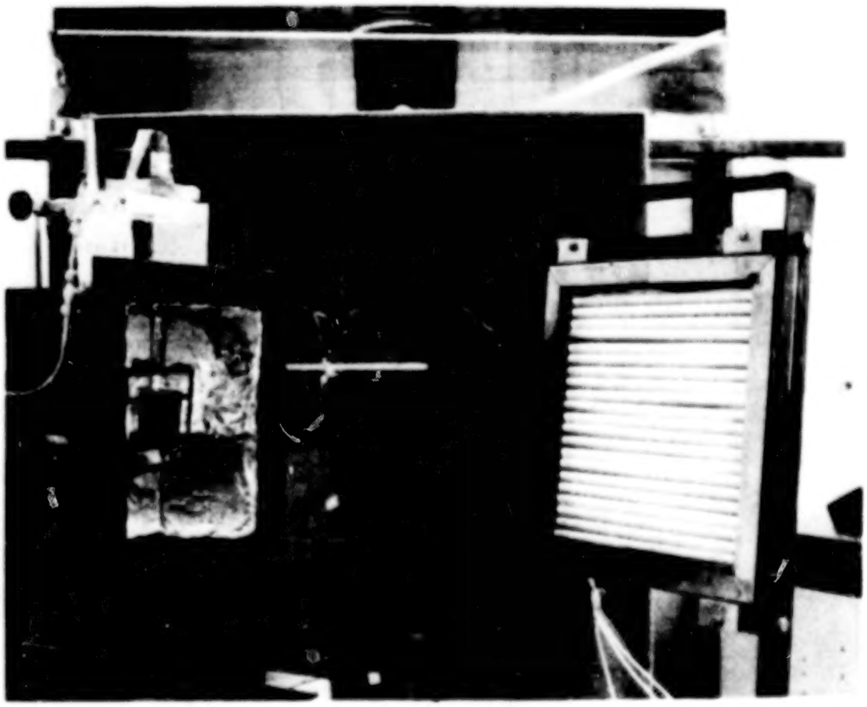

Figure 2.- Sample test area.

SCRUBBER

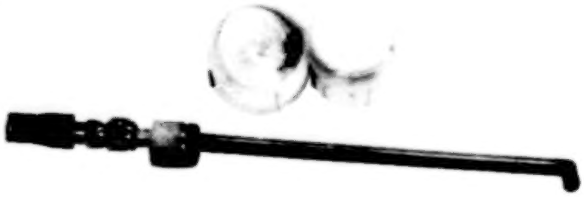

AEROSOL PROBE

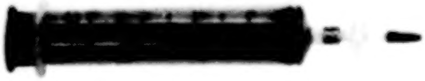

GAS SAMPLER

Figure 3.- Atmospheric test probes.

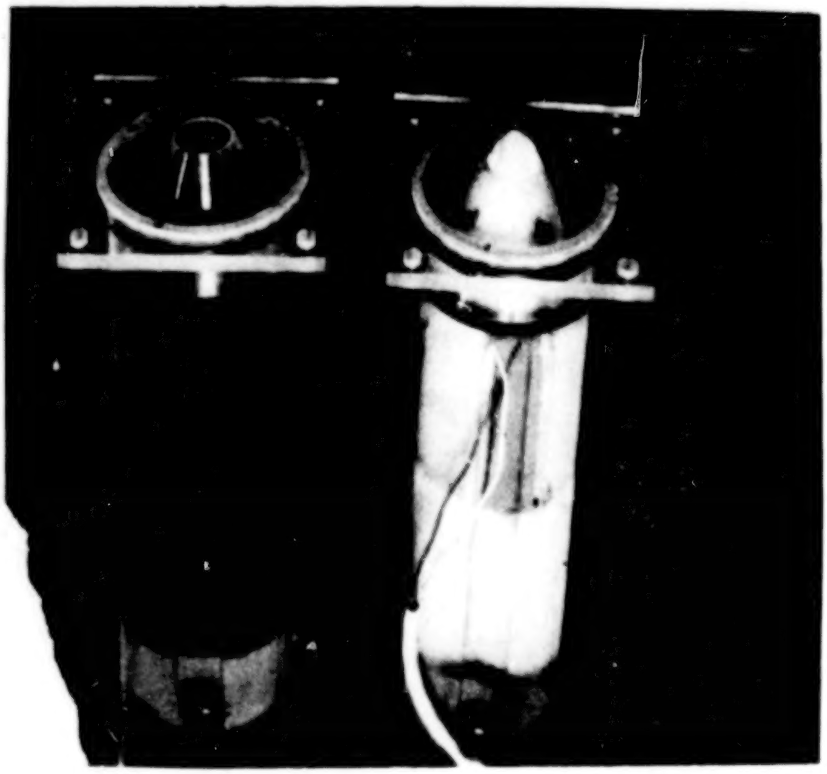

Figure 4.- Animal test area - rat module.

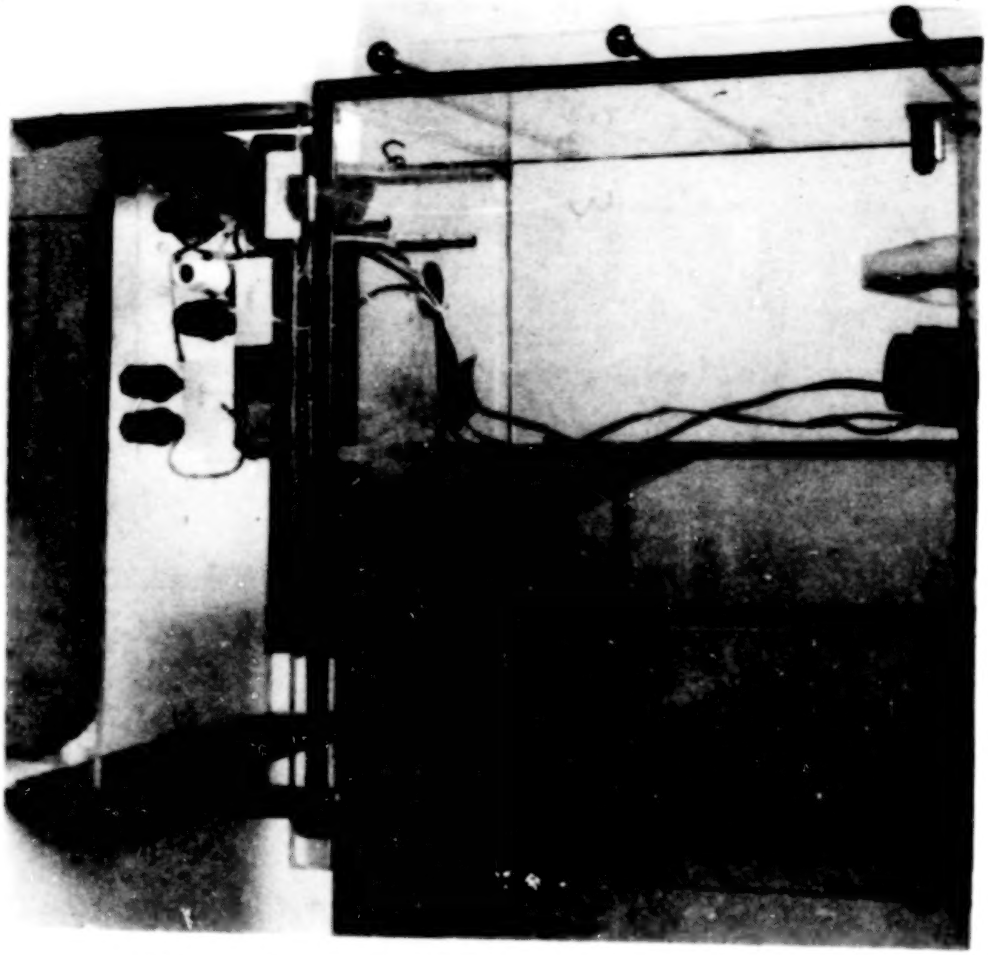

Figure 5.- Animal test area - mouse chamber.

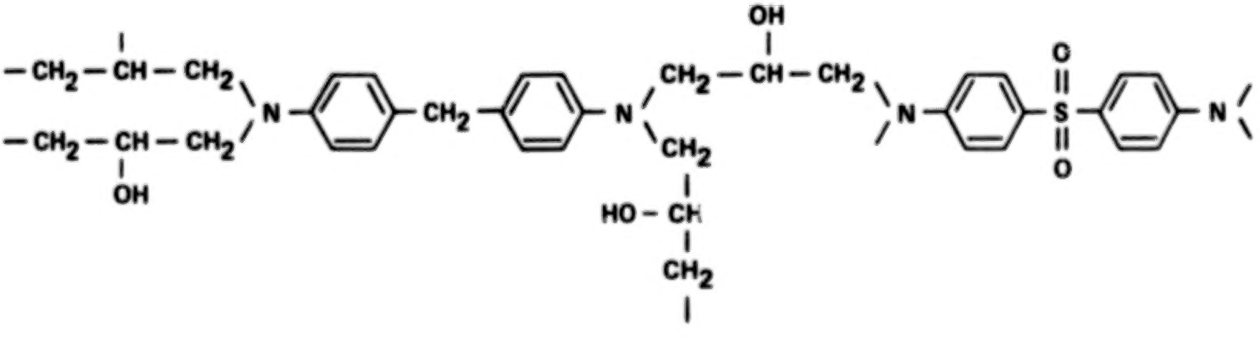

Figure 6.- Resin molecular structure.

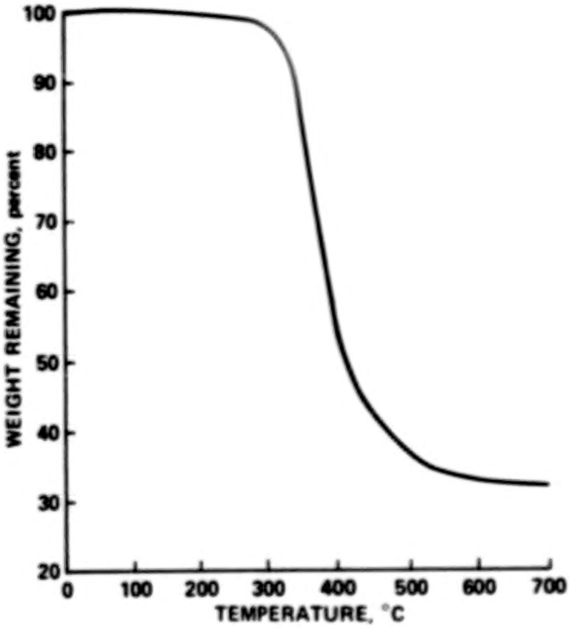

(a) N_2.

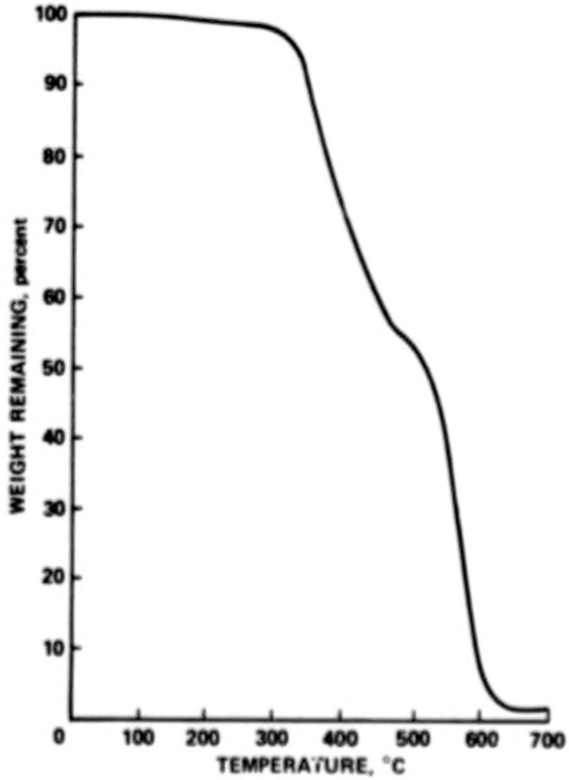

(b) Air.

Figure 7.- Thermogravimetric analysis of resin.

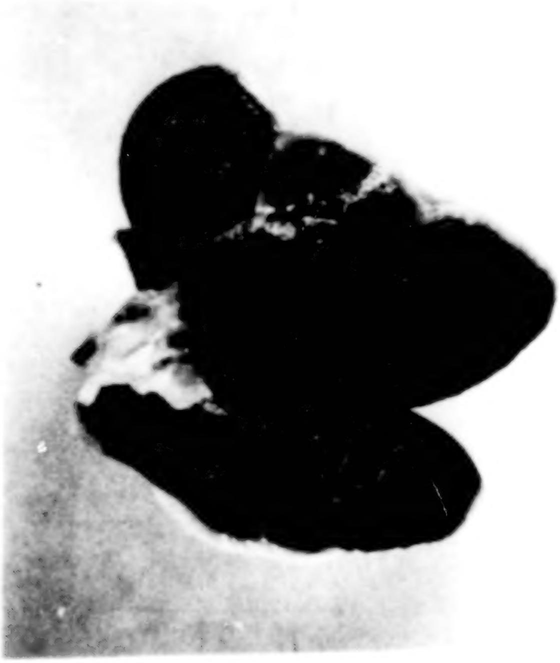

Figure 8.- Pulmonary edema.

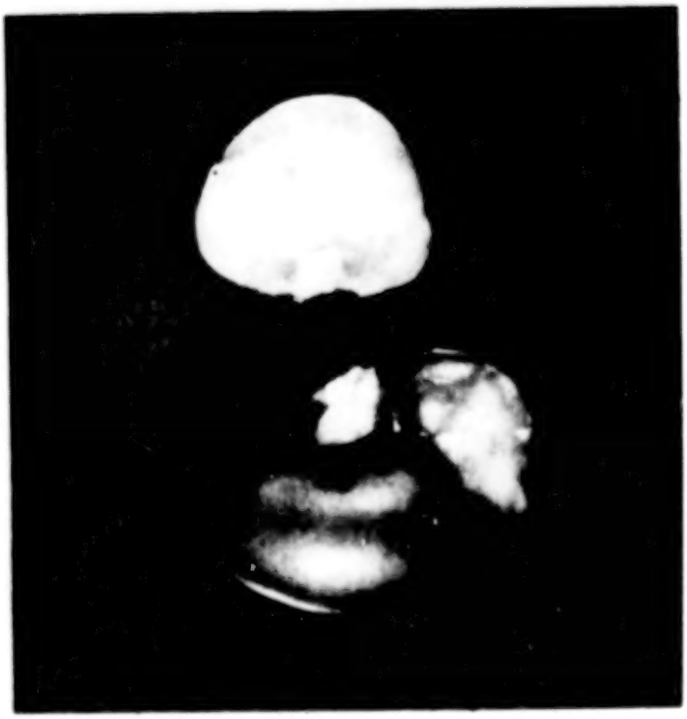

Figure 9.- Tissue necrosis. Radiant panel test 3501-6AS-5.

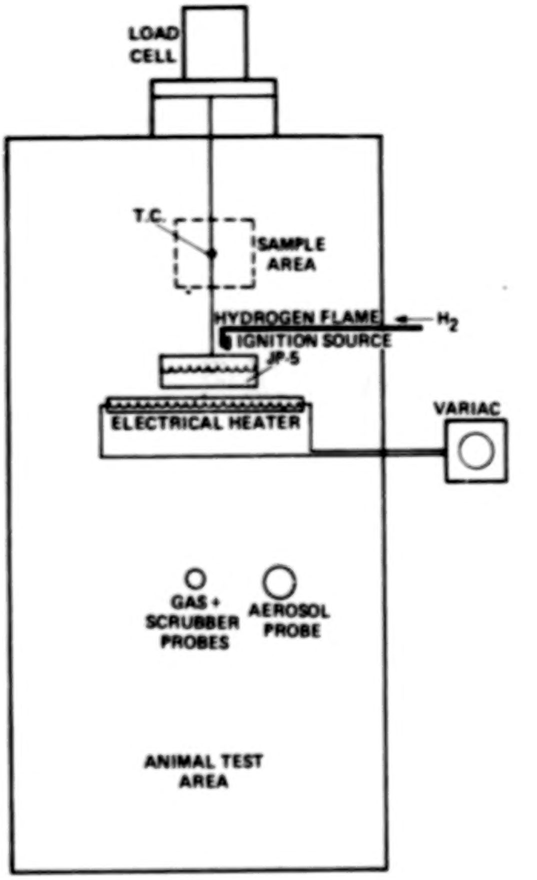
LOAD CELL
T.C.
SAMPLE AREA
HYDROGEN FLAME
H2
IGNITION SOURCE
JP-5
ELECTRICAL HEATER
VARIAC
GAS + SCRUBBER PROBES
AEROSOL PROBE
ANIMAL TEST AREA

Figure 10.- Modified radiant panel facility for JP-5 tests.

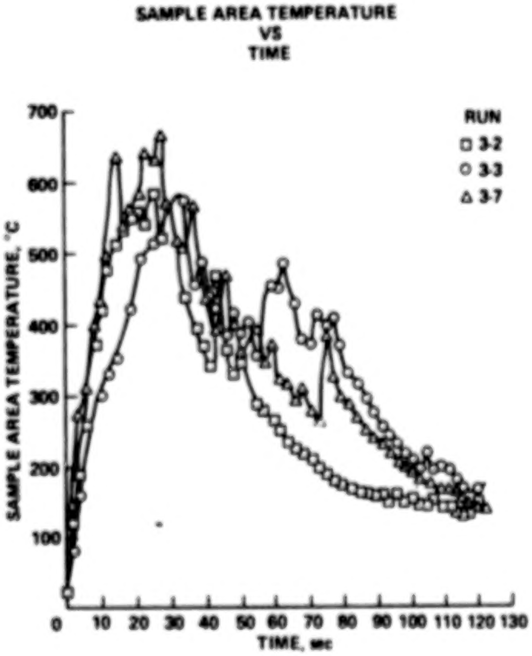

Figure 11.- Sample temperature vs time for JP-5 fire test.

BLANK PAGE

BLANK PAGE

THE USE OF ANTIMISTING KEROSENE (AMK) IN TURBOJET ENGINES

Harold W. Schmidt
NASA Lewis Research Center

SUMMARY

Test conducted by the FAA have demonstrated the crash-fire resistance of antimisting kerosene (AMK), a jet fuel containing an antimisting additive. This additive, a high-molecular-weight polymer, causes the fuel to resist atomization and liquid shear forces, which also affect flow characteristics in the engine fuel system. The flow rate of AMK is not a constant function of the pressure differential as in the case of Newtonian liquids. However, this shear resistance and its resultant non-Newtonian flow characteristics can be negated by molecular shear degradation. The purpose of this program was to evaluate the effect of AMK flow characterisitcs on fan-jet engines and the impact of degradation requirements on the fuel system.

It has been determined from the present program that AMK fuel cannot be used without predegradation, although some degradation occurs throughout the fuel feed system, especially in the fuel pumps. Although the technical feasibility of a mechanical fuel degradation system has been demonstrated, the practicability and cost effectiveness must be established. Several potential problem areas have been identified.

There is a tendency toward FM-9 AMK additive agglomeration and gel formation when the liquid flows at a critical velocity through very small passages. The data indicate this phenomenon to be a function of the degree of degradation, the passage size, the differential pressure, the fluid temperature, and the accumulated flow time. Additionally, test results indicate that the long-term cumulative effects of this phenomenon may require more degradation than the theoretical requirement determined from short-term tests.

INTRODUCTION

Antimisiting kerosene is a kerosene-fraction jet fuel containing an additive which reduces the flammibility of the fuel in an aircraft crash. The most promising AMK additives are high-molecular-weight polymers that are dissolved in Jet A fuel in concentrations in the range of 0.3 percent. These additives have demonstrated their ability to inhibit ignition and flame propagation of the released fuel in simulated crash tests.

The AMK fuel resists misting and atomization from wind shear and impact forces and instead tends to form globules. This agglomeration significantly reduces ignitibility and flame propagation.

The antimisting additive (FM-9) selected for more comprehensive testing in this program was developed by the Imperial Chemical Industries and the Royal Aircraft Establishment (RAE) of the United Kingdom and is being evaluated for crash-fire resistance by the FAA and RAE.

The properties of AMK that make it fire resistant also give it undesirable flow characteristics in the engine fuel feed system. The main problems are its non-Newtonian flow characteristic, which results in lower friction losses at low flow rates; a variable onset of turbulent flow rates, which depend on the degree of degradation; and the tendency for the additive to agglomerate with gel formation when the liquid is throttled (accelerated) through small clearances or passages.

In cooperation with the FAA, NASA conducted a program to evaluate AMK for airline use through a contract the Pratt & Whitney Aircraft Group who tested and evaluated the effects of FM-9 AMK on the fuel feed system of the JT8D engine. The purpose of the tests was to identify operating problems, assess the adaptability of existing engines to AMK, and to determined the potential viability of this fuel in present and future fan-jet engines. The data presented herein were obtained in that program.

Critical fuel system components and subsystems were tested and evaluated for AMK compatibility. Components tested included the fuel pump, the fuel controller, system filters, nozzles, and combustors.

The program included laboratory tests for fuel characterization, chemical compability, thermal stability, heat transfer, and rheological properties. System tests included nozzle spray-pattern tests, filtration limits, controller function, pump performance, ignition start, and relight tests.

AMK CHARACTERISTICS

Antimisting kerosene fuel exhibits the greatest shear resistance and crash-fire resistance before exposure to shear, such as pumping flow through pipes and fittings, filters, or other components. Successive exposure to any of these shear forces tends to break the polymeric molecules, thereby reducing the average molecular weight and the subsequent shear resistance. Continuation of such shear degradation causes AMK to revert to the original properties of the base fuel.

This characteristic provides the possibility of using AMK in existing engines if the level of degradation required for acceptable performance for each critical component is assured.

The AMK additives have a molecular weight of over 5 000 000, and these molecules tend to resist the turbulent flow in liquid boundary layers and extend the viscous flow regime, thereby acting as a drag reducer. The resistance to shear and droplet breakup also affects nozzle performance. For example, figure 1(a) shows the typical atomization of Jet A fuel in a standard JT8D nozzle at ignition flow rates. Figure 1(b) shows the behavior of undegraded AMK in the same nozzle. Similarly, figure 2 shows fuel behavior for the standard nozzle, and figures 3 and 4 for nozzles with successively increased atomization capabilities built into their designs. As shown in figure 5, the calibration curve for turbine flowmeters with antimisting fuel does not exhibit constant K (cycle per cubic meter); therefore, the flowmeter must be recalibrated for any given conditions (degradation level and temperature) to be used.

With the use of a micromotion mass meter, the flow rate of AMK can be accurately measured at any level of degradation (fig. 6). It was determined that, at the level of degradation required by the propulsion system, the normal accuracy of turbine flowmeters is obtained.

Heat-transfer measurements show a marked reduction in the heat transfer with undegraded AMK in the turbulent flow range, because of the boundary-layer turbulence suppression of the undegraded FM-9 molecules (fig. 7). Note that increasing levels of degradation causes the heat-transfer coefficient to approach Jet A values. The thermal stability of AMK (table I) was better than Jet A, and further study is planned to determine the reason for this apparent improvement.

Two additional characteristics were tested: water solubility and materials compatibility. The results of the water solubility tests are shown in table II. Although the unsheared Jet A/FM-9 appears to absorb less water than the Jet A fuel, further investigation is required because some of the FM-9 additive separated from the solution during the tests. The standard test procedure used for this test may not be representative of the actual AMK/water compatibility, but this will have to be thoroughly explored.

Some incompatibilities of component materials were observed and measured with the FM-9 AMK tested. The hardness and tensile strength of Buna-N and fluoro-silicone elastomers were lowered after a 30-day exposure, and there was a tendency towards swelling. Also, chemical interaction was measured in alloys containing copper, although bronze materials in the test components were not adversely effected by the AMK during the test program.

FUEL SYSTEM COMPONENTS TESTS WITH FM-9 AMK

The non-Newtonian flow behavior, caused by these large FM-9 molecules, is more pronounced in flow through small passages or close clearances (such as through filters and fuel flow controllers). The flow velocity of AMK through a capillary or filter increases (in Newtonian fashion) as a function of pressure until a "critical" transition occurs, requiring a sharply increased rate of pressure increase to cause a continuing flow-rate increase (fig. 8). During this transition, the AMK molecules have an increased tendency to agglomerate, forming a gel precipitate. (This "critical region is also a function of the degree of degradation.)

These critical velocity effects can be controlled or accommodated in several ways:

(1) By increasing the level of degradation
(2) By increasing the flow area of filters
(3) By increasing the flow passage length to diameter ratio, thereby reducing the flow-rate increase for a given change in pressure
(4) By increasing the temperature, which increases the velocity at which critical flow occurs

As the pressure and flow rate is increased past the critical velocity, a second critical velocity is reached when the shear forces are sufficient for molecular fragmentation and AMK degradation. Two parameters effect the degradation process:

(1) Time of exposure to degradation process
(2) The amount of stress or energy at or above degradation stress levels

The use of AMK for crash-fire mitigation requires the fuel in the aircraft fuel tanks to be maintained in a relatively undegraded state, and, as the fuel is metered to the engine, a degradation level, as required to permit the AMK flow through all critical components, must be provided. This will require an energy efficient degrader that can provide the highest molecular shear stress with the lowest possible power requirement.

The major problem in the effort to evaluate the effects of AMK on the performance of fuel system components was the accurate measurement of the degree or percent of degradation of the test fuel. The filtration rate ratio of AMK versus Jet A provided the best discrimination of the viscosity change as a function of the degree of shear degradation of three viscosity measurement techniques used (fig. 9).

Seventeen-micrometer mesh metal filters were used as the measurement standard, which gave a good discrimination of degradation as a function of stress time to a filtration rate ratio (AMK/Jet A) of approximately 4; but below 4 the curve flattens out. However, by measuring the amount of flow as a function of shear exposure and using 8- and 10-micrometer filters, better viscosity discrimination was achieved at the higher degradation levels.

The JT8D fuel pump assembly was used to degrade the AMK test fuel to desired levels. Figure 10 shows the degradation achieved as a function of the number of passes through the pump.

The difference in the power input into the pump was not measurable, even though significant degradation was achieved in the process. Preliminary data tend to support the possibility that the drag reduction characteristic of the polymer additive in part compensates for the energy used in the degradation process. Follow-on experimental tests are expected to quantify the degradation energy requirement and to identify the best method of degrading the fuel.

Qualitative comparisons of the emissions characteristics of AMK versus Jet A using the standard nozzle and the later low-emissions nozzle are shown in figure 11. It should be pointed out that 3-pass AMK (i.e., AMK after 3 passes through the fuel pump) is only partially degraded, and it is expected that AMK degraded to full system requirements will meet Jet A emission values. Subsequent testing will determine the optimum level of degradation.

Tests were conducted to compare engine-ignition and altitude-relight characteristics of AMK and Jet A. Partially degraded AMK required approximately 25 percent higher fuel flows to achieve full ignition in the nine-can burner test rig (fig. 12). Further tests are expected to show fully degraded AMK to be equivalent to Jet A.

The altitude relight tests at an air flow of 2.27 kilograms were the same for AMK and Jet A; at all other flow rates, the AMK relights were poorer.

Performance testing of the fuel controller with 16-pass AMK was completed without detrimental effects in comparative performance between Jet A and 16-pass AMK. An 8-hour closed-loop cycle test was subsequently completed without measurable differences or effects from the AMK.

Pump testing and calibration with undegraded AMK showed no detrimental effects. An apparent improvement in the flow rate and differential pressure for a given speed was observed with partially degraded and undegraded fuel. This drag reduction influence became negligible with increasing degradation, and pump performance with 16-pass AMK was the same as for Jet A fuel.

RESULTS AND CONCLUSIONS

1. It is technically feasible to operate JT8D engines with 0.3 percent FM-9 AMK fuel.

2. The degree of degradation that is necessary for AMK fuel compatibility with existing fuel system designs has been determined to be in the filter ratio range of 1.2, or lower, using a 17-micrometer filter.

3. The primary modification requirements for turbofan jet engines to accommodate FM-9 AMK will be the addition of a fuel degrader before the fuel pump, which will provide the selected level of degradation.

4. Methods of predegrading AMK fuel in a flight certified system must be evaluated for practicability, cost, and energy effectiveness.

5. Data obtained with JT8D engine are applicable to other engines because the characteristic limiting parameters of AMK are the critical flow velocity and the degradation level, and these are a function of filter mesh sizes and clearance specification of component parts.

TABLE I. – THERMAL STABILITY OF UNSHEARED ANTIMIST FUEL AND FUEL CONTAINING NO ADDITIVE

Temperature, °C	Parent fuel		Fuel containing additive	
	Deposit code	Differential pressure, mPa (mm Hg)	Deposit code	Differential pressure, mPa (mm Hg)
230	1	0.53 (4.0)	-	----------
245	1	7.3 (55)	-	----------
260	4	6.8 (51)	1	0.03 (0.2)
275	-	----------	4	.07 (.5)
290	-	----------	4	.13 (1.0)
320	-	----------	4	.20 (1.5)

Fuel	Breakpoint temperature, °C	Failure mode
Jet A	230 - 245	ΔP
3-Pass	275 - 290	Deposit code
1-Pass	260 - 275	Deposit code
Undegraded	260 - 275	Deposit code

TABLE II. - WATER SOLUBILITY TESTS

[Parts per million]

	Jet A	AMK unsheared
Before test	22	32
After test	60 - 64	40

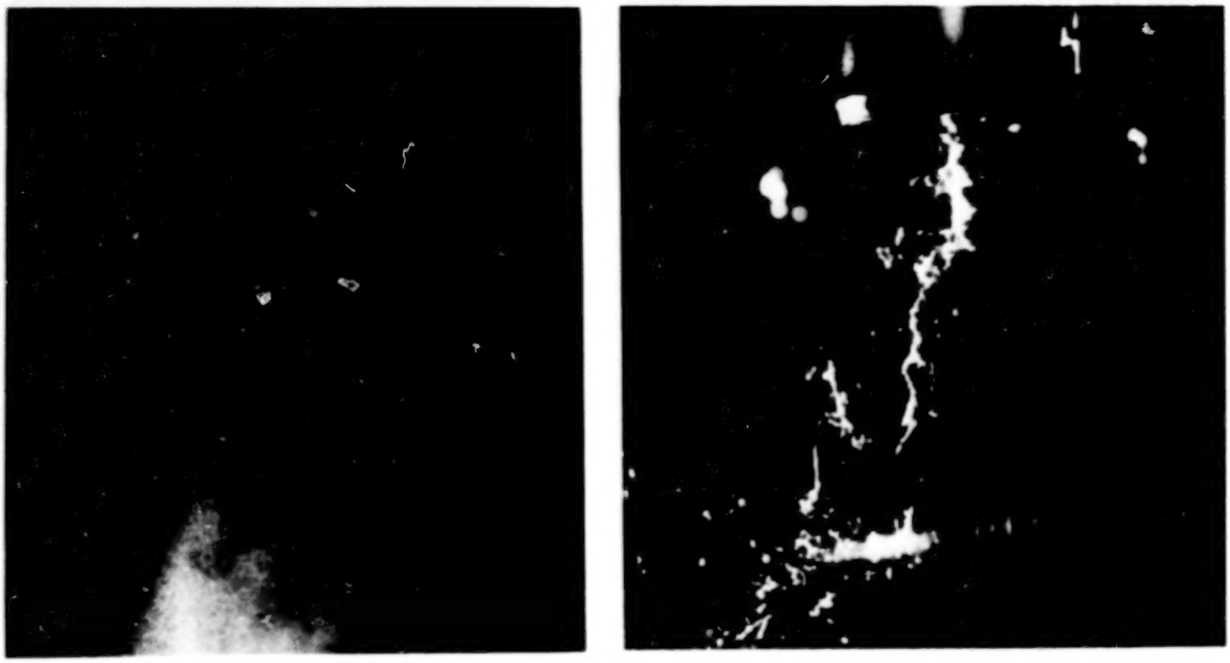

(a) Jet A.
(b) Undegraded antimisting fuel.

Figure 1.- Comparison of spray patterns with JT8D production-pressure atomizing nozzle and Jet A undegraded antimisting fuel.

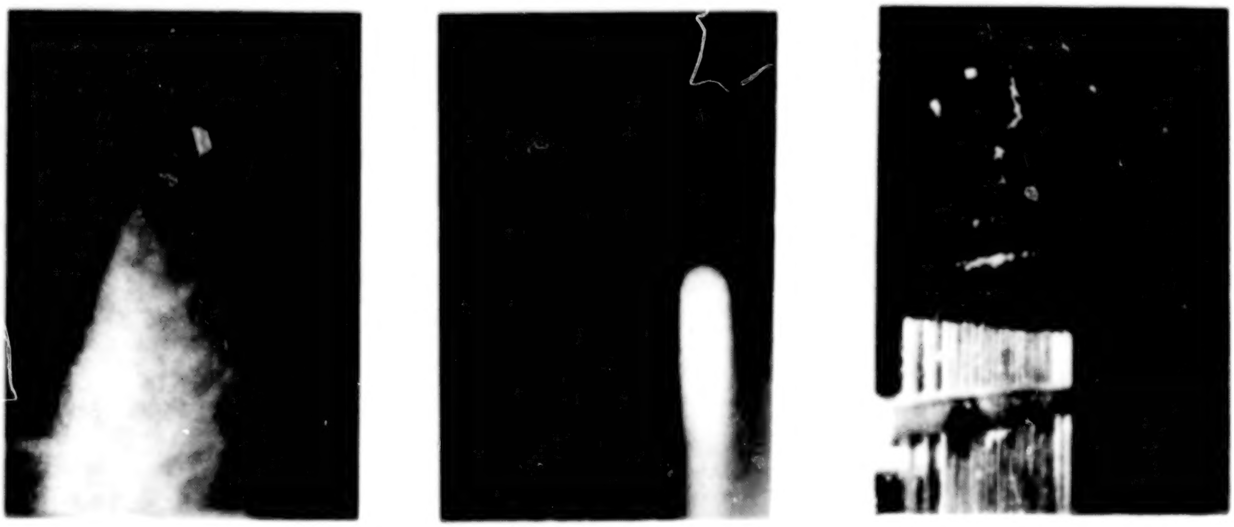

(a) Jet A.
(b) Degraded FM-9.
(c) Undegraded FM-9.

Figure 2.- Spray pattern with standard JT8D engine at ignition conditions.

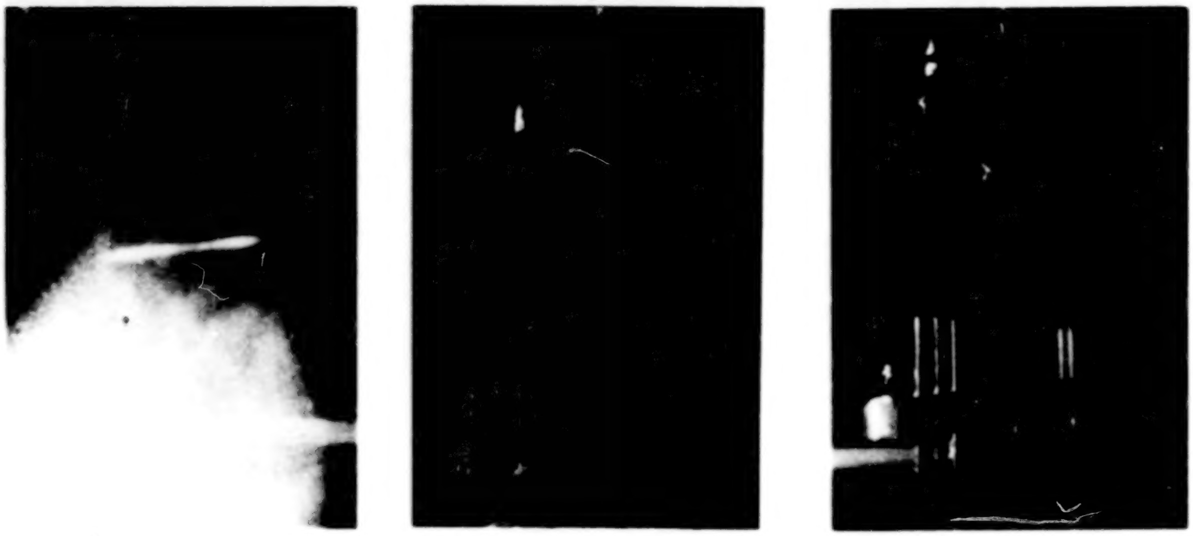

(a) Jet A. (b) Degraded FM-9. (c) Undegraded FM-9.

Figure 3.- Spray pattern with JT8D low-emission engine at ignition conditions.

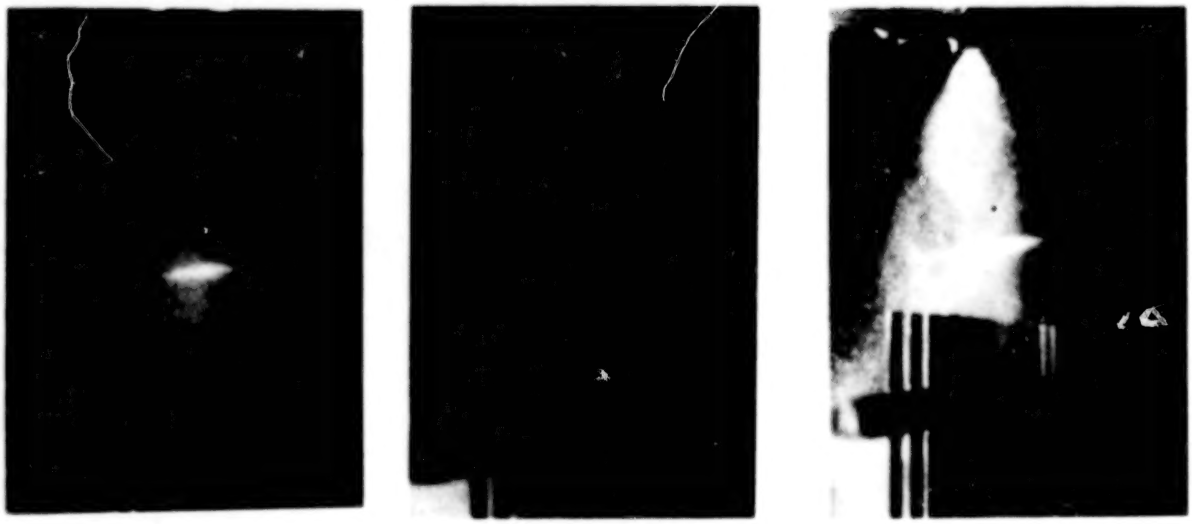

(a) Jet A. (b) Degraded FM-9. (c) Undegraded FM-9.

Figure 4.- Spray pattern with JT8D air-boost engine at ignition conditions.

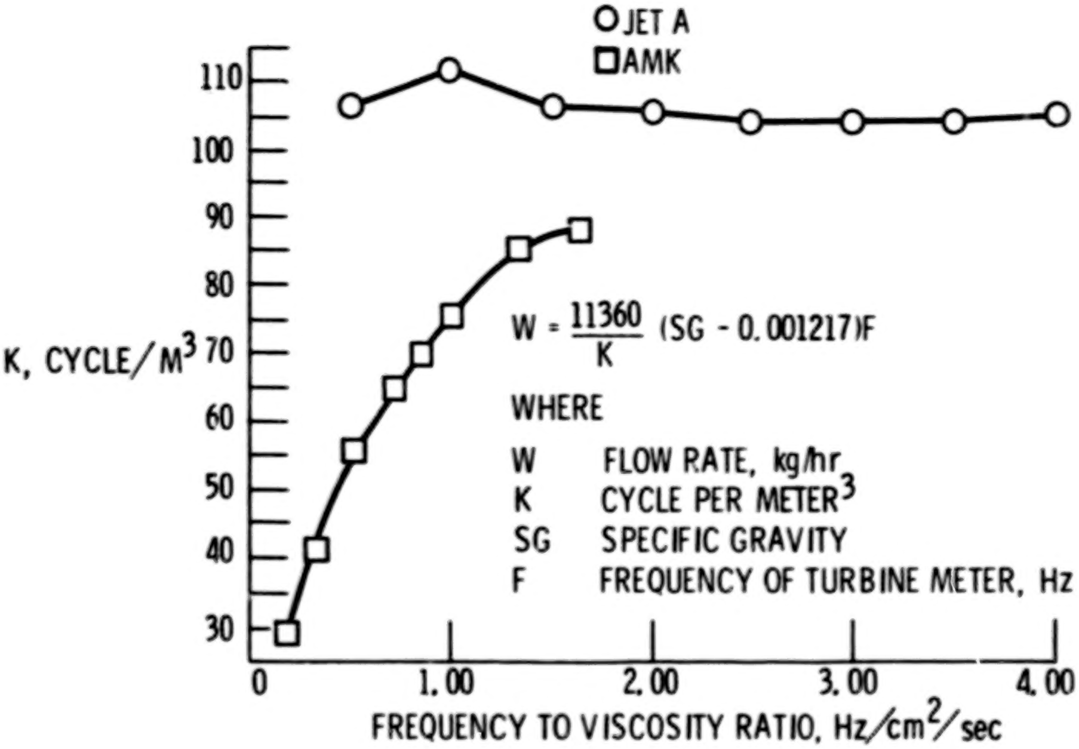

Figure 5.- Calibration curve for No. 8 turbine flowmeter.

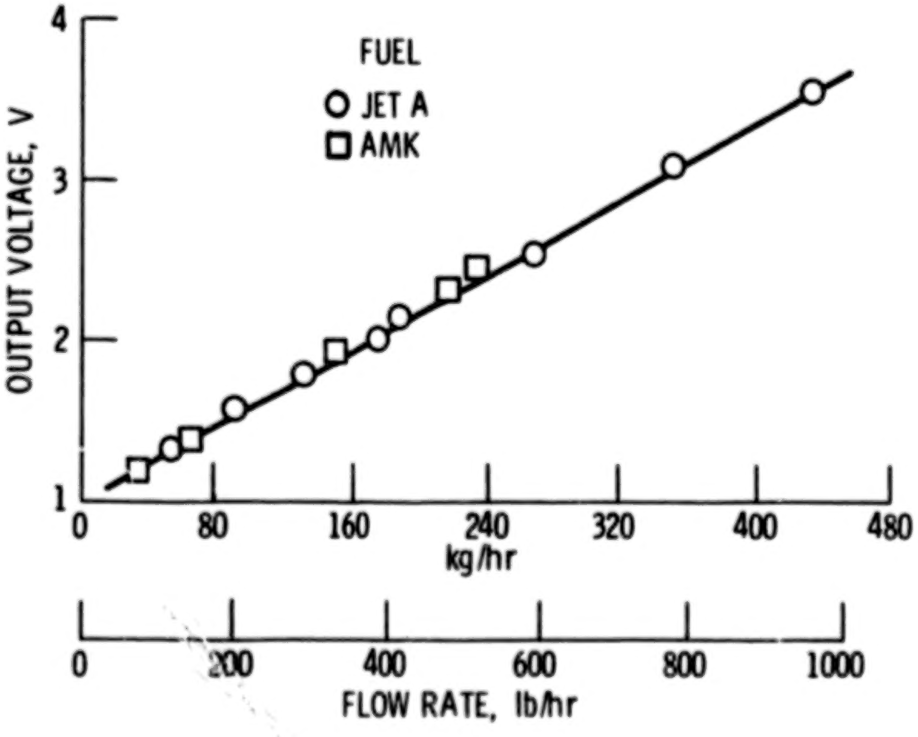

Figure 6.- Calibration data for a micrometer mass flowmeter.

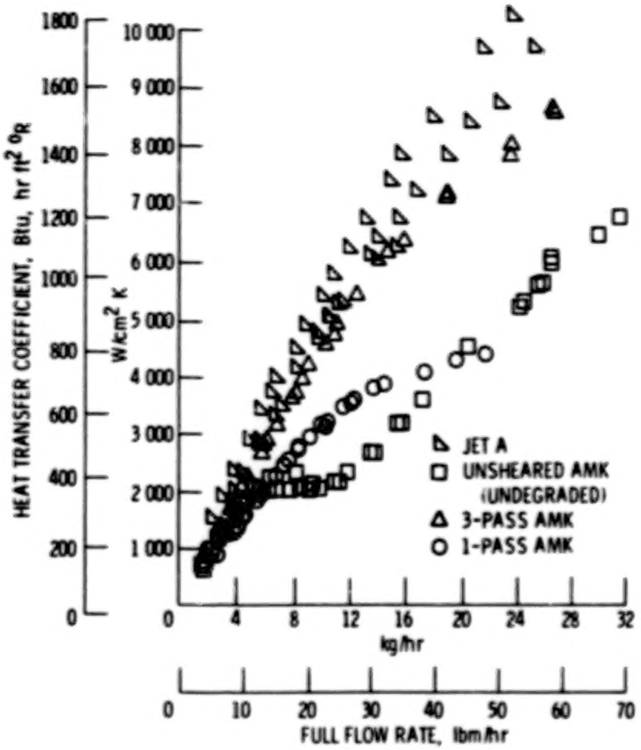

Figure 7.- Effect of anitmisting additives on heat transfer in fuel-oil cooler tubes.

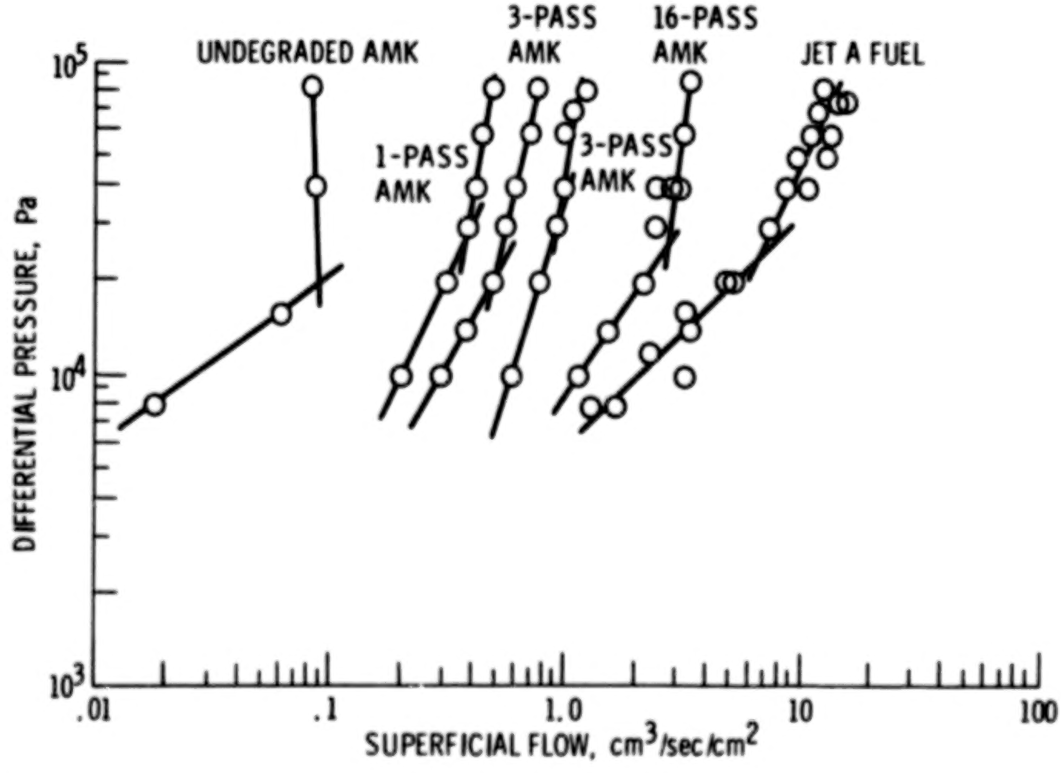

Figure 8.- Degree of AMK degradation as function of superficial flow velocity and differential pressure.

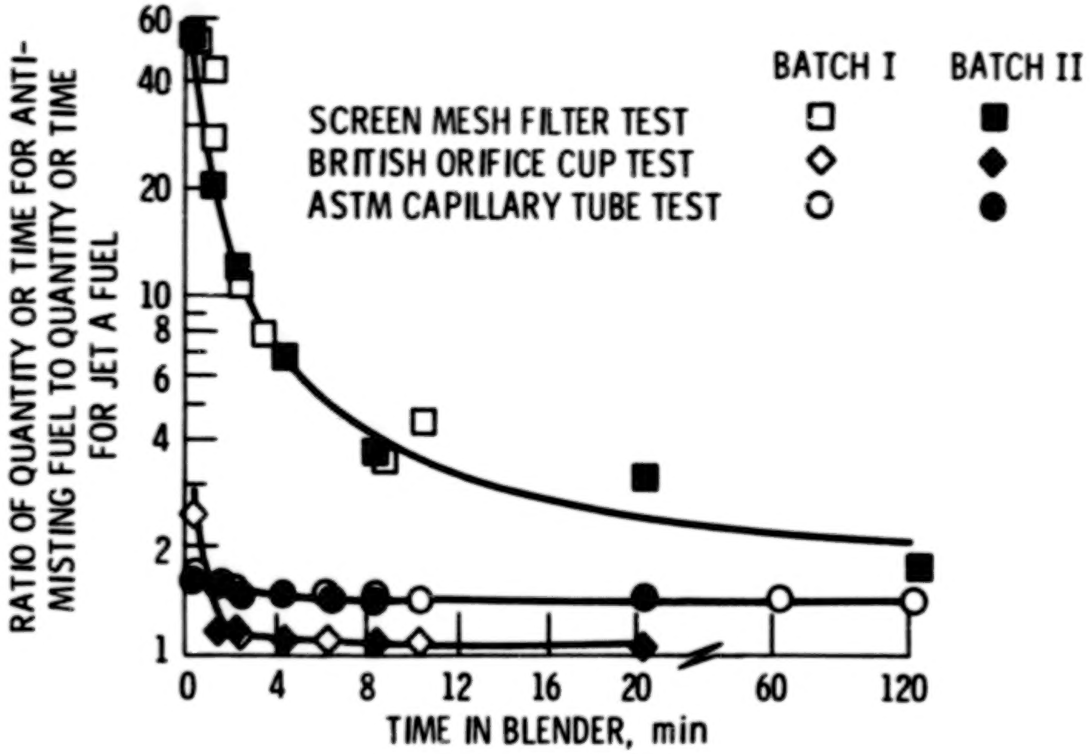

Figure 9.- Correlation of three viscosity measuring devices.

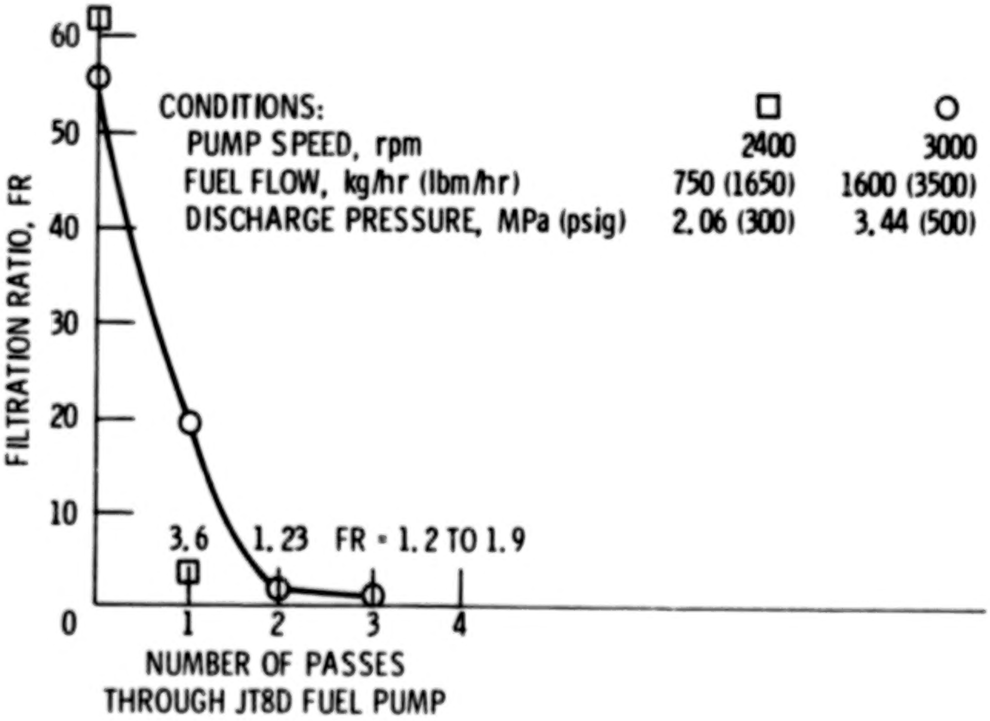

Figure 10.- Typical antimisting kerosene (AMK) shearing characteristics filter ratio (AMK time to Jet A time through 17-μm screen) sampled at collection tank.

EMISSION	STANDARD JT8D		LOW EMISSION JT8D	
	1-PASS AMK	3-PASS AMK	1-PASS AMK	3-PASS AMK
NO_x SMOKE	SAME[a] SAME	SAME SAME	SAME SAME	SAME SAME

[a] AS JET A.

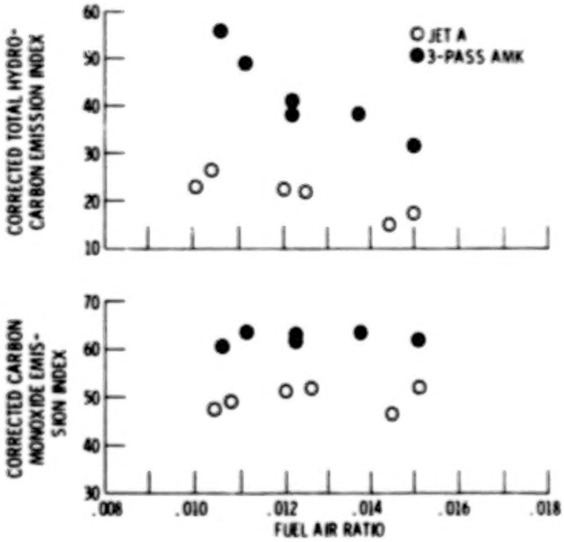

Figure 11.- Comparison of degraded antimisting kerosene (AMK) with Jet A fuel, tested in JT8D nozzles.

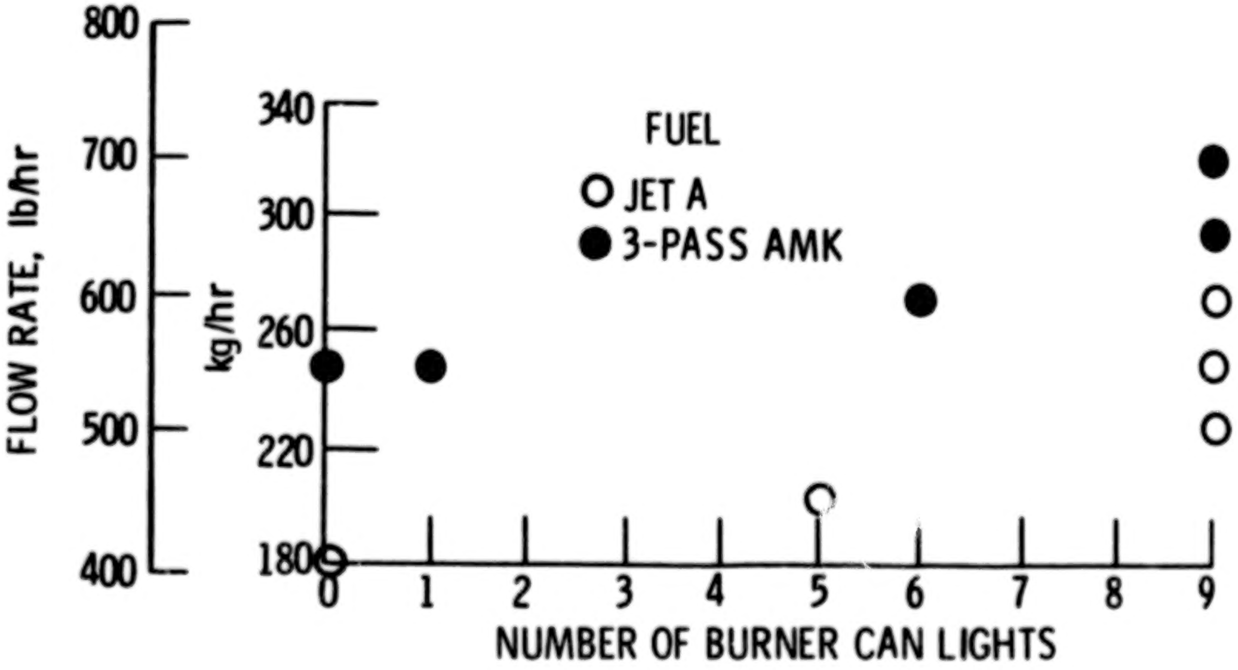

Figure 12.- Sea-level ignition behavior for antimisting kerosene (AMK) and Jet A fuels.

NASA/FAA GENERAL AVIATION CRASH DYNAMICS PROGRAM

Robert G. Thomson, Robert J. Hayduk, and Huey D. Carden
Langley Research Center

SUMMARY

The objective of the Langley Research Center General Aviation Crash Dynamics program is to develop technology for improved crash safety and occupant survivability in general aviation aircraft. The program involves three basic areas of research: controlled full-scale crash testing, nonlinear structural analyses to predict large deflection elastoplastic response, and load attenuating concepts for use in improved seat and subfloor structure. Both analytical and experimental methods are used to develop expertise in these areas. Analyses include simplified procedures for estimating energy dissipating capabilities and comprehensive computerized procedures for predicting airframe response. These analyses are being developed to provide designers with methods for predicting accelerations, loads, and displacements on collapsing structure. Tests on typical full-scale aircraft and on full- and subscale structural components are being performed to verify the analyses and to demonstrate load attenuating concepts.

A special apparatus has been built to test Emergency Locator Transmitters (ELT's) when attached to representative aircraft structure. The apparatus is shown to provide a good simulation of the longitudinal crash pulse observed in full-scale aircraft crash tests.

INTRODUCTION

In 1972, NASA embarked on a cooperative effort with the FAA and Industry to develop technology for improved crashworthiness and occupant survivability in general aviation aircraft. The effort includes analytical and experimental work and structural concept development. The methods and concepts developed in this ongoing effort are expected to make possible future general aviation aircraft designs having enhanced survivability under specified crash conditions with little or no increase in weight and acceptable cost. The overall program is diagramed in figure 1 with agency responsibility indicated by the legend.

Crashworthiness design technology is divided into three areas: environmental, airframe design, and component design. The environmental technology consists of acquiring and evaluating field crash data to support and validate parametric studies being conducted under controlled full-scale crash testing, the goal being to define a crash envelope within which the impact parameters allow human tolerable acceleration levels.

Airframe design has a twofold objective: to assess and apply current, on-the-shelf, analytical methods to predict structural collapse; and to develop and validate new and advanced analytical techniques. Full-scale tests are also used to verify analytical predictions, as well as to demonstrate improved load attenuating design concepts. Airframe design also includes the validation of novel load-limiting concepts for use in aircraft subfloor designs.

Component design technology consists of exploring new and innovative load-limiting concepts to improve the performance of the seat and occupant restraint systems by providing for controlled seat collapse while maintaining seat/occupant integrity. Component design also considers the design of non-lethal cabin interiors.

Langley's principal research areas in the joint FAA/NASA Crash Dynamics program are depicted pictorially in figure 2. These areas include full-scale crash testing, nonlinear crash impact analyses, and crashworthy seat and subfloor structure concept development. Subsequent sections deal with these topics, as well as Emergency Locator Transmitter (ELT) testing.

FULL-SCALE CRASH TESTING

Full-scale crash testing is performed at the Langley Impact Dynamics Research Facility (ref. 1) shown in figure 3. This facility is the former lunar landing research facility modified for free-flight crash testing of full-scale aircraft structures and structural components under controlled test conditions. The basic gantry structure is 73 m (240 ft) high and 122 m (400 ft) long supported by three sets of inclined legs spread 81 m (267 ft) apart at the ground and 20 m (67 ft) apart at the 66 m (218 ft) level. A movable bridge with a pullback winch for raising the test specimen spans the top and traverses the length of the gantry.

Test Method

The aircraft is suspended from the top of the gantry by two swing cables and is drawn back above the impact surface by a pullback cable. An umbilical cable, used for data acquisition, is also suspended from the top of the gantry and connects to the top of the aircraft. The test sequence is initiated when the aircraft is released from the pullback cable, permitting the aircraft to swing pendulum style into the impact surface. The swing cables are separated from the aircraft by pyrotechnics just prior to impact, freeing the aircraft from restraint. The umbilical cable remains attached to the aircraft for data acquisition, but it also separates by pyrotechnics before it becomes taut during skid out. The separation point is held relatively fixed near the impact surface, and the flight path angle is adjusted from 0° to 60° by changing the length of the swing cable. The height of the aircraft above the impact surface at release determines the impact velocity which can be varied from 0 to 26.8 m/s (60 mph). The movable bridge allows the pullback point to be positioned along the gantry to insure that the pullback cables pass through the center of gravity and act at 90° to the swing cables.

To obtain flight path velocities in excess of 26.8 m/s (60 mph) a velocity augmentation method has been devised which uses wing-mounted rockets to accelerate the test specimen on its downward swing. As shown in figure 4, two Falcon rockets are mounted at each engine nacelle location and provide a total thrust of 77 850 N. The aircraft is released after rocket ignition, and the rockets continue to burn during most of the downward acceleration trajectory but are dormant at impact. The velocity augmentation method provides flight path velocities from 26.8 to 44.7 m/s (60 to 100 mph) depending on the number and burn time of rockets used.

Instrumentation

Data acquisition from full-scale crash tests is accomplished with extensive photographic coverage, both interior and exterior to the aircraft using low-, medium-, and high-speed cameras and with onboard strain gages and accelerometers. The strain gage type accelerometers (range of 250 g and 750 g at 0 to 2000 Hz) are the primary data-generating instruments, and are positioned in the fuselage to measure accelerations both in the normal and longitudinal directions to the aircraft axis. Instrumented anthropomorphic dummies (National Highway Traffic Safety Administration Hybrid II) are onboard all full-scale aircraft tests conducted at LaRC. The location and framing rate of the cameras are discussed in reference 1. The restraint system arrangement and type of restraint used vary from test to test.

Test Conducted

A chronological summary of the full-scale crash tests conducted at the Impact Dynamics Research Facility is represented in figure 5. The shaded symbols are crash tests that have been conducted, the open symbols are planned crash tests. Different symbols represent different types of aircraft under different impact conditions, for example the □ represents a twin-engine specimen impacting at 26.8 m/s (60 mph) while the ◇ represents the same twin-engine specimen, using the velocity augmentation method, impacting at 40.2 m/s (90 mph). Various types of aircraft have been successfully crash tested at LaRC from 1974 through 1978 including CH-47 helicopters, high and low wing single-engine aircraft, and aircraft fuselage sections. Data from these tests are presented in references 2 to 4. The aircraft fuselage section tests are vertical drop tests conducted to simulate full-scale aircraft cabin sink rates experienced by twin-engine aircraft tested earlier. The response of the aircraft section, two passenger seats, and two dummies are being simulated analytically (see "Nonlinear Crash Impact Analysis"). Some single-engine crash tests were conducted using a dirt impact surface while most crash tests were conducted on a concrete surface. The dirt embankment was 12.2 m (40 ft) wide, 24.4 m (80 ft) long, and 1.2 m (4 ft) in depth. The dirt was packed to the consistency of a ploughed field. The variation of full-scale crash test parameters is not complete and does not consider such secondary effects as aircraft sliding, overturning, cartwheeling, or tree and obstacle impact.

Controlled-Crash Test and Las Vegas Accident

On August 30, 1978, a twin-engine Navajo Chieftain, carrying a pilot and nine passengers crash landed in the desert shortly after taking off from the North Las Vegas Airport. All ten persons on board were killed. A comparative study of this Navajo Chieftain crash and a similar NASA controlled-crash test was made. The purposes of the study were to compare damage modes and estimate acceleration levels in the Chieftain accident with Langley tests and to assess the validity of Langley's full-scale crash simulation. The controlled-crash test chosen employed the velocity augmentation method wherein the aircraft research a flight path velocity of 41.4 m/s (92.5 mph) at impact. The pitch angle was -12^{0}, with a 5^{0} left roll and 1^{0} yaw. Figure 6 shows photographs of the two aircraft. The NASA specimen is a twin-engine pressurized Navajo, which carries from six to eight passengers, and although the cabin is shorter in length, it is similar in structural configuration to the Chieftain.

Structural damage to the seats and cabin of the Navajo Chieftain and to the seats and cabin of the NASA test specimen are shown for illustrative purposes in figure 7. Much more corroborating structural damage is discussed in reference 5. The Chieftain apparently contacted the nearly level desert terrain at a location along the lower fuselage on the right side opposite the rear door. An instant later, the rest of the fuselage and the level right wing impacted. The Chieftain's attitude just prior to impact was concluded to have been the following: pitched up slightly, rolled slightly to the right and yawed to the left. The two aircraft differ in roll attitude at impact but are comparable. The structural damage to the cabin of the Chieftain was much greater than that exhibited by the NASA controlled-crash test under correspondingly similar impact attitudes. The damage pattern to the standard passenger and crew seats of the Chieftain was similar to that in the NASA tests, but generally exhibited more severe distortion. The damage patterns suggests similar basic failure modes and in the case of the seat distortion of flight impact velocity in excess of 41.4 m/s (92.5 mph) for the Chieftain. Acceleration time histories from the first passenger seat and floor of the NASA controlled-crash test are shown in figure 8 where the first passenger seat corresponds to the damaged seat shown in figure 7.

Because of the similarity in the damage, patterns exhibited by seats 6 and 8 of the Chieftain and the first passenger seat of the NASA controlled test, generalized conclusions can be drawn relative to certain seat accelerations experienced by those passengers in the Chieftain. The peak pelvic accelerations of passengers 6 and 8 in the Chieftain accident were probably in excess of 60 g's normal (to aircraft axis), 40 g's longitudinal, and 10 g's transverse.

NONLINEAR CRASH IMPACT ANALYSIS

The objective of the analytical efforts in the crash dynamics program is to develop the capability to predict nonlinear geometric and material behavior of sheet-stringer aircraft structures subjected to large deformations and to demonstrate this capability by determining the plastic buckling and collapse response of such structures under impulsive loadings. Two specific computer programs are being developed, one focused on modeling concepts applicable to large plastic deformations of realistic aircraft structural components, and the other a versatile seat/occupant program to simulate occupant response. These two programs are discussed in the following sections.

Plastic and Large Deflection Analysis of Nonlinear Structures (PLANS)

Description

For several years LaRC has been developing a sophisticated structural analysis computer program which includes geometric and material nonlinearities (refs. 6 and 7). "PLANS" is a finite element program for the static and dynamic nonlinear analysis of aircraft structures. PLANS computer program is capable of treating problems which contain bending and membrane stresses, thick and thin axisymmetric bodies, and general three-dimensional bodies. PLANS, rather than being a single comprehensive computer program, represents a collection of special purpose computer programs or modules, each associated with a distinct class of physical problems. Using this concept, each module is an independent finite element computer program with its associated element library. All the programs in PLANS employ the "initial strain" concept within an incremental procedure to account for the effect of plasticity and include the capability for cyclic plastic analysis. The solution procedure for treating material nonlinearities (plasticity) alone reduces the nonlinear material analysis to the incremental analysis of an elastic body of identical shape and boundary conditions, but with an additional set of applied "pseudo loads." The advantage of this solution technique is that it does not require modification of the element stiffness matrix at each incremental load step. Combined material and geometric nonlinearities are included in several of the modules and are treated by using the "updated" or convected coordinate approach. The convected coordinate approach, however, requires the reformation of the stiffness matrix during the incremental solution process. After an increment of load has been applied, increments of displacement are calculated and the geometry is updated. In addition to calculating the element stresses, strains, etc., the element stiffness matrices and mechanical load vector are updated because of the geometry changes and the presence of initial stresses. A further essential ingredient of PLANS is the treatment of dynamic nonlinear behavior using the DYCAST module. DYCAST incorporates various time-integration procedures, both explicit and implicit, as well as the inertia effects of the structure.

Comparison With Experiment

PLANS is currently being evaluated by comparing calculations with experimental results on simplified structures, such as a circular cylinder, a tabular frame structure, an angular frame with joint eccentricities, and the same angular frame covered with sheet metal. Static and dynamic analyses of these structures loaded into the large deflection plastic collapse regime have been conducted with PLANS and compared with experimental data in references 8 and 9.

An analytical simulation of a vertical drop test of an aircraft section has recently been compared with experimental full-scale crash data in reference 10. Figure 9 shows the fuselage section prior to testing and figure 10 shows the DYCAST finite element fuselage, seat, and occupant model. The vertical impact velocity of the specimen was 8.38 m/s (27.5 fps). The 50-percentile anthropomorphic dummies each weighed 74.8 kg (165 lb). The occupant pelvis vertical accelerations compared with analysis are shown in figure 11. The DYCAST and ACTION models predicted an accurate mean pelvis acceleration level. The computer program KRASH gave better results with several masses representing the lower and upper torso and predicts an oscillatory response similar to that exhibited by the test.

Modified Seat Occupant Model for Light Aircraft (MSOMLA)

Description

Considerable effort is being expended in developing a good mathematical simulation of occupant, seat, and restraint system behavior in a crash situation. MSOMLA was developed from a computer program SOMLA funded by the FAA as a tool for use in seat design (ref. 11). SOMLA is a three-dimensional seat, occupant, and restraint program with a finite element seat and an occupant modeled with twelve rigid segments joined together by rotational springs and dampers at the joints. The response of the occupant is described by Lagrange's equations of motion with 29 independent generalized coordinates. The seat model consists of beam and membrane finite elements.

SOMLA was used previously to model a standard seat and a dummy occupant in a NASA light aircraft section vertical drop test. During this simulation, problems were experienced with the seat model whenever the yield stress of an element was exceeded. Several attempts to correlate various finite element solutions of the standard seat with OPLANE-MG, DYCAST, and SOMLA using only beam and membrane elements, to experimental data form static vertical seat loading tests were only partially successful. Consequently, to expedite the analysis of the seat/occupant, the finite element seat in SOMLA was removed and replaced with a spring-damper system. Additional modifications to SOMLA added nonrigid occupant contact surfaces (nonlinear springs) and incorporated a 3-D computer graphics display. This modified SOMLA is called MSOMLA. A more complete discussion of MSOMLA, its computer input requirements, and additional comparisons of experiments and analysis can be found in reference 12.

Comparison With Experiment

A comparison of full-scale crash test data from the -30^{0}, 26.8 m/s (60 mph) crash test and occupant simulation using MSOMLA is presented in figure 11 in two-dimensional graphics. Although three-dimensional graphics are available in MSOMLA, only two-dimensional graphics were chosen for the pictorial comparison in figure 12. Note the similarity between the response of the occupant in the simulation and the occupant as seen through the window of the aircraft during crash test. Note also that in the simulation, the dummy's head passes through the back of the seat in front of him, a fact that could explain differences in the computed and measured head accelerations as presented in figure 13. The comparisons of this figure, between measured and computed acceleration pulses are excellent, considering the seat and occupant were subjected to forward, normal, and rotational accelerations. This comparison, using full-scale crash data, demonstrates the versatility of the program's simulation capability.

CRASHWORTHY SEAT AND SUBFLOOR STRUCTURE CONCEPTS

The development of structural concepts to limit the load transmitted to the occupant is another research area in LaRC's crashworthiness program. The objective of this research is to attenuate the load transmitted by a structure either by modifying its structural assembly, changing the geometry of its elements, or adding specific load-limiting devices to help dissipate the kinetic energy. Recent efforts in this area at LaRC have concentrated on the development of crashworthy aircraft seat and subfloor systems.

The concept of available stroke is paramount in determining the load attenuating capabilities of different design concepts. Shown in figure 14 are the three load attenuating areas which exist between an occupant and the impact surface during vertical descent: the landing gear, the cabin subfloor, and the aircraft seat. Attenuation provided by the landing gear will not be included in this discussion since it is more applicable to helicopter crash attenuators. Using the upward human acceleration tolerance of 25 g as established in ref. 13, a relationship between stroke and vertical descent velocity can be established for a constant stroking device which fully strokes in less than the maximum time allowable (0.10 s) for human tolerance. This relationship is illustrated in fig. 14. Under the condition of a constant 25 g deceleration stroke the maximum velocity decrease for the stroking available is 12.2 m/s (40 fps) for the seats and 8.2 m/s (27 fps) for the subfloor (assuming 30 cm (12 in.) and 15 cm (6 in.) in general for a twin-engine light aircraft). For a combination of stroking seat and stroking subfloor the maximum velocity decrease becomes 15.2 m/s (50 fps). These vertical sink rates are comparable to the Army Design Guide recommendations (ref. 13) for crashworthy seat design.

Seat

Figure 15 shows a standard passenger and three load-limiting passenger seats that were developed by the NASA and tested at the FAA's Civil Aeromedical Institute (CAMI) on a sled test facility. The standard seat is typical of those commonly used in some general aviation airplanes and weighs approximately 11 kg (25 lbm). The ceiling-mounted load-limiting seat is similar in design to a troop seat designed for Army helicopters (ref. 14) and weighs 9 kg (20 lbm). This seat is equipped with two wire bending load limiters which are located inside the seat back and are attached to the cabin ceiling to limit both vertical and forward loads. Two additional load limiters are attached diagonally between the seat pan at the front and the floor at the rear to limit forward loads only. The seat pan in the design remains parallel to the floor while stroking. The length of the stroke is approximately 30 cm (12 inches) in the vertical direction and 18 cm (7 inches) forward (fig. 16(a)). The components of a wire bending load limiter are shown in the photograph of fig. 17. In operation, the wire bending trolley, which is attached to the top housing sleeve, translates the wire loop along the axis of the wire during seat stroking at a constant force. This type of load limiter provides a near constant force during stroking thus making it possible to absorb maximum loads at human tolerance levels over a given stroking distance.

The floor-mounted load-limiting seat weighs 10 kg (23 lbm) and employs two wire bending load limiters which are attached diagonally between the seat pan at the top of the rear strut and the bottom of the front legs. While stroking, the rear struts pivot on the floor thus forcing the load-limiter housing to slide up inside the seat back (fig. 16(b)). The third load-limiting concept tested uses a rocker swing stroke to change the attitude of the occupant from an upright seated position to a semisupine position.

In the dynamic tests conducted at CAMI, the sled or carriage is linearly accelerated along rails to the required velocity and brought to rest by wires stretched across the track in a sequence designed to provide the desired impact loading to the sled. A hybrid II, 50 percentile dummy instrumented with accelerometers loaded the seats and restraint system on impact. The restraint system for these seats consisted of a continuous, one-piece, lap belt and double shoulder harness arrangement.

Time histories of dummy pelvis accelerations recorded during two different impact loadings are presented in figure 18 with the dummy installed in a standard seat and in a ceiling-mounted load-limiting seat. The vertical impulse of figure 18(a) positioned the seats (and dummy) to impact at a pitch angle (angle between dummy spine and direction of sled travel) of -30° and roll angle of 10°. In the "longitudinal" pulse (fig. 18(b)) the seats were yawed 30° to the direction of sled travel. The sled pulses are also included in the figure and represent the axial impulse imparted to the inclined dummies. The X and Z axes of the dummy are local axes perpendicular and parallel to its spine, respectively. The figure shows that for both impact conditions the load-limiting seat in general provide a sizeable reduction in pelvis acceleration over those recorded during similar impacts using the standard seat.

The impact condition associated with a dummy passenger in one of the full-scale NASA crash tests were quite similar to those defined by the sled test of figure 18(a), particularly in terms of velocity change, thereby permitting a gross comparison of their relative accelerations. Figure 19 shows that comparison. The dummy accelerations traced from the two tests are similar in both magnitude and shape, however some phase shift is evident. This agreement suggests that sled testing provides a good approximation of dummy/seat response in full-scale aircraft crashes.

Subfloor Structure

The subfloor structure of most medium size general aviation aircraft offers about 15-20 cm (6-8 in) of available stroking distance which suggests the capability to introduce a velocity change of approximately 8.2 m/s (27 fps) (see fig. 14). Aside from the necessary space for routing hydraulic and electrical conducts, considerable volume is available within the subfloor for energy dissipation through controlled collapse. A number of energy absorbing concepts have been advanced and figure 20 presents sketches of five prominent candidates. The first three concepts, moving from left to right, would replace existing subfloor structure and allow for (a) the metal working of floor beam webs filled with energy dissipating foam, (b) the collapsing of precorrugated floor beam webs filled with foam, or (c) the collapsing of precorrugated foam-filled webs interlaced with a notched lateral bulkhead. The remaining two concepts eliminate the floor beam entirely and replace it with a precorrugated canoe (the corrugations running circumferentially around the cross section) with energy dissipation foam exterior to the canoe, and foam-filled Kevlar cylinders supporting the floor loads. These five promising concepts have been tested both statically and dynamically to determine their load-deflection characteristics. Some examples of the static load-deflection behavior obtained from four of the five concepts are shown in figure 21.

A number of energy absorbing subfloor specimens were constructed using the results of the concept study. Each of the sections could replace existing subfloor structure and would consist of a relatively strong upper floor for maintaining seat-to-aircraft integrity and a crush zone to allow for a more uniform collapse and distribution of load. These five subfloors have been tested statically and their load-deflection characteristics are shown in figure 22 along with results for a comparable unmodified subfloor structure.

The unmodified subfloor load-deflection characteristics indicate several sudden substantial losses in load carrying capability which were the results of undesirable loss of structural integrity, that is, the seat rails broke loose, the floor webs and floor covering ripped free from the floor beams. On the other hand, the results for the five new concepts indicate that they perform well in that the the upper floor remained intact throughout the loading and did not break apart. Some concepts did, however, collapse with more desirable load-deflection characteristics than others. For example, the result for the corrugated beams with notched corner web attachments, as shown in more detail in figure 23, indicate that the crush zone collapsed at a more desirable lower (essentially) constant load characteristic than the unmodified structure while the energy absorbed at the reduced crushing load was essentially the same as the unmodified subfloor. Dynamic vertical tests of all the load-limiting aircraft sections are currently being conducted at vertical velocities up to 7.3 m/s (24 fps) to evaluate their impact performance as compared to unmodified subfloor structure.

Emergency Locator Transmitter (ELT) Tests

General aviation airplanes are required to carry an Emergency Locator Transmitter (ELT) (normally crash activated) to expedite the location of crash aircraft by searchers. However, the ELT is plagued with many problems that severely limited the usefulness of these potentially life-saving devices. The National Transportation Safety Board recently reviewed the ELT problems and efforts to find solutions (ref. 15). The ELT has a high rate of nondistress activation and failure to activate in a crash situation. Suspected problem sources are, among others, improper mounting, the location in the aircraft, short circuits, vibration sensitivity, battery failures, and antenna location. NASA Langley is assisting the FAA and industry through Radio Technical Commission for Aeronautics (RTCA) Special Committee 136 formed to study in depth the ELT problems and to seek solutions.

NASA Langley is demonstrating ELT sensor activation problems by mounting a sampling of ELT specimens in full-scale crash test aircraft and in a special test apparatus to simulate longitudinal crash pulses. This very definitive demonstration of some specific ELT performance problems and evaluation of the test results will increase understanding and lead to solutions. Langley is also studying the antenna radiation problem by fly-over examination of the radiation patterns emanating from ELT's mounted in situ.

An apparatus has been constructed to permit laboratory tests to be conducted on ELT's in a realistic environment. The test setup, shown in figure 24, consists of a large cylindrical section with an actual airplane tail section mounted in its interior. Wedges attached to the test apparatus shape the "crash" pulse upon impact in a bed of glass beads. The cylinder can be rotated relative to the wedges to vary the vector inputs. Decelerations at the base of the airplane section, responses of the bulkheads and webs, and the response of the ELT are recorded along with activation/no activation signals.

The test apparatus permits an extension of test data on ELT's acquired during crash tests of full-size aircraft at the Impact Dynamics Facility. For example, the data in figure 25 is a comparison of the longitudinal deceleration on an ELT in a recent crash test with a simulated crash pulse in the test rig. As indicated in the figure, both the characteristic shape of the crash pulse and structural resonances are reproduced by the test apparatus. A representative sampling of in-service ELT's tests in this apparatus is discussed in reference 16.

CONCLUDING REMARKS

Langley Research Center (LaRC) has initiated a crash safety program that will lead to the development of technology to define and demonstrate new structural concepts for improved crash safety and occupant survivability in general aviation aircraft. This technology will make possible the integration of crashworthy structural design concepts into general aviation design methods and will include airframe, seat, and restraint-system concepts that will dissipate energy and properly restrain the occupants within the cabin interior. Current efforts are focused on developing load-limiting aircraft components needed for crash load attenuation in addition to considerations for modified seat and restraint systems as well as structural airframe reconfigurations. The dynamic nonlinear behavior of these components is being analytically evaluated to determine their dynamic response and to verify design modifications and structural crushing efficiency. Seats and restraint systems with incorporated deceleration devices are being studied that will limit the load transmitted to the occupant, remain firmly attached to the cabin floor, and adequately restrain the occupant from impact with the cabin interior. Full-scale mockups of structural components incorporating load-limiting devices are being used to evaluate their performance and provide corroboration to the analytical predictive techniques.

In the development of aircraft crash scenarios, a set of design crash parameters are to be determined from both FAA field data and LaRC controlled-crash test data. The controlled-crash test data will include crashes at velocities comparable with the stall velocity of most general aviation aircraft. Close cooperation with other governmental agencies is being maintained to provide inputs for human tolerance criteria concerning the magnitude and duration of deceleration levels and for realistic crash data on survivability. The analytical predictive methods developed herein for crash analyses are to be documented and released.through COSMIC.

A new Emergency Locator Transmitter (ELT) test apparatus has been made operational at NASA Langley Research Center. Testing of a representative sample of in-service ELT's is underway. Results of this study will form the basis for specific recommendations by Radio Technical Commission for Aeronautics (RTCA) Special Committee 136. These recommendations to the FAA and Industry will lead to improvements in ELT reliability.

REFERENCES

1. Vaughan, Victor L; and Alfaro-Bou, Emilio: Impact Dynamics Research Facility for Full-Scale Aircraft Crash Testing. NASA TN D-8179, 1976.

2. Castle, Claude B.: Full-Scale Crash Test of a CH-47 Helicopter. NASA TM X-3412, 1976.

3. Alfaro-Bou, Emilio; and Vaughan, Victor L.: Light Airplane Crash Tests at Impact Velocities of 13 and 27 m/sec. NASA TP-1042, 1977.1977.

4. Castle, Claude B.; and Alfaro-Bou, Emilio: Light Airplane Crash Tests at Three Flight-Path Angles. NASA TP-1210, 1978.1978.

5. Hayduk, Robert J.: Comparative Analysis of PA-31-350 Chieftain (N44LV) Accident and NASA Crash Test Data. NASA TM-80102, 1979.

6. Pifko, A.; Levine, H. S.; Armen, H., Jr.: PLANS - A Finite Element Program for Nonlinear Analysis of Structures - Volume I - Theoretical Manual. NASA CR-2568, 1975. 975.

7. Pifko, A.; Armen, H., Jr.; Levy, A.; and Levine, H.: PLANS - A Finite Element Program for Nonlinear Analysis of Structures - Volume II - User's Manual. NASA CR-145244, 1977.977.

8. Thomson, R. G.; and, Goetz, R. C.: NASA/FAA General Aviation Crash Dynamics Program - A Status Report. AIAA/ASME/ASCE/AHS 20th Structures, Structural Dynamics, and Materials Conference, St. Louis, MO, April 4-6, 1979, AIAA Paper No. 79-0780.

9. Winter, Robert; Pifko, Allan B.; and Armen, Harry, Jr.: Crash Simulation of Skin-Frame Structures Using a Finite Element Code. SAE Business Aircraft Meeting, Wichita, KS, March 29-April 1, 1977, SAE paper 770484.

10. Hayduk, Robert J.; Thomson. Robert G.; Wittlin, Gil; and Kamat, Manohar P: Nonlinear Structural Crash Dynamics Analyses. SAE Business Aircraft Meeting, Wichita, KS, April 3-6, 1979, SAE Paper 790588.

11. Laananen, David H.: Development of a Scientific Basis for Analysis of Aircraft Seating Systems. FAA-RD-74-130, Jan. 1975.

12. Fasanella, Edwin L.: NASA General Aviation Crashworthiness Seat Development, SAE Business Aircraft Meeting, Wichita, KS, 1979.

13. Dynamic Science Report: Crash Survival Design Guide. USAAMRDL TR-71-22, Ft. Eustis, VA, 1971.

14. Reilly, M. J.: Crashworthy Troop Seat Investigation. USAAMRDL TR-74-93, Ft. Eustis, VA, 1974

15. Anon.: Emergency Locator Transmitters: An Overview. National Transportation Safety Board Special Study, Report NTSB-AAS-78-1, January 26, 1978.

16. Carden, Huey D.: Evaluation of Emergency-Locator-Transmitter Performance in Real and Simulated Crash Tests. 1980 Aircraft Safety and Operating Problems, NASA CP-2170, 1981.(Paper 35 of this compilation.)

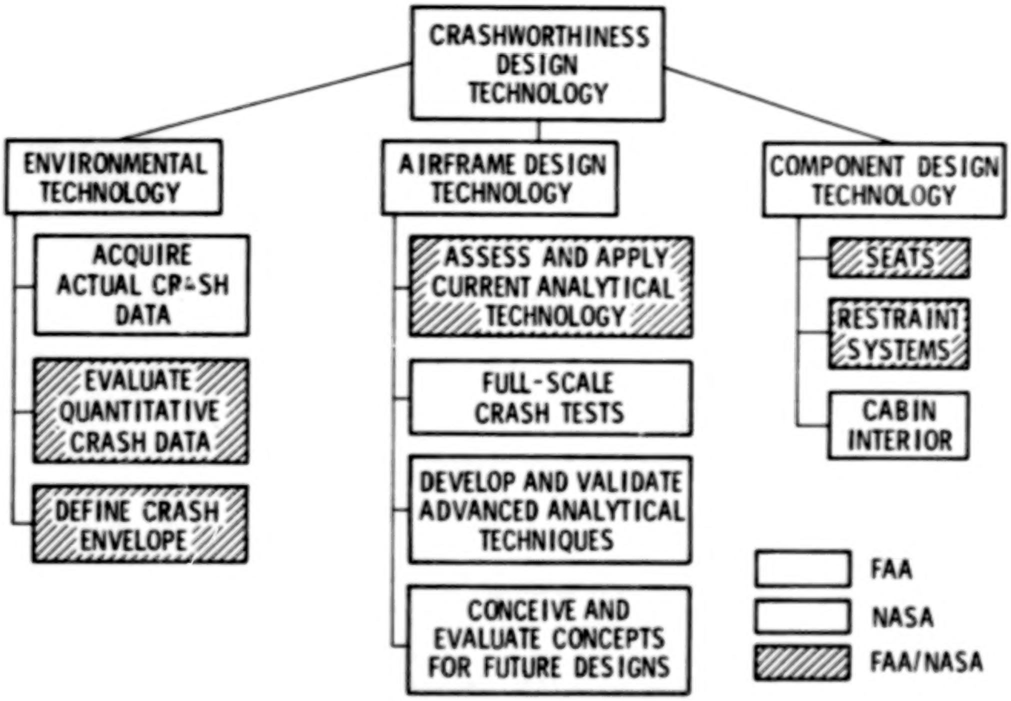
CRASHWORTHINESS DESIGN TECHNOLOGY
ENVIRONMENTAL TECHNOLOGY
AIRFRAME DESIGN TECHNOLOGY
COMPONENT DESIGN TECHNOLOGY
ACQUIRE ACTUAL CRASH DATA
EVALUATE QUANTITATIVE CRASH DATA
DEFINE CRASH ENVELOPE
ASSESS AND APPLY CURRENT ANALYTICAL TECHNOLOGY
FULL-SCALE CRASH TESTS
DEVELOP AND VALIDATE ADVANCED ANALYTICAL TECHNIQUES
CONCEIVE AND EVALUATE CONCEPTS FOR FUTURE DESIGNS
SEATS
RESTRAINT SYSTEMS
CABIN INTERIOR
FAA
NASA
FAA/NASA

Figure 1.- Agency responsibilities in joint FAA/NASA General Aviation Crashworthiness program.

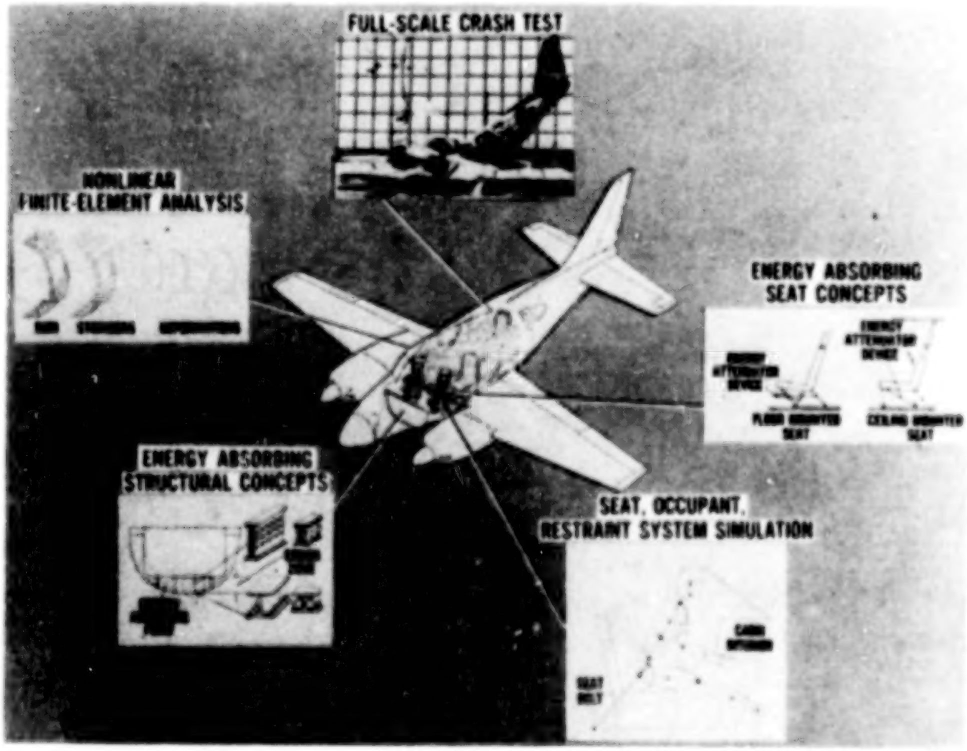
FULL-SCALE CRASH TEST
NONLINEAR FINITE-ELEMENT ANALYSIS
ENERGY ABSORBING SEAT CONCEPTS
ENERGY ATTENUATOR DEVICE
ENERGY ATTENUATOR DEVICE
FLOOR MOUNTED SEAT
CEILING MOUNTED SEAT
ENERGY ABSORBING STRUCTURAL CONCEPTS
SEAT, OCCUPANT, RESTRAINT SYSTEM SIMULATION
SEAT BELT

Figure 2.- Research areas in LaRC General Aviation Crash Dynamics program.

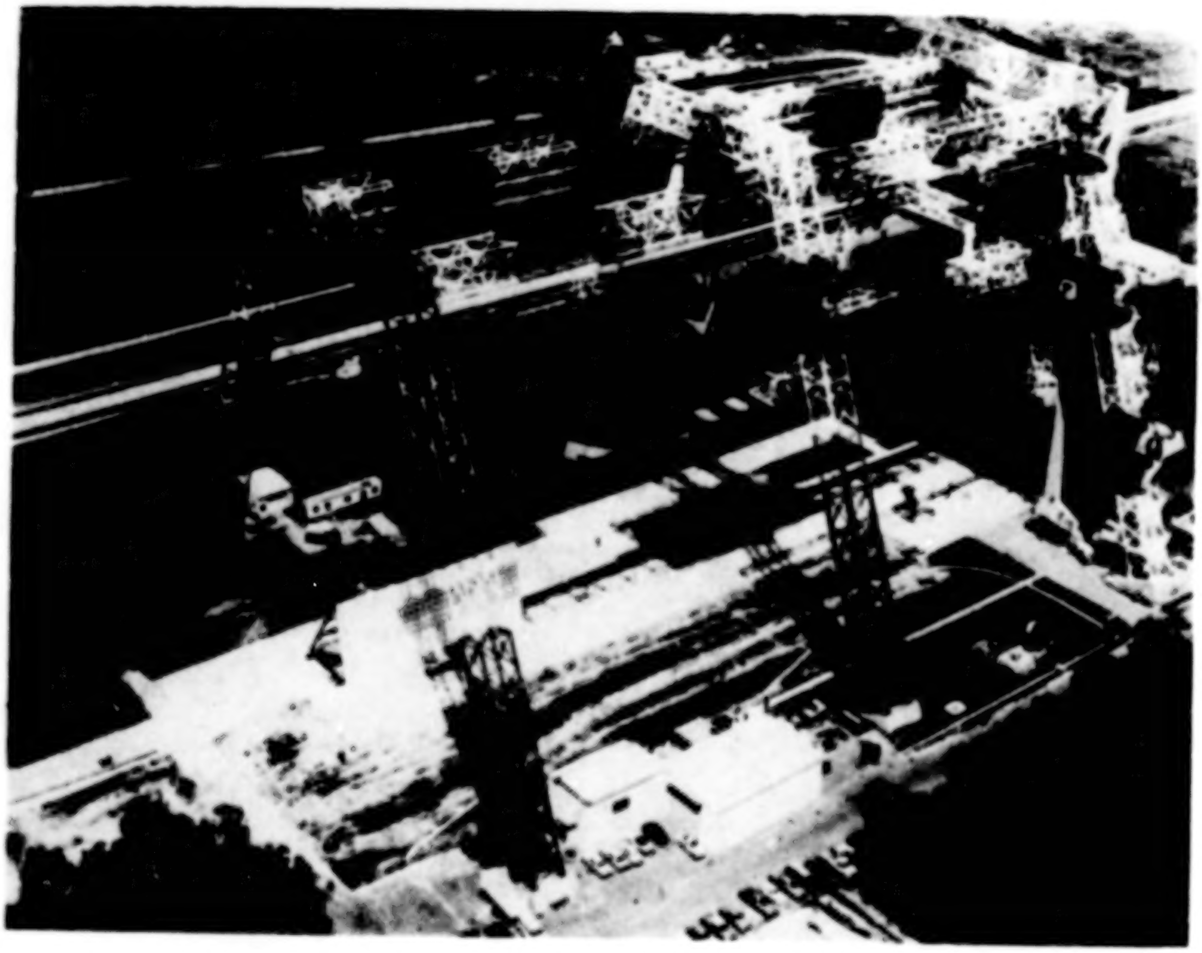

Figure 3.- Langley Impact Dynamics Research Facility.

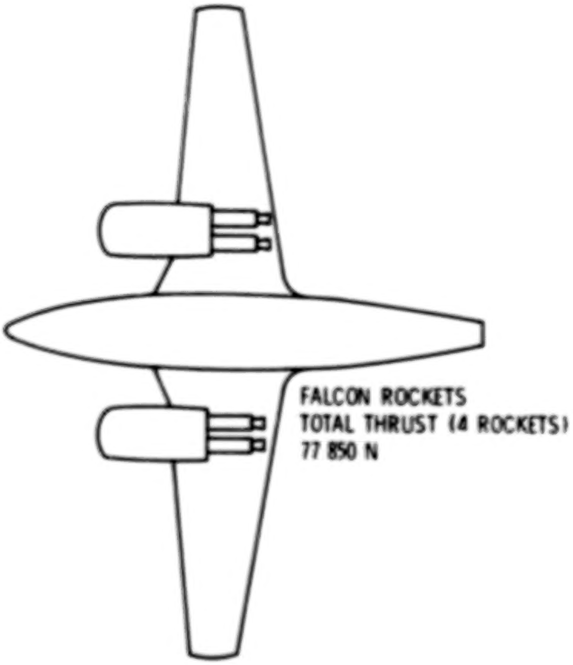
FALCON ROCKETS
TOTAL THRUST (4 ROCKETS)
77 850 N

(a) Schematic of rocket location.

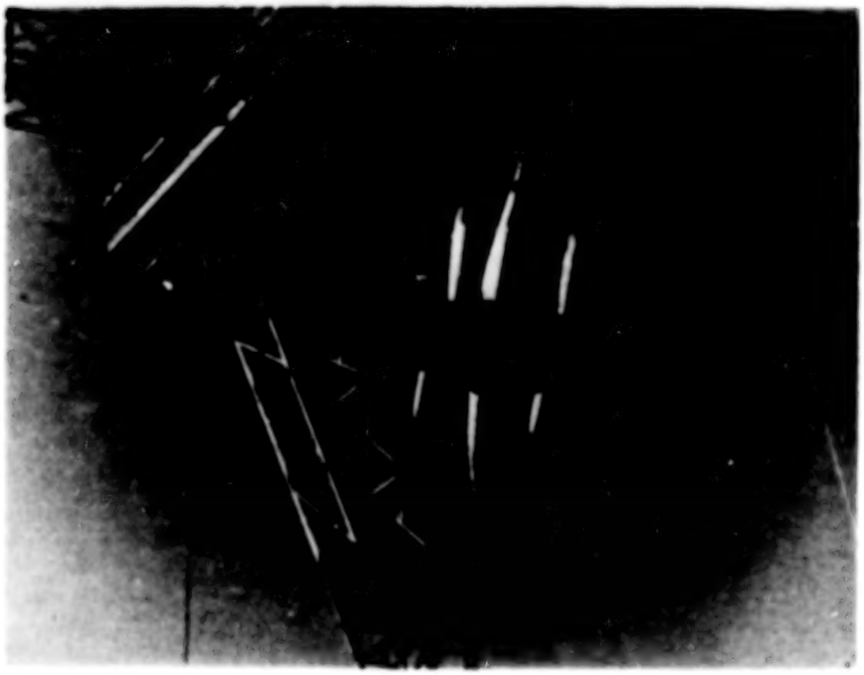

(b) Photograph of rocket ignition during test.

Figure 4.- Velocity augmentation crash test method.

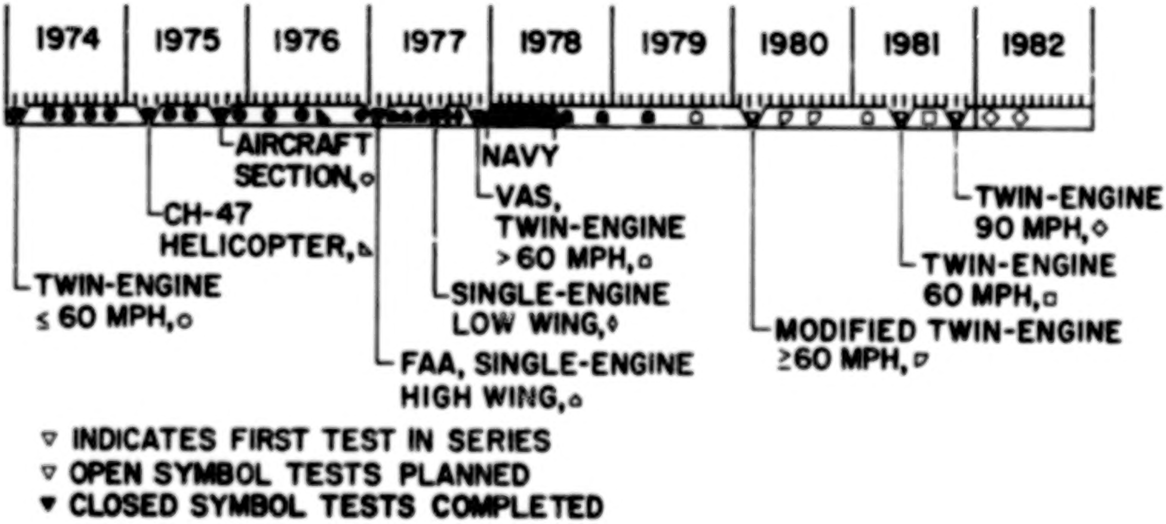

Figure 5.- General aviation crash test schedule. (1 mph = 0.45 m/s.)

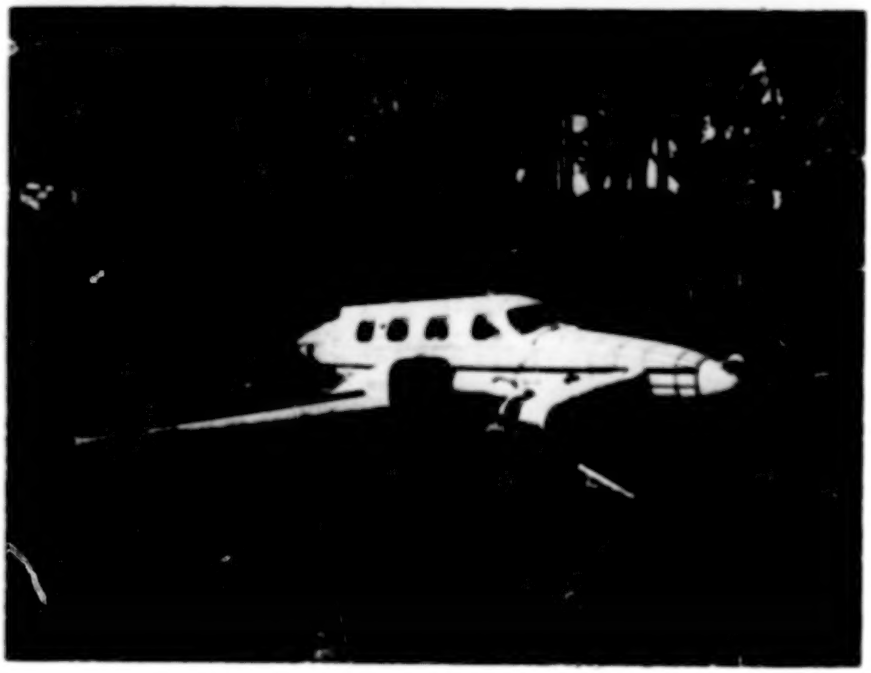

(a) Controlled crash.

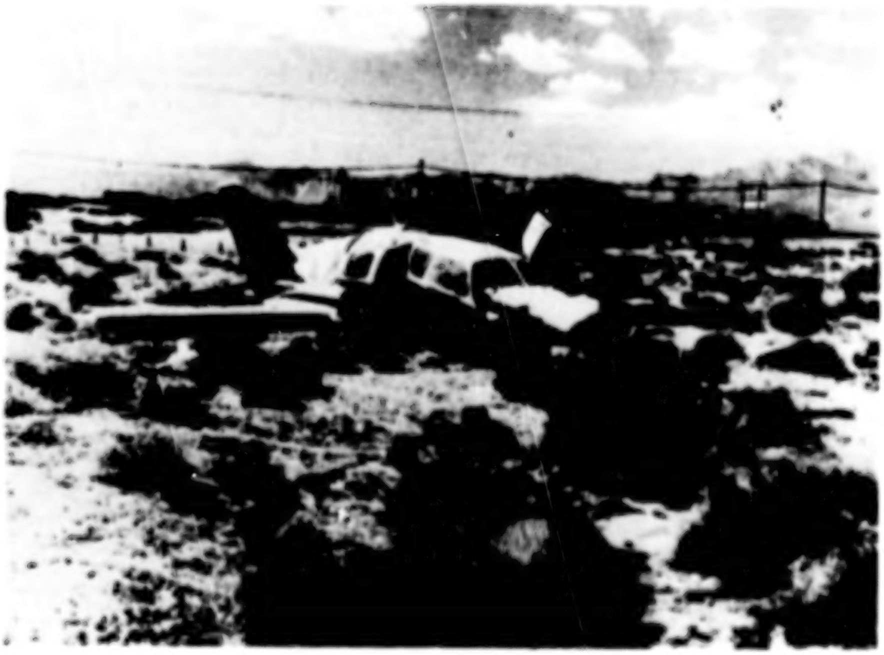

(b) Las Vegas accident.

Figure 6.- Controlled-crash test and Las Vegas accident.

LAS VEGAS ACCIDENT
PASSENGER SEAT-71.7 Kg PASSENGER

CONTROLLED TEST
PASSENGER SEAT-74.8 Kg DUMMY

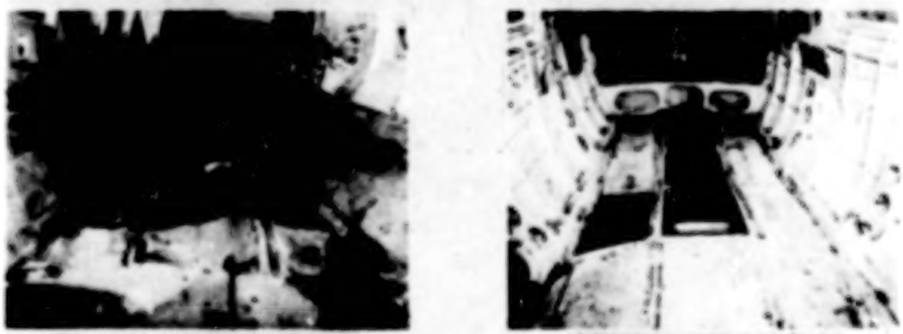

LAS VEGAS ACCIDENT CABIN FLOOR

CONTROLLED TEST CABIN FLOOR

Figure 7.- Damage comparison between controlled test and Las Vegas accident.

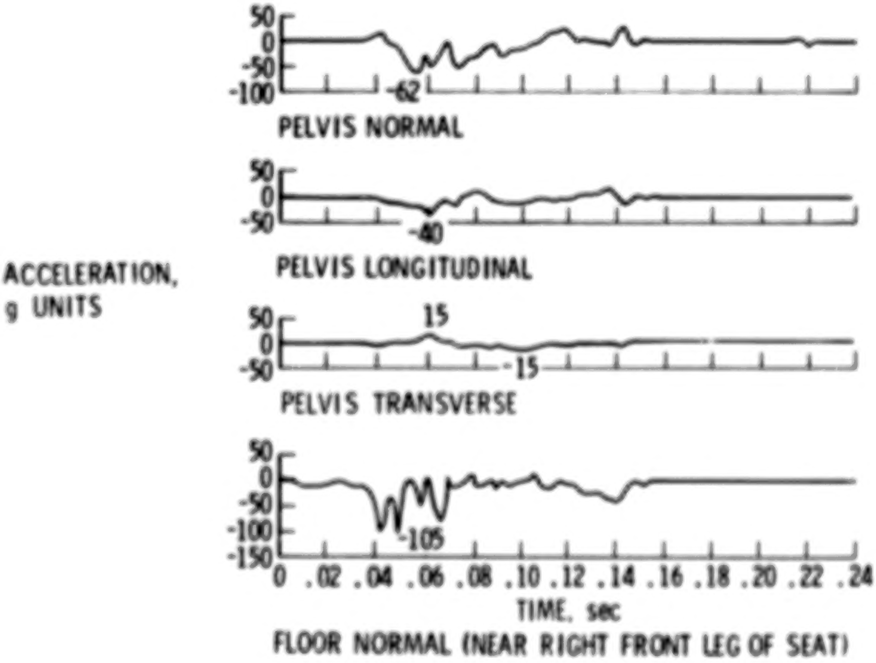

Figure 8.- Acceleration time histories from first passenger and floor of controlled-crash test (-12° pitch, 41.4 m/s flight path velocity with 5° left roll, 1° yaw).

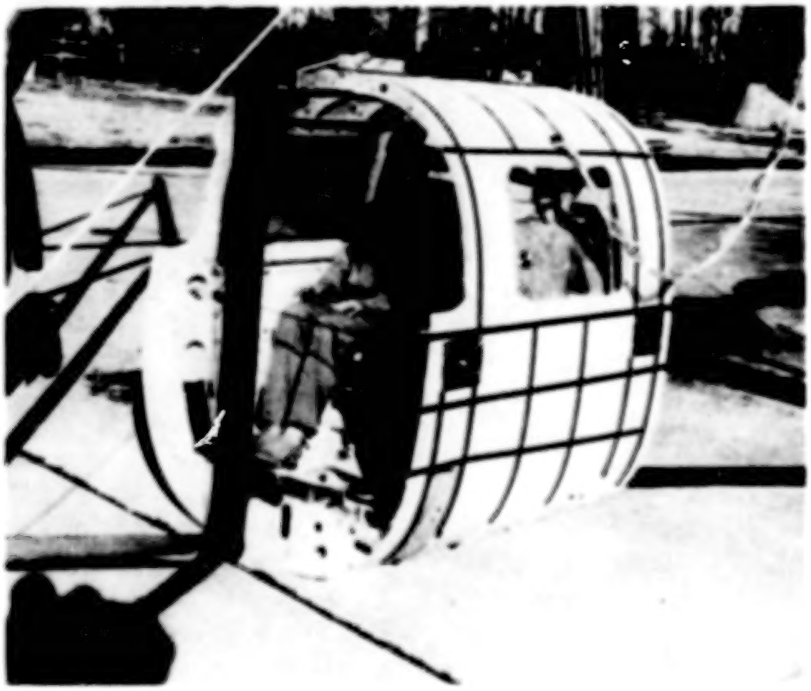

Figure 9.- Fuselage section drop-test specimen.

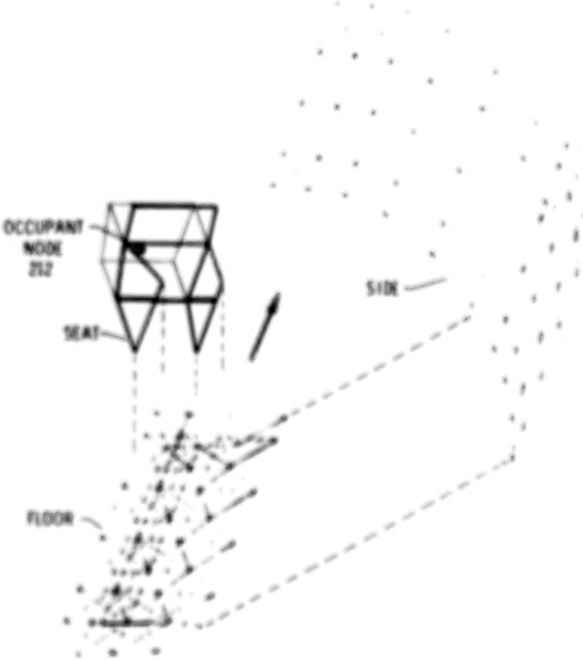
OCCUPANT
NODE
212
SEAT
SIDE
FLOOR

Figure 10.- DYCAST fuselage, seat, and occupant model.

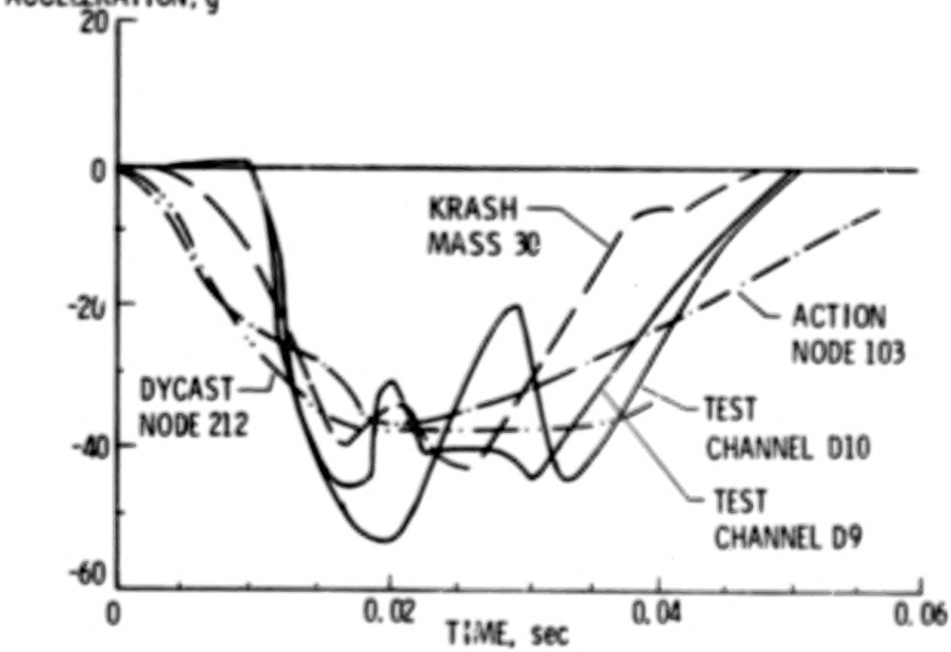

Figure 11.- Comparison of occupant pelvis vertical accelerations from test and analyses.

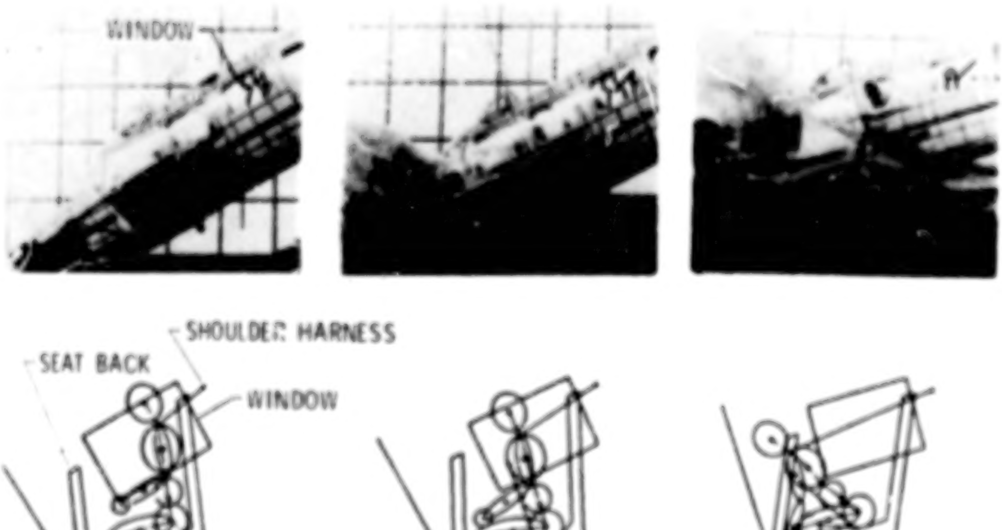
WINDOW
SHOULDER HARNESS
SEAT BACK
WINDOW
T = 0.05 SEC
T = 0.10 SEC
T = 0.15 SEC

Figure 12.- Two-dimensional computer graphics display of motion of third passenger of -30°, 27 m/s full-scale crash test.

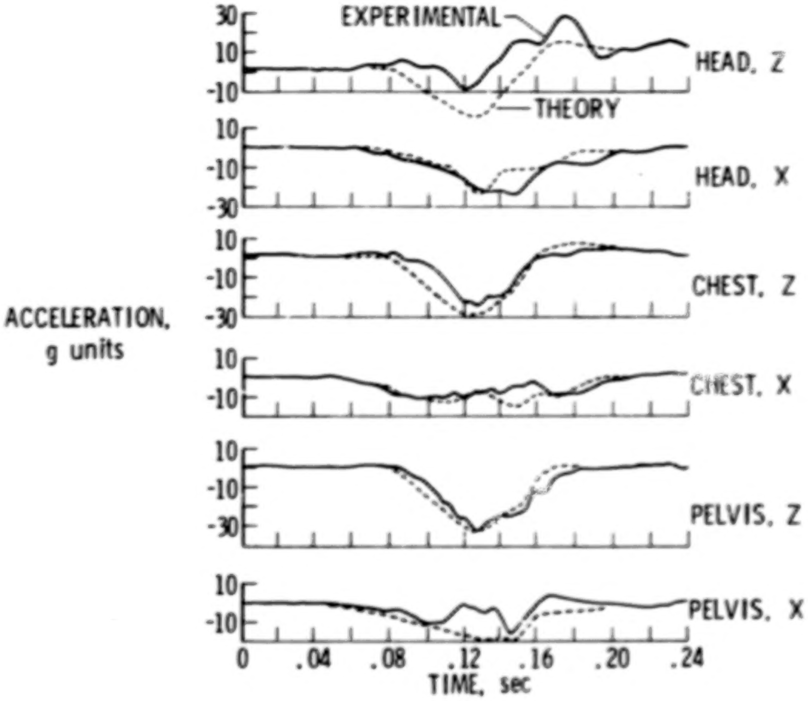

Figure 13.- Experimental and computer dummy accelerations for -30°, 27 m/s full-scale crash test.

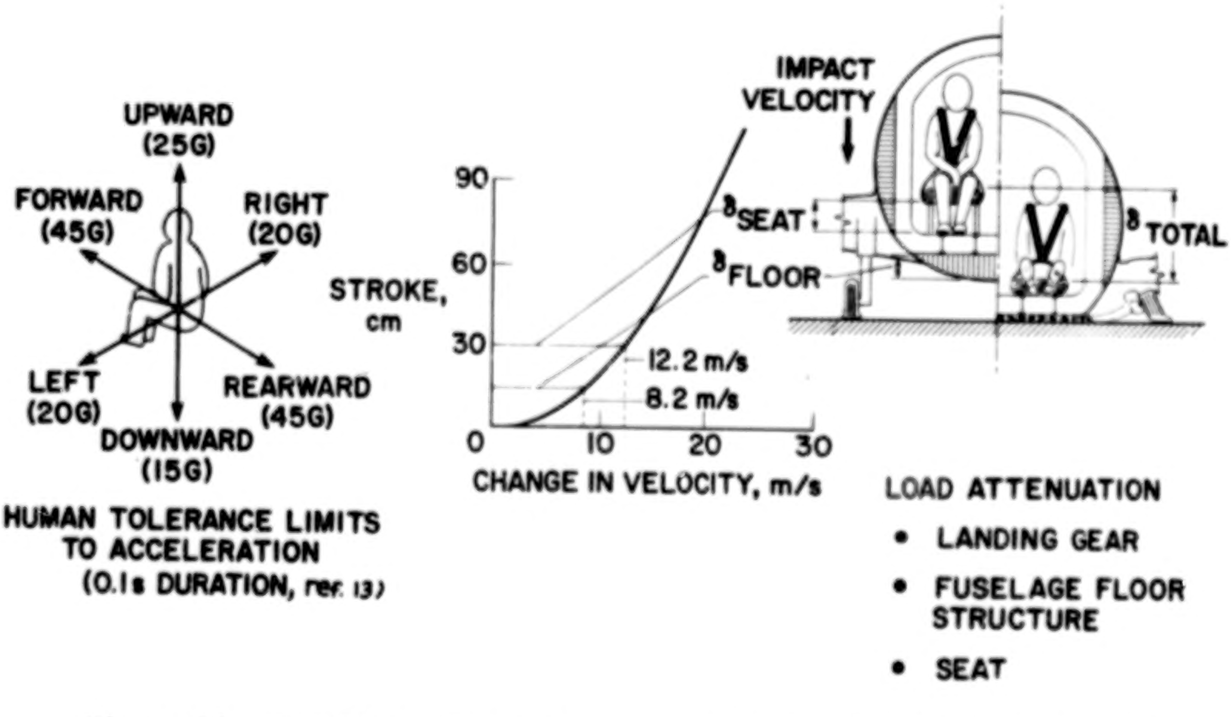
UPWARD (25G)
FORWARD (45G)
RIGHT (20G)
LEFT (20G)
REARWARD (45G)
DOWNWARD (15G)
HUMAN TOLERANCE LIMITS TO ACCELERATION (0.1s DURATION, ref. 13)
STROKE, cm
90
60
30
0
10
20
30
CHANGE IN VELOCITY, m/s
12.2 m/s
8.2 m/s
IMPACT VELOCITY
δSEAT
δFLOOR
δTOTAL
LOAD ATTENUATION
• LANDING GEAR
• FUSELAGE FLOOR STRUCTURE
• SEAT

Figure 14.- Available stroke for energy dissipation in typical twin-engine general aviation aircraft.

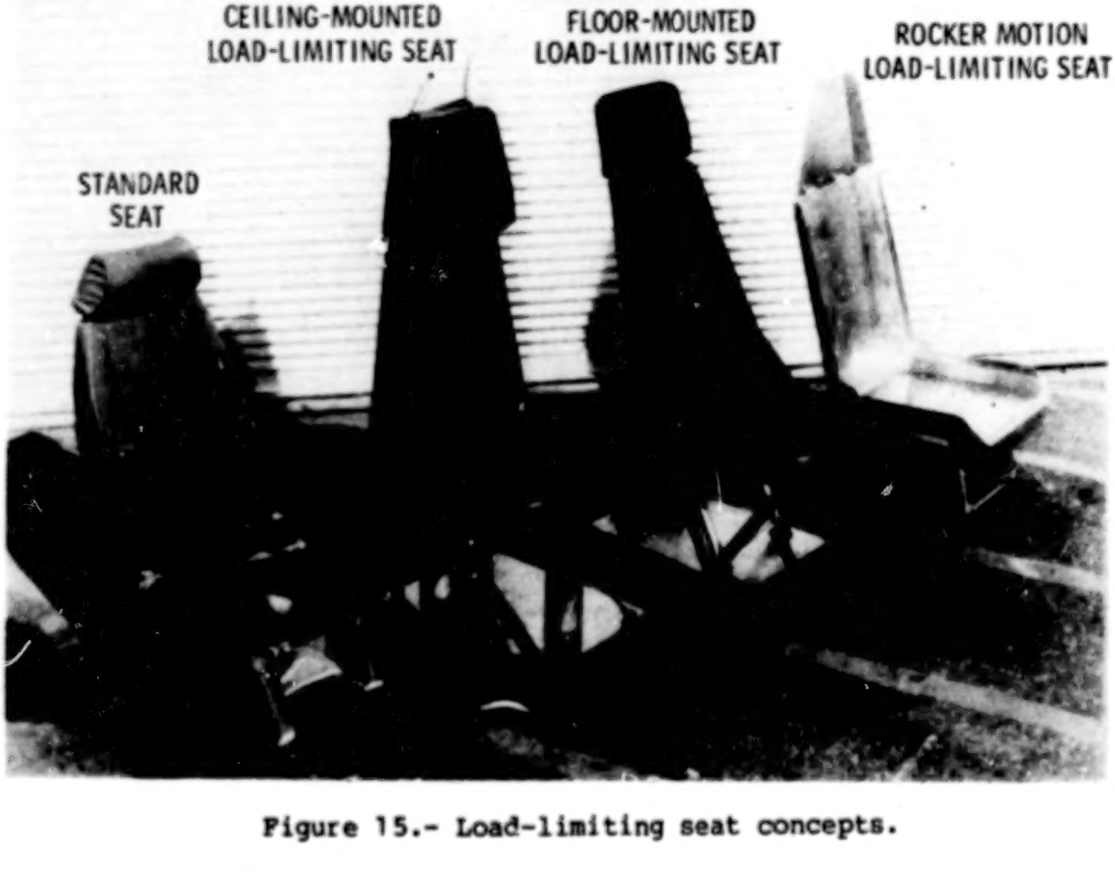
CEILING-MOUNTED
LOAD-LIMITING SEAT
FLOOR-MOUNTED
LOAD-LIMITING SEAT
ROCKER MOTION
LOAD-LIMITING SEAT
STANDARD
SEAT

Figure 15.- Load-limiting seat concepts.

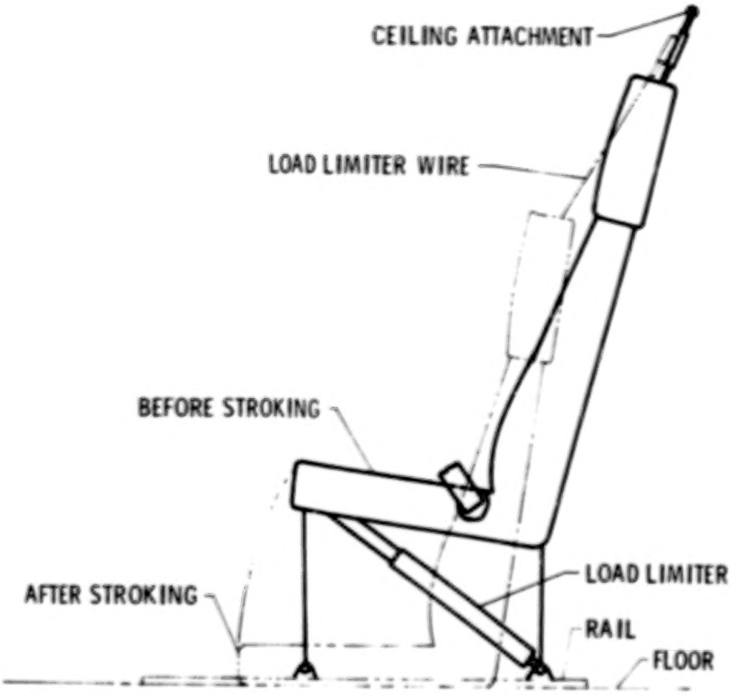
CEILING ATTACHMENT
LOAD LIMITER WIRE
BEFORE STROKING
AFTER STROKING
LOAD LIMITER
RAIL
FLOOR

(a) Ceiling-mounted passenger seat.

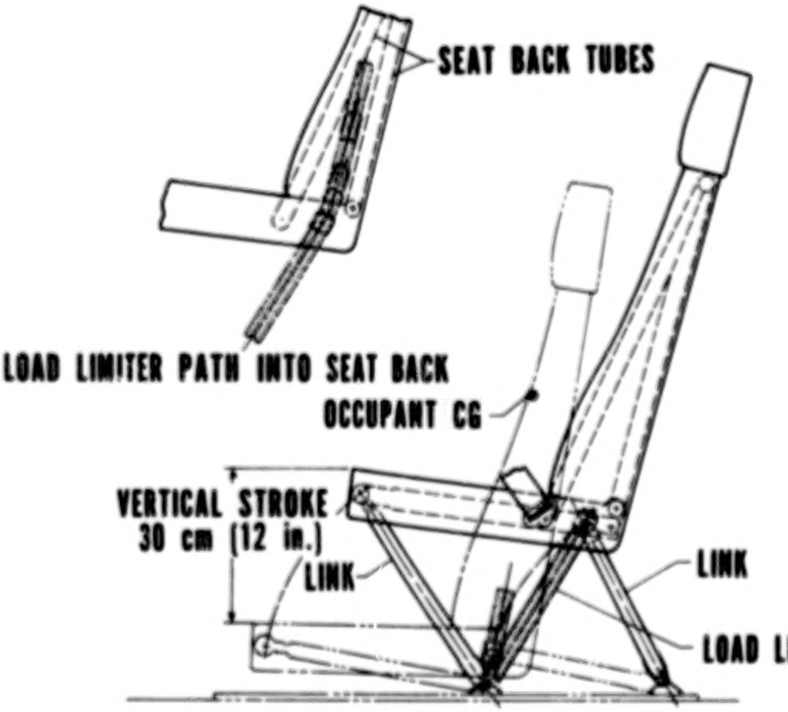
SEAT BACK TUBES
LOAD LIMITER PATH INTO SEAT BACK
OCCUPANT CG
VERTICAL STROKE
30 cm (12 in.)
LINK
LINK
LOAD LIMITER

(b) Floor-mounted passenger seat.

Figure 16.- Passenger seats with wire bending load limiters.

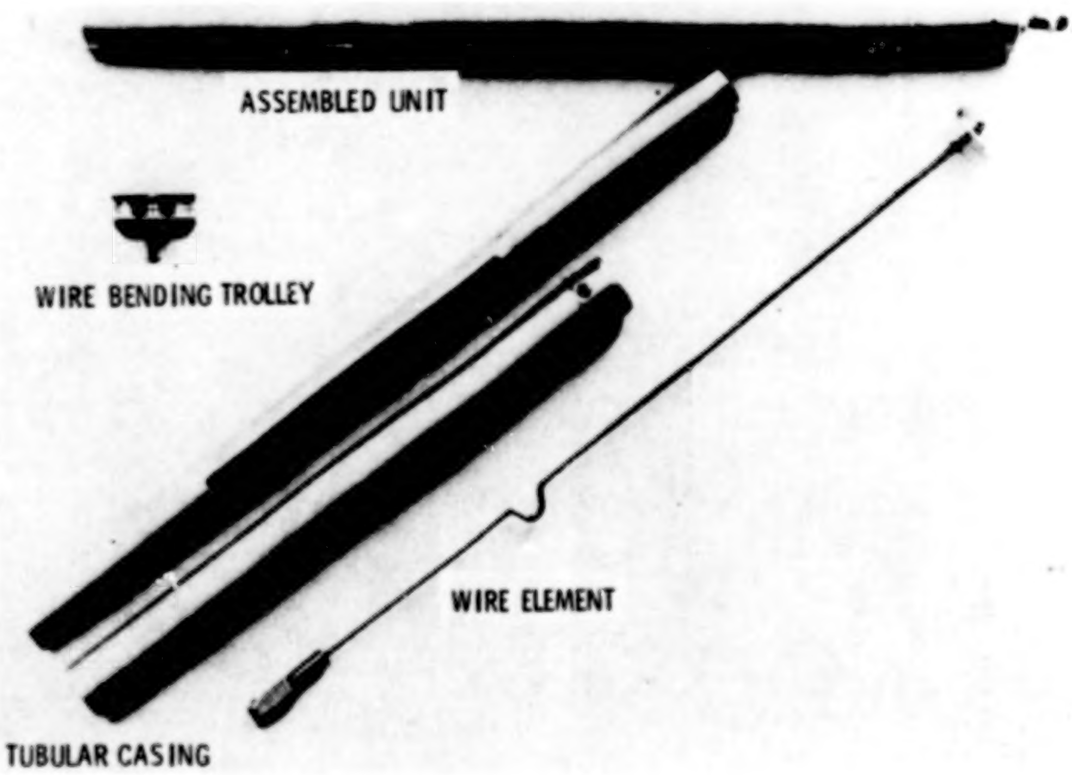
ASSEMBLED UNIT
WIRE BENDING TROLLEY
WIRE ELEMENT
TUBULAR CASING

Figure 17.- Wire bending load limiter.

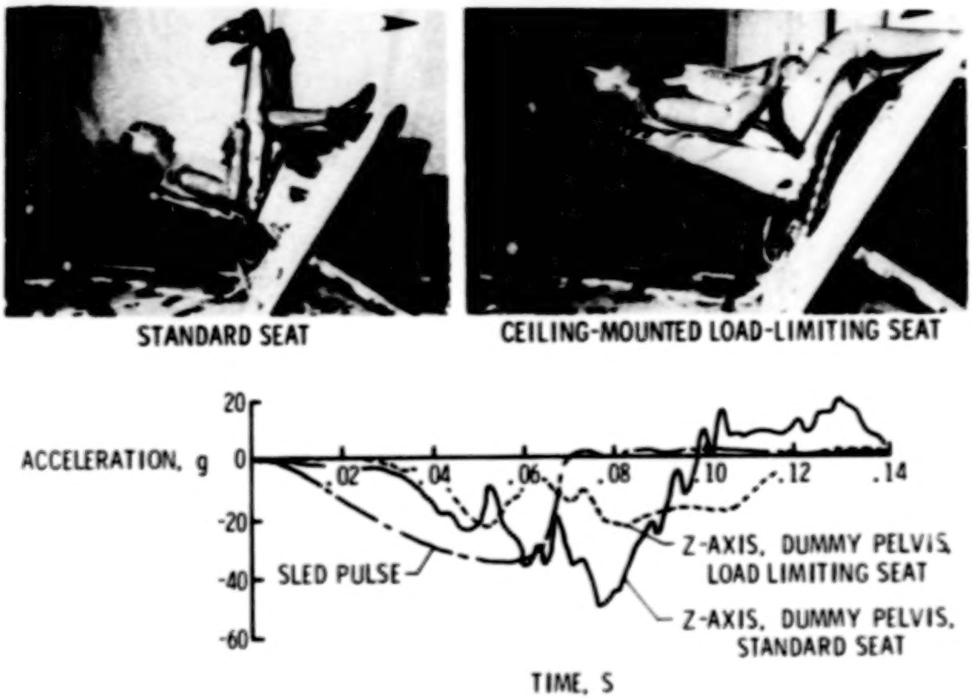

(a) "Vertical" (-30° pitch, 10° roll).

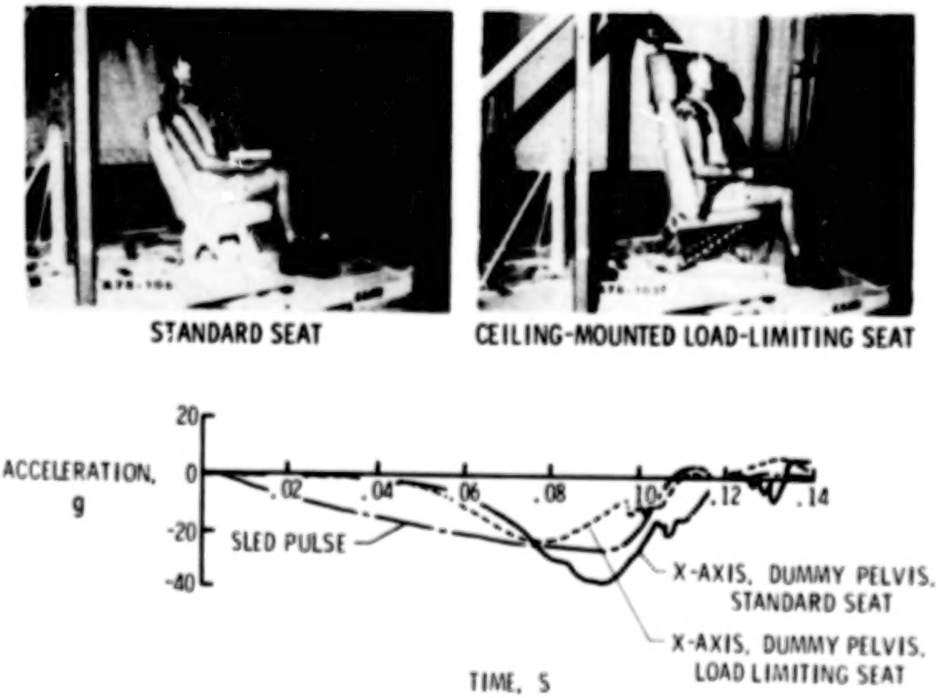

(b) "Longitudinal" (30° yaw).

Figure 18.- Pelvis accelerations for dummy in conventional and ceiling-mounted (load-limiting) seat subjected to "vertical" and "longitudinal" sled pulses.

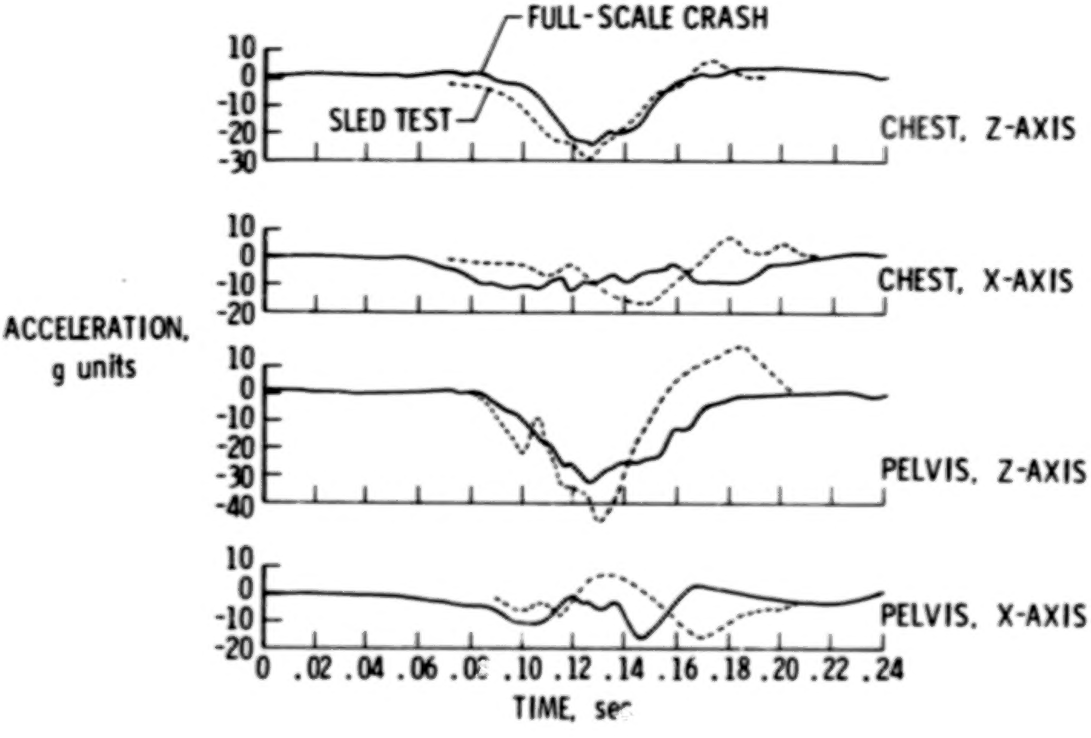

Figure 19.- Dummy accelerations from sled test and from a full-scale test under similar impact conditions.

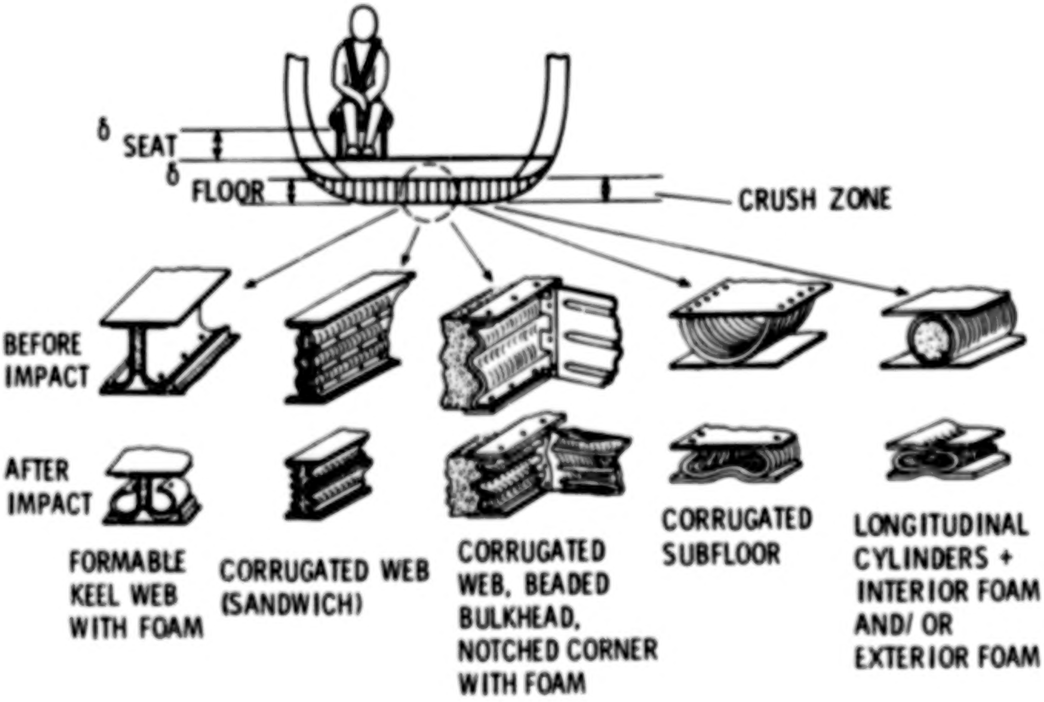
δ SEAT
δ FLOOR
CRUSH ZONE
BEFORE IMPACT
AFTER IMPACT
FORMABLE KEEL WEB WITH FOAM
CORRUGATED WEB (SANDWICH)
CORRUGATED WEB, BEADED BULKHEAD, NOTCHED CORNER WITH FOAM
CORRUGATED SUBFLOOR
LONGITUDINAL CYLINDERS + INTERIOR FOAM AND/ OR EXTERIOR FOAM

Figure 20.- Load-limiting subfloor concepts.

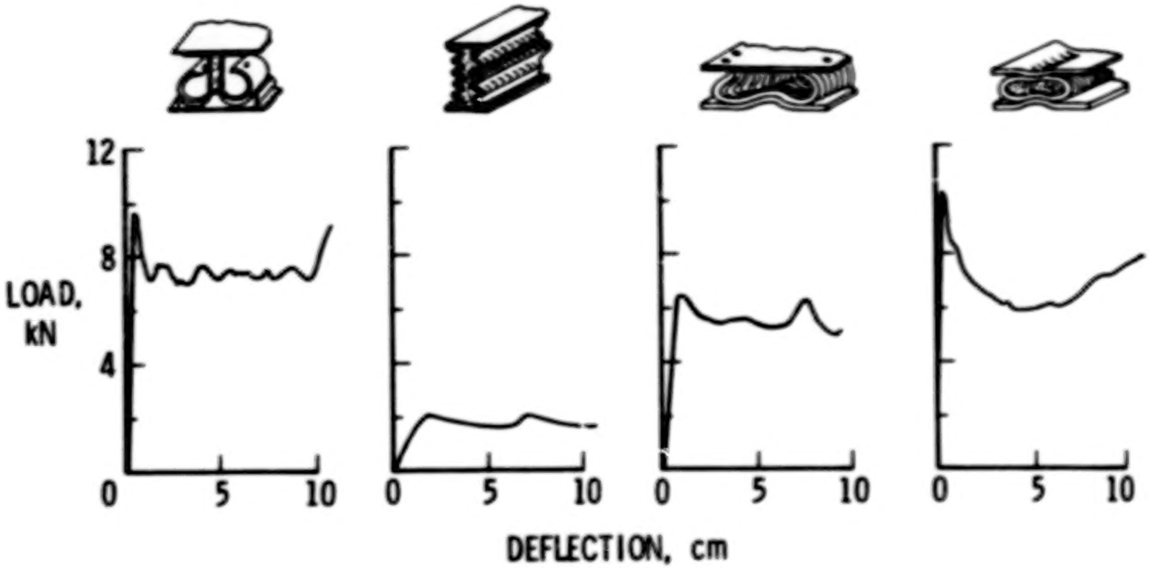

Figure 21.- Load-deflection curves for load-limiting concepts.

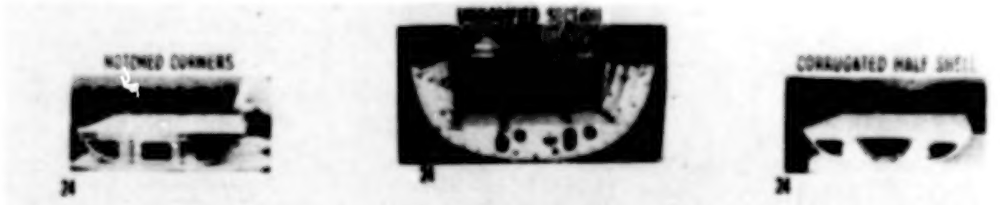

Figure 22.- Load-deflection curves for five load-limiting subfloor sections and an unmodified subfloor section. (1 kip = 4.5 N; 1 in. = 2.54 cm.)

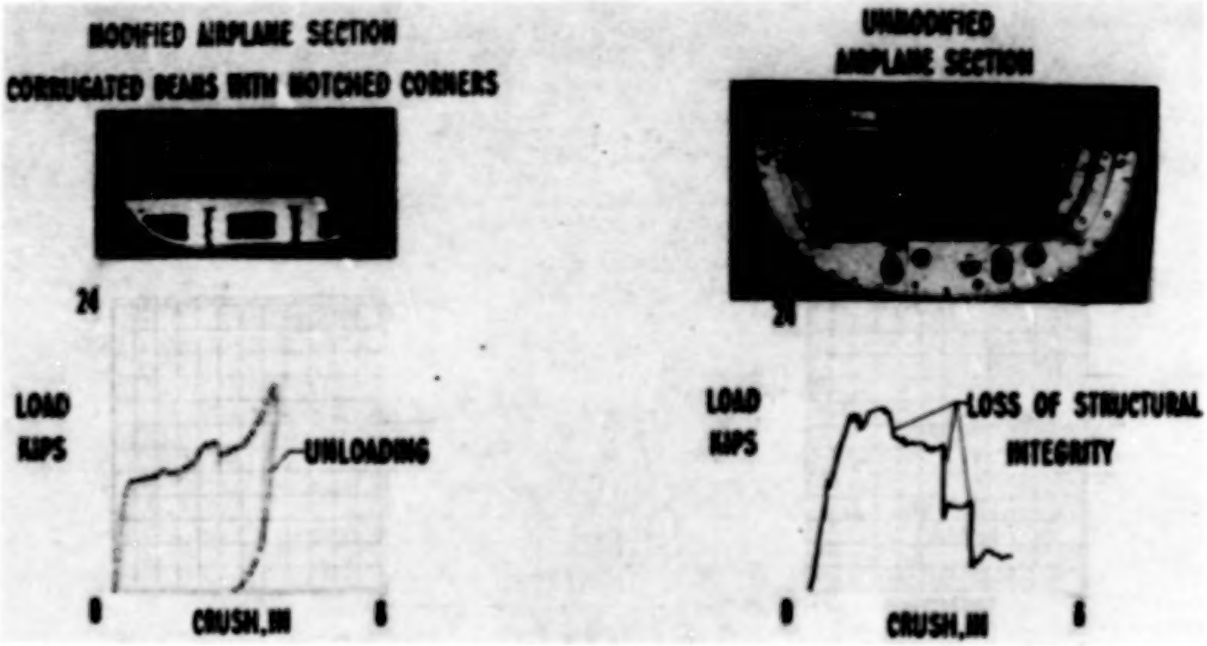

Figure 23.- Comparison of load-deflection curves for corrugated beams with notched corners with unmodified subfloor section. (1 kip = 4.5 N; 1 in. = 2.54 cm.)

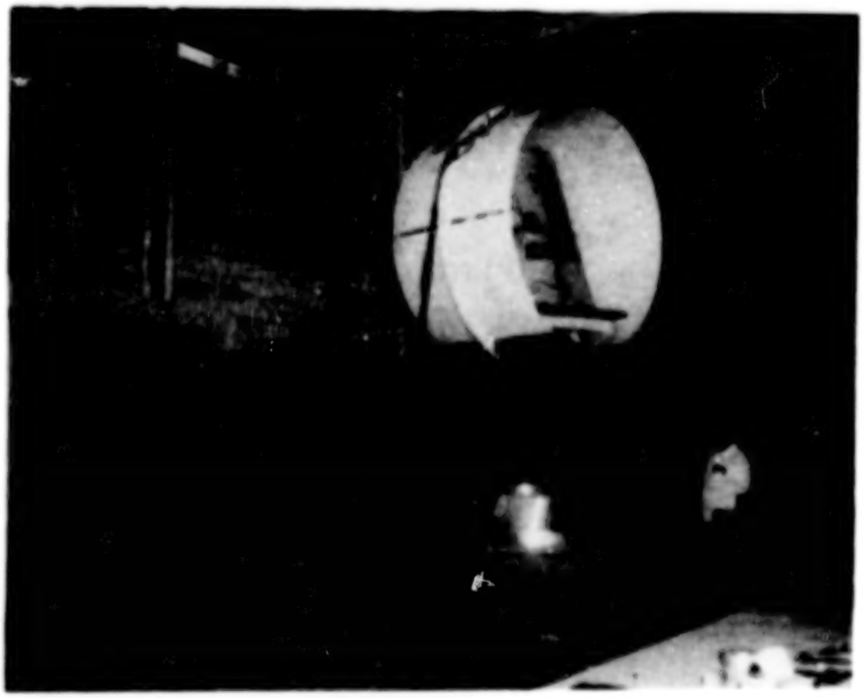

Figure 24.- Emergency Locator Transmitter (ELT) test apparatus.

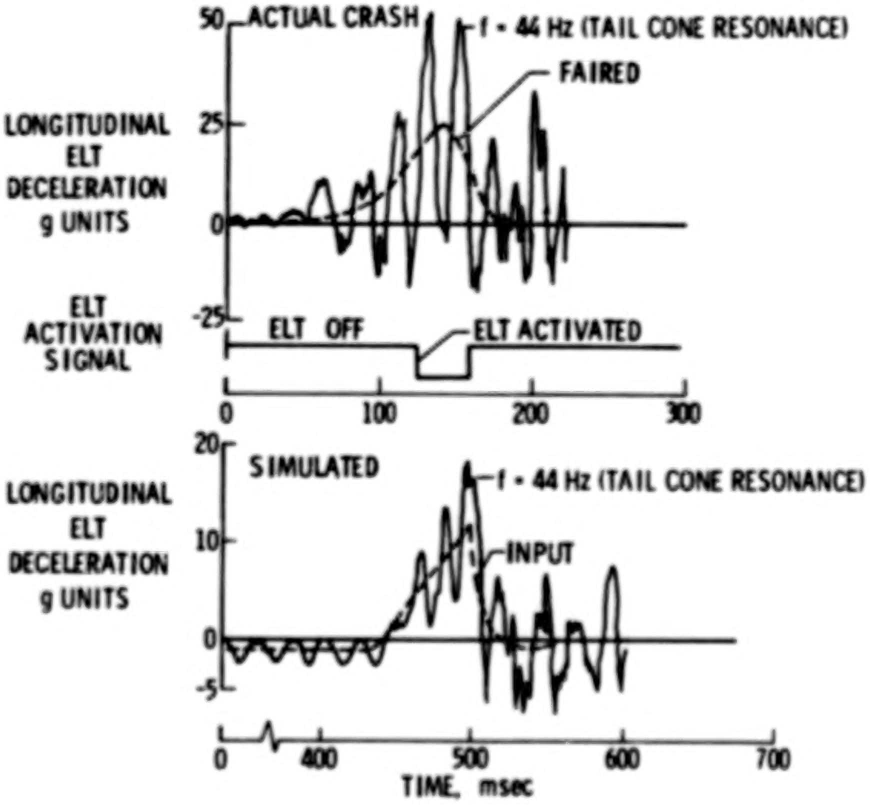

Figure 25.- Actual and simulated longitudinal crash pulses on ELT's.

SESSION V - FLIGHT EXPERIENCES AND GROUND OPERATIONS

BLANK PAGE

BLANK PAGE

CURRENT RESEARCH IN AIRCRAFT TIRE DESIGN AND PERFORMANCE

John A. Tanner and John L. McCarty
NASA Langley Research Center

S. K. Clark
University of Michigan

SUMMARY

A review of the NASA experimental and analytical tire research programs which address the various needs identified by landing gear designers and airplane users is presented in this paper. The experimental programs are designed to increase tire tread lifetimes, relate static and dynamic tire properties, establish the tire hydroplaning spin-up speed, study gear response to tire failures, and define tire temperature profiles during taxi, braking and cornering operations. The analytical programs are aimed at providing insights into the mechanisms of heat generation in rolling tires and developing the tools necessary to streamline the tire design process and to aid in the analysis of landing gear problems.

INTRODUCTION

For many years tire researchers at Langley have maintained a close working relationship with the aircraft landing gear community, namely, the airframe manufacturers and the airline operators. This relationship has allowed NASA to keep abreast of constantly changing tire research needs and to adjust its program priorities accordingly. Recent inputs from various sources have indicated that research is needed to (1) improve tire lifetimes both in terms of reduced tread wear and greater blowout resistance; (2) solve such landing gear dynamic problems as shimmy, gear walk, truck pitching, and braking and cornering performance in adverse weather; and (3) streamline the tire design process. NASA currently has several research programs underway to address these needs and the purpose of this paper is to present a status report on these activities and to provide some indication as to the direction of future research efforts.

TREAD WEAR

Tire replacement due to tread wear is a major safety and economic concern of airline operators. For this reason, NASA has since the early 1970's (refs. 1 to 3) been involved in a program to examine the effects of tire tread wear attributed to the various ground operations of an airplane. In addition, attempts are underway to develop new elastomeric materials which would provide improved tire tread wear and blowout resistance without degrading traction characteristics. For the purpose of this program, braking and cornering tests are being conducted on specially-prepared test tires using the instrumented vehicle shown in figure 1. The main feature of this vehicle is the test fixture which is cantilevered from the rear of the truck and supports the test tire. For braking tests at fixed slip ratios the test tire and wheel assembly is driven through a universal coupling by interchangeable gears, which in turn are chain-driven by a driving wheel on the truck. Changing the slip ratio entails merely changing the gears in the drive unit and in this program the slip ratios are being varied from 0% to 50%. For cornering tests the universal coupling is disconnected and the fixture is rotated to the desired steering or yaw angle and clamped in place. Yaw angles to 25-degrees are being evaluated. The braking tests are being conducted on both asphalt and concrete runway surfaces, but the cornering tests are being limited to a relatively smooth asphalt surface.

A sample of the wear, friction, and temperature data obtained during this test program is presented in figure 2. These data are for size 22 × 5.5, type VII, 12-ply rating aircraft tires which had been retreaded with four different elastomers whose compositions were as follows:

Elastomer	Composition
A	100% natural rubber
B	75% natural rubber and 25% cis-polybutadiene
C	75% natural rubber and 25% vinyl-polybutadiene
D	75% natural rubber and 25% trans-polypentenemer

Elastomer A was tested because natural rubber has been considered the elastomer best suited to meet the tire requirements for supersonic transport-type aircraft. Elastomer B comprises a stock representative of the current state-of-the-art treads for jet transports, and elastomers C and D are experimental blends developed specifically for this program. A fifth experimental elastomer which consists of a tri-blend of natural rubber, cis-polybutadiene, and vinyl-polybutadiene, is currently being evaluated. Presented on the left of figure 2 are plots of the tire wear rate as a function of the slip ratio from the braking tests and yaw angle from the cornering tests; a lower wear rate indicates a longer tire tread life. The data indicate that the 100-percent natural rubber tread (elastomer A) has the highest wear rate and the state-of-the-art tread (elastomer B) has the lowest wear rate of the elastomers tested to date. Treads fabricated from the two experimental elastomers had similar wear characteristics but neither had a wear resistance as good as the present state-of-the-art elastomer. Other characteristics of the experimental treads such as heat buildup, cut growth, and heat blowout resistance could, however, tip the balance in favor of one of the experimental elastomers for some applications. It is apparent from the figure that extended operations at high slip ratios and/or high yaw angles significantly shorten tread life for all tread materials.

While experimenting with the composition of the tire tread to improve its wear characteristics it is important that the tire friction capabilities not be compromised. The friction measurements obtained from the various tires in either the braking or cornering modes are faired by a single curve in figure 2.

thereby suggesting that the various tread elastomers studied to date do not significantly affect the tire friction performance.

Also presented in figure 2 are the maximum tread temperatures as obtained from an optical pyrometer mounted on the tire fixture which continuously monitored the tread temperature of a point on the rotating tire approximately 3/8 of a revolution out of the footprint. Tread temperatures were observed to be independent of the elastomer and the figure shows that this temperature increases with increasing slip ratio and increasing yaw angle.

STATIC AND ROLLING TIRE BEHAVIOR

NASA research on static and rolling behavioral characteristics of the pneumatic aircraft tire is concerned with studies of gear response to tire failures (blowouts); tire carcass temperatures during various aircraft ground operations; wet runway friction/hydroplaning; and certain key tire mechanical properties. The following paragraphs briefly discuss each of these planned or on-going programs.

Gear Response to Tire Failures

The need for a study of landing gear response to tire failures has become more critical in recent years due to the increasing number of tire failures experienced by the wide-body airplane fleet. A tentative test matrix has been outlined for a NASA program which calls for studies of the friction forces developed by deflated (blown) tires and by wheels rolling on rims; an assessment of debris trajectory patterns associated with tire blowouts; and the response of the strut, antiskid braking system, and the demands placed on the nose gear steering system following a main gear tire failure. A planning session has been scheduled with representatives from airline, tire, and other aviation industries and interested government agencies to finalize the test matrix and testing will probably commence in mid-1981.

Tire Carcass Temperatures

The generation of heat in aircraft tires is undergoing study to determine the temperature profiles which are necessary to define the strength and fatigue limitations of the tire carcass structure. Both experimental and analytical efforts are currently underway in this study. The experimental tests are being carried out on size 22 × 5.5 aircraft tires and the test vehicle is the same instrumented truck shown in figure 1. For these tests, the tires are equipped with a number of thermocouples located within the tire carcass on one side of the tire centerline as illustrated in the schematic of figure 3. A photograph of one such tire installed on the test vehicle is presented in figure 4 which also shows the modified hub and slip ring assembly for transmitting the thermocouple signals to the on-board recording equipment. Temperature data are being acquired while the tire is operated under free-rolling, light-braking, and yawed-rolling conditions. Since only one side of each tire is instrumented, symmetry is presumed about the tire centerline for free-rolling and light-braking conditions. For yawed rolling conditions, tests are run at yaw angles of equal magnitude on either side of 0° to account for any asymmetrical heating conditions. Typical results from the free-rolling tests are presented in figure 5 which shows the carcass temperature profiles of a test tire after travelling distances of 1500 m, 3000 m, and 4500 m at a ground speed of 17 knots. The data indicate that the hottest portions of the tire carcass are beneath the tread near the shoulder area and along the inner surface of the sidewall.

The analytical effort to model the heat generation mechanisms within an aircraft tire is being conducted at the University of Michigan under a NASA grant. The model employs an assembly of finite elements to represent the tire cross section and treats the heat generated within the tire as a function of the strain energy associated with the predicted tire flexure.

Figure 6 presents a comparison between the experimental data and the results from a preliminary analysis performed on a free-rolling tire. The figure shows the temperature rise as a function of time as measured and calculated at two thermocouple positions for two tire deflection conditions. The thermocouple positions include the inner and outer surface of the tire sidewall near the bead, and their positions are denoted on figure 3 by asterisks. The data presented in figure 6 show good agreement between the experimental and the calculated temperature rises. Current analytical work is aimed at refining the strain energy terms in the model to provide even closer agreement in the free-rolling case and to address the braking and cornering cases.

Wet Runway Friction/Hydroplaning

For many years the Langley Research Center has been associated with friction and hydroplaning research. (See refs. 4 and 5 for examples.) As a result of these early research efforts, the critical hydroplaning speed at which the tire begins to spin down when water is encountered on the runway has been well established. These early tests also indicated that a speed reduction to a second, lower critical speed is necessary to allow the tire to spin up again, but this critical hydroplaning spin-up speed has not been well documented. Tests are currently underway on the Langley Landing-Loads Track to establish the speed reduction necessary to allow tire spin-up, and to measure the hydrodynamic pressures within the footprint.

Tire Mechanical Properties

NASA's continuing investigation of tire mechanical properties (refs. 6 and 7 are typical of earlier work in this area) was recently expanded to support a program sponsored by the Society of Automotive Engineers (SAE) to measure both the static and dynamic properties of two sizes of modern aircraft tires. Data were generated using 49 × 17 and 18 × 5.5, type VII tires and provided some insight into the relationship of certain static and dynamic tire properties. An example is shown in figure 7, which presents the lateral spring rates determined from static and dynamic tests performed on a 49 × 17 size tire. The key to relating the static and dynamic data lies in the interpretation of static load-deflection curves similar to the one sketched in figure 7. As will be noted, tire static load-deflection curves generate a substantial hysteresis loop. It has been customary to assign a single value to the tire spring rate and generally, as in references 6 and 8, this rate was defined by the slope of the line which connected the loop extremes. Unfortunately, these spring rates were always lower than those obtained during dynamic tests. Observations from the SAE test program suggested that two spring rates would be more representative of tire response to static loadings. One rate would be the slope of the loading portion of the static hysteresis loop and the other rate would be defined by the initial slope of the load relaxation curve following attainment of the peak static load. Both of these rates and that obtained from dynamic (free vibration) tests are presented in figure 7. The figure suggests that the two statically determined rates define an envelope which would include all the possible spring rates obtained under dynamic loading conditions, with the lower bound of the envelope defined by the static loading curve and the upper bound defined by the initial static relaxation curve.

ANALYTICAL TIRE MODEL DEVELOPMENT

NASA is developing a family of analytical tire models which will be useful in tire design and landing gear analysis. This is a joint venture between NASA, the College of William and Mary, and George Washington University. The approach being taken is to use finite elements based on nonlinear shell theory (refs. 9 and 10). The shell theory is limited to small strains but can handle anisotropic, nonhomogeneous, elastic material characteristics; bending extensional coupling; large deformations; and moderate rotations. To date two quadrilateral shell finite-element models have been developed which feature the use of a reduced-basis solution algorithm and automatic selection of load or displacement incrementation (refs. 11 and 12). One model is a 16-node finite element based upon the displacement formulation and the second model is a finite element based upon a mixed formulation with 9 nodes along the periphery where displacements are the fundamental unknowns and 4 internal nodes where the stress resultants are the unknowns. For the mixed formulation the internal stress resultants are discontinuous across the interelement boundaries and the stress parameters and their path derivatives are eliminated on the element level. The performance of these two shell tire models is being verified by applying inflation pressure loads. Typical results from these verification studies are presented in figure 8 for a 10-ply tire of elliptical cross section mounted on a rigid wheel. A schematic of the model cross section is presented on the left of the figure. Also presented in the figure is a plot of the pressure load against the crown displacement of the tire illustrating the hardening spring characteristic of the tire. The drawing of the uninflated and inflated tire model geometries are shown to scale and illustrate the large deformations associated with this simple loading system.

Future work in tire analytical model development will be concentrated in the major areas of material characterization, modeling techniques, and load determination. In the area of material characterization the next effort will be aimed at the extension of the current linear elastic material model to include the nonlinear effects of viscoelastic material behavior. This effort will also include studies of the effects of elevated temperature on the material strength and its mechanical properties. Modeling techniques in the future will include rational approximations to the comprehensive nonlinear shell theory and solution algorithm refinements that reduce computer costs while maintaining solution accuracy. Future loading systems imposed upon the model will be consistent with studies of the tire/runway contact problem, the inclusion of braking and cornering forces, and the investigation of the dynamic effects of rolling.

The importance of the analytical tire model development program can best be expressed in terms of its anticipated applications. A mature family of tire models should furnish a means of streamlining new tire development and qualification procedures. Furthermore, these analytical tools should be able to predict tire failure modes during the design phase so that appropriate steps can be taken to prevent undue tire failures during aircraft ground operations. The family of tire models should provide the means of solving such landing gear dynamic problems as wheel shimmy, truck pitching, and gear walk. Eventually these models could provide the information necessary to tailor the mechanical properties of aircraft tires to make them more compatible with aircraft antiskid braking and nose gear steering systems and, thereby, optimize the ground handling capability of modern aircraft.

CONCLUDING REMARKS

Langley Research Center is conducting both experimental and analytical tire research programs to address the various needs identified by the landing gear designers and the airplane users. The experimental programs are designed to increase tire tread lifetimes, relate static and dynamic tire properties, establish the tire hydroplaning spin-up speed, study gear response to tire failures, and define tire temperature profiles during taxi, braking and cornering operations. The analytical programs are aimed at providing insights into the mechanisms of heat generation in rolling tires and developing the tools necessary to streamline the tire design process and to aid in the analysis of landing gear problems.

REFERENCES

1. McCarty, John Locke: Wear and Related Characteristics of an Aircraft Tire During Braking. NASA TN D-6963, 1972.

2. Yager, Thomas J.; McCarty, John L.; Riccitiello, S. R.; and Golub, M. A.: Development in New Aircraft Tire Tread Materials. Aircraft Safety and Operating Problems, NASA SP-416, 1976, pp. 247-256.

3. McCarty, John L.; Yager, Thomas J.; and Riccitiello, S. R.: Wear, Friction, and Temperature Characteristics of an Aircraft Tire Undergoing Braking and Cornering. NASA TP-1569, 1979.

4. Horne, Walter B.; and Dreher, Robert C.: Phenomena of Pneumatic Tire Hydroplaning. NASA TN D-2056, 1973.

5. Horne, Walter B.; and Leland, Trafford J. W.: Influence of Tire Tread Pattern and Runway Surface Condition on Braking Friction and Rolling Resistance of a Modern Aircraft Tire. NASA TN D-1376, 1962.

6. Smiley, Robert F.; and Horne, Walter B.: Mechanical Properties of Pneumatic Tires with Special Reference to Modern Aircraft Tires. NASA TR R-64, 1960.

7. Tanner, John A.: Fore-and-Aft Elastic Response Characteristics of 34 × 9.9, Type VII, 14 Ply-Rating Aircraft Tires of Bias-Ply, Bias-Belted, and Radial-Belted Design. NASA TN D-7449, 1974.

8. Sleeper, Robert K.; and Dreher, Robert C.: Tire Stiffness and Damping Determined From Static and Free-Vibration Tests. NASA TP-1671, 1980.

9. Saunders, S. L.: Nonlinear Theories for Thin Shells. Q. Appl. Math.; Vol. 21, No. 1, 1963, pp. 21-36.

10. Budiansky, B.: Notes on Nonlinear Shell Theory. J. Appl. Mech., Vol. 35, 1968, pp. 392-401.

11. Noor, Ahmed K.: Recent Advances in Reduction Methods for Nonlinear Problems. Computers and Structures, Vol. 13, 1981, pp. 31-44.

12. Noor, Ahmed K.; and Andersen, C. M.: Computerized Symbolic Manipulation in Nonlinear Finite Element Analysis. Computers and Structures, Vol. 13, 1981, pp. 379-403.

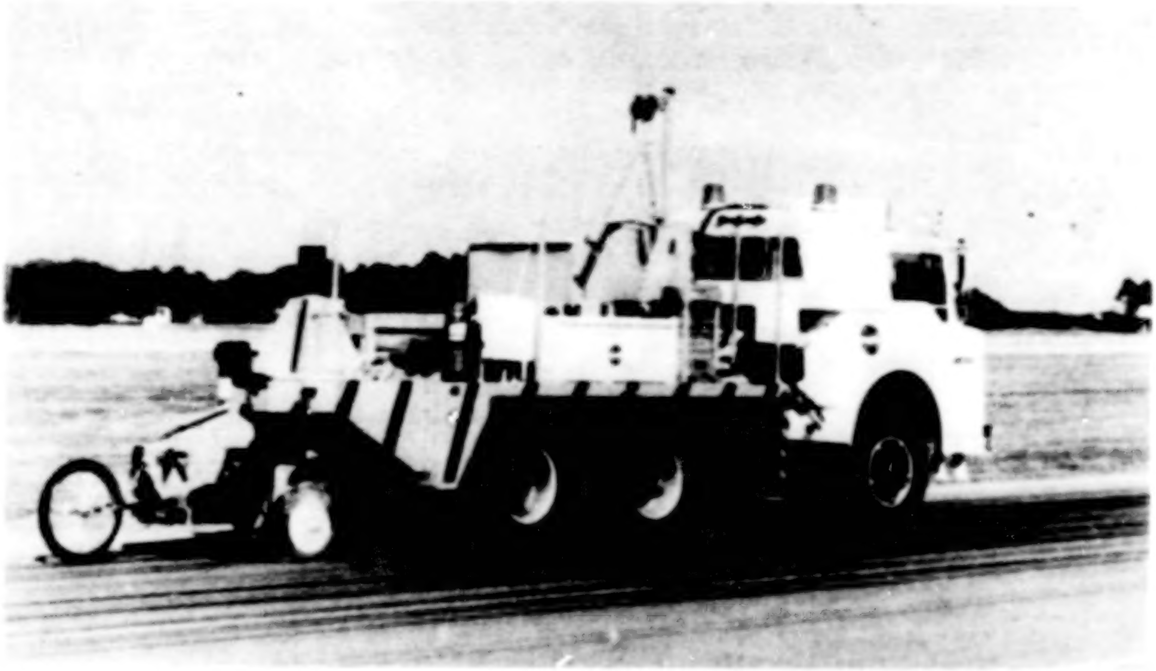

Figure 1.- Instrumented test vehicle.

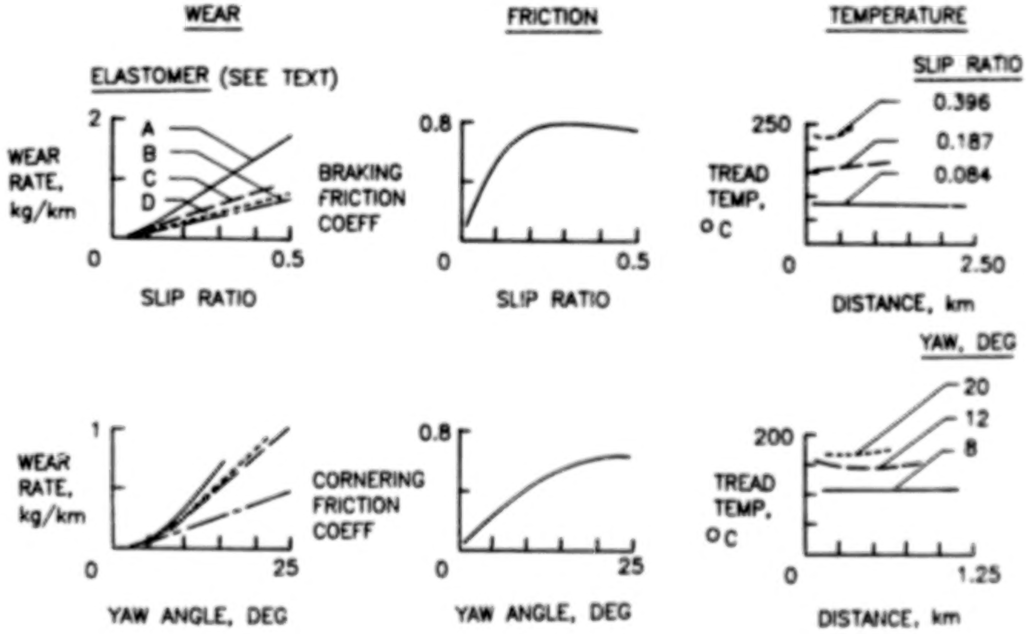

Figure 2.- Wear, friction, and temperature characteristics of a size 22 × 5.5 tire on a smooth asphalt surface.

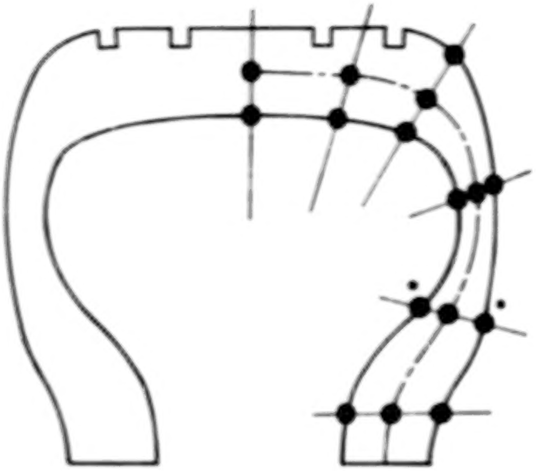

•: DATA FROM THESE THERMOCOUPLES COMPARED WITH MODEL PREDICTIONS

Figure 3.- Location of thermocouples in tire carcass.

Figure 4.- Size 22 × 5.5 test tire with thermocouples installed.

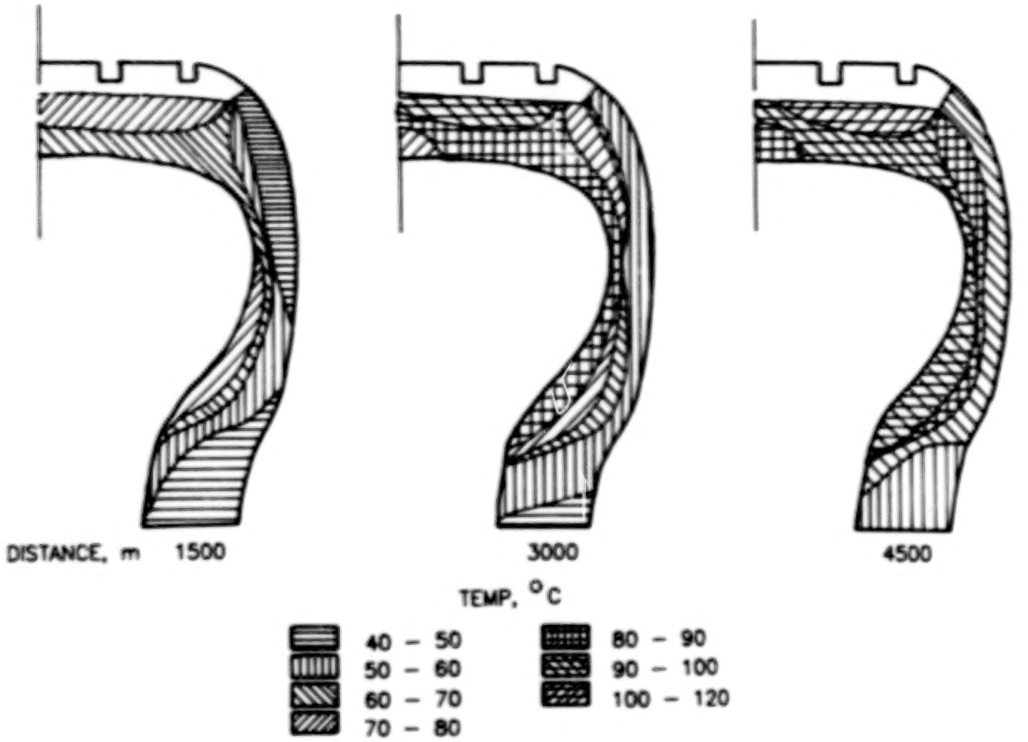
DISTANCE, m
1500
3000
4500
TEMP, °C
40 - 50
50 - 60
60 - 70
70 - 80
80 - 90
90 - 100
100 - 120

Figure 5.- Temperature profiles during free roll. 22 × 5.5, 12-ply tire; ground speed, 17 knots.

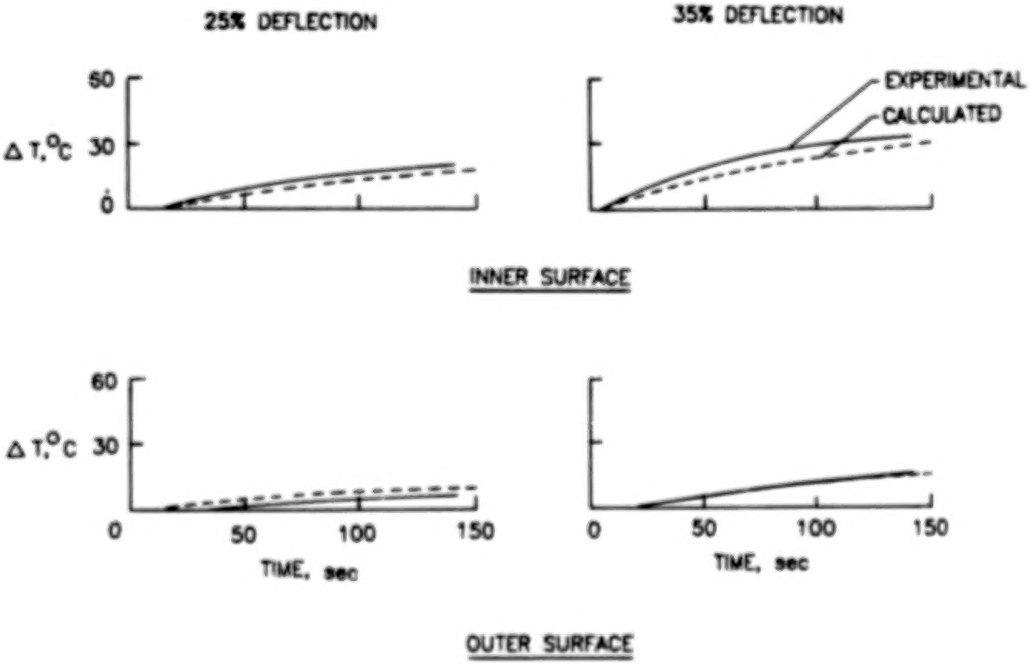

Figure 6.- Comparison of experimental and calculated temperature rise. 22 × 5.5 tire; ground speed, 17 knots.

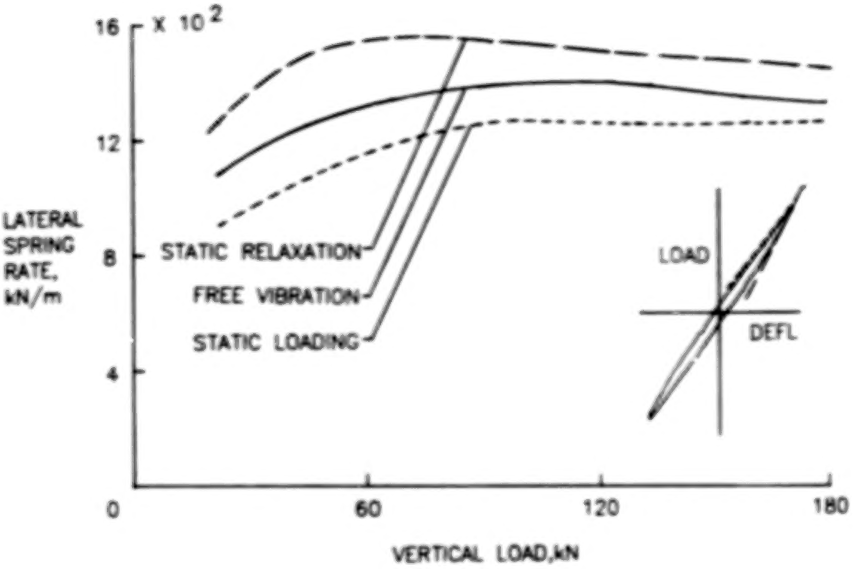

Figure 7.- Comparison of static and dynamic lateral tire spring rates for a 49 × 17 tire.

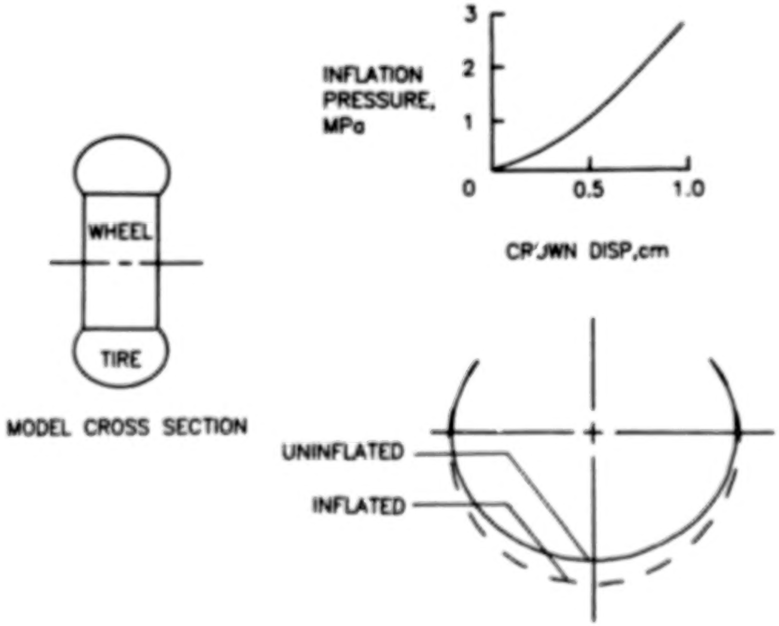

Figure 8.- Typical model results. 10-ply elliptical tire on a rigid wheel.

BLANK PAGE

BLANK PAGE

554

REVIEW OF ANTISKID AND BRAKE DYNAMICS RESEARCH

Sandy M. Stubbs and John A. Tanner
NASA Langley Research Center

SUMMARY

In an effort to establish the reasons for degraded performance of aircraft braking systems which sometimes occur on wet runways, Langley Research Center, with support from the FAA, has been involved in a program to study the behavior of various antiskid systems under the controlled conditions afforded by the Aircraft Landing Dynamics Facility. Results from this study utilizing a single main wheel of a DC-9 aircraft suggest that the systems investigated perform well under most circumstances but there may be room for improvement. For example, it has been demonstrated that pressure-bias-modulation can adversely affect the response of antiskid systems to rapid changes in the runway friction level. Results also indicate that antiskid systems designed to operate at a slip ratio of approximately 0.1 can provide a maximum braking effort without undue loss in the cornering capability of the tire. Time histories of braking friction coefficient were shown to provide a means of determining antiskid system performance and for systems that employed pressure-bias-modulation it was shown that performance could also be estimated from time histories of brake pressure and torque. Brake dynamic behavior from these tests has yielded the potential for more accurate mathematical models of the brake pressure-torque response which will be useful in future antiskid designs.

INTRODUCTION

Over the years, the number and variety of airplanes using antiskid braking systems have steadily increased until now most current commercial and military jet airplanes are equipped with various skid control devices. The earliest antiskid systems were generally designed to prevent wheel lockups and excessive tire wear on dry pavements. Modern skid control devices, however, are more sophisticated and are designed to provide maximum braking effort while maintaining full antiskid protection under all weather conditions. Operating statistics of modern jet airplanes indicate that these antiskid systems are both effective and dependable; the several million landings that are made each year in routine fashion with no serious operating problems attest to this fact However, it has also been well established, both from flight tests and from field experience, that the performance of these systems is subject to degradation on slippery runways; consequently, dangerously long roll-out distances and reduced steering capability can result during some airplane landing operations (refs. 1 to 3). Thus, there exists a need to study different types of antiskid braking systems in order to find reasons for the degraded braking performance that occurs under adverse runway conditions; there is also a need to obtain data for the development of more advanced systems that will insure safe ground handling operations under all weather conditions.

In an effort to meet these needs, an experimental research program was undertaken by NASA with support from the Federal Aviation Administration to study the single-wheel behavior of several different airplane antiskid braking systems under the controlled conditions afforded by the Langley Aircraft Landing Loads and Traction Facility. The types of skid control devices studied in this program included a velocity-rate-controlled system, a slip-ratio-controlled system with ground reference from an unbraked nose wheel, a slip-velocity-controlled system, and a mechanical-hydraulic system. The investigation of all these systems was conducted with a single main wheel, brake, and tire assembly of a McDonnell Douglas DC-9 series 10 airplane.

The purpose of this paper is to present some of the significant findings which became evident during the test of the antiskid systems under maximum braking effort. The parameters varied in the study included test speed, tire loading, tire yaw angle, tire tread condition, brake-system operating pressure, and runway wetness condition; a detailed discussion of the effects of these parameters on three of the systems studied can be found in references 4, 5, and 6. This paper touches briefly on several aspects of antiskid system design philosophy, discusses techniques for evaluating antiskid performance, and discusses brake dynamics during antiskid cycling.

APPARATUS AND TEST PROCEDURE

Test Facility

The investigation was performed using the test carriage shown in figure 1. Also shown in figure 1 is a close-up view of the test wheel and the instrumented dynamometer which was used instead of a landing-gear strut to support the DC-9 tire, wheel, and brake assembly because it provided an accurate measurement of the tire-ground forces. The test tire was a 40x14, type VII retreaded tire inflated to .97 MPa.

The test runway can also be seen in figure 1. Approximately 244 m of the flat concrete test runway were used to provide braking and cornering data on a dry surface, on an artificially damp surface, on an artificially flooded surface, and on a natural-rain wet surface. The test speeds used in the investigation were 50, 75, and 100 knots, and fixed tire yaw angles of 0, 1, 3, 6, and 9 degrees were examined. Vertical load was varied from 58 kN to 124 kN, and effects of three brake system pressures of 10, 14, and 21 MPa were studied.

Skid Control Systems

The brake system hardware used in the investigation is shown in figure 2. The brake system components were a pilot metering valve, brake selector valve, and a hydraulic fuse, all DC-9 aircraft components. The antiskid control valve is peculiar to each antiskid system investigated. The line sizes and lengths were those of the DC-9 but line bends were not simulated.

A schematic of a typical brake system is shown in figure 3. The supply pressure is fed through the pilot metering valve (which for these tests was set to give maximum braking effort) to the antiskid control valve and on to the brake. A speed sensor located on the braked wheel was used as input to the antiskid control box (the heart of the system) which produces a signal to regulate the antiskid control valve.

Four antiskid systems have been tested in this investigation. A velocity-rate controlled and a slip-velocity controlled system both having pressure bias modulation as a key element in their logic circuits are similar to the schematic shown in figure 3. A slip-ratio controlled antiskid system was investigated that used (in addition to the items illustrated in the sketch of figure 3) an input from an unbraked nose wheel to obtain the aircraft ground speed. The fourth system tested was a mechanical-hydraulic system not at all like the schematic of figure 3; instead, it had an internal flywheel spun-up by the free rolling wheel through an over-running clutch before application of brakes. The speed of the flywheel was mechanically compared with the braked wheel speed so that when the braked wheel angular velocity decreased at a rapid rate, brake pressure was released.

RESULTS AND DISCUSSION

The pargraphs in this section will discuss some factors that adversely affect antiskid performance on slippery runways; the use of pressure, torque, and friction information to estimate antiskid performance, and brake dynamics during antiskid cycling including the mathematical modeling of the brake pressure-torque response.

Optimum Slip Ratio For Antiskid Control

The drag force friction coefficient is plotted as a function of slip ratio in figure 4 to illustrate the advantages of using slip ratio as the parameter for antiskid control. By definition, a slip ratio of one is a locked wheel skid, and a slip ratio of zero is a freely rolling tire. Figure 4 presents data for three separate runs at 0° yaw conditions on dry, damp, and flooded runway surfaces. During the course of antiskid cycling, hysteresis loops or eddies can be seen which result in variations in the drag force for a given slip ratio. The maximum drag force friction coefficient is shown to occur initially at about a 0.1 slip ratio and to hold fairly constant out to a slip ratio of approximately 0.4 for all three surface conditions.

The variation of the drag force friction coefficient and the corresponding side force friction coefficient with slip ratio is presented in figure 5 for a yawed tire undergoing braking on a damp concrete surface. Again, the maximum drag force friction coefficient occurs initially at about 0.1 slip ratio, as was shown in figure 4, but the maximum side force friction coefficient is shown to occur at 0 slip ratio when the tire is unbraked. Furthermore, the side force friction decreases rapidly such that at slip ratios above approximately 0.2 the tire cornering capability has been reduced to essentially an insignificant value. For this reason a slip ratio of approximately 0.1 is suggested as the optimum for antiskid system design, since that value provides near-maximum braking force while retaining a fairly high percentage of the side force which is necessary for steering control.

If an antiskid braking system is to operate on the principle of slip ratio control, then measurements of the aircraft ground speed and the braked wheel speed are needed as inputs to the antiskid system logic circuits. Figure 6 shows braked wheel speed as a function of time for two different antiskid systems. The top curve is for a slip-ratio controlled antiskid system and the lower one is for a system without slip ratio control. The dashed lines on both plots indicate the ground speed decay of the aircraft, or in this case, the test carriage. The lower plot indicates that the system without slip ratio control cycled as designed with several instances wherein the brakes were released to permit the tire to spin up to the speed of the test carriage. Hence, for this system, the information from the braked wheel can be used to establish both the vehicle ground speed and the braked wheel speed.

On the other hand, the slip-ratio controlled system (top plot of figure 6) attempts to maintain the braked wheel speed at about 10% below the carriage ground speed for this test and, as such, never allows spin-up of the braked wheel to approach the carriage ground speed. Thus, for this type of system to properly function it is necessary to obtain a ground speed reference from some source independent of the braked wheel such as the unbraked nose wheel or an inertia platform.

Antiskid System Control Logic

Figure 7 addresses the issue of pressure bias modulation and its effect on antiskid control. Pressure bias modulation is an antiskid logic design feature used on some systems to enhance performance by increasing the operating time on the front side (positive slope) of the μ-slip curve. This logic may be satisfactory under conditions of constant available friction, but, as shown in figure 7, may be less satisfactory when friction surface conditions are changing rapidly. Time histories of wheel speed, skid signal, brake pressure, and drag force friction are presented in the figure for a test on a dry runway that has one damp spot about .6 m in diameter approximately midway down the test section. The figure shows that the wheel speed is cycling as designed on the dry surface such that wheel spin-down as at A causes a skid signal build-up B which closes the antiskid control valve, thereby reducing the brake pressure C. When the wheel spins back up D, the skid signal reduces and the brake pressure is reapplied. At approximately 6 seconds into the test, the wheel encounters the damp spot on the runway and immediately goes into a deep skid causing a saturated skid signal E and a corresponding reduction in brake pressure. When the wheel spins back up on this occasion the skid signal is only slightly reduced F because the pressure bias modulation system causes a slow reduction in skid signal and a consequent slow reapplication of brake pressure G. The resulting drag force friction coefficient trace shows that while the tire is being braked on a dry surface, the friction coefficient is effectively maintained at a level of about .6, but when it reaches the damp spot, the friction coefficient drops abruptly and remains below that level over a considerable time period because of the slow rate of brake application following the deep skid. An ideal system would allow a rapid reapplication of the brake pressure and bring the friction coefficient back up quickly to take advantage of that available on the dry surface.

Figure 8 shows the same type of test but without pressure bias modulation in the antiskid system. Again, when the tire reaches the damp spot on the runway, the wheel speed drops suddenly, causing the skid signal to saturate with a corresponding drop in brake pressure. When the wheel spins back up, the skid signal drops almost immediately to zero since it is not modulated and the brake pressure is rapidly reapplied. The drag-force friction coefficient indicates good antiskid action since it drops only momentarily when the damp spot is encountered. This type of reaction should greatly enhance antiskid performance under variable runway friction conditions.

Estimating Antiskid Braking Performance

References 7, 8, and 9 discuss several different sources from which antiskid-system efficiencies can be calculated. Ideally, antiskid efficiency should be based upon the friction developed between the tire and the runway surface. However, friction measurements are not readily obtained in practice and other characteristics such as brake torque or brake pressure must be employed. Figures 9, 10, and 11 are presented to illustrate the agreement, or lack thereof, between efficiencies as determined from friction, brake torque, and brake pressure measurements. Shown in figure 9 are typical time histories of brake pressure, torque, and friction for an antiskid system which employs pressure bias modulation. Following brake application, denoted by the rapid rise in all three measurements, the friction and brake torque gradually increase to maximum levels while the pressure is held constant, and when the tire enters into a deep skid all three drop suddenly. Four such cycles are observed during the course of the run shown. To compute the braking performance index (antiskid efficiency) β, the average pressure, torque, and friction developed during a run are divided by the respective average maximum value which, for this run, is the average of four measurements. Observe that for this test all three sources yielded essentially the same performance index.

Not all runs are as easy to analyze as the run shown in figure 9, however. Figure 10 presents time histories of the brake pressure, torque, and friction for a run on a wet surface using the same antiskid system. Maximum values for the pressure trace can be readily identified and when divided into the average value define a performance index of .81. The brake torque can also be analyzed in this fashion and gives an index of .80. The drag-force friction trace, however, shows no incipient skid points like those of the other two traces or like those in figure 9. In an effort to be unbiased, the maximum friction for such cases was taken at fixed time steps over the entire run. In

Part 2

SESSION IV - OPERATING PROBLEMS AND POTENTIAL SOLUTIONS
Chairman: H. W. Schmidt

22. WAKE VORTEX ATTENUATION FLIGHT TESTS: A STATUS REPORT 387 1/A14
Marvin R. Barber and Joseph J. Tymczyszyn

23. BASIC RESEARCH IN WAKE VORTEX ALLEVIATION USING A VARIABLE TWIST WING 409 1/C8
Dana J. Morris and G. Thomas Holbrook

24. PNEUMATIC BOOT FOR HELICOPTER ROTOR DEICING 425 1/D11
Bernard J. Blaha and Peggy L. Evanich

25. AIRCRAFT OPERATING EFFICIENCY ON THE NORTH ATLANTIC - A CHALLENGE FOR THE 1980'S 445 1/F3
Robert Steinberg

26. FIREWORTHINESS OF TRANSPORT AIRCRAFT INTERIOR SYSTEMS 453 1/F12
John A. Parker and D. A. Kourtides

27. COMBUSTION TOXICOLOGY OF EPOXY/CARBON FIBER COMPOSITES 481 2/A14
D. E. Cagliostro

28. THE USE OF ANTIMISTING KEROSENE (AMK) IN TURBOJET ENGINES 499 2/C10
Harold W. Schmidt

29. NASA/FAA GENERAL AVIATION CRASH DYNAMICS PROGRAM 511 2/D8
Robert G. Thomson, Robert J. Hayduk, and Huey D. Carden

SESSION V - FLIGHT EXPERIENCES AND GROUND OPERATIONS
Chairman: J. L. McCarty

30. CURRENT RESEARCH IN AIRCRAFT TIRE DESIGN AND PERFORMANCE 543 2/F12
John A. Tanner and John L. McCarty

31. REVIEW OF ANTISKID AND BRAKE DYNAMICS RESEARCH 555 2/G10
Sandy M. Stubbs and John A. Tanner

32. STUDIES OF SOME UNCONVENTIONAL SYSTEMS FOR SOLVING VARIOUS LANDING PROBLEMS 569 3/A12
T. J. W. Leland, J. R. McGehee, and R. C. Dreher

33. RECENT PROGRESS TOWARDS PREDICTING AIRCRAFT GROUND HANDLING PERFORMANCE 583 3/B12
Thomas J. Yager and Ellis J. White

34. THE NASA DIGITAL VGH PROGRAM - EARLY RESULTS 613
Norman L. Crabill and Garland J. Morris
3/D14

35. EVALUATION OF EMERGENCY-LOCATOR-TRANSMITTER PERFORMANCE IN REAL AND SIMULATED CRASH TESTS 625
Huey D. Carden
3/E12

36. EXTINGUISHING IN-FLIGHT ENGINE FUEL-LEAK FIRES WITH DRY CHEMICALS 655
Robert L. Altman
3/G14

SESSION VI - ACOUSTICS AND NOISE REDUCTION

Chairman: H. G. Morgan

37. RECENT DEVELOPMENTS IN AIRCRAFT ENGINE NOISE REDUCTION TECHNOLOGY 671
James R. Stone and Charles E. Feiler
4/B4

38. SOURCES, CONTROL, AND EFFECTS OF NOISE FROM AIRCRAFT PROPELLERS AND ROTORS 699
John S. Mixson, George C. Greene, and Thomas K. Dempsey
3/D4

39. NASA PROGRESS IN AIRCRAFT NOISE PREDICTION 721
J. P. Raney, S. L. Padula, and W. E. Zorumski
4/E12

40. AIRPORT NOISE IMPACT REDUCTION THROUGH OPERATIONS 759
Richard DeLoach
5/A13

ATTENDEES 779
5/C5

the run described by figure 10, when the average friction is divided by the maximum obtained by this technique, the performance index is computed to be .84. Thus, it appears that either pressure, torque, or friction may be used to obtain the performance index for this type of antiskid system.

Use of pressure or torque for determining antiskid performance can be misleading for a fast-responding antiskid system, however. Figure 11 shows time histories of brake pressure, torque, and friction for a slip-ratio controlled antiskid system that has high-frequency, high-amplitude oscillations in the brake pressure and torque traces. For this run, if the average pressure is divided by the maximum pressure, the resulting performance index is .77 and the index as computed from the brake torque is .85. In the friction trace, if the maximum friction values are obtained at fixed time intervals, a performance index of .91 is obtained. Thus, for this type of antiskid system, pressure and torque data will give estimates of braking performance which appear to be too low and the performance estimates based upon friction data should be used.

Brake Dynamic Pressure-Torque Relationship

A major finding of this study of antiskid braking systems has been the discovery of the true nature of brake dynamic behavior while under antiskid control. The plots on the left side of figure 12 show typical examples of the pressure input to the brake during antiskid operation, the resulting torque output from the brake, and the relationship between the brake pressure and brake torque as observed during a typical antiskid-braking test. This pressure-torque relationship defines brake behavior during antiskid operations and plays a critical role in establishing the braking efficiency of an antiskid braking system. The relationship depicted in figure 12 is characterized by fairly large hysteresis loops which imply a wide range of torque values for a given pressure.

Computer simulations of antiskid braking systems are needed to tune existing antiskid systems to optimize their braking and cornering performance for specific aircraft applications and to aid in future antiskid system designs. Sometimes these simulations are used to estimate antiskid-system efficiencies. These computer simulations typically model the brake pressure-torque response either as a linear spring with viscous damping or as an undamped nonlinear spring. When these current models are exercised with the actual pressure input from a typical antiskid braking test, however, they do not adequately represent the complicated hysteresis conditions that routinely exist in the brake pressure-torque response, as shown on the right in figure 12.

Recently, a nonlinear hysteresis model was developed at the Langley Research Center that captures the essence of the brake response characteristic. This improved model is based upon a variable, nonlinear spring with coulomb or friction damping. When this model is exercised with the actual brake pressure input there is a significant improvement in the fidelity of the pressure-torque response. By comparing the torque outputs from each model with the actual torque response of the brake for the same pressure input it is possible to carry out an error analysis, and the results of such an analysis based on percent torque error for each of the models are presented in the bar chart in the middle of the figure. The data indicate that the Langley model reduces the torque errors significantly. Currently this improved mathematical model is being intorduced into a ground handling simulator to better represent antiskid control for future studies.

CONCLUDING REMARKS

The results obtained to date from a study of the single-wheel behavior of antiskid braking systems suggest that the systems investigated perform well under most circumstances but that there is room for improvement. For example, it was demonstrated that pressure-bias-modulation can adversely affect the response of aircraft antiskid braking systems to rapid changes in the runway friction level. The results of this study also indicate that antiskid braking systems designed to operate at a fixed slip ratio of approximately 0.1 can provide a maximum braking effort without undue loss in the cornering capability of the tire.

It was demonstrated that the braking performance of systems which employ pressure-bias-modulation can be estimated from time histories of the brake pressure or torque when friction data are not available.

Finally, data from these tests have provided significant insights into brake dynamic behavior during antiskid cycling and yield the potential for more accurate mathematical models of the brake pressure-torque response which will be useful in the design of future aircraft antiskid braking systems.

REFERENCES

1. Tracy, William V., Jr.: Wet Runway Aircraft Control Project (F-4 Rain Tire Project). ASD TR-74-37, U.S. Air Force, Oct. 1974. (Available from DTIC as AD A0 [illegible]).

2. Danhof, Richard H.; [illegible], Jerauld R.: RF-4C Wet Runway Performance Evaluation. FTC-T [illegible] Air Force, May 1966. (Available from DTIC as AD 486 049).

3. Horne, Walter B.; McCarty, John L.; and Tanner, John A.: Some Effects of Adverse Weather Conditions on Performance of Airplane Antiskid Braking Systems. NASA TN D-8202, 1976.

4. Stubbs, Sandy M.; and Tanner, John A.: Behavior of Aircraft Antiskid Braking Systems on Dry and Wet Runway Surfaces - A Velocity-Rate-Controlled, Pressure-Bias-Modulated System. NASA TN D-8332, 1976.

5. Tanner, John A.; and Stubbs, Sandy M.: Behavior of Aircraft Antiskid Braking Systems on Dry and Wet Runway Surfaces - A Slip-Ratio-Controlled System With Ground Speed Reference From Unbraked Nose Wheel. NASA TN D-8455, 1977.

6. Stubbs, Sandy M.; and Tanner, John A.: Behavior of Aircraft Antiskid Braking Systems on Dry and Wet Runway Surfaces - A Slip-Velocity-Controlled, Pressure-Bias-Modulated System. NASA TN D-1051, 1979.

7. Skid Control Performance Evaluation. ARP 862, Soc. Automot. Eng., Mar. 1, 1968.

8. Lester, W. G. S.: Some Factors Influencing the Performance of Aircraft Anti-Skid Systems. Tech. Memo. EP 550, British R.A.E., July 1973.

9. Brake Control Systems, Antiskid, Aircraft Wheels, General Specifications for Mil. Specif. MIL-B-8075D, Feb. 24, 1971.

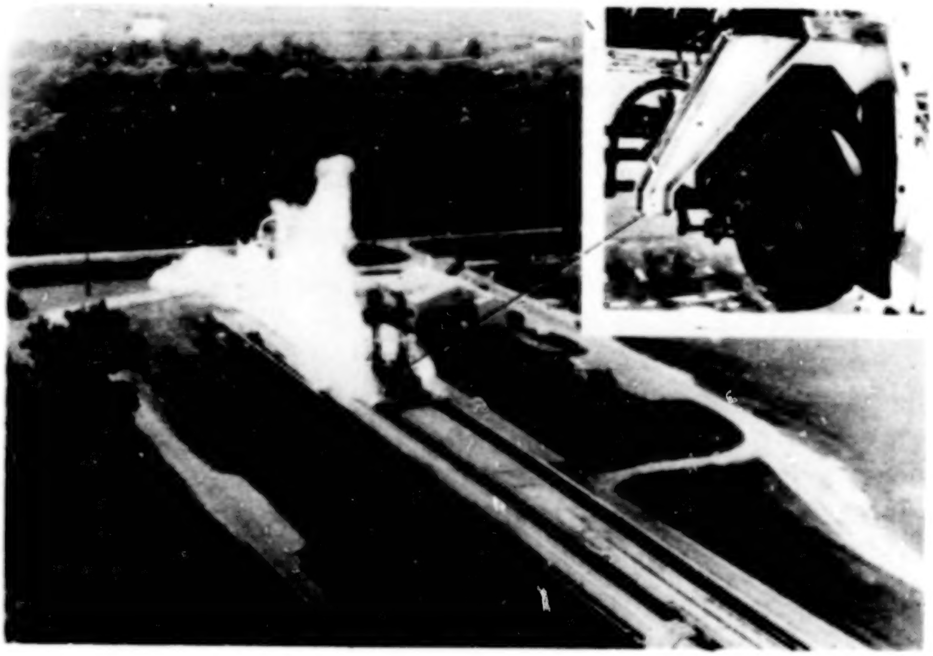

Figure 1.- Landing loads track test carriage.

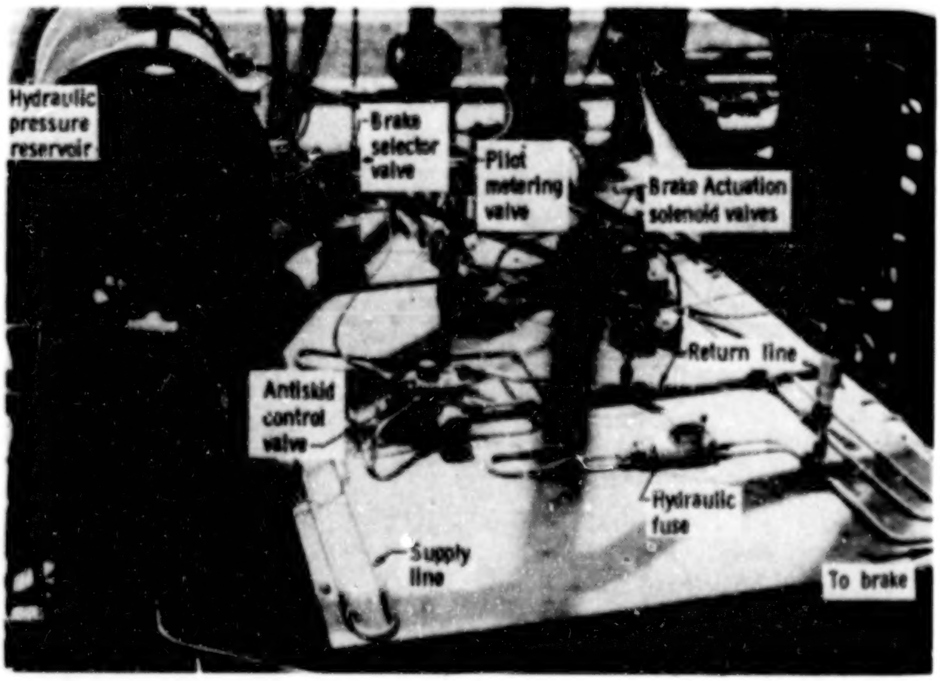
Hydraulic pressure reservoir
Brake selector valve
Pilot metering valve
Brake Actuation solenoid valves
Return line
Antiskid control valve
Hydraulic fuse
Supply line
To brake

Figure 2.- DC-9 (Series 10) brake system simulation.

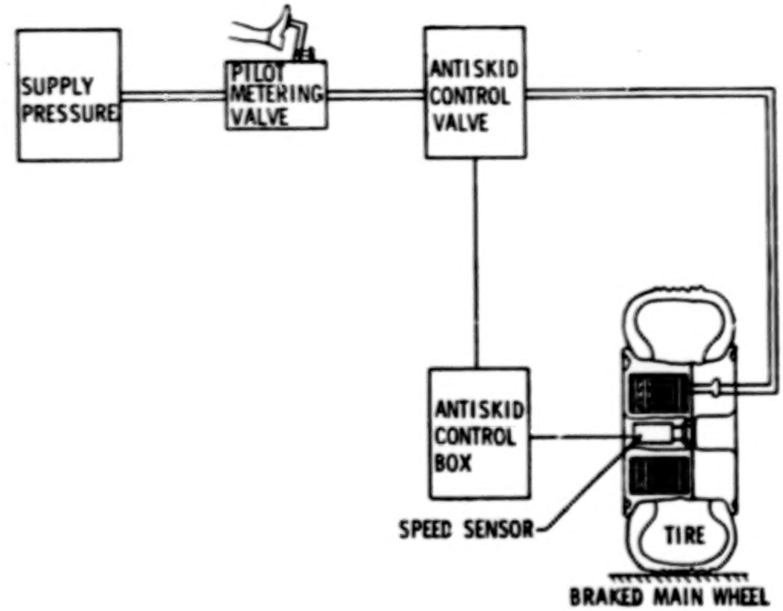
SUPPLY PRESSURE
PILOT METERING VALVE
ANTISKID CONTROL VALVE
ANTISKID CONTROL BOX
SPEED SENSOR
TIRE
BRAKED MAIN WHEEL

Figure 3.- Schematic of typical brake system.

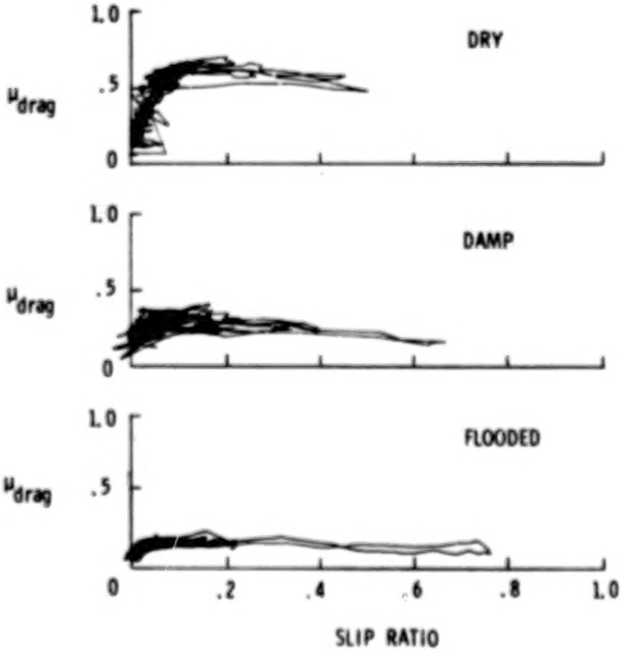

Figure 4.- Tire friction variations with slip ratio.

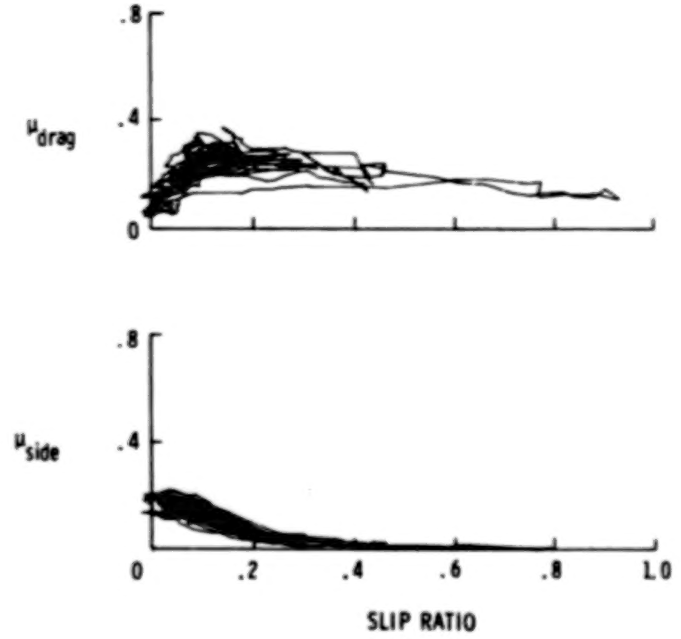

Figure 5.- Drag and side friction variations with slip ratio.

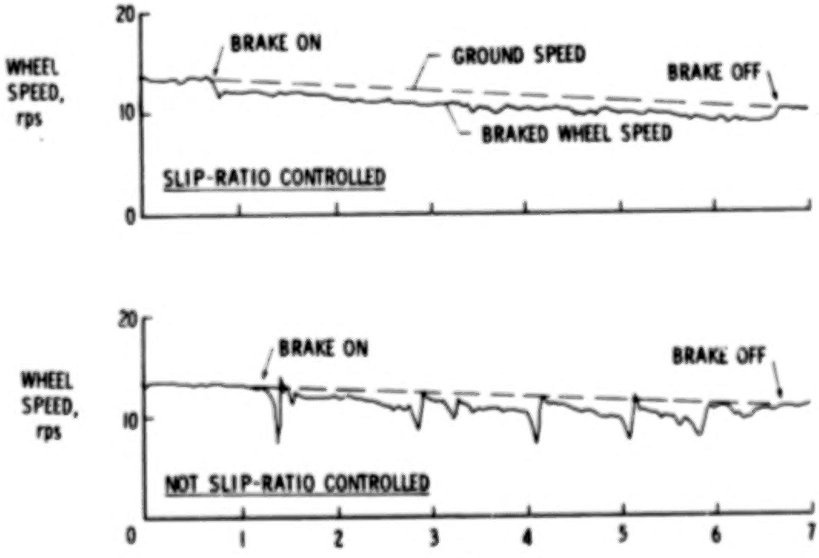

Figure 6.- Wheel speed response with and without slip-ratio control.

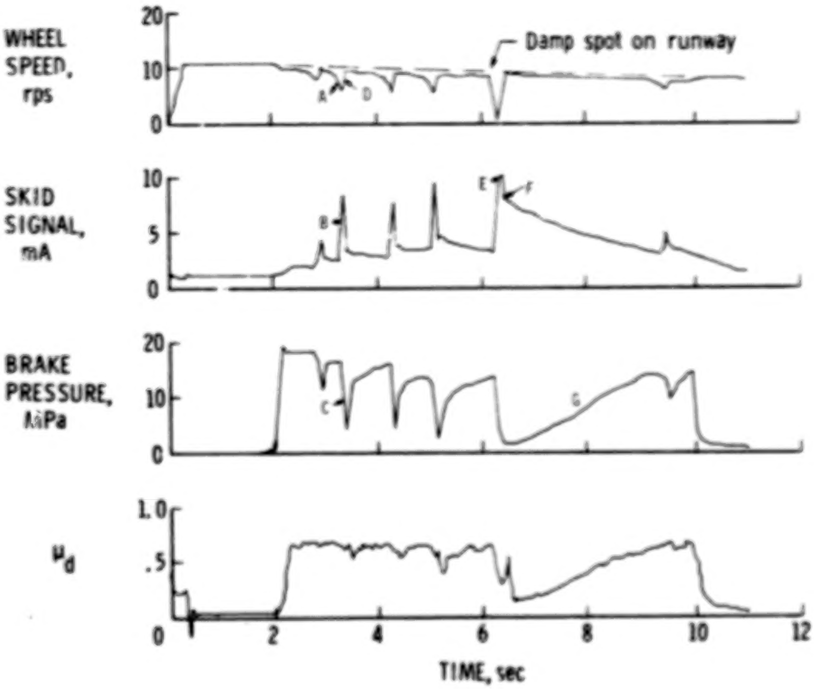

Figure 7.- Antiskid response with pressure bias modulation.

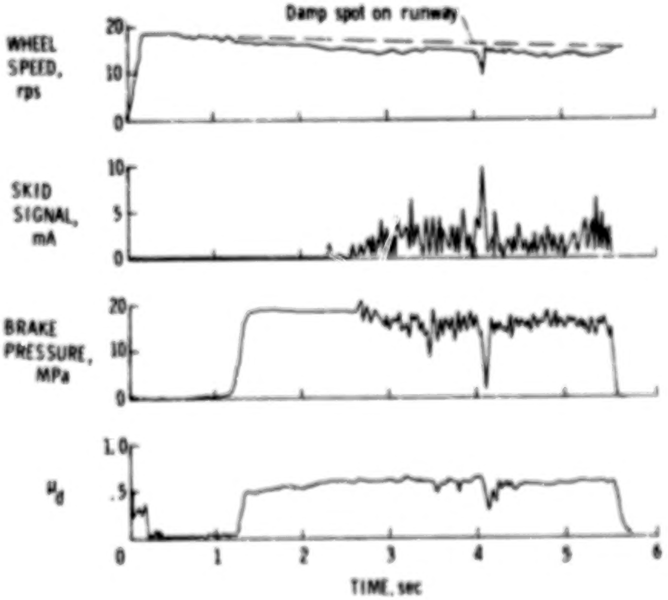

Figure 8.- Antiskid response without pressure bias modulation.

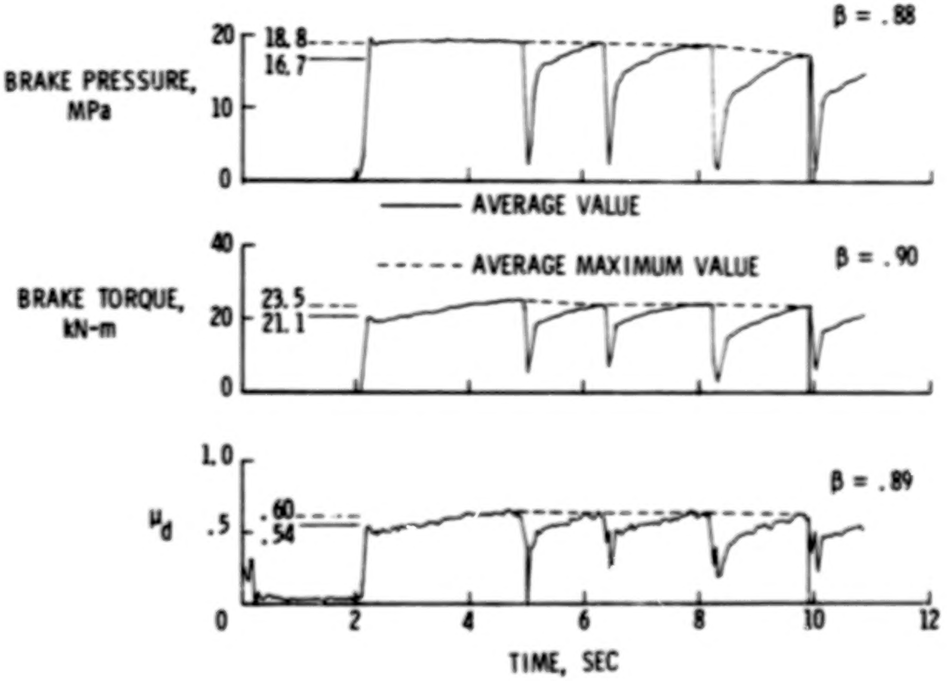

Figure 9.- Methods of estimating antiskid braking efficiency. Antiskid with pressure bias modulation on a dry runway.

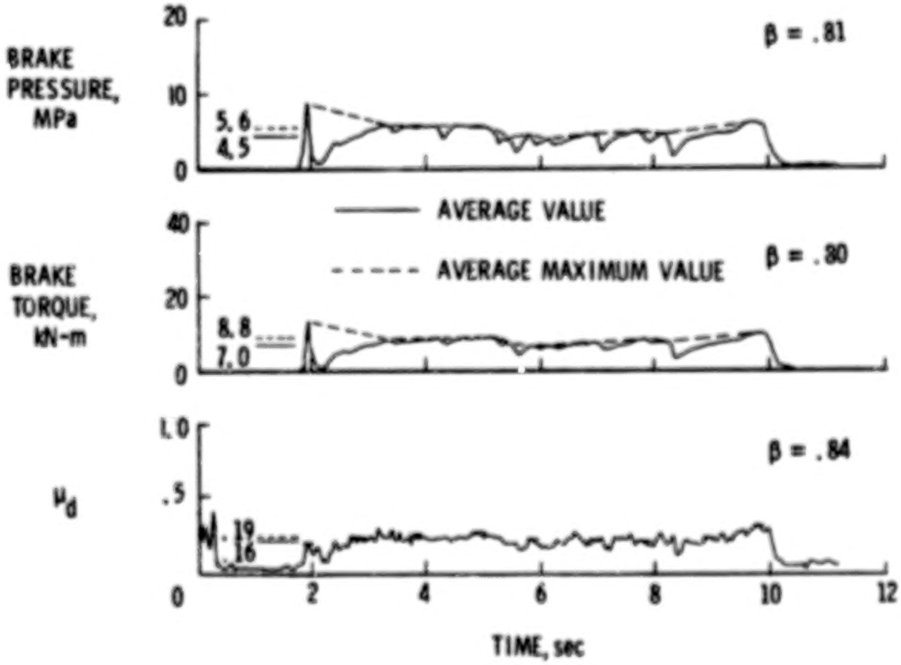

Figure 10.- Methods of estimating antiskid braking efficiency. Antiskid with pressure bias modulation on a damp runway.

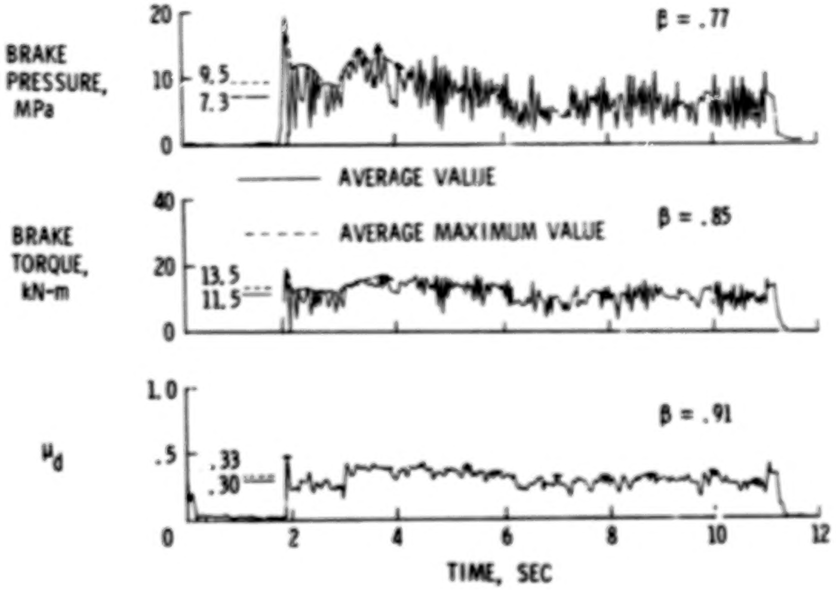

Figure 11.- Methods of estimating antiskid braking efficiency. Antiskid without pressure bias modulation on a damp runway.

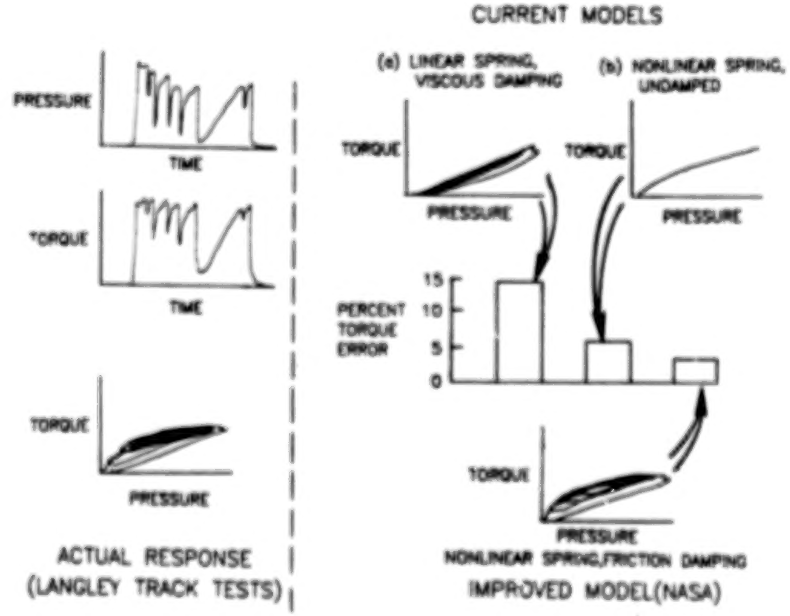

Figure 12.- Aircraft brake pressure-torque response.

STUDIES OF SOME UNCONVENTIONAL SYSTEMS FOR SOLVING VARIOUS LANDING PROBLEMS

T. J. W. Leland, J. R. McGehee, and R. C. Dreher
NASA Langley Research Center

SUMMARY

A review of three research programs which seek solutions to various landing problems through unconventional systems is presented in this paper. The programs, discussed individually, include first, the air cushion landing system (ACLS) where current efforts are concentrated on development of adequate ACLS braking and steering systems and on improved understanding of scaling laws and behavior. The second program is concentrated on use of a wire brush skid as a drag-producing device, which has been shown to have good friction coefficients and reasonable wear rates at ground bearing pressures up to 689 kPa (100 psi) and forward speeds up to 80 km/hr (50 mph). The third program shows great promise in an active control landing gear where significant airframe load reductions are possible during landing impact and subsequent rollout. Work in this area is continuing with studies concentrated on adaptation of the landing gear to a tactical fighter aircraft.

INTRODUCTION

In any discussion of the landing and ground handling problems of aircraft, particularly those with unusual mission requirements, the need often becomes apparent to look beyond the current, conventional systems to more unorthodox unconventional systems which may have some benefit in certain applications. This paper will discuss those current landing gear system research programs which might fall into the unconventional category, each in its own way exploring new or improved landing system concepts which address current or potential aircraft landing/ground handling problems. The most unconventional of these programs, the air cushion landing system, will be discussed first, followed by a presentation of studies of a wire brush skid as a landing gear or a drag-producing device. The last program to be discussed is an active control landing gear and will include some preliminary test results. Included in each discussion will be a status summary of current efforts and an indication of future directions.

AIR CUSHION LANDING SYSTEMS

General.- The air cushion landing system (ACLS) is designed to replace the conventional aircraft landing gear with a flexible toroidial trunk resembling, in the simplest version, a rubber life raft turned upside down and attached directly to the bottom fuselage of the aircraft. As shown in the sketch of figure 1, low-pressure, high-volume air is introduced into the trunk through ducts in the fuselage, and the air is exhausted through peripheral jet holes located in the bottom of the trunk. A portion of this air is trapped in the cavity to provide the necessary lifting force, while the rest of the air is dumped outboard and provides an effective air bearing between trunk and ground. The result is a vehicle having nearly zero ground friction and an extremely low ground bearing pressure of perhaps 7-14 kPa (1-2 psi), which makes possible a wide choice of potential landing and take-off sites including water.

An ACLS may take a variety of forms, as shown in figure 2, depending upon the aircraft size, configuration and mission requirements. Larger aircraft, particularly, may require two or more trunk systems, but no very severe structural penalties ensue since the ACLS distributes the airframe load and no "hard points" are required for attachment as with the conventional landing gear. The trunk or trunks are of course retracted or otherwise stowed during flight, and several workable schemes have been proposed to accomplish this, as in references 1 and 2 for examples. One major ground operational problem for which no completely satisfactory solution exists is development of adequate steering and braking controls for an ACLS, and to study this and other problems the specialized test vehicle shown in the center of figure 2 was developed at Langley.

ACLS Test Vehicle.- The vehicle, shown in figure 2 with a small ACLS installed and in figure 3 supported by a larger ACLS, is a much-modified airboat 5.5 m (18 ft) in length and weighing approximately 2360 kg (5200 lb). A retractable tricycle landing gear taken from a light aircraft was installed as shown to provide a safety back-up in case of an ACLS failure or for steering and braking in case of emergency. Forward propulsion is provided by a 250 hp aircraft engine and propeller at the rear, as shown, and a small jet engine is installed amidships to provide a bleed air source for the ACLS fan. The vehicle was developed primarily to study various braking and steering schemes suitable for ACLS, and is large enough, and portable enough, so that such schemes can be tested in potential real-world conditions of paved or unpaved runways, sod fields, sand, and water.

The air cushion landing system shown installed on the vehicle in figure 3 is a generalized concept involving four separate trunks of circular cross-section arranged in a rectangular planform, each trunk supplied with air from a plenum through the flexible ducts visible in the figure. A hub-turbine fan located on the plenum is used to convert high-pressure, low-volume jet engine bleed air to the low-pressure, high-volume air required for ACLS operation. The four-trunk system was chosen to provide a stable ACLS for steering and braking studies, and also for the inherent control possibilities offered by the separate air supply to each trunk.

An additional advantage of the ACLS test vehicle is the relative ease with which major configuration changes may be made, or any sort of desirable structure or apparatus added on. This feature is illustrated by the photograph of figure 4 which shows the installation of a fixed retractable wheel and tire installed as a steering aid in the ACLS cavity. The wheel is down-loaded to a maximum of about 90 kg (200 lb) with a double-acting hydraulic cylinder, which also serves to retract the assembly. Taxi tests had shown that the air rudders located in the propeller slipstream could, under the influence of a crosswind or runway crown, change with ease the heading of the vehicle but not its direction of travel. It was thought that a single, centrally located, lightly loaded tire might provide sufficient lateral resistance so that the rudders could change both heading and direction of travel. Qualitatively this proved to be the case, but detailed quantitative studies have been interrupted by a failure of the hub-turbine fan and no results can be shown in this paper.

Scale Model Studies.- As an aid to better understanding of air cushion landing system behavior and to provide initial design guidelines, a research contract was awarded to Foster-Miller Associates to develop a rational mathematical model and computer simulation of a generalized ACLS. The results of this study, summarized in reference 3, were quite promising, and to provide experimental corroboration, as well as a first approximation to scaling studies, a 1/3-scale model of the ACLS test vehicle was constructed as shown in figure 5. The model is roughly 1.5 m (5 ft) long and .9 m (3 ft) wide, and comparison with figure 3 will show the physical resemblance between 1/3-scale and full-scale trunks and air supply system. The computer simulation was adjusted to represent the 1/3-scale model, and replicate computer runs and experimental model tests were conducted. A sample comparison of results is shown in figure 6 for a 15 cm (6 in.) drop at 0^o pitch attitude and indicates reasonably good agreement between analysis and experiment. The differences observed may be due to an incorrect scaling of trunk material stiffness or of the trunk air supply characteristics, both of which are extremely difficult to model adequately. This study will be continued for a wide variety of test conditions and, as soon as the full-scale ACLS test vehicle becomes available, replicate tests will be conducted in an attempt to define basic scaling relationships through comparison of math model, 1/3-scale model and full-scale results.

WIRE BRUSH SKIDS

General.- Skids have been used as landing gear from the first days of aviation, with the most recent adaptation probably being for research aircraft such as the X-15. In most cases use of the skid was dictated, not by any inherent benefit, but as a compromise solution forced by other operating problems (weight, simplicity, thermal protection, stowage volume, etc.). Skid research conducted by NASA in the early sixties (ref. 4) involving studies of many different types of skid materials showed that a skid constructed of wire brushes had a surprisingly good friction-speed relationship compared with flat-plate skids. Revived interest in skids as a drag-producing device led to further studies of the characteristics of wire brush skids at bearing pressures much higher than the 152 kPa (22 psi) of reference 4 since in modern applications the weight and volume of a skid should be as small as possible.

Skid Research Program.- This paper will summarize the results of the skid program described in detail in reference 5, wherein wire brush skids were constructed of 17-7 PH stainless steel spring wire as shown in figure 7. Two different diameter wires and two bundle sizes were employed to explore the effects of wire density, and the instrumented tire test vehicle was adapted as shown in figure 8 to test the skids on several runway surfaces at Wallops Flight Center, at forward speeds up to 80 km/hr (50 mph). Loading on each skid was arranged to give actual ground bearing pressures of 345, 517, and 689 kPa (50, 75, and 100 psi), and measurements were made of developed skid friction and skid wear over sliding distances up to 1585 m (5200 ft). During the test program an attempt was also made to determine the extent of runway surface damage due to skid operations.

A sample of the test results of this program is presented in figure 9 where friction coefficient and wear index as a function of forward speed for one of the skids operating at two bearing pressures on two surfaces is shown. The figure shows that the drag friction coefficient is relatively insensitive to forward speed, but is affected by bearing pressure and by runway surface character. The wear index is seen to increase moderately with bearing pressure, as might be expected, and again a dependency on runway surface character is noted.

In evaluating the utility of a wire brush skid as a drag producer, it should be borne in mind that the drag friction coefficients are constant; that is, they are not constantly cycling as is the case with a braked wheel and tire under anti-skid control. Further, tests showed that the friction coefficient was unaffected by water on the runway. These facts indicate that, for certain applications (and braking for an ACLS comes immediately to mind), a wire brush skid is an extremely attractive alternative braking device and could conceivably replace wheel brakes on a conventional landing gear as used on returning spacecraft.

ACTIVE CONTROL LANDING GEAR

General.- Ground loads imposed on an airplane are important factors in the dynamic loading and hence fatigue damage of the airframe structure, and ground-inducted structural vibrations may also be a source of crew and passenger discomfort. Analytical studies (ref. 6) have determined the feasibility of applying active loads control to the main landing gear to limit the ground loads transmitted to the airframe. As shown in figure 10, the analysis was capable of handling many of the non-linear parameters encountered during ground operations and featured a hydraulic control in series with the main gear oleo-pneumatic strut. The results indicated that significant load reductions were possible using this scheme, and so the analysis was used as a design tool in constructing the hardware necessary to provide an experimental validation of the analytical results.

Basic System Description.- The active control landing gear concept is shown schematically in figure 11 to consist essentially of a modified oleo-pneumatic landing gear strut, an electronic controller, and a hydraulic servo valve. The landing gear strut is modified as shown by an annular, fluid-carrying tube running from the top of the strut to well down into the fluid portion of the strut. This annular tube is connected through the servo-valve to the hydraulic system, with the position of the servo valve spool determining whether high-pressure fluid is added to or removed from the strut. The spool is positioned by the electronic controller (see ref. 7), the heart of the system, which compares the kinetic energy at landing impact (a function of airplane mass and sink rate) with the work capability remaining in the strut (a function of strut stroke and strut hydraulic pressure). When these two energies are equal, a limit force command is generated and the controller acts to position the servo valve spool to maintain this value during the remainder of the impact. During the roll-out phase of the landing, a control bias returns the gear to the design stroke and will tend to maintain this level during ground operation.

Experimental Test Program.- For the experimental program a hand valve was added as shown in figure 11 to permit both conventional (passive) and active landing gear studies to be conducted by isolating the active portion of the system. The landing gear strut was taken from a light twin-engine aircraft, modified as shown in figure 11, and installed on the landing loads track test carriage as shown in figure 12. The fixture included a rigid airframe representation restricted to vertical and pitching motions, and a series of tests was conducted at various forward and sink speeds, and initial pitch attitudes. A sample of preliminary results is shown in figure 13 comparing active and passive landing gear impacts for the conditions shown, where a 19% c.g. force reduction was achieved by the active control system. This reduction was accomplished at the expense of added strut stroke, as shown, but the increased stroke required was much less than half the available stroke.

Similar striking load reductions are possible during the roll-out phase of the landing as shown in figure 14, where c.g. force reduction of 62% is obtained when the landing gear encounters the relatively uneven runway surface shown at the bottom of the figure. Results such as these are extremely encouraging, and the program is going forward with design of modifications necessary to install an active control landing gear on a tactical fighter aircraft.

CONCLUDING REMARKS

This paper has presented a review of three research programs which seek solutions to various landing problems through unconventional systems. The first, and most unconventional, of these is the air cushion landing system (ACLS), where current efforts are concentrated on development of adequate braking and steering systems and an improved understanding of scaling laws and behavior. The second program is concentrated on use of a wire brush skid as a drag producing device, which has been shown to have good friction coefficients and reasonable wear rates at ground bearing pressures up to 689 kPa (100 psi) and forward speeds up to 80 km/hr (50 mph). The third program shows great promise in an active control landing gear where significant load reductions are possible during landing impact and subsequent rollout. Work in this area is continuing with studies concentrated on adaptation of the active control landing gear to a tactical fighter aircraft.

REFERENCES

1. Buzzard, Wallace C.; Perez, David J.; Wyen, Gerald; and Randall, (CAF) John, Maj.: Tests of the Air Cushion Landing System on the XC-8A. AFFDL-TR-78-61, April 1978.

2. Saha, Hrishikesh, Compiler: Air Cushion Landing Systems. Univ. of Tennessee Space Inst., c. 1973.

3. Boghani, A. B.; Captain, K. M.; and Wormley, D. N.: Heave-Pitch-Roll Analysis and Testing of Air Cushion Landing Systems. NASA CR-2917, February 1978.

4. Dreher, Robert C.; and Batterson, Sidney A.: Coefficients of Friction and Wear Characteristics for Skids Made of Various Metals on Concrete, Asphalt, and Lakebed Surfaces. NASA TN D-999, 1962.

5. Dreher, Robert C.: Friction and Wear Characteristics of Wire-Brush Skids. NASA TN D-1495, 1979.

6. McGehee, John R.; and Carden, Huey D.: Analytical Investigation of the Landing Dynamics of a Large Airplane With a Load-Control System in the Main Landing Gear. NASA TP-1555, 1979.

7. Ross, Irving; and Edson, Ralph: An Electronic Control for an Electrohydraulic Active Control Aircraft Landing Gear. NASA CR-3113, 1979.

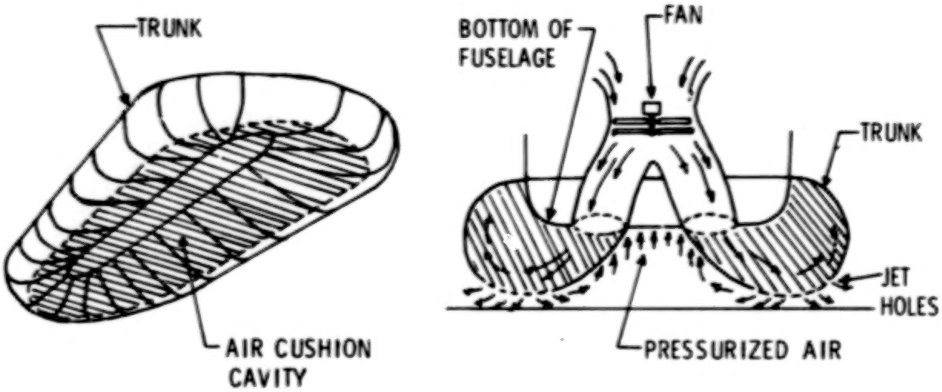
TRUNK
AIR CUSHION CAVITY
BOTTOM OF FUSELAGE
FAN
TRUNK
JET HOLES
PRESSURIZED AIR

Figure 1.- Schematic representation of an air cushion landing system.

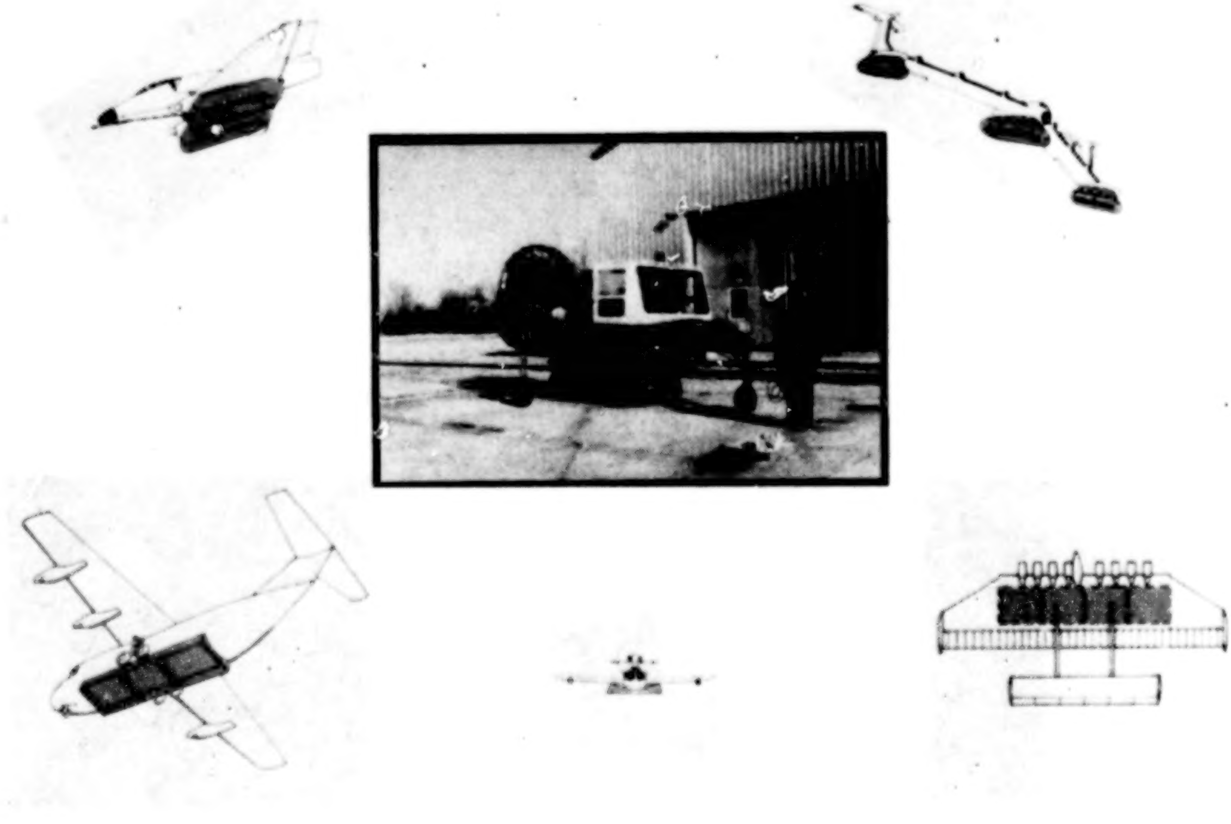

Figure 2.- Some advanced air cushion landing system configurations.

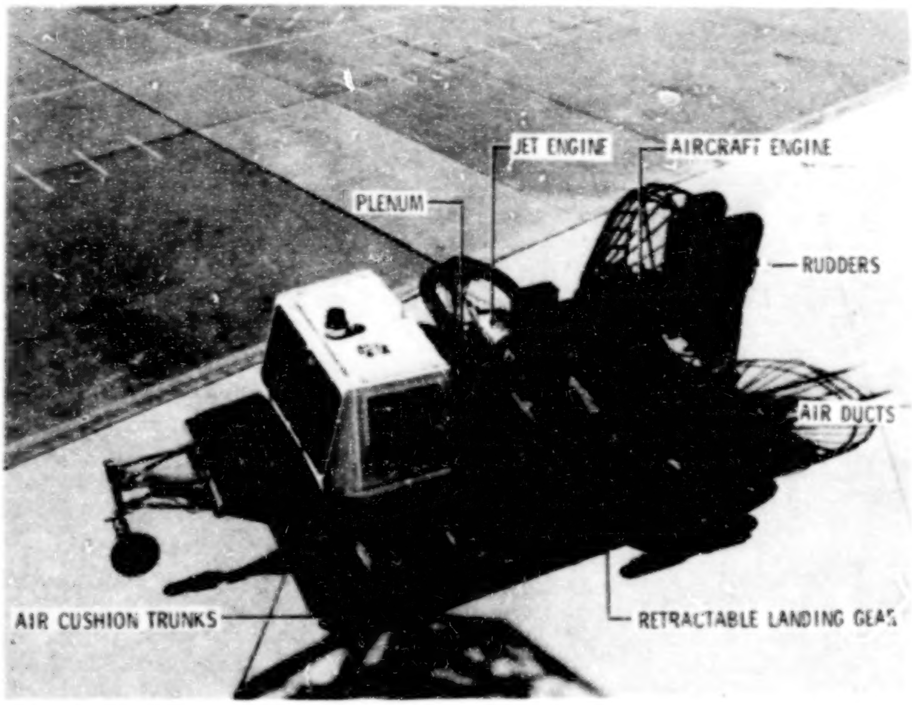
JET ENGINE
AIRCRAFT ENGINE
PLENUM
RUDDERS
AIR DUCTS
AIR CUSHION TRUNKS
RETRACTABLE LANDING GEAR

Figure 3.- Air cushion landing system test vehicle.

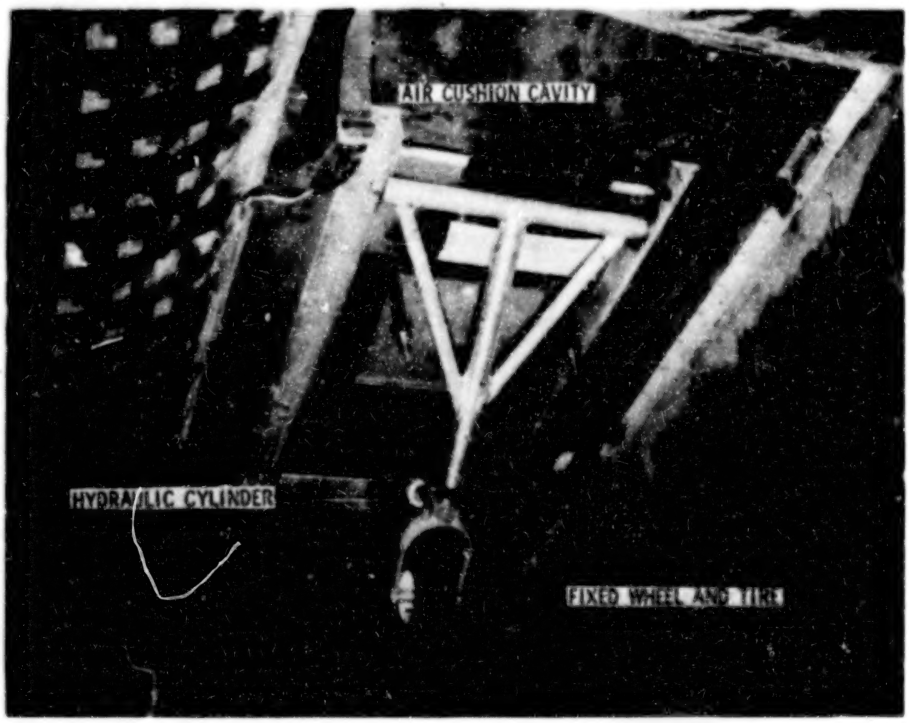
AIR CUSHION CAVITY
HYDRAULIC CYLINDER
FIXED WHEEL AND TIRE

Figure 4.- Auxiliary wheel for ACLS steering.

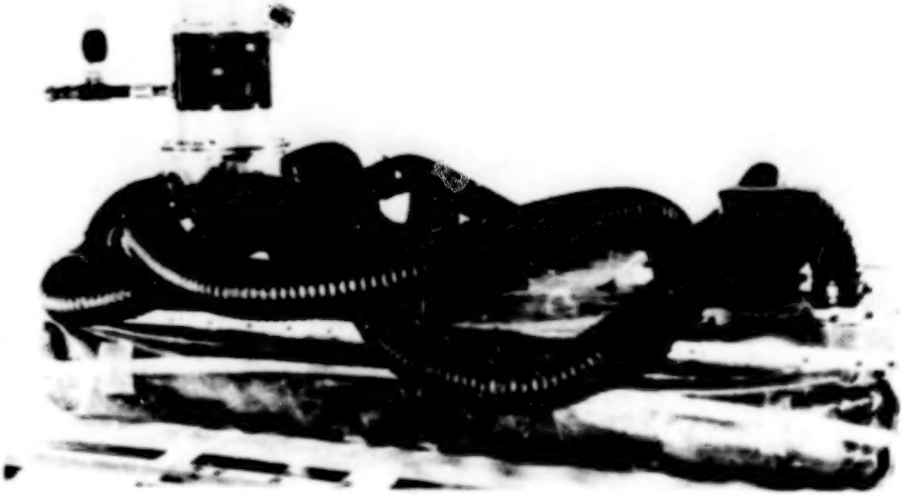

Figure 5.- Photograph of 1/3-scale model ACLS test vehicle.

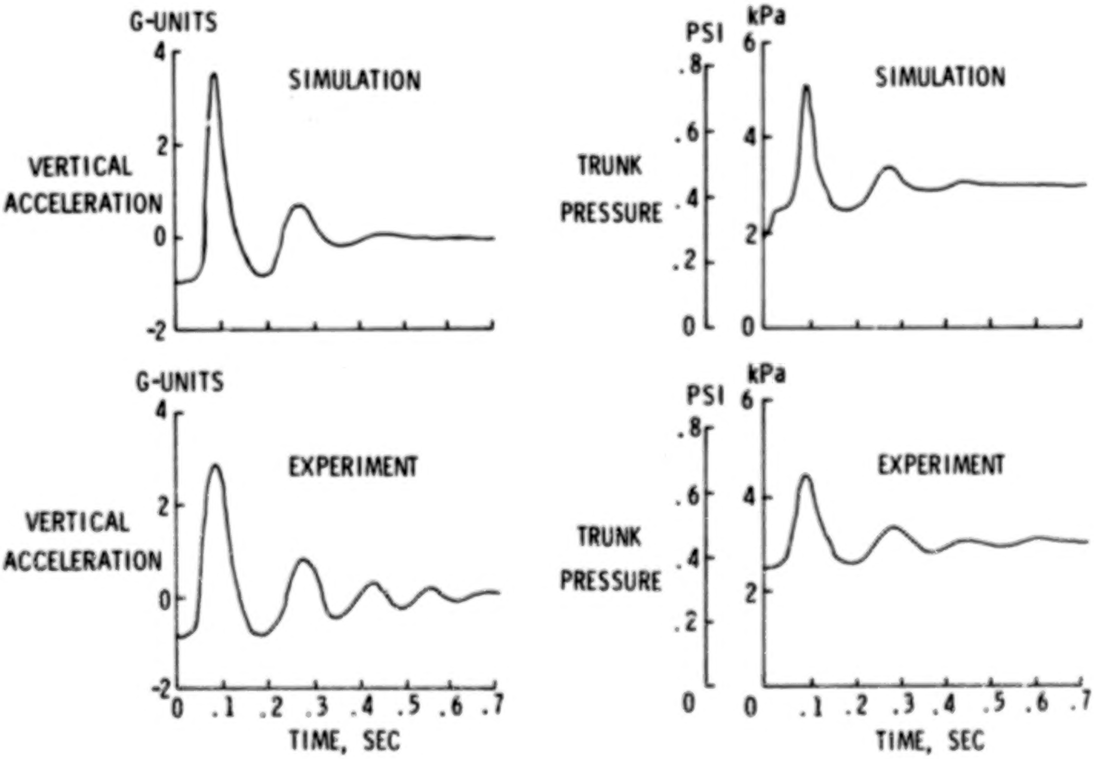

Figure 6.- Comparison of analytical and experimental test results of 1/3-scale model ACLS test vehicle. Static drop height = 15 cm (6 in); pitch attitude = 0^{o}.

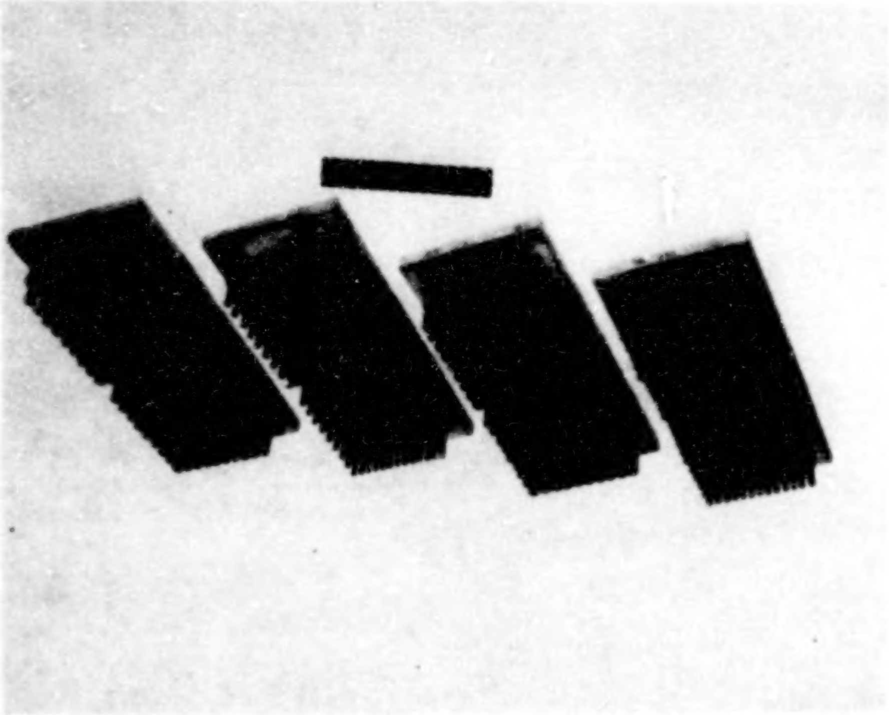

Figure 7.- Wire brush skids used in the research program.

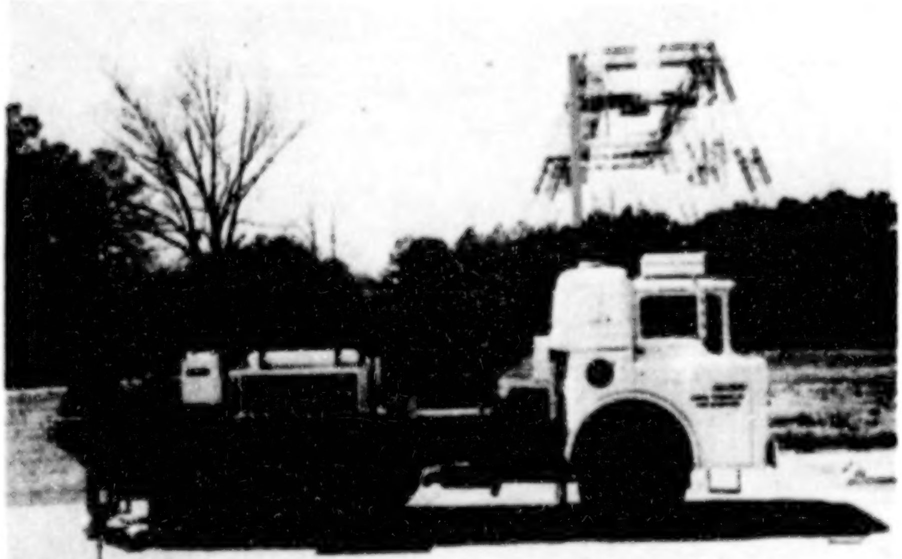
WIRE BRUSH SKID

Figure 8.- Instrumented ground vehicle as used for wire brush skid tests.

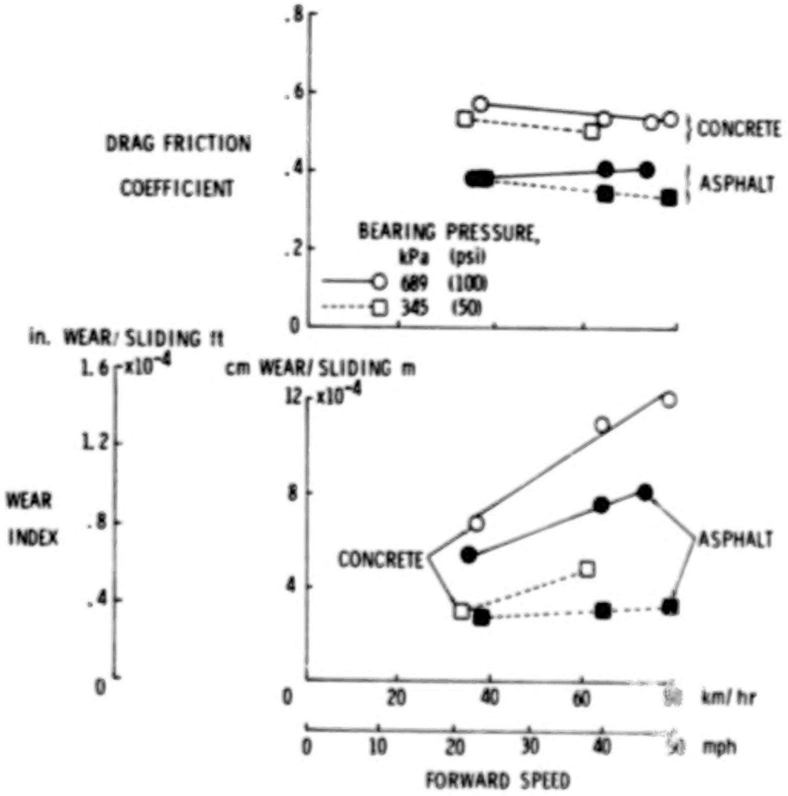

Figure 9.- Drag friction coefficient and wear index for a wire brush skid.

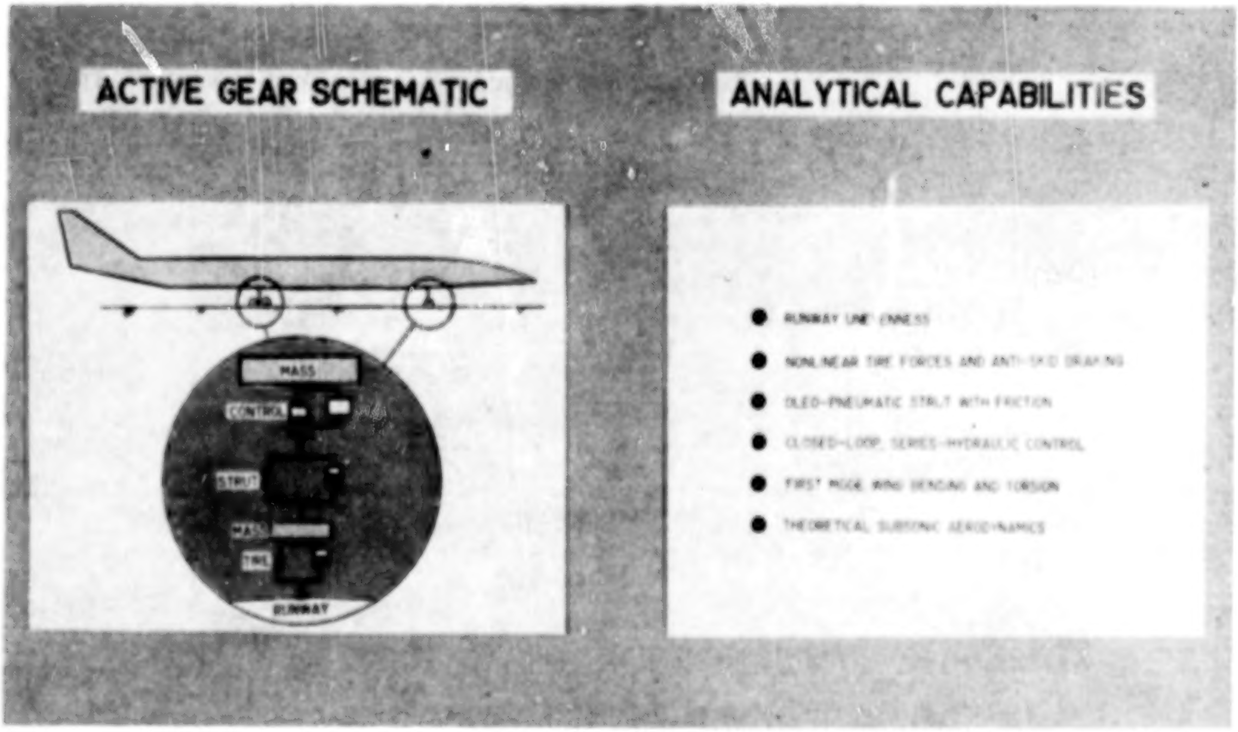

ACTIVE GEAR SCHEMATIC

ANALYTICAL CAPABILITIES

- RUNWAY UNEVENNESS
- NONLINEAR TIRE FORCES AND ANTI-SKID BRAKING
- OLEO-PNEUMATIC STRUT WITH FRICTION
- CLOSED-LOOP, SERIES-HYDRAULIC CONTROL
- FIRST MODE WING BENDING AND TORSION
- THEORETICAL SUBSONIC AERODYNAMICS

Figure 10.- Active control landing gear analysis.

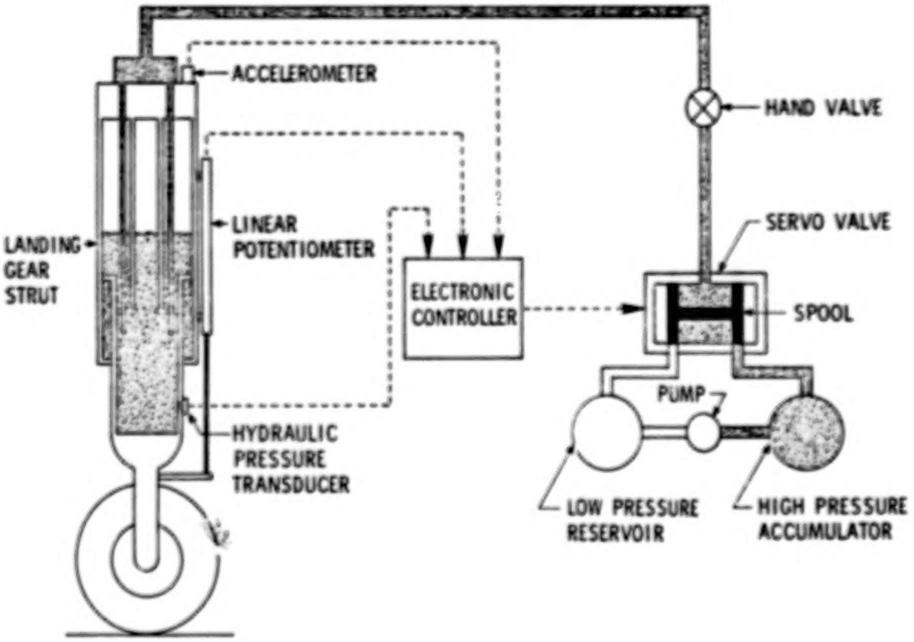
ACCELEROMETER
HAND VALVE
LINEAR POTENTIOMETER
LANDING GEAR STRUT
SERVO VALVE
ELECTRONIC CONTROLLER
SPOOL
PUMP
HYDRAULIC PRESSURE TRANSDUCER
LOW PRESSURE RESERVOIR
HIGH PRESSURE ACCUMULATOR

Figure 11.- Active control landing gear experimental test schematic.

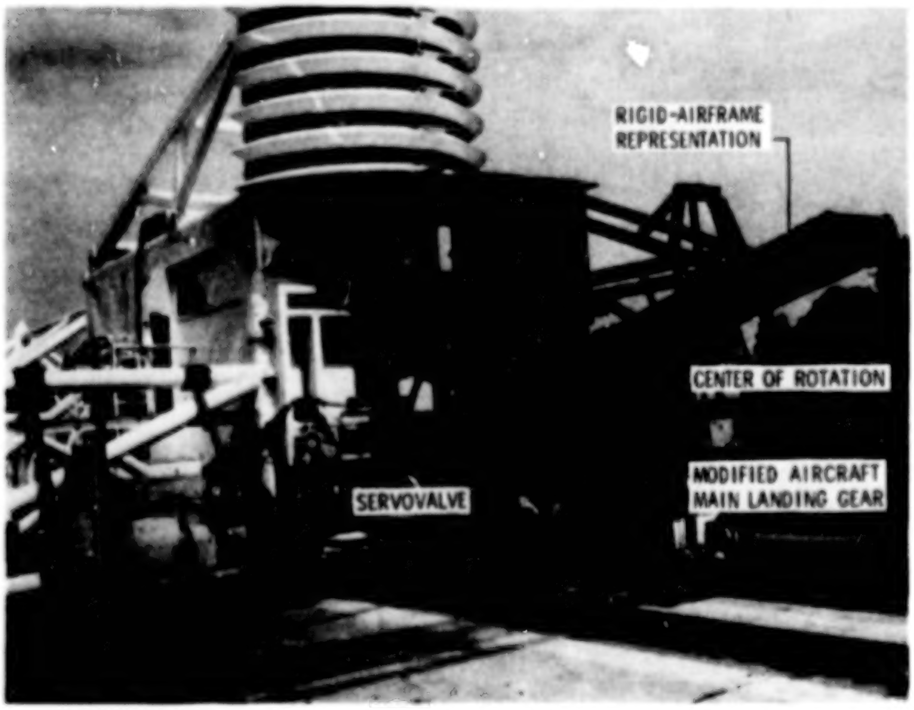
RIGID-AIRFRAME REPRESENTATION
CENTER OF ROTATION
MODIFIED AIRCRAFT MAIN LANDING GEAR
SERVOVALVE

Figure 12.- Active control landing gear installed on test carriage.

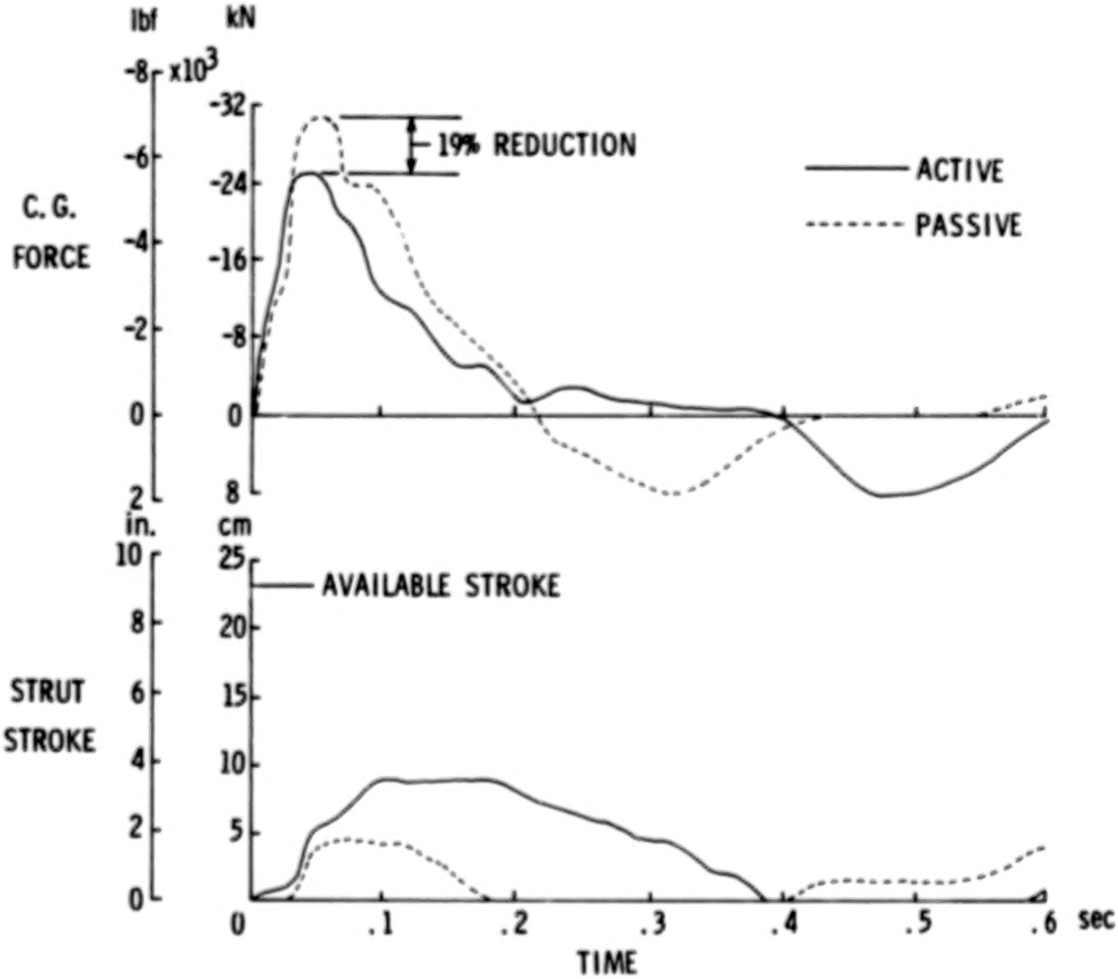

Figure 13.- Comparison of active and passive landing gear impact. Forward velocity = 80 knots; vertical velocity = 1.5 m/sec (5 ft/sec); pitch angle = 13°.

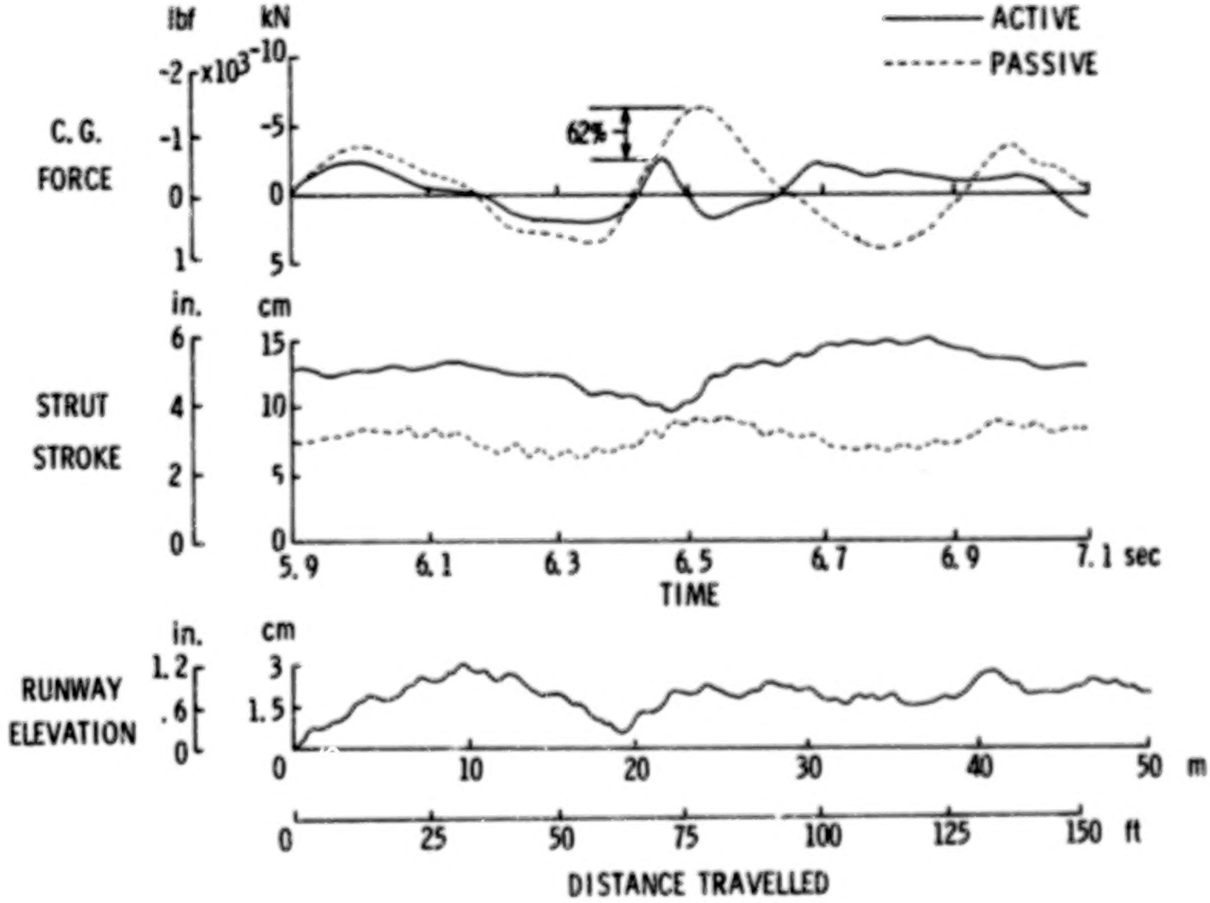

Figure 14.- Comparison of active and passive landing gear rollout. Forward velocity = 75 knots.

RECENT PROGRESS TOWARDS PREDICTING AIRCRAFT GROUND HANDLING PERFORMANCE

Thomas J. Yager and Ellis J. White
Langley Research Center

SUMMARY

The current capability implemented at Langley in simulating aircraft ground handling performance is reviewed and areas for further expansion and improvement are identified. The problem associated with providing necessary simulator input data for adequate modeling of aircraft tire/runway friction behavior is discussed and recent efforts to improve tire/runway friction definition, and hence simulator fidelity, are described. Aircraft braking performance data obtained on several wet runway surfaces are compared to ground vehicle friction measurements and, by use of empirically derived methods, agreement obtained between actual and estimated aircraft braking friction from ground vehicle data is shown. Further research efforts to improve methods of predicting tire friction performance are discussed including use of an instrumented tire test vehicle to expand the tire friction data bank and a study of surface texture measurement techniques. Future development plans directed towards improving the capability and fidelity of the aircraft ground handling simulation program are discussed relative to achieving "total simulation" and providing a valuable research tool for use in solving aircraft ground operational problems.

INTRODUCTION

Flight simulation is as old as powered flight itself if one considers the gliders the Wright brothers built to solve control problems before risking their lives and airplane. Since then we have had a number of simulation devices but it was not until the 1940's that flight simulation provided an electronic equivalent of the airplane, its flight crew input-output cues and indications of all instruments, systems, and flight control units. Over the intervening years, motion cues have been added together with out-of-cockpit visual cues not only to greatly enhance simulation capability, but also to provide impetus for expanded usage of the simulator as a training tool. A 1978 American Airlines survey of 18 scheduled U.S. airlines revealed that more than 70 modern flight simulators were owned and operated for air crew proficiency checks and transition training. Data from this survey also indicated that the annual fuel savings will exceed 380 kL (100 million gal) through the use of flight simulators for recurrent training requirements alone; over 760 kL (200 million gal) of fuel will be saved annually for all simulator applications in lieu of actual airplane flights. In addition to this proven energy conservation and a noticeable increase in quality and effectiveness of crew training, many airlines have identified improved safety in both training and operations as one of the major contributions of the flight simulator.

More recent progress in technology and rapid development of advanced simulator systems have encouraged airline training executives to seriously consider "total simulation" as a near term reality. The Federal Aviation Administration (FAA) has further stimulated this move toward total simulation with a proposed plan involving an incremental program that would lead to providing 100% training in simulators, followed by routine line checks. At present, airline simulator training is supplemented by at least several hours flying in the real thing. It is thus vitally important that simulators reproduce aircraft behavior as accurately as possible and pursuit of total simulation for crew training is generally conceded to require better visual systems and improved, more comprehensive, aircraft data. Significant progress has been achieved in meeting visual system requirements with development of daylight computer-generated image displays; but the paucity of data available for aircraft in ground effect (how an aircraft behaves during the last 90 m (295 ft) or so of a landing approach) and, to a lesser extent, aircraft performance on the ground continues to compromise total simulation fidelity. Flight test programs and research studies using instrumented aircraft have proven helpful in defining airplane braking performance, but because of limitations imposed by safety constraints, rising costs, and the ability to control test parameters, researchers have turned to development of new test techniques, computational methods, and improved simulation capabilities for acquiring complete aircraft ground handling characteristics.

This paper discusses NASA's program effort to expand flight simulator capability to confidently address aircraft ground handling performance, and hence aid in the development of total simulation as well as provide a useful tool for research studies. A description of the development and implementation of Langley's aircraft ground handling simulation facility is given together with an explanation of how the necessary tire/runway friction models were determined. The problems confronting researchers trying to accurately and adequately define the influence of this complex factor on aircraft ground performance are examined, and the need to improve and expand test data sources is identified. The use of empirically derived methods of estimating tire friction capability is explained and recent efforts to improve fidelity and expand usefulness of test methods and procedures to acquire better tire/runway friction models are discussed. The paper concludes with anticipated future developments to improve the simulator capability.

AIRCRAFT GROUND HANDLING SIMULATION FACILITY

Background

The rapid growth of jet-powered, high-performance aircraft usage in the civil and military fleets, coupled with improvements in airport landing aids, has resulted in an increased number of aircraft takeoff and landing operations under adverse weather conditions. Aircraft ground operational safety margins are severely compromised by combinations of such factors as slippery runways, crosswinds, windshears, extended touchdown points, excessive velocity, equipment malfunction, piloting techniques, and reduced visibility. Joint NASA, FAA, and USAF aircraft braking studies (see refs. 1 to 6) have indicated that on many runways, tire traction capability can be significantly degraded in the presence of rain, ice, or other pavement surface contaminants. These studies also provided the stimulus to investigate and improve the equally important directional control aspect of aircraft ground handling performance, particularly under conditions of crosswind and low runway friction. However, safety constraints as well as unpredictability of surface winds preclude full-scale flight testing as a viable means of fully defining aircraft directional control limitations. As a result of this impasse, NASA initiated in 1973 a feasibility study to expand available flight simulation capability to include the complex ground phase of aircraft operations. The feasibility of this approach was verified in a contracted study by McDonnell Aircraft Company using an F-4 fighter aircraft. The implementation of this initial contractor study and the results from piloted validation runs are documented in reference 7 and described in a paper (ref. 8) presented during the 1976 NASA conference on aircraft safety and operating problems.

Subsequent contractor development and expansion efforts, reported in references 9 and 10, resulted in validating a DC-9 aircraft ground handling simulation program in 1977. This simulation program has been implemented at Langley, using existing simulation equipment and computer facilities, and verified through piloted evaluation runs and agreement with available aircraft test data. Aircraft landings, ground maneuvers, takeoffs, and aborted takeoffs have been simulated and the effects of many parameters on aircraft ground performance are being studied, including crosswinds, runway roughness and friction levels, reverse thrust, and antiskid brake system operation. Although development of an adequate simulation of the ground phase of aircraft operations is an essential step in achieving total aircraft simulation, NASA Langley's primary interest is in using this expanded simulator capability as a research tool for study and solution of aircraft ground operational problems.

Motion Base Simulator

The motion simulation is provided to a general-purpose cockpit (adapted to represent a DC-9 aircraft) by a six-degree-of-freedom synergistic motion base as shown in figure 1. The six-axis motion is provided by six hydraulic jacks arranged in a configuration developed by the Franklin Institute, with the performance limits listed as follows:

Degree of Freedom	Position		Velocity	Acceleration
Horizontal X	Forward	1.245 m	±0.610 m/sec	±0.6g
	Aft	1.219 m		
Lateral Y	Left	1.219 m	±0.610 m/sec	±0.6g
	Right	1.219 m		
Vertical Z	Up	0.991 m	±0.610 m/sec	±0.6g
	Down	0.762 m		
Yaw ψ	$\pm 32^0$		$\pm 15^0/\text{sec}$	$\pm 50^0/\text{sec}^2$
Pitch θ	$+30^0$ -20^0		$\pm 15^0/\text{sec}$	$\pm 50^0/\text{sec}^2$
Roll ϕ	$\pm 22^0$		$\pm 15^0/\text{sec}$	$\pm 50^0/\text{sec}^2$

The base does not have independent drive systems for each degree of freedom, but achieves motion in all degrees of freedom by a combination of actuator extensions. Software is provided for the actuator extension, inverse transformation, the centroid transformation, and the washout algorithm necessary to return the base to the neutral point once the onset motion cues have been commanded. The washout algorithm is a Langley adapted version (ref. 11) of Schmidt and Conrad's coordinated washout circuitry, with the parameters modified slightly for ground handling. Figure 2 shows the interior of the cockpit with seats provided for the pilot and first officer or observer. The visual display is provided to both seats. Instruments showing airspeed, attitude, glide slope deviation, heading, localizer deviation, altitude, and vertical speed are active for the pilot. The column, wheel, and rudder pedals furnish primary flight inputs to the computer. Throttles with reverse thrust, flap control, and manual or automatic spoilers are available. Engine pressure ratio instruments, reverse thrust bucket indicator lights, and other instrumentation are available.

Visual Landing Display System

The visual landing display system (VLDS) is a camera/model board system designed to generate a six-degree-of-freedom, visual, out-the-window scene for the pilot of a simulated aircraft. The system shown in figure 3 consists of an 18.3x7.3 m (60x24 ft) dual-scaled terrain model, a lamp bank to illuminate the model, a three-degree-of-freedom translation motion system to position the camera, and a three-degree-of-freedom optical/rotational system mated to a color television camera. The terrain model contains two airports sufficiently separated to facilitate a scale factor of 1500:1 at the three-runway airport layout and a scale factor of 750:1 at the two-runway and heliport airport layout. With the minimum camera "look-point" height of the optical probe limited to 0.178 cm (0.070 in.), which equates to 2.74 m (9 ft) at 1500:1 or 1.37 m (4.5 ft) at 750:1, the dual scale provides the capability of simulating both large and small aircraft during landings, ground maneuvers, and takeoffs. The two long runways at the larger airport represent runways which are 3505 m (11 500 ft) in length and 81 m (267 ft) in width, and it is on these two runways that piloted test runs are conducted in the DC-9 aircraft ground handling program. The visual scene, displayed to the pilot by the color television camera signals transmitted to an external cockpit cathode ray tube screen, provides a horizontal and vertical field of view of 48 and 36 degrees, respectively. Figure 3 also shows a typical scene presented to the simulator pilot during approach for landing. Options available for the visual scene display include daytime, dusk, or nighttime conditions as well as limited visibility. Reference 12 contains additional information about the equipment, operation and performance of the Langley VLDS.

Computer Program Capability and Characteristics

The simulation was implemented at Langley as shown in figure 4. The six-degree-of-freedom equations of motion representing the airframe, the aerodynamic and control system, the engines, the environment, landing gear and brake system, and auxiliary equations are all computed on a CDC Cyber 175 computer. The Cyber computer also provides computations for the VLDS drive signals and the motion base washout and drive equations, as well as all cockpit instrument signals. The computer is interfaced with the VLDS, the motion base, and cockpit as shown in the figure. The loop is closed by the pilot providing the control deflections and thrust settings from the cockpit back to the computer.

The implementation of the model on the computer requires approximately 132 000 octal locations of memory and approximately 45% of the available control processor unit (CPU) time. Since the range of the mission is large (an aircraft during landing approach through a complete stop on the ground), and the ground model is complex and extensive (composed of full strut and tire dynamics for individual landing gears as well as a variety of runway slipperiness ranges), some special programing techniques were required. The landing gear dynamics are characterized by a set of lightly damped, high frequency, differential equations. To maintain stability of these solutions in a real-time environment with a reasonable number of iterations/sec to hold down CPU time without compromising the landing gear behavior, a local linearization integration algorithm (ref. 13) was used. The second order Adams-Bashforth algorithm was used for all other equations and the iteration rate for the whole model was 32/sec. Other special implementation techniques were required to accommodate the aircraft reaching zero velocity, crosswind effects on aircraft at zero forward velocity, trimming the aircraft at zero velocity, and a piloting technique of holding "brakes-on" during thrust buildup for takeoff while waiting at the end of the runway.

Validation of ground handling simulators in general is hampered to some degree by lack of flight data, although data does exist for stopping distances and lateral deviations from the centerline of the runway under various conditions. Table I summarizes the extent of the validation effort completed at Langley in the simulation program. The quantity of solutions in different categories and whether they were quantitative (compared to measurable data) or qualitative (subjective opinion from pilot or researchers) are shown. Also indicated is the source of comparison data for each category, whether it be actual flight data or Douglas Aircraft Co. (DAC) simulator results. The first three categories of solutions, longitudinal trim, longitudinal dynamic damping, and lateral direction damping, were "in-flight" checks. The remaining four categories, three of which were piloted, were for validation on the ground. The last category of selected piloted cases covered the majority of runway friction variations, wind conditions, and aircraft ground maneuvers. The results of the Langley validation checks compared favorably with the flight data and the DAC simulation results.

Simulation Models

The aircraft system, which must be defined mathematically and programmed in the computer to provide the simulation capability, consists of five principal models: aerodynamics, engines, landing gear, antiskid brake system, and tire/runway friction. A mathematical description of the aircraft motion is formed by establishing a fixed reference plane representing the earth and equations are written to define the displacements, velocities, and accelerations of the aircraft. The principal force inputs to these equations of motion come from gravity and the aircraft aerodynamics, engines, and landing gear. This aircraft force data, derived from both wind tunnel and flight test data, is compiled in a form suitable for use with the equations of motion. The complete DC-9 airframe mathematical model, based on a combination of these equations of motion with mathematical representations of aircraft control and guidance systems, wind and turbulence, runway roughness, and other pertinent elements, was provided by Douglas Aircraft Company, under contract to Langley, and documented in reference 14. This reference also describes how the digital antiskid brake system performance was derived and modeled from both NASA track test data reported in reference 15 and flight test data documented in reference 5.

Of all the mathematical models developed to implement the aircraft ground handling simulation program, the environmentally sensitive tire/runway friction modeling proved to be the most challenging to define. Available data sources from various flight test studies and track test investigations (see refs. 1 to 6 and 16 to 18) were found insufficient to completely determine the aircraft ground operation envelope of braking and cornering friction performance for the range of runway contamination conditions desired in the simulation. As a result of this lack of experimental data, NASA assisted the contractor in obtaining the desired friction models using analytical methods based on empirically derived tire friction relationships discussed in references 19 and 20. The tire friction curves (see ref. 14) generated from this mix of analytical and experimental test data described the unbraked cornering force friction coefficient variation with yaw angle for both main and nose gear tires, and the combined cornering and braking friction coefficient variation with yaw angle and slip ratio for the main gear tires at ground speeds from 0 to 150 knots on a variety of runway contamination conditions.

The runway conditions simulated by these tire friction curves included continuous dry, wet, flooded, or icy pavements. Combinations of these conditions, described by the term "patchy", were also modeled to expose the aircraft main gear tires to simulated symmetrical and unsymmetrical variations in friction while traveling down the runway. In general, the 15 line and test pilots that have flown the simulation during checkout, validation, demonstration, and parameter evaluation runs have been favorably impressed with the simulated aircraft ground handling performance but several areas related to the tire/runway friction model have been identified for improvement (see ref. 10). Consequently, NASA has initiated efforts involving new equipment and test techniques directed toward acquiring additional data necessary to enhance the fidelity of the tire/runway friction model and concurrently, to refine and improve the empirically derived methods used for estimating tire friction performance.

SOME RECENT EFFORTS TO IMPROVE TIRE/RUNWAY FRICTION DEFINITION

An adequate ground handling simulation for a particular aircraft type depends substantially on how accurately the tire friction envelope, including free rolling, braking, cornering, and combinations thereof, is defined for meeting demands imposed during ground operations under a wide variety of loading, speed, and environmental conditions. Determination of aircraft tire friction performance, however, is difficult at best considering the varied influence of both tire and runway surface characteristics and the effects of aircraft landing gear geometry and brake system performance. Review of test results from previous studies (including refs. 1-6, 8, 15-19, 21-23) has provided researchers with sufficient friction data on a large number of different-sized pneumatic tires to permit determination of empirically derived equations and relationships for use in estimating a particular tire friction performance. Figure 5 indicates in block diagram form how this methodology is used to transform tire friction-speed gradient data obtained experimentally in one operational mode (e.g. ground vehicle, locked-wheel tire friction) into estimated aircraft tire locked-wheel skidding (μ_{skid}), maximum (μ_{max}), and side (μ_{side}) friction coefficient variations with speed for different surface conditions and tire yaw angles. Using an antiskid brake system efficiency term (η), the estimated aircraft tire effective braking friction coefficient (μ_{eff}) variation with speed can be determined from the derived maximum friction values. Details of the procedures and equations currently used in this methodology are given in reference 20. Further refinements and improvements of these methods are planned based on results obtained from several ongoing tire friction studies (see ref. 24) and antiskid brake system evaluations (see ref. 25) conducted at the Langley Landing-Loads Track, in addition to the aircraft/ground vehicle tests and surface texture measurement study discussed in the following sections.

Aircraft/Ground Vehicle Friction Measurements

A joint NASA/FAA runway friction program was initiated in 1978 with several major objectives: (1) to establish a safe and reliable instrumented aircraft test technique for evaluating runway friction; (2) to obtain comparative friction data with old and new technology ground vehicle friction measurement systems; and (3) to determine the degree of correlation between different ground vehicle friction measurements and between ground vehicle and aircraft friction readings. The aircraft and the three ground vehicles selected for testing in this program are shown in figure 6. The FAA Sabreliner-80 aircraft is a swept-wing, twin-engined jet airplane equipped with antiskid brake units on the dual main landing gear wheels. A portable accelerometer package coupled to an analog tape recorder was installed in the aircraft to provide continuous time history records of aircraft deceleration during maximum-braking test runs. The mu-meter is a British-developed side-force measuring trailer which was towed with a light truck. The two friction-measuring tires are operated at a 7.5° toe-out angle and the third (rear central) wheel drives a chart recorder for monitoring the variation in side force friction during test runs. The diagonal-braked vehicle (DBV) friction measuring system was developed by NASA to safely obtain locked-wheel friction data at high speeds using smooth ASTM E524 tires on the braked, diagonal pair of wheels. An on-board oscillograph recorder provides time histories of several test parameters including vehicle ground speed, stopping distance, and longitudinal deceleration during braking. Additional details concerning the mu-meter and the DBV are given in references 3, 4, and 5. The friction tester vehicle is a relatively new friction measuring device, and is equipped with front wheel drive and a hydraulically retractable measuring wheel installed behind the rear axle. The measuring wheel, which is designed to operate at a constant 15 percent braking slip ratio, is connected to the axle of the free rolling rear wheels by a chain transmission. The forces acting on this measuring wheel and the distance traveled are fed into a digital computer where the information is converted into friction coefficient form and location on the runway. Friction tests with this device can be conducted at speeds up to 161 km/hr (100 mph) and an on-board wetting system is available for obtaining wet surface friction data.

The NASA Wallops Flight Center was chosen as the test site because of the variety of grooved and ungrooved runway surfaces and the large data bank compiled from other aircraft braking performance tests (see refs. 1 to 5). A series of instrumented aircraft braking runs were made on each surface under dry and artificially wet conditions. Since many of the test surfaces were only 107 m (350 ft) long, several runs were required to obtain friction measurements over the desired speed range. A large water tank truck, equipped with a wide dispersal nozzle, was used to wet the surface before each series of tests. In order to minimize the effects of time-related changes in surface wetness conditions, the time of ground vehicle measurements taken before and after each aircraft test run was noted and later the measurements were corrected, by linear interpolation, to the time of the aircraft test run. These corrected ground vehicle friction measurements reflect the same runway slipperiness condition as encountered by the aircraft.

Table II provides a compilation of the friction readings obtained at speeds of 17, 35, and 52 knots with the test aircraft and the three ground vehicles under artificially wetted conditions on all five types of runway surfaces. Since the friction data obtained with each test vehicle on the two concrete and two asphalt transversely grooved surfaces did not differ significantly, all the grooved surface friction data were faired to determine average friction values at each speed increment. Agreement in ranking the surfaces was obtained by the four test vehicles despite significant differences in the type of friction coefficient measured by the aircraft and each ground vehicle. Friction readings on the well-textured, damp, slurry-seal asphalt surface were the highest (ranking of 1) whereas the poorly textured, wet, canvas belt-finished concrete surface produced the lowest (ranking of 5) friction readings for all vehicles. Friction readings on the grooved surfaces were somewhat less than that measured on the slurry-seal asphalt because of the influence of several isolated puddles which were observed on the grooved surfaces after artificial wetting.

A further comparison of the aircraft and ground vehicle friction measurements obtained on each of these fives types of surfaces with artificial wetting is given in figure 7. The faired friction-speed gradient curves indicate the wide range of friction values determined from the aircraft and ground vehicle tests. The significant differences in the aircraft and ground vehicle tire characteristics, operating test modes, and braking system operations contributed to this friction data dispersion. Further evidence of the effect of tire characteristics is shown by the difference in the friction tester data obtained using both a high pressure, 3-groove tire and a low pressure, patterned tread tire. The data curves in figure 7 also illustrate the complexity of the problem faced in relating ground vehicle friction measurements obtained in one tire operational mode (e.g., locked wheel μ_{skid}) with that developed by an aircraft equipped with an antiskid brake system.

Calculations were made, however, to estimate the effective Sabreliner-80 aircraft braking friction coefficient variation with speed based on the friction measurements obtained by each ground vehicle and using the empirically derived methods discussed earlier in this paper. In general, the actual aircraft braking performance and that estimated from the ground vehicle friction measurements are shown in figure 8 to be in relatively good agreement on each of the five different test surfaces. The friction tester device shows great promise in providing runway friction measurements for use in estimating aircraft friction performance. Further evaluation of the test tires used by each ground vehicle is in progress using an instrumented tire test vehicle (truck), and test results may justify some modifications in the transformation relationships to provide closer agreement with the aircraft friction measurements.

Instrumented Tire Test Vehicle Friction Evaluations

The main features of the instrumented tire test vehicle (ITTV) used in previous tire friction and wear studies (see ref. 26) are identified in figure 9. Vertical load on the test tire up to 22.2 kN (5000 lb) is applied by means of two pneumatic cylinders and this load, together with the drag and side loads developed on the tire during test runs, is measured by strain gage beams centered about the wheel and mounted above the wheel-axle support structure. Continuous time histories of the output from these strain gages are recorded on an oscillograph mounted in the vehicle cab compartment. A pneumatic system to lower or raise the test tire from the surface is controlled in the cab compartment by the vehicle operator. Simulated tire braking at fixed slip ratios is accomplished by driving the test wheel with an adjustable steel shaft connected through a universal coupling (see fig. 9(b)) to interchangeable sprocket gears, which in turn, are chain driven by a sprocket replacing one left rear driving wheel of the vehicle. Changing the slip ratio involves replacement of the sprocket gear positioned at the driving end of the universal coupling. For locked-wheel braking tests, the universal shaft and coupling are removed and a mechanical locking device is installed on the test wheel axle to prevent wheel rotation. For yawed rolling tire tests, the test fixture is rotated manually to the preselected angle and locked in place. The output from the instrumented trailing wheel, providing an accurate measurement of vehicle speed and distance, and a cam-operated microswitch mounted on the test wheel axle, transmitting a signal for each test wheel revolution, is recorded on the oscillograph as well as displayed to the vehicle operator on digital counters in the cab compartment.

Braking and cornering tests have been conducted on several different runway surfaces at NASA Wallops Flight Center using the ITTV equipped with the bias-belted ASTM E501 and E524 test tires used on skiddometer trailers and diagonal-braked vehicles. The E501 tire has a 6-groove rib-tread pattern and the E524 tire has no tread (smooth) pattern. Wet surface tire braking results from these tests indicated that throughout the speed range evaluated, the rib-tread E501 tire developed higher friction compared to the smooth E524 tire. Figure 10 shows similar results that were obtained on an asphalt and a concrete surface at a test track in San Angelo, Texas using a skiddometer trailer device equipped with an on-board wetting system. Several locked-wheel friction (μ_{skid}) measurements were taken at each of six speed increments up to 97 km/hr (60 mph) and the data points shown in the figure indicate numerical averages of the μ_{skid} values obtained at each speed. In general, the locked-wheel friction developed by both tires on the two wet surfaces decreased with increasing speed as expected (see ref. 22) but the higher friction levels developed on the asphalt surface are contrary to previously noted trends of higher friction with higher surface texture depths. Measurements of surface macro-texture depth using the silicone putty sample technique described in reference 27 indicate the asphalt surface has considerably less macro-texture than the concrete surface. Apparently surface micro-texture characteristics as well as aggregate shape and surface finish treatment must significantly contribute to the ability of the test tires to develop friction forces on the wet surfaces.

Surface Texture Measurement Study

It has long been recognized that the friction forces which a pneumatic tire can develop for the purposes of braking, cornering, or driving are greatly influenced by the finish of the runway or road surface. Many different volumetric, profile, topography, and drainage techniques (see ref. 27) have been developed by reseachers to provide quantitative measurements of surface macro-texture (large scale) and to a lesser degree of success, surface micro-texture (small scale). Results from previous tire friction evaluations (e.g., see ref. 28) have indicated that the slope and the magnitude of the friction-speed gradient curve are functions of the surface macro- and micro-texture features, respectively.

A study of surface texture measurement techniques was recently started to determine the correlation between values obtained with several different techniques and to further define the relationship of these measurements with tire friction performance. Figure 11 shows an example of the correlation established between surface macro-texture depth values measured on a variety of concrete and asphalt pavements using the grease sample and sandpatch methods. Both techniques (see photographs in fig. 11) involved spreading a known volume of material (grease or sand) over the surface, measuring the area covered, and calculating an average texture depth. The data points shown in the figure represent average values determined from six measurements on a given surface with each method and the correlation equation was calculated using a least squares linear data fit. The grease sample technique results in a lower (approximately half) texture depth value than that measured by the sandpatch method, probably because of the manner in which the two materials are applied to the surface. The sand is spread by a lightly loaded, hard rubber disc which makes contact with only the high points in the pavement aggregate, whereas the grease is spread by a relatively soft rubber squeegee with a force that tends to wipe the high pavement peaks and fill the voids. Factors influencing this correlation are currently being evaluated, together with several other techniques including static drainage measurements obtained with outflowmeters.

An outflowmeter consists of a transparent cylinder with a rubber ring attached to the bottom face. When placed on a pavement surface, the cylinder is loaded so that the rubber ring will drape over the aggregate particles in a manner similar to that expected of tire tread elements. Water is poured into the open-topped cylinder, and the operator initiates water discharge by raising a rubber stopper at the bottom of the cylinder. The time required for a known volume of water to escape through any pores or channels in the pavement, as well as between the rubber ring and the pavement surface, is then measured. Short drainage times (high rates of flow) are thus associated with high surface macro-textures. The wide variation in outflowmeter water drainage times shown in figure 12 indicates the effect of various surface finishes and treatments on a surface macro-texture. These drainage measurements were taken on a canvas belt-finished concrete runway which was constructed level, both longitudinally and transversely, at NASA Wallops Flight Center. The runway centerline paint markings significantly reduced the ungrooved surface macro-texture (as indicated by the long drainage times) and the saw-cut grooving greatly improved the surface drainage rates. The outflowmeter drainage time measured on the 51 mm (2 in.) spaced groove pattern was approximately twice as long as that measured on the 25 mm (1 in.) spaced groove pattern. The drainage time differences shown between the two groove patterns may be partially due to the placement of the outflowmeter with respect to the groove configuration since the water discharge opening is only 51 mm (2.0 in.) in diameter.

CONCLUDING REMARKS

The significant progress which has been achieved in development of aircraft ground handling simulation capability at Langley is reviewed with additional improvements in software modeling identified. The problem associated with providing necessary simulator input data for adequate modeling of aircraft tire/runway friction behavior is discussed and recent efforts to improve this complex model, and hence simulator fidelity, are described. Aircraft braking performance data obtained on several wet runway surfaces is compared to ground vehicle friction measurements and, by use of empirically derived methods, good agreement between actual and estimated aircraft braking friction from ground vehicle data is shown. The performance of a relatively new friction measuring device, the friction tester, showed great promise in providing data applicable to aircraft friction performance. Additional research efforts to improve methods of predicting tire friction performance are discussed including use of an instrumented tire test vehicle to expand the tire friction data bank and a study of surface texture measurement techniques.

Future plans for the aircraft ground handling simulation program include development of a tire failure model and better antiskid brake system performance through test track investigations. Although attaining the capability to adequately simulate the ground phase of aircraft operations is an essential step in achieving total aircraft simulation, NASA Langley's primary interest is in using this expanded simulator capability as a research tool for study and solution of aircraft ground operational problems.

REFERENCES

1. Yager, Thomas J.: Comparative Braking Performance of Various Aircraft on Grooved and Ungrooved Pavements at the Landing Research Runway, NASA Wallops Flight Center. Pavement Grooving and Traction Studies, NASA SP-5073, 1969, pp. 35-65.

2. Joyner, Upshur T.; Phillips, W. Pelham; and Yager, Thomas J.: Recent Studies on Effects of Runway Grooving on Airplane Operations. AIAA Paper No. 69-773, July 1969.

3. Yager, Thomas J.; Phillips, W. Pelham; Horne, Walter B.; and Sparks, Howard C. (appendix D by R. W. Sugg): A Comparison of Aircraft and Ground Vehicle Stopping Performance on Dry, Wet, Flooded, Slush-, Snow-, and Ice-Covered Runways. NASA TN D-6098, 1970.

4. Horne, Walter B.; Yager, Thomas J.; Sleeper, Robert K. (LRC); and Merritt, Leslie R. (FAA): Preliminary Test Results of the Joint FAA-USAF-NASA Runway Research Program, Part I - Traction Measurements of Several Runways Under Wet and Dry Conditions with a Boeing 727, a Diagonal-Braked Vehicle, and a Mu-Meter. NASA TM X-73909, 1977.

5. Horne, Walter B.; Yager, Thomas J.; Sleeper, Robert K.; Smith, Eunice G. (LRC); Merritt, Leslie R. (FAA): Preliminary Tests Results of the Joint FAA-USAF-NASA Runway Research Program, Part II - Traction Measurements of Several Runways Under Wet, Snow-Covered, and Dry Conditions with a Douglas DC-9, a Diagonal-Braked Vehicle, and a Mu-Meter. NASA TM X-73910, 1977.

6. Merritt, Leslie R.: Concorde Landing Requirement Evaluation Tests. Report No. FAA-FS-160-74-2, 1974.

7. Anon.: Expansion of Flight Simulator Capability for Study and Solution of Aircraft Directional Control Problems on Runways - Phase I. NASA CR-145084, March 1975.

8. Stubbs, Sandy M.; and Tanner, John A.: Status of Recent Aircraft Braking and Cornering Research. Aircraft Safety and Operating Problems, NASA SP-416, 1976, pp. 257-269.

9. Anon.: Expansion of Flight Simulator Capability for Study and Solution of Aircraft Directional Control Problems on Runways - Phase II. NASA CR-145044, August 1976.

10. Kibbee, G. W.: Expansion of Flight Simulator Capability for Study and Solution of Aircraft Directional Control Problems on Runways. NASA CR-2970, April 1978.

11. Parrish, Russell V.; Dieudonne, James E.; and Martin, Dennis J., Jr.: Motion Software for a Synergistic Six-Degree-of-Freedom Motion Base. NASA TN D-7350, 1973.

12. Rollins, John D.: Description and Performance of the Langley Visual Landing Display System. NASA TM-78742, 1978.

13. Barker, Lawrence E.; Bowles, Roland L.; and Williams, Louise H.: Development and Application of a Local Linearization Algorithm for the Integration of Quaterion Rate Equations in Real-Time Flight Simulation Problems. NASA TN D-7347, 1973.

14. McGowan, J. A.: Expansion of Flight Simulator Capability for Study and Solution of Aircraft Directional Control Problems on Runways - Appendixes. NASA CR-145281, January 1978.

15. Stubbs, Sandy M.; and Tanner, John A.: Behavior of Aircraft Antiskid Braking Systems on Dry and Wet Runway Surfaces - A Velocity-Rate-Controlled, Pressure-Bias-Modulated System. NASA TN D-8332, 1976.

16. Byrdsong, Thomas A.: Experimental Investigation of the Directional Control Capability of 18x5.5, Type VII, Aircraft Tires on Wet Surfaces. NASA TN D-6202, 1971.

17. Dreher, Robert C.; and Tanner, John A.: Experimental Investigation of Braking and Cornering Characteristics of 30x11.5-14.5, Type VII, Aircraft Tires with Different Tread Patterns. NASA TN D-7743, 1974.

18. Horne, Walter B.; Yager, Thomas J.; and Taylor, Glenn R.: Review of Causes and Alleviation of Low Tire Traction on Wet Runways. NASA TN D-4406, 1968.

19. Smiley, Robert F.; and Horne, Walter B.: Mechanical Properties of Pneumatic Tires with Special Reference to Modern Aircraft Tires. NASA TR R-64, 1960. (Supersedes NACA TN 4110).

20. Horne, Walter B.: Status of Runway Slipperiness Research. Aircraft Safety and Operating Problems, NASA SP-416, 1976, pp. 191-245.

21. Horne, Walter B.; and Dreher, Robert C.: Phenomena of Pneumatic Tire Hydroplaning. NASA TN D-2056, 1963.

22. Leland, Trafford J. W.; Yager, Thomas J.; and Joyner, Upshur T.: Effects of Pavement Texture on Wet-Runway Braking Performance. NASA TN D-4323, 1968.

23. Yager, Thomas J.; and Dreher, Robert C.: Traction Characteristics of a 30x11.5-14.5, Type VII, Aircraft Tire on Dry, Wet, and Flooded Surfaces. NASA TM X-72805, 1976.

24. Tanner, John A.; McCarty, John L.; and Clark, S. K.: Current Research in Aircraft Tire Design and Performance. 1980 Aircraft Safety and Operating Problems. NASA CP-2170, 1981. (Paper 30 of this compilation.)

25. Stubbs, Sandy M.; and Tanner, John A.: Review of Antiskid and Brake Dynamics Research. 1980 Aircraft Safety and Operating Problems. NASA CP-2170, 1981. (Paper 31 of this compilation.)

26. McCarty, John L.; Yager, Thomas J.; and Riccitiello, S. R.: Wear, Friction, and Temperature Characteristics of an Aircraft Tire Undergoing Braking and Cornering. NASA TP 1569, 1979.

27. Rose, J. G.; Hutchinson, J. W.; and Gallaway, B. M.: Summary and Analysis of the Attributes of Methods of Surface Texture Measurement. Skid Resistance of Highway Pavements, ASTM STP 530, American Society for Testing and Materials, 1973, pp. 60-77.

28. Horne, W. B.; and Joyner, U. T.: Traction of Pneumatic Tires on Wet Runways. Conference on Aircraft Operating Problems, NASA SP-83, 1965, pp. 9-17.

TABLE I.- SCOPE OF AIRCRAFT GROUND HANDLING SIMULATOR VALIDATION.

TYPE OF SOLUTION (COMPARISON)	QUANTITY	TYPE OF EVALUATION		SOURCE OF COMPARISON DATA	
		QUANTITATIVE	QUALITATIVE	DAC SIMULATION RESULTS	FLIGHT TEST
LONGITUDINAL TRIM	9	√		√	√
LONGITUDINAL DYNAMIC DAMPING (PHUGOID)	2	√		√	√
LATERAL DIRECTION DAMPING (DUTCH ROLL CHARACTERISTICS)	2	√		√	√
MINIMUM CONTROL SPEED GROUND (V_{MCG}) -- PILOTED	4	√		√	√
STOPPING DISTANCE (BRAKES ONLY) -- PILOTED	4	√		√	√
GEAR DYNAMICS AND OVERALL LANDING AND ROLL OUT CONDITIONS	6	√		√	
SELECTED CASES COVERING MOST IMPORTANT PARAMETERS -- PILOTED	59		√	√	

TABLE II.- RUNWAY SURFACE RANKINGS BASED ON COMPARATIVE TEST AIRCRAFT AND GROUND VEHICLE FRICTION READINGS.
(Artificial wetting condition which differed between surfaces)

TEST DEVICE	TEST SPEED			TEST SURFACE FRICTION READING (RANKING*)				
	KNOTS	km/hr	MPH	SLURRY SEAL ASPHALT	GROOVED**	SMALL AGGREGATE ASPHALT	BURLAP DRAG FINISHED CONCRETE	CANVAS BELT FINISHED CONCRETE
SABRELINER-80 AIRCRAFT, μ_{EFF}	17	32	20	0.41 (1)	0.41 (1)	0.40 (3)	----	0.32 (5)
	35	65	40	0.40 (1)	0.40 (1)	0.35 (3)	0.34 (4)	0.28 (5)
	52	98	60	0.38 (1)	0.38 (1)	0.28 (4)	0.29 (3)	0.24 (5)
MU-METER, μ_{SIDE}	17	32	20	0.82 (1)	0.73 (2)	0.65 (4)	0.66 (3)	0.58 (5)
	35	65	40	0.80 (1)	0.68 (2)	0.38 (4)	0.57 (3)	0.26 (5)
	52	98	60	0.78 (1)	0.64 (2)	0.25 (4)	0.51 (3)	0.12 (5)
FRICTION TESTER;*** μ_{MAX}	17	32	20	0.98 (1)	0.86 (2)	0.71 (3)	0.71 (3)	0.63 (5)
	35	65	40	0.94 (1)	0.80 (2)	0.62 (4)	0.64 (3)	0.48 (5)
	52	98	60	0.86 (1)	0.74 (2)	0.43 (4)	0.56 (3)	0.23 (5)
DIAGONAL BRAKED VEHICLE, μ_{SKID}	17	32	20	0.73 (1)	0.62 (2)	0.56 (3)	0.48 (4)	0.45 (5)
	35	65	40	0.58 (1)	0.54 (2)	0.25 (4)	0.26 (3)	0.17 (5)
	52	98	60	0.51 (1)	0.47 (2)	0.13 (4)	0.18 (3)	0.06 (5)

*RANKING OF (1) INDICATES HIGHEST VALUE, (5) INDICATES LOWEST VALUE

**AVERAGE OF COMPARATIVE DATA OBTAINED ON FOUR DIFFERENT SURFACES TRANSVERSELY GROOVED WITH A 25 × 6 × 6 mm (1 × 1/4 × 1/4 In.) PATTERN

***FRICTION DATA OBTAINED WITH LOW PRESSURE, PATTERNED TEST TIRE

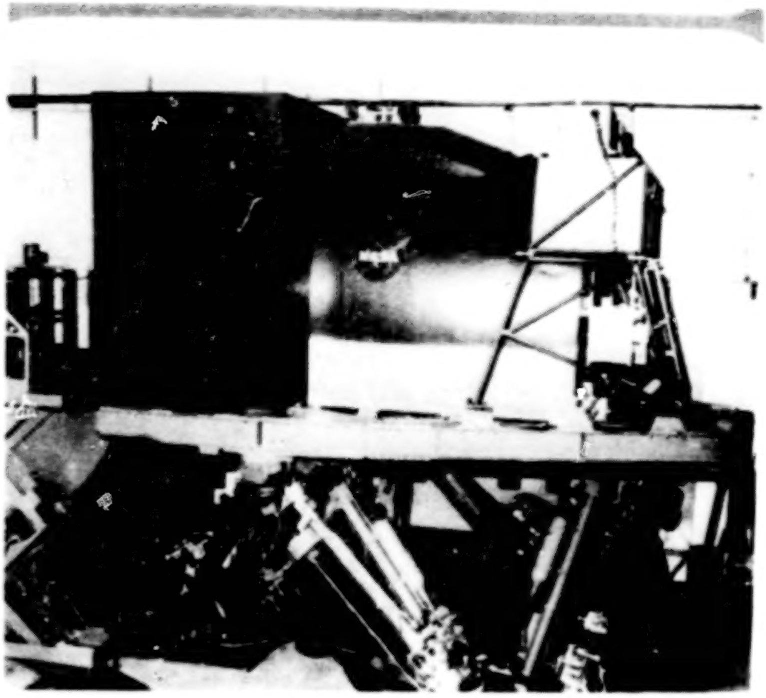

Figure 1.- Motion base simulator.

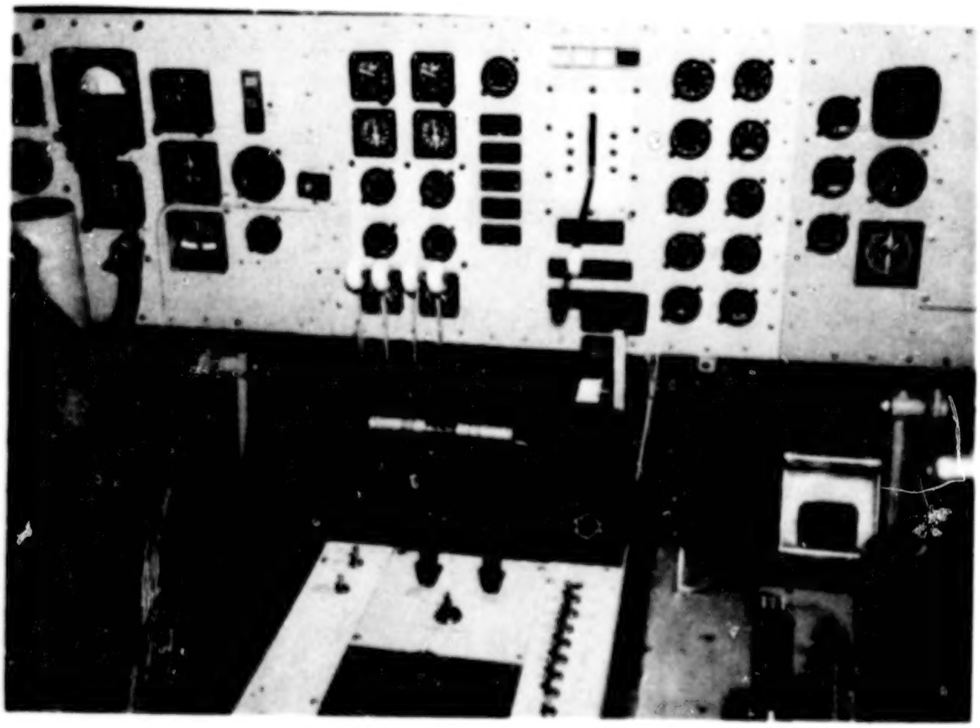

Figure 2.- Motion base cockpit interior.

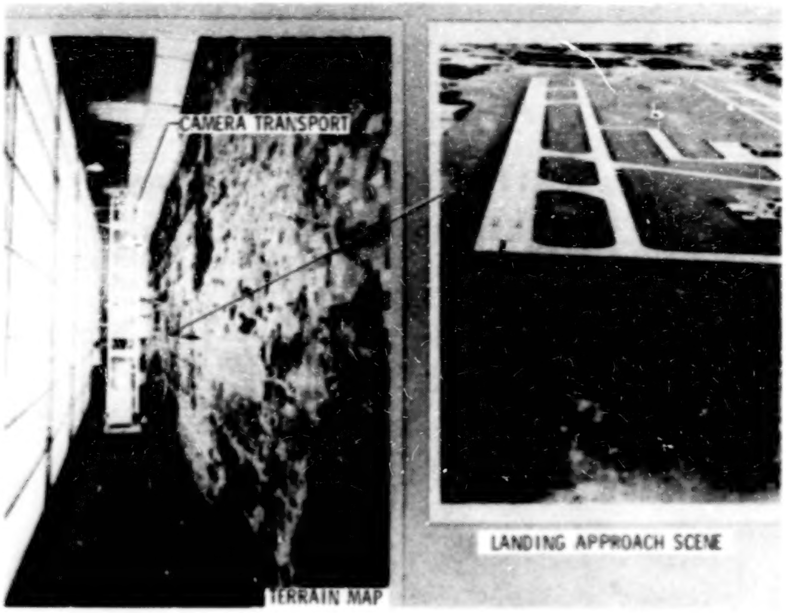
CAMERA TRANSPORT
LANDING APPROACH SCENE
TERRAIN MAP

Figure 3.- Visual landing display system.

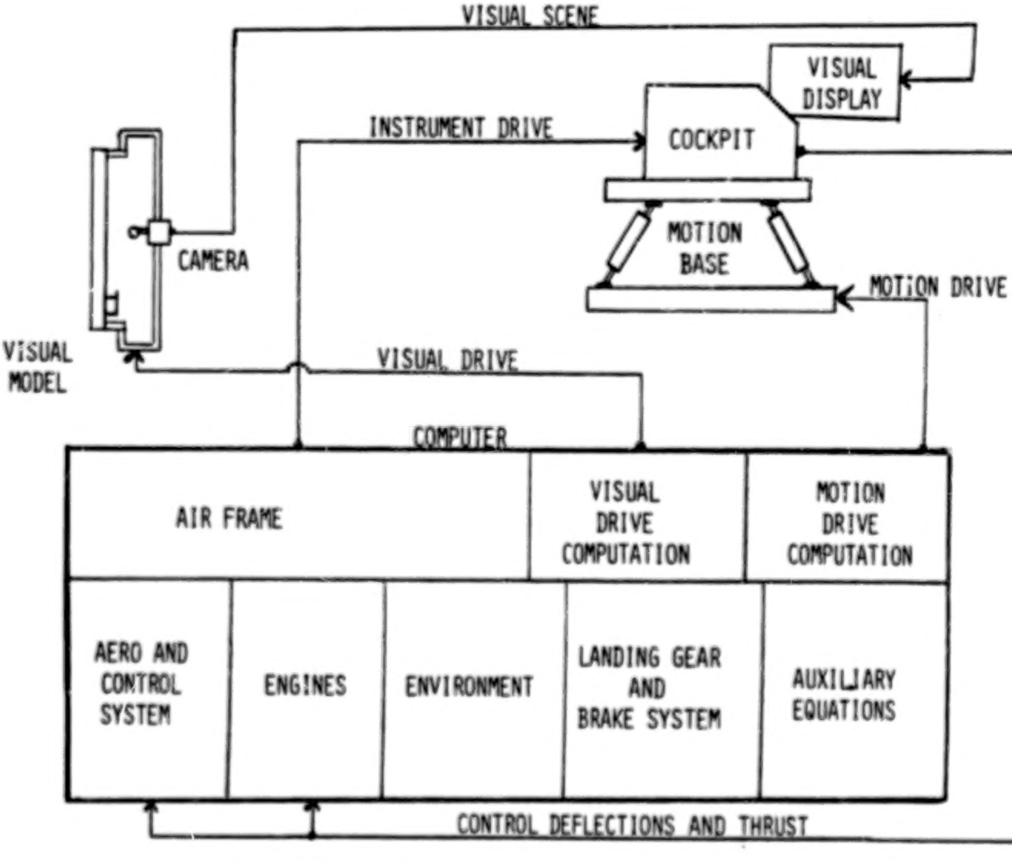
VISUAL SCENE
VISUAL DISPLAY
INSTRUMENT DRIVE
COCKPIT
MOTION BASE
CAMERA
MOTION DRIVE
VISUAL MODEL
VISUAL DRIVE
COMPUTER
AIR FRAME
VISUAL DRIVE COMPUTATION
MOTION DRIVE COMPUTATION
AERO AND CONTROL SYSTEM
ENGINES
ENVIRONMENT
LANDING GEAR AND BRAKE SYSTEM
AUXILIARY EQUATIONS
CONTROL DEFLECTIONS AND THRUST

Figure 4.- Block diagram indicating implementation of aircraft ground handling simulation facility.

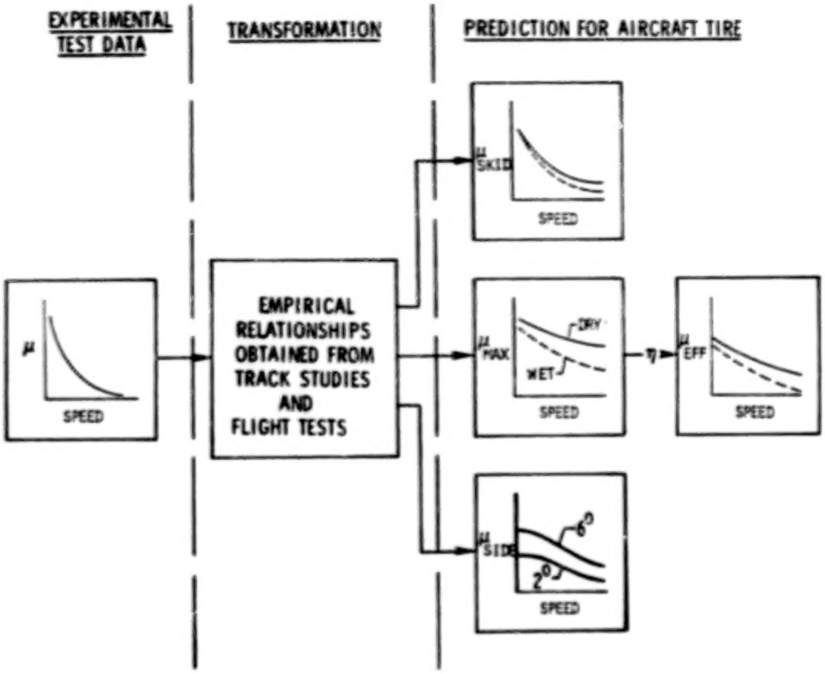
EXPERIMENTAL TEST DATA
TRANSFORMATION
PREDICTION FOR AIRCRAFT TIRE
μ
SPEED
EMPIRICAL RELATIONSHIPS OBTAINED FROM TRACK STUDIES AND FLIGHT TESTS
μ SKID
SPEED
μ MAX
DRY
WET
SPEED
η
μ EFF
SPEED
μ SIDE
6°
2°
SPEED

Figure 5.- Methodology used to estimate aircraft tire friction performance.

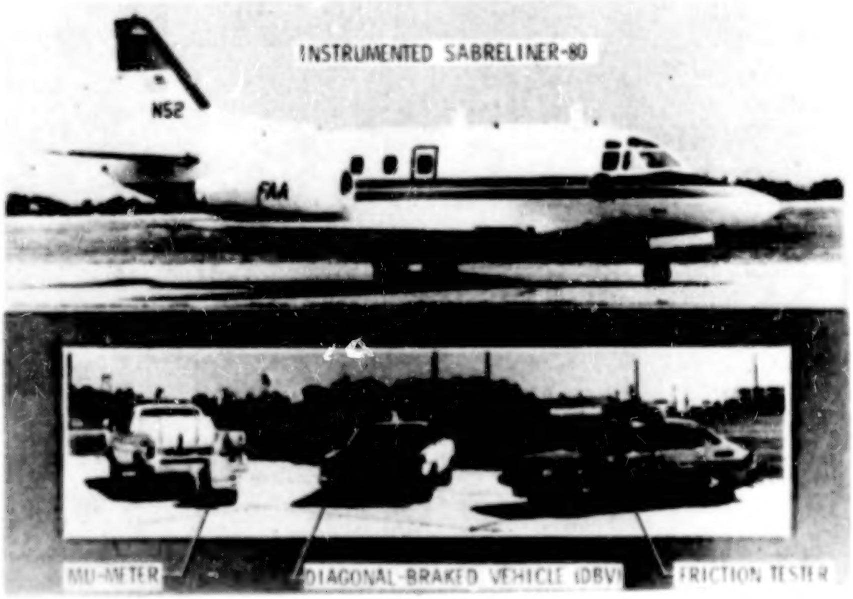
INSTRUMENTED SABRELINER-80
N52
FAA
MU-METER
DIAGONAL-BRAKED VEHICLE (DBV)
FRICTION TESTER

Figure 6.- Test aircraft and ground friction measuring vehicles used in joint NASA/FAA program.

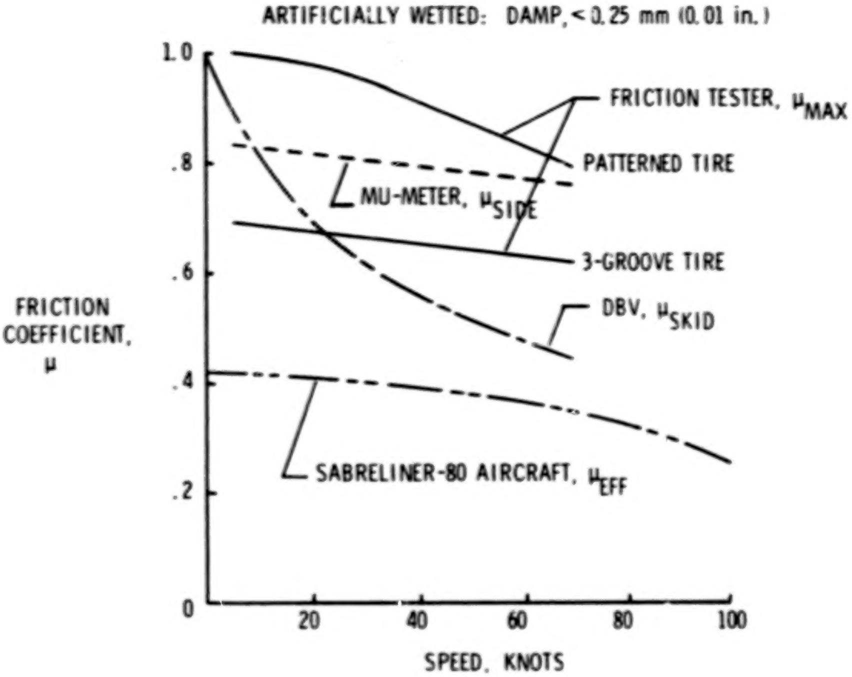

(a) Slurry seal asphalt surface.

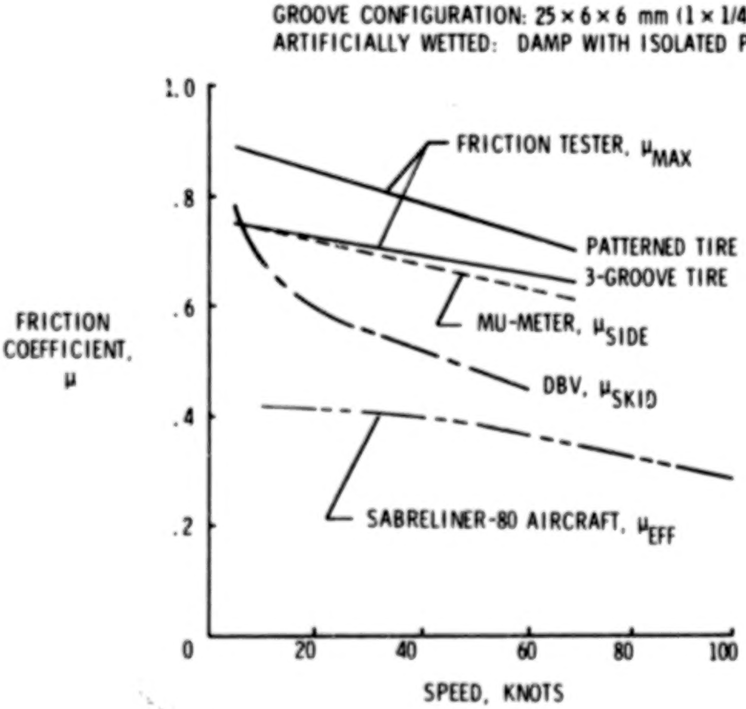

(b) Transverse grooved surfaces.

Figure 7.- Range of aircraft and ground vehicle friction data obtained on different wet runway surfaces at NASA Wallops Flight Center.

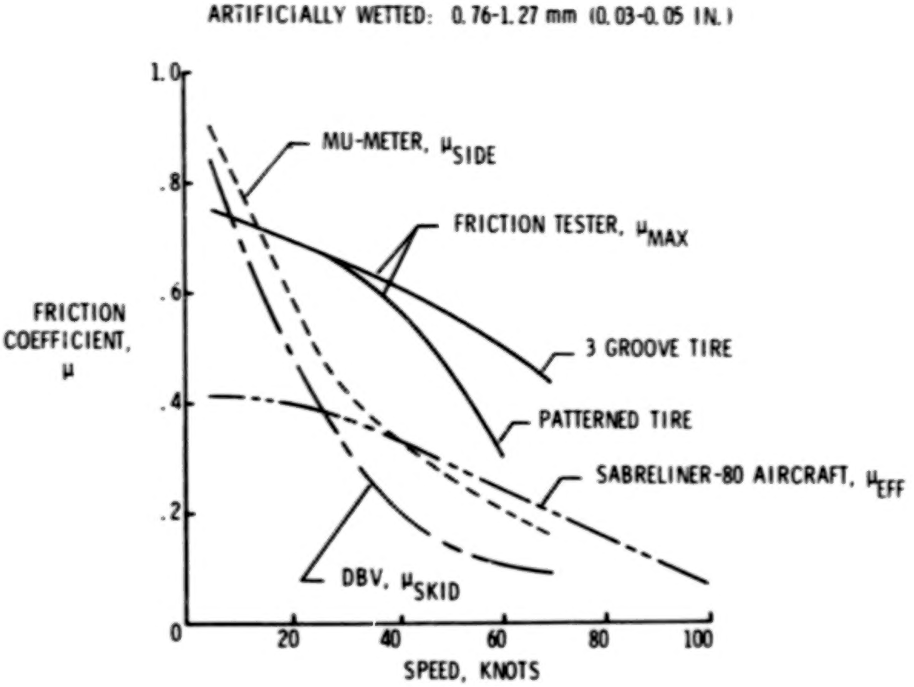

(c) Small aggregate asphalt surface.

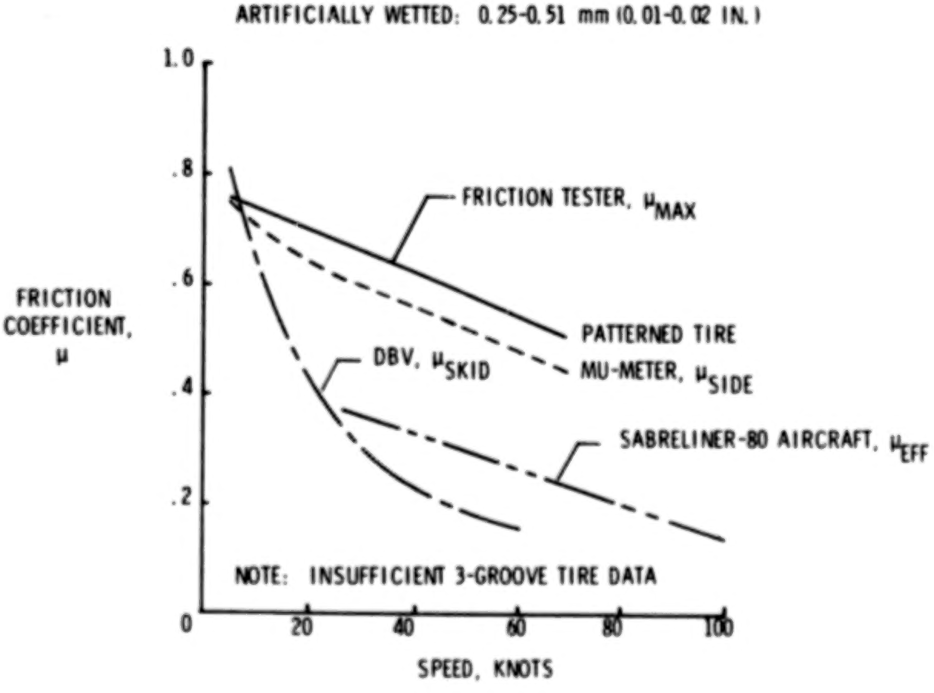

(d) Burlap drag-finished concrete surface.

Figure 7.- Continued.

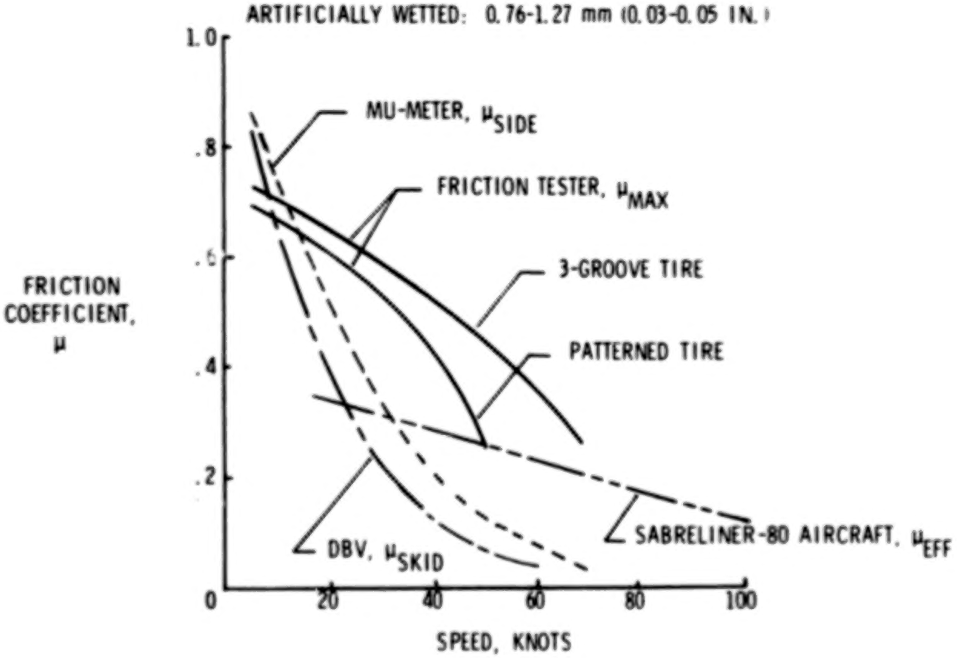

(e) Canvas belt-finished concrete surface.

Figure 7.- Concluded.

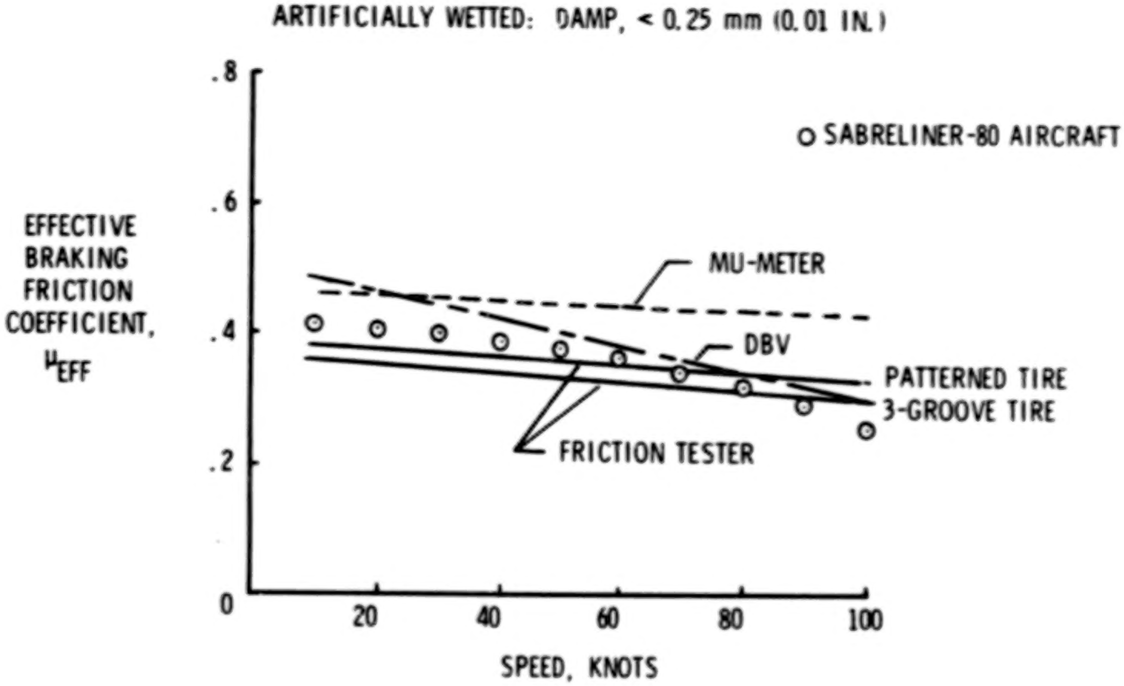

(a) Slurry seal asphalt surface.

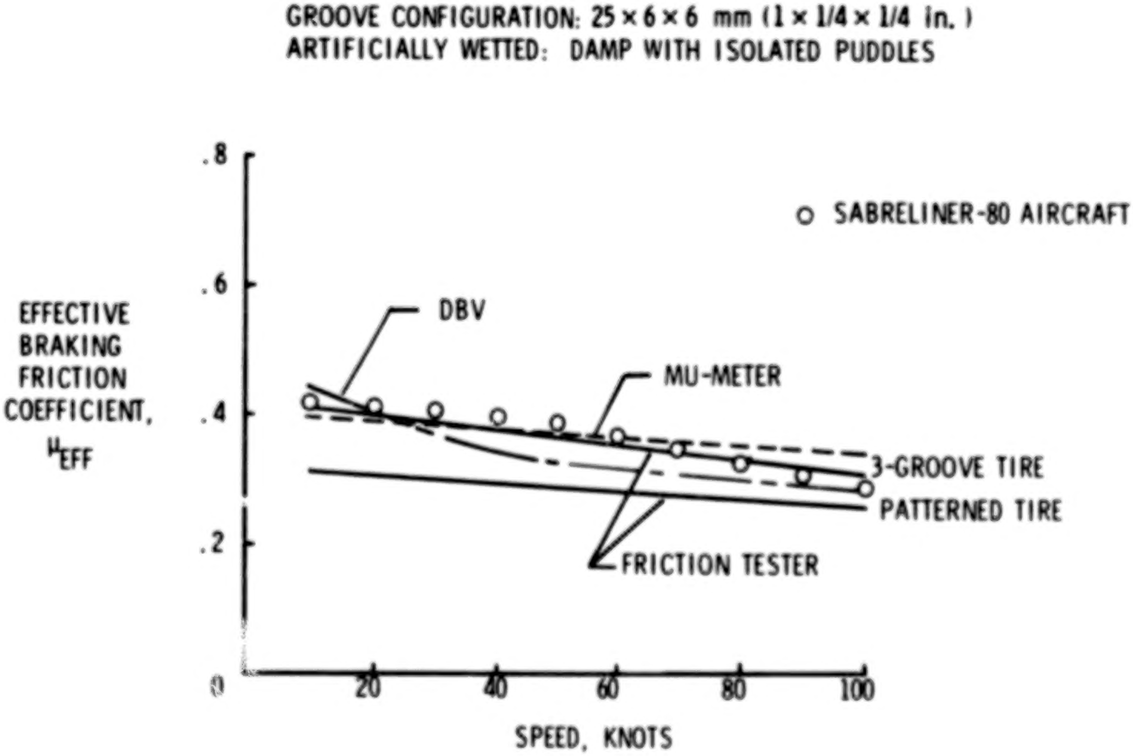

(b) Transverse grooved surfaces.

Figure 8.- Agreement between actual and estimated aircraft braking performance from ground vehicle friction measurements.

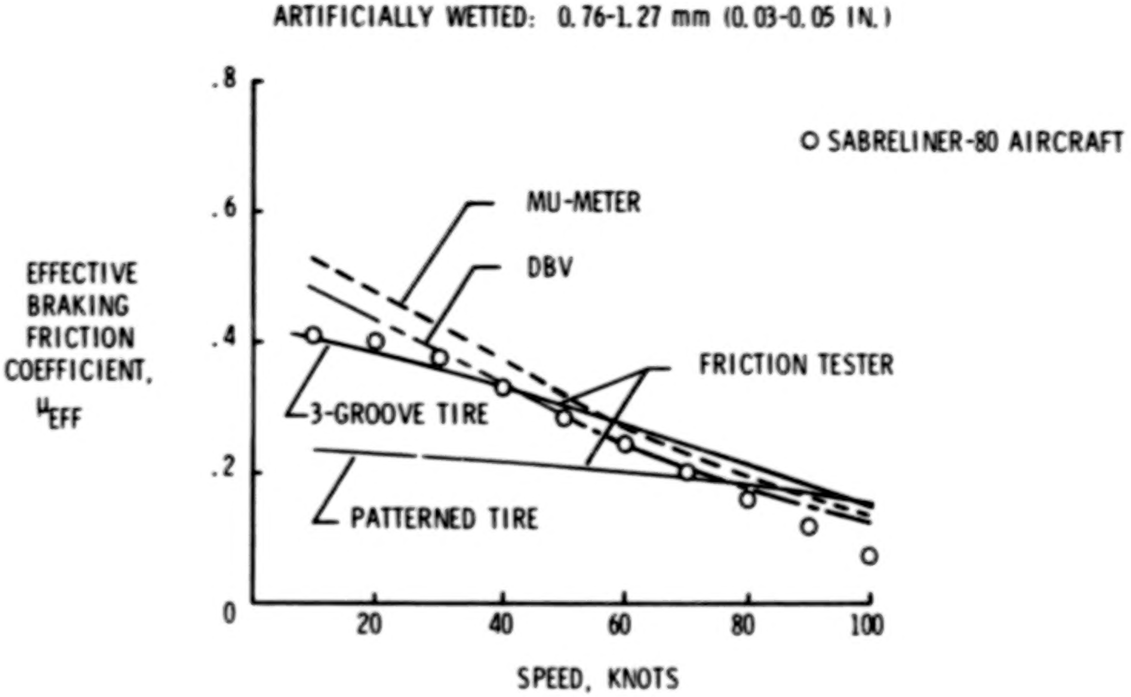
ARTIFICIALLY WETTED: 0.76-1.27 mm (0.03-0.05 IN.)

(c) Small aggregate asphalt surface.

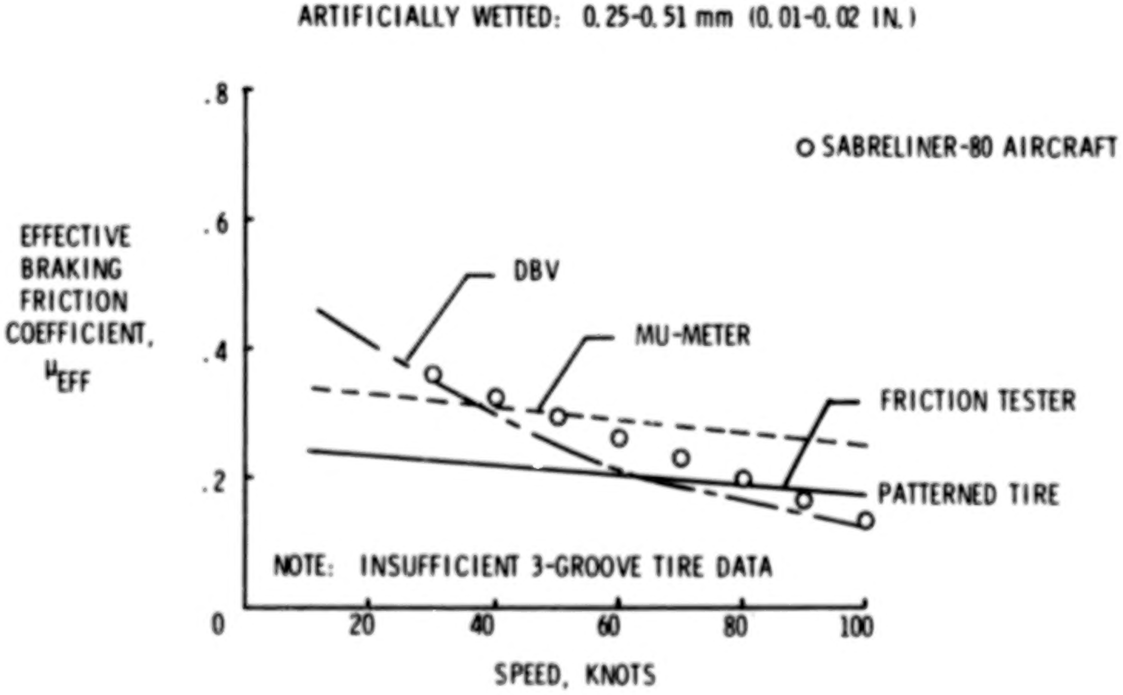
ARTIFICIALLY WETTED: 0.25-0.51 mm (0.01-0.02 IN.)

(d) Burlap drag-finished concrete surface.

Figure 8.- Continued.

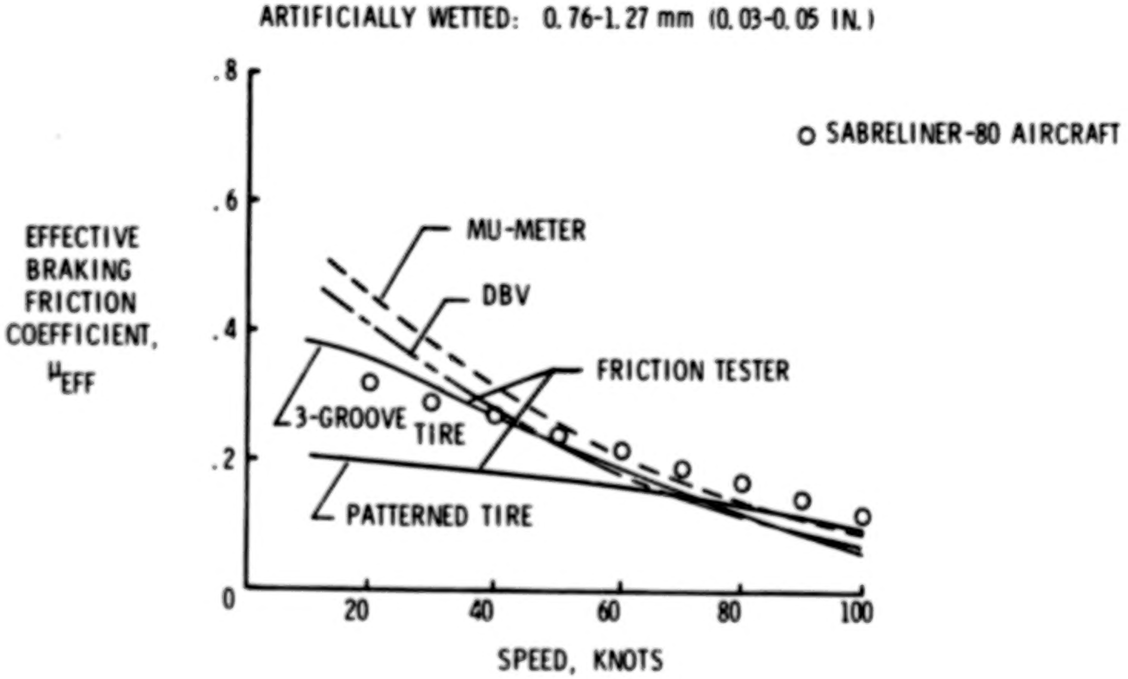

(e) Canvas belt-finished concrete surface.

Figure 8.- Concluded.

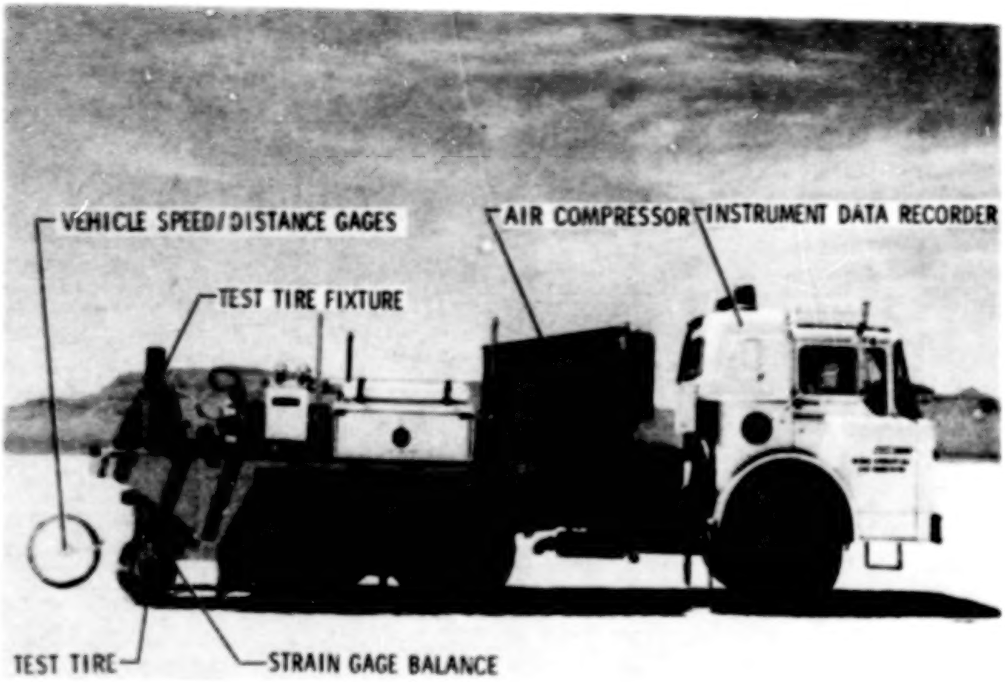
VEHICLE SPEED/DISTANCE GAGES
AIR COMPRESSOR
INSTRUMENT DATA RECORDER
TEST TIRE FIXTURE
TEST TIRE
STRAIN GAGE BALANCE

(a) Side view.

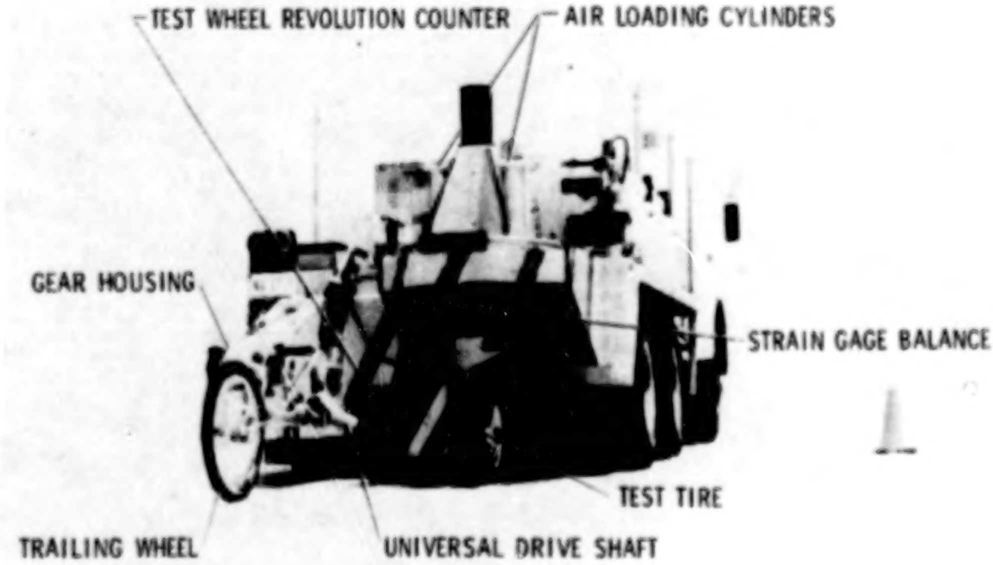
TEST WHEEL REVOLUTION COUNTER
AIR LOADING CYLINDERS
GEAR HOUSING
STRAIN GAGE BALANCE
TEST TIRE
TRAILING WHEEL
UNIVERSAL DRIVE SHAFT

(b) Rear view.

Figure 9.- Instrumented tire test vehicle.

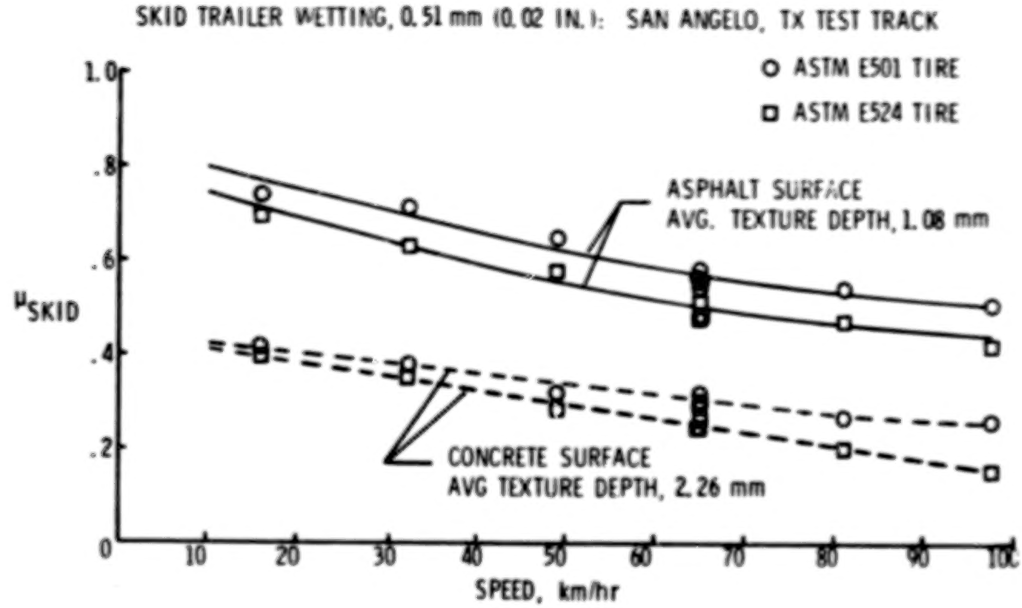

Figure 10.- Friction performance of two ground vehicle test tires.

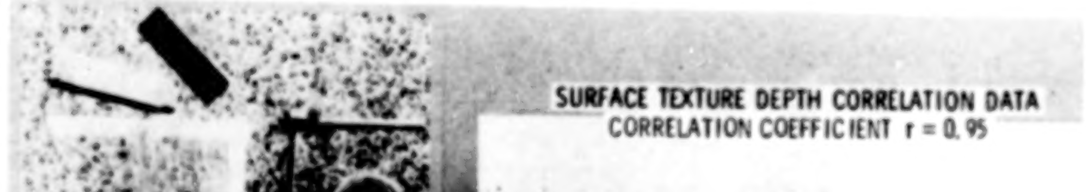

Figure 11.- Example of surface texture measurement correlation.

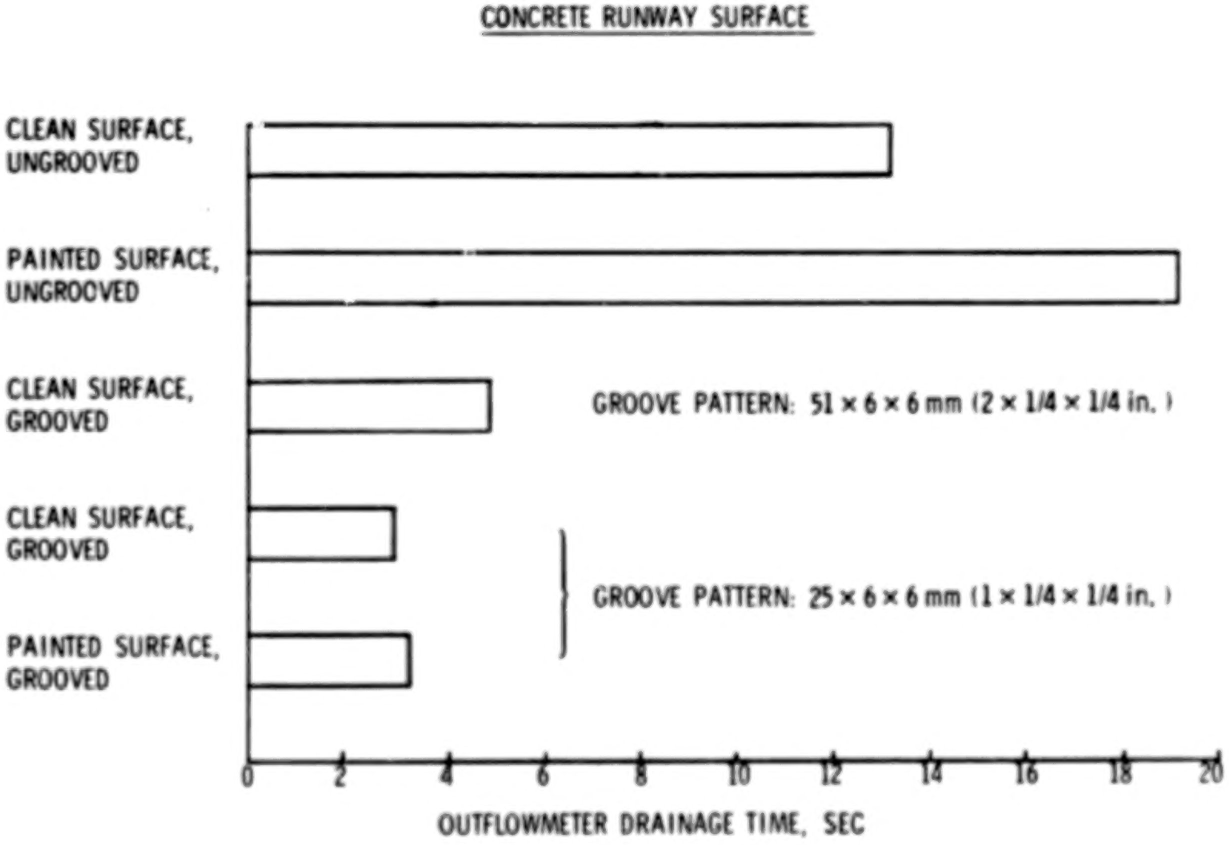

Figure 12.- Effect of surface treatments on outflowmeter drainage measurements.

BLANK PAGE

BLANK PAGE

THE NASA DIGITAL VGH PROGRAM--EARLY RESULTS

Norman L. Crabill and Garland J. Morris
Langley Research Center

SUMMARY

NASA has recently revived the "VGH" measurement program for airline transports to fulfill a need within the airline industry for realistic data describing flight operations of airline transports. These data will be used by transport designers to make better estimates of fatigue life consumption of current aircraft and to update design criteria for future aircraft. This program, using digital data recorded on magnetic tape was started in 1977. Several examples of the statistical outputs are reviewed to illustrate the types of analyses and results becoming available.

INTRODUCTION

NASA has recently revived the "VGH" measurement program for airline transports to fulfill a need within the airline industry for realistic data describing flight operations of airline transports. Data needed include operating altitude, airspeed, weight, loads, and control usage. These data will be used by transport designers to make better estimates of fatigue life consumption of current aircraft and to update design criteria for future aircraft.

NACA/NASA has historically provided such data, starting in the 1930's with the NASA "VG" program which gave velocity and load factor from operating aircraft for direct comparison with the designer's VG diagrams. Later, starting in the 1950's, a new dimension of altitude was added in the NACA/NASA-supplied film recorder, which provided time histories of velocity, load factor, and height which were read up and analyzed principally by manual processes. These analogue recorder programs for airline transports ceased in 1971, due to changing priorities within NASA.

In 1977, NASA revived the program for airline transports with some changes (ref. 1). It was decided to determine if data from digital recorders already existing on many wide-body aircraft for accident investigation purposes could be utilized to fulfill the Digital VGH Program objectives. More parameters would be attempted, since they are readily available. The present report gives several examples of the statistical outputs evolved for a Lockheed L-1011 aircraft using data obtained in routine flight operations in 1973, and compares them with results from 1978 operations. In addition, the report discusses several interesting operational effects obtained from an inspection of the time histories.

The service areas for the two data sets discussed are given in figure 1. The oldest data set was obtained for flights flown in February through May 1973 along the east coast with Chicago and San Juan added. This set consists of 83 flights, about 200 hours of flight time, and about 169 000 km (91 000 nautical miles). The data tapes for this 1973 data set were obtained in 1977 and were used to develop the analysis techniques, computer programs, and output formats. The newest set covers March 1978 through July 1979 and is for much the same routing, but with the addition of Mexico City, Acapulco, Seattle, and Portland, for 918 flights, about 1600 hours, and 1 300 000 km (700 000 nautical miles). For each data set, the data are for the same airplane obtained continuously, or as nearly as possible.

DISCUSSION

The data are recorded on existing Digital Flight Data Recorders on a 25-hour loop-tape on airliners in routine airline service (figure 2). The airline company reads out the data once or twice a week, transcribes the selected parameters into an IBM compatible format, and sends it and the support data (weights and trip length from flight logs) to NASA. NASA plots these data and edits them both manually and automatically and processes them into two basic statistical outputs--loads statistics and flight profile statistics--as described in reference 1 and illustrated in figures 3 and 4. The matrix of statistical data types output for this first program phase is shown in figure 4. Not all these data types will be discussed in this paper. Instead, this paper will show typical statistical outputs for altitude, weight, airspeed, and acceleration, as shown by the numbers 1, 2, 3, and 4 on figure 4. Complete statistical results for the L-1011, B-727, and B-747 airplanes are expected to be published within the next year, in separate reports.

Maximum Altitude Per Flight

The 83 flights of the 1973 operations, figure 5, show the maximum altitude per flight was about equally divided between 8892-10516 and 10516-12040 meters (30-35 000 and 35-40 000 feet). For the larger sample of 918 flights starting in 1978 over a broader route structure, the 10516-12040 m (35-40 000 feet) altitude was by far the most popular and two flights actually went to 12800 m (41 000 feet). At the 10516-12040 m (35-40 000 feet) maximum altitude level, the 2-2.5-hour trip was most prevalent for both sets of data. About 17 percent of all trips had peak altitudes less than 5944 m (19 500 feet) in 1978-1979.

Landing Fuel

Landing fuel mass is given for the L-1011 operation in figure 6 for the 83 flights, February to May 1973, and for 918 flights, 1978-1979 operations.

In 1973, the most popular trip of 2-2.5-hours duration almost always landed with 13 608-22 680 kg (30-50 000 lbs) of fuel. In 1978-1979, the most popular landing fuel mass by a factor of 2 was 4536-13 608 kg (10-30 000 lbs) for the same 2.5 hour trip length. However, the 1.0-1.5-hour trip landed with more fuel, 13 608-22 680 kg (30-50 000 lbs), twice as often as it did with the minimum 4536-13 608 kg (10-30 000 lbs). The 13 608-22 680 kg (30-50 000 lbs) landing fuel mass was still the most probable mass for all trip lengths. The distributions of trip duration for all fuel masses in 1978-1979 show more shorter trips than in 1973. The differences in trip duration distributions for the 83 flights and the 918 flights in 1978-1979, shown in figures 5 and 6, can be attributed to the effects of sample size and possibly other factors such as changes in fuel cost and availability.

Landing Flap Usage

The time spent at various airspeed intervals in each flap detent is given in figure 7 for 83 landings of the L-1011-1 aircraft in 1973 operations; flap placard speeds are also noted. These data are actual flap surface position indications collected into standard "bins" or detents of 5 to 8 degrees. It can be seen that flap deployment above the placard speed is minimal, the general trend is for broad speed distributions in small detents, and narrow distributions close to the placard speeds in the landing detents.

Loads

The measure of load on the aircraft is the body-axis normal acceleration at the center of gravity. As explained in reference 1, the basic counting technique employed is the "level crossing method" as opposed to the "peak count method" of the previous NACA/NASA VGH Program. Sample results for the L-1011-1 operation are given in figure 8 and compared with previous wide-body data extracted from the data set reported in reference 2.

The previous wide-body results are within a factor of 2 of the present results at a given load increment. However, at a given counting rate, the loads are within 10 to 15 percent. However, since they were not derived exactly the same way as the present results, the comparison must be made cautiously. The previous wide-body results are total peak counts per hour obtained by adding separately determined maneuver counts and gust counts to get the total counts; the present results are total level crossing counts per hour obtained directly from the trace of total normal accelerations. Results in reference 3 indicate the level crossing technique can sometimes give up to twice the crossing rate of the peak count method.

The present results, figure 8, provide data all the way to zero load. At these low levels, the counts are considerably higher than at the 0.2-g level previously available, as would be expected.

Examination of many power spectra of center-of-gravity normal acceleration showed the presence of sharply peaked responses just below 1 hz, whereas, the aircraft short period response (or gust response frequency) is characteristically 0.2 to 0.5 hz for the L-1011 with stick fixed. From the flight conditions, it was surmised that autopilot operation was involved; however, the 1973 data set did not include autopilot status. When the 1978 data set was obtained with autopilot status, it was possible to clearly see that the high frequency response was occurring with autopilot on, as in figure 9.

Figure 9 shows power spectra of L-1011 c.g. normal acceleration plotted after the manner of reference 4, to show the relative power under each peak. Thus, the vertical scale is linear with power spectral density times frequency versus log frequency horizontally. The measured data are for autopilot off and on under similar operating conditions. For autopilot off, the peak response is at about 0.3 hz, which is the aircraft stick-fixed short period frequency. For autopilot on, the peak is at about 0.8 hz, which was surmised to be the short period response with autopilot on. Subsequent calculations by the manufacturer and NASA confirmed this frequency shift.

There are at least two effects of this shift to be noted. First, the higher frequency motion is considered to be less disturbing to the passengers according to reference 5, which indicates 0.2 to 0.7 hz as the critical motion sickness region. Secondly, the average zero crossing rate of interest to fatigue analysis is increased 10 to 20 percent when the response is integrated across all frequencies.

Autopilot Operation

To assess the importance of these effects of autopilot operation, statistics on autopilot usage were compiled from 400+ hours of the 1978-1979 data set. The results are given in figure 10 and indicate for the L-1011 that the most frequently used altitude band for autopilot turn-on is ~2896 to 4420 m (10-15 000 ft) in the departure, but the most popular turn-off altitude is in the last 1372 m (5000 ft) in descent. In about 5 percent of the cases, it was on at touchdown; in about 8 percent of the flights, it was not on at all. Thus, the L-1011 autopilot was used approximately 75 percent of the time it was operating.

Detailed examination of the normal acceleration trace showed the occasional presence of a low-amplitude low-frequency oscillation. This "limit cycle" phenomenon is illustrated in figure 11. Peak-to-peak amplitudes averaged about .07 g's. This low-amplitude low-frequency motion, associated with the altitude hold mode according to the theoretical studies, is below the region associated with passenger discomfort (reference 5) and is not considered a factor in fatigue life consumption. Similar effects were noted on the 727 and 747 aircraft, figure 12, with the smaller shorter-range aircraft experiencing it more than 20 percent of the time, and the large long-range type less than 10 percent of the time the autopilot is on. It is estimated the effect of this limit cycle is to increase the fuel consumption a few tenths of 1 percent.

CONCLUDING REMARKS

Data from airline digital flight data recorders can provide relevant statistical data for estimating fatigue life consumption of the current airliner fleet and for design criteria updating for future designs. In addition, the data have indicated real operating effects due to the autopilot, i.e., gust response frequency peak increase by 2 or 3 times, and the existence of the low-frequency low-amplitude limit cycle motion in altitude hold. Extension of the program to more data types for ground operations is planned, along with acquisition of DC-10 data. Finally, on-board processing of simple data types is being considered. Throughout the program, industry feedback is sought and received.

REFERENCES

1. Morris, Garland J.; and Crabill, Norman L.: Air Transport Flight Parameter Measurements Program - Concepts and Benefits. SAE 1980 Aero-Space Congress, October 1980.

2. Zalovcik, J. A.; Jewel, Joseph W., Jr.; and Morris, Garland, J.: Comparison of VGH Data from Wide-Body and Narrow-Body Long-Haul Turbine-Powered Transports. NASA TN D-8481, July 1977.

3. Crooks, W. M.; Hoblit, F. M.; Mitchel, F. A.: Project HICAT. High Altitude Clear Air Turbulence Measurements and Meteorological Correlations. AFFDL TR 68-127, Vol. 1, Final Report, March 13, 1967 to July 31, 1968.

4. Houbolt, John C.: Design Manual for Vertical Gusts Based on Power Spectral Techniques. AFFDL-TR-70-106, pp. 11 and 12, December 1970.

5. Aeromedical Aspects of Vibration and Noise. AGARDOGRAPH No. 151, Chap. 5, November 1972.

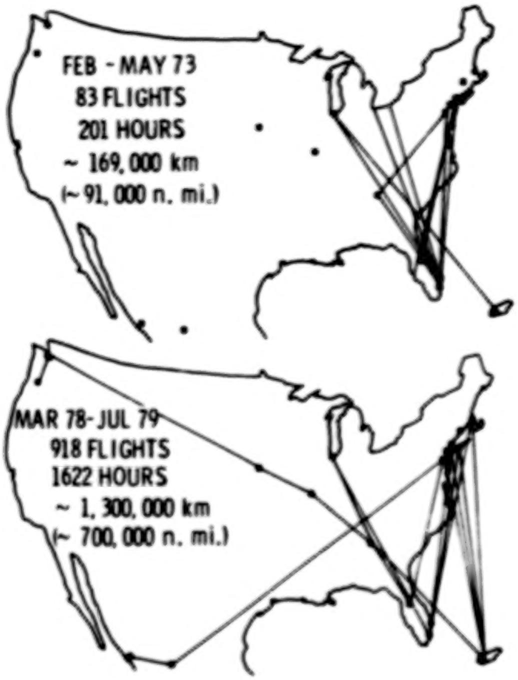
FEB - MAY 73
83 FLIGHTS
201 HOURS
~ 169,000 km
(~ 91,000 n. mi.)
MAR 78 - JUL 79
918 FLIGHTS
1622 HOURS
~ 1,300,000 km
(~ 700,000 n. mi.)

Figure 1.- Location of service areas for L-1011 operations.

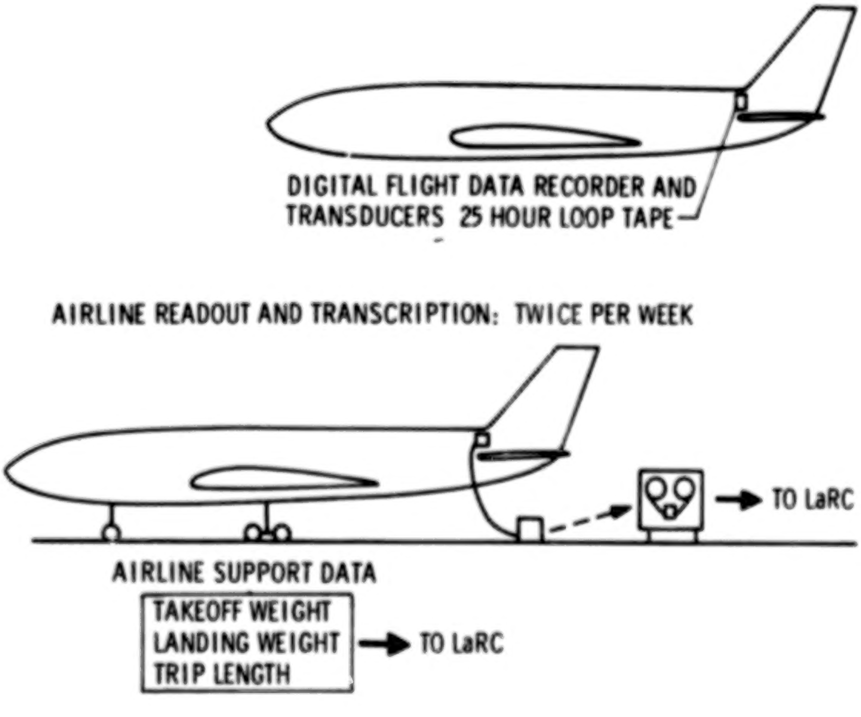
DIGITAL FLIGHT DATA RECORDER AND
TRANSDUCERS 25 HOUR LOOP TAPE
AIRLINE READOUT AND TRANSCRIPTION: TWICE PER WEEK
TO LaRC
AIRLINE SUPPORT DATA
TAKEOFF WEIGHT
LANDING WEIGHT
TRIP LENGTH
TO LaRC

Figure 2.- Digital VGH program data source.

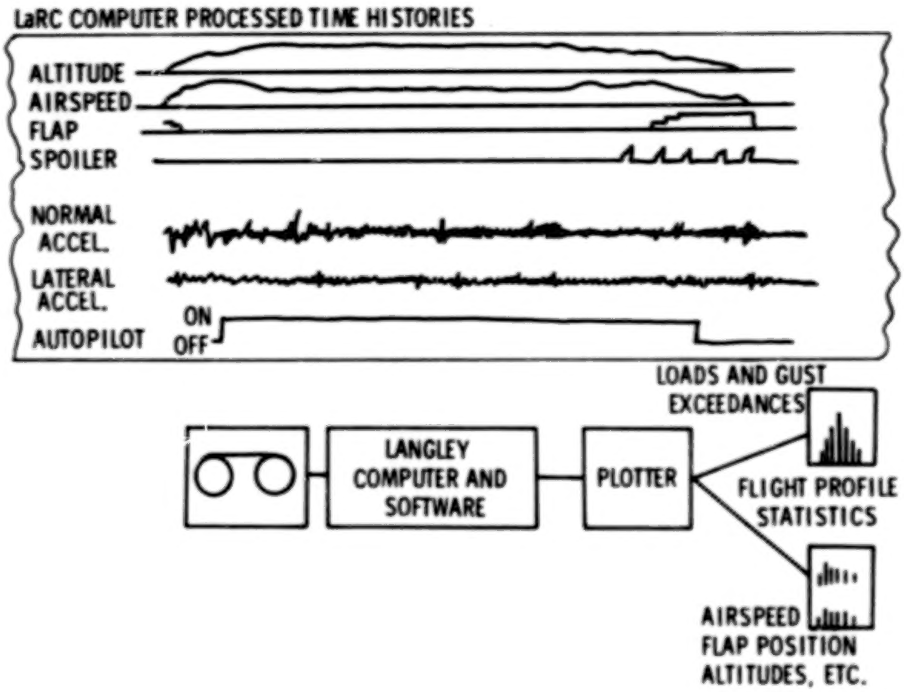
LaRC COMPUTER PROCESSED TIME HISTORIES
ALTITUDE
AIRSPEED
FLAP
SPOILER
NORMAL ACCEL.
LATERAL ACCEL.
AUTOPILOT
ON
OFF
LOADS AND GUST EXCEEDANCES
LANGLEY COMPUTER AND SOFTWARE
PLOTTER
FLIGHT PROFILE STATISTICS
AIRSPEED
FLAP POSITION
ALTITUDES, ETC.

Figure 3.- Data processing and analysis.

		COUNTS/hr	PERCENT OF TIME	PERCENT OF FLIGHTS
FLAPS UP OR DOWN	ACCELS AND GUST VELOC.	FOR ALTITUDE INTERVALS ④	—	MAX ACCELS AND GUST VEL. FOR ALT INTERVALS
	WEIGHTS	—	FOR CLIMB, LEV. FLT AND DESC. VS ALT.	FOR TAKE-OFF AND LANDING VS DURATION ②
	AIRSPEEDS	—	TOTAL, CLIMB, LEV. FLT AND DESC. VS ALT.	—
	ALTITUDE	—	SEE WEIGHTS AND AIRSPEED	MAX ALTITUDE VS DURATION ①
FLAPS > 2°	FLAP DETENTS	—	FOR TAKE-OFF AND LANDING	TIME OF FLAP CHANGE FROM TAKE-OFF AND LANDING
	WEIGHTS	—	FOR EACH DETENT ③	—
	ALT. ABOVE GROUND	—		—
	AIRSPEED	—		EQUIV. AIRSPEED AT FLAP DETENT CHANGE
	ACCELS	FOR TAKE-OFF AND LANDING FOR EACH DETENT	—	—
		MAX NORMAL ACCEL EACH DETENT VS AIRSPEED		

NUMBERS 1, 2, 3, AND 4 REFER TO TOPICS DISCUSSED IN TEXT

Figure 4.- Statistical data outputs.

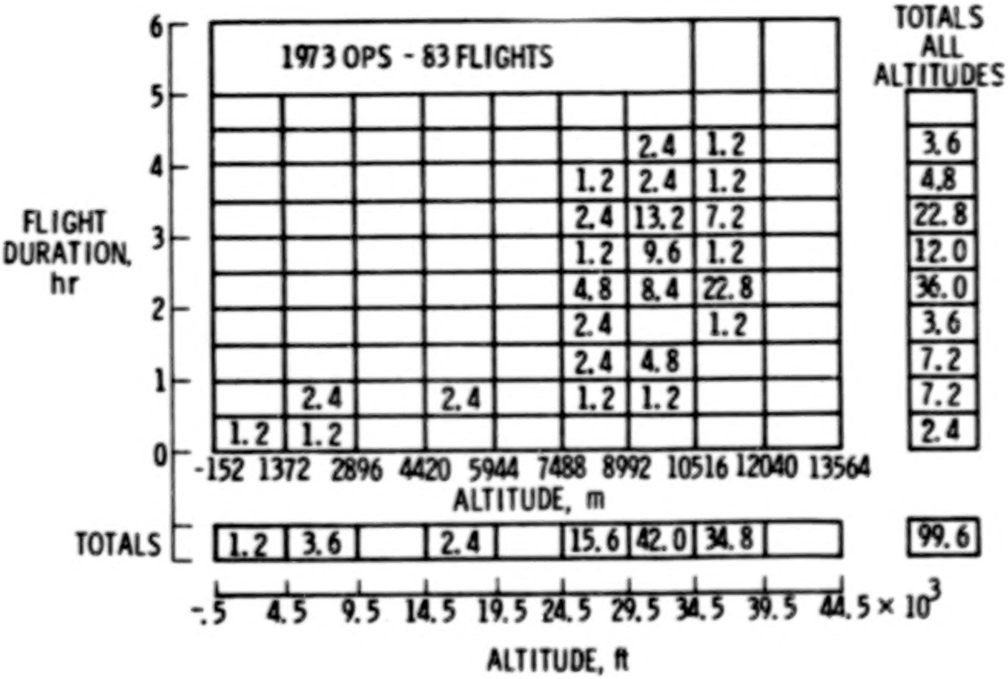

FLIGHT DURATION, hr	-152–1372	1372–2896	2896–4420	4420–5944	5944–7488	7488–8992	8992–10516	10516–12040	12040–13564	TOTALS ALL ALTITUDES
4.5–5										
4–4.5							2.4	1.2		3.6
3.5–4						1.2	2.4	1.2		4.8
3–3.5						2.4	13.2	7.2		22.8
2.5–3						1.2	9.6	1.2		12.0
2–2.5						4.8	8.4	22.8		36.0
1.5–2						2.4		1.2		3.6
1–1.5						2.4	4.8			7.2
.5–1		2.4		2.4		1.2	1.2			7.2
0–.5	1.2	1.2								2.4
TOTALS	1.2	3.6		2.4		15.6	42.0	34.8		99.6

(a) 1973 operations, 83 flights.

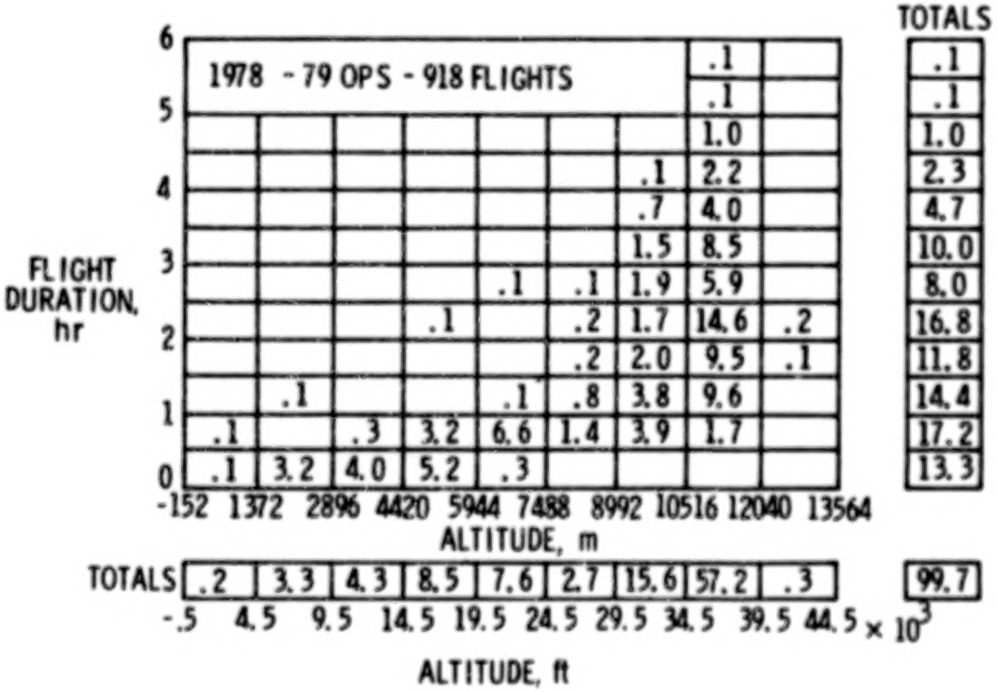

FLIGHT DURATION, hr	-152–1372	1372–2896	2896–4420	4420–5944	5944–7488	7488–8992	8992–10516	10516–12040	12040–13564	TOTALS
5.5–6								.1		.1
5–5.5								.1		.1
4.5–5								1.0		1.0
4–4.5							.1	2.2		2.3
3.5–4							.7	4.0		4.7
3–3.5							1.5	8.5		10.0
2.5–3					.1	.1	1.9	5.9		8.0
2–2.5				.1		.2	1.7	14.6	.2	16.8
1.5–2						.2	2.0	9.5	.1	11.8
1–1.5		.1			.1	.8	3.8	9.6		14.4
.5–1	.1		.3	3.2	6.6	1.4	3.9	1.7		17.2
0–.5	.1	3.2	4.0	5.2	.3					13.3
TOTALS	.2	3.3	4.3	8.5	7.6	2.7	15.6	57.2	.3	99.7

(b) 1978-1979 operations, 918 flights.

Figure 5.- Percent of flights to maximum altitude per flight versus flight duration.

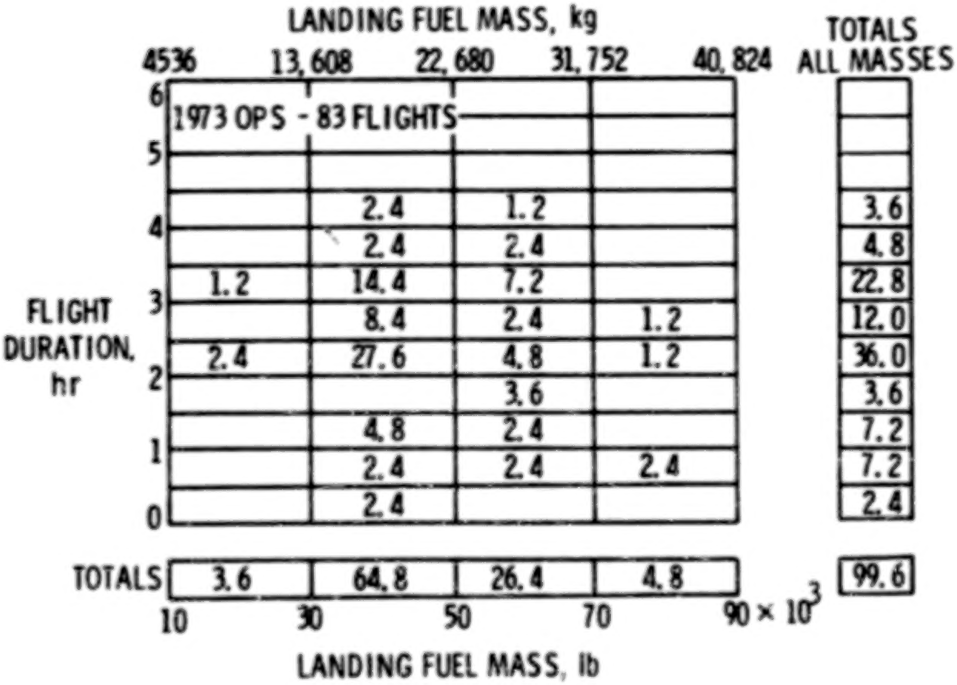

FLIGHT DURATION, hr	4536–13,608 kg (10–30 × 10³ lb)	13,608–22,680 kg (30–50 × 10³ lb)	22,680–31,752 kg (50–70 × 10³ lb)	31,752–40,824 kg (70–90 × 10³ lb)	TOTALS ALL MASSES
6–5.5	1973 OPS - 83 FLIGHTS				
5.5–5					
5–4.5					
4.5–4		2.4	1.2		3.6
4–3.5		2.4	2.4		4.8
3.5–3	1.2	14.4	7.2		22.8
3–2.5		8.4	2.4	1.2	12.0
2.5–2	2.4	27.6	4.8	1.2	36.0
2–1.5			3.6		3.6
1.5–1		4.8	2.4		7.2
1–0.5		2.4	2.4	2.4	7.2
0.5–0		2.4			2.4
TOTALS	3.6	64.8	26.4	4.8	99.6

(a) 1973 operations, 83 flights.

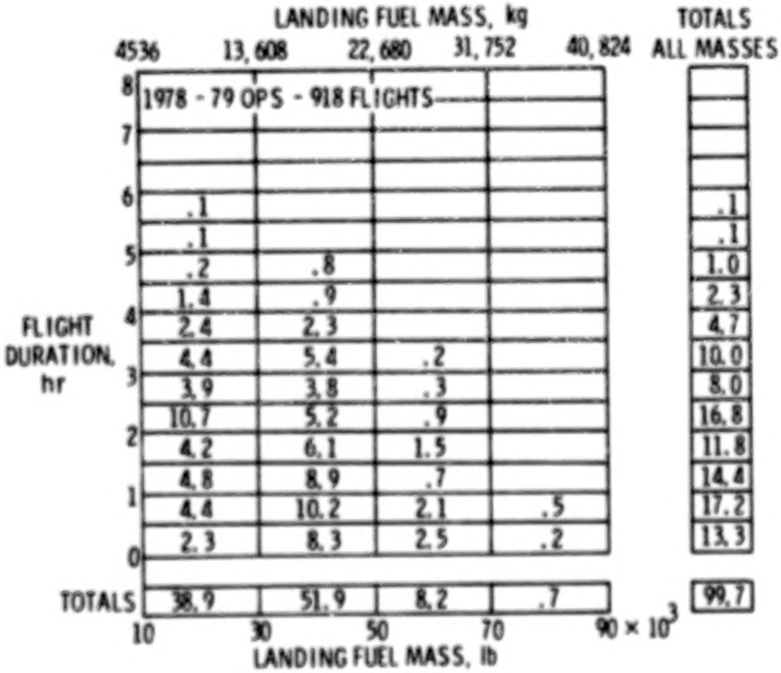

FLIGHT DURATION, hr	4536–13,608 kg (10–30 × 10³ lb)	13,608–22,680 kg (30–50 × 10³ lb)	22,680–31,752 kg (50–70 × 10³ lb)	31,752–40,824 kg (70–90 × 10³ lb)	TOTALS ALL MASSES
8–7.5	1978 - 79 OPS - 918 FLIGHTS				
7.5–7					
7–6.5					
6.5–6					
6–5.5	.1				.1
5.5–5	.1				.1
5–4.5	.2	.8			1.0
4.5–4	1.4	.9			2.3
4–3.5	2.4	2.3			4.7
3.5–3	4.4	5.4	.2		10.0
3–2.5	3.9	3.8	.3		8.0
2.5–2	10.7	5.2	.9		16.8
2–1.5	4.2	6.1	1.5		11.8
1.5–1	4.8	8.9	.7		14.4
1–0.5	4.4	10.2	2.1	.5	17.2
0.5–0	2.3	8.3	2.5	.2	13.3
TOTALS	38.9	51.9	8.2	.7	99.7

(b) 1978-1979 operations, 918 flights.

Figure 6.- Landing fuel mass versus flight duration.

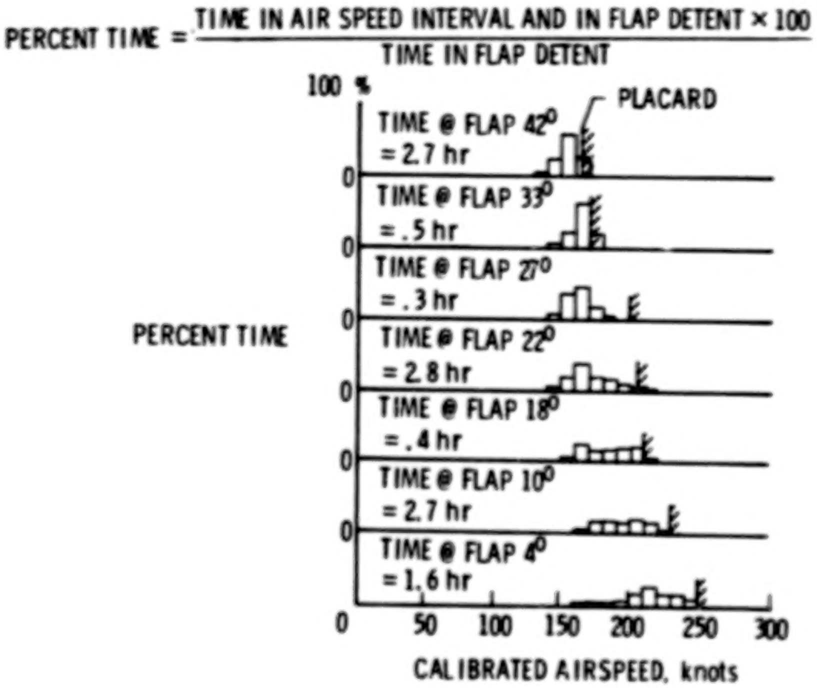

Figure 7.- L-1011 flap position versus airspeed during landing.

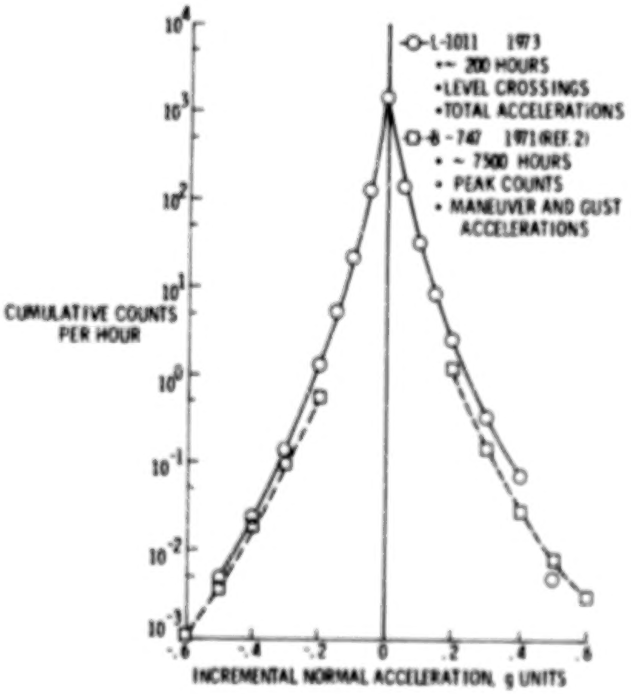

Figure 8.- Loads exceedances.

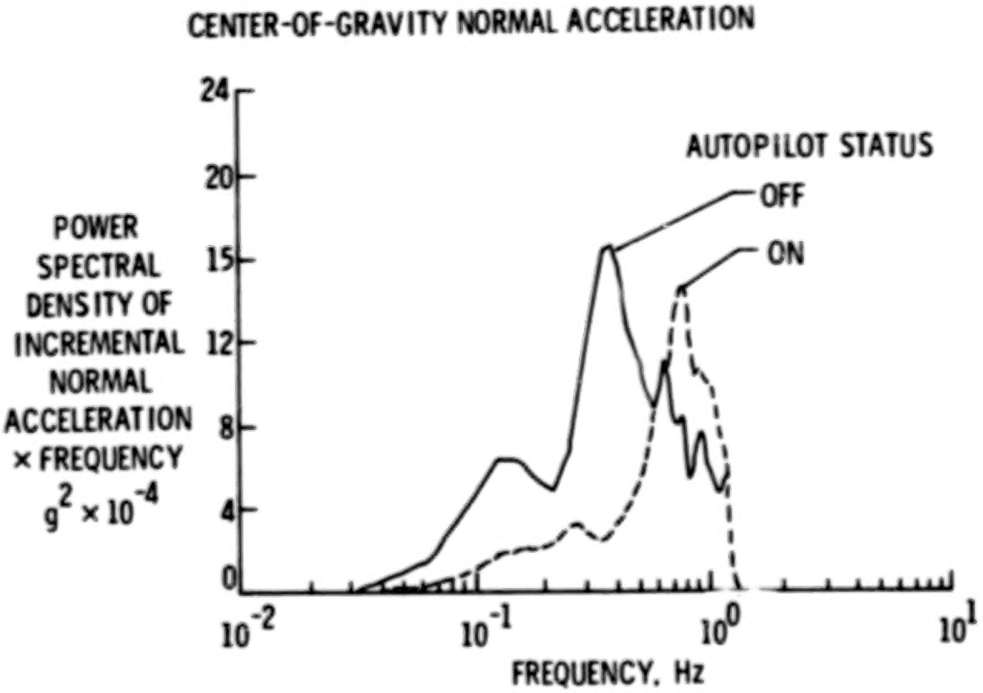

Figure 9.- Effects of autopilot on L-1011 measured power spectra.

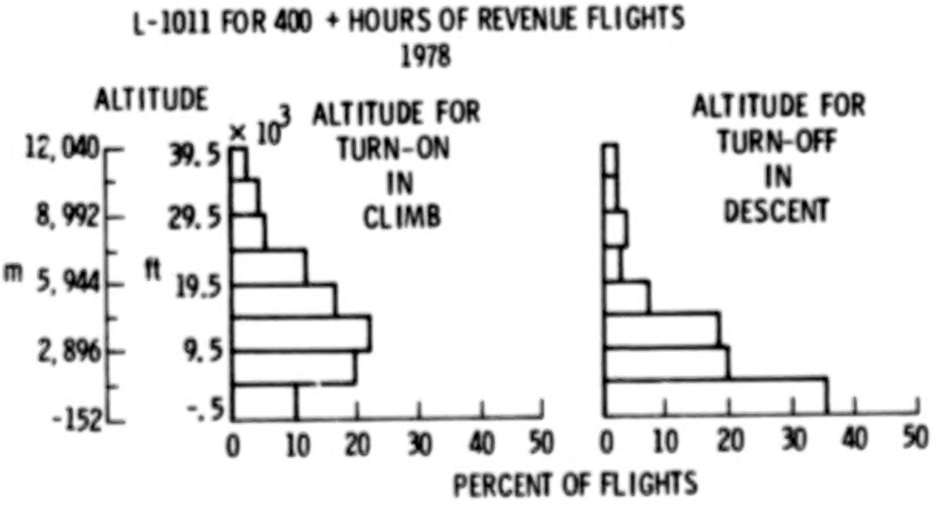

SUMMARY

- AUTOPILOT WAS "ON" ABOUT 75% OF THE TIME
- AUTOPILOT WAS "ON" AT TOUCHDOWN FOR 5% OF THE FLIGHTS
- AUTOPILOT WAS NOT USED ON 8% OF THE FLIGHTS

Figure 10.- Autopilot on-off statistics.

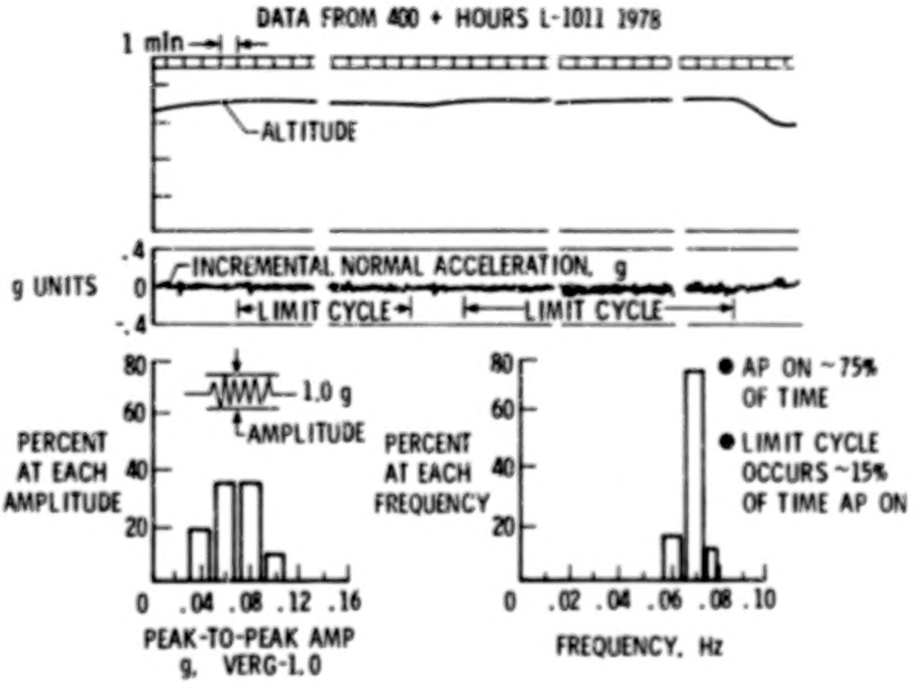

Figure 11.- Autopilot "limit cycle" experience.

AIRPLANE	% TIME AUTOPILOT ON	% TIME AUTOPILOT ON WHICH HAVE LIMIT CYCLE	DOMINANT FREQ. Hz	PEAK-TO-PEAK LOAD, g
B-727	56.42	23.69	.06	.068
L-1011	75.14	15.14	.07	.07
B-747	92.12	7.48	.066	.074

Figure 12.- Summary of autopilot-on and limit cycle times.

EVALUATION OF EMERGENCY-LOCATOR-TRANSMITTER
PERFORMANCE IN REAL AND SIMULATED CRASH TESTS

Huey D. Carden
NASA Langley Research Center

SUMMARY

Emergency-locator-transmitter (ELT) activation problems were investigated by testing a sampling of ELT units in actual airplane crashes and in a special test apparatus which simulated longitudinal crash pulses with superimposed local structural resonances. The objective of the study was to determine probable causes of excessive false alarms and nonactivations of ELT's during crash situations and to seek solutions to the current operational and technical problems. Experimental results from the study, which considered placement, mounting, and activation of ELT's under simulated crash impacts, and an evaluation of the sensitivity of ELT impact switches to orientation and to local structural vibrations are discussed.

INTRODUCTION

Most general-aviation airplanes have been required by law since the early 1970's (ref. 1) to carry emergency locator transmitters (ELT's). ELT units are self-contained, battery-powered, emergency-radio-transmitter beacons. Functionally, the ELT is triggered or activated by the deceleration imposed on the unit during a crash and are intended to aid Search and Rescue (SAR) in locating the crash site. From the outset, ELT's have suffered an excessive false-alarm rate as well as nonactivation problems during crashes. Initial efforts to overcome many of the technical and operational problems which occurred relative to the minimum performance standards of reference 2 were addressed in reference 3; however, the proposals were made without significant research to define the exact causes and to substantiate the proposed solutions to the problems. Consequently, many of the same problems still persist. For example, references 4 and 5 indicate from records examined that malfunctions of the deceleration sensitivity switch, corrosion problems, and human errors are still among the reported causes for unwanted ELT activations and that approximately 95 percent of all ELT alarms are nondistress situations. Thus, reliability and believability have severely limited the usefulness of these emergency devices.

Evaluation of the activation of ELT's in full-scale crash tests at Langley Research Center has been a part of the joint NASA/FAA Crash Dynamics Program which is aimed at developing technology for improved crash safety and occupant survivability in general-aviation aircraft (refs. 6 to 12). More recently, however, laboratory experiments on ELT sensor activation problems have been undertaken to support the work of Radio Technical Commission for Aeronautics

Special Committee 136. This committee was formed to assist the FAA and industry in seeking solutions to current ELT operational and technical problems. This paper presents the results of experiments on the activation of ELT's mounted in airplane structures and subjected to realistic crash impacts. The data are believed to be of general importance in understanding and dealing with the probable causes of the ELT false activations and providing solutions.

APPARATUS AND TEST PROCEDURE

Typical Emergency-Locator-Transmitter Units

Description of ELT units.- Figure 1 is a photograph of nine emergency locator transmitters (ELT's) typical of the units from various manufacturers. The units are among those used for evaluating the performance of sampling of in-service and off-the-shelf units under realistic crash impacts to determine the basic causes of ELT false activations and/or nonactivation.

The ELT is a relatively inexpensive, self-contained, battery-powered beacon designed to broadcast an emergency 121.5-MHz or 243.0-MHz radio signal automatically when triggered by the deceleration characteristic of an airplane crash. ELT's of primary concern in this study are of the "AF" or "AP" type. AF equipment is intended for permanent or fixed installation on the airframe; AP equipment may be attached or be portable. Typically, ELT's are less than 0.3048 m (1 ft) long and weigh only a few kilograms.

ELT mounts vary by type, airplane, and manufacturer's make and model as do the mounting locations in the airplanes. Locations can vary all the way from the cockpit area to the baggage compartment to the tail cone region. Typical mounts can vary from sturdy mounts, to mounts using velcro,[1] plastic ties, and mounts on non-airframe structure in the airplanes. This diversity in mounting techniques include improper and/or inadequate mounting of many ELT's and is likely to be one source of problems of nonfunctioning and/or false activations of some units. Installation was not variable for the study of this report, however, since each ELT was attached to the tail cone structure using state-of-the-art techniques. Figure 2 shows a typical mounting assembly used during the tests.

ELT impact sensor specifications.- The units are triggered by an impact sensor which is an acceleration-sensitive switch (a primary component of ELT's) activated by a force along one or more axes. Present specifications for automatic activation of ELT's are: for decelerations equal to or greater than $5.0g\,{}^{+2.0}_{-0.0}g$ ($1g = 9.80\ \text{m/sec}^2$ ($32\ \text{ft/sec}^2$)) and durations equal to or greater than $11\,{}^{+5.0}_{-0.0}$ msec, the unit must activate; for decelerations and times below these, the ELT must not activate. (See ref. 2.) These specifications apply primarily to crash decelerations parallel to or coincident with the longitudinal axis of the aircraft. More recently a recommendation (ref. 3) to change a criterion for activation has received some consideration. The new proposal is: for decelerations equal to or greater than 2.0g ± 0.3g and a velocity change (ΔV) greater than or equal to 1.067 ± 0.152 m/sec (3.5 ± 0.5 ft/sec), the sensor must activate the ELT; under all other conditions, the sensor must not activate. If the switches do not operate within the specified crash parameters, the unit may be susceptible to unwarranted activation or nonactivation under situations that should or should not activate them. Of the ELT's tested, three different switch types were represented: a cantilever beam (wire) with tip mass; a ball and magnet; and a rolomite[2] switch. Details of the switches are discussed in subsequent sections.

---

[1] Trade name of Velcro Corporation.

Crash Environment Determination

The initial step in the program for evaluating the performance of ELT's during crash situations was to record the longitudinal decelerations on FM tape during the various NASA full-scale crash tests of references 6 to 12. These data were analyzed (1) to determine the type of crash environment one might expect the ELT's to be subjected to during crash situations (for example, the primary loads and any secondary inputs) and (2) to help establish the crash pulse needed for simulation in a laboratory apparatus to permit repetitive, quick-turn-around tests on ELT's.

Crash pulses.- Typical measured longitudinal decelerations are presented in figure 3 for crashes of three different airplanes on concrete and dirt surfaces. The data are from accelerometers located on relatively rigid structure in the cabin area of the airplanes. These data show the nature of an actual environment the ELT can be subjected to in a crash situation. Figure 3(a) is for the crash test onto concrete. The top trace is the measured data with substantial high-frequency structural vibrations superimposed on the much lower frequency crash pulse. The bottom trace is smoothed data which show the underlying low-frequency, triangular-shaped crash pulse. The smoothing was accomplished using a least-squares fit reduction technique discussed in reference 7.

Two crash test decelerations for impacts on dirt are shown in figure 3(b). Basically no difference is noted between the crash pulses on dirt and on a concrete surface. (Compare fig. 3(a) and fig. 3(b).) The data of figure 3(b) also show the same high-frequency, local structural vibrations of the airplane overlayed on the low-frequency pulse evident in the smoothed data.

Structural resonances.- Since the basic crash pulses almost always have structural resonances superimposed on them, limited vibration data were obtained on several different types of general-aviation airplanes to determine the typical frequency range for airplane structural resonance.

---

[2] Invention of Sandia Laboratories.

Accelerometers with conditioning equipment and an oscillograph recorder were used for determining the characteristic airplane resonances. The accelerometer was mounted to bulkheads, ELT mounts or beams in the cabin, and/or tail cone region of seven different airplanes. A large rubber mallet was used to rap some hard point of the airplane to excite the structure in the longitudinal direction. Oscillograph traces of the vibrations were used to determine the predominant frequency. Characteristic resonances in the seven airplanes range from approximately 35 to 200 Hz.

The data for figure 3 indicate that the longitudinal deceleration pulse measured in actual crash tests at the Langley Research Center (LaRC) is basically a low-frequency, triangular-shaped pulse well below 10 Hz with superimposed structural vibrations also evident in the range of 35 to 200 Hz depending upon the mounting location and type of light airplane. Although the airplane crash test parameters associated with these data cannot be considered comprehensive for all crash situations encountered by light airplanes, they are believed to be typical of a majority of crashes, especially those where some structural crushing occurs.

ELT Impact Test Apparatus

Based upon observations made of the nature of basic crash deceleration pulses from actual experimental LaRC crash tests and the structural resonances from seven general-aviation airplanes, a test apparatus capable of being repetitively used was fabricated for testing various ELT units in a realistic simulated crash environment. (See fig. 4.) The apparatus provides a convenient, realistic, and economical laboratory method of extending the test data on ELT's acquired during crash tests of full-sized airplanes at the Langley Impact Dynamics Research Facility. For example, figure 5 is a comparison of the longitudinal deceleration on an ELT in a crash test with a simulated crash pulse in the impact test apparatus. As indicated in the figure, both the characteristic shape of the crash pulse and structural resonances are reproduced by the test apparatus. It should be noted that the test apparatus was designed to give the same basic deceleration pulse with superimposed structural resonances but with lower maximum deceleration values than actual crash tests. The function of the apparatus was to test ELT's which are supposed to activate in the 5g to 7g range of impact decelerations.

Description of impact apparatus.- The laboratory apparatus for testing ELT's to evaluate their performance is shown in figure 4. The test setup (an adaptation of the concept in ref. 13) consists of a 1.83 m (6 ft) diameter by 1.23 m (4 ft) long steel cylindrical section with a 1.23 m (4 ft) length of an actual airplane tail cone section mounted on a platform inside the cylindrical section. A number of attachments between a ring frame at the base of the tail section and the platform permitted tuning of the basic tail cone natural frequency. The oscillations noted on the deceleration traces with the test apparatus were the vibrations of the tail cone at its natural frequency on the platform. The sudden release of the apparatus excites this vibration during free fall and the impact excites the much higher amplitude vibration superimposed on the basic deceleration pulse. (See fig. 5.) Two 1.22 m (4 ft) long by 0.46 m (1.5 ft) deep, 60° wooden wedges attached to the test apparatus shape the crash pulse upon impact into a 0.609-m (2-ft) depth of glass beads. The glass beads ranging in size from 420 to 595 μm (0.0165 to 0.0234 in.) were used as the impact medium because of their uniformity and reduced susceptibility to moisture and for repeatability. The steel cylinder can be rotated relative to the wedges to vary the vector input for off-axis studies.

Instrumentation.- The ELT impact test apparatus was instrumented with strain-gauge-type accelerometers having flat frequency response from dc to 2000 Hz. The accelerometer signals were routed through a calibration unit and a galvanometer driver to oscillograph recorders with galvanometers (fig. 4) which had flat frequency responses from dc to 2500 Hz. Decelerations at the base of the tail cone, on bulkheads, on webs, at the ELT brackets, and on the ELT units were recorded along with ELT activation/no activation signals whenever possible. A radio receiver tuned to 121.5 MHz was also used to monitor all the ELT activations.

Test procedure.- Once accelerometers (oriented perpendicular and parallel to the ELT sensitivity axis) were attached to the ELT, the unit was installed in the tail cone and the ELT was armed to ready the unit. The entire apparatus was then raised to a given drop height above the impact surface by an overhead hoist using a cargo hook for quick release. A push-button switch activated the oscillograph recorders. A second switch was then used to electrically release the cargo hook to drop the apparatus. Penetration of the wedges into the bed of glass beads decelerated the system; thus, loads were imposed on the test apparatus and ELT. If the deceleration from a drop was too low to activate the ELT, the drop height was increased, the glass beads releveled, and the test repeated until the impact loads were sufficient to activate the ELT unit. Tests were repeated at drop heights just above and below the activation threshold to bracket the deceleration level for activation. The drop height ranged between 0 and 1.07 m (0 and 3.5 ft). Except for the orientation angle of the tail cone relative to the wedges, the off-axis studies were carried out with the same procedure.

ELT Switch Vibration Test Apparatus

Because of the possible sensitivity of the ELT impact sensors or switches to high-frequency vibrations, additional impact tests and sinusoidal vibration tests were conducted to evaluate the sensitivity of the impact sensors to vibratory inputs.

Description of ELT inertia switches.- As noted previously, three different switch types were used in the ELT's examined in the study: (1) a cantilever beam (wire) with tip mass and silicone oil medium (fig. 6(a)), (2) a ball and magnet with a calibrated field intensity (fig. 6(b)), and (3) a rolomite switch (fig. 6(c)). The first two switch types work in conjunction with a holding transistor (SCR) which electronically latches the transmitter in the ON position after a chosen time delay or contact level.

The principle of operation of the cantilever beam switch is that when a force deflects the tip mass against the metal ring of the switch case for sufficient time, the ELT electronics are activated. For the ball and magnet when the force due to an acceleration exceeds the holding force of the magnet, the ball moves away from the magnet and closes the ELT electronics circuit. The rolomite switch does not necessarily require a holding circuit. In this switch, an inertial mass (hollow brass cylinder) is held by a blade spring wrapped around it. A second buckled blade spring is held close to two contacts. Under sufficient impact, the inertial mass strikes the blade spring causing it to snap through in the opposite direction to close the contacts and remain (theoretically) in this position until manually reset.

To aid the study and understanding of switch behavior, an experimental, low-frequency switch of the cantilever beam type was built for testing. A photograph of the assembled and disassembled switch is shown in figure 7. The switch had a thin brass cylindrical case with a metal cap on one end and a threaded insert for holding the cantilever beam on the other. The cantilever beam with tip mass was tuned to have a resonance of 14 Hz; the activation level was set for 5g to 7g; silicone oil provided the desired damping. A frequency of 14 Hz for the switch was chosen since it was between the 4 to 6 Hz basic force pulses and the local structural resonances of 30 to 200 Hz.

Description of switch vibration apparatus.- In addition to the instrumentation used with the impact apparatus, figure 8 shows the additional apparatus used for conducting the ELT switch vibration study. A permanent magnet shaker with required electronics was used for vibrating the base of a beam clamped in a vise. The inertia switches were mounted to the tip of the beam. The cantilever beam approach permitted the necessary displacements at the low-frequency vibrations with the limited ±0.635-cm (±0.25-in.) displacement capability of the shaker.

Instrumentation.- The same accelerometers and conditioning and recording equipment used for the impact tests were also used during the switch studies. Along with a test switch, an accelerometer for measuring the acceleration on the switch was attached to the tip of the cantilever beam. An oscillator signal routed through a power amplifier was used to drive the permanent magnet shaker. A 9-V dc battery wired across the switch provided a means of detecting switch closure. An oscillograph recorder was used to record the vibratory accelerations and the switch closure signals.

Test procedure.- With the ELT switch and accelerometer mounted to the tip of the cantilever beam, the length of the beam was adjusted in the vise clamp to give frequencies between approximately 5 and 100 Hz. The calibration unit was used to calibrate the accelerometer output on the oscillograph recorder to a desired range. The oscillator frequency was tuned to the beam resonance and the amplitude slowly increased until switch closure was noted. An oscillograph record was then made of the acceleration and switch closure signals for determining the activation level of the switch. The length of the beam was again adjusted for a different resonant frequency and the process repeated to obtain switch activation acceleration levels versus excitation frequency.

RESULTS AND DISCUSSION

Field Crash Tests of ELT's

Test data on ELT's have been acquired during crash tests of full-size aircraft at the Langley Impact Dynamics Research Facility. For example, figure 9 shows the different ELT's mounted in the cabin and tail cone area of a test airplane. Tests were conducted on the ELT's in two separate crash tests. The impact parameters were 27 m/sec (60 mph) for the two tests onto a concrete surface at (a) -30° flight path, -30° pitch and (b) -15° flight path, -15° pitch. Figure 10 presents the longitudinal decelerations on the airplane structure and the ELT units for the tests.

-30° flight path.- Decelerations at the -30° flight path are presented in figure 10(a). The top of figure 10(a) shows the recorded and filtered (20-Hz low pass filter) decelerations in the cabin area. The two histories at the top are on the cabin structure whereas the next two are on the ELT unit. The bottom of figure 10(a) presents similar data for the tail area. The data indicate the presence of similar high-frequency local vibrations prevalent in the crash tests discussed in the section "Crash Environment Determinations." The filtered data show that the low-frequency underlying crash pulse was approximately 15g which is well above the 5g to 7g threshold for ELT activation. A comparison of the ELT data in the tail cone area with those in the cabin indicates that the superimposed high-frequency vibrations were of somewhat lower magnitude in the tail than in the cabin, however; the basic crash pulse loading in this region of the airplane was also approximately 15g. The ELT in the cabin activated during the crash. In the tail, one of the two ELT's failed to activate; yet when the ELT was removed from the airplane immediately after the crash test and swung by hand, it did activate.

-15° flight path.- Figure 10(b) presents decelerations for the identical locations and the identical ELT units for the -15° flight-path crash test. A comparison of figure 10(b) with figure 10(a) indicates that both the superimposed local structural vibrations and the underlying crash pulse were lower for the -15° flight-path crash test. Likewise a comparison of the decelerations in the tail with decelerations in the cabin area (at the -15° flight path) indicate the attenuation of the magnitude of the local vibrations in the tail. The lower deceleration in the tail is reasonable since the area is further behind the initial contact region than the cabin. Furthermore the low-frequency crash pulse, between 5g and 10g (also above the 5g to 7g ELT activation threshold), is lower in magnitude and longer in duration than the -30° crash because at the lower angle there is less energy taken out in the initial impact and the airplane slides forward at a higher speed. ELT activations and nonactivations were identical to the previous -30° flight-path crash test. Once again when the ELT which failed to activate during the crash was removed and swung by hand, it activated. These types of behavior are typical of what has occurred in many cases and is one reason for exploring the vibration sensitivity of ELT inertia switches.

Impact Tests of ELT's

Figure 11 presents experimental results from the laboratory impact tests of 11 ELT units representing 7 different manufacturers. The ELT's represent both in-service and off-the-shelf units. Decelerations on the ELT units are presented as a function of time in milliseconds and activation status is noted.

Out of specifications - below threshold.- Typical longitudinal decelerations on three of five ELT units that activated during the impact study well below the proper specified threshold activation level of 5g are shown in figure 11(a). The structural resonance of the airplane tail cone may be noted on all the deceleration traces. Typically for these ELT units, the impact apparatus had to be lowered until the impact wedges (fig. 4) were just touching or actually penetrating the glass beads before activation of the units would not occur upon impact of the test apparatus.

Out of specification - above threshold.- Figure 11(b) presents longitudinal decelerations on two of three ELT units that did not operate at the proper specified deceleration level although, as noted in the figure, the ELT units experienced sufficient deceleration magnitude and time (T) durations to have activated even at the upper allowed 7g level. These particular ELT units also failed to properly activate even from the upper limit of impact velocity of the apparatus of approximately 4.57 m/sec (15 ft/sec).

Within specifications.- Decelerations for two of three units that activated within the ELT activation specification levels are shown in figure 11(c). The top traces are for one unit; the two bottom traces are for a second ELT. The upper traces for each ELT (labeled "ELT ON") show that when the ELT's experienced a deceleration pulse greater than 5g for at least 12.5 msec, activation of the unit occurred (activation verified by radio receiver). Similarly, the deceleration on the same unit at a slightly lower impact velocity shows that the magnitude of the deceleration was not above 5g for sufficient time and the ELT properly did not activate (traces labeled "ELT OFF"). A comparison of the measured time to reception of signal from ELT's indicates a wide spread in delay time for transmission to occur. Whether some part of the delay was a result of some of the units being out of specifications could not be assessed from these tests.

Off-Axis Impacts

The previous data are for impacts along the longitudinal axis of the tail cone in the ELT impact test apparatus. Tests were also conducted to evaluate off-axis impacts on the activation of ELT's. The cylindrical section with the airplane tail cone mounted on the platform (fig. 4) can be rotated relative to the impact wedges of the ELT impact test apparatus. Any angle between 0° and 90° can be obtained in this fashion so that the impact wedges can be set at any desired angle to the sensitivity axis of the ELT mounted in the tail cone. Figure 12 illustrates typical results of the off-axis deceleration input study. Angles, α, of 0°, 15°, 30°, 45°, and 90° were used in the investigation. An ELT which was within the activation specification levels was used in the tests. The data illustrated in figure 12 are for an angle of 30°. In the top part of the figure, the component of the impact deceleration acting along the longitudinal sensitivity axis of the ELT was of sufficient magnitude to exceed the activation threshold and the ELT activated. On the other hand, the bottom figure shows that at a slightly lower deceleration level, the magnitude of the component along the sensitivity axis of the ELT was not sufficient to activate the ELT. Analysis of all the off-axis data indicated that, as expected, if the component of deceleration along the ELT sensitivity axis is greater than the 5g threshold, the ELT activates and forces perpendicular to the sensitive axis of the ELT did not cause activation problems.

Anomalous Activations

Figure 13 illustrates anomalous behavior exhibited by an ELT unit used in the impact tests. The deceleration trace at the top of the figure is for an impact with the ELT mounted in the tail cone of the ELT impact test apparatus. As may be noted in the first two traces in the figure, the ELT experienced deceleration magnitude and duration well exceeding the 5g and 7g threshold levels but the ELT did not properly activate. However, when the ELT was removed from the tail cone and whirled by hand to produce the deceleration (bottom trace) that just exceeded the 5g threshold, the ELT activated. Based upon these results, it was concluded that the cantilever beam inertia switch was being affected by the higher frequency vibrations. Additional results on the evaluation of the sensitivity of the impact sensors to local vibrations are discussed in subsequent sections.

ELT Switch Vibrations and Analysis

Several of the ELT impact switches were mounted in the ELT impact test apparatus (fig. 4) for evaluation, and sinusoidal vibration tests with the apparatus shown in figure 8 were also conducted to evaluate the sensitivity of impact sensors. Results of these tests are shown in figures 14 to 16.

Inertia switch chatter.- Figures 14(a) and 14(b) indicate that ELT sensors respond to the structural vibrations superimposed on the lower frequency input deceleration pulse obtained with the impact test apparatus. Figure 14(a) shows results for two cantilever beam switches. The top trace in the figure is the impact deceleration, whereas the lower two traces are switch contacts for both a 5g and a 7g threshold switch. The contact of the switches is being affected by the higher frequency vibrations on the input deceleration pulse. Responses of a ball and magnet and a rolamite switch to pulse inputs with higher frequency vibrations are shown in figure 14(b). The top traces are the input to the ball and magnet switch and the switch contact behavior. The two bottom traces are for the rolamite switch. Both sensors show chatter from the superimposed higher frequency structural vibrations.

The impact behavior of the experimental low-frequency switch is shown in figure 14(c). The top trace in the figure shows the deceleration pulse with the higher frequency vibrations, which was imposed on the experimental switch. Neither the underlying deceleration pulse nor the vibrations caused the switch to make contact in this case. In the bottom trace, a deceleration pulse exceeded the activation threshold of the low-frequency switch, and switch contact occurred. Data for these tests indicate that the switch made contact as it should have but was not affected by or was sensing the higher frequency structural vibrations present on the basic input pulse. This behavior is highly desirable to minimize possible false activations from structural vibrations during noncrash situations or nonactivations during crashes because of the vibration-induced on-off—on-off contact of the switch which may prevent ELT electronic latching times from being achieved.

Switch vibration sensitivity.- In figure 15, a classical plot used to describe the behavior of a simple oscillator is presented to allow a comparison between the response of the experimental low-frequency switch (14-Hz cantilever) and a commercial switch (44-Hz cantilever). In nondimensional terms, the ratio of the switch gap displacement Δ (for switch contact to occur) to the switch base acceleration $\ddot{U}$ at contact is given as a function of the ratio of sinusoidal forcing frequency ω to the undamped switch natural frequency ω_n. Three curves for damping ratios C/C_c of 0.0, 0.7, and 2 are presented out of the family of curves possible depending on the damping values (C is actual damping and C_c is critical damping). As indicated in the figure, the experimental 14-Hz switch had a damping ratio of 0.7. The switch will respond identically to the amplitude of input frequencies up to essentially its undamped frequency of 14 Hz ($\omega/\omega_n = 1$) but becomes less responsive to those frequencies above 14 Hz. For example, at approximately 42 Hz, 3 times the natural frequency ($\omega/\omega_n = 3$), the response ratio is only 0.1. On the other hand with its higher natural frequency, the commercial 44-Hz switch (with $C/C_c = 2$) still has a ratio of 1/10 at approximately 88 Hz ($\omega/\omega_n = 2$). The important point to note is that, even being more highly damped, the commercial switch is too sensitive to the frequencies in the range of 30 Hz and above which places it too much into the purely local structural vibration regime of airplanes. Data on switches presented in the form of this figure also allow one to readily determine the damping ratio in the sensor during experimentation with a switch design of a known undamped natural frequency. By testing the switch at $\omega/\omega_n = 1$, the switch damping can be found from a nondimensional plot such as shown here.

In figure 16, additional results from the switch sensitivity tests are presented for both the experimental 14-Hz cantilever switch and the 44-Hz commercial cantilever switch of the previous figure along with ball and magnet switches, one a unidirectional and one with a radial sensitivity. Switch base displacement for switch contact to occur is plotted as a function of the excitation frequency. Lines of constant g units are also shown in the figure for reference. The data indicate that below approximately 20 Hz the experimental cantilever switch, the commercial switch, and the two ball and magnet switches respond essentially the same. The only difference between the 44-Hz commercial cantilever and the other switches is that it is a 7g threshold switch instead of a 5g switch. Note, however, that, above approximately 20 Hz, the displacement of the switch base for switch contact to occur approaches the switch gap of 6.35 mm (0.25 in.) in the 14-Hz experimental switch whereas the 44-Hz switch displacement continues to decrease and approaches its switch gap of 0.635 mm (0.025 in.) at much higher frequencies. At the higher frequencies, the accelerations of the low-frequency 14-Hz switch must be very large before switch contact can occur. On the other hand, the 44-Hz commercial switch makes contact at substantially lower displacements; for example, at 44 Hz the commercial switch will make contact at 24g, whereas 50g is required for the 14-Hz switch. Similarly, at 100 Hz, the commercial switch will contact at 54g, but the low-frequency switch requires 260g for contact to occur.

Data for the two different ball and magnet switches are quite revealing. At the low end below 20 Hz, the response is essentially the same as the other type of switches. However, with increasing frequency the g level for contact of the switch continues to be essentially 5g to 6g. At approximately 90 Hz, the level increased to only 9g. It is interesting to note that in reference 5, an ELT brand which had one of the worst false activation records was one that uses the ball and magnet switch. Based upon the data in this figure, that record can be better understood.

Thus from the switch sensitivity study, it can be seen that, by the design of the switch resonance, the sensor can be made less sensitive to higher frequency structural responses but at the same time still be sensitive to the low-frequency crash-type pulses of actual interest. The less sensitivity to the higher frequencies is beneficial both during normal operations and during crash situations. During normal operations the g units would have to be extremely high (very unlikely) before switch contact could occur. During crash situations, although present on the crash pulse, the sensor would be less likely to be confused by the responses if they were large enough in magnitude to cause switch contact. Furthermore, it is not difficult to see local resonances with periods both below and above ELT electronic latching times. This could lead to activation problems as well as false activations from vibratory input.

SUMMARY OF RESULTS

This paper has presented the results of full-scale crash tests and laboratory impact tests and vibration studies on emergency-locator-transmitter (ELT) activation problems. The results from these studies are summarized as follows:

(1) Data from crash tests at the Langley Research Center indicate that the longitudinal crash environment imposed on ELT's in crash situations is basically a low-frequency loading pulse well below 10 Hz; however, high amplitude, local structural resonances which may be between 30 to 200 Hz, are superimposed on the crash pulse.

(2) With regard to frequency of structural vibrations and basic shape of deceleration pulse, good correlation was obtained between simulated crash pulses with superimposed structural vibrations in a special ELT impact test apparatus and actual crash test results.

(3) Crash tests and laboratory impact tests indicated similar erratic activation behavior of ELT units.

(4) Many ELT units did not operate within the specified activation threshold.

(5) Impact sensors typical of those used in ELT's were found to be too sensitive to structural vibrations.

(6) The vibration sensitivity of the impact sensors is undesirable since local structrual vibrations of the airplane could cause unwarranted activations during normal airplane operations or prevent the sensors from properly activating the ELT in a crash situation (depending on the frequency of the vibrations).

(7) A low-frequency switch design was found to possess desirable response characteristics in that it is sensitive to low-frequency crash pulses and the inherent nature of the design is less sensitive to higher frequencies in the range of local structural vibrations.

(8) Research results from this study and others will form the basis of recommendations to FAA and Industry on ELT's through a Radio Technical Commission for Aeronautics (RTCA) report.

REFERENCES

1. The Occupational Health and Safety Act of 1970. Public law 91-596, Section 31, 1970.

2. RTCA SC-119: Minimum Performance Standards - Emergency Locator Transmitters. Doc. No. DO-147, Radio Tech. Comm. Aeronaut., Nov. 1970. (Superseded by RTCA Doc. No. DO-168.)

3. RTCA SC-127: Minimum Performance Standards - Emergency Locator Transmitters. Doc. No. DO-168, Radio Tech. Comm. Aeronaut., Jan. 1979. (Supersedes RTCA Doc. No. DO-147.)

4. Special Study - Emergency Locator Transmitters: An Overview. NTSB-AAS-78-1, Jan. 26, 1978.

5. Toth, S.; and Gershkoff, I.: Control of ELT False Alarms. Publ. 1362-01-1-2032 (Contract NASW-3229), ARINC Res. Corp., Oct. 1979. (Available as NASA CR-162502.)

6. Vaughan, Victor L., Jr.; and Alfaro-Bou, Emilio: Impact Dynamics Research Facility for Full-Scale Aircraft Crash Testing. NASA TN D-8179, 1976.

7. Alfaro-Bou, Emilio; and Vaughan, Victor L., Jr.: Light Airplane Crash Tests at Impact Velocities of 13 and 27 m/sec. NASA TP-1042, 1977.

8. Castle, Claude B.; and Alfaro-Bou, Emilio: Light Airplane Crash Tests at Three Flight-Path Angles. NASA TP-1210, 1978.

9. Fasanella, Edwin L.; and Alfaro-Bou, Emilio: NASA General Aviation Crashworthiness Seat Development. [Preprint] 790591, Soc. Automot. Eng., Apr. 1979.

10. Castle, Claude B.; and Alfaro-Bou, Emilio: Light Airplane Crash Tests at Three Roll Angles. NASA TP-1477, 1979.

11. Hayduk, Robert J.: Comparative Analysis of PA-31-350 Chieftain (N44LV) Accident and NASA Crash Test Data. NASA TM-80102, 1979.

12. Vaughan, Victor L., Jr.; and Alfaro-Bou, Emilio: Light Airplane Crash Tests at Three Pitch Angles. NASA TP-148, 1979.

13. Brooks, George W.; and Carden, Huey D.: A Versatile Drop Test Procedure for the Simulation of Impact Environments. Noise Contr., Shock & Vib., vol. 7, no. 5, Sept.-Oct. 1961, pp. 4-8.

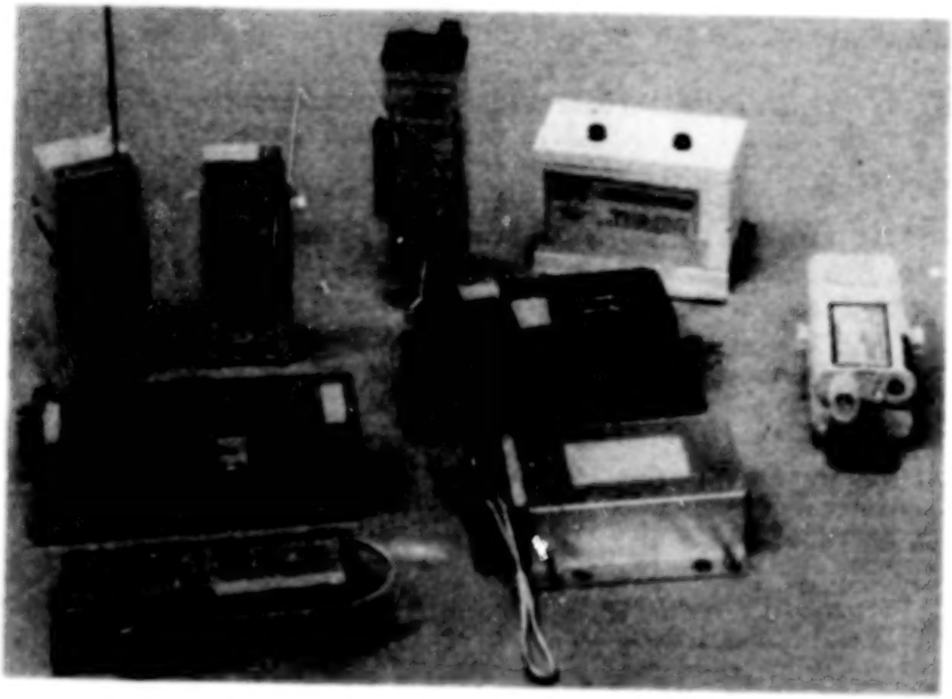

Figure 1.- Typical ELT's.

ELT
ELT MOUNTING BRACKET

Figure 2.- Typical mounting assembly used in tests.

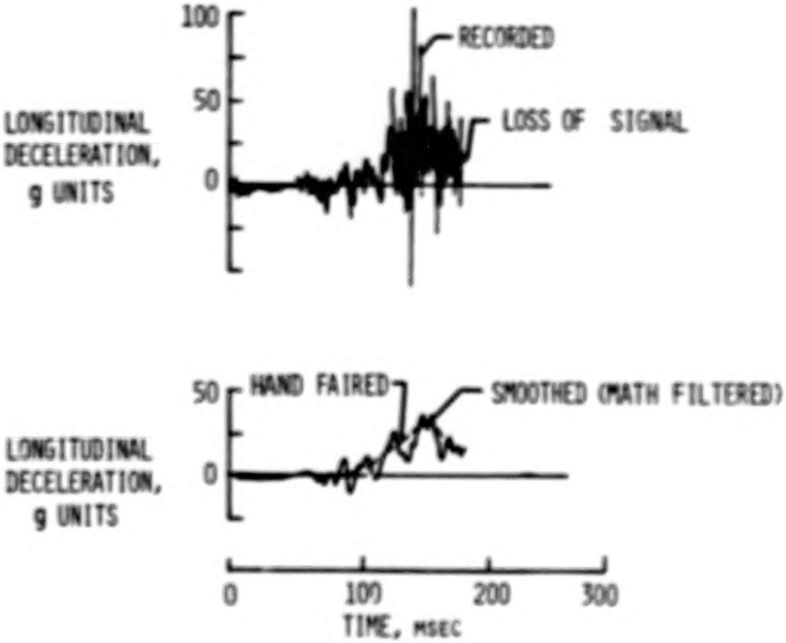

(a) Concrete surface.

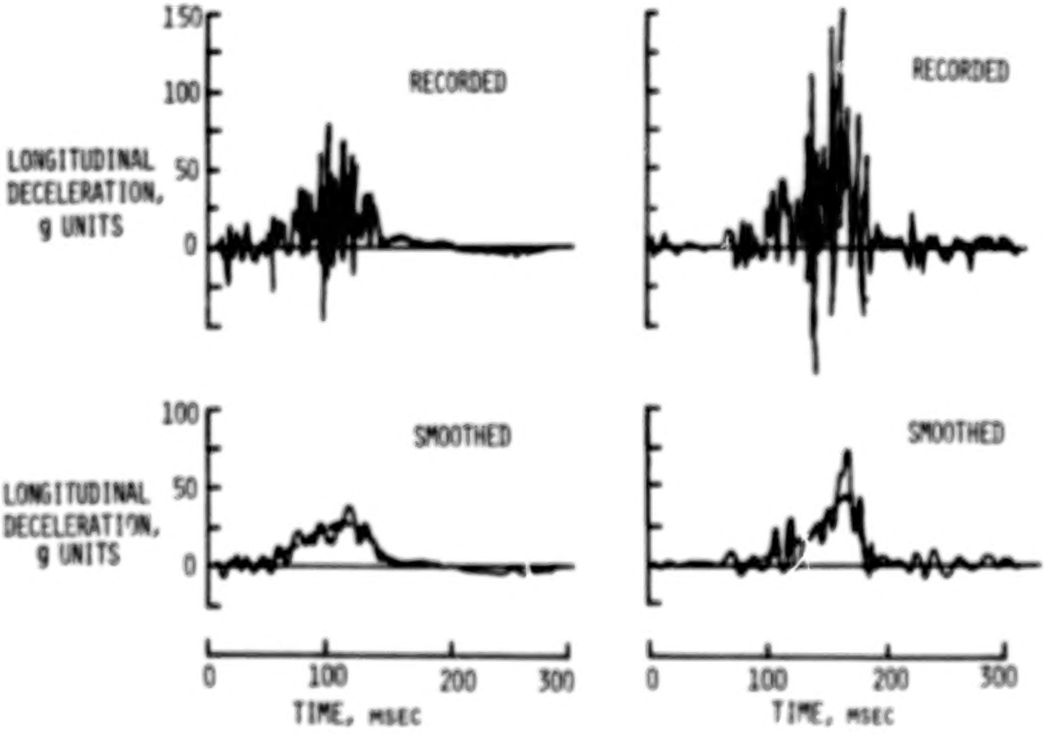

(b) Dirt surfaces.

Figure 3.- Typical measured longitudinal deceleration pulses for three different airplanes.

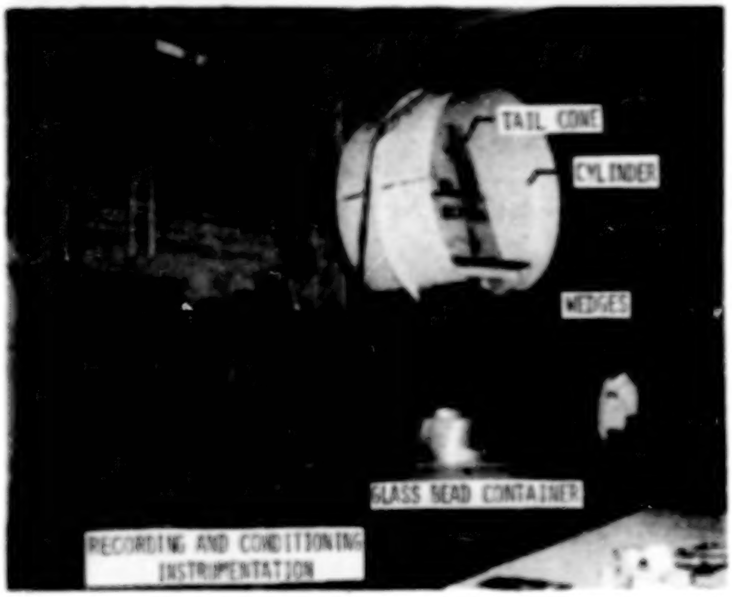
TAIL CONE
CYLINDER
WEDGES
GLASS BEAD CONTAINER
RECORDING AND CONDITIONING INSTRUMENTATION

Figure 4.- Laboratory ELT impact test apparatus.

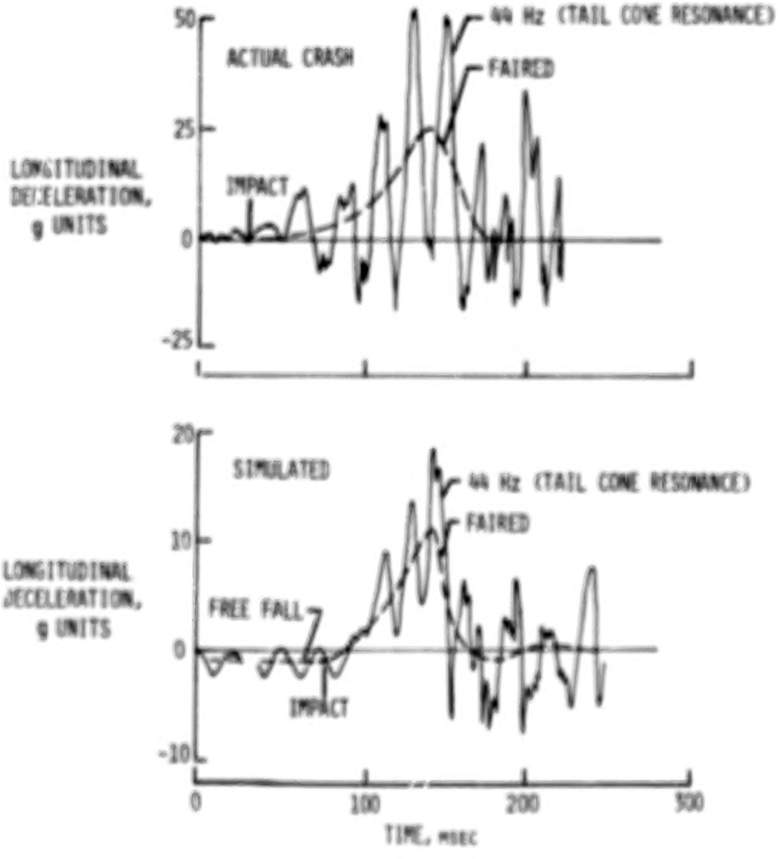

Figure 5.- Comparison of actual and simulated longitudinal deceleration crash pulse on ELT.

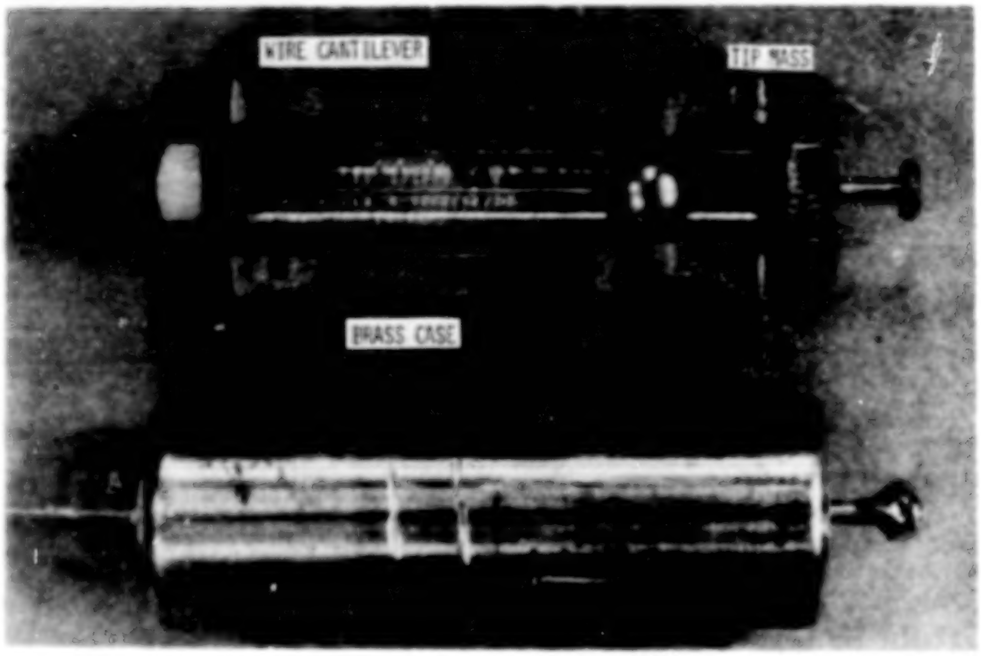
WIRE CANTILEVER
TIP MASS
BRASS CASE

(a) Cantilever beam switch.

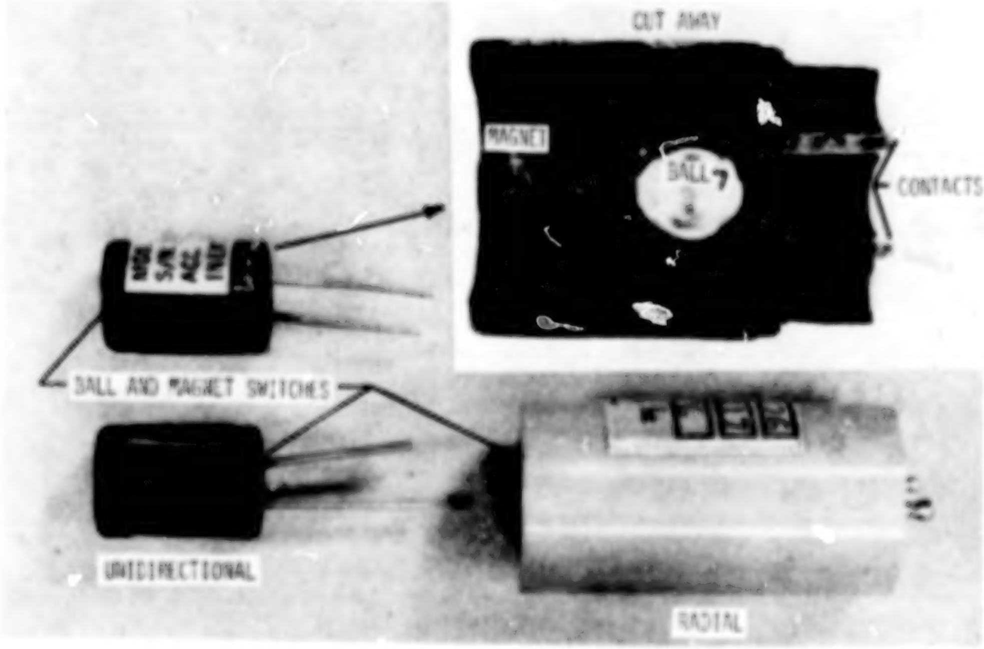
CUT AWAY
MAGNET
BALL
CONTACTS
BALL AND MAGNET SWITCHES
UNIDIRECTIONAL
RADIAL

(b) Ball and magnet switches.

Figure 6.- Typical ELT inertia switches.

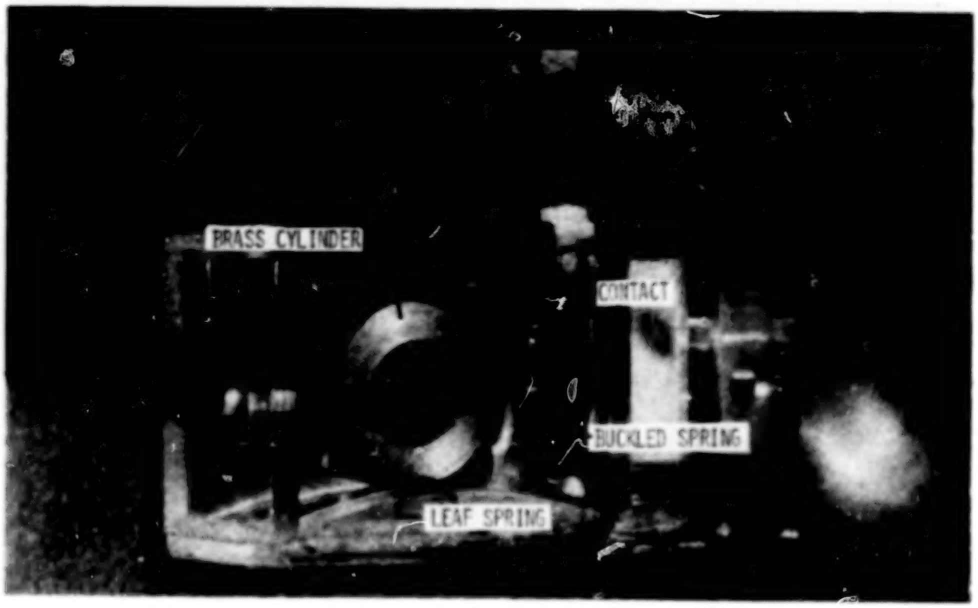
BRASS CYLINDER
CONTACT
BUCKLED SPRING
LEAF SPRING

(c) Rolomite switch.

Figure 6.- Concluded.

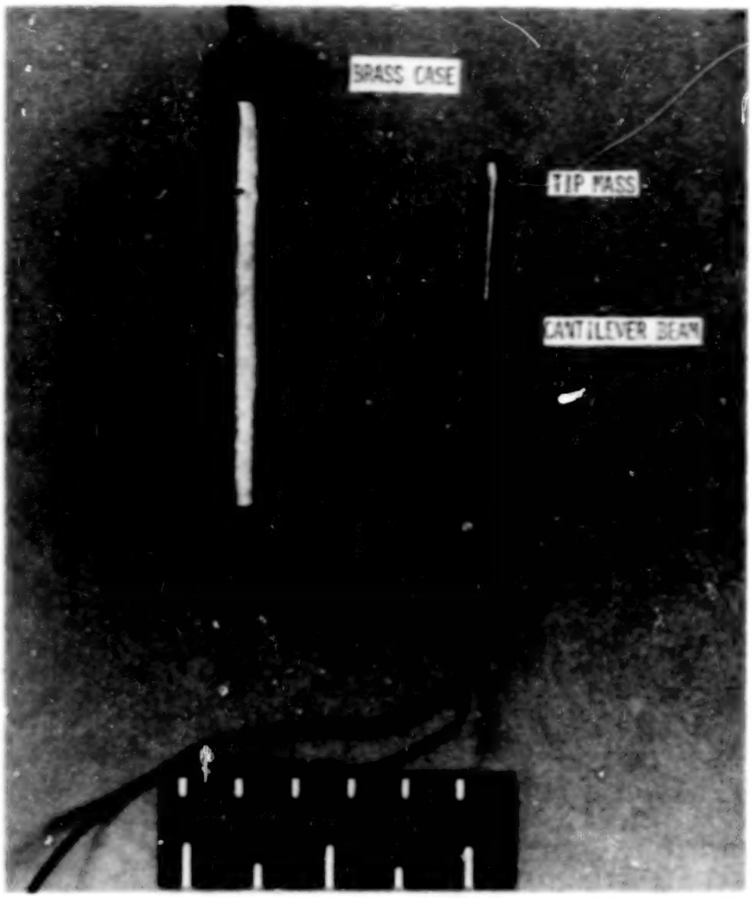
BRASS CASE
TIP MASS
CANTILEVER BEAM

(a) Disassembled.

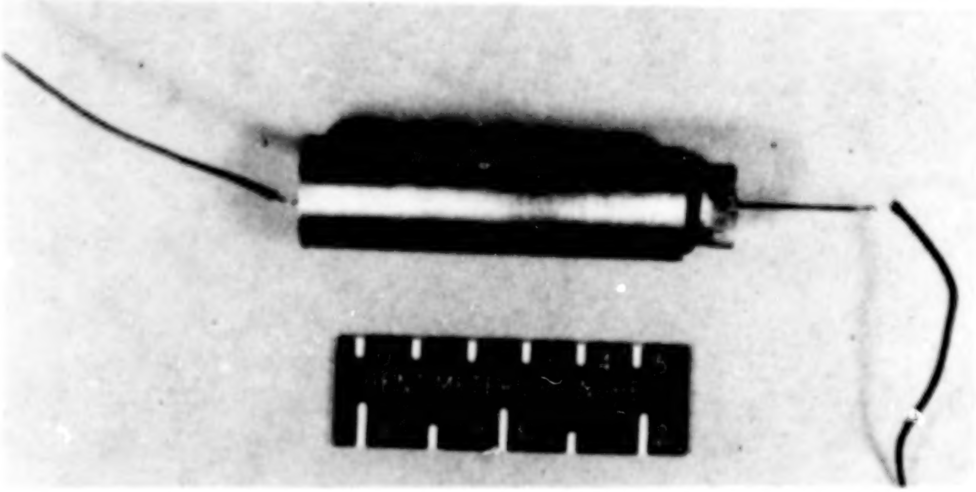

(b) Assembled.

Figure 7.- Experimental low-frequency switch.

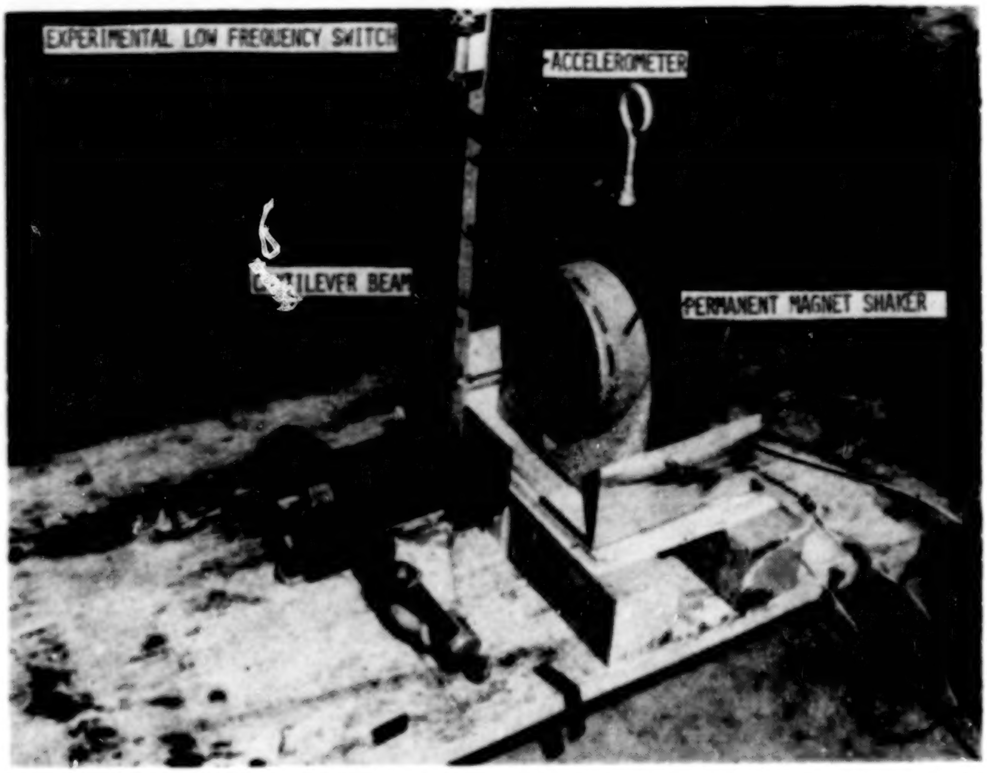
EXPERIMENTAL LOW FREQUENCY SWITCH
ACCELEROMETER
CANTILEVER BEAM
PERMANENT MAGNET SHAKER

Figure 8.- Switch vibration apparatus.

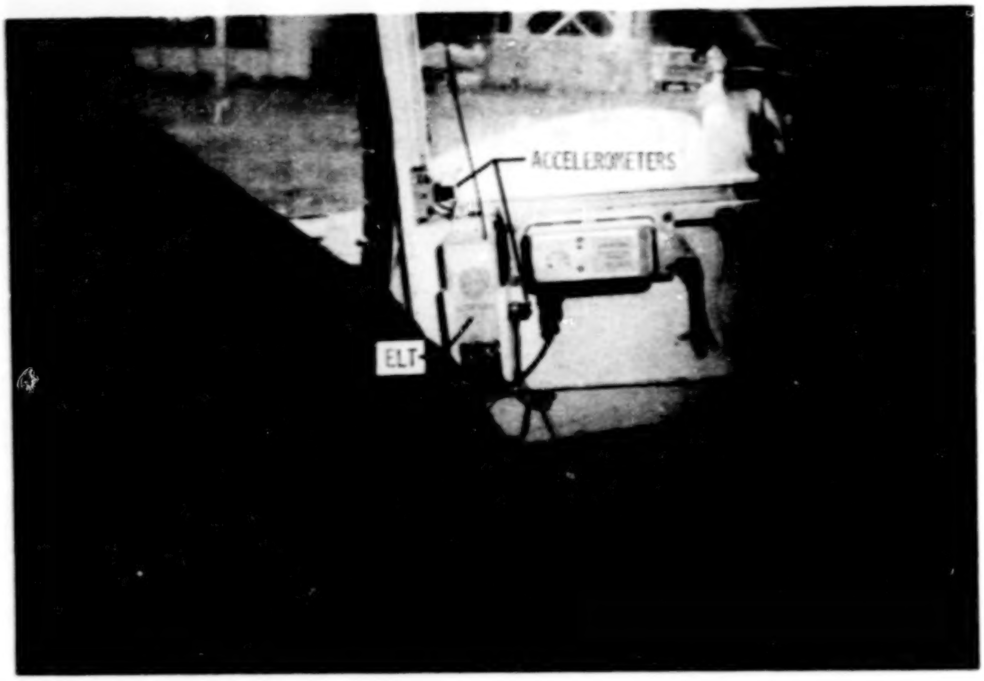
ACCELEROMETERS
ELT

(a) Cabin area.

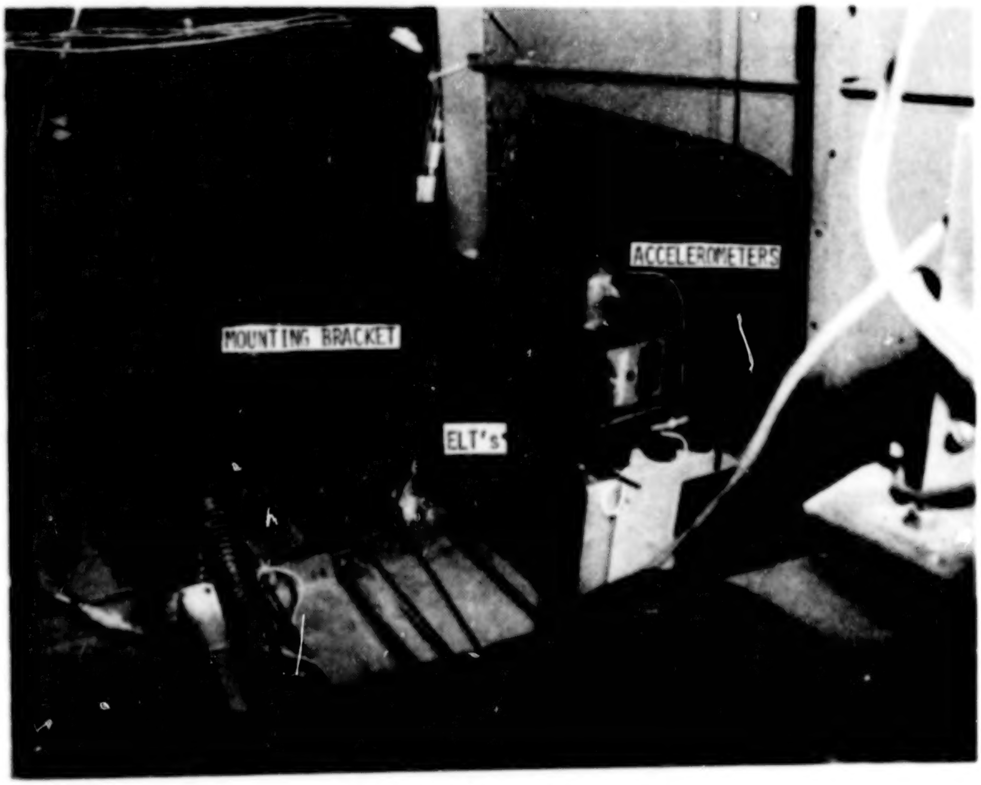
ACCELEROMETERS
MOUNTING BRACKET
ELT's

(b) Tail cone area.

Figure 9.- ELT's mounted in test airplane for crash tests.

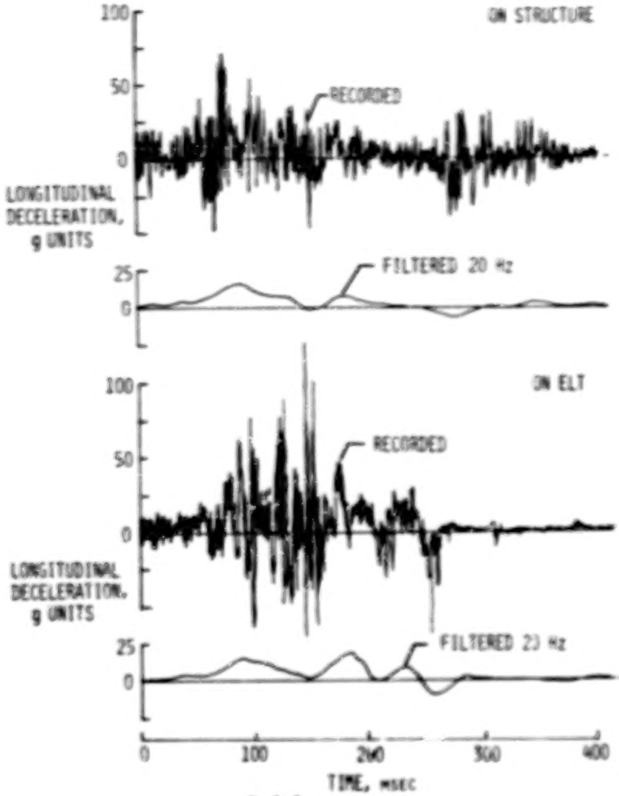

Cabin area

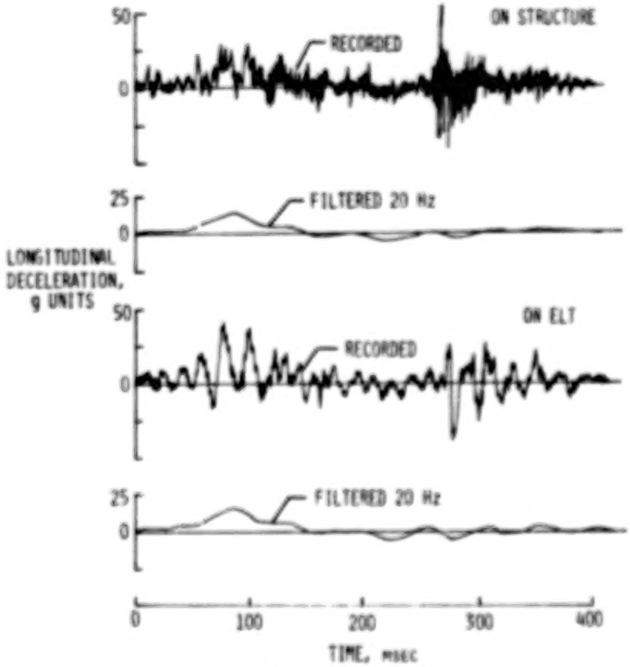

Tail cone area

(a) Flight path, -30°; pitch angle, -30°.

Figure 10.- Longitudinal decelerations in crash test airplane. Velocity, 27 m/sec (60 mph).

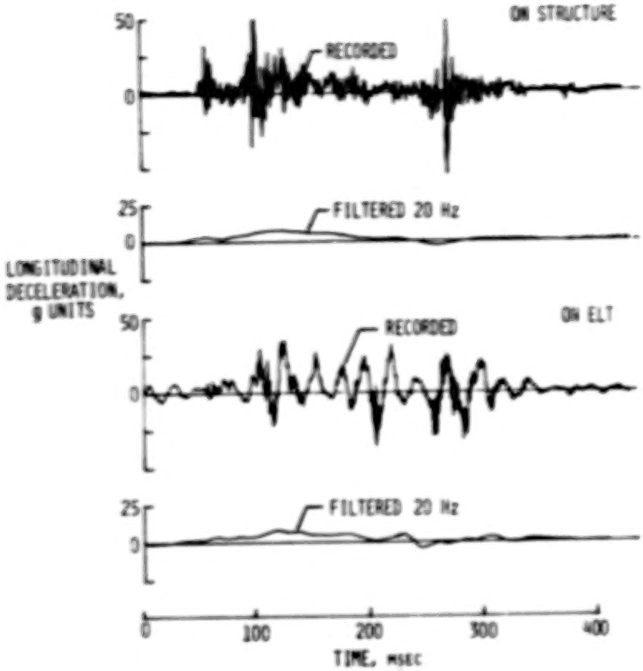

Cabin area

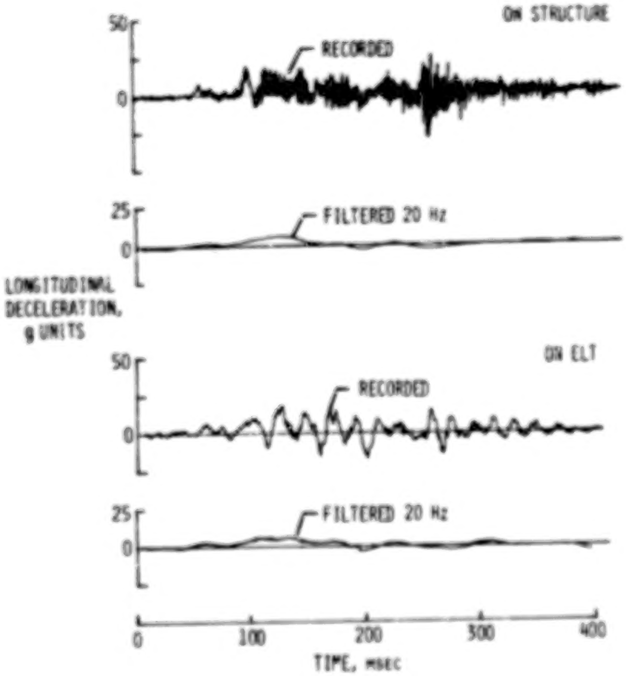

Tail cone area

(b) Flight path, -15°; pitch angle, -15°.

Figure 10.- Concluded.

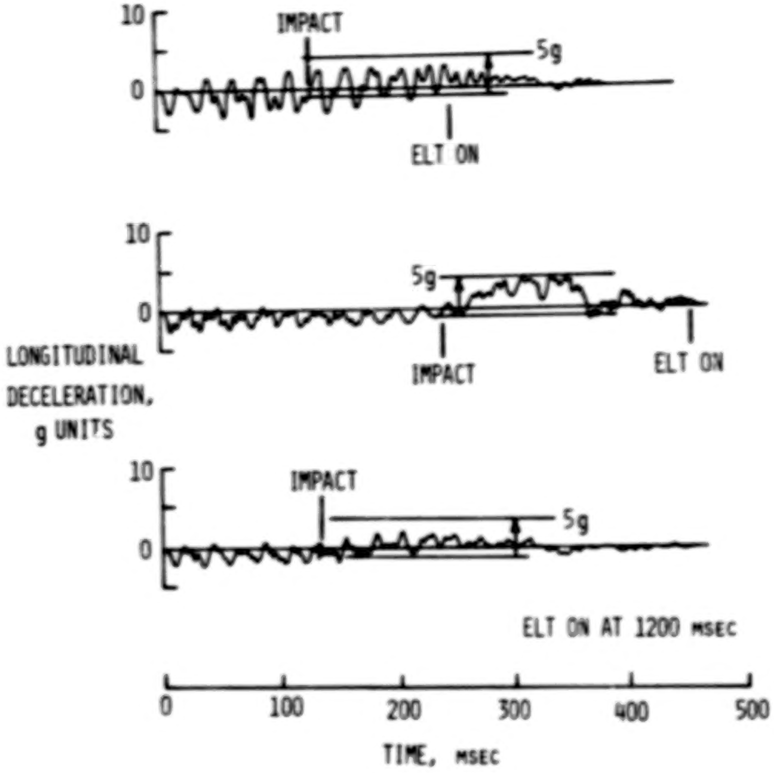

(a) Out of specifications - below threshold.

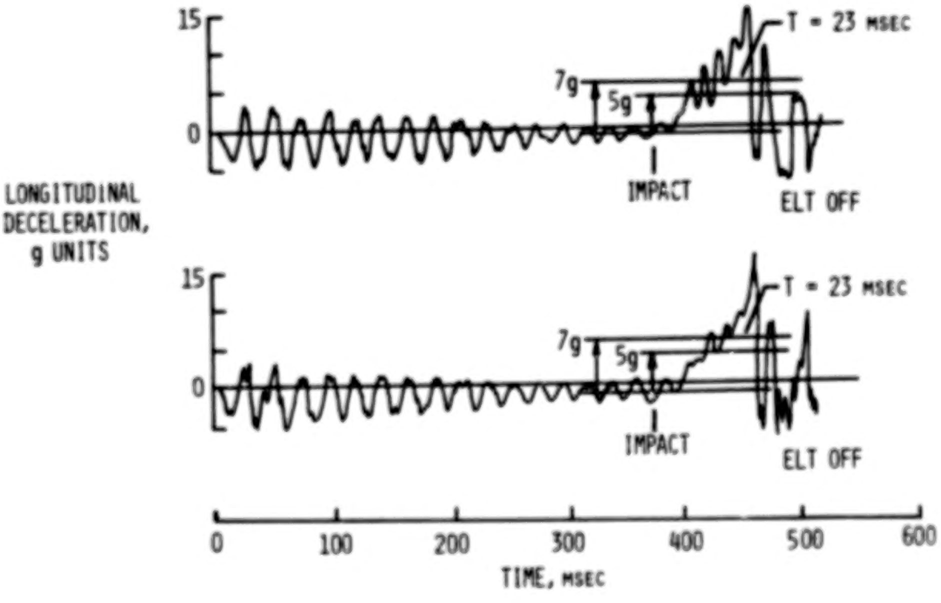

(b) Out of specifications - above threshold.

Figure 11.- Typical laboratory impact test results on ELT activation.

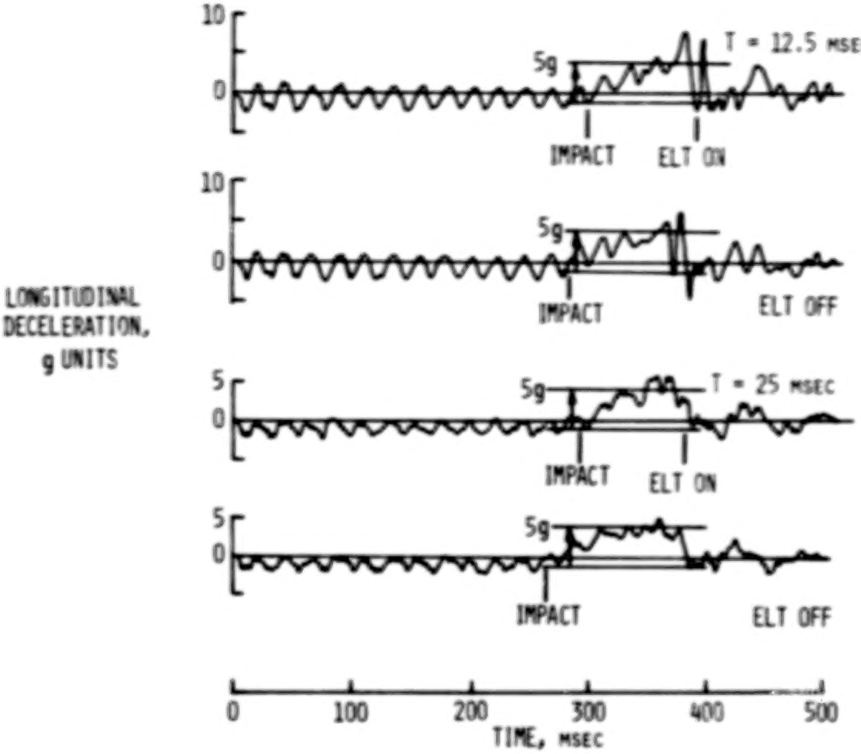

(c) Within specifications.

Figure 11.- Concluded.

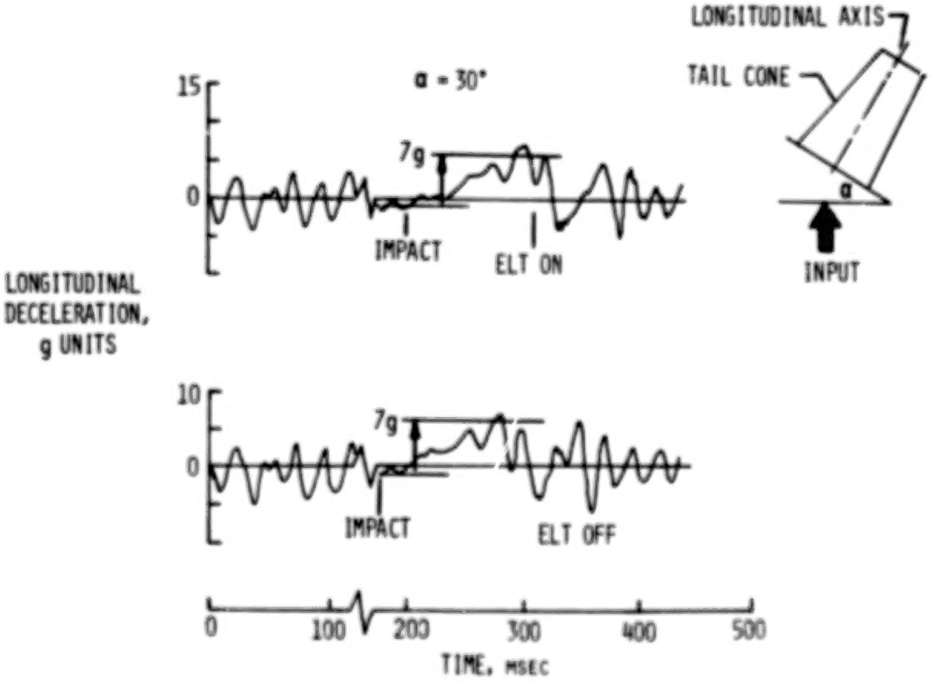

Figure 12.- Off-axis impact results.

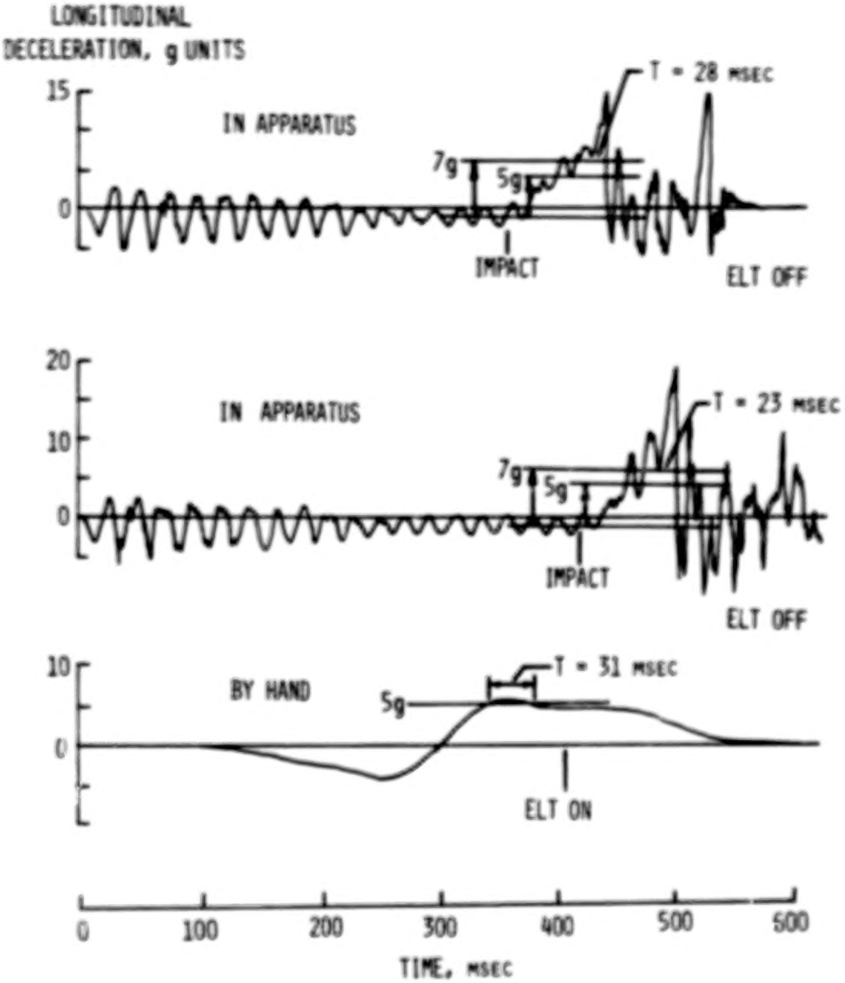

Figure 13.- Anomalous ELT activation behavior.

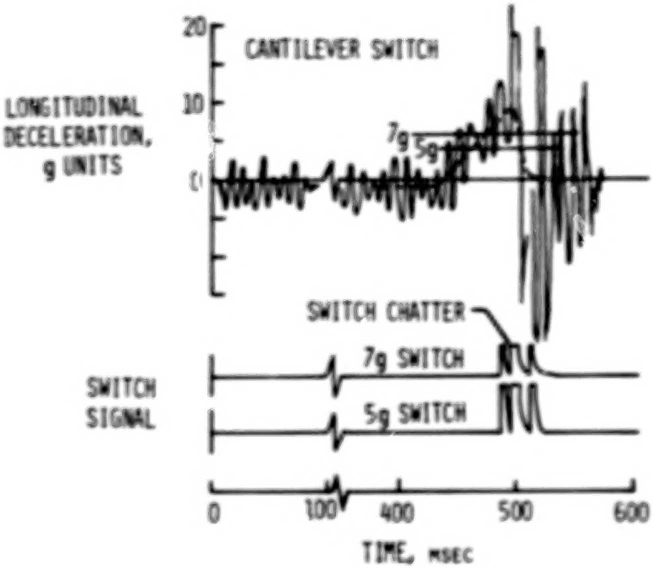

(a) Cantilever beam switch.

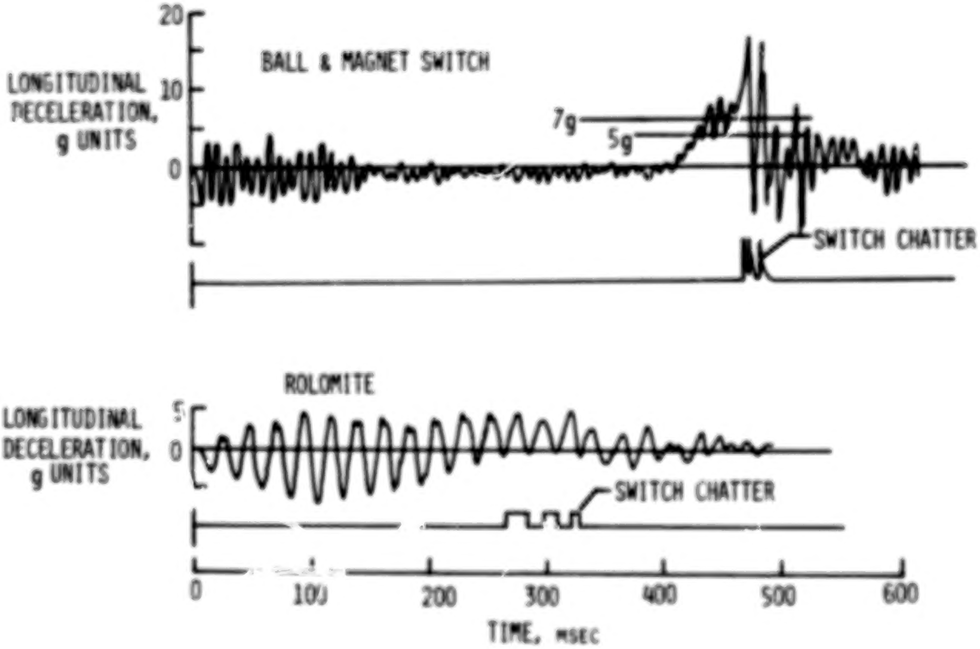

(b) Ball and magnet and rolomite switches.

Figure 14.- Inertia switch chatter during impact tests.

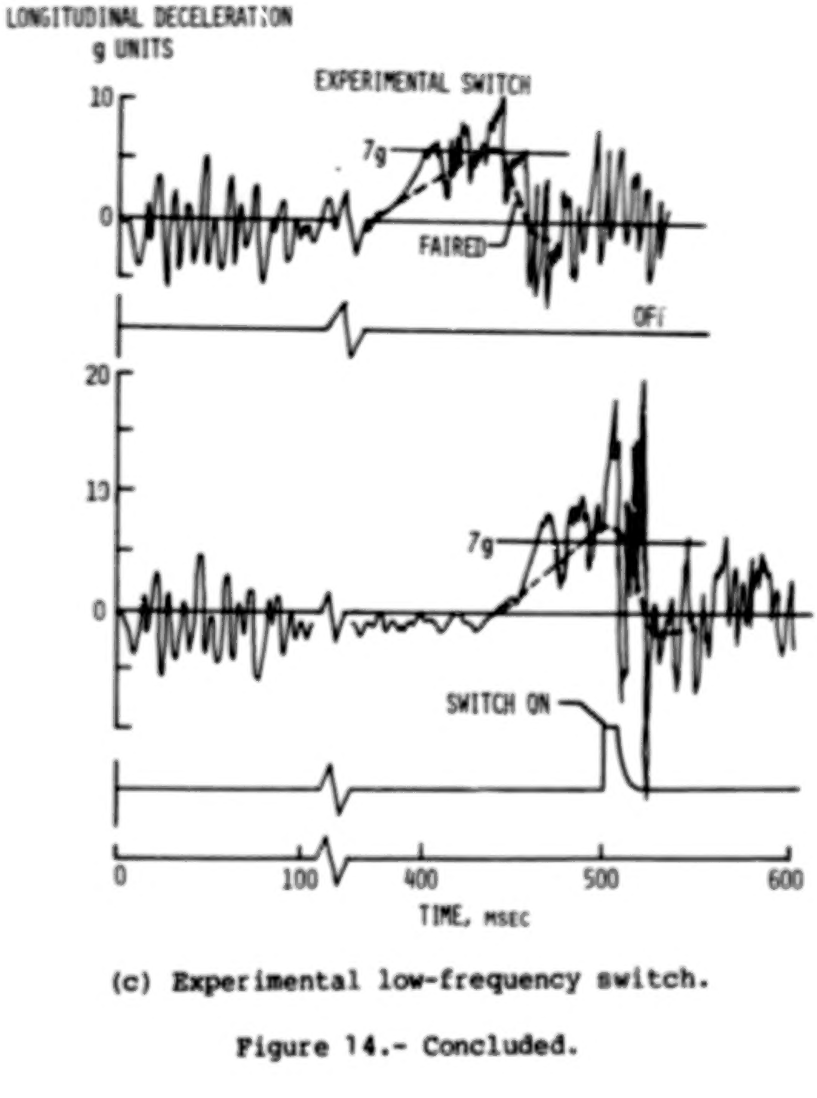

(c) Experimental low-frequency switch.

Figure 14.- Concluded.

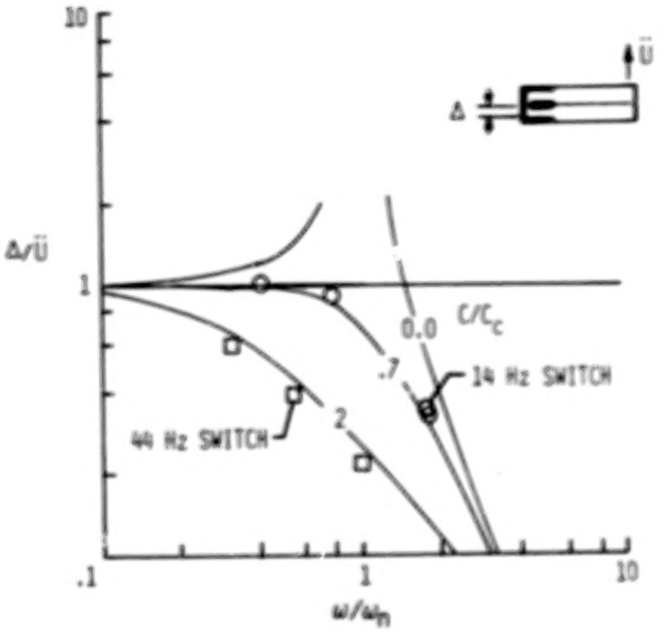

Figure 15.- Sinusoidal vibration test results for ELT switches.

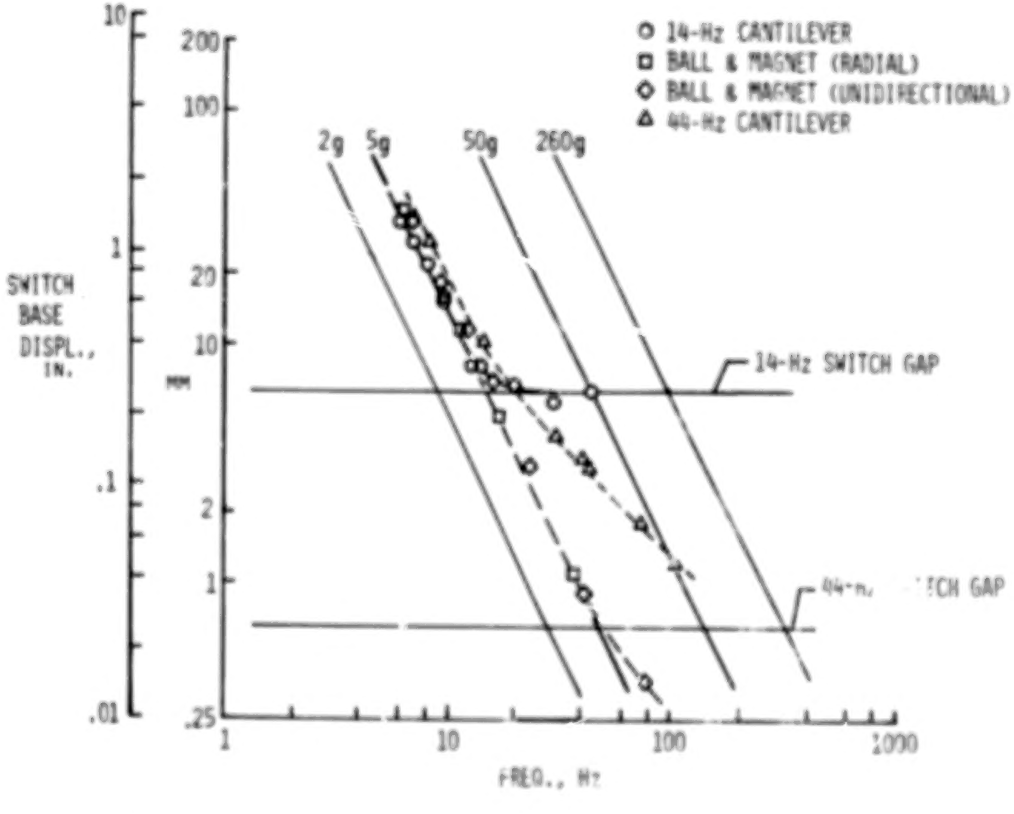

Figure 16.- ELT switch vibration displacement as a function of excitation frequency.

BLANK PAGE

BLANK PAGE

EXTINGUISHING IN-FLIGHT ENGINE FUEL-LEAK FIRES WITH DRY CHEMICALS

Robert L. Altman

Ames Research Center

SUMMARY

When fuels leak onto surfaces of an operating engine they can ignite when engine case temperatures exceed 540°C (1000°F). As aircraft flight speeds are increased, engine case temperatures, bleed air temperatures, maximum air velocities, and fire extinguishant storage temperature requirements also increase, making the task of extinguishing fuel-leak fires in flight even more difficult. We have undertaken to find new fire extinguishants that are more effective than the CF_3Br, CF_2Br_2, and CF_2ClBr now in use. Besides testing commercially available dry chemicals, such as $NaHCO_3$, $KHCO_3$, KCl, and $KC_2N_2H_3O_3$(ICI Monnex ®), we have tried to develop and test new dry-powder fire extinguishants. Specifically, our interest has been in developing new dry-powder extinguishants that, when discharged into a jet engine fuel-leak fire, would stick to the hot surfaces. Moreover, after putting out the initial fire, these extinguishants would act as anti-reignition catalysts, even when the fuel continued to leak onto the heated surface.

INTRODUCTION

Previous fire extinguishment tests with Halons like CH_3Br, CH_2ClBr, CF_3Br, and CF_2ClBr have shown that the minimum Halon concentration in the gas phase above a liquid pool or spray fire required to extinguish the fire at first increases with increased airflow at low flow rates but then decreases at still higher flow rates. In both situations, however, the total weight of extinguishant required to put out the fire increased with increasing airflow (refs. 1, 2). To counter this, an increase in the Halon discharge rate by increasing the stored nitrogen pressure or by increasing the extinguishant discharge temperature will decrease the total weight of Halon required for complete extinguishment (refs. 3, 4). The reduced weight effectiveness of Halons with increased airflow has induced Graviner, the manufacturer of the Concorde nacelle fire extinguishing system, to install a pair of airflow-reducing flaps upstream of the compressor; the flaps reduce the nacelle airflow to a minimum before Halon is discharged after an engine fuel-leak fire has been detected (ref. 5).

The longer fuel-leak fires burn before extinguishment is begun, the harder they are to extinguish; also, long-burning fires can start up again once the extinguishant is exhausted because the surroundings are then hot

Part 2

SESSION IV - OPERATING PROBLEMS AND POTENTIAL SOLUTIONS
Chairman: H. W. Schmidt

22. WAKE VORTEX ATTENUATION FLIGHT TESTS: A STATUS REPORT 387 1/A14
Marvin R. Barber and Joseph J. Tymczyszyn

23. BASIC RESEARCH IN WAKE VORTEX ALLEVIATION USING A VARIABLE TWIST WING 409 1/C8
Dana J. Morris and G. Thomas Holbrook

24. PNEUMATIC BOOT FOR HELICOPTER ROTOR DEICING 425 1/D11
Bernard J. Blaha and Peggy L. Evanich

25. AIRCRAFT OPERATING EFFICIENCY ON THE NORTH ATLANTIC - A CHALLENGE FOR THE 1980'S 445 1/F3
Robert Steinberg

26. FIREWORTHINESS OF TRANSPORT AIRCRAFT INTERIOR SYSTEMS 453 1/F12
John A. Parker and D. A. Kourtides

27. COMBUSTION TOXICOLOGY OF EPOXY/CARBON FIBER COMPOSITES 481 2/A14
D. E. Cagliostro

28. THE USE OF ANTIMISTING KEROSENE (AMK) IN TURBOJET ENGINES 499 2/C10
Harold W. Schmidt

29. NASA/FAA GENERAL AVIATION CRASH DYNAMICS PROGRAM 511 2/D8
Robert G. Thomson, Robert J. Hayduk, and Huey D. Carden

SESSION V - FLIGHT EXPERIENCES AND GROUND OPERATIONS
Chairman: J. L. McCarty

30. CURRENT RESEARCH IN AIRCRAFT TIRE DESIGN AND PERFORMANCE 543 2/F12
John A. Tanner and John L. McCarty

31. REVIEW OF ANTISKID AND BRAKE DYNAMICS RESEARCH 555 2/G10
Sandy M. Stubbs and John A. Tanner

32. STUDIES OF SOME UNCONVENTIONAL SYSTEMS FOR SOLVING VARIOUS LANDING PROBLEMS 569 3/A12
T. J. W. Leland, J. R. McGehee, and R. C. Dreher

33. RECENT PROGRESS TOWARDS PREDICTING AIRCRAFT GROUND HANDLING PERFORMANCE 583 3/B12
Thomas J. Yager and Ellis J. White

34. THE NASA DIGITAL VGH PROGRAM - EARLY RESULTS 613 3/D14
Norman L. Crabill and Garland J. Morris

35. EVALUATION OF EMERGENCY-LOCATOR-TRANSMITTER PERFORMANCE IN REAL AND SIMULATED CRASH TESTS 625 3/E12
Huey D. Carden

36. EXTINGUISHING IN-FLIGHT ENGINE FUEL-LEAK FIRES WITH DRY CHEMICALS 655 3/G14
Robert L. Altman

SESSION VI - ACOUSTICS AND NOISE REDUCTION
Chairman: H. G. Morgan

37. RECENT DEVELOPMENTS IN AIRCRAFT ENGINE NOISE REDUCTION TECHNOLOGY 671 4/B4
James R. Stone and Charles E. Feiler

38. SOURCES, CONTROL, AND EFFECTS OF NOISE FROM AIRCRAFT PROPELLERS AND ROTORS 699 3/D4
John S. Mixson, George C. Greene, and Thomas K. Dempsey

39. NASA PROGRESS IN AIRCRAFT NOISE PREDICTION 721 4/E12
J. P. Raney, S. L. Padula, and W. E. Zorumski

40. AIRPORT NOISE IMPACT REDUCTION THROUGH OPERATIONS 759 5/A13
Richard DeLoach

ATTENDEES 779 5/C5

enough to reignite the fuel (refs. 6-8). Therefore, we have devised an experimental procedure for rating the effectiveness of fire extinguishants in controlling fuel-leak fires. In this technique, the effectiveness of an extinguishant is measured in terms of the delay between initial extinguishment and reignition; throughout the test fuel continues to drip on the heated surface until reignition occurs.

This program was sponsored by Wright-Patterson AFB, but most of the experimental work was done in the facilities of the Chemical Research Projects Office of Ames Research Center. The program was conducted with the assistance of Professors A. C. Ling, L. A. Mayer, and D. J. Myronuk, San Jose State University, and their students.

TEST PROCEDURES

Static Test

The initial experimental setup devised by Altman and Myronuk is shown schematically in figure 1 and in actual operation in figure 2. The fire was started by dripping JP-4 fuel onto a heated semicylindrical stainless steel surface. The surface was heated to a temperature between 700°C and 900°C by a Nichrome heating element placed below the curved surface. The ambient air in the cavity above the stainless steel surface was also heated by a combination of hot-surface radiation and gas convection to a temperature below that of the hot surface; however, we made no attempt to control this process. One of the two parameters used to rank the effectiveness of fire extinguishants was the hot-surface temperature, which was imprecisely determined by an uncalibrated Chromel-Alumel thermocouple. The thermocouple was welded to the semicylindrical surface at a point close to that where the fuel drop made initial contact with the hot surface.

To further describe the experimental procedure, suppose that the steady-state temperature of the hot surface was a nominal 700°C, as determined from the recorded emf output of the thermocouple. The dripping of the JP-4 fuel was then started, and very soon after the first fuel drop hit the hot surface, the temperature of the surface dropped, to, say, 650°C (because of fuel evaporative cooling). Shortly thereafter, the thermocouple temperature began to rise because the fuel drops had burst into flame. When the nominal temperature had returned to 700°C a given weight of dry chemical fire extinguishant was discharged onto the plate in the same area where the drops had first landed. If the flame was extinguished, the continuous stream of nonburning fuel drops striking the hot surface induced further evaporative cooling and the temperature dropped again. Because the fire extinguishing powder now blanketed the thermocouple-to-surface weld, the nominal temperature rose again when the drops burst into flame, although to a temperature higher than 700°C; the higher temperature was a result of the insulating effect of the powder blanket. The time from first extinguishment to second reignition, the so-called reignition delay time, was the prime measurement used in ranking the effectiveness of the dry chemical fire extinguishants.

Some of the reignition time delay results obtained from an initial survey of commercial and reagent dry chemicals made from Na- and K-bicarbonate, carbonate, and chloride, etc., on a 775°C hot surface are given in figure 3. The rank order obtained

$$K_2CO_3 > KHCO_3 > KCl > NaHCO_3 > Na_2CO_3 > NaCl$$

is about the same as that reported by other investigators (refs. 9-13). Our experiments with two different particle size distributions of $KHCO_3$ and K_2CO_3, all made from reagent chemicals, demonstrated that reduction in particle size increased the reignition time delay just as it increased fire extinguishant weight effectiveness. In agreement with these earlier investigations, the data in figure 3 also show that given the effectiveness of any sodium salt, the analogous potassium salt always seemed to be still more effective. We were, however, surprised to observe the special effectiveness of K_2CO_3 and $NaAl(OH)_2CO_3$; as a result, we undertook the preparation of a commercial dry chemical from K_2CO_3 with an additive to reduce the spontaneous hydration and also developed an alternative method of preparing Na- and K-$Al(OH)_2CO_3$ by heating dry powder mixtures of $Al(OH)_3$ and Na- or K-HCO_3 in a CO_2 atmosphere (ref. 14).

Van Tiggelen et al. (ref. 15) separate fire extinguishants into two classes: (1) those that interfere with the flame chemical reactions and (2) those that cool the flame, that is, change the mechanism of flame propagation rather than merely reduce the overall rate of chemical reaction. Since, as mentioned in the description of our experimental procedure, the presence of fire extinguishing powder altered the hot surface heat-transfer properties, we also tried alumina, Al_2O_3 and silicic acid, H_2SiO_3, as reignition delay "baseline" test materials; alumina because no chemical change would be expected and silicic acid because it could decompose to yield only water and SiO_2. At least in amounts of 7 g or less these possible flame temperature reducers were no less effective than the poorest chemical flame reaction interference agents, $NaHCO_3$, Na_2CO_3, $NaCl$, $NH_4H_2PO_4$, or $KC_2N_2H_3O_3$ (ICI Monnex ®).

The initial fire test apparatus was modified somewhat as shown in figure 4 in order to better control the fuel flow rate and make the reignition delay results more reproducible (ref. 14). Some of the results obtained with this newer apparatus (designed by Professors Ling and Mayer) are given in figure 5. We were, of course, pleased to see that the commercial K_2CO_3 preparation was the best of the lot of commercial dry chemicals. Because early experimental work at WPAFB (ref. 16) had demonstrated that the most weight-effective Halon was one containing iodine, that is, CH_3I, we tried to develop a dry chemical iodide. Of such iodides tested — SnI_2, KI, NAI, and CI_4 — CI_4 was ineffective in delaying reignition even at 700°C; all the other iodides turned out to be less effective at 900°C than the commercial dry chemicals. The other tin salts listed in figure 5 were tried to see whether the increased effectiveness of SnI_2 over CI_4 had something to do with the tin. Sodium tungstate, Na_2WO_4, with and without water, was tested because Lewis and Von Elbe (ref. 17) cited some experimental data on the greater effectiveness of Na_2WO_4 over that of KCl as a surface coating on glass in removing H free radicals. Obviously, the effect of water release from NA_2WO_4 dihydrate in delaying hot-surface reignition is as great as the chemical effectiveness of Na_2WO_4 by itself.

Figure 6 shows some of the results obtained with other experimental dry chemicals. Obviously, Na- and K-$Al(OH)_2CO_3$, sodium and potassium dawsonite, are superior to Na- and K-bicar [illegible] Since either of the dawsonites can be considered to be an addition [illegible] of boemite, AlOOH, and the appropriate alkali metal bicarbonate, the e [illegible] of K-dawsonite (KD) might then be expected to be some mole-fractio [illegible] sum of the effectiveness of $KHCO_3$ and AlOOH. But the effectiveness o [illegible] clearly greater than the effectiveness of any combination of $KHCO_3$ and [illegible] Boron trioxide, B_2O_3, was tested because it melts at 450°C to form a glass; however, it seems to be no more effective than Al_2O_3, and a mixture of KD and B_2O_3 is even less effective than pure KD. We conclude this section by noting that the effectiveness of both mechanical and preheated mixtures of KI with either Al_2O_3 or KD seems superior to that of either constituent, particularly at the higher temperatures, but further discussion is deferred until the presentation of the effect of airflow rate on extinguishment effectiveness.

Dynamic Test

A schematic of the dynamic fire test facility designed by Professor Myronuk and Richard Fish of ARC, is shown in figure 7. The test section downstream of the blower contains a stainless steel surface heated to 800°C-900°C. Ambient air flowed over the surface at rates from 6 to 36 m/sec and JP-4 fuel was leaked onto the surface at a rate of 250 cm^3/min. As in the static testing, once a steady hot-surface temperature was obtained at a given airflow rate, the fuel leak was initiated and made to ignite on the hot surface within 1 sec. After ignition a specific mass of extinguishant was discharged within 1 sec onto the heated surface, and, with the fuel leak uninterrupted, the time between initial extinguishment and reignition was recorded as the prime parameter of extinguishment effectiveness. The other variables were airflow rate and hot-surface temperature.

Because of their potential toxicity we could not obtain static reignition delay time data with Halon extinguishants. Therefore, our first objective was to obtain dynamic results with these materials in order to establish a baseline; some of the results are given in figure 8. To explain the data tabulation, all four of the Halons tested extinguished the fuel-leak fire at an airflow rate of 6 m/sec and did prevent its reignition for 2 sec; however, 39 g of CH_2ClBr were required but only 21 g of CF_2Br_2. In all these tests the fire reignited after 2 sec because the Halon was being continuously diluted by the airflow after the first second of discharge time. When the airflow was increased to 36 m/sec, even more Halon extinguishant was required to keep the fire from reigniting for as long as 20 sec — 40 g of either CF_2Br_2 or CF_2ClBr and 60 g of either CF_3Br or CH_2ClBr. Twenty seconds is the upper limit of the reignition delay time reported because when the fire was kept from reigniting for a longer time the hot-surface temperature declined significantly as a result of fuel evaporative cooling. From data such as this we rank these extinguishants as follows:

$$CF_2Br_2 \approx CF_2ClBr \geq CF_3Br \approx CH_2ClBr$$

A similar procedure was then carried out with commercial dry chemicals; these results are given in figure 9. As shown in figure 9, the extinguishment effectiveness of these chemicals was ranked as follows:

$$K_2CO_3 > KC_2N_2H_3O_2 > KHCO_3 > NaHCO_3 > KCl$$

Potassium carbonate, K_2CO_3, is reported to be more than three times as effective as Na_2CO_3 or KCl in fire extinguishment and Na_2CO_3 is reported to be about twice as effective as Li_2CO_3 or $NaHCO_3$ (ref. 15). Since the best of the commercial lots reported in figure 9 was Ansul's K_2CO_3, Li- and Na-carbonate dry powders prepared from reagent chemicals were also tested as an exercise in varying the alkali metal element in the carbonate; the results are shown in figure 10. The parallelism between the recorded literature effectiveness and ours indicates that increased reignition delay time is directly related to extinguishment effectiveness. Figure 10 also shows that while the effectiveness of pure KD is nil at an airflow rate of 36 m/sec, a 2:1 mixture of KD and KCl by weight increased the weight effectiveness of KCl three to five times. The results were similar for a 9:1 mixture of KD and KI when compared with the results for pure KI. Since both KCl and KI are volatile at these temperatures, the increase in KI and KCl effectiveness in these mixtures with KD could be due to the creation of a diffusion barrier for the gaseous alkali halide molecules by the KD or to the creation of some new chemical compound between the alkali metal halide and KD thus reducing the volatility of both the alkali metal halide and decomposition products of KD.

To shed some light on these alternatives, a mixture of alumina and KI having approximately the same KI content as the mixtures of KI with KD was tested. Since no reignition delay resulted over the entire airflow range with even twice the total mass as the KD plus KI mixture, the diffusion barrier idea seems incorrect. Still another way of testing this idea is to try to increase the stickiness of KD, for if KD makes either the KCl or KI stick to the hot surface longer, thereby increasing the effectiveness, then increasing the stickiness of KD should increase its own effectiveness to something like its static effectiveness, shown in figure 6. For this test a mixture of KD with 10% B_2O_3 was prepared, but as shown in figure 10 it was no more effective than pure KD, even though some evidence of glass formation was apparent because the steel surface was very difficult to clean.

As for the possibility of some new chemical compound between KCl or KI and KD being produced by the hot surface when mechanical mixtures of alkali metal halides and KD are tested, an intimate mixture of KI and the starting materials for making KD was heated as if to make KD. Since no chemical reaction is expected between KI and either of the $KHCO_3$ or $Al(OH)_3$ materials for making KD, the preheated mixture should show similar fire extinguishing properties to those of the mechanical mixture of KI and KD given in figure 10. Various such mixtures of the precursors of KD with 5% to 18% KI were heated as if to make KD; their reignition delay time properties, which are tabulated in figure 11, do not seem to be significantly different from those of a mechanical mixture of KI and KD.

In a separate study, we have shown that heating SnI_2 with the precursors of KD, that is, $KHCO_3$ and $Al(OH)_3$, yields KI, AlOOH, and SnO_2 by the following gross reaction:

$$SnI_2 + 2KAl(OH)_2CO_3 \rightarrow SnO_2 + 2KI + 2AlOOH + H_2\uparrow + 2CO_2\uparrow$$

An infrared investigation of the solid after it was heated demonstrated the presence of SnO_2, KI, and AlOOH, and the entire disappearance of SnI_2 and KD when the starting mole ratios of SnI_2 to KD-precursors were 1:1 or 1:2. As expected, KD remained when the SnI_2-to-KD-precursors were 1:4. For all three samples of the KD·SnI_2 end product reported in figure 11, the KD is in great enough excess to give a product containing SnO_2, AlOOH, KD, and KI. Further experimental work is necessary to determine why the fire extinguishment effectiveness of this material is better than that of the KD·KI preparations.

CONCLUSION

Certain dry chemicals developed and tested in our laboratories seem to have greater weight effectiveness than the Halons in current use for controlling fuel-leak fires, particularly in the presence of high airflow rates. However, the experimental variables and their role in the results obtained are insufficiently understood and the understanding of fire extinguishment has not been advanced much by this study. A further discussion of the many uncertainties is, therefore, deferred until more detailed publication in a scientific journal.

The applicability and effectiveness of these materials, namely potassium dawsonite mixed mechanically with KCl or KI, in controlling engine nacelle fires have yet to be demonstrated. However, we plan to participate further in such a test activity that will be conducted at the FAA Technical Center in Atlantic City, New Jersey, in the not too distant future.

REFERENCES

1. Hirst, R.; Farenden, P. J.; and Simmons, R. F.: The Extinction of Fires in Aircraft Jet Engines - Part I, Small-Scale Simulation of Fires. Fire Tech., vol. 12, 1976, p. 266.

2. Hirst, R.; Farenden, P. J.; and Simmons, R. F.: The Extinction of Fires in Aircraft Jet Engines - Part II, Full-Scale Fire Tests. Fire Tech., vol. 13, 1977, p. 59.

3. Dyer, J. H.; Majoram, M. J.; and Simmons, R. F.: The Extinction of Fires in Aircraft Jet Engines - Part III, Extinction of Fires at Low Airflows. Fire Tech., vol. 13, 1977, p. 126.

4. Dyer, J. H.; Majoram, M. J.; and Simmons, R. F.: The Extinction of Fires in Aircraft Jet Engines - Part IV, Extinction of Fires by Sprays of Bromochlorodifluoromethane. Fire Tech., vol. 13, 1977, p. 223.

5. Davis, R. A.: Concorde Power Plant Fire Protection System. Aircraft Eng., vol. 43, 1971, p. 26.

6. Klueg, E. P.; and Demaree, J. E.: An Investigation of In-Flight Fire Protection with a Turbofan Powerplant Installation. Rep. NA-69-26, Federal Aviation Administration, Apr. 1969.

7. Simulated Flight Test Investigation of the Effectiveness of a Lightweight, Aircraft, Fixed, Fire-Extinguishing System. Fenwal Inc., Ashland, Mass., Navy Bureau of Aeronautics Contract N600(19)59572, 23 June 1964.

8. Sommers, D. E.: Fire Protection Tests in a Small Fuselage-Mounted Turbojet Engine and Nacelle Installation. Rep. RD-70-57, Federal Aviation Administration, Nov. 1970.

9. Dolan, J. E.: The Suppression of Methane/Air Ignitions by Fine Powders. Sixth Symposium (International) on Combustion, Reinhold Publishing Corp., 1957, p. 787.

10. Lafitte, P.; and Bouchet, R.: Suppression of Explosion Waves in Gaseous Mixtures of Means of Fine Powders. Seventh Symposium (International) on Combustion, Butterworths Scientific Publications, 1959, p. 504.

11. Lafitte, P.; Delbourgo, C. R.; Combourieu, J.; and Dumont, J. C.: The Influence of Particle Diameter on the Specificity of Fine Powders in the Extinction of Flames. Comb. & Flame, vol. 9, 1965, p. 357.

12. Friedrich, M.: Mode of Action of Dry Fire Extinguishing Agents. U.S. Naval Research Laboratory Translation No. 804, Wash., D.C., 1960.

13. Lee, T. G.; and Robertson, A. F.: Extinguishment Effectiveness of Some Powdered Materials on Hydrocarbon Fires. Fire Res. Abst. Rev., vol. 2, 1960, p. 13.

14. Altman, R. L.; Ling, A. C.; Mayer, L. A.; and Myronuk, D. J.: Development and Testing of Dry Chemicals in Advanced Extinguishing Systems for Jet Engine Nacelle Fires. Final Rep. 1975-1979, Wright-Patterson Air Force Base, Ohio, 1980.

15. Van Tiggelen, A.; Vrebosch, J.; Dewitte, M.; De Geest J.; and Remmerie, P.: Inhibition of Flame Reactions. Tech. Documentary Rep. RTD-TDR-63-4011, Wright-Patterson Air Force Base, Ohio, 1963.

16. Muench, N. P.; and Klein, H. A.: Fire Protection of Jet Engine Aircraft. Memorandum Rep. No. MCREXE-664-466-K, Wright-Patterson Air Force, Ohio, 1949.

17. Lewis, B.; and Von Elbe, G.: Combustion, Flames and Explosions of Gases. Second ed., Academic Press, New York, 1961, p. 27.

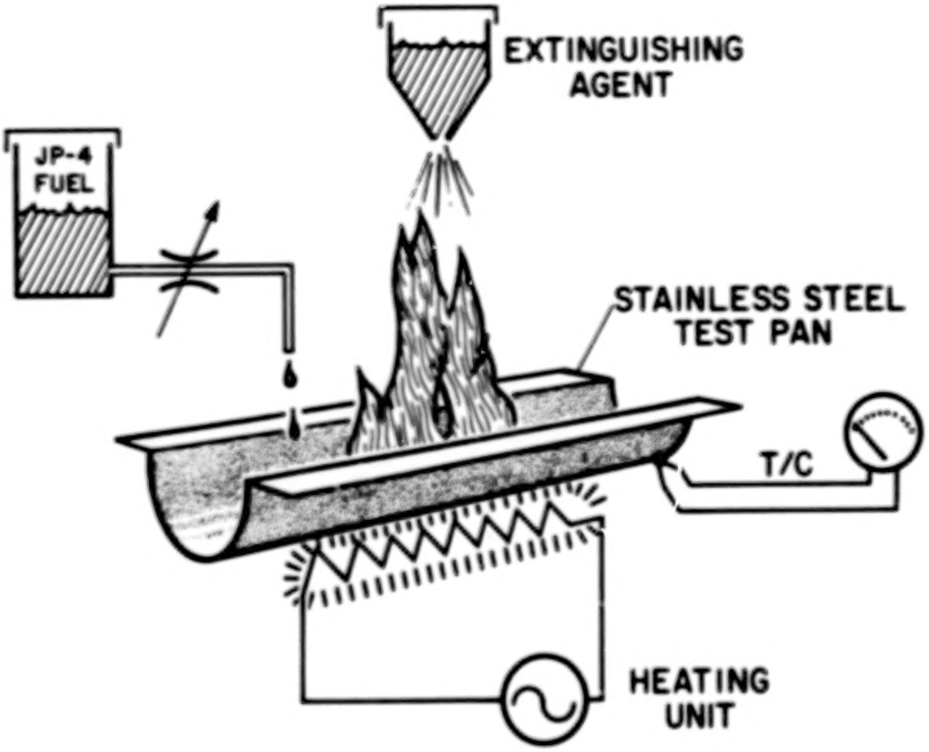
EXTINGUISHING AGENT
JP-4 FUEL
STAINLESS STEEL TEST PAN
T/C
HEATING UNIT

Figure 1.- Static nacelle fire test facility (schematic).

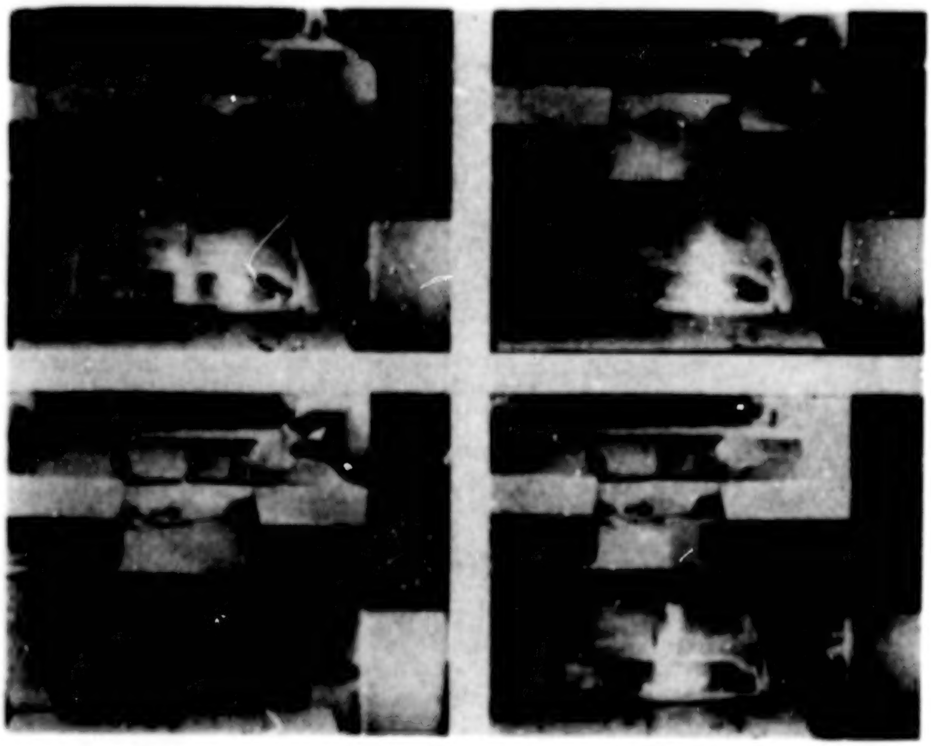

Figure 2.- Static nacelle fire test facility (actual).

DRY CHEMICAL FIRE EXTINGUISHANT POWDER	SAMPLE SIZE, grams		
	2.5	5	7.5
	SECONDS TO REIGNITE		
$KHCO_3$ (ANSUL PURPLE K*)	30	100	220
$KC\ell$ (PYROCHEM SUPER K*)	3	17	70
$NaHCO_3$ (ANSUL DRY POWDER*)	3	4	8
$NH_4H_2PO_4$ (ANSUL FORAY*)	3	2	2
$KC_2N_2H_3O_3$ (ICI MONNEX*)	2	2	2
Na_2CO_3 (ANSUL NaX*)	1	1	1
$NaC\ell$ (ANSUL MET-L-X*)	0	0	2
$NaA\ell(OH)_2CO_3$ (KAISER DAWSONITE)	40	125	340
K_2CO_3 (REAGENT POWDER)	20	300	NO IGN.
K_2CO_3 (REAGENT GRANULAR)	12	38	260
$KHCO_3$ (REAGENT POWDER)	40	60	200
$KHCO_3$ (REAGENT GRANULAR)	15	40	150
$A\ell_2O_3$ (REAGENT ALUMINA)	2	2	15
H_2SiO_3 (REAGENT SILICIC ACID)	2	2	12

*THESE ARE COMMERCIAL EXTINGUISHANTS

Figure 3.- Average time for reignition of JP-4 fuel drip on 775°C hot surface.

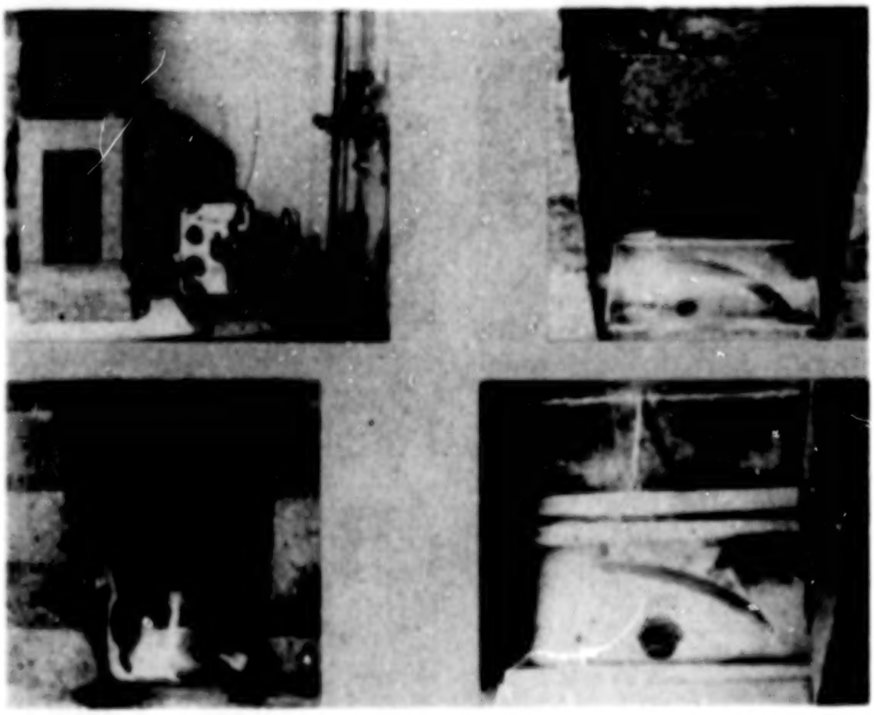

Figure 4.- Modified static nacelle fire test facility.

DRY CHEMICALS	DELAY TIME, sec	
	700°C	900°C
K_2CO_3 (ANSUL PREP)	150 ± 80	–
$KHCO_3$ (ANSUL PURPLE-K)	69 ± 20	7 ± 4
$KC_2N_2H_3O_3$ (ICI MONNEX)	55 ± 30	7 ± 2
$KC\ell$ (PYROCHEM SUPER-K)	33 ± 4	–
$NaC\ell$ (PYROCHEM BCD)	33 ± 15	5 ± 2
$(NH_4)H_2PO_4$ (ANSUL FORAY)	12 ± 2	–
$(NH_4)H_2PO_4$ (PYROCHEM TUW-156)	8 ± 3	–
SnI_2 (68% I)	380 ± 80	2 ± 2
KI (76% I)	>900	2 ± 2
NaI (85% I)	600 ± 60	3 ± 2
CI_4 (98% I)	NONE	–
$SnC\ell_4 \bullet 2H_2O$	26 ± 3	–
SnO	15 ± 5	–
$Na_2WO_4 \bullet 2H_2O$	17 ± 2	–
Na_2WO_4	8 ± 2	–

Figure 5.- Reignition delay time for JP-4 fuel drip on hot surface with 10 g of commercial and experimental dry chemicals.

DRY CHEMICALS	DELAY TIME, sec	
	750°C	900°C
$NaA\ell(OH)_2CO_3{}^{\dagger}$	296 ± 50	6 ± 3
$KA\ell(OH)_2CO_3{}^{\dagger}$	153 ± 15	10 ± 4
$A\ell(OH)_3$	100 ± 30	3 ± 2
$A\ell OOH^{\dagger}$	48 ± 35	NONE
$A\ell_2O_3$	28 ± 12	NONE
B_2O_3	5 ± 3	2 ± 1
H_3BO_3	10	–
KD + B_2O_3 (10%)	62 ± 28	6 ± 2
$K_3A\ell F_6$	14 ± 5	–
$A\ell(OH)_3 + SnI_2$ (7% I)	204 ± 20	8 ± 1
$A\ell(OH)_3$ + KI (8% I)	233 ± 56	–
$A\ell(OH)_3 \bullet$ KI (7% I)	72 ± 3	8 ± 1
$A\ell OOH \bullet$ KI (7% I)	131 ± 7	15 ± 4
$A\ell_2O_3 \bullet$ KI (7% I)	>900	50 ± 12
$KA\ell(OH)_2CO_3 + SnI_2$ (6% I)	520 ± 52	51 ± 3
$KA\ell(OH)_2CO_3 \bullet SnI_2$ (6% I)	419 ± 61	50 ± 2
$KA\ell(OH)_2CO_3$ + KI (7% I)	500 ± 90	13 ± 4
$KA\ell(OH)_2CO_3 \bullet$ KI (7% I)	>900	50 ± 14

+ MECHANICAL MIXTURE

• MECHANICAL MIXTURE PREHEATED BEFORE TEST (WEIGHT PERCENT IODINE IN MIXTURE)

† PREPARED AT ARC FROM REAGENT CHEMICALS

Figure 6.- Reignition delay time for JP-4 fuel drip on hot surface with 10 g of experimental dry chemicals.

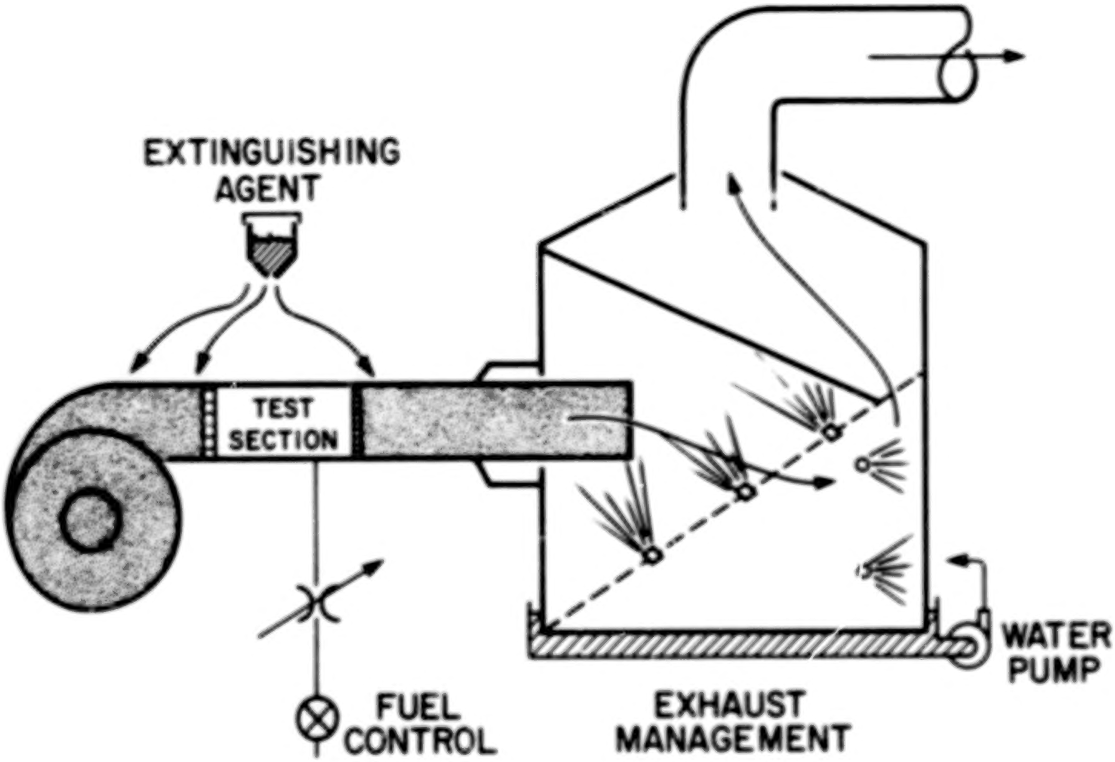
EXTINGUISHING AGENT
TEST SECTION
FUEL CONTROL
EXHAUST MANAGEMENT
WATER PUMP

Figure 7.- Dynamic nacelle fire test facility.

HALON	GRAMS	DELAY TIME, sec, AT VARIOUS AIRFLOWS, mps	
		6	36
1202 CF_2Br_2	21	2	–
	40	–	20
1211 CF_2ClBr	24	2	–
	40	–	20
1301 CF_3Br	35	2	–
	60	–	20
1011 CH_2ClBr	39	2	–
	60	–	20

EXTINGUISHMENT EFFECTIVENESS

$CF_2Br_2 \approx CF_2ClBr > CF_3Br \approx CH_2ClBr$

Figure 8.- Reignition delay time versus airflow rate for JP-4 fuel drip on 800°C hot surface for various Halon extinguishants.

DRY CHEMICALS	GRAMS	DELAY TIME, sec, AT VARIOUS AIRFLOWS, mps 6	36
$KHCO_3$* (ANSUL PKP)	30	20	2
	50	—	20
$KHCO_3$* (ANSUL X)	20	20	<1
	30	—	20
$NaHCO_3$* (ANSUL +50C)	30	20	0
	50	—	<1
$KC_2N_2H_3O_3$* (ICI MONNEX)	10	2	0
	20	20	20
KCl* (PYROCHEM SUPER - K)	30	<1	0
	50	—	20
K_2CO_3* (ANSUL PREP)	8	0	20
	20	2	20
	30	20	—

*800°C
EXTINGUISHMENT EFFECTIVENESS
$K_2CO_3 > KC_2N_2H_3O_3 > KHCO_3 > NaHCO_3 > KCl$

Figure 9.- Reignition delay time versus airflow rate for JP-4 fuel drip on hot surface with commercial dry chemicals.

DRY CHEMICALS	GRAMS	DELAY TIME, sec, AT VARIOUS AIRFLOWS, mps 6	36
	‡		
Li_2CO_3†	30 - 40	<1	0
Na_2CO_3†	30 - 40	<1	0
$KAl(OH)_2CO_3$* ("KD")	30	20	0
KD + KCl (32%)*	10 - 20	2	20
KI†	50	<1	0
KD + KI (10%)*	20	3	20
Al_2O_3 + KI (9%)*	40	0	0
KD + B_2O_3 (10%)*	20	20	0

*800°C
†900°C
‡POWDER MIXTURE

Figure 10.- Reignition delay time versus airflow rate for JP-4 fuel drip on hot surface with experimental dry chemicals.

DRY CHEMICALS	GRAMS	DELAY TIME, sec, AT VARIOUS AIRFLOWS, mps	
		6	36
KD • KI (5%)	20	1	<1
	25	20	—
KD • KI (9%)	15	<1	20
KD • KI (18%)	20	<1	20
$A\ell_2O_3$ • KI (9%)	40	0	0
KD • SnI_2 (5%)	15	20	20
KD • SnI_2 (10%)	15	20	20
KD • SnI_2 (20%)	10	20	20

• MECHANICAL MIXTURE PREHEATED BEFORE USE

Figure 11.- Reignition delay time versus airflow rate for JP-4 fuel drip on 800°C hot surface with experimental dry chemicals.

SESSION VI - ACOUSTICS AND NOISE REDUCTION

BLANK PAGE

BLANK PAGE

RECENT DEVELOPMENTS IN AIRCRAFT ENGINE NOISE REDUCTION TECHNOLOGY

James R. Stone and Charles E. Feiler
Lewis Research Center

SUMMARY

This paper reviews some of the more important developments and progress in jet and fan noise reduction and flight effects made in the past several years. Experiments are reported which show that nonaxisymmetric coannular nozzles have the potential to reduce jet noise for conventional and inverted velocity profiles. It now appears that an improved understanding of suppressive liner behavior, coupled with the new understanding of fan source noise, will soon allow the joint optimization of acoustic liner and fan design for low noise. It is also shown that fan noise source reduction concepts are applicable to advanced turboprops. Advances in inflow control device design are reviewed that appear to offer an adequate approach to the ground simulation of in-flight fan noise. This approach will be assessed by flight experiments currently being conducted on a JT15D engine in a joint program of the Lewis, Langley, and Ames Research Centers. Also in regard to flight effects, it is shown that static jet engine exhaust noise can be projected to flight with reasonable accuracy on an absolute basis.

INTRODUCTION

Aircraft noise has been a major environmental concern for many years. One indication of the public pressure to reduce noise is the number of airports around the world that have noise restrictions such as curfews on nighttime operations, flight routing and operating restrictions, and use of preferential runways. Some data on noise restraints at major world airports are shown in figure 1 for the years 1968, 1973, and 1978 (ref. 1). It can be seen that in 10 years the number of airports with restrictions has doubled. This has happened even though during this time the Federal Aviation Administration (FAA) has issued increasingly stringent noise certification standards that are critical design constraints on new aircraft. To alleviate this noise problem, which is a major constraint to the growth of the civil aviation industry, NASA is conducting research and technology studies to advance the state of the art. The Lewis Research Center has concentrated primarily on propulsion noise reduction technology.

Propulsion noise research is focused on understanding the noise-producing processes, or sources, so that noise can be reduced in efficient and economical ways that do not penalize the engine performance or weight significantly. An additional objective is to develop prediction procedures for each noise source that will allow aircraft noise to be estimated accurately. This paper deals primarily with high-bypass-ratio turbofan engines, although the application of this technology to advanced turboprops is also discussed. Recent advances in supersonic cruise noise technology are not dealt with specifically in this paper but are reported in reference 2.

The noise sources for a turbofan engine are illustrated in figure 2. The sources are both internal and external to the engine. The internal sources are the fan, the compressor, the combustor, the turbine, and the flow over the support struts. The last three sources have usually been considered collectively as engine core noise. Sound from the internal sources must propagate through the engine ducts and nozzles, where it can be reduced by acoustic treatment. Thus acoustic treatment and sound propagation in ducts are very important elements in engine noise reduction. The external sources are the high-velocity jet exhausts mixing with each other and with the ambient air. An important aspect of the engine noise problem is the effects of flight on the various noise sources. As is shown, the effects of flight, or forward velocity, differ for the several noise sources.

SYMBOLS
(S. I. Units unless noted)

D	diameter of nozzle
f	frequency
H	annular height of nozzle
M_0	flight Mach number
OASPL	overall sound pressure level, dB re 20 $\mu N/m^2$
PNL	perceived noise level, PNdB
PR_i	inner-stream-total- to ambient-pressure ratio
PR_o	outer-stream-total- to ambient-pressure ratio
SPL	sound pressure level, dB re 20 $\mu N/m^2$
T_j	jet total temperature
T_s	shielding stream total temperature
V_j	jet velocity
V_s	shielding stream velocity
V_0	flight velocity

θ	polar directivity angle referred to inlet, deg
φ	azimuthal angle, deg
φ_s	azimuthal angular extent of shielding stream, deg

FAN NOISE

The fan is a dominant noise source in current high-bypass-ratio turbofan engines, particularly during landing approach. Furthermore advanced turbofan design studies, such as those associated with the Energy Efficient Engine program, indicate that the fan will continue to be a dominant noise source in future high-bypass-ratio engines (ref. 3). The ultimate goals of fan noise research are to develop noise-reducing design features that are compatible with good aerodynamic performance and to confirm experimentally the acoustic effectiveness of these designs. The approaches to noise reduction include source strength reduction and unified design of the fan and liner to obtain the optimum synergistic effects. The NASA research programs are aimed at understanding the noise-generating mechanisms and describing in detail the fan source characteristics (e.g., ref. 4). Describing the source is important because propagation, liner suppression, and radiation all strongly depend on the initial conditions at the source (refs. 5 to 9). An important constraint on experimental work in static facilities is that the test environment must lead to noise levels that correctly simulate flight (ref. 10), as discussed further in a later section.

Two primary source mechanisms that are addressed in research to reduce fan noise are shown in the turbofan cross section in figure 3. Rotor-stator interactions in the form of rotor wakes and vortices impinging on the stators can be particularly important at the subsonic tip speeds that occur during landing approach. The corresponding narrowband spectrum is shown in the upper portion of figure 4. The blade passing tone and its harmonics, which are due to periodic interactions of the rotor wakes with the stator blades, are superimposed on the broadband levels that result from interactions involving random flow disturbances. Rotor-alone noise production occurs because of nonuniformities in the rotor-locked shock wave patterns that form at the leading edges at supersonic tip speeds. These patterns radiate multiple pure tones during takeoff and have a spectrum of the type shown in the lower portion of figure 4. Multiple pure tones can occur at all multiples of fan shaft rotation frequency, and some of the individual tone levels often exceed the level of the blade passing frequency and its harmonics.

One of the concepts that has been investigated to reduce shock-generated, multiple-pure-tone noise is to sweep the rotor-blade leading edges. An experimental swept-rotor fan designed to explore the acoustic performance of swept blades is shown in figure 5. The acoustic design of this fan was performed by Bolt, Beranek and Newman, Inc., and the aerodynamic and mechanical designs were developed by the Lycoming Division of AVCO Corp. (ref. 11). The blade leading edges are swept forward to midspan and then rearward to the tip in order to limit the maximum blade root stresses. These stresses would be unacceptably high if the sweep were only in one direction. The sweep is varied spanwise in such a manner that the normal component of blade leading-edge relative Mach number is subsonic over the entire span. It is this component that controls leading-edge shock formation. Thus except for blade end effects and the sweep-reversal point this design should essentially eliminate the leading-edge shock system and thereby reduce the multiple-pure-tone noise.

The swept-rotor fan shown in figure 5 was acoustically tested in the NASA Lewis Research Center anechoic chamber (ref. 12), and the major results are shown in figure 6. The multiple-pure-tone power levels for an unswept fan and the swept-rotor fan are compared as a function of fan-tip relative Mach number. Rotor sweep delayed the onset of multiple pure tones to higher relative Mach numbers, about 1.25 instead of 1.0, and reduced the levels over a large portion of the tip-speed range, including speeds representative of takeoff. The aerodynamic performance of the fan did not meet the design goals (e.g., the efficiency was 9 percent low), but this is not surprising since this was the first build of a new design concept for which there are no established design procedures. These initial results are encouraging, and refinement of the aerodynamic design may lead to further multiple-pure-tone noise reductions with more acceptable aerodynamic performance.

APPLICATION OF SWEPT-ROTOR TO ADVANCED TURBOPROPS

The swept-rotor concept, described earlier, is also being considered for advanced high-speed turboprops, which have a potential cabin noise problem at cruise due to propeller noise. Blade sweep also helps reduce aerodynamic losses caused by compressibility effects. Three basic blade planforms pictured in figure 7 were tested in the NASA Lewis 8- by 6-Foot Supersonic Wind Tunnel (ref. 13). Blade sweep angles of 0°, 30°, and 45° were used for these designs. Wall-mounted pressure transducers were used to obtain near-field acoustic data. (Further details are given in refs. 14 and 15.)

The beneficial effects of sweep on propeller noise reduction are shown in figure 8, which compares 45° sweep with no sweep. Maximum blade passing tone level is plotted against helical tip Mach number (total, including flight and rotation). The advance ratio and the power coefficient for all cases are approximately the design values. Variation in helical-tip Mach number was obtained by taking data at various free-stream Mach numbers. The plots for both the 0° and 45° swept blades exhibit a sharp noise increase with increasing helical-tip Mach number; this is then followed by a region where noise levels off. The tailored sweep of the 45° design provides noise reduction over the complete range of tip speeds. Near the cruise design tip Mach number of 1.14, the reduction is about 5 to 6 dB and appears to be even larger at the lower tip speeds tested. Data in reference 14, obtained with a 30° swept blade, support the behavior shown in figure 8.

EXHAUST NOISE

The various noise sources associated with the exhaust are considered in this section. Exhaust noise sources include jet mixing noise, jet shock-cell noise, and core noise. The aft-radiated turbomachinery noise is not included. However, noise transmission through the turbine is an important element in the core noise problem, and recent results are given in references 16 and 17. Core noise generally becomes important at low power settings, particularly in flight. Recent results of core noise investigations are reported in references 18 to 23. Jet shock-cell noise is a potentially important source for supersonic cruise aircraft but is generally not a factor for high-bypass-ratio turbofan engines. For jet-powered aircraft the most important source at takeoff is usually jet mixing noise, and so the present discussion focuses on this noise source. Considerable research has been conducted on jet mixing noise reduction, particularly for supersonic cruise application (ref. 24). Progress has also been made in developing jet noise reduction concepts applicable to subsonic aircraft. Two basic approaches that have received considerable attention are shown in figure 9.

One approach is to mix the fan and core streams; this reduces the maximum jet velocity and consequently reduces jet noise. In addition, this approach offers the potential added benefits of increasing thrust and reducing specific fuel consumption. Such internal mixers have been investigated by the industry (refs. 25 and 26), with some support from the FAA (ref. 27). NASA has also supported mixer-nozzle development studies for large and small turbofan engines (refs. 24 and 13, respectively). Model-scale research is currently being conducted at the Lewis Research Center to help develop internal mixer noise technology for high-bypass-ratio turbofan engines such as the Energy Efficient Engine.

The other approach is to use asymmetry in the jet exhaust in the form of a noise shielding concept. Two variations to this approach that have been investigated on a preliminary basis at the Lewis Research Center are discussed in the following sections.

Thermal Acoustic Shielding

Velocity and temperature profiles in the jet flow field affect noise generation and propagation (e.g., ref. 28), and these phenomena can lead to noise suppression concepts (e.g., ref. 29). It has been shown that a relatively quiet jet can shield a noisier jet (refs. 30 and 31). On the basis of these considerations the thermal acoustic shield concept, illustrated in figure 10, is receiving considerable attention.

Previous experimental studies (ref. 32) have shown that jet exhaust noise can be reduced by using a full ($\Phi_s = 360°$) annular thermal acoustic shield consisting of a high-temperature, low-velocity gas stream surrounding the high-velocity central jet exhaust. It has also been recognized for some time that even a low-temperature annular flow reduces the noise of the central jet, as in a conventional bypass engine (e.g., ref. 33). The reductions obtained with a full-annular shielding stream are believed to be limited by multiple reflections within the jet. It has been suggested that a semiannular shield ($\varphi_s = 180°$) would not be limited in this manner. Therefore an exploratory study of this concept was begun at the Lewis Research Center (ref. 34).

The semiannular thermal acoustic shield configuration was obtained by blocking the flow in half of the outer stream of a coplanar, coannular nozzle, as shown in figure 11. Typical noise spectra for a subsonic primary jet at three angles - $\theta = 45°$ (forward quadrant), $\theta = 90°$ (overhead), and $\theta = 135°$ (aft quadrant) are shown in figure 12. It can be seen that the partial shield provides high-frequency noise reduction at all angles, but the effect is most pronounced in the aft quadrant ($\theta = 135°$). Since it is in the aft quadrant where jet noise peaks, significant peak perceived noise level (PNL) reductions should result. Perceived noise level directivities, scaled up to a nominally full-size engine, are shown in figure 13 for these same conditions. The shielding benefits can be observed at all angles, and the reduction in peak PNL is about 4 PNdB. These promising results indicate that the thermal acoustic shield should be further investigated since the present study was exploratory and the geometry by no means optimized. Lewis has recently begun a model-scale contract study of the thermal acoustic shield integrated with an annular plug nozzle. Although this study is motivated primarily by the possibility of supersonic cruise application, promising results might lead to concepts applicable to high-bypass-ratio turbofans.

Nozzle Shaping

Other means of using asymmetry in the flow field of dual-stream exhausts have been proposed to control noise. As shown in figure 14, for a conventional-velocity-profile coannular nozzle, increasing the annular height H for fixed velocities and temperatures reduces the noise. However, for the inverted-velocity-profile case, the opposite trend occurs (ref. 35). It seems reasonable then that favorable acoustic results might be obtained by proper introduction of asymmetry. Specifically, the passage height should be increased on the side toward the observer for a conventional profile, and for an inverted profile the passage height should be decreased in the direction of the observer. These trends were observed in exploratory experiments with the nozzle shown in figure 15. The outer nozzle was mounted eccentrically to produce a 70 percent reduction in passage height in one direction and a corresponding 70 percent increase in passage height in the opposite direction.

The expected type of results was obtained for the conventional-velocity-profile case, most likely to be applicable to high-bypass-ratio turbofans, and typical results (ref. 36) are shown in figure 16. Measured spectra for the concentric and eccentric nozzles are compared at a directivity angle θ of 125°, which is at or near the peak noise angle. A significant suppression is obtained with the eccentric nozzle for model-scale frequencies above 1000 Hz. For lower frequencies the effects are minimal. Also given on the abscissa is a second scale showing the corresponding frequencies for a typical full-scale engine (0.69-m diam). It is apparent that the suppression occurs in a frequency range where it would be beneficial at full scale. Similar results were obtained for the inverted-velocity-profile case and show potential for supersonic cruise application (ref. 37).

For purposes of practical application noise suppression is generally desired both in the sideline plane ($\varphi \cong 65°$) and the flyover plane ($\varphi = 0°$). The eccentric nozzle provides maximum suppression in the flyover plane, with decreasing suppression as φ increases toward 90°. However, by shaping the annulus with a constant wide width to $\varphi = 90°$, or even greater, sideline suppression should be achievable. In this procedure the annulus width must be decreased for φ values larger than the φ for the wide-width annulus. This in essence yields an asymmetric passage (fig. 17) for the present nozzle concept.

It is expected that further substantial noise suppression can be achieved with shaped nozzles by incorporating suppressor elements into the design concept. Such nozzle concepts could include either full-core stream suppressors or partial-core stream suppressors. The application of such suppressors could not only reduce the jet noise, but could also enhance the usual suppressor noise reduction of the baseline nozzles by advantageously altering the jet plume velocity profile.

FLIGHT EFFECTS

To assess the effect of aircraft noise on the environment in the vicinity of an airport, it is necessary to predict the effects of flight on the various components of engine noise. For new or proposed aircraft such predictions must often be made on the basis of only static data for the full-scale engine, since costs limit the number of configurations that can be flight tested. Therefore it is essential that methods be developed for obtaining valid static data for projection to flight as well as analytical procedures for making such projections. The general problem is complicated by the fact that the effects of flight are not the same for all the noise components. The Lewis Research Center programs focus on the different problems of inlet and exhaust noise flight effects and simulation.

Fan Inlet Noise

Modern turbofan engines exhibit less fan noise in flight than is projected from ground static tests. A major reason for this discrepancy is the apparent existence of an additional noise source in ground static tests that is not present in flight. This extraneous noise mechanism, illustrated in figure 18, is due to rotor interaction with inflow disturbances. The rotor blades cut externally produced turbulence, wakes, or vortices that are drawn into the inlet. At subsonic fan tip speeds this source often obscures or completely masks the rotor-stator interaction source expected to be dominant in flight.

The reason for the prominence of the inflow source statically and its greatly reduced importance in flight (ref. 10) are illustrated in figure 19. The nature of the fan inlet flow field for both the static and flight cases is shown on the left side of the figure, and the corresponding fan spectra are shown on the right. In the static case turbulence in the atmosphere as well as wakes and vortices from the proximity of the test stand and ground plane are drawn into the inlet through the greatly contracting stream tubes. The contraction intensifies transverse turbulent fluctuations and stretches the disturbances axially so that the rotor blades cut each intensified disturbance many times. Tone bursts are generated that appear as a strong blade passing tone and harmonics in the fan spectrum. In contrast, in the flight case the stream tubes do not contract to intensify and elongate the atmospheric turbulence, and test-stand and ground-plane disturbances are not present. Thus for fan stages that have been designed to limit the noise produced by rotor-stator interaction, the tone levels, particularly those of the fundamental tone, are greatly reduced.

Several investigators (refs. 38 to 44) have shown that honeycomb-screen structures mounted over the test inlet can reduce inflow disturbances and the resultant tone noise. Recent tests have been conducted at the Lewis Research Center to evaluate several types of inflow control devices (ICD) similar to that shown in figure 20 (ref. 45). These tests were conducted on a JT15D engine with a massive exhaust muffler, as shown in figure 21. The ICD's ranged from 1.6 to 4 fan diameters in size and differed in shape and fabrication method. The results obtained with the ICD shown in figures 20 and 21 are summarized in figure 22. All the ICD's significantly reduced the blade passing tone in the far field, but the smallest ICD's apparently introduced propagating modes that could be identified by additional lobes in the directivity patterns. Other recent experiments on fan source noise with this type of ICD are reported in reference 46. Flight tests are being conducted by the Langley Research Center for this engine mounted on an OV-1 airplane as shown in figure 23. Thus actual flight data will be obtained that will permit an evaluation of how well the ICD's reproduce the flight type of inflow condition.

Jet Exhaust Noise

The subject of flight effects on jet exhaust noise has been a rather controversial one in recent years. Some of the terminology needed to describe flight effects is defined in figure 24. The cases considered herein are level flyovers at an airplane velocity of V_0. The observer is located at an angle θ from the engine inlet axis.

According to classical jet noise theory in-flight jet noise should follow a fairly simple relation, as the velocity arrows at the bottom of figure 24 suggest. For a given absolute jet velocity V_j (shown by the upper, longer arrow), increasing the flight velocity V_0 (shown by the lower, shorter arrow) reduces the velocity of the jet relative to the air. This reduces the shear, and therefore the noise should be less in flight.

The current interest in flight effects was greatly stimulated several years ago when Rolls-Royce (refs. 47 and 48) reported results like those shown in figure 25, where the overall sound pressure level is plotted as a function of directivity angle. The static case is shown by the solid curve, and the corresponding flight case is shown by the dash-dot and curve. The noise in the rear quadrant was reduced, as expected. However, in some cases, such as the one shown here, the noise in the forward quadrant increased in flight. Further confusing the issue is the fact that model-jet simulated flight tests indicate that in-flight noise should be reduced at all angles, as shown by the dashed curve. Studies conducted or sponsored by NASA suggest that these apparent anomalies can be resolved when the engine internal noise is considered (refs. 49 to 55). The internal noise is amplified by a sufficient amount (ref. 56) that the total in-flight noise exceeds the static level even though the jet noise is reduced.

Based on the favorable comparisons with flight data when internal noise is accounted for, a methodology has been developed for predicting in-flight exhaust noise for single-stream exhausts from static data (ref. 57). This methodology is illustrated in figure 26. The experimentally determined static total noise is compared with the jet mixing and shock-cell noise predicted from reference 58. The predicted jet noise and shock noise are antilogarithmically subtracted from the total measured noise to produce an inferred excess noise. The inferred excess noise is correlated with similar data for other angles and power settings to produce an empirical excess noise correlation. The correlated excess noise and the shock noise are then projected to flight, as shown on the right side of figure 26, with the assumption of a Doppler frequency shift and an amplification of $-40 \log (1 - M_0 \cos \theta)$. The jet mixing noise in flight is predicted from reference 58, and the total projected flight noise is obtained by antilogarithmic addition.

Typical static results are shown in figure 27 for an Orenda turbojet on an F-86 airplane at high jet velocity (596 m/sec). The results were obtained by Boeing (ref. 59) and made available to NASA. Noise spectra are shown at three angles - $\theta = 50°$ (forward quadrant), $\theta = 90°$ (overhead), and $\theta = 130°$ (peak noise, aft quadrant). It can be seen that the importance of the various noise sources varies with the different angles. Shock noise is dominant in the forward quadrant, and jet mixing noise is dominant in the aft quadrant. At lower power settings the excess noise becomes more important. The projection of these data to flight is compared with actual flyover data in figure 28. The relative importance of jet mixing noise is reduced as compared with the static case (fig. 27), and the projection agrees rather well with the experimental data. Additional comparisons are shown for the Orenda engine on the F-86 in reference 58 and for the J85 turbojet on the Bertin aerotrain in reference 60.

CONCLUDING REMARKS

This paper reviews some of the recent important developments in engine noise reduction technology. Some developments of particular interest are as follows:

1. Sweeping of the fan blades has been shown to be useful in reducing multiple-pure-tone noise. Similarly, increasing sweep has been shown to reduce the noise of advanced turboprop models.

2. Two methods of using nozzle asymmetry have been shown to reduce jet exhaust noise: nonconcentric dual-stream exhausts and the thermal acoustic shield.

3. Inlet flow control devices have been developed that appear to allow static fan noise tests to be made with inflow conditions approximating those encountered in flight. Flight tests are planned to more fully resolve the issue.

4. It is shown that static jet engine exhaust noise can be accurately projected to flight on an absolute basis.

REFERENCES

1. Russell, R. E.: The State of Aircraft Noise Technology. Presented at the EPA Noise Technology Research Symposium, Dallas, Texas, Jan. 29, 1979.

2. Bliss, D. B.; et al.: Design Considerations for a Novel Low Source Noise Transonic Fan Stage. AIAA Paper 76-577, July 1976.

3. Owens, R. E.: Energy Efficient Engine: Propulsion System - Aircraft Integration Evaluation. (PWA-5594-48, Pratt & Whitney Aircraft, NASA Contract NAS3-20646.) NASA CR-159488, 1979.

4. Kobayashi, H.; and Groeneweg, J. F.: Effects of Inflow Distortion Profiles on Fan Tone Noise Calculated Using a 3-D Theory. AIAA Paper 79-0577, Mar. 1979.

5. Rice, E. J.: Spinning Mode Sound Propagation Ducts with Acoustic Treatment. NASA TN D-7913, 1975.

6. Rice, E. J.; and Heidelberg, L. J.: Comparison of Inlet Suppressor Data with Approximate Theory Based on Cutoff Ratio. NASA TM-81386, 1979.

7. Rice, E. J.; Heidmann, M. F.; and Sofrin, T. G.: Modal Propagation Angles in a Cylindrical Duct with Flow and Their Relation to Sound Radiation. AIAA Paper 79-0183, Jan. 1979. (Also NASA TM-79030, 1979.)

8. Homicz, G. F.; and Lordi, J. A.: A Note on the Radiative Directivity Patterns of Duct Acoustic Modes. J. Sound Vib., vol. 41, no. 3, Aug. 1975, pp. 283-290.

9. Saule, A. V.; and Rice, E. J.: Far-Field Multimodal Acoustic Radiation Directivity. NASA TM-73839, 1977.

10. Feiler, C. E.; and Groeneweg, J. F.: Summary of Forward Velocity Effects on Fan Noise. AIAA Paper 77-1319, Oct. 1977. (Also NASA TM-73722, 1977.)

11. Hayden, R. E.; et al.: Analysis and Design of a High Speed, Low Noise Aircraft Fan Incorporating Swept Leading Edge Rotor and Stator Blades. (BBN-3332, Bolt, Beranek and Newman, Inc.; NASA Contract NAS3-18512.) NASA CR-135092, 1977.

12. Lucas, J. G.; Woodward, R. P.; and MacKinnon, M. J.: Acoustic Evaluation of a Novel Swept-Rotor Fan. AIAA Paper 78-1121, July 1978. (Also NASA TM-78878, 1978.)

13. General Aviation Propulsion. NASA CP-2126, 1980.

14. Dittmar, J. H.; Blaha, B. J.; and Jeracki, R. J.: Tone Noise of Three Supersonic Helical Tip Speed Propellers in a Wind Tunnel at 0.8 Mach Number. NASA TM-79046, 1978.

15. Dittmar, J. H.; Jeracki, R. J.; and Blaha, B. J.: Tone Noise of Three Supersonic Helical Tip Speed Propellers in a Wind Tunnel. NASA TM-79167, 1979.

16. Doyle, V. L.; and Matta, R. K.: Attenuation of Upstream-Generated Low Frequency Noise by Gas Turbines. (R77AEG482, General Electric Co.; NASA Contract NAS3-19435.) NASA CR-135219, 1977.

17. Matta, R. K.; and Mani, R.: Theory of Low Frequency Noise Transmission Through Turbines. (R77AEG570, General Electric Co.; NASA Contract NAS3-20027.) NASA CR-159457, 1979.

18. Reshotko, M.; and Karchmer, A. M.: Combustor Fluctuating Pressure Measurements In-Engine and in a Component Test Facility: A Preliminary Comparison. NASA TM-73845, 1977.

19. Reshotko, M.; et al.: Core Noise Measurements of a YF-102 Turbofan Engine. AIAA Paper 77-21, Jan. 1977.

20. Karchmer, A. M.; and Reshotko, M.: Core Noise Source Diagnostics on a Turbofan Engine Using Correlation and Coherence Techniques. NASA TM X-73535, 1976.

21. Karchmer, A. M.; Reshotko, M.; and Montegani, F. J.: Measurement of Far Field Combustion Noise from a Turbofan Engine Using Coherence Functions. AIAA Paper 77-1277, Oct. 1977. (Also NASA TM-73748, 1977.)

22. von Glahn, U. H.: Correlation of Combustor Acoustic Power Levels Inferred from Internal Fluctuating Pressure Measurements. NASA TM-78986, 1978.

23. Miles, J. H.; and Raftopoulos, D. D.: Spectral Structure of Pressure Measurements Made in a Combustion Duct. NASA TM-81471, 1980.

24. Aeropropulsion 1979. NASA CP-2092, 1979.

25. Kester, J. D.; and Peracchio, A. A.: Noise Technology for Future Aircraft Power Plants. Mech. Eng., vol. 99, no. 1, Jan. 1977, pp. 40-47.

26. Pennock, A. P.: Mixer Nozzle Noise Characteristics. AIAA Paper 80-0166, Jan. 1980.

27. Packman, A. B.; and Eiler, D. C.: Internal Mixer Investigation for JT8D Engine Jet Noise Reduction. Vol. 1: Results. PWA-5582-VOL-1, Pratt & Whitney Aircraft Group, 1977. (FAA-RD-77-132-1-VOL-1, AD-A057309.)

28. Mani, R.; et al.: High Velocity Jet Noise Source Location and Reduction, Task 2 - Theoretical Developments and Basic Experiments. R78AEG323, General Electric Co., 1978. (FAA-RD-76-79,II.)

29. Cowan, S. J.; and Crouch, R. W.: Transmission of Sound Through a Two-Dimensional Shielding Jet. AIAA Paper 73-1002, Oct. 1973.

30. Bhat, W. V.: Experimental Investigation of Noise Reduction from Two Parallel Flow Jets. AIAA Paper 77-1290, Oct. 1977.

31. Shivashankara, B. N.; and Bhat, W. V.: Noise Characteristics of Two Parallel Jets of Unequal Flow. AIAA Paper 80-1068, Jan. 1980.

32. Ahuja, K. K.; and Dosanjh, D. S.: Heated Fluid Shroud as an Acoustic Shield for Noise Reduction - An Experimental Study. AIAA Paper 77-1286, Oct. 1977.

33. Olsen, W. A.; and Friedman, R.: Jet Noise from Co-Axial Nozzles over a Wide Range of Geometric and Flow Parameters. AIAA Paper 74-43, Jan. 1974. (Also NASA TM X-71503, 1974.)

34. Goodykoontz, Jack H.: Effect of a Semi-Annular Thermal Acoustic Shield on Jet Exhaust Noise. NASA TM-81615, 1980.

35. Goodykoontz, J. H.; and Stone, J. R.: Experimental Study of Coaxial Nozzle Noise. AIAA Paper 79-0631, Mar. 1979. (Also NASA TM-79090, 1979.)

36. Goodykoontz, J.; and von Glahn, U.: Noise Suppression due to Annulus Shaping of an Inverted-Velocity-Profile Coaxial Nozzle. NASA TM-81460, 1980.

37. von Glahn, U.; and Goodykoontz, J.: Noise Suppression due to Annulus Shaping for a Conventional Coaxial Nozzle. NASA TM-81461, 1980.

38. Jones, W. L.; McArdle, J. G.; and Homyak, L.: Evaluation of Two Inflow Control Devices for Flight Simulation of Fan Noise Using a JT15D Engine. AIAA Paper 79-0654, Mar. 1979.

39. Shaw, L. M.; et al.: Inlet Turbulence and Fan Noise Measured in an Anechoic Wind Tunnel and Statically with an Inlet Flow Control Device. NASA TM-73723, 1977.

40. Woodward, R. P.; et al.: Effectiveness of an Inlet Flow Turbulence Control Device to Simulate Flight Fan Noise in an Anechoic Chamber. NASA TM-73855, 1977.

41. Hodder, B. K.: An Investigation of Possible Causes for the Reduction of Fan Noise in Flight. AIAA Paper 76-585, July 1976.

42. Ho, P. Y.; Smith, E. B.; and Kantola, R. A.: An Inflow Turbulence Reduction Structure for Scale Model Fan Testing. AIAA Paper 79-0655, Mar. 1979.

43. Kantola, R. A.; and Warren, R. E.: Reduction of Rotor-Turbulence Interaction Noise in Static Fan Noise Testing. AIAA Paper 79-0656, Mar. 1979.

44. Ginder, R. B.; Kenison, R. C.; and Smith, A. D.: Considerations for the Design of Inlet Flow Conditioners for Static Fan Noise Testing. AIAA Paper 79-0657, Mar. 1979.

45. McArdle, J. G.; Jones, W. L.; Heidelberg, L. J.; and Homyak, L.: Comparison of Several Inflow Control Devices for Flight Simulation of Fan Tone Noise Using a JT15D-1 Engine. AIAA Paper 80-1025, June 1980.

46. Woodward, R. P.; and Glaser, F. W.: Effect of Inflow Control on Inlet Noise of a Cut-On Fan. AIAA Paper 80-1049, June 1980. (Also NASA TM-81487, 1980.)

47. Brooks, J. R.; and Woodrow, R. J.: The Effects of Forward Speed on a Number of Turbojet Exhaust Silencers. AIAA Paper 75-506, Mar. 1975.

48. Bushell, K. W.: Measurement and Prediction of Jet Noise in Flight. AIAA Paper 75-461, Mar. 1975.

49. Stone, J. R.: On the Effects of Flight on Jet Engine Exhaust Noise. NASA TM X-71819, 1975.

50. Merriman, J. E.; et al.: Forward Motion and Installation Effects on Engine Noise. AIAA Paper 76-584, July 1976.

51. Blankenship, G. L.; et al.: Effect of Forward Motion on Engine Noise. (MDC-J7708, Douglas Aircraft Co., Inc.; NASA Contract NAS3-20031) NASA CR-134954, 1977.

52. Stone, James R.: Prediction of In-Flight Exhaust Noise for Turbojet and Turbofan Engines. Noise Control Eng., vol. 10, no. 1, Jan.-Feb. 1978, pp. 40-46.

53. Stone, J. R.: On the Use of Relative Velocity Exponents for Jet Engine Exhaust Noise. NASA TM-78873, 1978.

54. Ahuja, K. K.; Tester, B. J.; and Tanna, H. K.: The Free Jet as a Simulator of Forward Velocity Effects on Jet Noise. NASA CR-3056, 1978.

55. Burcham, F. W., Jr.; Lasagna, P. L.; and Oas, S. C.: Measurements and Predictions of Flyover and Static Noise of a TF-30 Afterburning Turbofan Engine. NASA TP-1372, 1978.

56. Morse, P. M.; and Ingard, K. U.: Theoretical Acoustics. McGraw-Hill Book Co., Inc., 1968.

57. Stone, J. R.: Prediction of Unsuppressed Jet Engine Exhaust Noise in Flight from Static Data. AIAA Paper 80-1008, June 1980. (Also NASA TM-81537, 1980.)

58. Stone, J. R.; and Montegani, F. J.: An Improved Prediction Method for the Noise Generated in Flight by Circular Jets. NASA TM-81470, 1980.

59. Strout, F. G.: Flight Effects on Uniform Flow Jet Noise. D6-48036, Boeing Commercial Airplane Co., 1978.

60. Clapper, W.; and Stringas, E. J.: High Velocity Jet Noise Source Location and Reduction, Task 4 - Development/Evaluation of Techniques for "In-flight" Investigation. R77AEG189, General Electric Co., 1977. (FAA-RD-76-79-4, AD-A041849.)

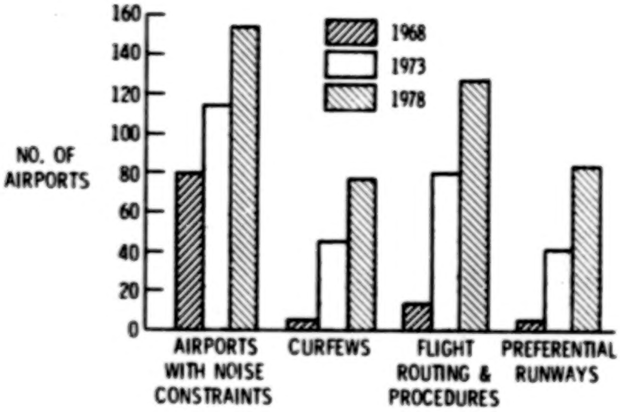

Figure 1.- Noise constraints at major world airports.

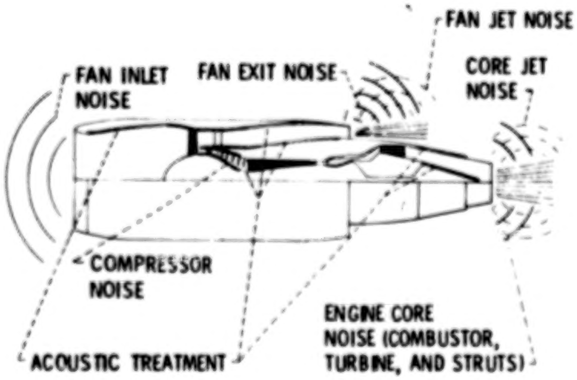
FAN JET NOISE
FAN INLET NOISE
FAN EXIT NOISE
CORE JET NOISE
COMPRESSOR NOISE
ENGINE CORE NOISE (COMBUSTOR, TURBINE, AND STRUTS)
ACOUSTIC TREATMENT

Figure 2.- Turbofan engine noise sources.

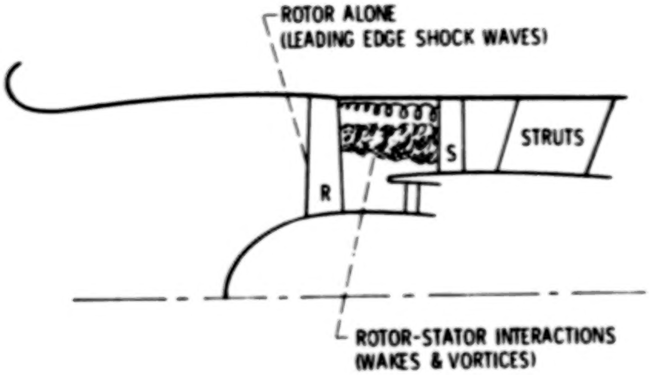
ROTOR ALONE
(LEADING EDGE SHOCK WAVES)
R
S
STRUTS
ROTOR-STATOR INTERACTIONS
(WAKES & VORTICES)

Figure 3.- Fan noise sources.

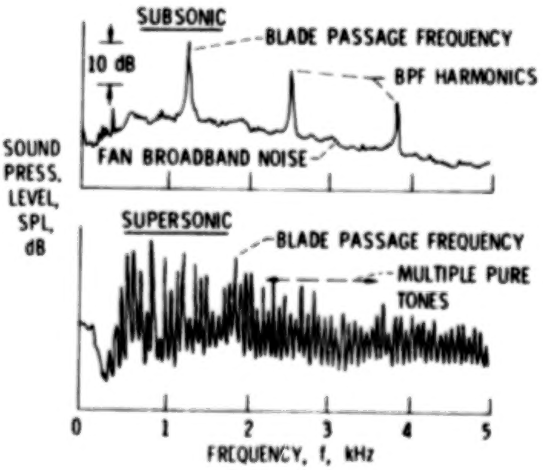

Figure 4.- Fan noise spectra at subsonic and supersonic tip speeds.

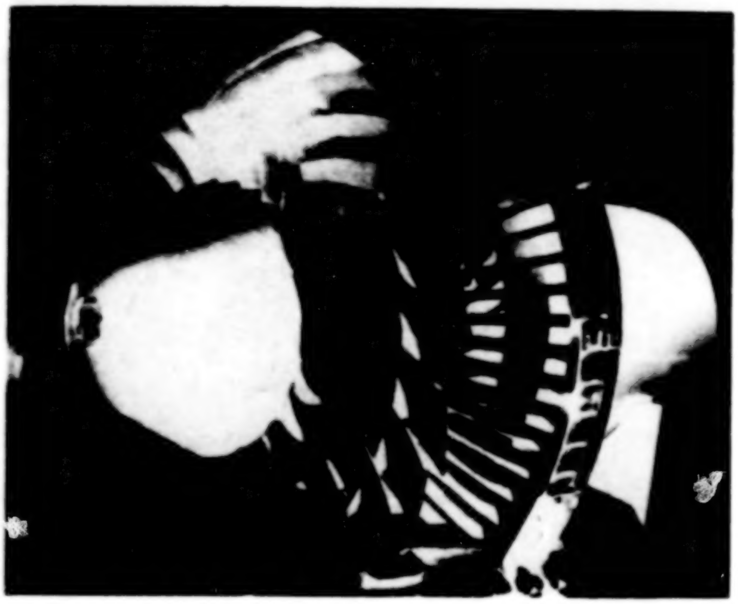

Figure 5.- Swept-rotor fan.

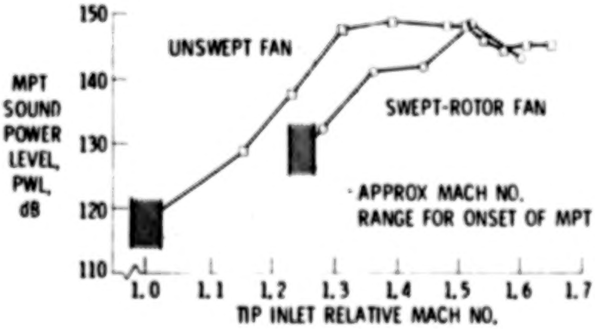

Figure 6.- Multiple-pure-tone generation of unswept- and swept-rotor fans.

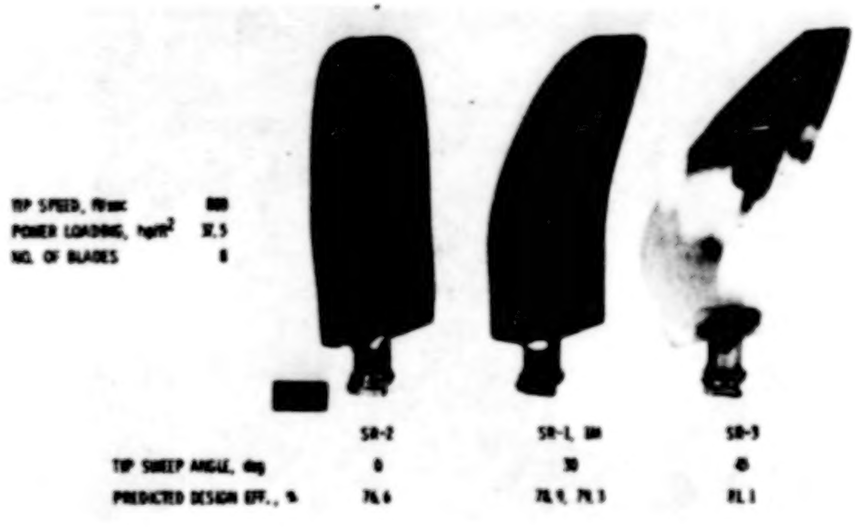
TIP SPEED, ft/sec 800
POWER LOADING, hp/ft² 37.5
NO. OF BLADES 8
SR-2
SR-1, 1M
SR-3
TIP SWEEP ANGLE, deg 0 30 45
PREDICTED DESIGN EFF., % 76.6 78.9, 79.3 81.1

Figure 7.- Propeller model comparison. (Note: 1 ft = 0.305 m and 1 hp/ft^2 = 8018 W/m^2.)

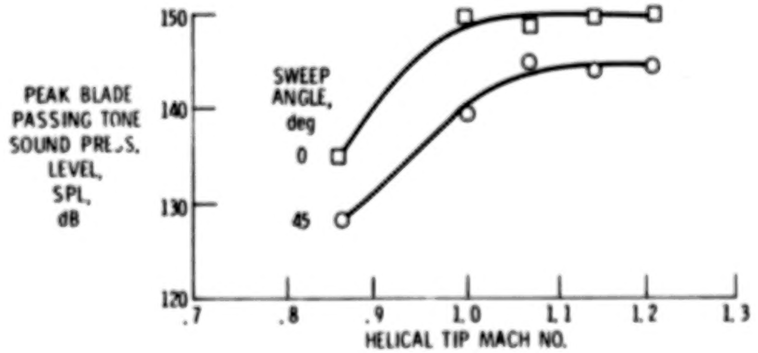

Figure 8.- Effect of tip Mach number on measured noise.

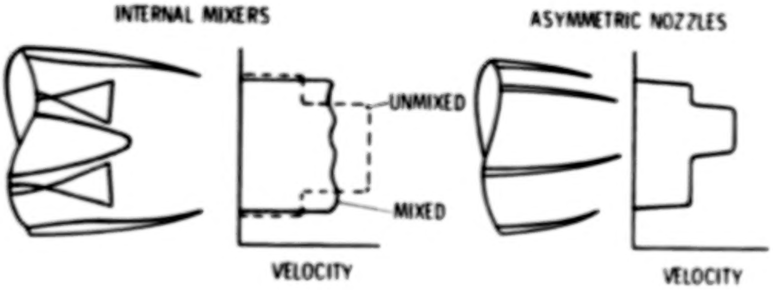
INTERNAL MIXERS
UNMIXED
MIXED
VELOCITY
ASYMMETRIC NOZZLES
VELOCITY

Figure 9.- Jet noise reduction concepts.

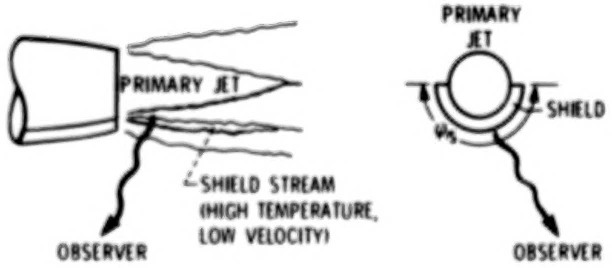
PRIMARY JET
SHIELD STREAM (HIGH TEMPERATURE, LOW VELOCITY)
OBSERVER
PRIMARY JET
SHIELD
ψs
OBSERVER

Figure 10.- Thermal acoustic shield schematic.

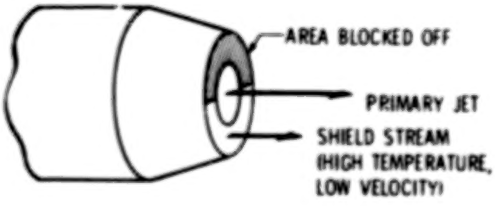
AREA BLOCKED OFF
PRIMARY JET
SHIELD STREAM (HIGH TEMPERATURE, LOW VELOCITY)

Figure 11.- Thermal acoustic shield test configuration.

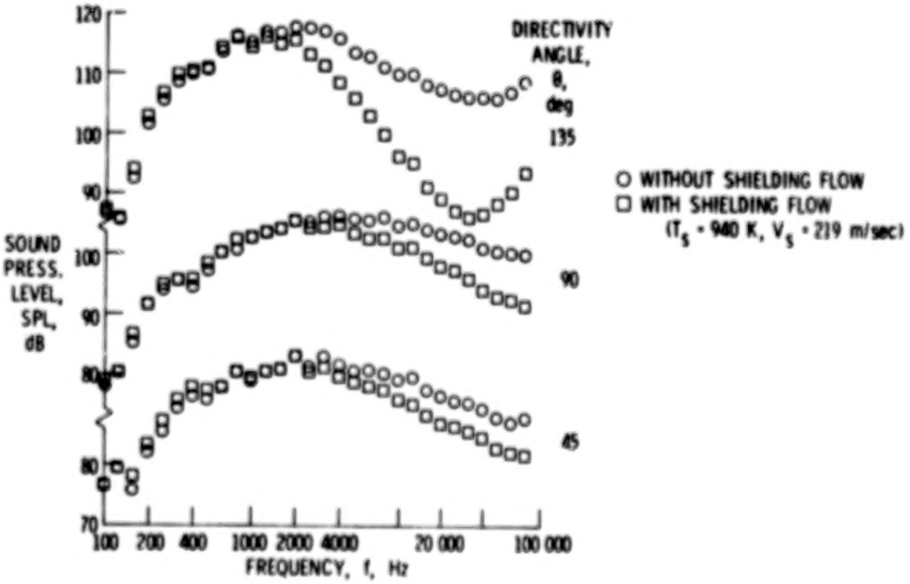

Figure 12.- Effect of shielding flow on subsonic jet noise for coplanar, coannular nozzle. Jet velocity, 575 m/sec.

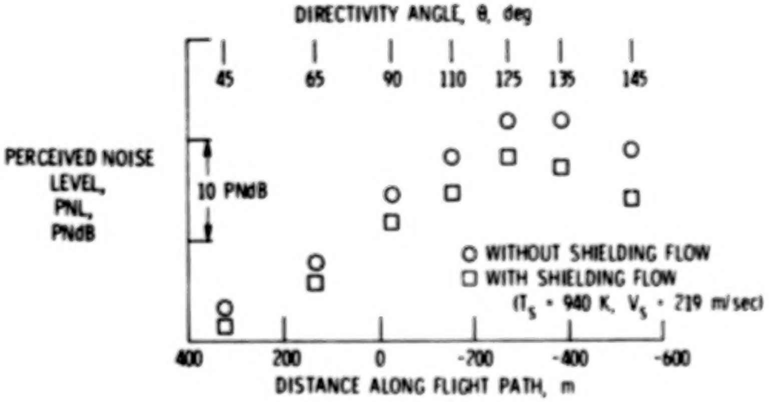

Figure 13.- Effect of shielding flow on flyover perceived noise levels for large scale conical nozzle. V_j = 575 m/sec; subsonic, flyover distance, 335 m.

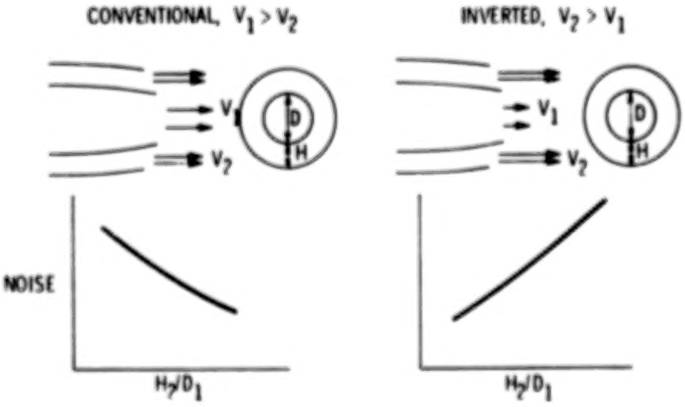
CONVENTIONAL, $V_1 > V_2$
INVERTED, $V_2 > V_1$
V_1
V_2
D
H
NOISE
H_2/D_1
H_2/D_1

Figure 14.- Coannular nozzle geometric effects.

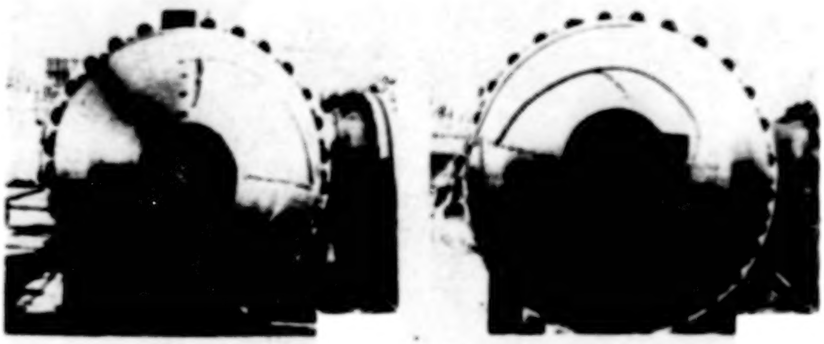
CONCENTRIC NOZZLE
ECCENTRIC NOZZLE

Figure 15.- Concentric and eccentric nozzles.

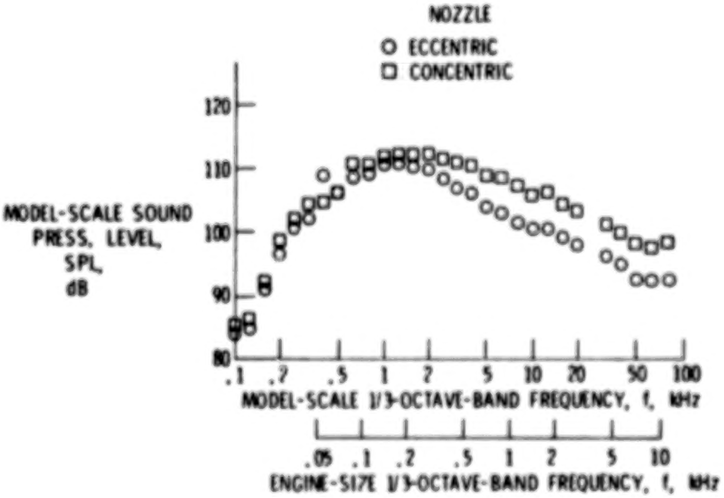

Figure 16.- Model-scale spectra. $\theta = 125^\circ$; $PR_i = 2.2$; $PR_o = 1.4$; $V_o = 496$ m/sec; $V_i = 229$ m/sec.

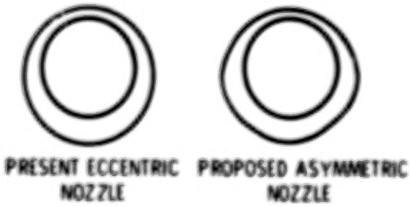
PRESENT ECCENTRIC NOZZLE
PROPOSED ASYMMETRIC NOZZLE

Figure 17.- Nonaxisymmetric application of suppression principle.

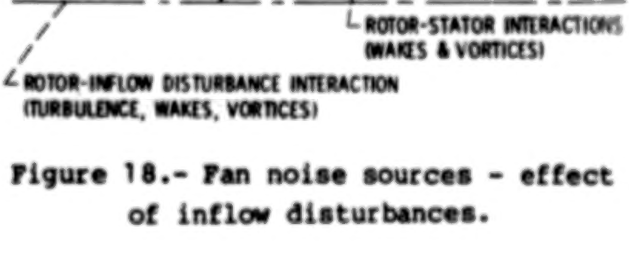
ROTOR ALONE (LEADING-EDGE SHOCK WAVES)
R
S
STRUTS
ROTOR-STATOR INTERACTIONS (WAKES & VORTICES)
ROTOR-INFLOW DISTURBANCE INTERACTION (TURBULENCE, WAKES, VORTICES)

Figure 18.- Fan noise sources - effect of inflow disturbances.

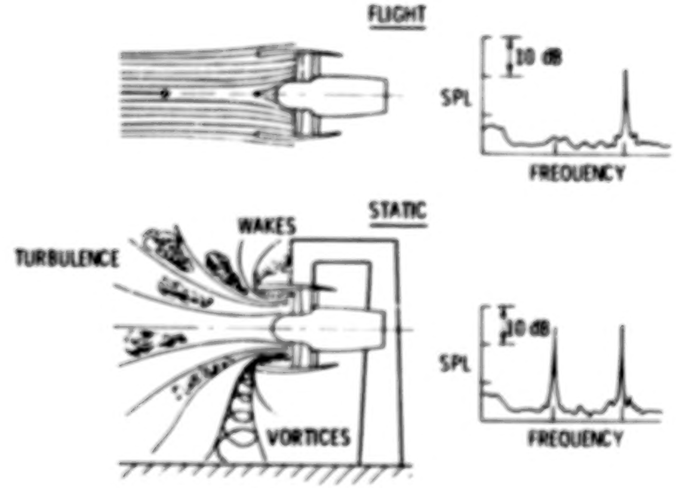
FLIGHT
10 dB
SPL
FREQUENCY
STATIC
WAKES
TURBULENCE
10 dB
SPL
VORTICES
FREQUENCY

Figure 19.- Forward velocity effects on inlet flow and noise.

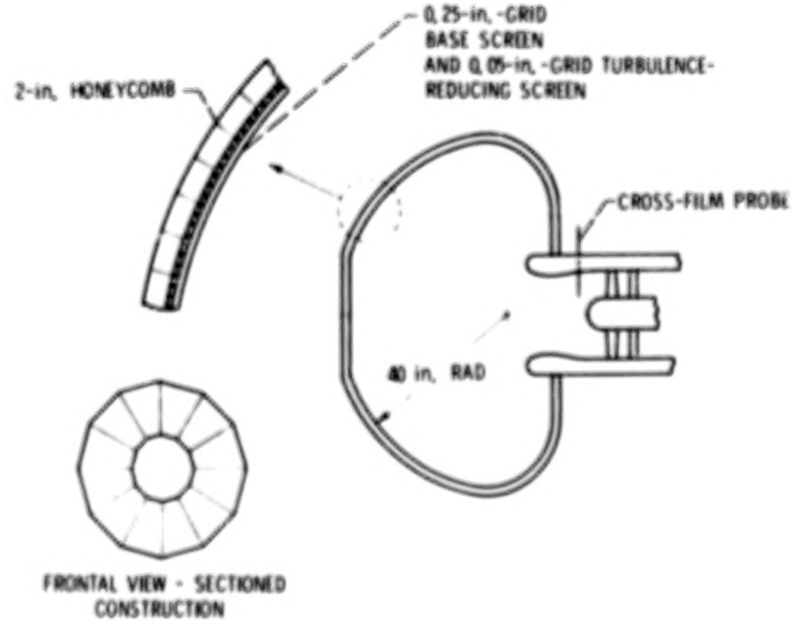
0.25-in.-GRID
BASE SCREEN
AND 0.05-in.-GRID TURBULENCE-
REDUCING SCREEN
2-in. HONEYCOMB
CROSS-FILM PROBE
40 in. RAD
FRONTAL VIEW - SECTIONED
CONSTRUCTION

Figure 20.- Inflow control device. (Note: 1 in. = 2.54 cm.)

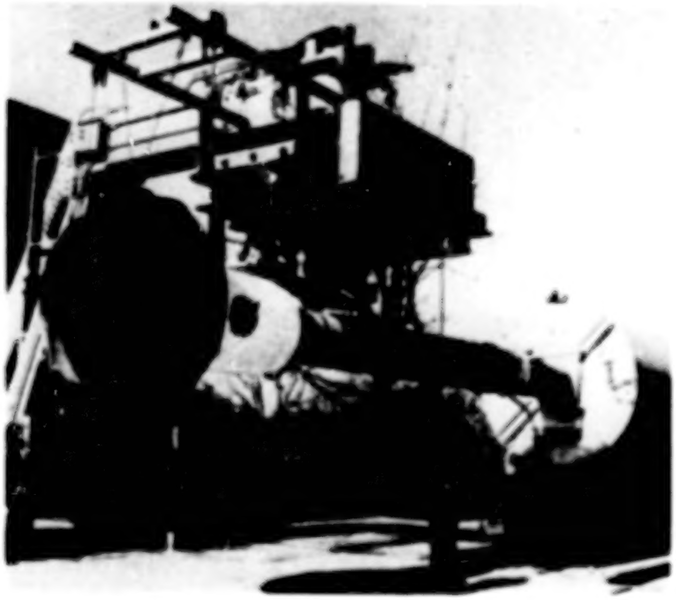

Figure 21.- JT15D engine with ICD installed.

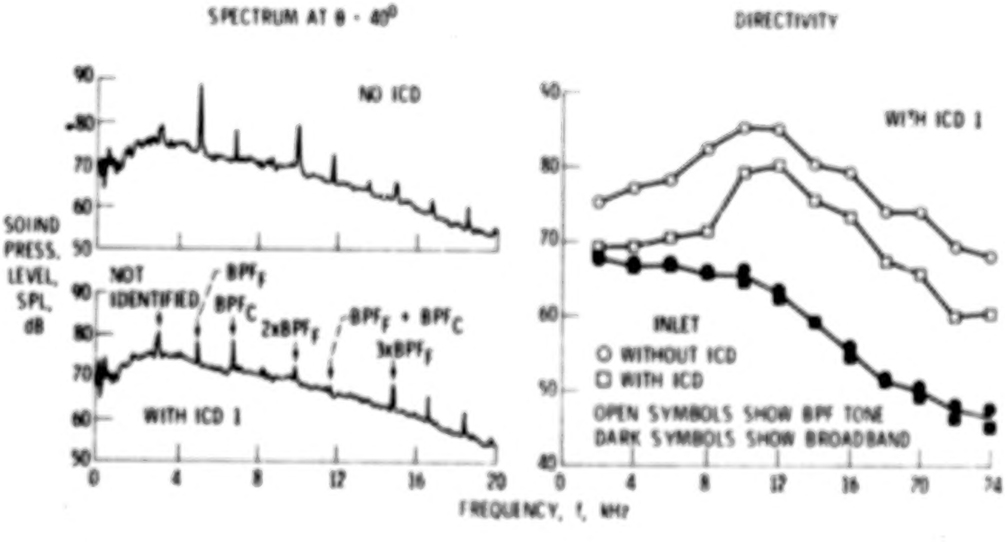

Figure 22.- Effect of inflow control device on fan noise generation.

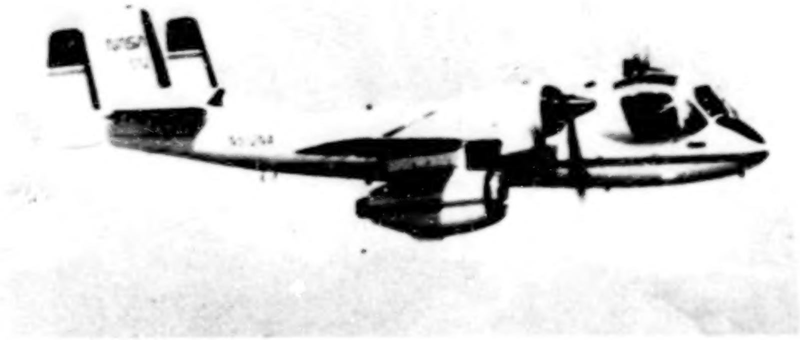

Figure 23.- OV-1 in flight with JT15D engine installed.

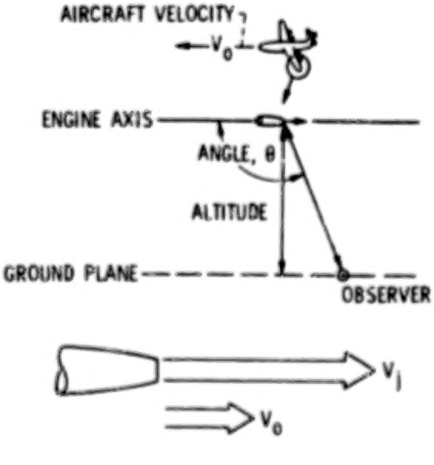
AIRCRAFT VELOCITY
V_0
ENGINE AXIS
ANGLE, θ
ALTITUDE
GROUND PLANE
OBSERVER
V_j
V_0

Figure 24.- Flight effects on exhaust noise.

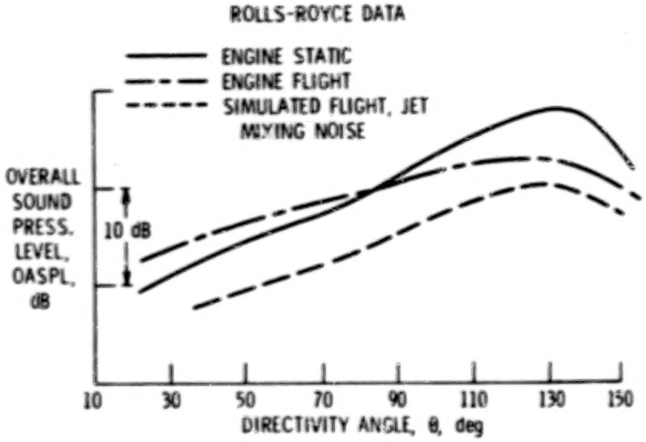

Figure 25.- Typical flight effects on exhaust noise.

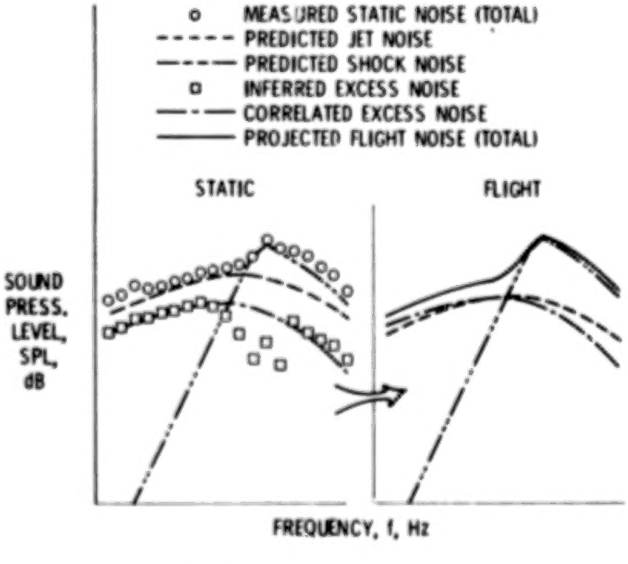

Figure 26.- Methodology for predicting in-flight noise from static data.

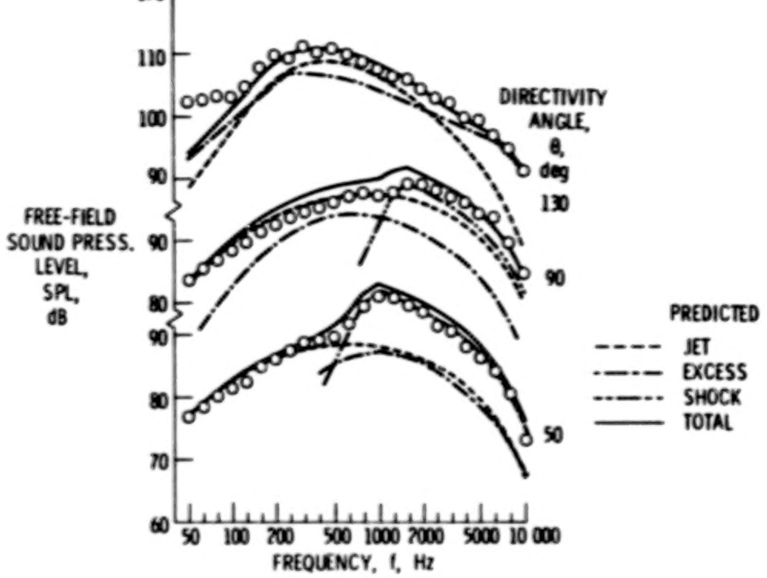

Figure 27.- Experimental and predicted static spectra for Orenda turbojet on F-86 airplane. High jet velocity (596 m/sec).

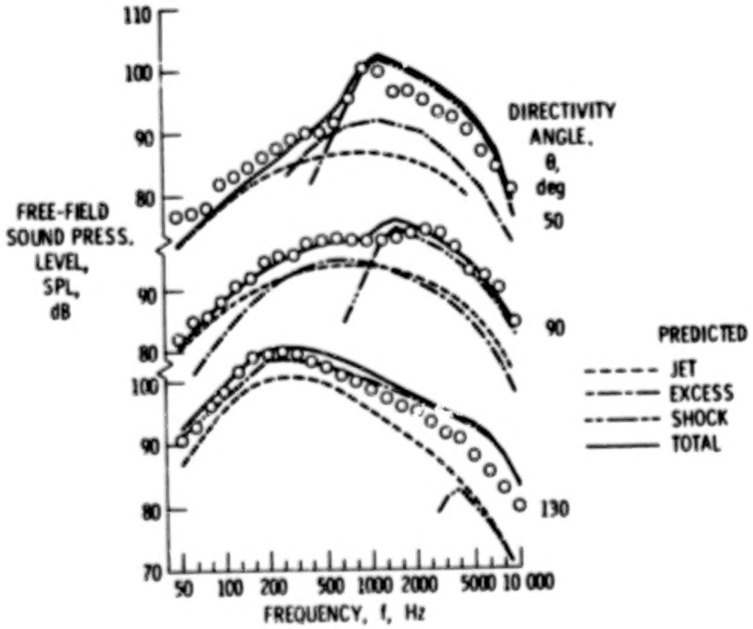

Figure 28.- Experimental and predicted flight spectra for Orenda turbojet on F-86 airplane. High jet velocity (596 m/sec).

SOURCES, CONTROL, AND EFFECTS OF NOISE FROM AIRCRAFT PROPELLERS AND ROTORS

John S. Mixson, George C. Greene, and Thomas K. Dempsey

SUMMARY

Control of noise generated by aircraft propellers and rotors is important to minimize annoyance or discomfort felt by community residents and aircraft passengers. This paper describes recent NASA and NASA-sponsored research on the prediction and control of propeller and rotor source noise, on the analysis and design of fuselage-sidewall noise control treatments, and on the measurement and quantification of the response of passengers to aircraft noise. Source noise predictions are compared with measurements for conventional low-speed propellers, for new high-speed propellers (propfans), and for a helicopter. Results from a light aircraft demonstration program are described, indicating that about 5-dB reduction of flyover noise can be obtained without significant performance penalty. Sidewall design studies are described for interior noise control in light general aviation aircraft and in large transports using propfan propulsion. The weight of the added acoustic treatment is estimated and tradeoffs between weight and noise reduction are discussed. A laboratory study of passenger response to combined broadband and tonal propeller-like noise is described. Subject discomfort ratings of combined tone-broadband noises are compared with ratings of broadband (boundary layer) noise alone, and the relative importance of the propeller tones is examined.

INTRODUCTION

Noise generated by aircraft propellers and rotors can propagate into the airport community and into the aircraft interior causing annoyance and discomfort of residents and passengers. The importance of control is indicated by the large number of general aviation aircraft, the increasing use of fixed-wing and rotary-wing business aircraft, and the increasing number of propeller-driven commuter aircraft. In addition, the need to reduce fuel consumption has lead to the study of high-speed, large capacity, propeller-driven aircraft to be used in scheduled airline service as alternates to current jet aircraft. While developing noise control methods, it is also important to minimize the impact of noise control on the aircraft performance and weight.

Control of the noise at the source can be expected to reduce the impact on both community and passengers. This paper describes recent studies of the prediction and control of source noise generated by conventional low-speed propellers, by new high-speed propellers (propfans), and by helicopter rotors. In addition to source noise reduction, noise control treatment is usually required in the aircraft sidewall to provide a comfortable environment for passengers. Recent studies of the analysis and design of acoustic treatment for aircraft sidewalls are described for application to light general aviation aircraft and to large transports using propfan propulsion. Approaches to minimizing the added weight are also discussed. Minimizing the aircraft weight or performance penalty while providing an acceptable environment requires a detailed understanding of the responses of people to the noise. Therefore, the final topic discussed in this paper is the measurement of passenger response to noise and vibration environments, including a recent laboratory study using combined broadband noise and tonal propeller-type noise. The paper summarizes the objectives, recent results, and future trends of NASA and NASA-sponsored research in the three areas, with specific attention to applications to general aviation aircraft, helicopters, and advanced high-speed turboprop aircraft.

PROPELLER AND ROTOR NOISE PREDICTION

The purpose of NASA's propeller and helicopter-rotor noise research program is to provide a technology base for reducing noise with a minimum of performance, weight, and economic penalties. Noise prediction technology represents the most basic part of the program. The emphasis of this activity is on the understanding and prediction of noise using basic principles of physics. This requires a knowledge of the geometry, operating conditions, and aerodynamic characteristics of the propeller/rotor.

Low-Speed Propellers

Examples of noise calculations for low-speed propellers using recently developed technology (refs. 1-3) are shown in figures 1 and 2. Figure 1 shows a comparison of measured and calculated noise for a light, twin-engine transport aircraft. The data, obtained during an extensive flight test program (ref. 1), were taken at a propeller-tip Mach number of approximately 0.85, at an airspeed of approximately 55 m/s, and with one engine shutdown. The acoustic measurements were made in the plane of the propeller with a microphone mounted on a boom on the aircraft wing. The noise calculations were made using the two methods described in reference 3, both giving the same numerical results. The good agreement shown is typical of the comparisons over a range of flight conditions.

Figure 2 shows another comparison of measured and calculated results for low-speed propellers (ref. 2). The measurements were made during the evaluation of quiet propeller designs in an anechoic wind tunnel, as shown in the schematic on the right side of the figure. The data are for a 1/4-scale model of a light, single-engine aircraft propeller at an airspeed of approximately 30 m/s. Noise data were measured with a microphone mounted in the airstream 1 diameter from the center of propeller rotation. The acoustic pressure time history is presented for approximately two revolutions of the propeller. The almost perfect agreement is a result of very careful acoustic measurements and accurate calculations of the propeller aerodynamic characteristics.

High-Speed Propellers

High-speed propeller/rotor noise prediction technology is evolving rapidly (refs. 3-7). It is a difficult problem because of the relatively high tip Mach numbers, advanced blade geometry, and complex aerodynamic flow field. In addition, there is little acoustic data available to evaluate the predictions because there are no high-speed acoustic facilities for testing propellers.

A comparison of predicted and measured noise for a compromise test condition (ref. 8) is shown in figure 3. These results are for a 0.61-m diameter, two-bladed version of the high-speed propeller shown in the photograph. This propeller was designed for a freestream Mach number of 0.8 and was tested in an open-jet wind tunnel at a freestream Mach number of 0.3 with the propeller rpm increased so that the tip Mach number was equal to the design value of approximately 1.13. The noise measurements were made in an anechoic chamber surrounding the free jet with corrections applied for the shear-layer effects. The noise calculations were made using the method of reference 9, which includes only the effects of blade thickness and loading. The agreement for the lower harmonics is good; however, there is a tendency to underpredict the level of the fundamental.

This tendency to underpredict the fundamental is different from results (ref. 10) obtained in a hard-wall wind tunnel at freestream Mach numbers between 0.6 and 0.85. Reference 10 indicates that the noise level at the fundamental frequency is nearly constant for tip Mach numbers above 1.07. At a tip Mach number of 1.14, the noise level predicted by the method of reference 9 is 5 to 10 dB higher than the values measured in the hard-wall tunnel. It has not been established whether the differences between measured and calculated noise are due to facility differences, measurement techniques, or difficulty in modeling the aeroacoustic phenomena. This uncertainty may be resolved during planned flight tests of the propellers used in the study described in reference 10.

Helicopters

Helicopter noise is more difficult to predict than propeller noise because of the complex aerodynamic environment in which the rotors operate. The noise field is highly dependent upon aircraft geometry and aerodynamic environment, and the dominant noise generating mechanism may change with flight condition or observer locations.

Helicopter noise prediction methodology has been under development for many years. In spite of significant advances (for example, ref. 11), there is still no generally accepted method which can accurately predict helicopter rotor noise. Efforts to develop better methods have been hampered by the proprietary nature of helicopter noise prediction methods and a reluctance to share noise data because of competitive pressure and pending noise regulations. The absence of a high-quality and complete data base for a wide range of helicopter configurations has had a negative impact on the development and general acceptance of noise prediction theory.

Acquisition of a data base has also been hampered by the general lack of ground facilities with capability for acoustic tests of helicopter models. The only facility specifically designed for helicopter noise research is the Army indoor hover facility at the Ames Research Center, which has proved to be a valuable research tool. A number of other facilities have been used for helicopter noise research including the Ames 40 x 80 wind tunnel, the Langley V/STOL tunnel, and several smaller wind tunnels. Although each of these facilities is limited to some degree by acoustic characteristics, model size, or forward speed capability, some useful results can be obtained if care is taken in the experiment design. This may entail measuring noise in the near field, signal averaging to minimize background noise effects, or testing one configuration relative to another. For a variety of reasons, it has proven difficult to obtain good, absolute level data in the wind tunnel. It is this absolute data which is required for verifying and developing better noise prediction methods.

Flight tests may prove to be the best source of high-quality noise data. Two efforts were recently initiated to assemble existing flight-test data and use it to assess the status of current noise prediction methods. The data being assembled consists of noise data and rotor-blade pressure measurements for two helicopter configurations, as well as a complete set of flight parameters, and will be prepared with complete documentation in a format suitable for computer processing. These measured data are currently being used to evaluate a new noise prediction method based on an extension of the computer program described in ref. 9 and linear acoustic theory of reference 11. In addition, calculated aerodynamic inputs are being used to determine the sensitivity of the predicted noise to the quality of the input data.

One of the configurations being studied is shown in figure 4. It is in the 15 000-kg gross-weight range and has a 22-m diameter, six-bladed rotor with a tip speed of about 216 m/s. Although the study is not complete, there have been a number of preliminary comparisons between the predicted and measured noise data. Figure 5 shows a comparison for a 49-m/s flyover at 152-m altitude. The comparison was made using calculated rotor airloads for an observer on the ground, 305 m ahead of the aircraft. The agreement between predicted and measured noise levels is encouraging for the limited number of harmonics shown. The agreement for greater observer distances is not as good. This is due, at least in part, to the fact that only spherical spreading effects are included in the current calculations. An additional concern is that the original measured data contained ground reflection effects which were removed with a relatively simple correction method. These effects will require further investigation.

PROPELLER NOISE/PERFORMANCE DEMONSTRATION

The propeller noise/performance program is a joint NASA/EPA program to demonstrate that propeller noise for general aviation aircraft can be reduced in an economically reasonable manner. The goal of this effort is to reduce light aircraft propeller noise by 5 dB(A) while maintaining or improving propeller performance. The effort consists of (1) optimization studies to assess the potential noise and performance benefits of various propeller parameters, (2) wind-tunnel tests to verify design concepts, and (3) flight tests to demonstrate the noise reduction technology. Parallel efforts are being conducted at the Massachusetts Institute of Technology and the Ohio State University.

The parameters which affect both noise and performance were analyzed to determine the tradeoffs required to optimize the propeller. The results of one such parameter variation are shown in figure 6. This figure shows the calculated effect of varying the position of the peak of the radial load distribution on both the propeller noise and efficiency. The significant point is that the noise level can be reduced several dB(A) without a significant effect on propeller efficiency. This change combined with several other parameter changes can result in a significant noise reduction with little or no performance penalty.

In order to test some of the concepts which were developed during the parametric studies, two 1/4-scale model propellers were tested in an anechoic wind tunnel (ref. 2). The baseline propeller was a model of a standard Cessna 172 propeller. A "quiet" propeller was also constructed which had a slightly smaller diameter and a wider blade chord. The noise reduction was achieved through a reduction in tip speed due to the smaller diameter and the movement of the load distribution inboard on the propeller blade.

These propellers were tested over a wide range of conditions on a propeller spinning rig with and without an afterbody to simulate an aircraft fuselage. Figure 7 shows the test configuration in the acoustic wind tunnel with a fuselage afterbody.

After demonstrating the noise reduction techniques in the wind tunnel, full-scale propellers were designed for flight tests. Figure 8 shows the standard and "quiet" propellers mounted on a Cessna 172 aircraft. The aircraft was flown over a ground microphone array at 305-m altitude to determine the noise reduction under FAA noise certification conditions. In addition, aircraft rate of climb was measured over a range of airspeeds to determine the relative performance of the two propellers. These noise and performance results are also shown in figure 8. The "quiet" propeller consistently produced a noise reduction of about 5 dB(A) while retaining climb performance characteristics comparable to the standard propeller.

PROPELLER NEAR-FIELD NOISE

Design of acoustic treatment for an aircraft sidewall requires knowledge of the exterior noise impinging on the sidewall and the interior noise level desired, as well as knowledge of the basic sidewall structure. Impinging noise has been defined for both low-speed and high-speed propellers and sample results are presented in figures 9 and 10.

Low-Speed Propeller

Impinging noise from a low-speed propeller is illustrated in figure 9. The measurements were made on the fuselage of a twin-engine, light aircraft. Noise was measured using an array of 10 flush-mounted microphones, seven of which were located in a horizontal line, and four of which were in a vertical line in the propeller plane. Minimum clearance between the sidewall and the propeller tip was about 0.05 of the propeller diameter. Tests were run at several rpm/power combinations in static conditions and for several forward speeds in taxi tests. Extensive results are presented in reference 12; sample results are shown at the right of the figure. The results indicate that the empirical prediction agrees with results for static tests and the analytical result agrees at low frequencies with measured data from taxi tests. The analytical results were obtained using the computer program of reference 9 with empirical corrections for the effects of the sidewall (ref. 12). The difference between static and taxi test results is due to the ingestion of turbulence that is generated by the propeller inflow interacting with the ground. The lower noise levels associated with the taxi condition were obtained with a forward speed of about 20 m/s or more. From this figure (in addition to figures 1 and 2), it can be concluded that prediction procedures are adequate for noise levels of low-speed, general aviation propellers.

High-Speed Propeller

Near-field noise of a high-speed, propfan propeller is illustrated in figure 10. Test data in this figure were obtained from reference 13. The test setup is indicated in the sketch at the upper left of the figure. The propeller tested (shown in figure 3) was a 0.61-m-diameter model of a swept-blade propeller designed to operate at a forward speed of Mach = 0.8 at an altitude of 10.67 km. The blade sweep is designed to reduce noise and maintain aerodynamic performance. The tests were carried out in an anechoic chamber of an acoustic wind tunnel having airflow capability at Mach = 0.3. At the power conditions of the tests, the propeller was fully immersed in the airflow. To compensate for the lower speed of the airflow, the model propeller was run at increased rpm so the helical tip speed was the same on the model as the full-scale design condition. A boilerplate cylinder was located at 0.8 propeller diameter clearance from the model propeller to simulate the aircraft fuselage, and the impinging noise was measured with an array of microphones flush-mounted in the cylinder.

Contours of equal sound pressure level at the blade-passage frequency from this test are shown at the lower left and predicted contours (ref. 13) are shown at the lower center of the figure. Comparing measured contours with predicted contours shows that the highest level and its location ahead of the propeller plane are in agreement. While the overall appearance of the contours shows reasonable agreement, there are differences in the detailed shapes. Improvements in the prediction procedures discussed earlier may improve agreement. The same analytical procedure used to calculate the model results was also used to predict impinging noise for full-scale flight conditions and the results are shown at the lower right. For this flight condition, the maximum noise occurs aft of the propeller plane. The figure indicates that the highest level is 150 dB with a large area subjected to 148 dB.

THEORETICAL METHODS FOR INTERIOR NOISE REDUCTION

Light Aircraft

Theoretical methods for predicting interior noise levels in light aircraft are under development (ref. 14). The methods are intended for use in designing minimum-weight sidewall structures having sufficient noise transmission loss to provide passenger comfort. A number of mathematical models of the sidewall structure are being investigated to find the simplest model that provides accurate results. Figure 11 shows three sidewall models that are under investigation. When using the flexible panel/rigid stiffener model or the flexible panel/flexible stiffener model, an array of subpanels is assembled to represent the complete sidewall area.

The graph indicates the sensitivity of interior noise to added weight for three candidate noise control approaches. The noise measured used is A-weighted dB to represent passenger comfort; these results were obtained using the panel/rigid stiffener model. All three treatments consist of modifications of the skin properties. Each treatment is applied separately to the structure. The figure indicates that the curves for a given treatment tend to flatten out as weight increases, suggesting a "diminishing returns" type of behavior. Comparing the treatments shows that the damping provides the most interior noise reduction for a given weight and that increasing skin thickness provides comparatively small reductions. The reductions obtained by damping are substantial; the original level of 104 dB(A) is uncomfortable while the level of about 85 dB(A) is reasonably comfortable. The weight required (about 36 kg) is larger than desired but small compared to the aircraft weight/payload.

The theoretical predictions have been verified using simple laboratory panel/box tests (ref. 15). The models are being extended by inclusion of acoustic treatments such as fiberglass wool and double walls, and the improved model is to be used in an investigation of optimum treatment for a twin-engine, light aircraft.

High-Speed Turboprop Aircraft

Theoretical studies have been carried out to determine the weight and configuration of fuselage sidewall acoustic treatment required to provide an 80-dB(A), cabin noise level in propfan-powered aircraft (refs. 16 and 17). Figure 12 summarizes the results. The study required the development of new, comprehensive interior noise prediction methods and considered wide-body, narrow-body, and executive aircraft flying at Mach = 0.8 at 9.14-km altitude. The fuselage sidewall structure consisted of skin, stringers, and rings and had dimensions and materials typical of current operational aircraft. The studies indicated that additional acoustic treatment weight is required in comparison with the treatment normally expected for turbofan powered versions of the study aircraft. Added treatment is required along the fuselage from a station slightly ahead of the forward propeller plane to the tail section and circumferentially around the fuselage above the passenger floor. The sidewall consists of the elements indicated in the sketch; however, the primary noise control action is provided by the masses of the inner trim panel and outer skin acting as a double-wall noise barrier. The weights required to provide the 80-dB(A) interior noise level are shown at the right. In general, these weights are less than 2.5 percent of gross weight. The shaded portion of the bar indicates the range of results obtained from variations of sidewall configuration and analysis methods. The weight penalty for the wide-body aircraft from these studies is slightly less than the weight obtained from the RECAT (reduced energy for commercial transportation) system study; thus, the previous result (RECAT) is confirmed by the more extensive and in-depth recent studies. The RECAT study showed that propfan-powered aircraft have a fuel-saving and direct-operating-cost advantage over turbofan aircraft, even after taking the acoustic weight penalty into account.

PASSENGER COMFORT

Comfort Prediction Model

A program at Langley Research Center has led to the development of a model for predicting passenger discomfort (or acceptance) for existing or future transportation vehicles. Input to the model, figure 13, is the passenger vibration and noise environment for the vehicle and output of the model is the total discomfort measured along a discomfort scale. Development of the model has involved: (1) empirical estimation of discomfort due to sinusoidal and/or random vibrations within single axes; (2) empirical estimation of the discomfort due to vibration in combined axes; and (3) application of empirically determined corrections for the effects of interior noise and duration of vibration. The discomfort scale used to measure the output of the model is displayed in figure 14. The scale is ratio in nature and anchored at discomfort threshold. The figure shows the relationship between the discomfort scale (ordinate of figure 14) and the corresponding percentage (abscissa of figure 14) of passengers who would rate that discomfort level as being uncomfortable. A value of unity along the discomfort scale corresponds to discomfort threshold, i.e., 50 percent of the passengers would be uncomfortable. Details of the methods and procedures used to derive this discomfort scale are given in references 18 and

19. A complete description of the relationship between vibratory inputs and discomfort can be obtained from references 20 and 21. The extensive information contained in these references has been incorporated in a computer program for ease of calculation. For purposes of illustration, figure 15 provides a comparison of various vehicles along the discomfort scale. The figure presents the discomfort level produced by various air and surface transportation vehicles, relative to discomfort threshold. The discomfort values for each vehicle were obtained by using actual measured vibration/noise levels as input to the ride comfort model. These results provide an estimate of absolute discomfort as well as a quantitative comparison (and ranking) between vehicles. For example, the commercial jet transport together with the Bay Area Rapid Transit system and a full-sized automobile provided the best ride quality, i.e., the discomfort levels of each are below discomfort threshold. The various rail vehicles (including the German Bundesbahn and magnetically levitated vehicle) produced estimates of passenger discomfort that were generally somewhat above discomfort threshold and discomfort was seen to increase as vehicle speed increased. A typical city bus produces a relatively large value of discomfort, although the most uncomfortable ride for which data are available was estimated for a helicopter interior noise and vibration environment. However, removal of the noise component of the helicopter ride environment resulted in a discomfort level estimate slightly below discomfort threshold, thus indicating that noise was the predominant source of passenger dissatisfaction within the helicopter. The absolute levels of discomfort and relative ranking of vehicles shown in the figure are in good agreement with actual passenger experience and, hence, provide face validity of the NASA ride comfort scale. Further, since the scale was developed as common to all types and combinations of vibration and noise, it provides a simple and concise index for comparing the individual/combined axis components of discomfort, as well as a design tool for estimating the tradeoffs to passenger ride quality of various noise/vibration vehicle inputs.

Combined Noise and Vibration

An important portion of this program has been directed at including in the model the effects of combined noise and vibration on passenger comfort. Figure 16 displays typical results of this research. The individual curves of figure 16 indicate the D-weighted noise level, dB, and vibration acceleration, g_{rms}, required to produce constant amounts of overall discomfort for combinations of noise and vibration. (See ref. 22 for additional information about development of the curves.) The solid curves of the figure represent subjective data for the range of physical factors investigated in these studies; whereas, the dashed curves represent extrapolations over an extended range of the physical factors. Although the extrapolations are felt to be reasonable, caution should be exercised in the use of the extrapolated values. The validity of the extrapolations remains to be verified by future research. As shown in figure 16, constant discomfort curves were generated for discomfort (DISC) values ranging from discomfort threshold (DISC = 1) to values as high as DISC = 6, corresponding to a very high degree of discomfort. The usefulness of figure 16 lies in the fact that it represents a very important source of information for determining the tradeoffs available between noise and vibration in terms of passenger discomfort. For example, at high levels of discomfort (e.g., DISC 5 or 6), variations of acceleration over the range shown result in small changes of discomfort level, indicating that noise level is the dominant factor in the determination of overall discomfort. For low levels of discomfort, however, the noise levels must be reduced substantially with increases of acceleration in order to maintain a constant degree of discomfort. This indicates that at the lower degrees of discomfort, both noise and vibration, contribute significantly to overall discomfort. Finally, it should be noted that the threshold of noise discomfort for the combined environment is approximately 75 to 78 dB, L_D.

Passenger Response to Tones

Recent fuel conservation measures have led to proposals for development of propeller-driven aircraft for use in commuter as well as high-speed, long-haul applications. The increased fuel efficiency of these vehicles could be offset, however, if passenger acceptance necessitates increased aircraft weight for purposes of noise reduction. A noise characteristic typical of such propeller-driven aircraft environments that may be critical to passenger comfort is the low-frequency tonal content. Research within the NASA Langley program to this point had not accounted for the effects of such noise on passengers. Consequently, an exploratory study was conducted to examine subjective response to propeller-type tone noises in combination with broadband (boundary layer) noise. The study was conducted in the Passenger Ride Quality Apparatus (PRQA) at Langley Research Center (ref. 23), shown in figure 17. The study involved a total of 96 subjects who evaluated synthesized noises using a 9-point discomfort category scale. The noises consisted of turbulent boundary layer noise combined with propeller-type noises in a factorial combination of blade-passage frequencies (50, 80, 100, 125, and 200 Hz), harmonic rolloff rates (0 and 10 dB/harmonic), tone/noise ratios (0, 10, and 20 dB), and noise levels (85, 90, 95, and 100 dB). The results of these tests indicated that noise level and blade-passage frequency (tones) were the primary noise characteristics that determine passenger reaction. The study results are summarized in figure 18, which displays mean subject ratings of discomfort as a function of A-weighted noise level. Mean subject rating was obtained by averaging the ratings of the 96 subjects for each noise. The mean subject ratings for the sounds with tones fell in the region between the dashed lines. For comparison, the subjects rated a sound containing no tones; the mean ratings for this sound are indicated by the solid line labeled "boundary layer noise" in the figure. There is a complex relationship between discomfort and various tonal characteristics (tone/noise ratio, fundamental frequency, and rolloff rate). Figure 18 indicates that the discomfort ratings of tonal noises range from slightly less than boundary layer (the lower dashed line), to more discomfort than boundary layer (the upper dashed line). The maximum difference between tonal noises and boundary layer noise can be quantified by comparing the upper dashed line with the solid line on the basis of equal subject rating, as indicated by the horizontal line at a rating of four. The data on this horizontal line indicate that the most uncomfortable tonal noise and the boundary layer noise are rated equal in discomfort when the tonal noise is

5 dB(A) lower in level than the boundary layer noise. Thus, to provide comfort in a propeller aircraft that is equal to the comfort in a turbofan aircraft, the noise level may need to be as much as 5 dB(A) less in the propeller aircraft, depending on the specific values of parameters such as tone/noise ratio, tone rolloff rate, and frequency of the fundamental tone. Currently, research is being planned to further examine subjective response and to develop a noise metric correction to account for the interior noise environments of this type of vehicle.

CONCLUDING REMARKS

This paper describes recent results of NASA and NASA-sponsored research on the prediction and control of noise from aircraft propellers and rotors. Control approaches considered include reduction of the noise generated by the propeller and reduction of the noise transmitted through the aircraft sidewall to the interior. Applications to general aviation aircraft, high-speed turboprop transports, and helicopters are reviewed, and an exploratory laboratory study of passenger response to propeller-like tonal noises is described.

Comparisons of predicted and measured noise from low-speed general aviation propellers indicate that the noise can be predicted with satisfactory accuracy provided sufficient effort is devoted to definition of detailed aerodynamic pressure distributions. Current prediction methods were used along with wind-tunnel model studies to develop a quiet propeller that was shown by flight test to reduce flyover noise by about 5 dB(A) in comparison with the standard propeller. Prediction of noise from high-speed propellers and helicopter rotors is more difficult because of the complex blade shape and aerodynamic flow field. However, fair agreement is obtained in the lower frequency harmonics, and several features of the noise generating mechanisms are under investigation to improve predictions. Theoretical studies have been carried out to design sidewall acoustic treatments for general aviation and high-speed turboprop aircraft. These studies indicate that sidewalls can be designed to provide acceptable cabin noise levels, but that additional weight is required. Passenger subjective ratings of tonal noises and comparison with ratings of broadband (boundary layer) noise indicated that tonal noise ratings range from slightly less uncomfortable to more uncomfortable than broadband, depending on the particular values of tone/noise ratio, tone fundamental frequency, and tone rolloff rate.

REFERENCES

1. Magliozzi, B.: The Influence of Forward Flight on Propeller Noise. NASA CR-145105, Feb. 1977.

2. Succi, George P.; Munro, David H.; and Zimmer, Jeffrey A.: Experimental Verification of Propeller Noise Prediction. AIAA Paper 80-0994, June 1980.

3. Farassat, F.; and Succi, George P.: A Review of Propeller Discrete Frequency Noise Prediction Technology with Emphasis on Two Current Methods for Time Domain Calculations. J. Sound and Vibration, vol. 71, no. 3, Aug. 1980.

4. Hanson, D. B.; and Fink, M. R.: The Importance of Quadrupole Sources in Prediction of Transonic Tip Speed Propeller Noise. J. Sound and Vibration, vol. 62, no. 1, Jan. 1979.

5. Boxwell, D. A.; Yu, Y. H.; and Schmitz, F. H.: Hovering Impulsive Noise - Some Measured and Calculated Results. NASA CP-2052, Part I, May 22-24, 1978.

6. Isom, M. P.: The Theory of Sound Radiated by a Hovering Transonic Helicopter Blade. Polytechnic Institute of New York Report, Poly-AE/AM No. 75-5, 1975.

7. Farassat, F.: Extension of Isom's Thickness Noise Formula to the Near Field. Letter to Editor, J. Sound and Vibration, vol. 67, no. 2, 1979.

8. Brooks, B. M.; and Metzger, F. B.: Acoustic Test and Analysis of Three Advanced Turboprop Models. NASA CR-159667, Jan. 1980.

9. Nystrom, P. A.; and Farassat, F.: A Numerical Technique for Calculation of the Noise of High Speed Propellers with Advanced Blade Geometry. NASA TP-1662, 1980.

10. Dittmar, James H.: A Comparison Between an Existing Propeller Noise Theory and Wind Tunnel Data. NASA TM-81519, May 1980.

11. Farassat, F.: Theory of Noise Generation from Moving Bodies with an Application to Helicopter Rotors. NASA TR-451, 1975.

12. Mixson, J. S.; Barton, C. K.; Piersol, A. G.; and Wilby, J. F.: Characteristics of Propeller Noise on an Aircraft Fuselage Related to Interior Noise Transmission. AIAA Paper 79-0646, Mar. 12-14, 1979.

13. Magliozzi, B.; and Brooks, Bennett M.: Advanced Turboprop Airplane Interior Noise Reduction-Source Definition. NASA CR-159668, Oct. 1979.

14. Vaicaitis, R.: Noise Transmission into a Light Aircraft. AIAA 78-197R, J. of Aircraft, vol. 17, no. 2, Feb. 1980.

15. Vaicaitis, R.; and Slazak, M.: Noise Transmission Through Stiffened Panels. J. Sound and Vibration, vol. 70, no. 3, 1980.

16. Rennison, D. C.; Wilby, J. F.; Marsh, A. H.; and Wilby, E. G.: Interior Noise Control Prediction Study for High-Speed, Propeller-Driven Aircraft. NASA CR-159200, Sept. 1979.

17. Revell, J. D.; Balena, F. J.; and Koval, L. R.: Analytical Study of Interior Noise Control by Fuselage Design Techniques on High-Speed, Propeller-Driven Aircraft. NASA CR-159222, July 1978.

18. Dempsey, T. K.: A Model and Predictive Scale of Passenger Ride Discomfort. NASA TM X-72623, Dec. 1974.

19. Dempsey, T. K.; and Leatherwood, J. D.: Vibration Ride Comfort Criteria. Proceedings of the Sixth Congress of the International Ergonomics Association, July 1976.

20. Dempsey, T. K.; Leatherwood, J. D.; and Clevenson, S. A.: Single Axis Vibration Discomfort Criteria. NASA TP-1422, May 1979.

21. Leatherwood, Jack D.; Dempsey, Thomas K.; and Clevenson, Sherman A.: A Design Tool for Estimating Passenger Ride Discomfort Within Complex Ride Environments. Human Factors Jour., vol. 22, no. 3, 1980.

22. Dempsey, T. K.; Leatherwood, J. D.; and Clevenson, S. A.: Development of Noise and Vibration Ride Comfort Criteria. J. Acoustical Society of America, vol. 65, no. 1, Jan. 1979.

23. Clevenson, S. A.; and Leatherwood, J. D.: On the Development of Passenger Vibration Ride Acceptance Criteria. Shock and Vibration Bulletin, vol. 43, no. 3, June 1973.

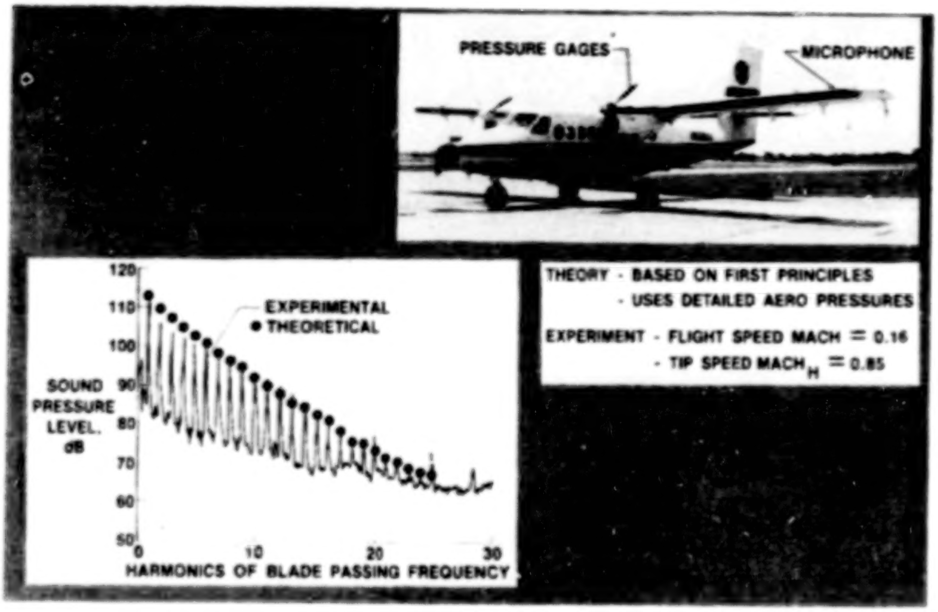

Figure 1.- Measured and predicted noise of general aviation propeller.

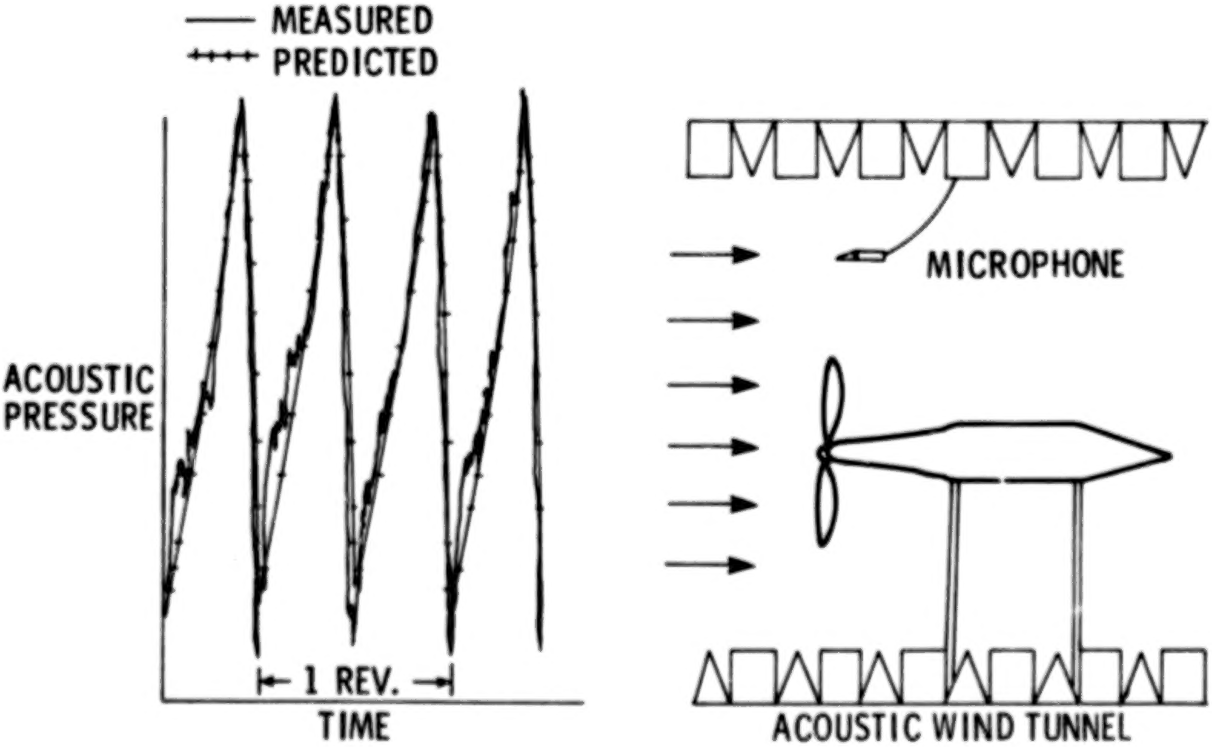

Figure 2.- Measured and predicted noise of general aviation propeller models.

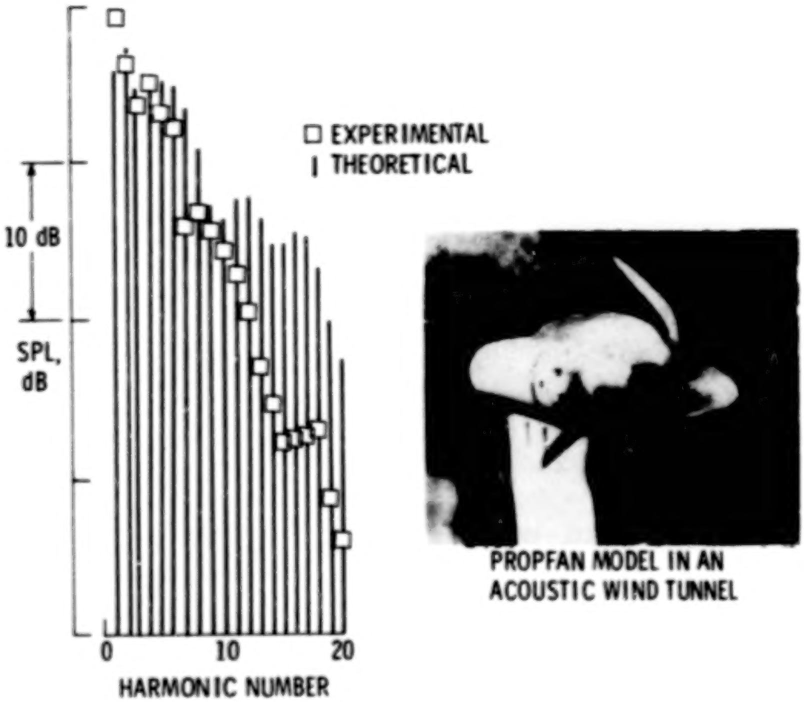

PROPFAN MODEL IN AN ACOUSTIC WIND TUNNEL

Figure 3.- Harmonic noise spectrum of model high-speed propeller. Diameter = 0.61 m.

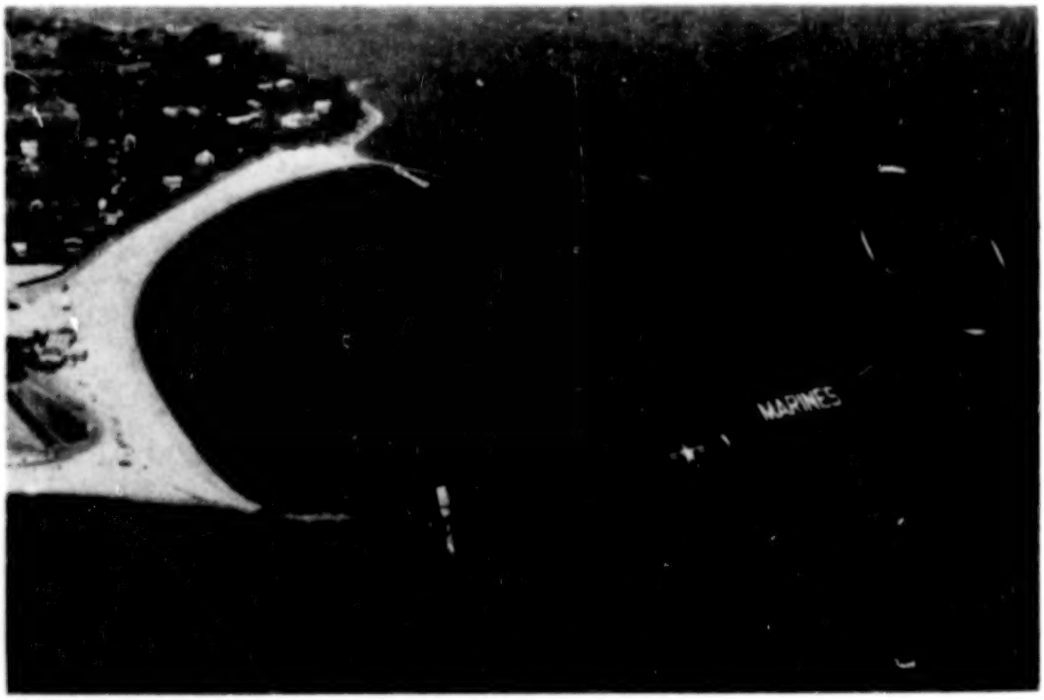

Figure 4.- Large helicopter type used in flyover noise tests.

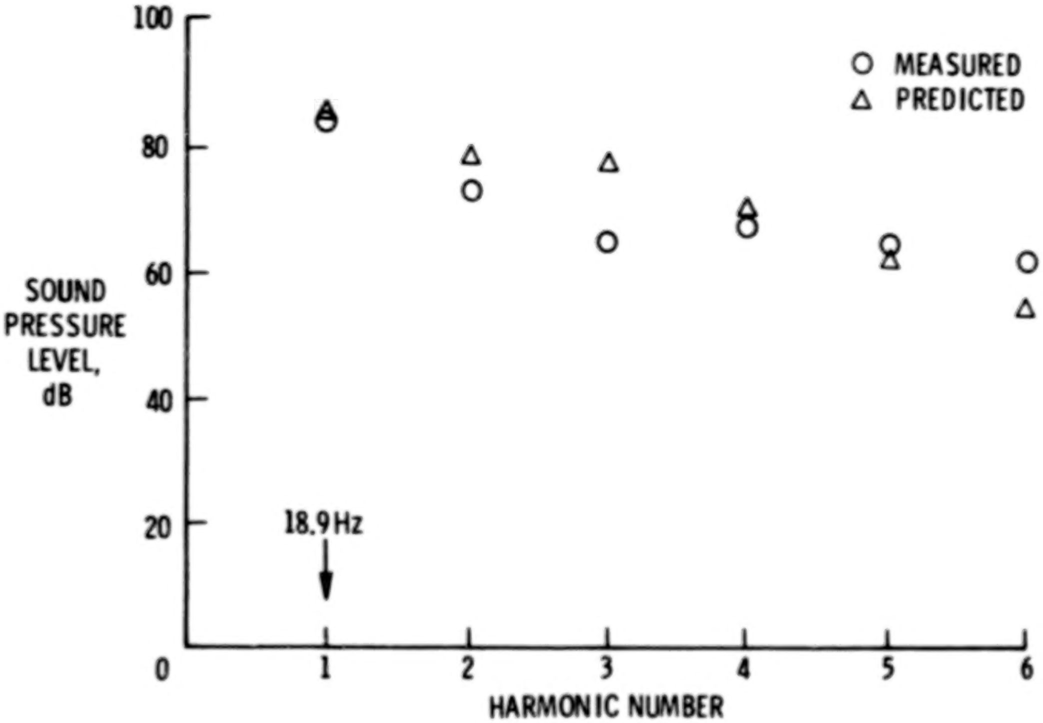

Figure 5.- Measured and predicted noise levels for helicopter in 49-m/s level flyover at 152-m altitude.

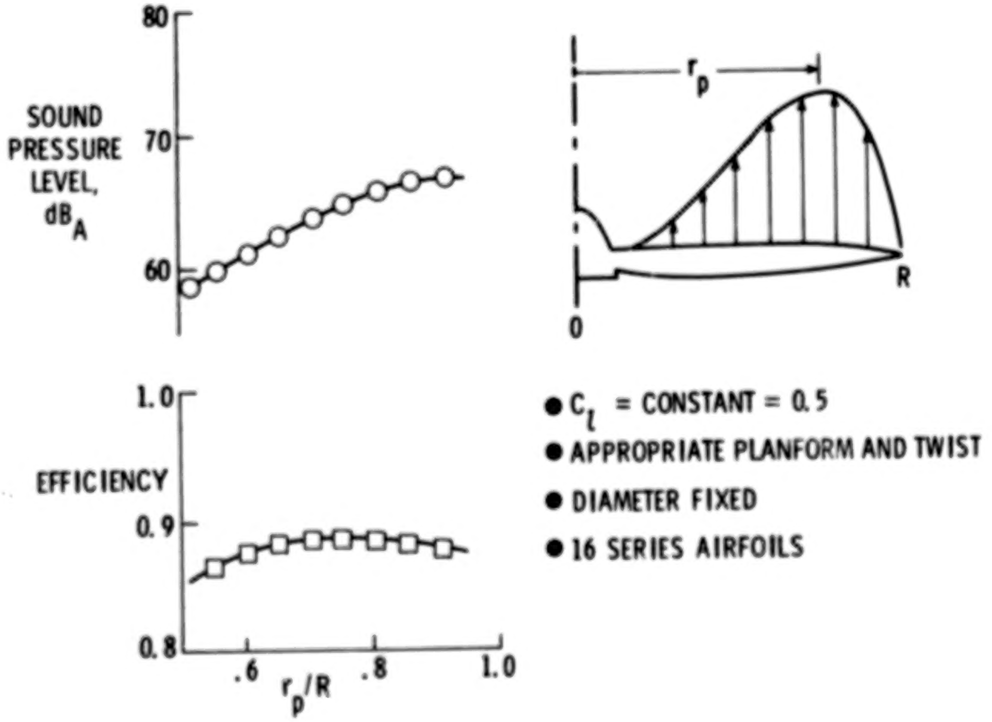

- C_l = CONSTANT = 0.5
- APPROPRIATE PLANFORM AND TWIST
- DIAMETER FIXED
- 16 SERIES AIRFOILS

Figure 6.- Calculated effect of varying radial load distribution.

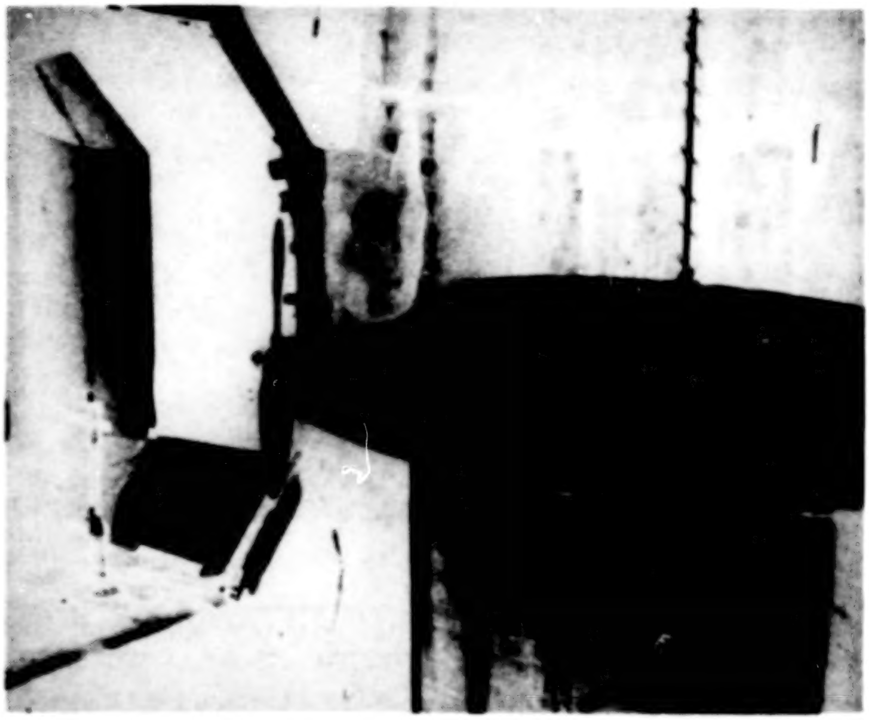

Figure 7.- Acoustic tests of quiet general aviation propellers in anechoic wind tunnel.

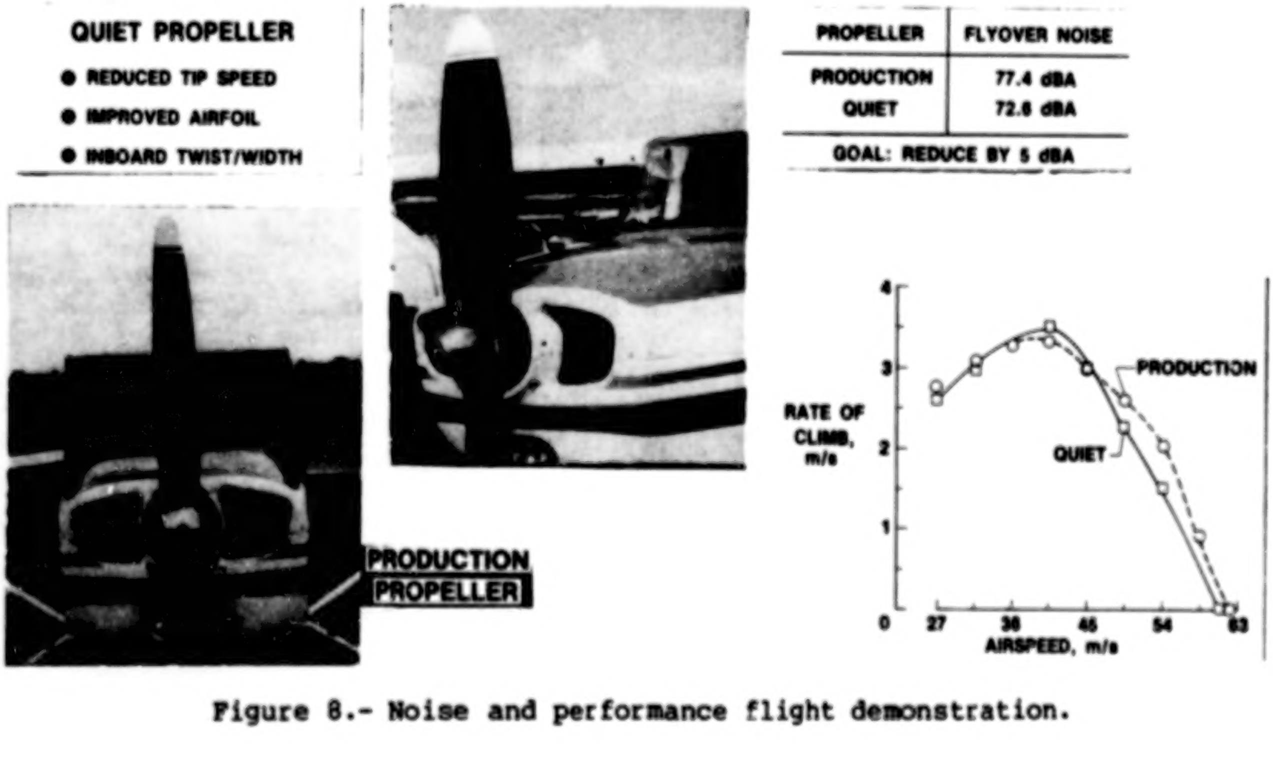

QUIET PROPELLER

- REDUCED TIP SPEED
- IMPROVED AIRFOIL
- INBOARD TWIST/WIDTH

PROPELLER	FLYOVER NOISE
PRODUCTION	77.4 dBA
QUIET	72.6 dBA

GOAL: REDUCE BY 5 dBA

Figure 8.- Noise and performance flight demonstration.

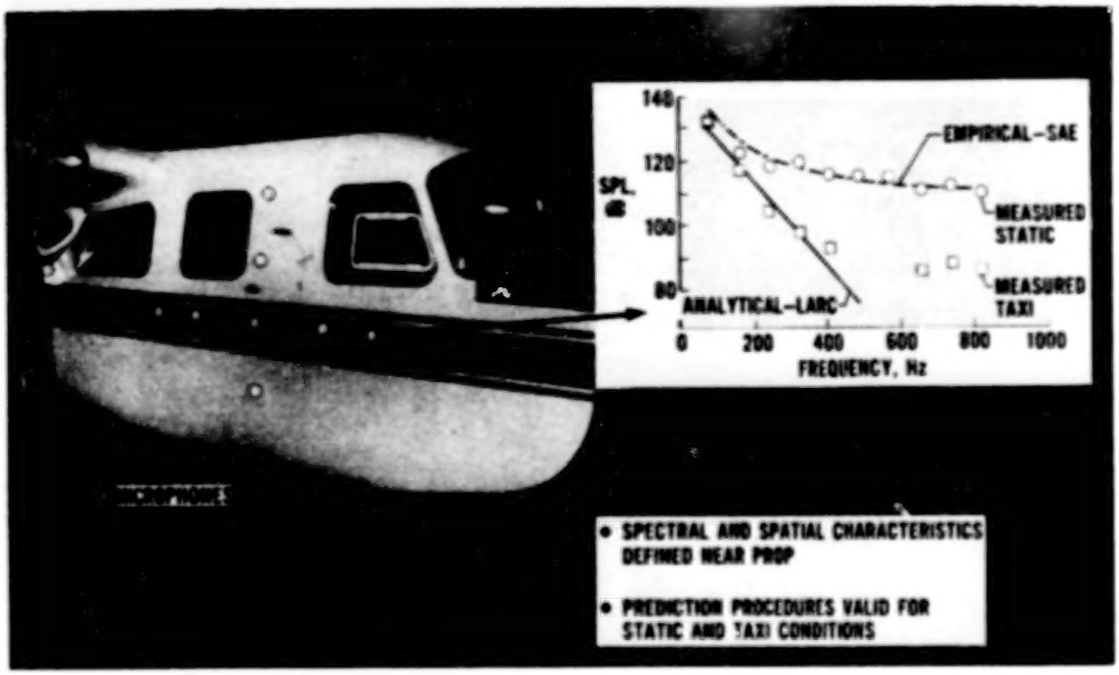

- SPECTRAL AND SPATIAL CHARACTERISTICS DEFINED NEAR PROP
- PREDICTION PROCEDURES VALID FOR STATIC AND TAXI CONDITIONS

Figure 9.- Propeller noise on fuselage of twin-engine, light aircraft.

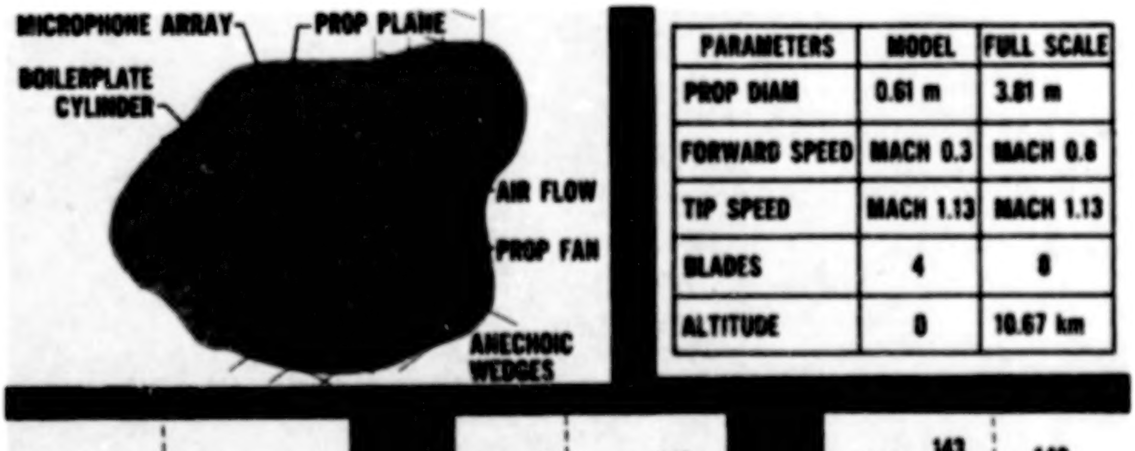

MICROPHONE ARRAY
PROP PLANE
BOILERPLATE CYLINDER
AIR FLOW
PROP FAN
ANECHOIC WEDGES
140
143
145
140
MODEL MEASURED, dB
140
143
145
143
MODEL PREDICTED, dB
140
143
140
FULL SCALE–PREDICTED, dB

PARAMETERS	MODEL	FULL SCALE
PROP DIAM	0.61 m	3.81 m
FORWARD SPEED	MACH 0.3	MACH 0.8
TIP SPEED	MACH 1.13	MACH 1.13
BLADES	4	8
ALTITUDE	0	10.67 km

Figure 10.- Noise from model high-speed propeller on simulated fuselage.

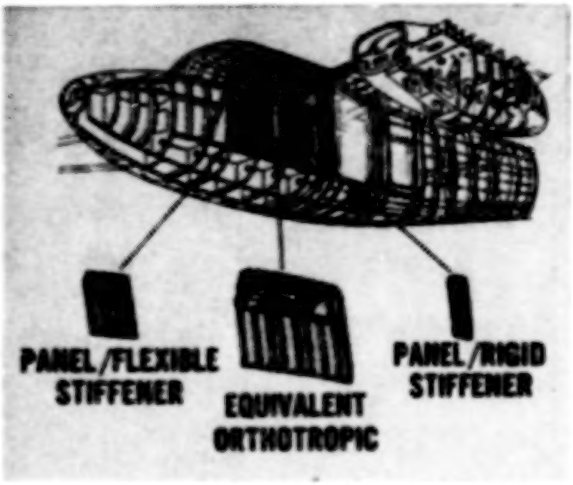
PANEL/FLEXIBLE STIFFENER
EQUIVALENT ORTHOTROPIC
PANEL/RIGID STIFFENER

CHARACTERIZATION OF SIDEWALL

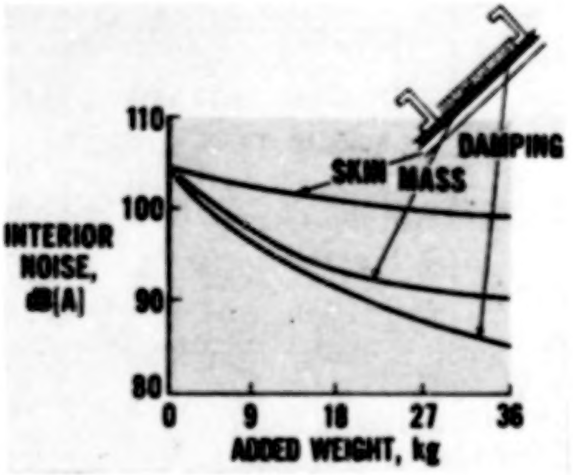

NOISE/WEIGHT SENSITIVITY STUDY

Figure 11.- Theoretical studies of interior noise control by sidewall treatment on light aircraft.

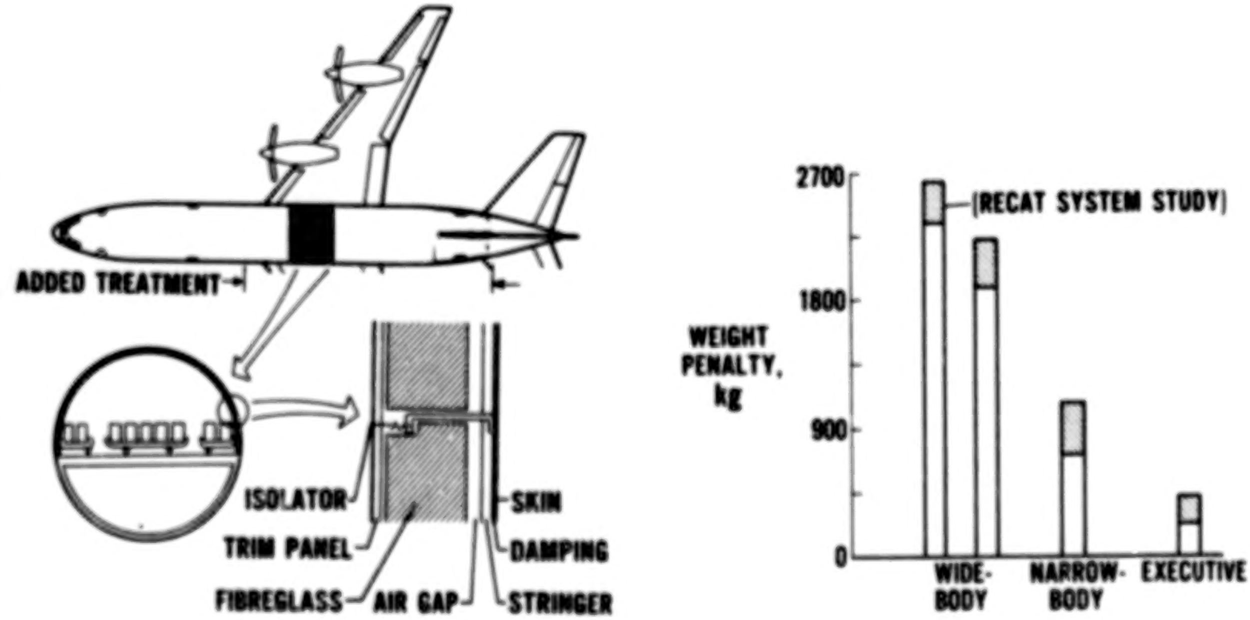

Figure 12.- Theoretical studies of sidewalls for interior noise control on high-speed turboprop aircraft.

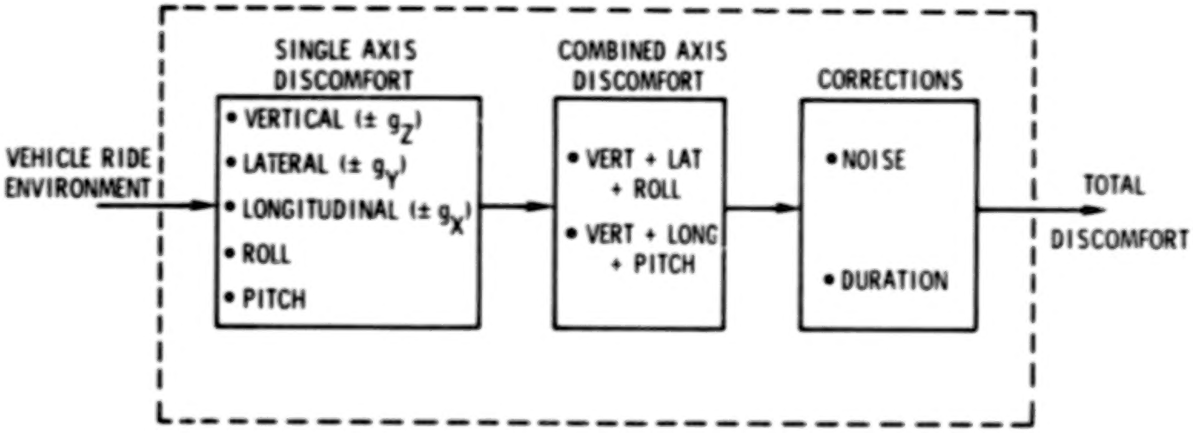
VEHICLE RIDE ENVIRONMENT
SINGLE AXIS DISCOMFORT
• VERTICAL (± g_Z)
• LATERAL (± g_Y)
• LONGITUDINAL (± g_X)
• ROLL
• PITCH
COMBINED AXIS DISCOMFORT
• VERT + LAT + ROLL
• VERT + LONG + PITCH
CORRECTIONS
• NOISE
• DURATION
TOTAL DISCOMFORT

Figure 13.- Ride quality model.

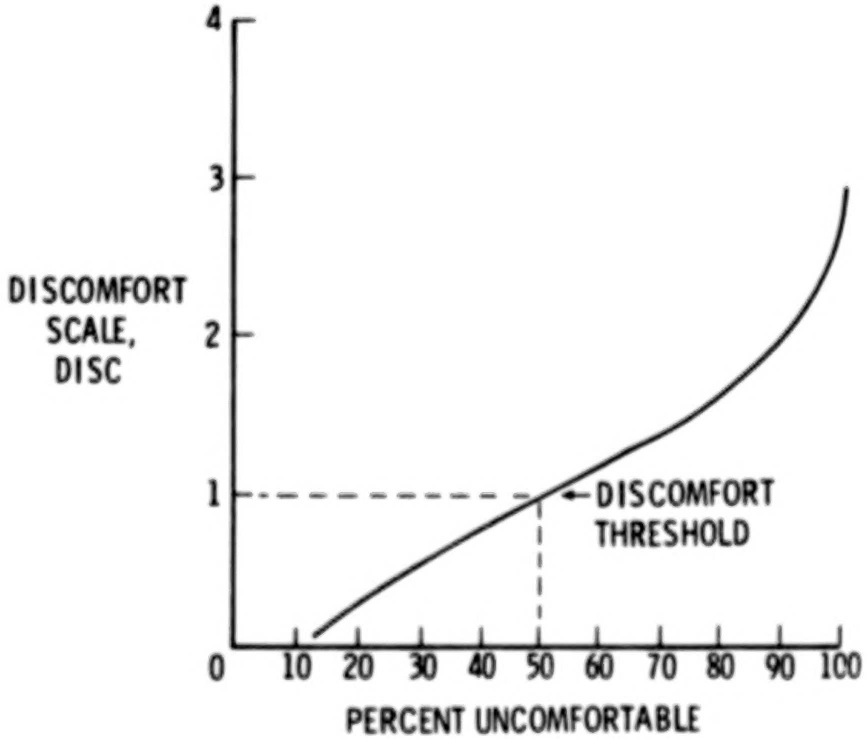

Figure 14.- Relation between discomfort scale and percent of passengers uncomfortable.

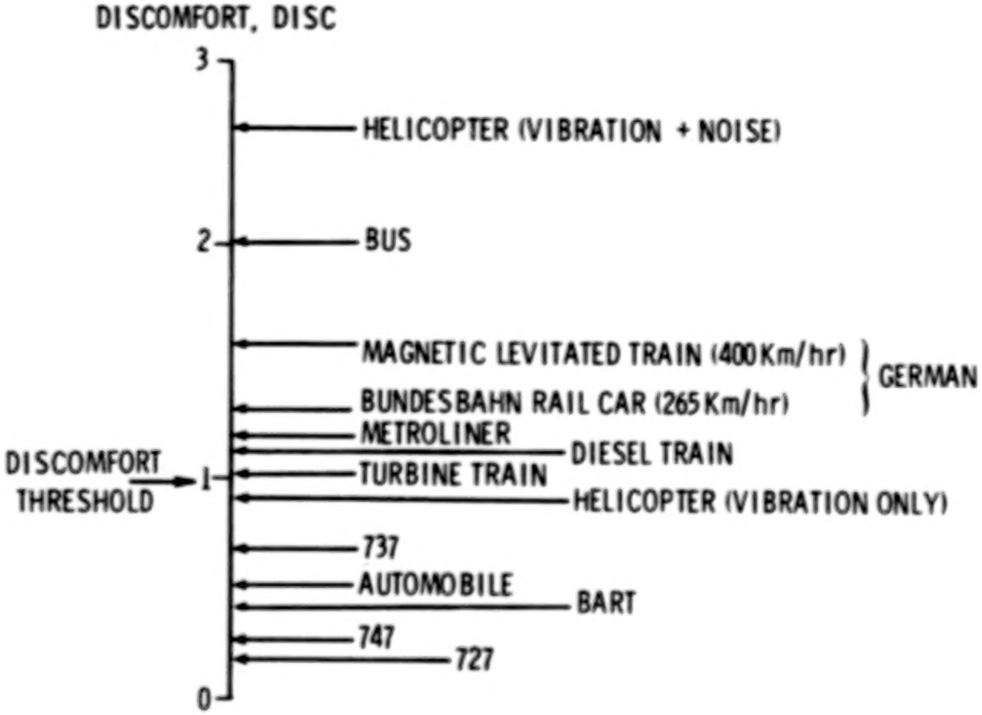

Figure 15.- Discomfort scale rating of transportation vehicles.

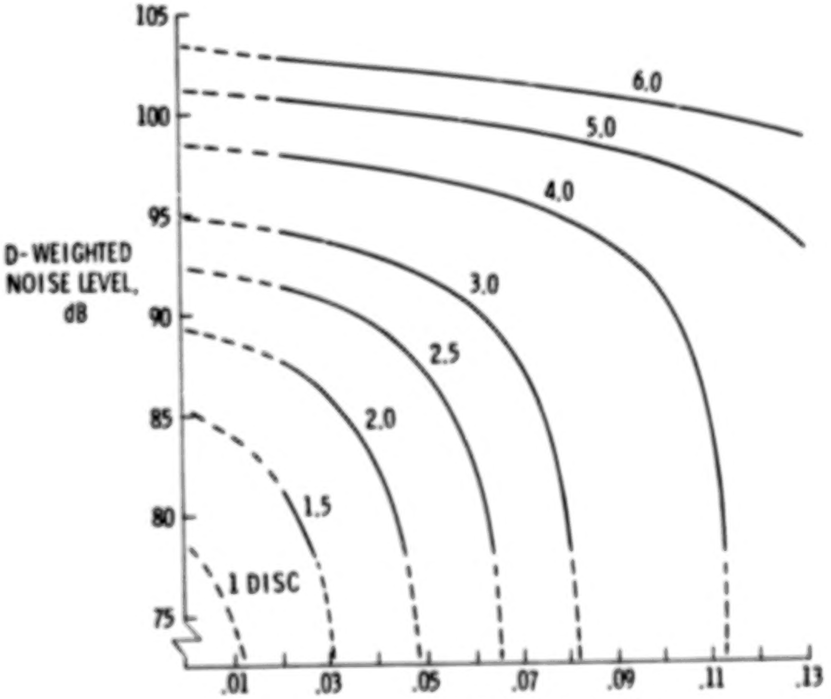

Figure 16.- D-weighted noise levels required to produce constant discomfort curves as function of vibration acceleration.

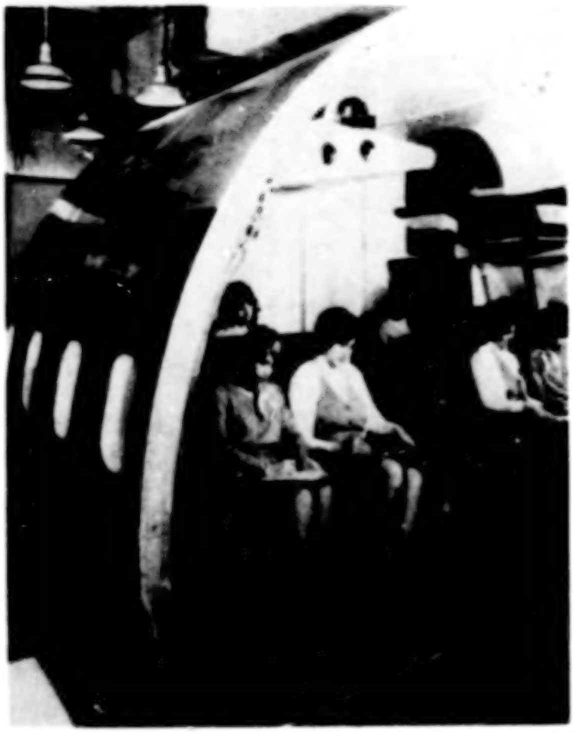

Figure 17.- The Passenger Ride Quality Apparatus at Langley Research Center.

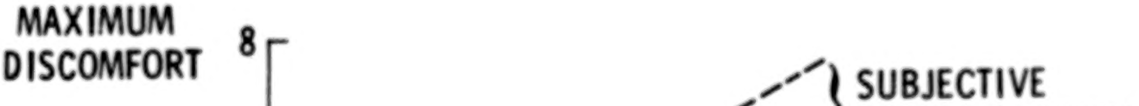

Figure 18.- Subjective response to tonal interior noise.

NASA PROGRESS IN AIRCRAFT NOISE PREDICTION

J. P. Raney, S. L. Padula and W. E. Zorumski
Langley Research Center

SUMMARY

For several years NASA has maintained an aircraft noise prediction activity at the Langley Research Center with the goal of developing methodology for predicting the effective perceived noise level (EPNL) produced by jet-powered CTOL aircraft to an accuracy of ± 1.5 dB. Another goal is to establish, in terms of fundamental acoustic theory, the relationship of noise to the design and operation of aircraft and to demonstrate the feasibility of incorporating aircraft noise constraints into the preliminary design process. Much progress has been made toward these goals. The Aircraft Noise Prediction Program (ANOPP) contains a complete set of prediction methods for CTOL aircraft which includes propulsion system noise sources, aerodynamic or airframe noise sources, foward speed effects, a layered atmospheric model with molecular absorption, ground impedance effects including excess ground attenuation (EGA), and a received-noise contouring capability. A method for calculating noise-constrained or noise-minimized aircraft operations is presently in the validation phase. Comparisons of ANOPP calculations with measured aircraft noise levels are encouraging and highlight areas where further improvements are required.

INTRODUCTION

In 1973, a focused aircraft systems noise prediction activity was established at the Langley Research Center. The mission was to develop a state-of-the-art computer system for calculating aircraft noise (refs. 1 and 2). The commitment to develop the Aircraft Noise Prediction Program (ANOPP) stemmed from the need for a credible means of quantifying the expected benefits from NASA's noise reduction research programs. It was also anticipated that this program could from time to time support the prediction needs of other government agencies concerned with aircraft noise and could be useful to NASA contractors.

One of the first major applications of ANOPP was to support the Supersonic Cruise Research (SCR) project at Langley; ANOPP continues to be applied to SCR research at this time. The next application was in conjunction with the FAA in an International Civil Aviation Organization (ICAO) study to determine economically reasonable and technologically feasible noise limits for future supersonic transports (ref. 3).

The ANOPP development group has a continuing commitment to assess and improve NASA's noise prediction capability. This is done by comparing predictions to measured data from both laboratory models and full-scale flight measurements. Recent prediction assessment, or validation studies, have included comparisons of prediction with flyover noise from the McDonnell-Douglas DC-9 and DC-10, the Boeing 747, and the Lockheed L-1011 aircraft.

Protocol established in conjunction with the SCR project has been improved and methodology for incorporating noise as a design constraint is being developed. An engine modeling capability which will allow investigation of the effects of variations in the relationships of engine control variables is planned, and a method for calculating noise-constrained takeoff procedures has recently been incorporated in ANOPP (ref. 4).

Several research projects which address critical weaknesses in noise prediction have been identified as a result of the focus provided by the ANOPP development and application activities. These include shock cell noise generation, ground effects on propagation, forward flight effects on jet noise, coaxial and inverted coaxial jet noise prediction, and jet-on-jet shielding effects.

The purpose of this paper is to describe ANOPP in its present state, to assess its accuracy and applicability to the preliminary aircraft design process, and to indicate where further theoretical and experimental research on noise prediction is required. The elements of the noise prediction problem which are incorporated in ANOPP will first be described. Next, the results of comparisons of ANOPP calculations with measured noise levels will be presented. Progress toward treating noise as a design constraint in aircraft system studies will then be discussed. The paper will conclude with a summary of noise-prediction-related research activities which have been initiated as a result of the need to improve aircraft noise prediction accuracy.

SYMBOLS

a_i	source noise prediction parameters
A	atmospheric propagation effects factor
c_a	ambient speed of sound, m/sec
D	overall source directivity factor
DI	directivity index
f	frequency, Hz
G	ground effects factor
H	altitude, m

I	source intensity, watt/m^2
M	aircraft Mach number
n	number of frequency bands
P	acoustic pressure, N/m^2
P_{ref}	reference pressure, N/m^2
ps	power setting, percent
R	aircraft position vector w.r.t. earth-fixed axes
r	noise propagation vector w.r.t. body axes
$\mathcal{R}$	relative spectrum factor
$\mathcal{R}L$	relative spectrum level (=10 log $\mathcal{R}$)
S	power spectrum factor
SL	power spectrum level (=10 log S)
t	time, sec
w	weighting factor
(x,y,z)	Cartesian coordinate system
α	angle of attack, deg
β	source elevation angle, deg
θ	source directivity angle, deg
Π	acoustic power, watt
π	= 3.1415926
ρ_a	ambient density, kg/m^3
σ	atmospheric attenuation
ϕ	source azimuth angle, deg
(ξ,η,z)	cylindrical polar coordinate system

Subscripts

f	final

i	index
max	maximum
min	minimum
o	observer
ref	reference
s	source

ABBREVIATIONS AND SPECIAL SYMBOLS

ANOPP	Aircraft Noise Prediction Program
CTOL	conventional takeoff and landing
(C_L/C_D)	lift-drag ratio
EGA	excess ground attenuation
EPNL	effective perceived noise level
ICAO	International Civil Aviation Organization
OASPL	overall sound pressure level
PNLT	tone-corrected perceived noise level
$\langle p^2 \rangle$	mean-squared pressure
SAE	Society of Automotive Engineers
SCR	Supersonic Cruise Research
SNECMA	Societé Nationale D'Etude et de Construction de Moteurs D'Aviation
SPL	sound pressure level
SST	Supersonic Transport
$(T/\dot{m}c_a)$	normalized specific thrust
(T/W)	thrust-weight ratio

ANOPP NOISE PREDICTION METHODOLOGY

The purpose of ANOPP is to predict noise from an aircraft by accounting for the effects of its engines, its operations, the atmosphere including ground effects, and other characteristics which may influence the noise it generates. The approach to this problem has been placed on a fundamental basis, as depicted in figure 1 (ref. 1). The aircraft follows an arbitrary flight path in the presence of an observer on the ground. During this operation, noise sources on the aircraft emit radiation with defined power, directionality, and spectral distribution characteristics, all of which may depend on time. This source noise propagates through the atmosphere (being attenuated) to the vicinity of the observer. The observer receives the noise signal from the direct ray plus a signal from a ray reflected by the local ground surface.

The essential ingredients of the aircraft noise prediction problem which are embodied in ANOPP are as follows: (1) the source intensity I, (2) the aircraft position given by vector R(t), (3) the aircraft orientation given by θ and ϕ, (4) the atmospheric and ground-impedance characteristics given by A and G, and (5) the location of the observer given by the vector r(t).

A number of approaches are available for this general prediction problem. These approaches are divided in ANOPP into four categories, called functional levels, which are depicted by the schematic in figure 2. The functional levels are defined by the amount of data which is processed and by the degree of approximation in the prediction methods (ref. 5). Level I predicts an effective measure of noise which depends on the observer location and assumes uniform flight conditions. Level II predicts a noise level which depends on the observer and time, but assumes standard atmospheric conditions. In Level III, frequency effects are predicted in addition to the effects of observer and time. Both nonstandard atmospheric effects and detailed flight procedures can be handled in Level III. In Levels II and III, the noise measured may be subdivided as to the noise source which generates them. Level IV predicts the same information as Level III, but with more detail in the spectral data. The present paper deals primarily with Level III noise prediction.

An ANOPP Level III noise prediction is characterized by the prediction of 1/3-octave band noise. The band centers are based on observer frequencies and are independent of time. All other inputs to the prediction modules are time dependent. The vectors from the source to the observer are naturally dependent on the observer and time so that the output from a source is a function of frequency, time, and observer.

The prediction of 1/3-octave band noise is a limitation which should not be passed over lightly. Some of the more important noise sources are actually tones, for example, from the fan rotor of a bypass-type engine. In the prediction module, these tones are assigned to a 1/3-octave band and subsequently treated as broadband noise. This will cause subsequent errors in the prediction of atmospheric attenuation, ground effects and even noise levels. Nevertheless, the added complexity of carrying a separate procedure for tones suggests that this is not an appropriate task for ANOPP Level III and this type of analysis has been assigned to Level IV.

Source Noise Prediction

ANOPP source modules use standard forms for the prediction equations. The standard equation of Level III prediction modules is shown in equation (1).

$$<P^2(f,\theta;a_i)> = \rho_a c_a \frac{\Pi(a_i)}{4\pi r_s^2} D(\theta;a_i)\, S(f;a_i) \mathcal{R}(f,\theta;a_i) \qquad (1)$$

where

$$\mathcal{R}(f,\theta;a_i) = \frac{S(f,\theta;a_i)}{S(f;a_i)} = \frac{D(\theta,f;a_i)}{D(\theta;a_i)}$$

The basic noise variable is mean-squared pressure, $<P^2>$. Within ANOPP, a dimensionless group is used, with $\rho_a c_a^2$ being the reference pressure. The equation is shown in dimensional form in equation (1) so that it will be more familiar to the reader. The use of mean-squared pressure allows noise from different sources to be added directly, thus avoiding the time consuming logarithmic and exponentiation operations required to add sound pressure level, SPL.

Each noise source is characterized by an acoustic power Π. This power, divided by the area of a sphere with radius r_s and multiplied by the characteristic impedance of the atmosphere, $\rho_a c_a$, gives the average overall mean-squared pressure for virtual observers at distances r_s from the source. The power is a function of source parameters a_i, which have been previously evaluated by analysis of the engine, and the aircraft flight.

The average overall mean-squared pressure is not adequate for most predictions. It must be known how the sound is directed and how the acoustic energy is distributed in different frequency bands. This information is contained in three factors: the overall directivity factor D, the power spectrum factor S, and the relative spectrum factor $\mathcal{R}$.

The overall directivity and power spectrum factors are defined in figure 3. The directivity factor is the ratio of the overall mean-squared pressure at angle θ to the average overall mean-square pressure on the virtual observer sphere of radius r_s. The equation shown in figure 3 is for an axisymmetric source, however, ANOPP provides the directivity effects in the azimuthal direction as well as in the polar angle θ shown here. The directivity factor is usually plotted as a directivity index, DI, which is simply ten-log of the directivity factor against θ, the polar directivity angle.

The power spectrum factor, S(f), is the ratio of the acoustic power in a band to the overall acoustic power. This factor may also be expressed in terms of integrals of the mean-squared pressure as shown in figure 3. Again, the equation shown is for an axisymmetric source. The integrals are used in computing S(f) from experimental data. The power spectrum factor is usually plotted in logarithmic form against frequency or Strouhal number. Since the factor must be less than one, its logarithm is negative and usually has a peak value at about -10 dB.

The overall directivity and the power spectrum give some information about how the mean-squared pressure is directed over angles and distributed over frequency bands, but this information is not complete. What is needed is either the spectrum factor for the mean-squared pressure at each angle or the directivity at each frequency band of the acoustic power. Either of these variables can be expressed in terms of the relative spectrum factor as shown in figure 4. In logarithmic form, the relative spectrum level is the difference between the mean-squared pressure spectrum level and the power spectrum level. It can be shown that this is identical to the difference between the directivity index of the frequency band and the overall directivity index. The reader may observe that many empirical prediction formulas assume a relative spectrum level of zero dB.

Forward flight effects on noise sources are not easily expressible in a standard form. This is a current research area and there is a tendency to use specialized procedures for each source. There are two definite relations, however, which distinguish the Level IV ANOPP system from the Level III and lower versions. These are shown in equations (2a) and (2b), where the subscripts o and s denote quantities at the observers and at the source, respectively.

$$f_o\ (M,\theta) = f_s\ (1-M\cos\theta)^{-1}$$

$$\text{where} \qquad a_i = a_i\ (M) \tag{2a}$$

is the relationship for Level IV moving source system and

$$f_s(M,\theta) = f_o(1-M\cos\theta)^{-1}$$

$$\text{where} \qquad a_i = a_i\ (M,\theta) \tag{2b}$$

is the relationship for Level III fixed source system. In Level IV, the frequencies are fixed at the source and the Doppler factor adjusts the observer frequency as a function of Mach number and directivity angle. In Level III, all sources are treated like broadband noise so that the observer frequency is fixed and the noise frequency is accordingly shifted by the Doppler factor. The noise source parameters in Level III may accordingly be a function of Mach number and directivity angle in some flight effect schemes.

Some of the ANOPP modules which are presently used for CTOL subsonic cruise aircraft and SST noise prediction are shown in Table I. Since the noise source modules fit within the standard form equation described previously, there is no need to go into further detail here. All ANOPP methods are fully referenceable and the reader may refer to the documents listed in Table I for full details on a particular method.

Propagation and Noise Effects

Having discussed source noise computations, the next task is to account for propagation effects as the sound travels through a real atmosphere to an observer on the ground. It is necessary to understand how the source noise information is organized and stored, how propagation effects are included and how the resulting noise is measured and reported. The final portion of this section will compare three different noise contouring methods available in ANOPP.

Level III propagation effects. - All of the source noise prediction methods covered above calculate mean-squared pressure at a given distance r_s from the center of the source. The geometry for any of the engine sources is shown in figure 5. Since these sources are axisymmetric, it is sufficient to define acoustic pressures on a half circle centered at the center of the jet nozzle. Usually, the predicted pressures are tabulated at eighteen values of directivity angle, θ, starting at the engine inlet axis and ending at the jet nozzle axis. Pressures are also tabulated at each 1/3-octave band center frequency from 50 Hz to 10,000 Hz as indicated in figure 6.

Level III propagation effects are represented schematically in figure 6 as correction factors which modify the near-field curve to become the far-field curve. Equation (3) contains a more detailed representation showing that mean-squared pressure at the observer equals mean-squared pressure at radius r_s multiplied by correction terms for impedance differences, spherical spreading, atmospheric attenuation, and ground effects.

$$\begin{aligned} \langle P^2(f,t)\rangle_o &= \frac{(\rho c)_o}{(\rho c)_s}\left[\frac{r_s}{r_o(t)}\right]^2 \langle P^2(f_s(t),\theta(t);a_i(t))\rangle_s \\ &\cdot \exp\left\{-\bar{\sigma}\,(f,t)\,\left[r_o(t)-r_s\right]\right\} G(f_o,\beta(t),r_o(t)) \end{aligned} \qquad (3)$$

where $\bar{\sigma}$ is an average atmospheric attenuation measure and G is a ground effects factor. Notice that propagation effects must be recomputed at each time step along the trajectory because the distance from source to observer, r_o, and the elevation angle between source and observer, β, are changing rapidly with time. The mean-squared pressure at the source $\langle P^2\rangle_s$ may not need to be recalculated at every time step since engine parameters vary slowly with time and since the variation of $<P^2>_s$ with θ can be accounted for by interpolation over a set of virtual observers.

Noise received by each observer is measured in terms of sound pressure level (SPL). Equation (4) gives a general expression for SPL and indicates two of the most common weighting functions.

$$\mathrm{SPL} = 10\ \mathrm{LOG}_{10}\ \frac{\sum_{i=1}^{n} w_i <P^2(f_i)>}{P^2_{ref}} \qquad (4)$$

where $w_i = \begin{cases} 1 & \text{if OASPL} \\ w(<P^2>,f) & \text{if PNLT} \end{cases}$

Actually, SPL is the logarithm of a ratio of the area under a weighted mean-squared pressure spectrum and the square of the reference pressure. Level III ANOPP approximates the integral over all frequencies by a summation of integrals over each third octave band. The weights, w_i, are chosen from many possible weighting functions used to evaluate the effect of sound on humans. Overall sound pressure level, OASPL, is a flat weighting function which gives equal importance to each frequency band. Perceived noise level, PNL, is a complicated weighting function based on empirical annoyance curves. The empirical data indicate that both the frequency content and the loudness of a sound contribute to its noisiness. The measure PNLT uses the same weights as PNL but includes corrections for discrete tones in the sound spectrum.

As the aircraft flies by an observer location, the perceived noise levels will reach a peak and then subside as indicated in figure 7. Psychoacoustic research suggests that the observer reacts to the peak noise level and to the duration of the almost-peak noise levels. Effective perceived noise level (EPNL) includes this duration effect by measuring the area of the shaded region in figure 7. The prescribed method of calculating EPNL is to approximate the integral of PNLT over time by applying the trapezoid rule at half-second time intervals.

Contouring methods. - Effective perceived noise contours are useful visual aids for representing the noise level received by a large number of observers. ANOPP provides two possible avenues toward producing contour plots in a reasonable amount of computer time. The user may either use Level I approximations to calculate a large number of EPNL values or he may use the ANOPP contour enhancement methods to produce smooth contours from a limited number of accurate EPNL values. Both approaches will be discussed below.

The simplest contouring method uses Level I approximations which are based on level flyover data corrected to standard day conditions. EPNL can be tabulated as a function of minimum approach distance, r_o, and engine power setting as pictured in figure 8. In addition to the EPNL table, the user must supply or compute aircraft position and power setting at each time step in the flight and must specify the directivity angle θ at which the maximum noise occurs. Plotting a given contour involves interpolating into the EPNL table for the value of r_o at which that noise level occurs. The values of r_o, θ, and aircraft position then define an observer location as shown in figure 9. This process is repeated at each time step and the contour is drawn by a graphics subroutine which connects the observer locations.

This simple contouring method has been the accepted practice for a number of years. It is clear, however, that this method can be no more accurate than the Level I predictions on which it is based. Using this method to draw noise contours for a maneuvering aircraft or for realistic takeoff and landing operations is not recommended.

A much more powerful and versatile method is illustrated in figure 10. Noise levels are predicted for an evenly spaced grid of observer locations using either Level II or Level III prediction methods. A standard contouring computer package can draw the noise footprint from these data which are appropriate for any nonuniform aircraft operation. The major drawback of this basic contouring method is the computing cost since a dense grid of observer locations is needed to produce smooth contours. A secondary problem is the quality of the contours produced. The standard contouring software is for general purpose application and utilizes no knowledge of the basic shapes of the noise contours. These shapes are roughly concentric ellipses which are symmetric about the runway centerline. Thus the noise footprints produced rarely conform to the user's expectations.

The advanced ANOPP contouring capability overcomes the difficulties mentioned above in two ways. First, it uses a more representative coordinate system, and second, it enhances the data before contouring. The method employs the conversion from Cartesian coordinates (x, y, z) to cylindrical polar coordinates (ξ, η, z). It is often advantageous to use stretched polar coordinates, achieved by dividing y by a constant before conversion to polar coordinates. By using this more natural representation, it is possible to produce reasonable contours with as few as sixteen observer locations. The ANOPP enhancement program fits a cubic surface through these sixteen points and interpolates to form a dense grid before contouring. Typical results are shown in figure 11, in which countours produced from the enhancement of sixteen calculated points compare favorably with contours produced from a very dense grid of calculated points.

ANOPP VALIDATION AND EVALUATION

The ICAO Study

In 1977 the International Civil Aviation Organization (ICAO) requested through its Civil Aircraft Noise (CAN) committee a recommendation for noise standards applicable to future SST's. Participating countries included the United States, the United Kingdom, France, and the USSR. Participating organizations included Boeing Aircraft Company, McDonnell-Douglas, Lockheed, British Aerospace, General Electric, Pratt & Whitney Aircraft, Rolls-Royce, SNECMA, and NASA Langley.

A prediction subcommittee was established and given the task of choosing a "Reference Prediction Procedure" which would serve as a common denominator for the parametric studies and noise calculations supporting each participant's recommendations.

In order to provide a basis for selection of the Reference Prediction Procedure it was decided to request participants to calculate component and total noise levels for a hypothetical very low bypass ratio SST engine specified by SNECMA. Noise data for several aircraft/engine combinations were also made available to any who wished to compare predicted noise levels against measured data.

Hypothetical SST engine. - The results of the hypothetical SST engine noise calculations are summarized in Table II. Calculations were made for each of three power settings representing takeoff, cruise, and landing approach. Total flyover noise is presented in terms of effective perceived noise level (EPNL) and the component levels presented in terms of peak perceived noise level (PNL) for jet, shock cell, and combustion noise. The highest and lowest levels calculated are shown to indicate the range of the results. The levels calculated using ANOPP are also indicated.

Two conclusions were drawn from the results of the paper SST engine noise calculations. The first is that there were large differences in the noise levels predicted by different methods. The second is that ANOPP produced results which compared very favorably with the average of those calculated by other organizations.

One additional observation should be recorded. The results for fan and turbine noise were disappointing and inconclusive. The range from high to low values exceeded 20 dB with no apparent concensus as to the best method. The SST engine prediction exercise, therefore, clearly identified the need for greatly improved turbo machinery prediction methodology especially for other than jet-noise-dominated aircraft.

Comparisons with measured aircraft noise data. - Noise levels for five aircraft including Concorde and for the Aerotrain were also calculated for comparison with measured data. The procedure followed for this portion of the ICAO study was first to calculate noise levels based on input data which was provided through the chairman of the prediction subcommittee. Later, the predicted and measured perceived noise levels (PNL) were transposed to the same plot for comparison and evaluation of the accuracy of the prediction methods.

The differences between measured and ANOPP-predicted values of EPNL for all of the aircraft in the ICAO study are summarized in figure 12. On average the ANOPP predictions were approximately 2 dB below measured levels. The dashed curve for the Concorde indicates underprediction of from 1 to 4 EPNdB depending on the jet velocity.

In summary, the ICAO study provided an early opportunity to compare ANOPP with other prediction methods and with measured aircraft data. The ICAO study also provided a basis for identifying future improvements, particularly in the turbomachinery area, in ANOPP methods. The results of the study were encouraging since the reference procedure selected by the noise prediction subcommittee in 1978 consisted mostly of ANOPP methodology.[1]

DC-9

Following the ICAO study, ANOPP noise predictions were made for a McDonnell-Douglas DC-9-32 powered by JT8D-9 so-called hardwall engines.[2] Noise levels, flight path, and aircraft data for actual test conditions were supplied by the manufacturer. Engine data were made available by Pratt & Whitney. Four flights of interest were drawn from a large set of tests done by McDonnell-Douglas at the Yuma test site (ref. 6). Tone corrected perceived noise level predictions were made by summing jet, core, and fan noise components. There were no shocks present. The fan noise was calculated in two stages using a modified Heidmann method, as per the ICAO recommended procedure.[3] Ground effects and atmospheric attenuation were included in the prediction scheme since these were present in the measured data. Finally, effective perceived noise levels were calculated.

The results of the DC-9 exercise are summarized in Table III and in figure 13. As seen in the table, the effective perceived noise levels predicted by ANOPP compare very well with the values supplied by the manufacturer. The 1 to 2 dB underprediction of EPNL value by ANOPP results primarily from an underprediction of peak perceived noise levels. The two graphs presented in figure 13 are representative. The first graph compares measured and predicted PNLT as a function of radiation angle. The two curves agree very well except in the region between 100° to 130°. The second graph compares measured and predicted sound pressure level spectra for one angle in this peak noise region. The measured and predicted curves agree in general shape; however, the predicted levels average about 3 to 5 dB lower than the measured data.

---

[1] The final report of the Subcommittee on SST Noise Prediction was given by the chairman, M. J. T. Smith, to a meeting of ICAO noise prediction specialists at the Department of State, Washington DC, June 15, 1978.

[2] LTV/HTC memorandum, 1-25-79, Subject: Tone Corrected Perceived Noise Level and Sound Pressure Level Comparisons of McDonnell-Douglas DC-9 Flight Data and NASA/ANOPP Predictions.

[3] See Footnote 1.

DC-10

In the first of three ANOPP validation studies for U.S. wide body aircraft, McDonnell-Douglas submitted comparisons of predicted to measured noise levels for six level flyovers of a DC-10 at power settings ranging from approach to full takeoff power (ref. 7). Inputs of noise critical engine data were prepared by the Douglas propulsion group while airplane tracking and noise data were taken from files of the flight test group. Remote computer terminal access to the Langley computer was arranged so that Douglas could run ANOPP at Langley from their Long Beach plant.

Comparisons were made on the basis of PNLT vs. angle from the inlet axis and on the basis of 1/3-octave band spectra at selected angles as shown in figure 14. Ground effects are apparent in both the predicted and measured noise spectra. EPNL comparisons were also made for each flight. Predictions included jet, fan, combustion, turbine and airframe component noise. Since the JT9D engine was installed in an acoustically treated nacelle, the effect of duct treatment was estimated. It was assumed that the duct treatment eliminated the fan tones but did not reduce the broadband noise. Even with this assumption, ANOPP tended to overpredict the high-frequency fan noise. On the other hand, the lower-frequency jet noise was consistently underpredicted. These effects are apparent in the frequency spectrum at $\theta = 120°$. The graph of PNLT versus radiation angle in figure 14 also shows overprediction in both the forward and rear arcs which is caused by the high predicted values of fan noise. On an EPNL basis, ANOPP overpredicted from 0.4 to 3.1 EPNdB with an average overprediction of 1.3 EPNdB for the six flyovers. For the example shown in figure 14, the overprediction was 1.6 EPNdB, which is a representative case.

The DC-10 was the first aircraft for which ANOPP had overpredicted the noise. This overprediction could probably be removed by a more accurate estimate of the attenuation of fan noise provided by duct treatment. It is also possible that beneficial forward flight effects on fan noise are responsible for these differences.

L-1011

The Lockheed-California Company participated in the second wide-body ANOPP validation study under contract to Langley Research Center. Under this contract, Lockheed selected an aircraft noise data base consisting of six flyovers at engine power settings from 60 percent to 100 percent of corrected fan speed. The noise data for these flyovers were accompanied by tracking data and engine performance information on the Rolls Royce RB-211 engines. Lockheed was linked to the Langley computer complex via a remote terminal so that the ANOPP noise prediction could be made by Lockheed's engineers.

The results of the L-1011 validation study as published in reference 8 are disappointing. While agreement between measured and predicted data at the low power settings is quite good, the noise produced at takeoff power settings is grossly overpredicted. The difference between measured and predicted noise levels is as much as 20 PNdB for the full power takeoff case. The agreement is particularly bad in the forward quadrant, that is, for radiation angles between 20 and 80 degrees.

A study of the predicted levels of the component noise sources suggests that the overpredictions are due to high levels for the fan combination tones which are generated by supersonic tip speed fans. This explains why the low power cases, where fan tip speed is subsonic, are not overpredicted. If the Lockheed engineers had eliminated fan tones, as was done by Douglas, the results would have been greatly improved.

Figure 15 and 16 are representative of the L-1011 validation study results. Each graph contains measured data, the original predicted noise levels obtained by Lockheed and the revised predicted levels obtained by eliminating the fan combination tone or buzz-saw noise. Figure 15 contains a perceived noise level plot and a spectra plot for the full power takeoff case. Even with the revision to the fan noise prediction, the takeoff noise is overestimated in the forward quadrant. Figure 16 is included to show that for reduced power settings, ANOPP can predict L-1011 flyover noise quite well. This figure compares the measured and predicted noise spectrums at a radiation angle of 60° and a power setting of 90% fan speed. Notice that once the buzz saw noise component is suppressed, the measured and predicted curves look very similar. Even the reinforcements and cancellations caused by ground reflection are correctly predicted. This figure is typical of all the reduced power results included in the validation study.

Boeing 747

The Boeing Aircraft Company has recently completed the third wide body validation study, which compared ANOPP predictions to 747 flyover data. The flyovers, depicted in figure 17, were made at constant 122 meter altitude (400 ft) with several engine power settings. Noise was measured by flush-mounted microphones on the airport runway. The predicted total noise was assumed to be the sum of jet, fan, core, turbine, and airframe noise components. The jet and fan noise components dominated the predicted levels in most cases.

Comparisons of predicted and measured tone-corrected perceived noise levels are shown in figure 17. At approach power, the predictions were less than the measured data at all directivity angles. The approach power prediction for EPNL was 5 dB below the measured data. At takeoff power, the perceived noise levels were overpredicted in the forward quadrant and underpredicted in the aft quadrant causing a 1 dB difference in effective perceived noise levels. No attempt to analyze the source of these discrepancies has been made except to note that buzz-saw noise was included in the ANOPP calculation by the Boeing engineers.

Discussion

The three wide body validation studies all indicate a need for improved fan noise prediction methods. The fan noise overprediction which often reaches 10 to 15 dB is thought to result from extrapolating static test stand data to flight conditions. Acceptable results for the DC-10 were obtained because of the Douglas engineers' decision to "model" fan noise by neglecting the buzz-saw component. For the Lockheed L-1011, results were shown with and without the buzz-saw component demonstrating significant improvement when the buzz-saw component was omitted. The Boeing 747 takeoff power noise levels were apparently overpredicted in the forward arc because of the buzz-saw term.

Improvement in jet noise prediction also appears necessary. Jet noise prediction methods are based on scale model data. The wide body validation studies indicate that significant underpredictions of jet noise may result from extrapolating these model data to full-scale engines. Flight effects on jet noise appear to be another source of prediction error.

The results of the three wide body validation studies will be documented as NASA Contractor Reports and will be available for detailed analysis by the prediction community. The intent in conducting these studies was to provide a component-by-component comparison of ANOPP prediction methods with measured noise levels of current technology aircraft. The results are encouraging. Deficiencies in fan and jet noise prediction methods have been pinpointed which will provide the focus of future prediction research.

SYSTEMS STUDIES

The application of ANOPP to preliminary design systems studies or parametric analyses is illustrated in figure 18. A few of the key dimensionless variables are the thrust-weight ratio, (T/W), which sizes the propulsion system; the lift-drag ratio, (C_L/C_D), which represents the aircraft's aerodynamic characteristics; and the normalized specific thrust, $(T/\dot{m}c_a)$, which is an indicator of source noise. The interrelationships among these and other dimensionless variables must be carefully studied before the ultimate compromise between noise at the FAA certification points, performance, and economics can be reached. The value of ANOPP for design studies and, consequently, for quantifying the benefits of proposed noise reduction technology has been established through the NASA SCR project interface and the ICAO/SCR studies. NASA is committed to continued cooperative development and improvement of ANOPP for application to future parametric and preliminary design studies of advanced aircraft system concepts.

An example of application of ANOPP to a systems study involving noise-constrained takeoff procedures is discussed in the next section.

Optimized Takeoff Procedures

The Aircraft Noise Prediction Program has facilitated a set of systematic noise reducing trajectory studies which is unique in a number of ways. First, a standard optimization program is used to adjust continuous control functions and produce realistic takeoff solutions. Second, multiple noise constraints surrounding the runway tend to reduce noise in every direction, not just at a single point. Third, detailed mathematical descriptions of flight path, engine operations, and noise tailor the solution to a specific aircraft. Both the completeness of the studies and the approach to the problem are unique.

The general optimization problem is illustrated in figure 19. The object is to find that takeoff trajectory which minimizes noise at each selected observer location. The range of physically possible and acceptable trajectories is represented by the shaded region in figure 19. The lower limit represents a minimal adherence to accepted safety practices and the upper limit represents the maximum power takeoff. Between these extremes lies the trajectory which produces minimum noise at the observers.

A key to the solution of this general class of optimal control problems is to realize that the inverse problem is easier to solve. In other words, rather than minimizing noise at multiple observer locations with the constraint that final altitude, H_f, exceeds some minimum safe altitude, it is more natural to maximize H_f with multiple noise constraints as summarized below.

Payoff:	Maximum altitude	
Controls:	$\alpha(t)$, $ps(t)$	
Constraints:	$EPNL_i < EPNL_{max}$	$i = 1, 2 \ldots$
Side Constraints:	$\alpha_{min} < \alpha < \alpha_{max}$	
	$ps_{min} < ps < ps_{max}$	

The optimization problem is to adjust the flight controls, angle of attack α and power setting ps, in order to maximize final altitude while restricting the noise at each observer to some acceptable limit. The acceptable noise limit can then be lowered until no feasible solution exists. The side constraints on α and ps establish a range of possible angle-of-attack values and a range of physically attainable engine settings. These constraints are equivalent to defining minimum and maximum possible trajectories bounding the shaded region in figure 19.

ANOPP is especially handy for solving optimization problems of this type. (See figure 20.) It contains a module to calculate the flight trajectory and one or more modules to evaluate Level II noise predictions at each observer. It also contains executive control statements which perform initialization and decision logic. The optimization code, while not strictly a part of ANOPP, can be introduced to the executive system and used as any other functional module. The optimizer in use was developed at NASA Ames Research Center by Gary Vanderplaats and is described in reference 9.

The optimization approach has already been applied to advanced design supersonic transport takeoffs. The details of this research, including a description of the flight dynamics module, are contained in reference 4. One issue left unresolved in that work is the applicability of optimized procedures to present commercial aircraft. A study of the L-1011 takeoff procedures has since clarified this point.

Optimized L-1011 Takeoff

The Lockheed L-1011 Tristar is selected for an optimized takeoff study for a number of reasons. The primary reason is that detailed engine performance and noise data are published in references 8 and 10. Moreover, the wide-body L-1011 with three high by-pass ratio RB-211 engines provides a sharp contrast to the supersonic transport concept studied previously. Finally, the L-1011 has a wide range of operating capabilities which make optimized procedures attractive. Even fully loaded, the L-1011 has a considerable amount of excess power capability so that the aircraft can maintain a climb in the event of an engine failure.

The test problem designed for the L-1011 is based on FAA certification procedures for large commercial aircraft. Two observer locations are situated along the FAR-36 sideline at 5500 m and 6000 m from brake release and a third observer location is on the runway centerline and 6486 meters from brake release. Noise levels at each observer are restricted to 96 EPNdB which proved to be the lowest feasible noise goal. (Here buzz-saw noise is omitted). Side constraints on the control functions are set very loosely at $\alpha_{min} = 4°$, $\alpha_{max} = 16°$, $ps_{min} = 70\%$, $ps_{max} = 100\%$.

The results of the L-1011 study are presented in figures 21-23. The initial conditions are based on a representative (constant power/constant velocity) takeoff procedure found in reference 10. The ANOPP flight dynamics routine can approximate this takeoff based on the initial aircraft position and the angle-of-attack and power setting schedules given in the reference. The optimization routine then adjusts the control functions in order to maximize final altitude and to conform to the noise constraint. Initial and optimal values of angle-of-attack, power setting, altitude and velocity are given in figure 21 and 22. Notice that the optimum thrust schedule is a gradual cutback such that minimum thrust occurs slightly before the aircraft flies over the centerline microphone. The thrust schedule plus the modified angle-of-attack schedule results in a slower rate of climb than in the initial takeoff. However, the optimal solution conforms to FAA safety standards in that the climb gradient remains above 4 percent and in that the thrust cutback occurs after the aircraft has reached 213 m (700 ft) altitude.

Use of the optimal flight procedure results in reduced effective perceived noise levels everywhere along the sideline and at the flyover monitor. (See figure 23.) This test problem demonstrates the use of optimization to reduce noise levels for certification purposes. The same technique could be applied to community noise abatement studies by positioning the observer locations in areas of high population density or in areas where citizen complaints are frequent.

NOISE PREDICTION RESEARCH

Several areas requiring further research have been identified as a result of systems studies using ANOPP to provide predicted noise levels. One of these noise-constrained or optimum takeoff procedures has been discussed in the previous section. Three others are indicated in figure 24.

Shock Cell Noise

Shock cell noise was identified as a critical research area during the Supersonic Cruise Research studies. Shock cell noise has a nearly omnidirectional radiation pattern which causes it to dominate the forward arc during takeoff. This forward radiated noise limits the benefits of power cutback as a noise reducing operational procedure. Consequently, the elimination of shock cell noise is critical to the success of a supersonic vehicle. NASA has a strong in-house program underway which is aimed at developing the ability to understand and control shock cell noise. The initial portion of this study has been described by Seiner and Norum (ref. 11). A new theory of shock cell noise has been developed and is presently in the validation process. As indicated in figure 24 the essential feature of this new model of shock cell noise is its more forgiving nature when the exhaust nozzle is operated in off design condition.

Lateral Attenuation Research

It became apparent during the Supersonic Cruise Research and ICAO studies that more information was needed on ground effects on aircraft noise. Quantifying the low angle of incidence phenomenon of excess (fig. 25) ground attenuation (EGA) was of particular interest. The only large data base available to check the theoretical predictions were the ground-to-ground propagation data taken by Parkin and Scholes in the mid fifties (ref. 12). There were almost no air-to-ground data available.

NASA conducted a series of flight tests at Wallops Island in 1979 in order to obtain this needed air-to-ground EGA data (ref. 13). Figure 25 shows a summary of the results of these tests in terms of a plot of the EPNdB attenuation as a function of elevation angle and distance to the observer. Similar curves are available for the attenuation as a function of frequency. These curves agree fairly well with theory, however, there is a tendency to measure slightly more attenuation than is predicted. Also, the actual data points from the experiment show a sizable amount of scatter. The timely acquisition and interpretation of this data set has supported the development of a credible method of calculating lateral attenuation which has been documented by the SAE (A-21 Aircraft Noise Committee) in an aerospace information report (ref. 14).

Static tests were made using a source mounted on a tower at the same Wallops Island site to provide a further comparison between prediction and experiment. It is hoped that these tests will exhibit reduced data scatter and explain any remaining difference between theory and experiment.

Jet Shielding Research

Lateral attenuation measurement on multi-engine aircraft often show greater attenuations than predicted by ground effect theory or than measured in the T-38 tests. The T-38 tests were made with only the engine nearest the microphones operating at full power so that there would be no jet shielding effect.

NASA has a program underway to determine the shielding effect of one jet on another as indicated in figure 24. An analytical study is being conducted to try to compute this effect. An in-house study is being conducted to measure the shielding of a point source. A contract study to provide experimental data of the shielding of a jet by a jet is also planned.

CONCLUDING REMARKS

This paper has attempted to describe some of the essential features of the ANOPP system for aircraft noise prediction and to provide a basis for evaluating its present capabilities and future potential. In just a few years ANOPP has progressed from a turbojet prediction capability to its present capability of predicting the noise from high-bypass-ratio engines with coaxial flow. By virtue of participation in SCR and ICAO systems studies, procedures for incorporating noise as a constraint at the preliminary design stage have been established. A takeoff noise optimizing procedure has been developed and installed in ANOPP which calculates a minimum noise takeoff procedure subject to multiple site noise constraints.

ANOPP provides the framework in which more sophisticated source prediction theories may be evaluated when, and if, these theories show the possibility of representing experimental data over a reasonable range of test conditions. It also provides the basis for evaluating new noise reduction concepts such as inverted flow vs. conventional jets by interchanging modules so that the user immediately sees the effect on flyover noise or on a takeoff noise contour of the inverted jet as compared to the conventional jet. The program is also useful in comparing the predictions of different theories to full-scale flight data. The ANOPP data base contains flyover spectra from three wide-body aircraft. New fan modules may be installed in ANOPP to have their predictions compared to these data. In this way, the more promising theories may be evaluated and selected for use. This procedure for the objective evaluation of noise prediction methods is an important contribution to noise research and futher suggests the use of ANOPP as a means of evaluating proposed noise reduction designs and techniques.

Future activities to improve prediction accuracy include the refinement of present empirical procedures and the development of first principles prediction methodology.

REFERENCES

1. Raney, John P.: Development of a New Computer System for Aircraft Noise Prediction. AIAA Paper 75-536, Mar. 1975.

2. Raney, John P.: Noise Prediction Technology for CTOL Aircraft. NASA TM-78700, 1978.

3. Staff of the Langley Research Center: Preliminary Noise Tradeoff Study of a Mach 2.7 Cruise Aircraft. NASA TM-78732, 1979.

4. Padula, S. L.: Prediction of Noise Constrained Optimum Takeoff Procedures. AIAA-80-1055, June 1980.

5. Zorumski, William E.: Aircraft Flyover Noise Prediction. NOISE-CON 77 Proceedings, George C. Maling, Jr., ed., Noise Control Found., c.1977, pp. 205-222.

6. Hosier, Robert N.: A Comparison of Two Independent Measurements and Analyses of Jet Aircraft Flyover Noise. NASA TN D-8379, 1977.

7. Kapper, C. Y.: Validation of Aircraft Noise Prediction Program. NASA CR-159047, 1979.

8. Godby, Larry: ANOPP Validation Study - Lockheed L-1011. NASA CR-159138, 1979.

9. Vanderplaats, Garret N.: CONMIN - A Fortran Program for Constrained Function Minimization: User's Manual. NASA TM X-62,282, 1973.

10. Shapiro, Nathan; et al.: Commercial Aircraft Noise Definition - L-1011 Tristar. Volumes I-IV. FAA-EQ-73-6, Sept. 1974. (Available from DTIC as AD A012 371 to A012 375.)

11. Seiner, J. M.; and Norum, T. D.: Aerodynamic Aspects of Shock Containing Jet Plumes. AIAA-80-0965, June 1980.

12. Parkin, P. H.; and Scholes, W. E.: The Horizontal Propagation of Sound From a Jet Engine Close to the Ground, at Radlett. J. Sound. Vib., vol. 1, no. 1, Jan. 1964, pp. 1-13.

13. Parkin, P. H.; and Scholes, W. E.: The Horizontal Propagation of Sound From a Jet Engine Close to the Ground, at Hatfield. J. Sound Vib., vol. 2, no. 4, Oct. 1965, pp. 353-374.

14. SAE Committee A-21: Prediction Method for Lateral Attenuation of Airplane Noise During Takeoff and Landing. SAE Aerospace Information Report 1751. (To be published Apr. 1981.)

TABLE I. - CURRENT LEVEL III METHODS.

Module	Origin	Authors	Documentation
Single Jet	Boeing/SAE	Jaeck/Tanna	SAE ARP 876, Boeing Doc. D6-42929 J. Sound Vib 50.3, 1977.
Coaxial Jet	NASA	Stone	NASA TM X-71618
Inverted Jet	NASA/Kentron	Pao/Russell	NASA TP 1301, NASA CR 3176
Fan	NASA	Heidmann	NASA TM X-71763
Combustion	GE/FAA/SAE	Matta/Cornell	SAE ARP 876 FAA RD-77-4, FAA-RD-74-125-III
Turbine	GE/FAA/Kentron	Matta/Rawls	FAA-RD-77-4, FAA-RD-74-125-III
Airframe	UTRC/FAA	Fink	FAA-RD-77-29
Attenuation	Wyle/DOT/ANSI	Sutherland	DOT-TST-75-87, ANSI STD S1.26
Ground Effects	NASA	Pao/Willshire	NASA TP-1104, NASA TP 1747

TABLE II. - RESULTS OF THE HYPOTHETICAL SST ENGINE ICAO NOISE PREDICTION EXERCISE.

		Freefield Total Noise	Freefield Source Noise Peak PNL		
		EPNL	Jet	Shock	Combustion
100% Power	High	114.5	116	114	101.5
at	Low	111.5	110	110	95
305 m (1000 ft)	ANOPP	113.5	113	112.5	96
66% Power	High	108	106	96	97
at	Low	99	98.5	84	91
305 m (1000 ft)	ANOPP	106	101	96	91.5
25% Power	High	114.5	100	NA	99
at	Low	99.5	84	NA	92
122 m (400 ft)	ANOPP	110.0	93	NA	92

TABLE III. - COMPARISON OF PREDICTED AND MEASURED EPNL VALUES.

Run No.	ANOPP	Measured (McDonnell-Douglas)
Takeoff		
1	96.7	97.9
2	95.7	97.1
Landing		
3	102.8	102.3
4	100.1	102.4

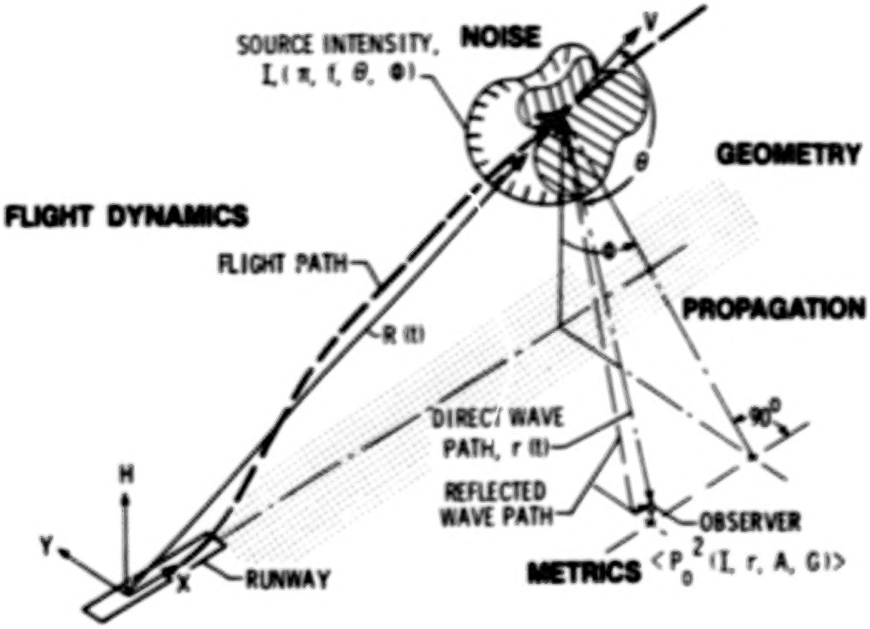
SOURCE INTENSITY,
I(π, f, θ, Φ)
NOISE
V
GEOMETRY
θ
FLIGHT DYNAMICS
FLIGHT PATH
R(t)
Φ
PROPAGATION
DIRECT WAVE PATH, r(t)
90°
REFLECTED WAVE PATH
OBSERVER
H
Y
X
RUNWAY
METRICS
<P_0^2(I, r, A, G)>

Figure 1.- ANOPP prediction methodology.

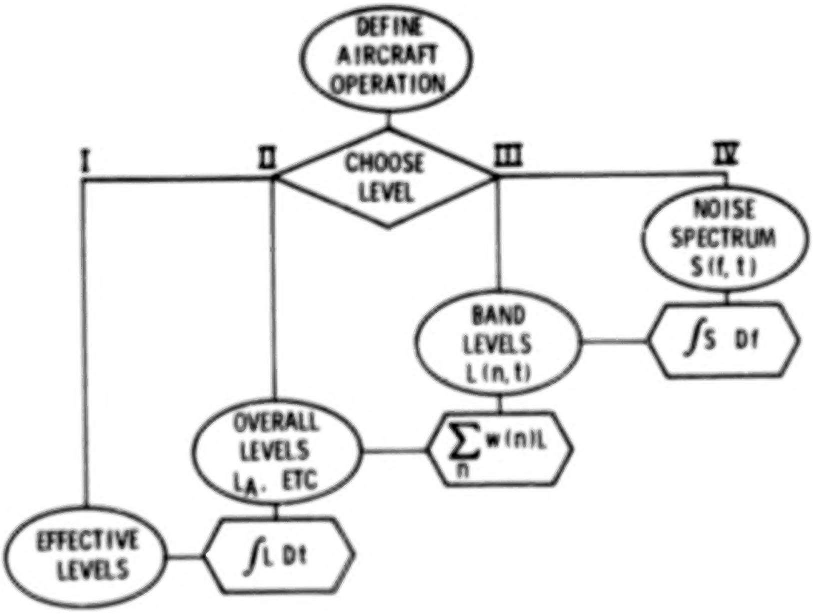
DEFINE AIRCRAFT OPERATION
CHOOSE LEVEL
I
II
III
IV
NOISE SPECTRUM S(f, t)
BAND LEVELS L(n, t)
∫S Df
OVERALL LEVELS L_A, ETC
Σ_n w(n)L
EFFECTIVE LEVELS
∫L Dt

Figure 2.- ANOPP functional level computation flow diagram.

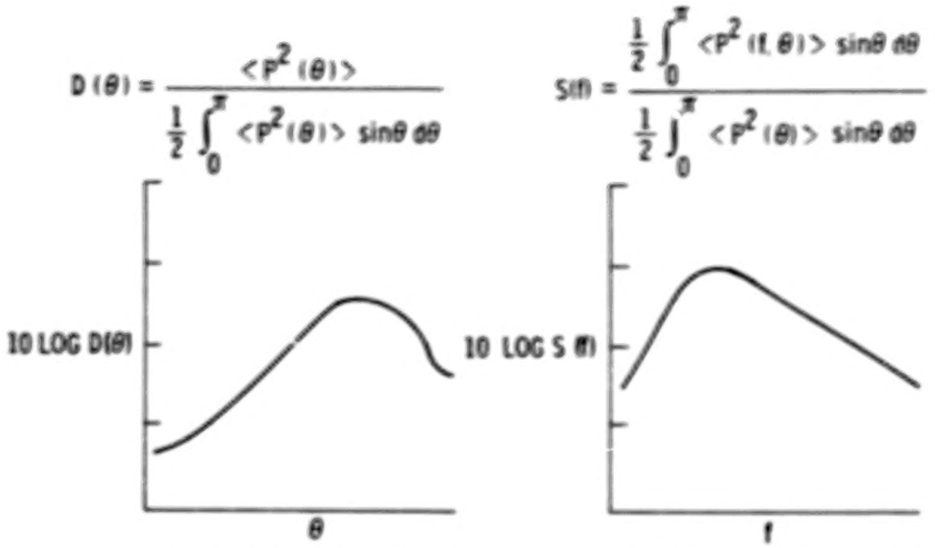

(a) OVERALL DIRECTIVITY (b) POWER SPECTRUM LEVEL

Figure 3.- Overall directivity and power spectrum levels.

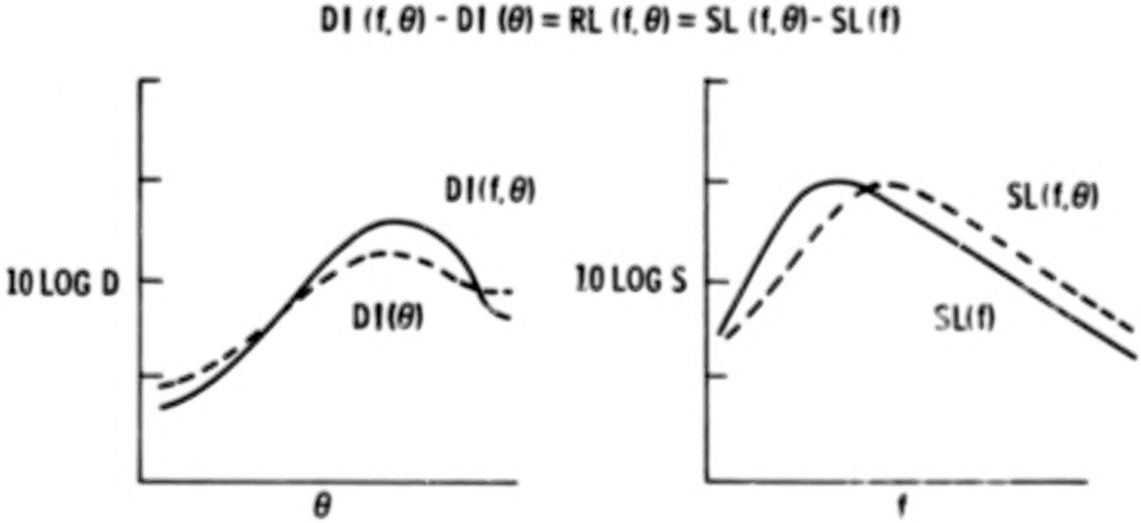

Figure 4.- Relative spectrum levels.

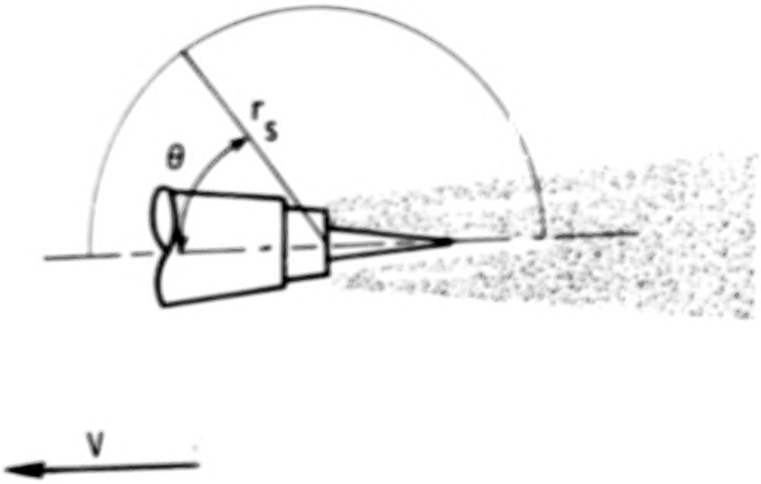

Figure 5.- Source noise prediction geometry.

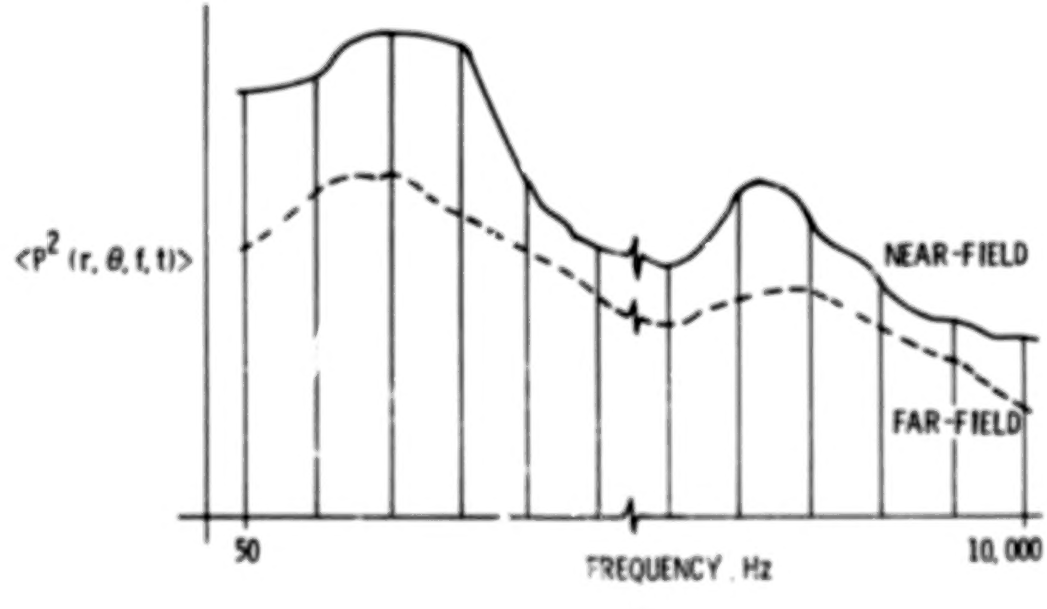

Figure 6.- Near-field and far-field noise spectra.

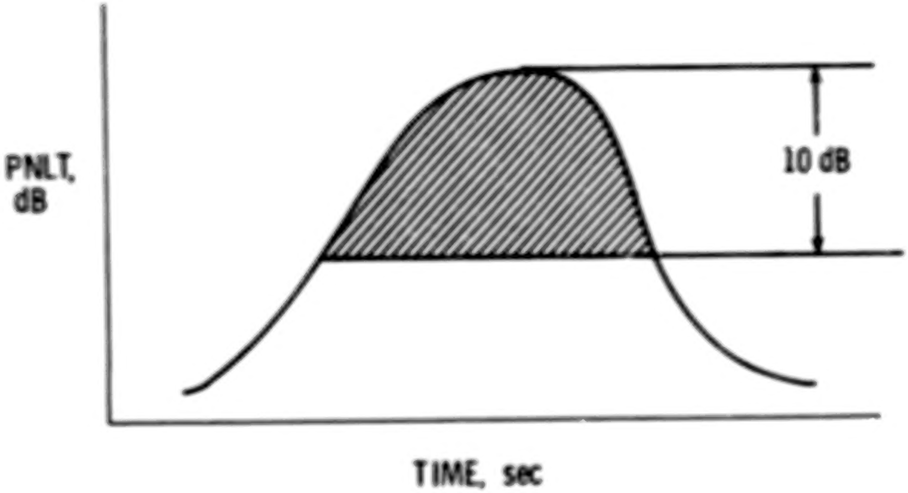
PNLT, dB
10 dB
TIME, sec

Figure 7.- Effective perceived noise level computation.

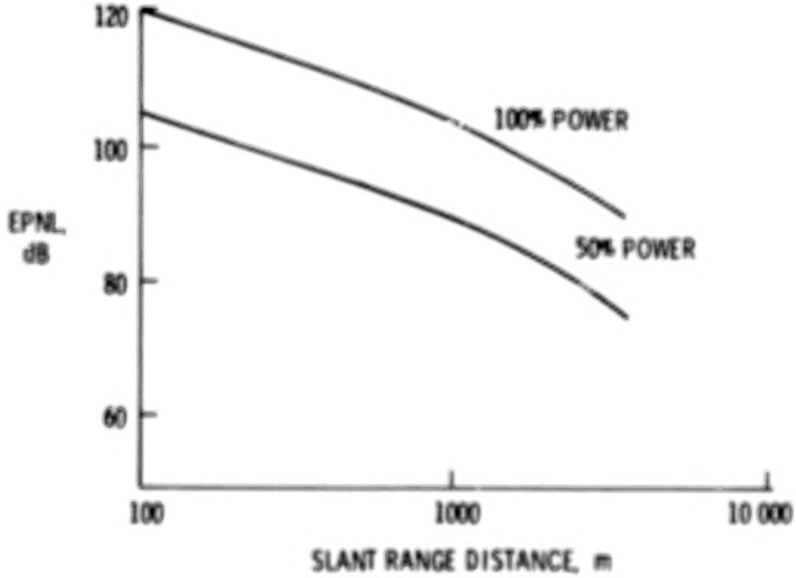

Figure 8.- Noise level/slant range curves.

Part 2

SESSION IV - OPERATING PROBLEMS AND POTENTIAL SOLUTIONS

Chairman: H. W. Schmidt

22. WAKE VORTEX ATTENUATION FLIGHT TESTS: A STATUS REPORT 387 1/A14
Marvin R. Barber and Joseph J. Tymczyszyn

23. BASIC RESEARCH IN WAKE VORTEX ALLEVIATION USING A VARIABLE TWIST WING 409 1/C8
Dana J. Morris and G. Thomas Holbrook

24. PNEUMATIC BOOT FOR HELICOPTER ROTOR DEICING 425 1/D11
Bernard J. Blaha and Peggy L. Evanich

25. AIRCRAFT OPERATING EFFICIENCY ON THE NORTH ATLANTIC - A CHALLENGE FOR THE 1980'S 445 1/F3
Robert Steinberg

26. FIREWORTHINESS OF TRANSPORT AIRCRAFT INTERIOR SYSTEMS 453 1/F12
John A. Parker and D. A. Kourtides

27. COMBUSTION TOXICOLOGY OF EPOXY/CARBON FIBER COMPOSITES 481 2/A14
D. E. Cagliostro

28. THE USE OF ANTIMISTING KEROSENE (AMK) IN TURBOJET ENGINES 499 2/C10
Harold W. Schmidt

29. NASA/FAA GENERAL AVIATION CRASH DYNAMICS PROGRAM 511 2/D8
Robert G. Thomson, Robert J. Hayduk, and Huey D. Carden

SESSION V - FLIGHT EXPERIENCES AND GROUND OPERATIONS

Chairman: J. L. McCarty

30. CURRENT RESEARCH IN AIRCRAFT TIRE DESIGN AND PERFORMANCE 543 2/F12
John A. Tanner and John L. McCarty

31. REVIEW OF ANTISKID AND BRAKE DYNAMICS RESEARCH 555 2/G10
Sandy M. Stubbs and John A. Tanner

32. STUDIES OF SOME UNCONVENTIONAL SYSTEMS FOR SOLVING VARIOUS LANDING PROBLEMS 569 3/A12
T. J. W. Leland, J. R. McGehee, and R. C. Dreher

33. RECENT PROGRESS TOWARDS PREDICTING AIRCRAFT GROUND HANDLING PERFORMANCE 583 3/B12
Thomas J. Yager and Ellis J. White

34. THE NASA DIGITAL VGH PROGRAM - EARLY RESULTS 613 **3/D14**
Norman L. Crabill and Garland J. Morris

35. EVALUATION OF EMERGENCY-LOCATOR-TRANSMITTER PERFORMANCE IN REAL AND SIMULATED CRASH TESTS 625 **3/E12**
Huey D. Carden

36. EXTINGUISHING IN-FLIGHT ENGINE FUEL-LEAK FIRES WITH DRY CHEMICALS 655 **3/G14**
Robert L. Altman

SESSION VI - ACOUSTICS AND NOISE REDUCTION
Chairman: H. G. Morgan

37. RECENT DEVELOPMENTS IN AIRCRAFT ENGINE NOISE REDUCTION TECHNOLOGY 671 **4/B4**
James R. Stone and Charles E. Feiler

38. SOURCES, CONTROL, AND EFFECTS OF NOISE FROM AIRCRAFT PROPELLERS AND ROTORS 699 **3/D4**
John S. Mixson, George C. Greene, and Thomas K. Dempsey

39. NASA PROGRESS IN AIRCRAFT NOISE PREDICTION 721 **4/E12**
J. P. Raney, S. L. Padula, and W. E. Zorumski

40. AIRPORT NOISE IMPACT REDUCTION THROUGH OPERATIONS 759 **5/A13**
Richard DeLoach

ATTENDEES 779 **5/C5**

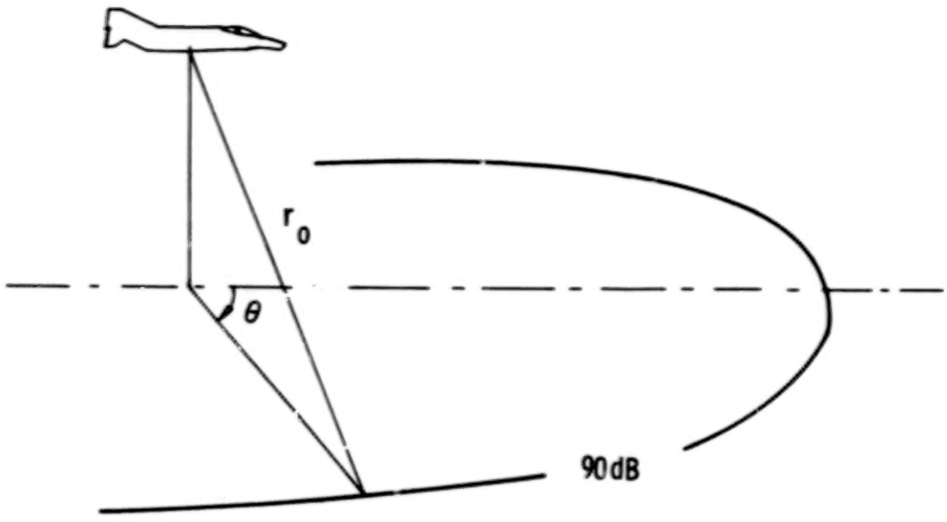

Figure 9.- Level I contouring procedure.

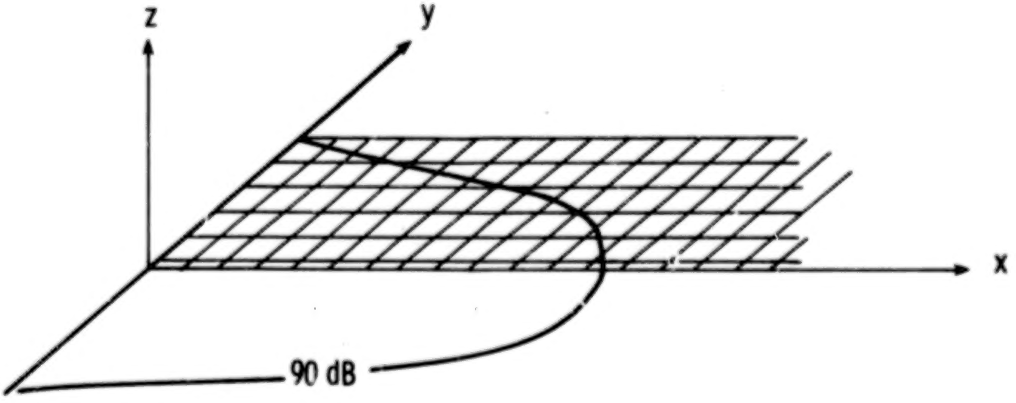

Figure 10.- Level II and III grid contouring method.

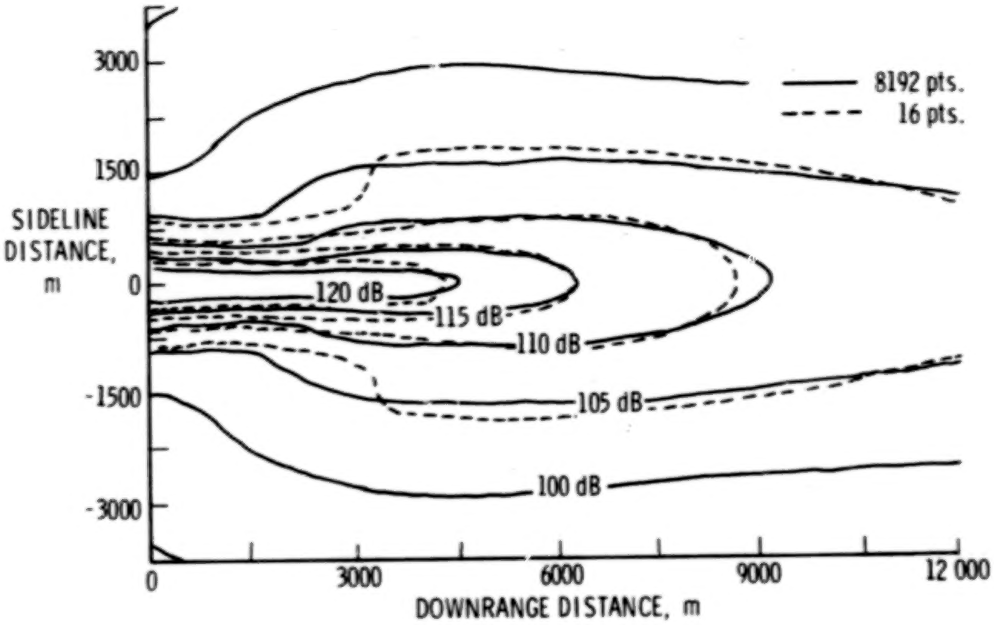

Figure 11.- Comparison of ANOPP enhanced EPNL contours with very accurate nonenhanced contours.

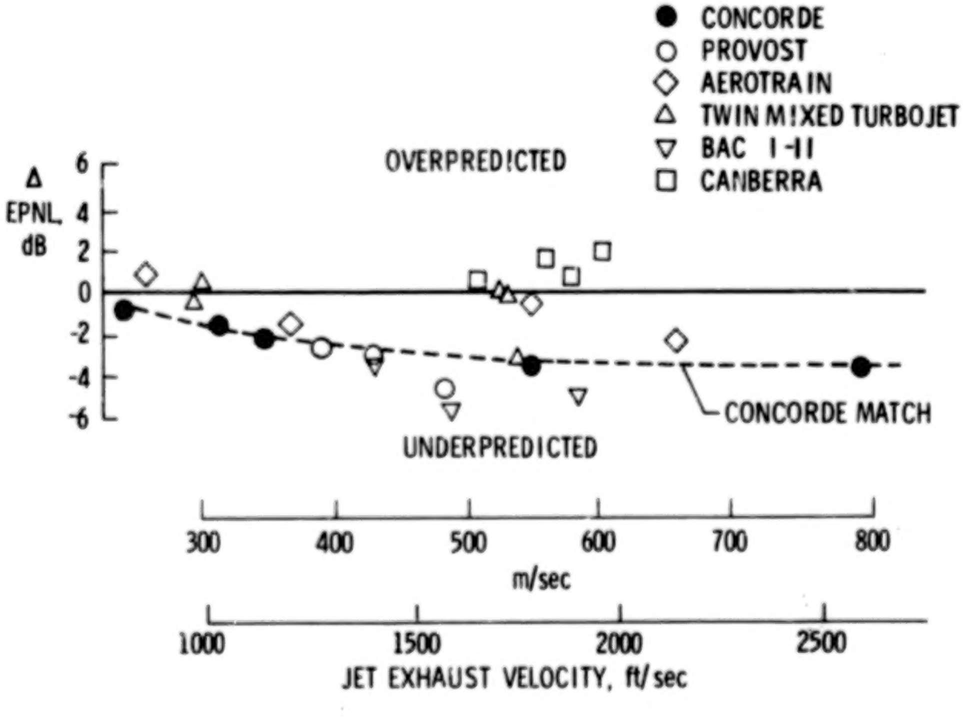

Figure 12.- Comparison of ANOPP predictions with measured data in the 1977 ICAO exercise.

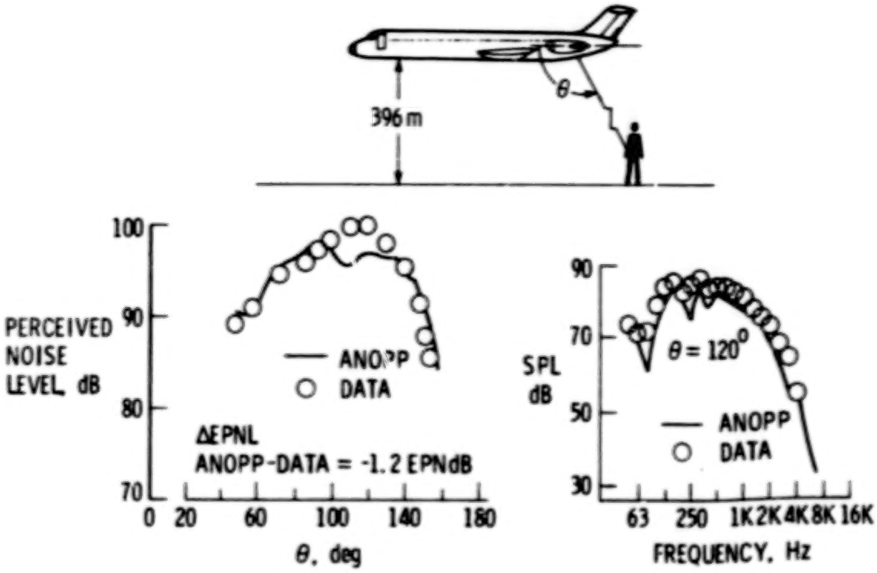

Figure 13.- Comparison of DC-9 noise prediction with measured data.

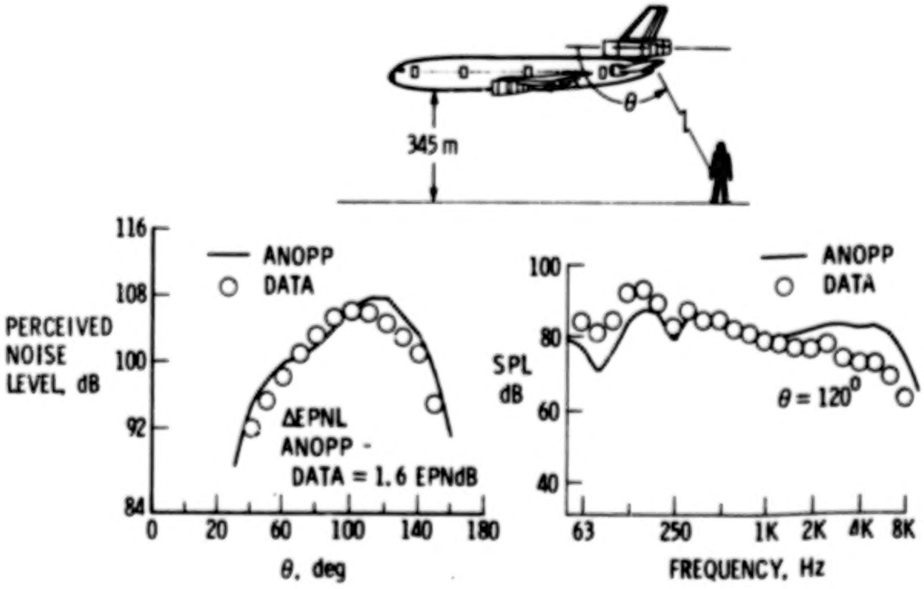

Figure 14.- Comparison of DC-10 noise prediction with measured data.

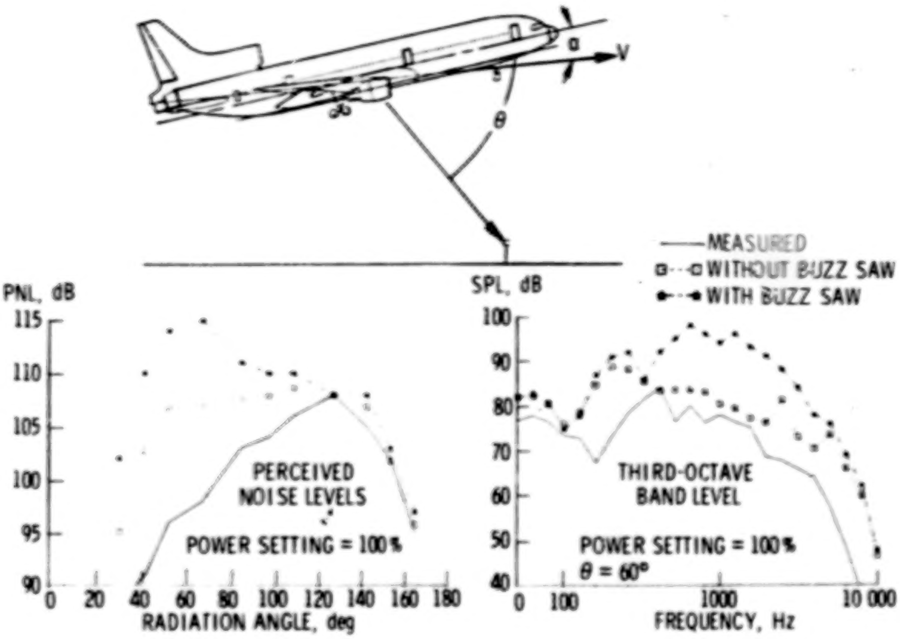

Figure 15.- Comparison of L-1011 noise prediction with measured data.

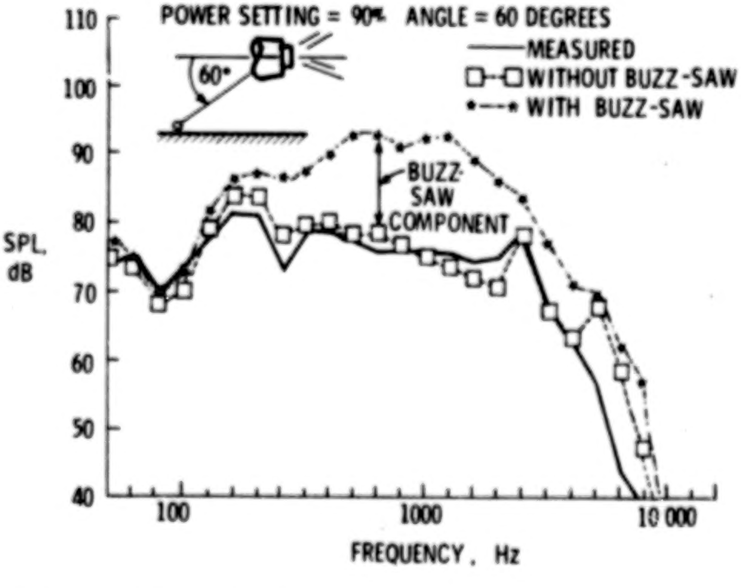

Figure 16.- L-1011 noise spectra for a reduced power flyover.

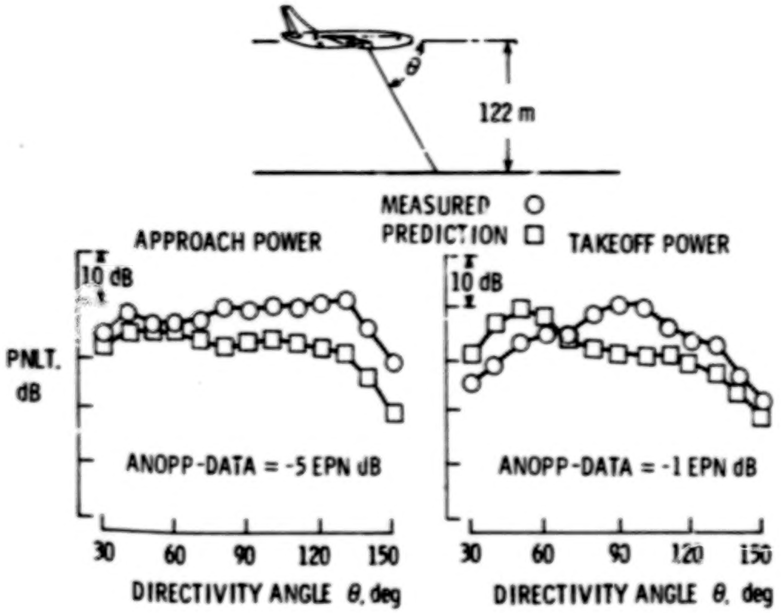

Figure 17.- Comparison of 747 noise prediction with measured data.

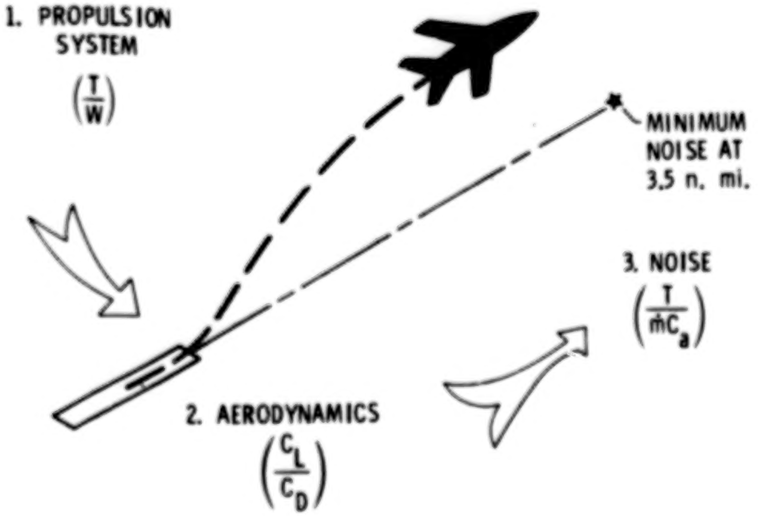
1. PROPULSION SYSTEM
(T/W)
MINIMUM NOISE AT 3.5 n. mi.
3. NOISE
(T/ṁC_a)
2. AERODYNAMICS
(C_L/C_D)

Figure 18.- ANOPP preliminary design systems studies.

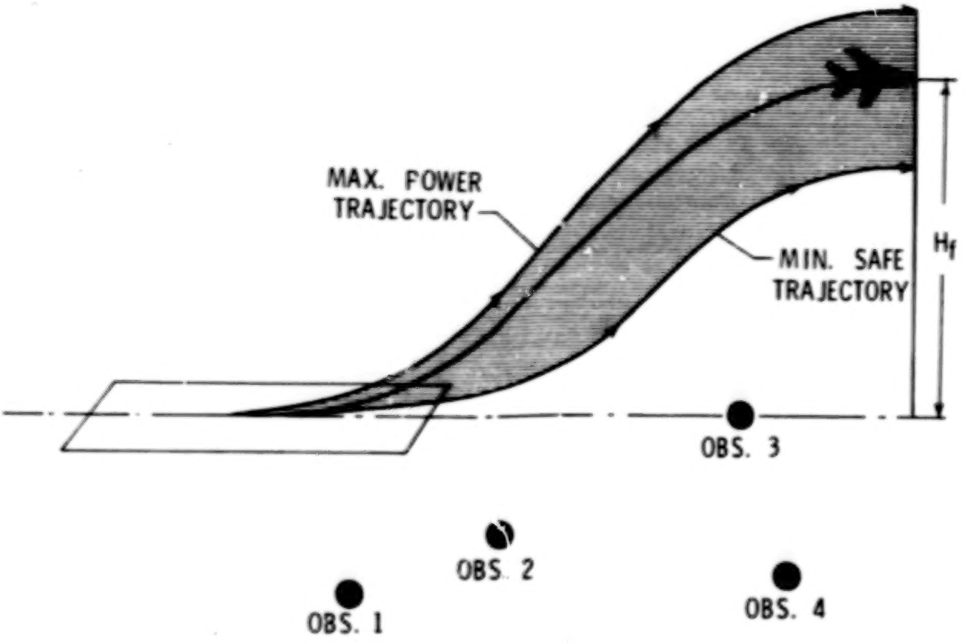
MAX. POWER
TRAJECTORY
MIN. SAFE
TRAJECTORY
H_f
OBS. 3
OBS. 2
OBS. 1
OBS. 4

Figure 19.- Noise reducing operational procedures.

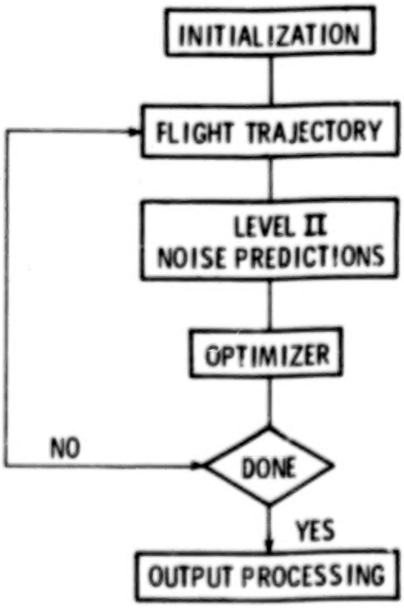
INITIALIZATION
FLIGHT TRAJECTORY
LEVEL II
NOISE PREDICTIONS
OPTIMIZER
NO
DONE
YES
OUTPUT PROCESSING

Figure 20.- Flow of the optimization computations.

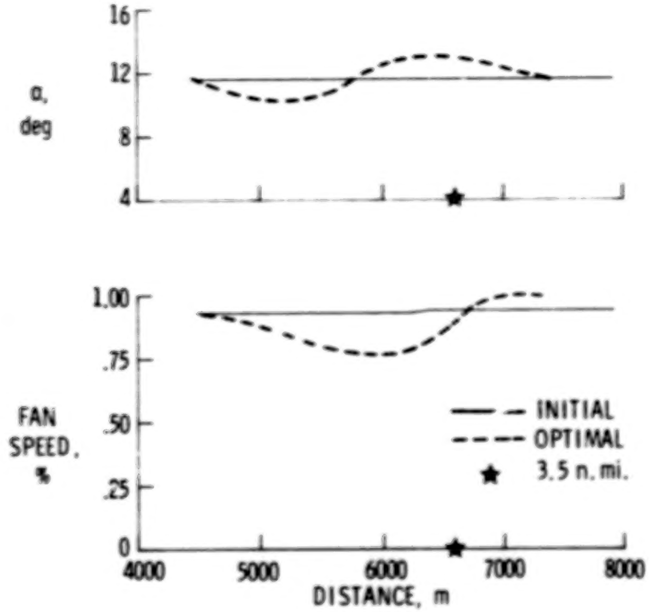

Figure 21.- Comparison of initial and optimal control functions.

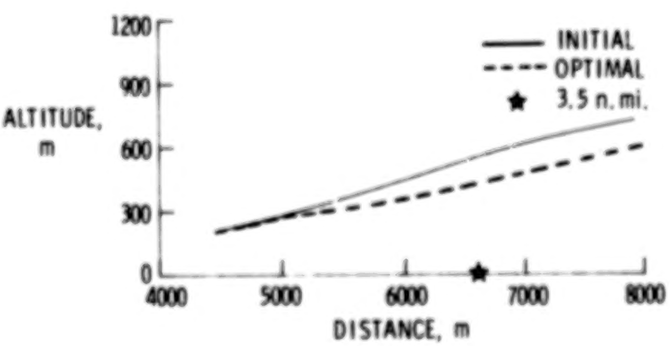

Figure 22.- Effect of optimal controls on L-1011 flight performance.

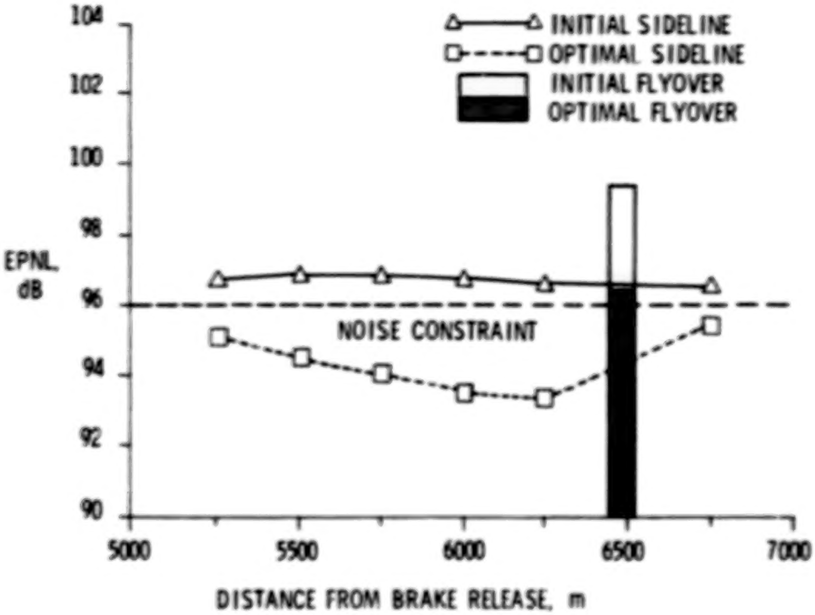

Figure 23.- Noise reduction obtained from optimized flight procedures.

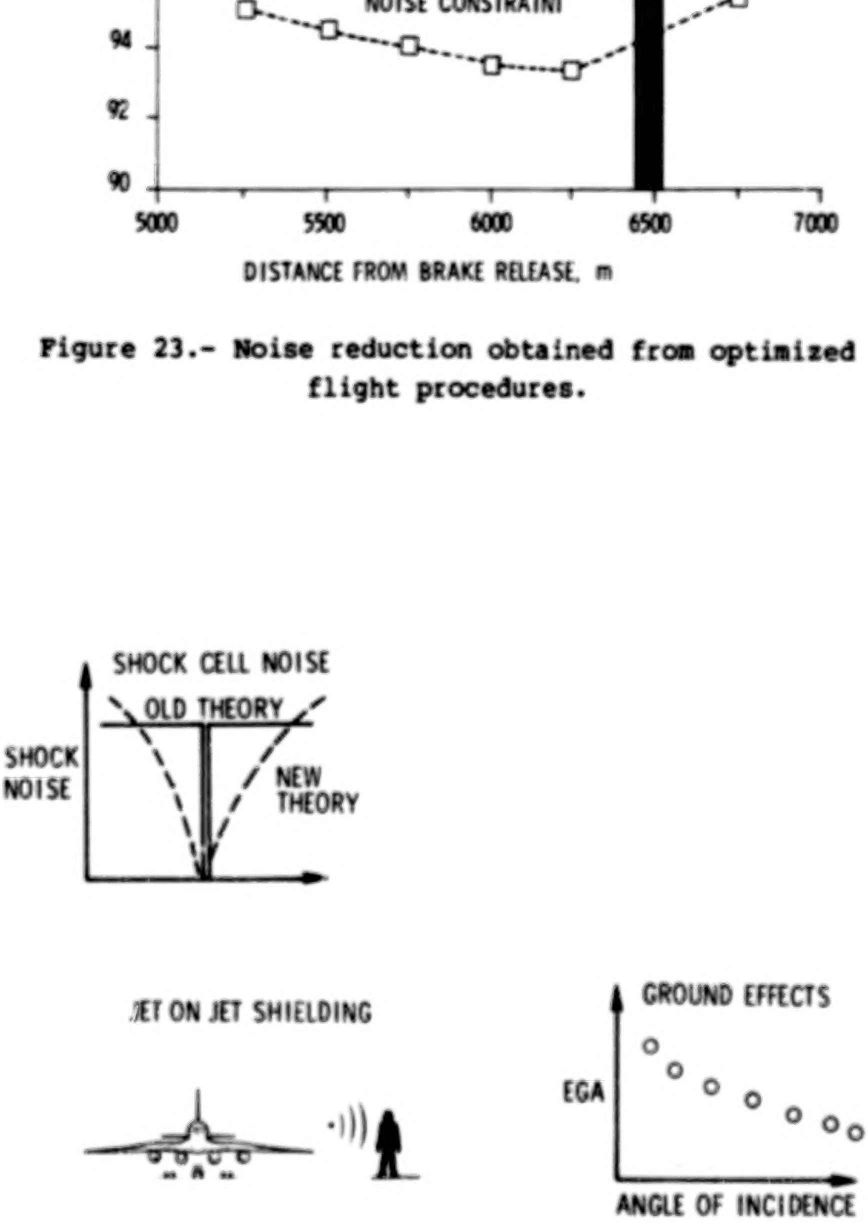
SHOCK CELL NOISE
OLD THEORY
SHOCK NOISE
NEW THEORY
JET ON JET SHIELDING
GROUND EFFECTS
EGA
ANGLE OF INCIDENCE

Figure 24.- New research areas identified by ANOPP.

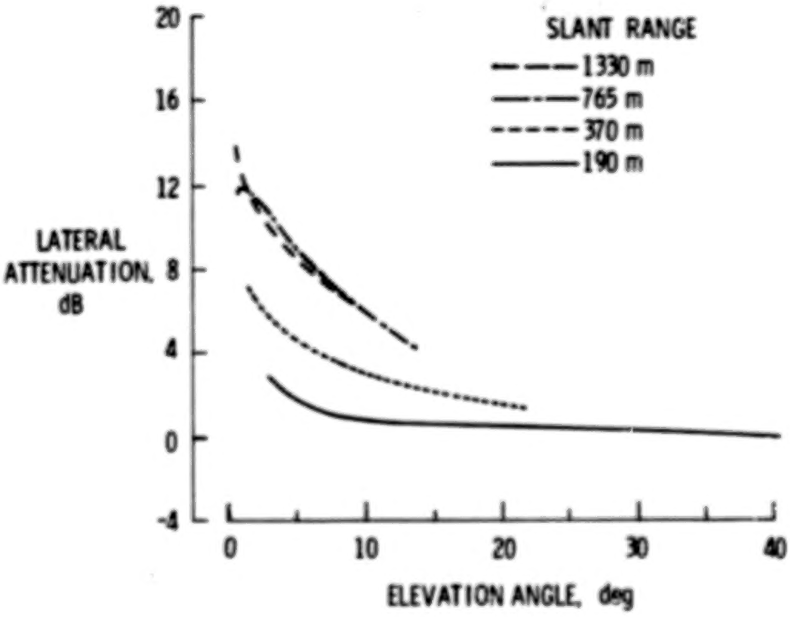

Figure 25.- Lateral attenuation in T-38 flyover data.

BLANK PAGE

BLANK PAGE

AIRPORT NOISE IMPACT REDUCTION THROUGH OPERATIONS

Richard DeLoach
Langley Research Center

SUMMARY

The objective of Langley Research Center's airport community noise impact modeling program is to develop the technology for noise impact assessment and minimization in airport communities. Focus for this program is an airport community computer simulation model called ALAMO (Airport-noise Levels and Annoyance MOdel) which is capable of overlaying distributions of aircraft noise level (footprints) on the population distributions of any U.S. airport community. Recently developed psychophysical relationships between noise exposure level and subjective response are then invoked to predict the overall impact of airport noise on the surrounding community, based on the number of individuals exposed to various levels of noise. Outputs of the program include a prediction of the number of residents expected to be "highly annoyed" with the airport noise, as well as several demographic variables listed as a function of noise level, including population, population density, and population growth rate. The ALAMO model can be used to quantify the degree of noise impact reduction which can be achieved by various candidate noise abatement strategies. For example, a number of runway selection alternatives might be compared with the imposition of a night curfew to see which strategy results in the greatest reduction of highly impacted residents. In a similar manner, various fleet mix and land-use alternatives can be assessed to determine which has the greatest potential for alleviating noise impact. Since each noise abatement strategy will have a cost associated with it, the ALAMO model can be used to determine an appropriate distribution of limited airport noise abatement resources.

In this paper, the effects of various aeronautical, operational, and land-use noise impact reduction alternatives are assessed for a major midwestern airport. Specifically, the relative effectiveness of adding sound absorbing material to aircraft engines, imposing curfews, and treating houses with acoustic insulation is examined.

INTRODUCTION

Concern for the impact of noise on airport communities represents a major impediment to the growth and development of commercial aviation, both in the United States and abroad. Noise effects are largely responsible for the fact that, in the United States, no construction has been initiated for new jet airports to serve major metropolitan communities in a decade even though the demand for air transportation has grown dramatically in the same period.

Figure (1) illustrates the growth in passenger-km/yr (mi/yr) in the United States since 1950, with the current trend extrapolated to 1990 (ref. 1). The increased demand for air carrier service has been partially absorbed through increased operations at established airports. Residents of the more severely impacted airport communities have organized themselves politically in order to impose various noise abatement operating constraints on the airports serving their communities. Figure 2 illustrates the trend toward increased operating constraints at airports worldwide. If the historical trend of increasing air carrier demand continues as expected, the trend toward more tightly constrained operations can also be expected to continue.

In addition to constraints on airport operating procedures which might take the form of night curfews, takeoff and landing profile restrictions, or restrictions on ground tracks, other abatement countermeasures are also of interest to airport operator and community planners. These nonoperational countermeasures can be classified as either aeronautical countermeasures or land-use countermeasures. Aeronautical countermeasures involve the development and implementation of source noise suppression technology to reduce noise levels emanating from the jet engines. Available technology options include new fan designs, acoustic liners, engine inlet designs, and internal flow mixers (ref. 2). Land-use countermeasures include zoning restrictions to discourage future residential construction in the airport vicinity, relocation of residents out of highly impacted areas, and insultation of impacted homes to provide noise relief.

The task of developing an effective noise abatement strategy is complicated by difficulties in defining quantitatively the degree of noise relief which is afforded by a particular countermeasure. Furthermore, the noise relief which a particular countermeasure provides can be much different for one airport than for another. For example, a takeoff procedure which involves a large cutback in thrust soon after takeoff will provide greater relief in communities with higher population densities near the airport than in communities with higher population densities further from the airport.

This paper describes the implementation of an assessment methodology which permits the quantitative assessment of a variety of noise abatement options on and airport-specific basis. The assessment method, which is implemented in a computerized community response model called the Airport-noise Levels and Annoyance MOdel (ALAMO), is demonstrated for the case of a major midwestern airport. Several potential aeronautical, operational, and land-use countermeasures are evaluated for this airport.

IMPACT ASSESSMENT METHODOLOGY

The Fractional Impact Method of assessing community response to airport noise is used in the impact assessments described in this paper. This method expresses noise impact in terms of the number of people exposed to noise of a particular level, in the following way: The number of people exposed to a particular noise level is multiplied by a dimensionless weighting function which depends on that noise level. The weighting function is based on Schultz's relationship between human subjective response to noise (percent "highly annoyed") and noise level as described by the L_{dn} metric (ref. 3). The weighting function is obtained by normalizing the Schultz dose-response transfer function to unity at 75 L_{dn} and represents the "fraction of impact" associated with various noise levels, assuming an impact of 100 percent at 75 L_{dn} (fig. 3). The product of this level-dependent weighting function and the number of people exposed to each noise level is summed for all noise levels in the airport community, resulting in a quantity called the level weighted population, which expresses noise impact in terms of both noise level (intensity) and population exposed (extensity).

Working Group 69 of the National Research Council's Committee on Hearing, Bioacoustics, and Biomechanics (CHABA) developed the level weighted population concept as it is used in this paper and has recommended this concept for quantifying noise impact in their "Guidelines for Preparing Environmental Impact Statements on Noise" (ref. 4), prepared at the request of the Environmental Protection Agency. Also described in reference 4 is a second noise impact descriptor called the Noise Impact Index (NII), which is defined as the ratio of the level weighted population (described above) to the total impacted population. The NII is a useful measure for comparing the noise impact in communities with different numbers of impacted residents.

IMPLEMENTATION OF ASSESSMENT METHODOLOGY

The idea that community response to noise should be described in terms of noise level and population exposed is not new. Early applications of the fractional impact concept are described in reference 5 for example. Even though the basic concept is not new, a practical means for routinely performing fractional impact calculations has had to await three technical developments, two of which have occurred only recently.

The first of these developments has to do with describing noise levels at arbitrary locations within an airport community. Methods for performing this task have been available for several years and involve the combining of aircraft source noise and performance data with noise prediction methodology to generate contours of constant noise exposure around an airport (refs. 6 and 7).

The second technical development to facilitate applications of the fractional impact method involves the recent introduction of census data base management computer programs which provide a cost-effective means of obtaining the demographic information required in fractional impact calculations. Before such census data were available in machine readable formats, the demographic data had to be acquired by tedious manual techniques, which were costly and time consuming. Now the population within a noise contour of essentially arbitrary size and shape can be determined quite easily for any airport community in the United States, with a resolution approaching half a square mile in densely populated areas (ref. 8).

The third and final technical development to facilitate routine applications of the fractional impact method is Schultz's identification of a stable relationship between noise level and human subjective response as described in the previous section. The weighting function used to determine the "fraction of impact" associated with a given noise level is based on this recently developed noise dose-response relationship.

The three major components required to assess airport community noise impact via the fractional impact method, namely, a community noise prediction program, a census data base management program, and the Schultz dose-response transfer function, have recently been incorporated into an airport community noise impact assessment model called ALAMO (Airport-noise Levels and Annoyance MOdel) (ref. 9). The ALAMO is a computerized implementation of the fractional impact method which can be used to assess noise impact for any airport community in the United States. (Assessments are limited to U.S. airports only because the demographic data base built into ALAMO is based on U.S. census data.) ALAMO reports the number of people impacted as a function of noise level, the number predicted to be "highly annoyed" (via the Schultz dose-response transfer function), the level weighted population and the Noise Impact Index. In addition, complete demographic profiles are generated which contain several quantities of interest to noise control planners, such as distributions of age, property values, homeowners, renters, single-family dwellings, and apartment buildings. Other demographic variables are also available which, while not of direct interest in a noise impact analysis, may provide insight into the prevailing attitude of the impacted population toward the airport. Family income, ethnic origin, occupation, and educational level are examples of such variables. ALAMO generates reports which display demographic variables and the results of noise impact calculations as a function of noise level for the community as a whole and for each of eight octants defined by superimposing an octant compass rose over the noise footprint, centered at the airport. Thus, it is possible to determine the numbers of residents living to the north-northeast of the airport who own their own homes and who are exposed to noise levels between 60 and 65 L_{dn}, for example.

The ALAMO has recently been used to assess both the current operating scenario and a number of hypothetical noise abatement scenarios at an existing large airport. Results of this assessment are presented in the next section.

Baseline Operating Scenario

Most of the operations information upon which the impact assessment in this example is based can be found in draft and final Environmental Impact Statements for the airport (refs. 10 and 11), required because of plans to extend its two major parallel runways. Operations information found in the EIS was augmented by information obtained from current flight schedules and from discussions with control tower personnel at the airport.

The ALAMO requires that the operating scenario for the airport under study be described in terms of four types of information: runway descriptions;

takeoff and landing profile descriptions; ground track descriptions; and descriptions of the operations schedule in terms of the number of operations by aircraft type, time of day, stage length (for takeoffs), ground tracks, and profiles. The runway descriptions are straightforward and simply involve recording the length and orientation of each of the runways. These data were obtained from the Airport Layout Plan (ref. 10) (fig. 4). The takeoff profiles for this airport were modeled after recommendations in FAA Advisory Circular 91-39 (ref. 12) which defines a standard takeoff procedure calling for a reduction from takeoff thrust to maximum climb thrust before flap retraction (cleanup). Ground tracks presented in the draft EIS (ref. 10) were used in the present impact assessment (fig. 5).

The ALAMO requires that flight operations be defined in terms of the number of operations of each aircraft type which occur on each ground track as a function of time of day (day or night) and stage length. The EIS did not contain operations data with quite this level of detail, although enough information was provided to develop an approximate model of the operating schedule, with augmentations from airline flight scheduling information. Percentage use rates given in the EIS for each ground track were multiplied by the number of daily operations given for each aircraft type in order to define the number of each aircraft type to assign to each track. These per track operations were further divided into day (7 a.m. to 10 p.m.) and night (10 p.m. to 7 a.m.) operations according to the following distribution, given in EIS:

	Day	Night
Air Carrier	90%	10%
Commuter	68.9%	31.1%
General Aviation	93.4%	6.6%

Stage length distributions for departing aircraft were not given in the EIS, but estimates were made of the number of departures by stage length based on airline scheduling information (ref. 13). A percentage distribution of takeoff operations by stage length was constructed from this information and applied to the per track day and night operations, with alterations to insure that aircraft types with takeoff roll lengths too long to use other runways were assigned to the longest runway. The results of this operations definition exercise was a table of the number of each aircraft type assigned to each ground track as a function of time of day and takeoff stage length.

Result of the Baseline Impact Assessment

Demographic reports and fractional impact reports were produced for the airport community as a whole and for each of the eight octants around the airport defined by overlaying an octant compass rose, centered on the airport. The compass rose thus divided the community into the north-northeast (NNE), east-northeast (ENE), east-southeast (ESE), south-southeast (SSE), south-southwest (SSW), west-southwest (WSW), west-northwest (WNW), and north-

northwest (NNW) octants. Figure 6 presents the number of people exposed to airport noise levels in excess of 55 L_{dn}, and includes the level weighted population and the number of people predicted to be highly annoyed by the aircraft noise, all as a function of community location, by octant. Figure 7 presents the corresponding Noise Impact Index and percent highly annoyed data. It is interesting to note that the octants which are most severely impacted (west-southwest and north-northwest) contain the fewest people. This suggests that either the airport noise distribution affects the population distribution around the airport, with fewer people choosing to live in the higher impacted areas, or that the current airport flight tracks avoid the most populated areas.

Figures 8 to 10 illustrate how population density, population growth rate, and average home values vary as a function of noise level in the airport community. The population density data are based on 1977 population figures and the growth rate data represent average annual percentage growth rates from 1970 to 1977. The average home value figures are from 1970 census data. The precision of these demographic data can be questioned because of the assumptions which must necessarily be made about the aircraft and airport operating scenario when computing the noise contours used to bound the airport community residents counted in these data. Furthermore, the average home values presented in figure 10 represent 1970 price levels, which are not relevant today. However, it is the trend of the data that is of interest, rather than the absolute values of the numbers.

The data in figure 8 indicate a maximum population density in the 65 to 70 L_{dn} band, with a decrease in population density both as the airport is approached (increasing noise levels) and as the distance from the airport gets larger (decreasing noise level). This is consistent with a general trend reported in ref. 14 for airport communities of this size.

The growth rate data in figure 9 indicate a general decline in the population residing inside the 55 L_{dn} contour. While the growth rate is negative for all the noise bands presented, the trend is for a greater decline in population in the higher impacted neighborhoods than in neighborhoods receiving less impact.

Average home values also exhibit a declining trend with increasing noise level (fig. 10). It should be noted, however, that trends in such parameters as average home values and population growth rate should not be associated exclusively with the influence of airport noise since many other factors of course play a role in determining these trends.

EVALUATION OF HYPOTHETICAL NOISE IMPACT COUNTERMEASURES

The previous section presented the results of a noise-impact assessment based on a model of the current operating scenario at a large midwestern airport. It is not necessary to limit such an assessment exercise to the current operating scenario, however. Alternate scenarios, including those which may have the potential for reducing noise impact, can be modeled as well. The relative effectiveness of several hypothetical noise abatement strategies can thus be readily determined. A number of such noise abatement countermeasures have been modeled and are presented in this section.

Description of Countermeasures

Seven noise abatement countermeasures which were modeled are described in this section. These include two aeronautical countermeasures, two operational countermeasures, two land-use countermeasures, and one combined aeronautical/operational countermeasure.

The first noise abatement scenario to be considered consisted of treating the engines of narrow-body jet transports with sound absorbing material (SAM treatment). This countermeasure was implemented by replacing the standard 727, 737, DC-9, 707, and DC-8 noise curves which reside in the data base of the ALAMO noise prediction subprogram with resident noise curves describing SAM-treated engines. It should be noted that as older, noisy aircraft are retired from the fleet, the fleet mix which evolves will contain a progressively larger fraction of aircraft which are powered by quieter engines, and the attractiveness of this engine modification alternative will, therefore, diminish with time. It is interesting, nonetheless, to compare this source-noise countermeasure with operational and land-use alternatives.

The second scenario consisted of diverting all general aviation aircraft to alternate airports. While it is recognized that such a policy would be impractical to implement, it is nonetheless of interest to assess the relative contribution of general aviation operations to the total airport noise impact.

A night curfew was modeled, in which all of the operations scheduled after 10 p.m. were rescheduled before 10 p.m. This case was run a second time, with the night curfew applied only to scheduled operations.

In the fourth scenario, all aircraft were modeled as landing further down the runway than in the baseline case, in which the landing threshold was modeled at 1000 feet from the end of the runway. This displaced threshold countermeasure is of particular interest since it has in fact been implemented at JFK International Airport for Concorde SST approaches. Two threshold displacements were modeled, 1000 feet and 2000 feet.

Two land-use countermeasures were modeled: vacating the 75 L_{dn} contour and insulating all homes inside the 65 L_{dn} contour to provide the equivalent of a 6 dB reduction in noise level. In the first land-use scenario, all residents inside the 75 L_{dn} contour were presumed to be relocated completely outside of the airport community and were neglected in the ensuing fractional impact calculations. In the second land-use scenario, 6 decibels were subtracted from all the contour values inside the 65 dB contour prior to performing the fractional impact calculations.

The final countermeasure to be modeled consisted of a combination of two of the countermeasures previously described. This case modeled both a night curfew and all narrow-body jet transports treated with sound absorbing material.

Besides the seven noise abatement countermeasures described above, one additional case was run which, while not a countermeasure option, is of interest nonetheless. In this case, all operations were doubled in order to assess the noise impact which such an increase in operations might have, assuming no change in the population distribution modeled in the baseline case.

Noise Effect of Alternative Airport Community Scenarios

The number of community residents predicted to be highly annoyed was calculated for each of the alternative airport community scenarios described in the previous section, and compared with the number predicted to be highly annoyed under the current scenario. The percentage reduction in population highly annoyed was then calculated in order to assess the relative effectiveness of each of the hypothetical noise abatement countermeasures. These calculations were performed for each of the eight compass rose octants around the airport, as well as for the community as a whole, and the results are presented in figures 11 to 18 and summarized in Table I.

TABLE I.- IMPACT COUNTERMEASURE EFFECTIVENESS

COUNTERMEASURE	REDUCTION IN ANNOYED POPULATION
SAM Engine Treatment	43%
Curfew - All Operations	30%
Curfew - Scheduled Operations	29%
House Treatment Inside 65 L_{dn}	26%
Vacate 75 L_{dn} Contour	4%
Ban All G/A Operations	2%
1000 Ft. Displaced Landing	2%
2000 Ft. Displaced Landing	1%
SAM + Curfew	68%

The most effective individual countermeasure modeled was to treat the aircraft engines with sound absorbing material. A 43 percent reduction in population highly annoyed is predicted. Next in predicted effectiveness is to impose a night curfew so that all operations after 10 p.m. are rescheduled for before 10 p.m. This noise abatement strategy is predicted to result in a 30 percent reduction in highly annoyed population. Restricting the curfew to scheduled jet transport operations was found to be almost as effective, with a 29 percent reduction in the most severely impacted residents. Treating houses inside the existing 65 L_{dn} contour with sufficient noise insulation to result in an effective L_{dn} reduction of 6 dB is predicted to cause a 26 percent reduction in highly annoyed population. The remaining individual countermeasures, banning G/A operations, using displaced landing thresholds, and relocating residents who live inside the 75 L_{dn} contour, were found to have a relatively small (1 percent to 4 percent) effect on the number of highly annoyed residents. When the two most effective countermeasures (SAM engine treatment and night curfew) were combined, the reduction in highly-annoyed population was found to be 68 percent, compared with 43 percent and 30 percent respectively, for the two countermeasures applied separately.

The data in Table I refer to the effects of various countermeasures on the airport community as a whole, while figures 11 to 18 indicated, in addition, the impact in each of the octants surrounding the airport. It is interesting to note that there is a relatively wide variation in the degree of relief associated with each countermeasure from octant to octant. For example, while providing acoustic insulation for homes inside the 65 L_{dn} contour is predicted to result in a community-wide reduction in noise impact of 26 percent, the noise impact reduction is predicted to vary from as little as 10 percent to the south-southwest of the airport, to as much as 38 percent to the north-northwest. These differences in the degree of impact reduction achievable in different areas of the same airport community are attributed to the nonuniform nature of both the noise and population distributions. Such differences in impact by area within the community are especially interesting for countermeasures such as insulating homes, which can be carried out in selected neighborhoods when limited noise abatement resources preclude applying the countermeasure to the airport community as a whole.

In addition to investigating potential noise abatement countermeasures, the noise impact of doubling the number of operations was also calculated (fig. 18). Noise impact is not a linear function of the number of flight operations, since doubling all operations increased the noise impact by a factor of only 1.5.

CONCLUDING REMARKS

The noise impact of current flight operations has been modeled for a major airport using the Fractional Impact Method, and predictions of the number of residents highly annoyed with aircraft noise have been made based on a recently-developed psychophysical relationship between noise level and human subjective response to noise. A number of aeronautical, operational, and land-use noise impact countermeasures were also modeled to assess their relative effectiveness in reducing the current noise impact.

Source noise reduction was found to be the most effective noise impact countermeasure (43 percent reduction in highly annoyed population), while banning night flights and insulating homes inside the 65 L_{dn} contour were also found to be effective (30 percent and 26 percent reduction in highly-annoyed population, respectively). Other countermeasures, such as displaced landing thresholds, diverting G/A aircraft, and relocating residents who live inside the 75 L_{dn} contour, were found to have a small (less than 4 percent) effect on the number of highly-annoyed airport community residents. Doubling the number of operations was found to increase the noise impact by a factor of 1.5.

The results obtained for this airport illustrate the potential effectiveness of various aeronautical, operational, and land-use noise-impact countermeasures which might be applied to a commercial jet airport. The specific results reported here apply only to the airport which was selected for analysis; other airports, with different noise and population distributions, may yield different results. In particular, the rank-ordering of countermeasures by effectiveness may vary from airport to airport, and general conclusions about the relative effectiveness of a particular countermeasure must be preceded by an analysis of more airports. The ALAMO community response model used in the present study was designed to facilitate such an analysis and provides a tool for studying the noise effects associated with a wide variety of actual or hypothetical operating scenarios on a site-specific airport community basis.

REFERENCES

1. Hearth, Donald P.: Vehicle Expectations in Air Transportation for the Year 2000. Presented at AIAA Global Technology 2000 Meeting, Baltimore, Md., May 5-11, 1980.

2. Hubbard, Harvey H.; and Morgan, Homer G.: Aircraft Noise Control in the 1980's. Presented at Inter-Noise 80 Meeting, Miami, Florida, Dec. 8-10, 1980.

3. Schultz, T. J.: Synthesis of Social Surveys on Noise Annoyance. J. Acous. Soc. Am., Vol. 64, No. 2, August 1978.

4. Anonymous: Guidelines for Preparing Environmental Impact Statements on Noise. Report of Working Group 69 on Evaluation of Environmental Impact of Noise. National Research Council, National Academy of Sciences, 1977.

5. Galloway, W. J.: Community Noise Exposure Resulting from Aircraft Operations: Technical Review. AMRL-TR-73-106, Aerospace Medical Research Laboratory, November 1974.

6. FAA Integrated Noise Model Version 1 - Basic User's Guide. FAA Report FAA-EQ-78-91, January 1978.

7. Horonjeff, R. D.; Kandakuri, R. R.; and Reddingius, N. H.: Community Noise Exposure Resulting from Aircraft Operations: Computer Program Description. AMRL-TR-73-109, Aerospace Medical Research Laboratory, October 1974.

8. Anonymous: Site II User's Guide. CACI, Inc. - Federal. 1815 North Fort Myer Drive, Arlington, Va, 1976.

9. DeLoach, R.: An Airport Community Noise Impact Assessment Model. NASA TM 80198, July 1980.

10. Anonymous: Draft Environmental Impact Statement. Lambert-St. Louis International Airport. St. Louis, Missouri, June 1979.

11. Anonymous: Final Environmental Impact Statement. Lambert-St. Louis International Airport. St. Louis, Missouri, May 1980.

12. Anonymous: Recommended Noise Abatement Takeoff and Departure Procedure for Civil Turbojet Powered Airplanes. FAA Advisory Circular AC 91-39, January 18, 1974.

13. Anonymous: Official Airline Guide - North American Edition. Published by the Reuben H. Donnelley Corporation. August 15, 1978.

14. Anonymous: Noise Exposure of Civil Aircarrier Airplanes Through the Year 2000. In 2 volumes. EPA 550/9-79-313-1, February 1979.

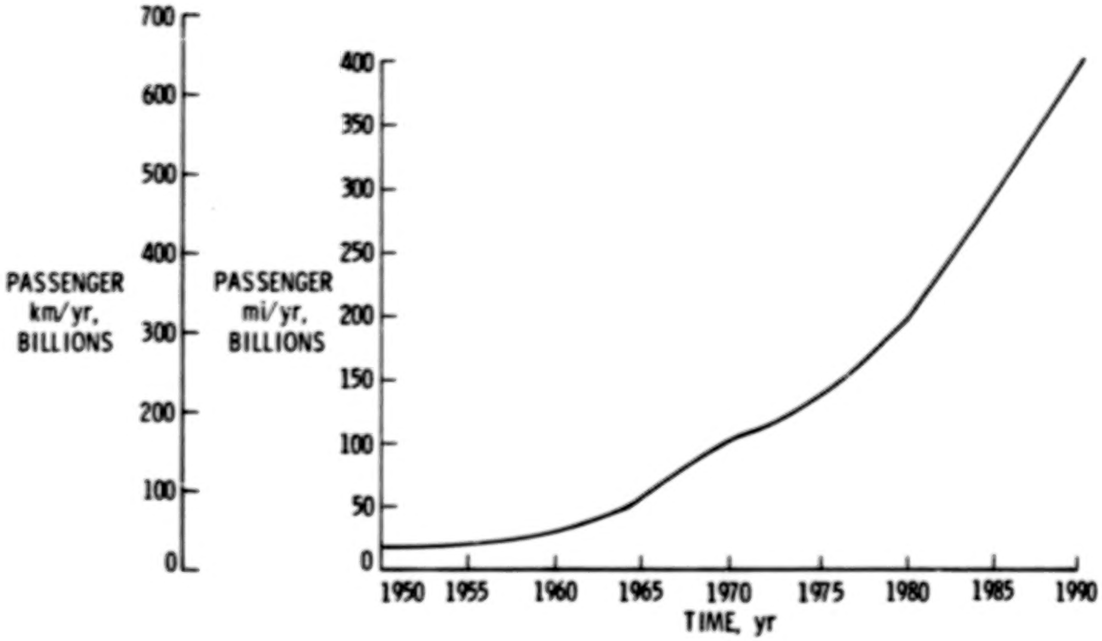

Figure 1.- Growth in U.S. air carrier service.

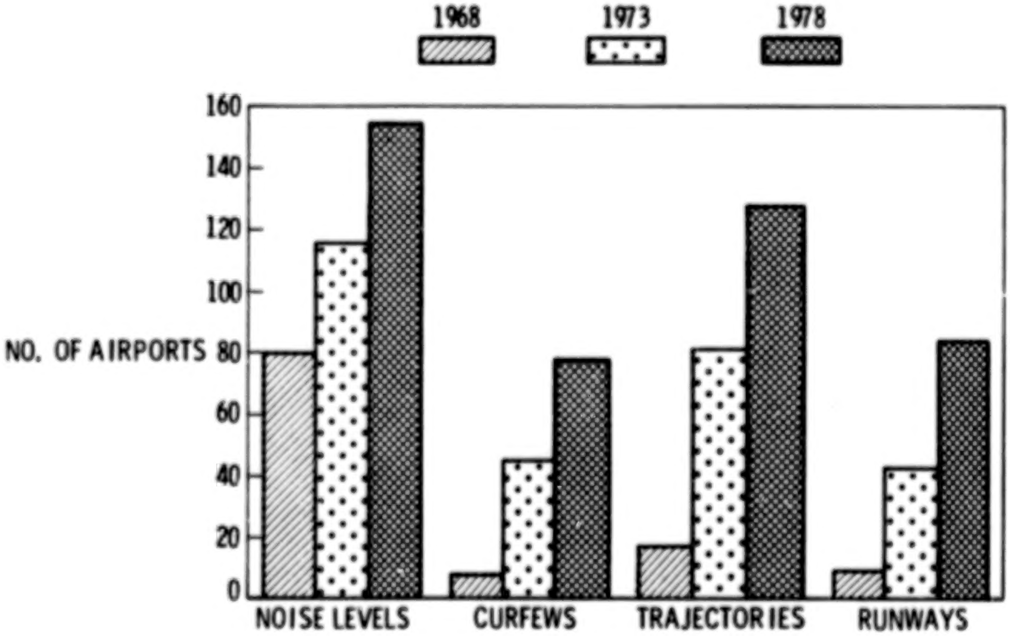

Figure 2.- Noise constraints at major world airports.

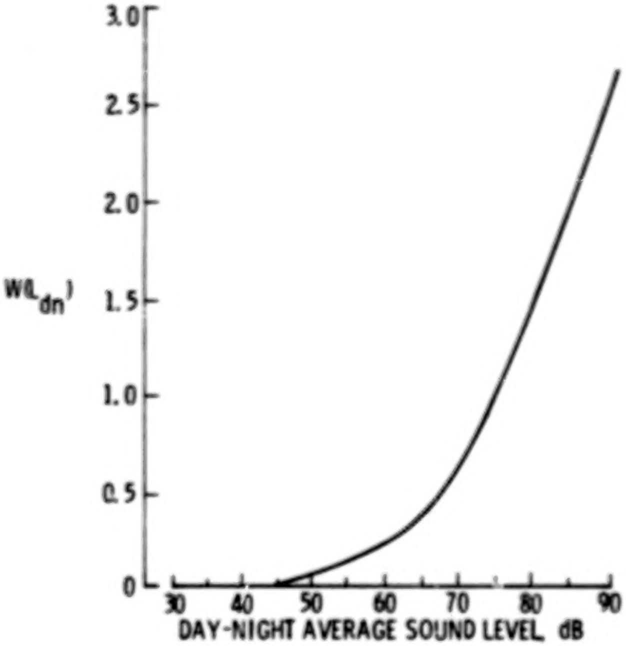

Figure 3.- Sound level weighting function (W) for fractional impact analysis.

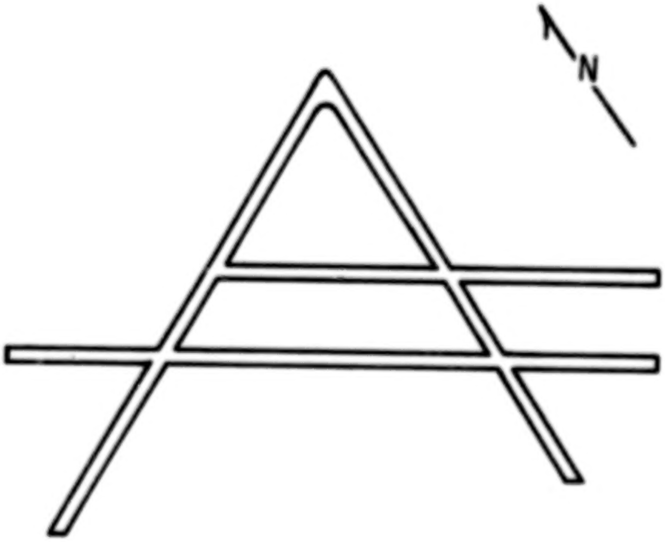

Figure 4.- Runway orientation.

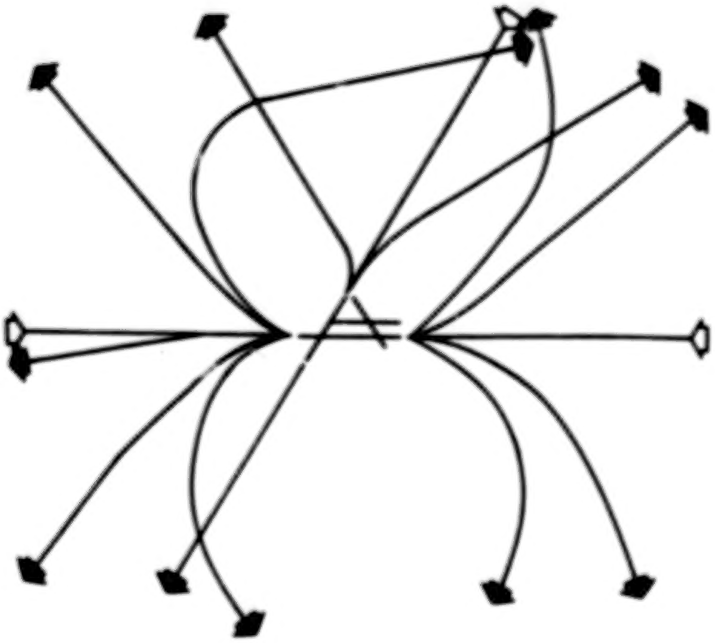

Figure 5.- Ground tracks.

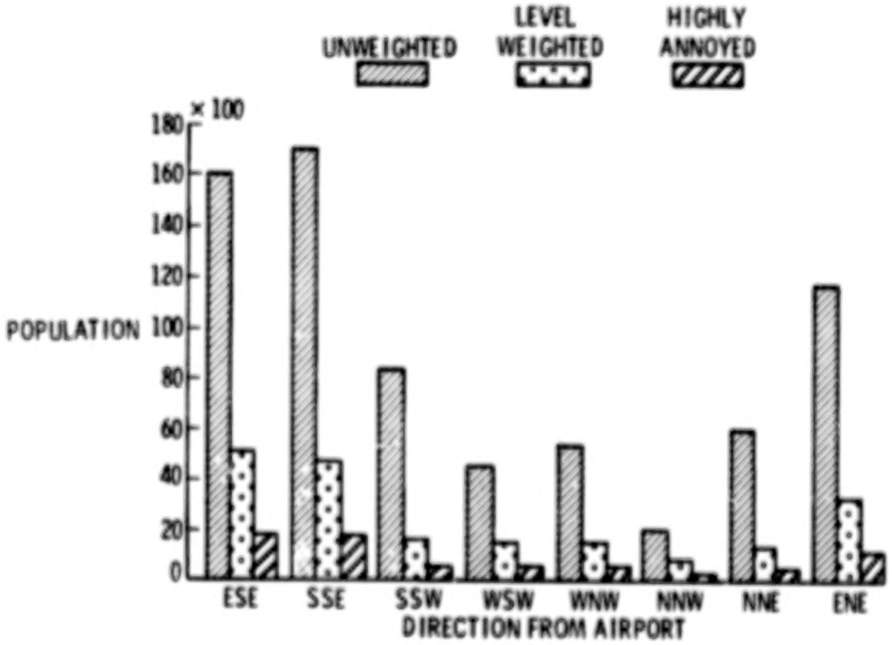

Figure 6.- Noise impact in terms of impacted population.

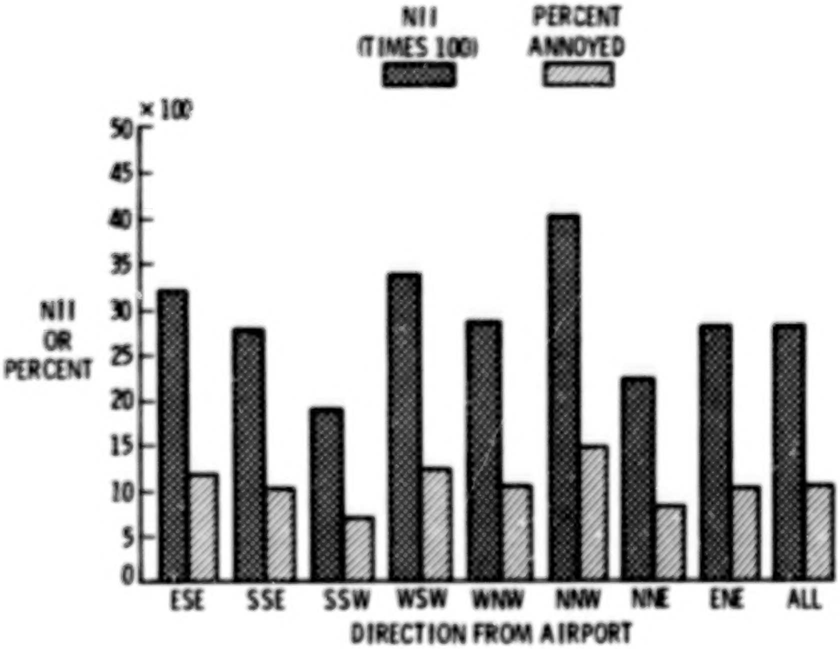

Figure 7.- Community noise impact levels.

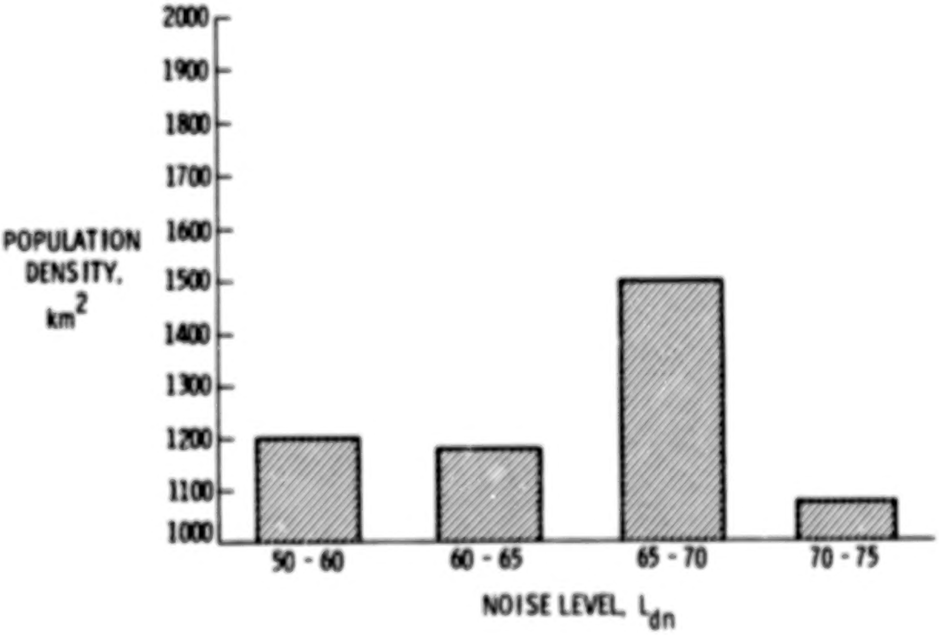

Figure 8.- Population density.

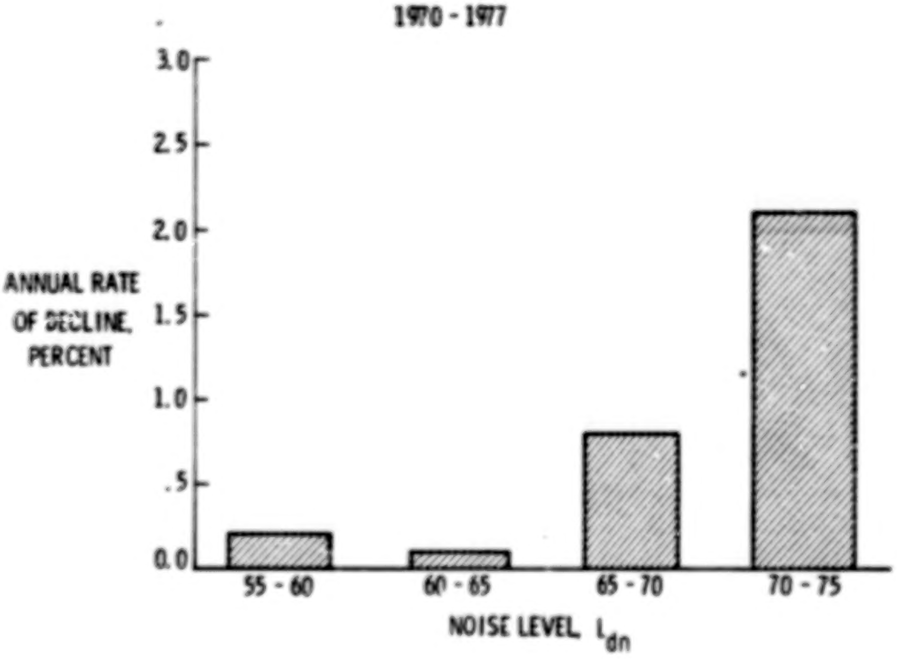

Figure 9.- Annual rate of decline in population.

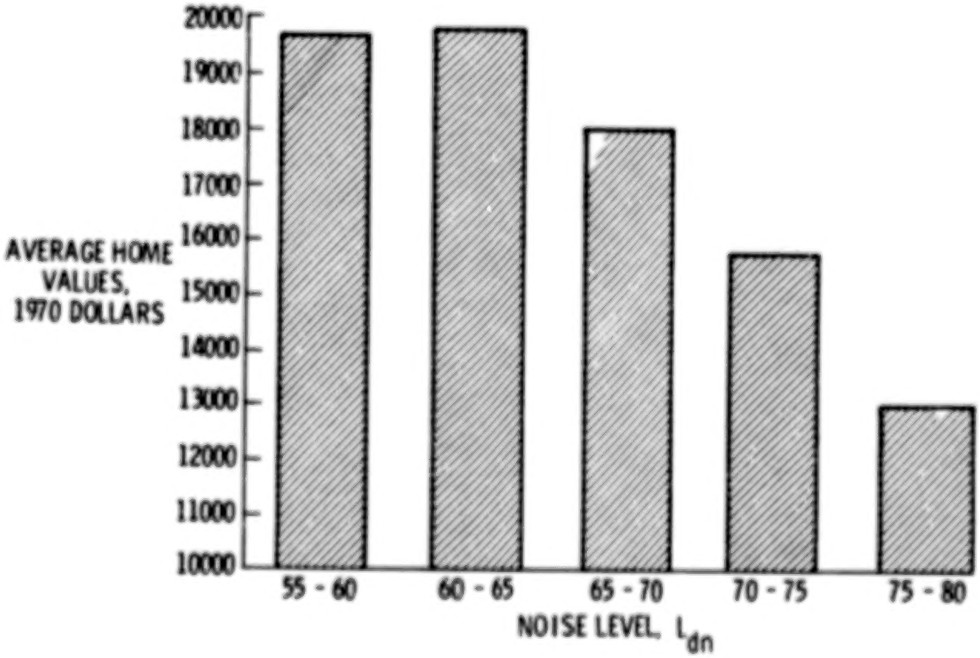

Figure 10.- Average home values.

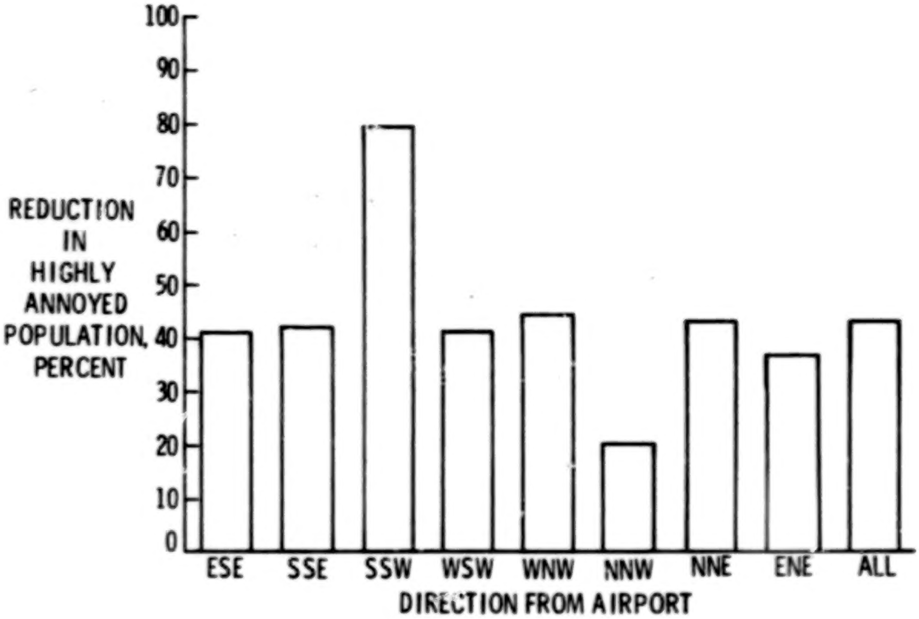

Figure 11.- Effect of adding sound-absorbing material to aircraft engines.

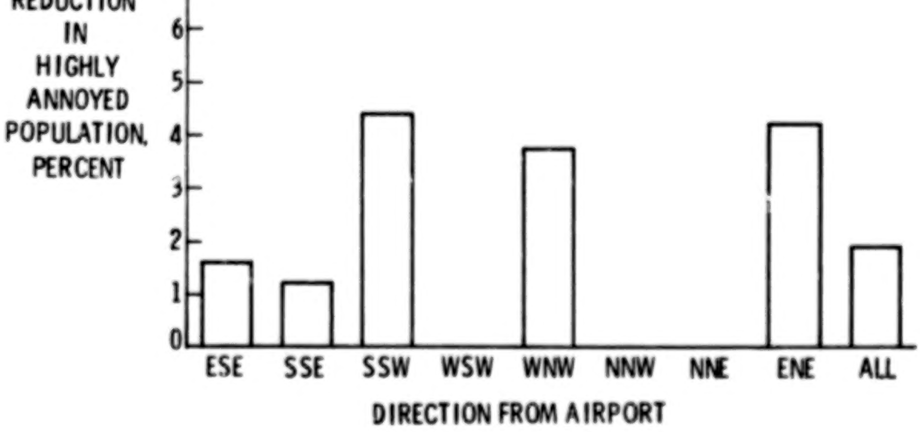

Figure 12.- Effect of eliminating general aviation operations.

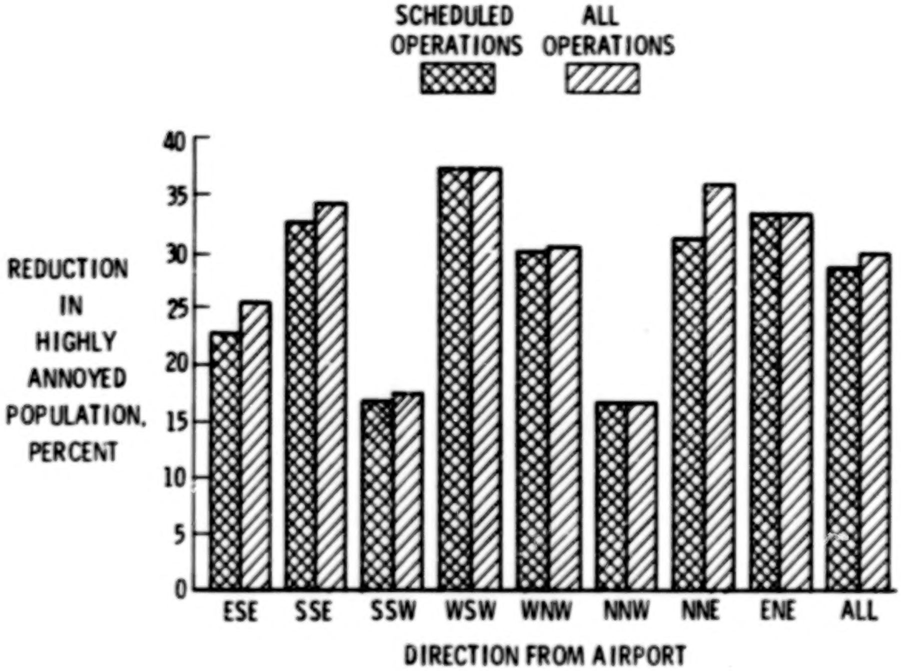

Figure 13.- Effect of imposing a night curfew.

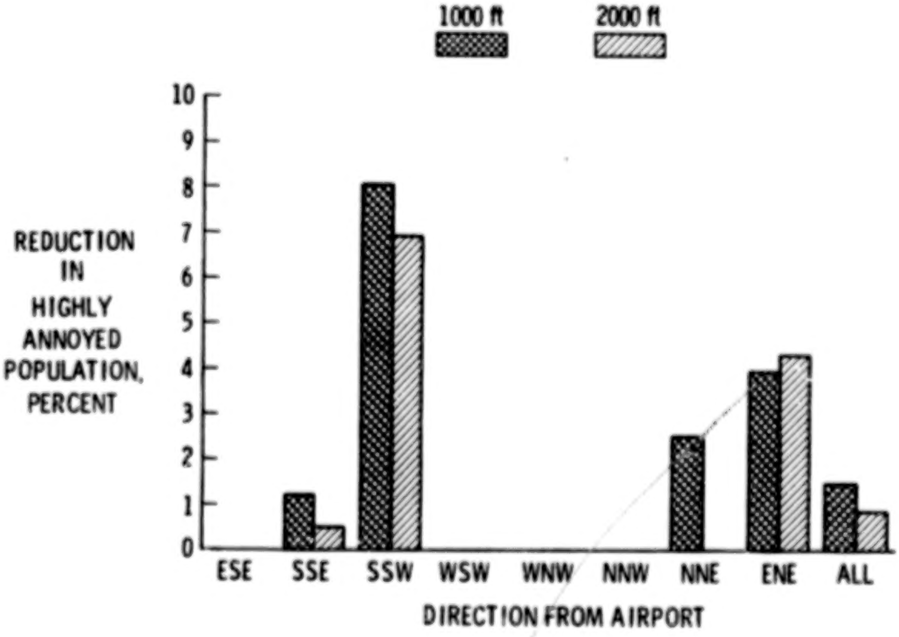

Figure 14.- Effect of displaced landing thresholds.

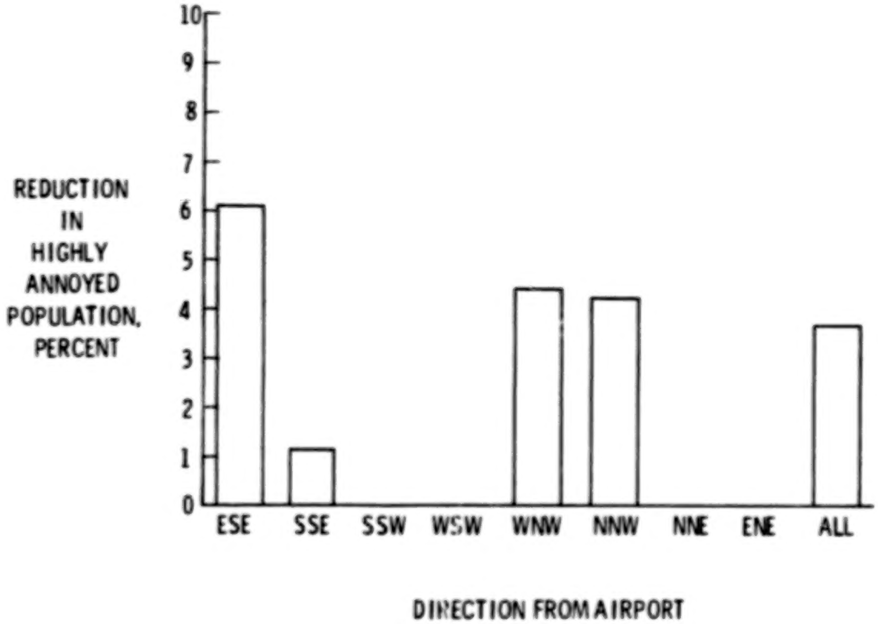

Figure 15.- Effect of vacating 75 L_{dn} contour.

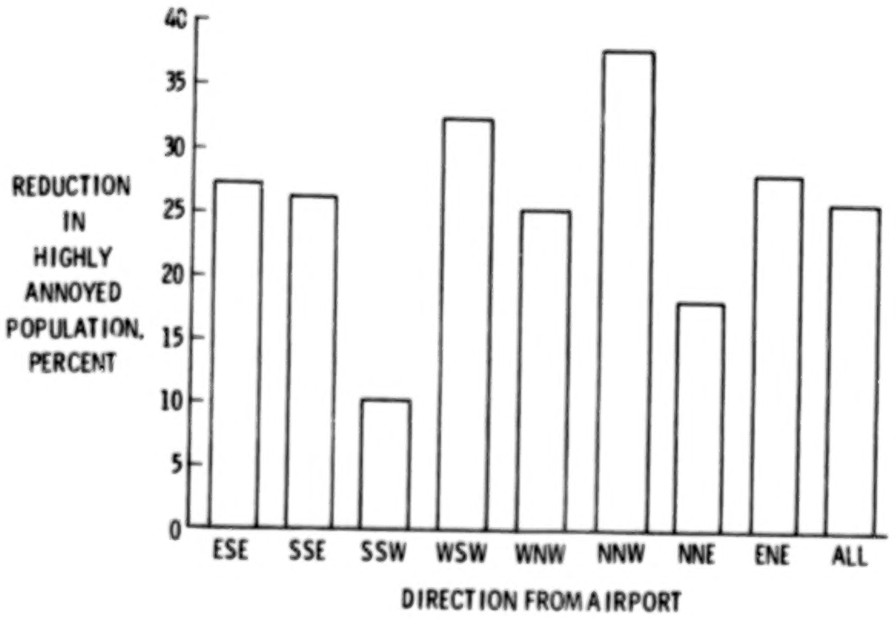

Figure 16.- Effect of a 6 dB acoustic treatment for homes inside 65 L_{dn}.

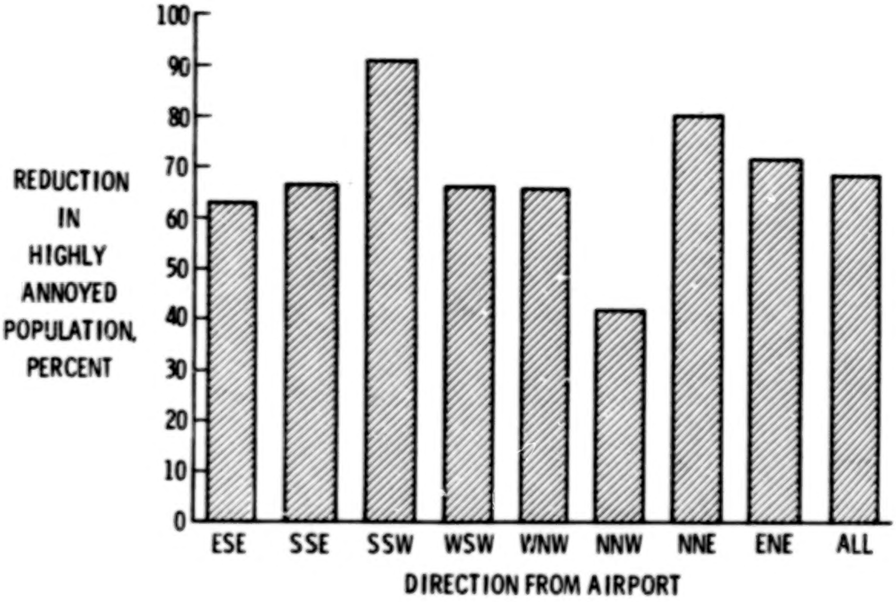

Figure 17.- Effect of sound-absorbing material plus night curfew.

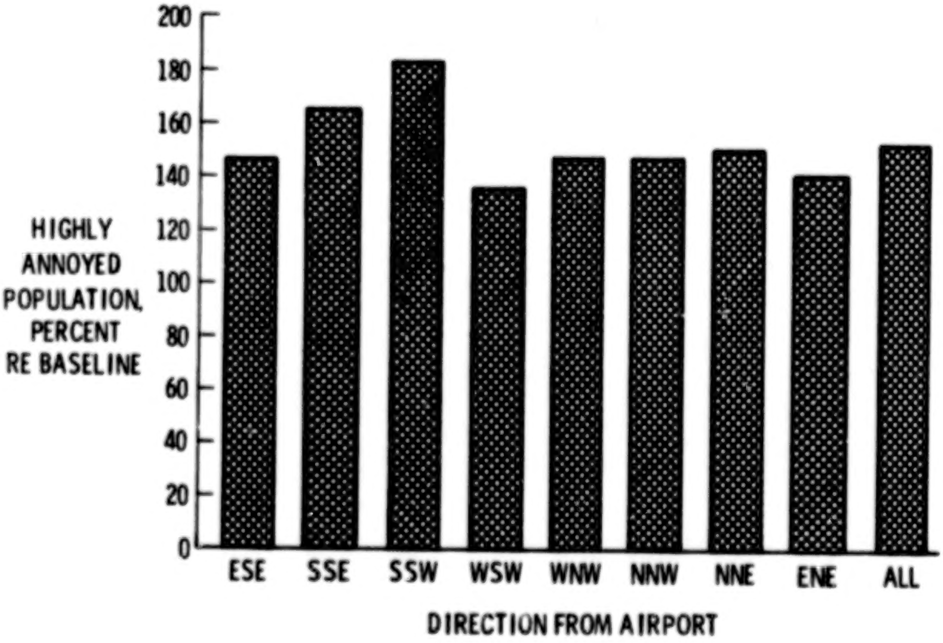

Figure 18.- Effect of doubling the number of operations.

LIST OF ATTENDEES

Philip J. Akers, AWS 130
Federal Aviation Administration
800 Independence Avenue, S.W.
Washington, DC 20591
Phone - 202 426-8395

Margaret B. Alexander
NASA Marshall Space Flight Center
ES82, B. 4481
Marshall Space Flight Center,
AL 35812
Phone - 205 453-2087
FTS 872-2087

Joseph S. Algranti
NASA Johnson Space Center
CC, B. 276
Houston, TX 77058
Phone - 713 483-7226
FTS 525-7226

Jesse T. Allen
Lockheed Georgia Company
Dept. 9801, Zone 366
Marietta, GA 30063
Phone - 404 424-9411

Dr. Willard W. Anderson
NASA Langley Research Center
Mail Stop 152
Hampton, VA 23665
Phone - 804 827-3049
FTS 928-3049

Marvin R. Barber
NASA Dryden Flight Research Center
Mail P-D
Edwards, CA 93523
Phone - 805 258-3275
FTS 984-3275

M. Craig Beard, AWS-1
Director, Office of Airworthiness
Federal Aviation Administration
800 Independence Avenue
Washington, DC 20591
Phone - 202 426-8235

Gary P. Beasley
NASA Langley Research Center
Mail Stop 152
Hampton, VA 23665
Phone - 804 827-2077
FTS 928-2077

Hugh P. Bergeron
NASA Langley Research Center
Mail Stop 152E
Hampton, VA 23665
Phone - 804 827-3917
FTS 928-3917

Roy A. Berube
Pan American Airlines
P. O. Box 592055 AMF
Miami, FL 33159
Phone - 213 624-0192

G. A. Birocco
Department of the Army
Ft. Eustis, VA 23604
Phone - 213 624-0192

Robert E. Bower
NASA Langley Research Center
Mail Stop 116
Hampton, VA 23665
Phone - 804 827-3285
FTS 928-3285

James R. Branstetter
FAA/LaRC Engineering and Development
Field Office
Mail Stop 250
Hampton, VA 23665
Phone - 804 827-4595
FTS 928-4595

Richard S. Bray
NASA Ames Research Center
MS 211-2, FSD
Moffett Field, CA 94035
Phone - 415 965-5000
FTS 448-6002

Anthony J. Broderick, AVS-4
Technical Advisor
Office of Associate Administrator
  for Aviation Standards
Federal Aviation Administration
800 Independence Avenue, S.W.
Washington, DC 20591
Phone - 202 426-3134

John S. Bull
NASA Ames Research Center
MS 210-9, FSN
Moffett Field, CA 94035
Phone - 415 965-5425
        FTS 448-5425

William T. Bundick
NASA Langley Research Center
Mail Stop 494
Hampton, VA 23665
Phone - 804 827-3744
        FTS 928-3744

Robert A. Byrd, Jr.
Delta Airlines, Inc.
Dept. 020
Atlanta Hartsfield Airport
Atlanta, GA 30320
Phone - 404 765-2600

Dennis W. Camp
NASA Marshall Space Flight Center
ES82, B. 4481
Marshall Space Flight Center,
AL 35812
Phone - 205 453-2087
        FTS 872-2087

Alan B. Chambers
NASA Ames Research Center
MS 239-1, LM
Moffett Field, CA 94035
Phone - 415 965-5729
        FTS 448-5729

Jerry Chavkin, AWS-100
Chief, Aircraft Engineering
  Division
Federal Aviation Administration
800 Independence Avenue, S.W.
Washington, DC 20591

E. S. Cheaney
Battelle Memorial Institute
505 King Avenue
Columbus, OH 43201
Phone - 614 424-6424

David A. Conner
NASA Langley Research Center
Mail Stop 461
Hampton, VA 23665
Phone - 804 827-2645
        FTS 928-2645

D. William Conner
Private Consultant
NASA Langley Research Center
  (Retired)
200 York View Road
Yorktown, VA 23692
Phone - 804 898-5580

Ralph C. Cockley
Lockheed-California Company
2555 N. Hollywood Way
Burbank, CA 91520
Phone - 213 847-6121

George Cooper
G. E. Cooper Associates
22701 Mt. Eden Road
Saratoga, CA 95070

Norman L. Crabill
NASA Langley Research Center
Mail Stop 247
Hampton, VA 23665
Phone - 804 827-3274
        FTS 928-3274

Bob Crafts
Trans World Airlines
605 Third Avenue
New York, NY 10016
Phone - 212 557-3000

Delwin R. Croom
NASA Langley Research Center
Mail Stop 286
Hampton, VA 23665
Phone - 804

James Danaher
Deputy Director for Operations
National Transportation
Safety Board (NTSB)
800 Independence Avenue, S.W.
Washington, DC 20594
Phone - 202 472-6100

J. L. DeCelles
Airline Pilots Association
9107 Lee Blvd.
Leawood, KS 66206

Richard Deloach
NASA Langley Research Center
Mail Stop 463
Hampton, VA 23665
Phone - 804 827-3561
FTS 928-3561

V. L. J. DiRito
USA Research and Technology
Laboratory
NASA Ames Research Center
Moffett Field, CA 94035
Phone - 415 965-5578
FTS 448-5578

Philip Donely
Consultant and Lecturer
NASA Langley Research Center
(Retired)
202 Cherry Point Road
Grafton, VA 23692
Phone - 804 898-8063

Dr. David R. Downing
NASA Langley Research Center
MS 494
Hampton, VA 23665
Phone - 804 827-3209
FTS 928-3209

M. P. DuBovy
Douglas Aircraft
3855 Lakewood Blvd.
Long Beach, CA 90846
Phone - 213 593-5511

Bobby M. Earnest
NASA Langley Research Center
Mail Stop 157D
Hampton, VA 23665
Phone - 804 827-2764
FTS 928-2764

Duane Edelman
Republic Airlines, Inc.
7500 Airline Drive
Minneapolis, MN 55450
Phone - 612 726-7411

William Edmonds
Airline Pilots Association
9107 Lee Blvd.
Leawood, KS 66206

W. T. Edwards
Federal Aviation Administration
Technical Center
Atlantic City, NJ 08405
Phone - 609 641-8200

Terry Emerson, AFWAL/FIGR
Wright-Patterson Air Force Base, OH 45433
Phone - FTS 775-6644
775-3644

John H. Enders
Flight Safety Foundation, Inc.
5510 Columbia Pike, No. 303
Arlington, VA 22204
Phone - 703 820-2779

Kenneth D. Ensslin
Director-Flight Safety
Trans World Airlines
605 Third Avenue
New York, NY 10158
Phone - 212 557-5158

James Erickson
Director, Southwestern Regional Office
Federal Aviation Administration
P. O. Box 1689
Fort Worth, TX 76101
Phone - 212 557-5158

Peggy Evanich
Safety Technology Section
NASA Lewis Research Center
21000 Brookpark Road
Cleveland, OH 44135
Phone - 216 433-6122
FTS 294-6122

William M. Fanning
National Business Aircraft Association
1 Farragut Square South
Washington, DC 20006
Phone - 202 783-9000

Donald L. Feller
NASA Wallops Flight Center
Wallops Island, VA 23337
Phone - 804 824-3411
FTS 928-5711

George G. Field
Douglas Aircraft Company
3855 Lakewood Blvd.
Long Beach, CA 90846
Phone - 213 593-5511

Bruce D. Fisher
NASA Langley Research Center
Mail Stop 247
Hampton, VA 23665
Phone - 804 827-3274
FTS 928-3274

G. Robert Flynn
The Boeing Company
Box 3707
Seattle, WA 98124
Phone - 206 655-2121

Reginald G. E. Furlonger
British Embassy
3100 Massachusetts Avenue, N.W.
Washington, DC 20008
Phone - 202 462-1340

John F. Garren
NASA Langley Research Center
Mail Stop 246B
Hampton, VA 23665
Phone - 804 827-3621
FTS 928-3621

B. L. Gary
NASA Jet Propulsion Laboratory
4800 Oak Grove Drive
Pasadena, CA 91103
Phone - 213 354-4321
FTS 792-3198

Richard Geiselhart, ASD/ENECH
Wright-Patterson Air Force Base, OH 45433
Phone - FTS 775-4258/5597

John Gerlach
NASA Wallops Flight Center
Wallops Island, VA 23337
Phone - 804 824-3411
FTS 928-5711

William P. Gilbert
NASA Langley Research Center
Mail Stop 355
Hampton, VA 23665
Phone - 804 827-2184
FTS 928-2184

Walton Graham
Questek
34 Mary's Lane
Centerport, NY 11721
Phone - 516 757-4670

G. C. Greene
NASA Langley Research Center
Mail Stop 461
Hampton, VA 23665
Phone - 804 827-2645
FTS 928-2645

Albert W. Hall
NASA Langley Research Center
Mail Stop 247
Hampton, VA 23665
Phone - 804 827-3274
FTS 928-3274

Dr. Randall L. Harris
NASA Langley Research Center
Mail Stop 152D
Hampton, VA 23665
Phone - 804 827-3871
FTS 928-3871

Major John H. Happ, Jr.
Hq., MAC/IGF
Scott Air Force Base, IL 62225

J. R. Harrison, ASF-1
Federal Aviation Administration
800 Independence Avenue, S.W.
Washington, DC 20591
Phone - 202 426-3704

Robert W. Harrison
Air Force Inspection and
Safety Center/SEDA
Norton Air Force Base, CA 92409

Hastings, E. C., Jr.
NASA Langley Research Center
Mail Stop 246B
Hampton, VA 23665
Phone - 804 827-3621
FTS 928-3621

Charles Hayes
Aviation Safety
NASA Johnson Space Center
Houston, TX 77058
Phone - 713 483-7272
FTS 525-7272

Maynard Hill
Applied Physics Laboratory
Johns Hopkins University
Johns Hopkins Road
Laurel, MD 20810
Phone - 301 953-7100

G. Thomas Holbrook
NASA Langley Research Center
Mail Stop 247
Hampton, VA 23665
Phone - 804 827-3274
FTS 928-3274

Thomas G. Horeff
Chief, Propulsion Branch
Federal Aviation Administration
800 Independence Avenue
Washington, DC 20591
Phone - 202 426-4000

Dick Hueschen
NASA Langley Research Center
Mail Stop 494
Hampton, VA 23665
Phone - 804 827-3350
FTS 928-3350

Charles R. Hyde
Kentron International, Inc.
Hampton Technical Center
3221 N. Armistead Avenue
Hampton, VA 23666
Phone - 804 838-1010

Vern Johnson
Corporate Director of Product
Integrity
AiResearch Manufacturing Co. of
Arizona
P. O. Box 5217
Phoenix, AZ 85010

Vicki Johnson
NASA Langley Research Center
Mail Stop 309
Hampton, VA 23665
Phone - 804 827-2611
FTS 928-2611

T. G. Jones
Lockheed Georgia Company
86 S. Cobb Drive
Marietta, GA 30063
Phone - 404 424-9411

Valerie Jones
Kentron International, Inc.
Hampton Technical Center
3221 N. Armistead Avenue
Hampton, VA 23666
Phone - 804 838-1010

Joe B. Jordan
Northrop
Box 7288
Hampton, VA 23666
Phone - 804 838-3360

Cathrine Kaoudis
Systems Development Corporation
3217 N. Armistead Avenue
Hampton, VA 23666
Phone - 804 838-4360

James R. Kelly
NASA Langley Research Center
Mail Stop 246B
Hampton, VA 23665
Phone - 804 827-3621
FTS 928-3621

Maj. Gerald L. Keyser, Jr.
NASA Langley Research Center
Mail Stop 255A
Hampton, VA 23665
Phone - 804 827-3061
FTS 928-3061

Dr. Ram Khatri
Fairchild Industries
20301 Century Blvd.
Germantown, MD 20767
Phone - 301 428-6000

Richard L. Kurkowski
NASA Ames Research Center
Moffett Field, CA 94035
Phone - 415 965-6219
FTS 448-6219

Clayton H. Lander
Rockwell International
Collins Division
MS 106-176
400 Collins Road, N.E.
Cedar Rapids, IA 52402
Phone - 319 395-1000

Donald L. Lansing
NASA Langley Research Center
Mail Stop 460
Hampton, VA 23665
Phone - 804 827-2617
FTS 928-2617

J. K. Lauber
NASA Ames Research Center
Moffett Field, CA 94035
Phone - 415 965-5717
FTS 448-5717

G. E. Leamon
NASA Langley Research Center
Mail Stop 309
Hampton, VA 23665
Phone - 804 827-2611
FTS 928-2611

Robert Leutwyler, DAVAA-G
U. S. Army Avionics R&D Activity
Fort Monmoth, NJ 07703

Laurence K. Loftin, Jr.
Distinguished Research Associate
NASA Langley Research Center
(Retired)
211 Anne Burras Lane,
Newport News, VA 23606
Phone - 804 596-4224

Donald L. Loving
NASA Langley Research Center
(Retired)
4 Crestmont Place
Newport News, VA 23606
Phone - 804 596-8181

Walter Luffsey, AVS-1
Federal Aviation Administration
800 Independence Avenue, S.W.
Washington, DC 20591
Phone - 202 426-3131

William D. Mace
NASA Langley Research Center
Mail Stop 117
Hampton, VA 23665
Phone - 804 827-3745
FTS 928-3745

D. J. Maglieri
NASA Langley Research Center
Mail Stop 249A
Hampton, VA 23665
Phone - 804 827-3838
FTS 928-3838

Richard J. Margason
NASA Langley Research Center
Mail Stop 286
Hampton, VA 23665
Phone - 804 827-3611
FTS 928-3611

Gil Maupin
New Jersey Division of Aeronautics
1035 Parkway Avenue
Trenton, NJ 08625
Phone - 609 292-3112

John L. McCarty
NASA Langley Research Center
Mail Stop 497
Hampton, VA 23665
Phone - 804 827-2796
FTS 928-2796

Thomas E. McSweeney
Chief, Airframe Branch
Federal Aviation Administration
800 Independence Avenue, S.W.
Washington, DC 20591
Phone - 202 426-4000

J. P. McVicker, ARD 414
Federal Aviation Administration
800 Independence Avenue, S.W.
Washington, DC 20591
Phone - 202 426-9350

Ed Melson
NASA Wallops Flight Center
Wallops Island, VA 23337
Phone - 804 824-3411
FTS 928-5711

James W. Messerly
B. F. Goodrich
Manager, Materials Science
Engineered Products Group
9921 Brecksville Road
Brecksville, OH 44141
Phone - 216 447-5368

C. O. Miller
System Safety, Inc.
McLean Hose
Suite 905
6800 Fleetwood Road
McLean, VA 22101
Phone - 703 356-5065

Dr. John S. Mixson
NASA Langley Research Center
Mail Stop 463
Hampton, VA 23665
Phone - 804 827-3561
FTS 928-3561

John T. Moehring, AEED/EPI
General Electric
Aircraft Engine Group
Mail Zone J60
Neumann Way
Cincinnati, OH 45215
Phone - 513 243-2000

Gene C. Moen
NASA Langley Research Center
Mail Stop 246B
Hampton, VA 23665
Phone - 804 827-3621
FTS 928-3621

Melvin D. Montemerlo, RTE-6
National Aeronautics and Space Administration
Washington, DC 20546
Phone - 202 755-8503
FTS 755-8503

Homer G. Morgan
NASA Langley Research Center
Mail Stop 462
Hampton, VA 23665
Phone - 804 827-3577
FTS 928-3577

Dana J. Morris
NASA Langley Research Center
Mail Stop 247
Hampton, VA 23665
Phone - 804 827-3274
FTS 928-3274

Richard Morris
NASA Langley Research Center
Mail Stop 157A
Hampton, VA 23665
Phone - 804 827-3073
FTS 928-3073

James P. Muldoon
The Port Authority of New York
and New Jersey
One World Trade Center
New York, NY 10048

James H. Muncey, ARD-412
Federal Aviation Administration
800 Independence Avenue, S.W.
Washington, DC 20591
Phone - 202 426-8427

Harold N. Murrow
NASA Langley Research Center
Mail Stop 243
Hampton, VA 23665
Phone - 804 827-3527
FTS 928-3527

J. F. Moran
NASA Langley Research Center
Mail Stop 309
Hampton, VA 23665
Phone - 804 827-2611
FTS 928-2611

Roger Neeland, ARD-312
Federal Aviation Administration
800 Independence Avenue, S.W.
Washington, DC 20591
Phone - 202 426-8605

James Neff
United Air Lines, Inc.
Suite 607
1825 K Street, N.W.
Washington, DC 20006
Phone - 703 892-7410

J. R. Nelson, ARD-330
Director, Flight and System
Safety
Federal Aviation Administration
800 Independence Avenue, S.W.
Washington, DC 20591
Phone - 202 426-3406

Stanley F. Nelson, SI-SAT-23
NASA Kennedy Space Center,
FL 32899
Phone - 305 867-7113
FTS 823-7113

Halyo Nesim
Information and Control
System, Inc.
25 Research Road
Hampton, VA 23666
Phone - 804 838-9391

David O'Strowski
Flight Test Branch
Federal Aviation Administration
Washington, DC 20591
Phone - 202 426-8323

Sharon L. Padula
NASA Langley Research Center
Mail Stop 461
Hampton, VA 23665
Phone - 804 827-2645
FTS 928-2645

Bill Paden
Lockheed Georgia
86 S. Cobb Drive
Marietta, GA 30063
Phone - 404 424-9411

John Park, ARD-321
Federal Aviation Administration
800 Independence Avenue, S.W.
Washington, DC 20591
Phone - 202 426-2072

J. A. Parker
NASA Ames Research Center
Moffett Field, CA 94035
Phone - 415 965-5225
FTS 448-5225

Dr. Lee W. Parker
Lee W. Parker, Inc.
252 Lexington Road
Concord, MA 01742
Phone - 617 369-5370

J. L. Parks, Jr.
Wallops Flight Center
Wallops Island, VA 23337
Phone - 804 824-3411
FTS 928-5711

J. C. Patterson, Jr.
NASA Langley Research Center
Mail Stop 359
Hampton, VA 23665
Phone - 804 827-2631
FTS 928-2631

Lee H. Person, Jr.
NASA Langley Research Center
Mail Stop 255A
Hampton, VA 23665
Phone - 804 827-3061
FTS 928-3061

J. B. Peterson
Republic Airlines
7500 Airline Drive
Minneapolis, MN 55450
Phone - 612 726-7411

Steve Pillow
Systems Development Corporation
3217 N. Armistead Avenue
Hampton, VA 23666
Phone - 804 838-4360

Bob Pitner
Hydro-Aire
Box 7722
3000 Winona Avenue
Burbank, CA 91510
Phone - 213 842-6121

Felix Pitts
NASA Langley Research Center
Mail Stop 477
Hampton, VA 23665
Phone - 804 827-3681
FTS 928-3681

S. B. Poritzky, Director
Systems Engineering Management
Federal Aviation Administration
800 Independence Avenue, S.W.
Washington, DC 20591
Phone - 202 426-8332

Otto Praeger
Boeing Military Airplane Co.
3801 S. Oliver
Wichita, KS 67210

William J. Quinlivan
Lockheed California Company
P. O. Box 551
Burbank, CA 91520
Phone - 213 847-6121

Bill Redeen, AGA-3
Federal Aviation Administration
800 Independence Avenue, S.W.
Washington, DC 20591
Phone - 202 426-8783

Arnold Reiner
Director, Flight Safety Analysis
and Information
Hangar 14
Room 356
Pan American
JFK International Airport
Jamaica, NY 11430
Phone - 305 637-6186

John E. Reed, ACT-340
Flight Safety Research Branch
Federal Aviation Administration
Technical Center
Atlantic City Airport, NJ 08405
Phone - 609 641-8200

John P. Reeder
NASA Langley Research Center
(Retired)
247 James River Drive
Newport News, VA 23601
Phone - 804 596-0628

Allen Royal
Department of the Army
Ft. Eustis, VA 23604
Phone - 213 624-0192

John Ruddy
Airline Pilots Association
9107 Lee Blvd.
Leawood, KS 66206

Maj. Gen. Len C. Russell, Commander
Air Force Inspection and
Safety Center (AFISC)
Norton Air Force Base, CA 92409

Dr. J. P. Raney
NASA Langley Research Center
Mail Stop 461
Hampton, VA 23665
Phone - 804 827-2645
FTS 928-2645

Edwin M. Ryan
Naval Air Systems Command
Washington, DC 20361
Phone - 202 692-2280

Harold W. Schmidt
NASA Lewis Research Center
21000 Brookpark Road
Cleveland, OH 44135
Phone - 216 433-6365
FTS 294-6365

Francis X. Schwartz
Vice President
Air North
P. O. Box 55
Woodbridge, VA 22191

George Sexton
Lockheed Georgia
86 S. Cobb Drive
Marietta, GA 30063
Phone - 404 424-9411

Gene Sharp
Vice President
Piedmont Airlines
Box 2720
Smith-Reynolds Airport
Winston-Salem, NC 27102
Phone - 919 767-5100

Brooks L. Shaw
Wallops Flight Center
Wallops Island, VA 23337
Phone - 804 824-3411
FTS 928-5711

Candy Shearls
Systems Development Corporation
3217 N. Armistead Avenue
Hampton, VA 23666
Phone - 804 838-4360

Dr. Jack Shelnutt
Seville Research Corporation
400 Plaza Blvd.
Pensacola, FL 32505
Phone - 904 434-5241

R. Drummond Simpson
Texas International Airlines
P. O. Box 12788
Houston, TX 77017
Phone - 713 641-7100

E. Dave Skelly
Collins Radio
Main Station 124-215
400 Collins Road, N.E.
Cedar Rapids, IA 52406

Ed Slattery
Pratt and Whitney
400 Main Street
East Hartford, CT 06108
Phone - 203 525-4321

Cmdr. John W. Smith, ATF-4
Federal Aviation Administration
800 Independence Avenue, S.W.
Washington, DC 20591
Phone - 202 426-3326

Lt. Col. Paul D. Smith, ASD/SE
Chief of Safety
Wright-Patterson Air Force Base,
OH 45433

Amos A. Spady
NASA Langley Research Center
Mail Stop 152D
Hampton, VA 23665
Phone - 804 827-3871
FTS 928-3871

Cary R. Spitzer
NASA Langley Research Center
Mail Stop 472
Hampton, VA 23665
Phone - 804 827-3318
FTS 928-3318

R. Steinberg
NASA Lewis Research Center
21000 Brookpark Road
Cleveland, OH 44135
Phone - 216 433-6677
FTS 294-6677

David G. Stephens
NASA Langley Research Center
Mail Stop 463
Hampton, VA 23665
Phone - 804 827-3561
FTS 928-3561

Gerald Stone
McDonnell Douglas Corporation
Douglas Aircraft Company
3855 Lakewood Blvd.
Long Beach, CA 90846
Phone - 213 593-5511

H. Paul Stough
NASA Langley Research Center
Mail Stop 247
Hampton, VA 23665
Phone - 804 827-3274
FTS 928-3274

Barry Strauch
Embry Riddle Aeronautical University
Daytona Beach Regional Airport
Dayton Beach, FL 32014
Phone - 904 252-5561

Sandy M. Stubbs
NASA Langley Research Center
Mail Stop 497
Hampton, VA 23665
Phone - 804 827-2796
FTA 928-2796

John A.Tanner
NASA Langley Research Center
Mail Stop 497
Hampton, VA 23665
Phone - 804 827-2796
FTS 928-2796

Robert J. Tapscott
NASA Langley Research Center
(Retired)
113 Dogwood Court
Yorktown, VA 23690
Phone - 804 898-6234

Robert T. Taylor
351 Level Green Court
Hampton, VA 23669
Phone - 804 851-4329

A. Richard Tobiason, RJT-2
National Aeronautics and
Space Administration
Washington, DC 20546
Phone - 202 755-3003

Barry L. Trotter
Eastern Airlines, Inc.
Miami International Airport
Miami, FL 33148
Phone - 305 873-2001

Harry A. Verstynen, Chief
FAA/LaRC Engineering and Development
Field Office
Mail Stop 250
Hampton, VA 23665
Phone - 804 827-4595
FTS 928-4595

Susan J. Voight
NASA Langley Research Center
Mail Stop 125A
Hampton, VA 23665
Phone - 804 827-2083
FTS 928-2083

Robert E. Waldron, IGF
AFSC Headquarters
Safety Office
Andrews Air Force Base, MD 20334
Phone - 301 981-2386

Dr. Thomas M. Walsh
NASA Langley Research Center
Mail Stop 265
Hampton, VA 23665
Phone - 804 827-2224
FTS 928-2224

D. M. Watson
NASA Ames Research Center
Moffett Field, CA 94035
Phone - 415 965-5433
FTS 448-5433

E. A. Weaver, EC 32
NASA Marshall Space Flight Center
Marshall Space Flight Center,
AL 35812
Phone - 205 453-1597
FTS 872-1597

Rick Weiss, ARD-312
Federal Aviation Administration
800 Independence Avenue, S.W.
Washington, DC 20591
Phone - 202 426-8605

Allen Whitehead
NASA Langley Research Center
Mail Stop 116
Hampton, VA 23665
Phone - 804 827-3285
FTS 928-3285

Raymond Wasson
Lockheed Georgia Company
86 S. Cobb Drive
Marietta, GA 30063
Phone - 404 424-9411

Dave Williams
NASA Langley Research Center
Mail Stop 246B
Hampton, VA 23665
Phone - 804 827-3621
FTS 928-3621

Bob Wilson
Naval Air Development Center
Warminster, PA 18974

Roger L. Winblade, RJT-2
National Aeronautics and Space
Administration
Washington, DC 20546
Phone - 202 755-3000
FTS 755-3000

Robert D. Witcofski
NASA Langley Research Center
Mail Stop 249A
Hampton, VA 23665
Phone - 804 827-3838
FTS 928-3838

E. C. Wood
Flight Safety Foundation, Inc.
5510 Columbia Pike, Suite 303
Arlington, VA 22204
Phone - 703 820-2777

James F. Woodall, ACT-300
Acting Chief, Aircraft Safety
Development Division
Federal Aviation Administration
Technical Center
Atlantic City, NJ 08405
Phone - 609 641-8200

Thomas J. Yager
NASA Langley Research Center
Mail Stop 497
Hampton, VA 23665
Phone - 804 827-2796
FTS 928-2796

Kenneth R. Yenni
NASA Langley Research Center
Mail Stop 255A
Hampton, VA 23665
Phone - 804 827-3061
FTS 928-3061

Douglas Young
NASA Wallops Flight Center
Wallops Island, VA 23337
Phone - 804 824-3411
FTS 928-5711

J. C. Young
NASA Langley Research Center
Mail Stop 494
Hampton, VA 23665
Phone - 804 827-3744
FTS 928-3744

John Young
Trans World Airlines
605 3rd Avenue
New York, NY 10016
Phone - 212 557-3000

Bud Zalesky
Lockheed California Company
2555 N. Hollywood Way
Box 551
Burbank, CA 91520
Phone - 213 847-6121

Compiler -

Joseph W. Stickle
NASA Langley Research Center
Mail Stop 246A
Hampton, VA 23665
Phone - 804 827-2037
FTS 928-2037

1. Report No.
NASA CP-2170, Part 2

2. Government Accession No.

3. Recipient's Catalog No.

4. Title and Subtitle
1980 AIRCRAFT SAFETY AND OPERATING PROBLEMS

5. Report Date
March 1981

6. Performing Organization Code
505-44-23-03

7. Author(s)
Joseph W. Stickle, Compiler

8. Performing Organization Report No.
L-14254

9. Performing Organization Name and Address
NASA Langley Research Center
Hampton, VA 23665

10. Work Unit No.

11. Contract or Grant No.

12. Sponsoring Agency Name and Address
National Aeronautics and Space Administration
Washington, DC 20546

13. Type of Report and Period Covered
Conference Proceedings

14. Sponsoring Agency Code

15. Supplementary Notes

16. Abstract

NASA maintains a continuing research effort on aircraft safety and operating problems. Periodic reports to the aviation community, usually 3 to 5 years apart, are presented in conference form with subsequent publication of the proceedings. This document contains the NASA program presented at the 1980 Aircraft Safety and Operating Problems Conference held at the Langley Research Center, Hampton, VA, November 5-7, 1980. Sessions for the conference included: Terminal-Area Operations; Avionics and Human Factors; Atmospheric Environment; Operating Problems and Potential Solutions; Flight Experiences and Ground Operations; and Acoustic and Noise Reduction.

17. Key Words (Suggested by Author(s))
Airplanes
Flight operations
Crashworthiness
Safety
Terminal area
Environment

18. Distribution Statement
Unclassified - Unlimited

Subject Category 03

19. Security Classif. (of this report)
Unclassified

20. Security Classif. (of this page)
Unclassified

21. No. of Pages
413

22. Price
A18

For sale by the National Technical Information Service, Springfield, Virginia 22161

NASA-Langley, 1981

END

June 18, 1981